Springer Series in Reliability Engineering

Srinivasan Gopalakrishnan · Massimo Ruzzene
Sathyanaraya Hanagud

Computational Techniques for Structural Health Monitoring

Springer

Springer Series in Reliability Engineering

For further volumes:
http://www.springer.com/series/6917

Srinivasan Gopalakrishnan
Massimo Ruzzene · Sathyanarayana Hanagud

Computational Techniques for Structural Health Monitoring

Springer

Srinivasan Gopalakrishnan
Department of Aerospace Engineering
Indian Institute of Science
Bangalore 560012
India
e-mail: krishnan@aero.iisc.ernet.in

Prof. Sathyanarayana Hanagud
School of Aerospace Engineering
Georgia Institute of Technology
Atlanta, GA 30332
USA
e-mail: hanagud@aerospace.gatech.edu

Massimo Ruzzene
School of Aerospace Engineering and
School of Mechanical Engineering
Georgia Institute of Technology
Atlanta, GA 30332
USA
e-mail: Ruzzene@gatech.edu

ISSN 1614-7839
ISBN 978-0-85729-283-4 e-ISBN 978-0-85729-284-1
DOI 10.1007/978-0-85729-284-1
Springer London Dordrecht Heidelberg New York

British Library Cataloguing in Publication Data
A catalogue record for this book is available from the British Library

Cover design: eStudio Calamar, Berlin/Figueres

Printed on acid-free paper

Springer is part of Springer Science+Business Media (www.springer.com)

To Samuel, Luca, Karthik and Keerthana

Preface

Philosophy of design of structures has undergone a sea change. Lighter and sleek structures have replaced bulky and heavy ones thanks to the increased emphasis on avoiding overly conservative design. These developments have introduced severe constraints on design methodologies that are currently in practice, which requires the use of new technologies to monitor the integrity of structures. Structural Health Monitoring (SHM) is one such technology, which can provide information on the state of the structure continuously or at periodic intervals.

The importance of SHM technology is demonstrated by the wealth of research activity and initiatives in this emerging area. The importance of SHM is expected to grow as new materials such as composites find increasing application in novel lightweight construction. Laminated composites also offer the opportunity for sensors to be embedded at the manufacturing stage, which can provide structural response information with unprecedented detail and therefore can substantially facilitate the assessment of structural integrity and the monitoring of its degradation.

SHM technology is a multidisciplinary field which requires a deep understanding of materials, sensors and electronics, along with the ability to perform sophisticated numerical and analytical modeling and signal processing. Each of these topics is a subject by itself, and writing a single textbook incorporating all the above aspects is indeed a tall order. Modeling forms an important component in SHM technology. Simulated data are used in support of the development of new algorithms for damage detection, or for an improved understanding on the effects of damage on the response of the structure. The objective of this book is therefore to present various computational tools which can be used for SHM.

Many of the numerical tasks described in this monograph can be accomplished through the application of Finite Element (FE) methodologies. The FE method, although very versatile, is affected by serious limitations when the high frequency response of structures needs to be evaluated, or when configurations with very small features need to be discretized. Both of these instances are very common in the simulation of SHM problems. Alternate methodologies are therefore presented, such as the Spectral Finite Element method, the bridging multi-scale techniques

and various simplified damage modeling methods. The choice of the mathematical model is very critical and dictated by various factors such as damage size, damage location, frequency content of exciting signals, model sizes, time of computation etc. In addition, robust and computationally fast damage detection methodologies that blend well with the chosen mathematical model are needed in order to obtain fast answers in regards to the damage location and extent. It is to be noted that many damage detection algorithms in most cases need to work with incomplete and noise polluted data. All of these computational aspects are necessary to the understanding of SHM technology and associated process. A book devoted to the modeling aspects of SHM tries to fill the need of the hour through the joint expertise in the field of the authors whose work over a decade provides most of the topics presented here.

This book is organized in modular form with the material is covered in 3 parts. A basic introduction to the theory of elasticity, composites and wave propagation, forms the foundations to the topics presented here. This is followed by a chapter on signal processing issues related to SHM. Two important modeling tools, namely the Finite Element Method and the Spectral Element Method are covered next, followed by three chapters on simplified damaged models. A separate chapter on modeling of piezoelectric actuators and sensors extensively used in the context of SHM, is given, while the last part is devoted to the description of various damage detection methodologies.

The material presented can be used to develop a graduate level course on SHM. While writing this book, we have assumed that the reader has the basic engineering mechanics and graduate level mathematics background. The book can also serve as a useful reference material for those working in the areas of structural integrity and wave propagation.

The completion of a work of this magnitude would not be possible without the help of many graduate students and collaborators who have worked on the material presented herein as part of their Doctoral and Masters thesis, and joint projects. Dr. Gopalakrishnan would like to thank his former graduate students Dr. Roy Mahapatra, Dr. A. Chakraborty, Dr. Mira Mitra, Mr.. Srikkanth, Mr. Garg and Mr. Nag. Dr. Ruzzene is very grateful to very bright, focused and committed co-workers such as Dr. Nicole Apetre, Dr. James Ayers, Dr. Filippo Casadei, Dr. Manuel Collet, Prof. Stefano Gonella, and Dr. Vinod Sharma whose efforts and ideas are documented in various parts of this monograph. Last but not the least, Drs. Gopalakrishnan and Ruzzene deeply thank their wives Anu and Elizabeth for their continuous patience, understanding and support without which this book would have not been possible.

Bangalore, India; Atlanta GA, USA
October 2010

S. Gopalakrishnan
M. Ruzzene
S. Hanagud

Contents

Part I
Introductory Concepts in Structural Health Monitoring

Chapter 1
Introduction

1.1 Overview on Structural Health Monitoring

Structural Health Monitoring (SHM) defines the process of assessing the state of health of a structure and of predicting its remaining life. Successful development and implementation of the SHM process involves the understanding of diverse disciplines such as sensor technology, materials technology, modeling aspects and computing technology. This book specifically focuses on the presentation of computational techniques which support the SHM process. The integration of effective simulation tools in SHM, in general requires the thorough understanding of the overall process. This chapter is therefore devoted to providing a general overview of SHM. Specifically, the chapter begins with definition of some of the commonly used terminologies in the health monitoring studies, which will be followed by a section on the various available health monitoring techniques. The role of simulation is introduced next, along with a general presentation of the content of the book.

1.1.1 Why Do We Need Structural Health Monitoring?

All man-made structures (machines bridges and aircrafts) have finite life spans and begin to degrade as soon as they are put into service. Processes such as corrosion, fatigue, erosion, wear and overloads degrade them until they are no longer fit for their intended use. Depending on the value of a structure, the cost of repairing it and the consequences of it failing, a number of actions can be taken

- Wait until the structure breaks and dispose of it (low sticker price relative to the repair cost, low criticality)
- Wait until the structure breaks and repair it (high sticker price relative to the repair cost, low criticality)

S. Gopalakrishnan et al., *Computational Techniques for Structural Health Monitoring*, Springer Series in Reliability Engineering, DOI: 10.1007/978-0-85729-284-1_1,

- Examine it at periodic intervals and determine whether or not remedial action is needed (high criticality).

Many engineering structures, such as ships, bridges, aircraft, buildings, fall in to the latter category. The consequences of a critical aircraft component failing in flight or of a bridge collapsing are such that regular inspections are performed by skilled engineers to assess the health of structures and systems. This inspection process is necessary, costly and usually finds no faults. It is also subject to human error, meaning that some unnecessary maintenance is performed and some faults go undetected. Examples of on-line machine health monitoring exist for rotating machinery and for machine tools, where the goal is to assess and compensate for tool wear. However, there are no equivalents for evaluating the health of most engineering structures.

Structural design has undergone a sea change, where stringent restrictions are placed on the design variables to produce lightweight structures having very high structural integrity. Such structures are normally shape-optimized to guarantee their resistance to sustain the design loads. However, they are more vulnerable to small and medium size damages such as horizontal, vertical or inclined cracks, corrosion in metallic structures, and delamination, fibre breakages or matrix cracks in the case of composites. These damages severely affect the structural integrity, which needs constant monitoring.

SHM has the objective of providing the tools for the constant or periodic monitoring of critical structural assets in order to determine the need for remedial action, and to prevent catastrophic failures. SHM has therefore potential application in many disciplines including aerospace, mechanical and civil engineering [10, 60]. The basic idea in SHM is to provide the structure of interest with sensing and analysis capabilities and to enable monitoring and evaluation to be carried out periodically or continuously, and autonomously. SHM potentially offers increased safety, since faults cannot grow to a dangerous level, avoids the vagaries of human behavior, and reduces ownership costs by replacing pre-planned precautionary servicing with targeted, responsive maintenance. Because the potential benefits of this embodiment of SHM are huge, a great amount of research is in progress worldwide into developing and improving systems that bring some degree of "self-awareness" to man-made structures [10, 38, 39, 51].

The benefits of SHM include:

1. to allow an optimal use of the structure, a minimized downtime, and the avoidance of catastrophic failures;
2. to give the designer an improvement in his products; and
3. to drastically change the work organization of maintenance services. This is achieved by replacing the scheduled and periodic maintenance inspection with performance-based (or condition-based) maintenance (long term) or at least (short term) by reducing the present maintenance labor. In particular dismounting of parts with no hidden defect can be avoided and human

involvement can be minimized which consequently reduces labor, downtime and errors, and thus improves safety and reliability.

1.1.2 Basic Elements of SHM Systems

An SHM system comprises of both hardware and software elements. The hardware elements are essentially the sensors and the associated instrumentation, while the software components consist of damage modeling and damage detection algorithms. A general vision for SHM is to develop structures featuring network of sensors, which periodically and continuously provide data. Sensors may be active or passive, whereby passive sensors such as strain gauges only receive (or sense) signals, while the active sensors both receive (or sense) and transmit (or actuate) signals. Commonly used active sensors include Poly Vinyle Dy Floride (PVDF) sensors piezoceramic sensors (made from Lead Zirconate Titanate, commonly called PZT sensors) or fiber optics sensors. There are also instances of TERFENOL-D, a type of magnetostrictive material, being used as an active sensor in SHM applications [55]. The data given out by the sensor depends on the type of sensors used. For example, if the sensor used is fibre optic sensor, (which works on the principle that the change in the strain condition in the structure, induces the change in the wavelength of the light spectrum), the output is essentially the strains or strain histories. On the other hand, if the sensors used is PZT or PVDF type, the output given by these sensors are essentially the voltage histories across the sensors. Voltage histories needs to be post processed to obtain quantities such as displacements, velocities or accelerations. More recently, non-contact sensors have become popular as they completely avoid wiring and direct contact with the surface. The most commonly used non-contact sensor is the*Scanning Doppler Laser Vibrometer* (SDLV). With no need for wiring and other connections, the region to be monitored can be chosen depending upon the level and location of excitation. The advantage of such measurements is that region-by-region monitoring is possible, which is crucial for determining local effects caused by defects.

SHM essentially has two components, namely the *Diagnosis* and the *Prognosis*. Diagnosis aims to give, at every moment during the life of a structure, a procedure to determine the state of the constituent materials of the different parts, and of the full assembly of these parts constituting the structure as a whole. Hence, the diagnosis procedure will notify the onset of damages such as cracks, its location and its extent. The diagnosis procedure can be further divided into two categories, namely the *passive diagnosis* and the *active diagnosis*. Passive diagnosis is based on distributed passive sensor measurement (such as strain gauges) to diagnose the state of structures. These methods provide limited information for estimation of damages. Active diagnosis, on the other hand, is based on actuator induced sensor measurements and as such unlimited information could be generated to diagnose the state of the structures. Active diagnosis SHM system can be built using smart sensors and

actuators. The prognosis procedure will involve computation of the severity of the crack in terms of fracture mechanics parameters, and its residual life.

Considering only the diagnosis function, one can think of SHM as a new and improved way of performing *Non destructive evaluation*. This is partially true, but SHM is much more. It involves the integration of sensors, possibly smart materials, data transmission, computational modeling, and processing ability inside the structures. This makes it possible to reconsider the design of the structure and the its lifetime management.

In summary, an SHM system encompasses the following components:

- The structure on which the SHM system will be placed.
- Sensors, which can be of contact or non-contact type.
- Data Acquisition systems.
- Signal Processing.
- Damage modeling and damage detection algorithms.
- Data transfer and storage mechanisms.
- Data handling and management.

SHM is therefore an essentially multi-disciplinary subject requiring thorough understanding of mechanics, materials and electronics. An alternate way of looking at SHM is a discipline combining the following four subjects [60] (see Fig. 1.1):

- Condition based monitoring
- Non Destructive Evaluation (NDE) technologies
- New modeling methods
- New sensor technologies

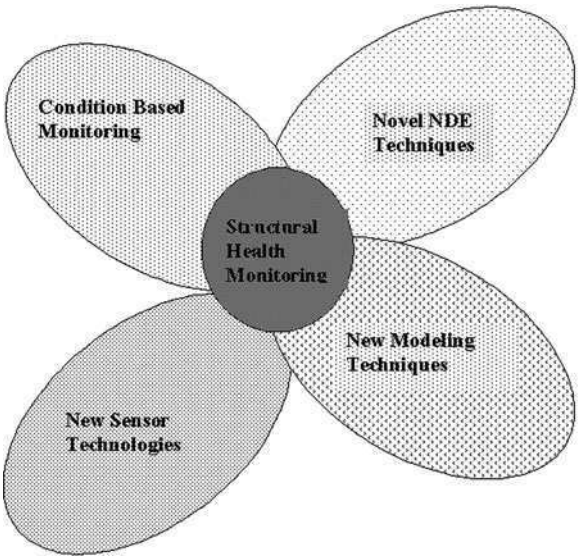

Fig. 1.1 Elements of structural health monitoring

Most of current practices followed in the maintenance of structural systems is time based. For example, an aircraft, after flying certain number of hours are retired to the hangar for thorough inspection. These inspections often need complete disassembly of components in order to subject them NDE inspections. This *inspection based on schedules* approach is time consuming and mostly driven by the fear of failure rather than a real necessity. If the fear factor is reduced by significant amounts, progress can be made towards an *inspection based on demand* approach, *i.e. monitor only when* it is absolutely necessary. This a process is also known as *Condition Based Monitoring*, or *Condition Based Maintenance* (CBM). The CBM concept is based on the notion that a sensing system on the structure monitors the integrity and notifies the operator when damage is detected. Life-safety and economic benefits associated with such a philosophy will only be realized if the monitoring system provides sufficient warning such that the corrective action can be taken before the damage evolves to a failure level. The trade-off associated with implementing such a philosophy is that it requires a sophisticated monitoring hardware to be deployed on the system along with a sophisticated data analysis procedure which interrogates the measured data.

NDE methods as Fig. 1.1 suggests, represent a subset of the overall SHM process. In classical NDE, a trigger is provided from a device that is external to the structure under examination and the data is measured, which will then be post-processed to asses the state of the structure. With the increase in the use of laminated composites in structural systems, it is now possible to embed these triggering devices called *actuators* into the host structure, which in many cases can also be used for sensing, say deformations, temperature, pressure, etc. In order to keep pace with the rapid changes in materials technologies, which can be successfully exploited in the SHM, new NDE methodologies are also needed to replace the conventional ones. One such method is the application of the SLDV as illustrated in the later part of this chapter.

Two other areas, which are paramount to the success of SHM are *Sensor Technologies* and *Modeling Methods*. The success of SHM depends on the ability of the number of sensors mounted on the structure to measure accurate data. The sensor performance is measured by its sensitivity. With the rapid advances made in the materials technologies, it is possible today to design a sensor material that can give high sensitivity. PZT and PVDF sensors are those which evolved from the advancement of material technologies, have higher sensitivity compared to the conventional strain gauges. More recently, Micro Electro-mechanical Systems (MEMS) based sensors have become quite popular as sensing device in the SHM systems. These sensors are not only minute, but are also quite cheap as compared to the conventional strain gauges. The advancement of the silicon technology has given great fillip to this development. Other most extensively used sensor for SHM is the Fiber Optic Sensors. Currently they are used in many aircrafts for load monitoring, which is one of the important part in the SHM process. Yet another area of rapid progress is that of wireless sensors. The range of effectiveness of these sensors is an important aspect that needs to be carefully evaluated when

considering the use of these type of sensors. Extensive applications of wireless sensors to bridge SHM is being pursued in the civil engineering domain.

Modeling is a critical part in the SHM process. The measured data as such does not say where the flaws are or what type flaw the structure has. These data need post-processing through robust mathematical tools that convert the measured data into meaningful quantities that help to not only locate the flaws, but also quantify their severity. Common modeling techniques employ the Finite Element Method (FEM), which is quite versatile in its ability to model complex geometries. However, when the flaw sizes are small, it is necessary to trigger a signal that has very high frequency content. At higher frequencies, the wavelengths are very small and it is necessary that the mesh sizes used in the FEM be comparable to wavelength. Typical recommendations suggest the use of at least 8–10 elements per wavelength of deformation for accurate capturing of wave phenomena and their interaction with defects. Hence, FEM requires the use of very fine mesh for such problems, which results in enormous computation time to get accurate results. Computational aspects of SHM in regards to FEM can be found for example in [17]. Methods like FEM are not quite suitable when the flaw sizes that requires determination, are small. The suitable mathematical model for such problems is the one based on wave propagation methods and the most common among them is the Spectral Finite Element Method (SFEM) [18].

Modeling has two components, namely the flaw modeling and the damage detection algorithms. In metallic structures, the commonly occurring flaws are the horizontal/vertical or inclined cracks, which are in some cases through the thickness cracks. The second kind flaw in metallic structure is corrosion. Although the corrosion types are many, modeling pitting corrosion is much simpler compared to other types of corrosion. Hence, simplified mathematical models for these types of flaws are required. If the structure is made from laminated composites, the failure modes are many as compared to metallic structures. The commonly occurring failure modes in composites are the *Delaminations*, *Fibre Breakage*, *Matrix Cracks* and *Debonds*. In addition, these structures are prone to large moisture absorbtion due to large porosity that creeps in during manufacturing. Hence, one needs simplified mathematical models to represent these failure modes.

The second aspect of modeling is in devising efficient damage detection algorithms that can blend with the chosen mathematical models. The damage detection algorithm should be able to work with incomplete and noise polluted data. Most damage detection methods requires the data from a structure in both the undamaged (baseline) and damaged configuration. By comparing the responses between the two, one can infer the state of the structure. This approach is not a practical one. The hosts of sensors embedded or surface mounted in a structure can give enormous amount of data. Not all such data will be useful, which requires a thorough screening. Data reduction and data cleaning methods need to be developed to eliminate the data that are not useful and/or noisy.

The above discussions make evident how modeling plays a huge part in the success of an SHM system. Significant advances have been made in the modeling aspects of SHM. However, to the authors' best of knowledge, there are no books

available that address the modeling aspects in relation to SHM. This book is essentially oriented in this direction.

1.1.3 Levels of Structural Health Monitoring

SHM is an inverse problem wherein the flaws in the structure is characterized using the measured data for some known input. Hence, SHM can be thought as a system identification problem. As mentioned earlier, SHM is classified into two categories, namely the Diagnosis and Prognosis. Through diagnosis, one can determine the presence of a flaws, their location, and their extent along with the possibility of looking at the delaying the propagation of flaws in the structure. The prognosis part uses the information of the diagnosis part and determines the remaining life of the structure. Hence the SHM can be broadly divided into following five levels [10].

- *Level 1:* Confirming the presence of damage
- *Level 2:* Determination of location and orientation of the damage
- *Level 3:* Evaluation of the severity of the damage
- *Level 4:* Possibility of controlling or delaying the growth of damage
- *Level 5:* Determining the remaining life in the structure (prognosis).

Level 1 SHM can be achieved by monitoring certain properties of the structure over time. Properties such as strain energy, fundamental natural frequency, phase information, stiffness reduction are some of the parameters, which can provide answers in regards to the presence of damage. The most extensively used method to confirm the presence of damage is by monitoring the natural frequencies. As damage reduces the stiffness, it induces changes in the natural frequencies. By comparing the baseline fundamental frequency with the fundamental frequency of the damaged structure, one can confirm the presence of damage. This is possible only when the damage can induce significant stiffness changes in the structure. Small damages such as delamination in composites, induces negligible stiffness change, which causes only negligible variations in the first few modal frequencies. This means one has to monitor higher order modes, which is often difficult to do. Wave propagation based techniques can be considered as effective alternatives for small or early damage detection.

Level 2 SHM is an order more difficult than Level 1 SHM. Here, from the known input and the measured output, it is necessary to determine the location of the flaw and possibly its extent and orientation. A simple way to perform this action is to trigger a signal experimentally that has high frequency content and measure the output at some location. The output will have an additional wave reflection from the flaw. Knowing the speed of the medium and the time of arrival of the reflected pulse, we can locate the flaw location. However, in many cases, due to number of boundary reflections, it is not possible to clearly identify the reflections due to the flaw accurately. In addition, the measured response itself may

be noise polluted, which makes identification of reflection due to a flaw extremely difficult. Hence, we need detection algorithms that does not suffer from the above problems. This is one of the primary focus of this book, wherein we develop algorithms, which converts the measured response into certain quantifying number, whose value indicates the status of the structure in regards the presence of the damage. The notable aspect of such algorithm is that these do not require baseline responses for damage detection.

After the damage is predicted at Level 2 stage, it is necessary to determine the severity of the damage. This forms the Level 3 SHM. If the damage is a crack, then we need to estimate the Stress Intensity Factor (SIF) or Strain Energy Release Rate (SERR) of the crack. If the SIF or SERR reaches its threshold values, then the crack will start growing. SIF is not a easily measurable quantity. In addition, in most cases, the measured output in SHM studies will be in the form of voltage histories given out by PZT type sensors. In order to asses the crack severity, it is necessary to correlate the voltage histories with the crack parameters such as SIF or SERR. This is indeed a tall order.

If the located crack is quite severe (SIF being greater than the SIF threshold), then immediate measures should be taken to arrest the growth of cracks. This is a part of Level 4 activity of SHM. The method adopted to delay or arrest the growth of flaw such as cracks are quite different for metallic or composite structures. In composite structures, delamination, can grow really fast. For such structures, the common method adopted is to reinforce the damaged area with a patch. Such patch repair delay the growth of the crack and probably can arrest it for low magnitude loads. This book does not address the Level 4 aspect of SHM. Level 5 SHM is closely associated with Level 4 SHM, wherein the estimation of fracture parameters are used to perform fatigue life analysis to determine the remaining life of the structure. The analysis here is mostly statistical. This by itself is a major subject, which is not covered in this book.

In summary, the scope of SHM is quite broad, requires understanding of many disciplines. In this book, we will not focus on all of these. The main focus here is to address the necessary computational tools required to post-process the measured data in order to locate and quantify the flaws present in the structure.

1.1.4 State-of-Art and Technological Needs

SHM can also be classified differently, especially in the context of aircraft health monitoring, namely *on-line* SHM and *off-line* SHM. In on-line SHM, the host of sensors is on-board the aircraft to provide outputs during its flight. The recorded data needs to be post processed to assess the state of the structures. This is indeed quite challenging. In off-line SHM, the aircraft is monitored when it is in the hanger. The enabling technologies required for each of these are quite different and these are summarized in the next two sub-sections.

1.1.4.1 On-Line SHM

The concept of on-line SHM can be represented as in Fig. 1.2, which shows a multitude of sensors used to monitor operating and material conditions during the in flight and/or ground operations, e.g. aircraft during taxiing or refueling. The sensors systems are networked and they communicate with each other. The vehicle maintains a neural system that can indeed be compared to the human nervous system which evaluates and diagnoses the compromises that the structures need to make that may affect its structural integrity during service. The system also posts requisite actions to be taken either through repair or replacement of the damaged part.

Sensor systems could be used as local monitoring systems to identify crack initiation and/or growth at critical locations or could be used to monitor entire structural components and subassemblies. Fiber-optic sensors can provide further support. Acoustical systems, based on *guided waves* technology, can also be efficiently applied. The most significant difference to conventional nondestructive technologies is that, with the maturity of the composite structures technologies, all sensor systems can be permanently installed (integrated) into the structure. Sensor systems based on piezoelectric materials are currently favored due to the high level of maturity attained in their manufacturing. It is of utmost importance to ensure that the embedded sensors do not impact the structural integrity of the structure. Structures made from composite materials are highly suitable for embedding of

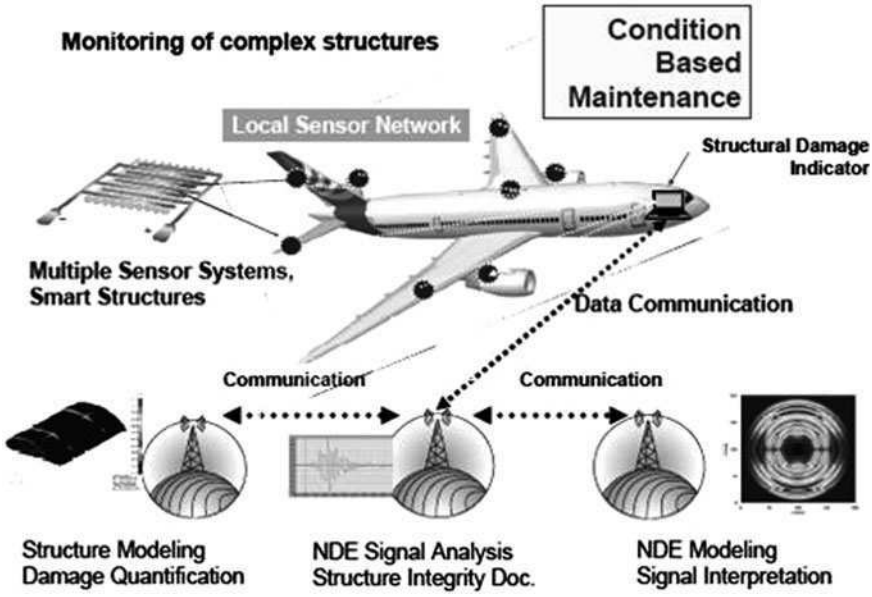

Fig. 1.2 Concept of on-line structural health monitoring

piezoelectric sensors, which allows the entire embedded part to develop sensory properties.

Acquired data are locally available and also can be transmitted to external systems and/or monitoring stations using wireless communication. The acquired data have to be pre-processed, typically by sensor integrated signal processors, prior to performing final data analysis, which is usually done at a relay station or at the monitoring station. Many modeling tools need to be developed that can be used for modeling of NDE techniques and the structure under investigation and thus permit for an integrity assessment of complex installations and systems in real-time. To successfully develop and apply such SHM technologies, it is required that the technical and scientific progress in various areas of expertise are vigorously investigated and exploited. New measurement techniques, based on traditional NDE methods, are required to provide information and data about material characteristics, material alterations and material discontinuities. The efficiency of such systems is largely dictated by the ability to apply the constantly evolving developments in the computational and data storage technologies. The longevity and reliability of such sensor platforms is currently an unsolved problem. SHM systems will become a commercial success if low-cost sensor systems can be applied in a simple manner, which requires new ideas and concepts for the packaging of integrated circuits assemblies, including polymer electronics. New data acquisition and signal processing techniques, such as *Acoustic Tomography* or *Random Acoustic Noise Technique* (RANT), must be developed. Both techniques utilize noise emissions and operating noise for component reconstruction and flaw detection, similarly to passive radar systems.

Programming of individual network nodes is time-consuming, manpower intensive and costly. Therefore, new networking concepts, allowing the automated integration of sensor systems need to be developed. Telemetric techniques to facilitate data transfers between individual nodes, SHM systems and the outside world are some of the enabling technologies that require development. In addition, new ideas to supply adequate power for such systems are also needed. Efficient, powerful battery systems, promising several years of lifetime are some of the critical technologies. Piezoelectric or magneto-inductive *energy harvesting systems*, thermoelectric generators or other power generation methods are also important technologies that will be extremely useful in the development of energy efficient power systems. Passive systems, receiving energy from external sources or through magnetic field irradiation are also promising alternatives.

Data evaluation and disposition of results will be a key aspect. The acquired signals have to provide all information necessary to assess the integrity of the structure under consideration and to predict residual operational lifetime or dictate the replacement of the monitored part or component.

1.1.4.2 Off-Line SHM

A SHM system that does not require real-time data and operates when the platform in question, say an aircraft, is not in operation is normally referred to as off-line SHM. It is quite well known that maintenance costs of an aircraft is a major contributor to the operating costs and it increases as the aircraft ages. Off-line SHM systems are required to reduce the maintenance costs of an aircraft through reduction in the maintenance time so that either the frequency of maintenance can be decreased or the structures can be designed with reduced factors of safety. The need for the off-line SHM will be clear if we look at Figs. 1.3 and 1.4, which show the action and manpower distribution for a typical commercial aircraft. From these two figures, it is quite clear that inspection accounts for significant manpower costs, which can be substantially reduced by using off-line SHM. Hence, there is a real need to pursue off-line SHM activities vigorously.

The critical technologies required for off-line SHM are quite similar to the on-line SHM and hence not repeated here. Although the off-line SHM does not require telemetry technology, significant efforts are still required in the areas of development of modeling and damage detection methodologies. One of the critical areas that is very useful for reduced maintenance is the development of non-contact measurement techniques such as Scanning Laser Doppler Vibrometer. Such a system can be used to monitor a large area in a very short period. However, post processing such large data requires data mining and data reduction methodologies coupled with a very robust mathematical model to represent the damage and detection algorithms.

Most active interrogation systems require a trigger signal provided by the actuator system. The frequency content of the trigger signal to be provided to the system is inversely proportional to the size of the flaw, that is, smaller the flaw size, larger will be the frequency content of the trigger signal. For predicting cracks of nano-meter size, trigger signal of very short duration (of the order of pico-secs, having frequency content in the order Tera-Hertz range) is required. The

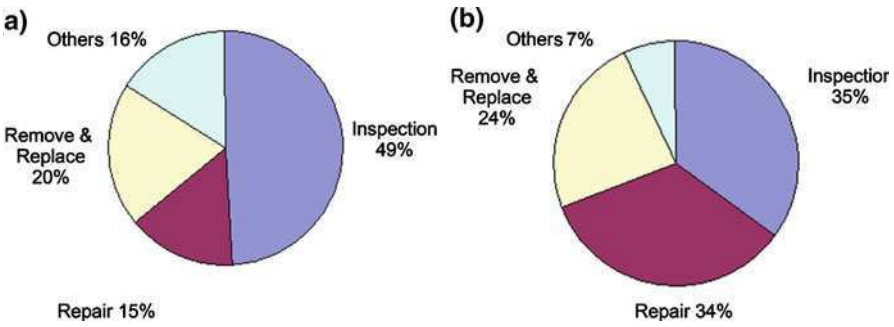

Fig. 1.3 Aircraft maintenance costs: (**a**) maintenance action distribution (**b**) maintenance manpower distribution [3]

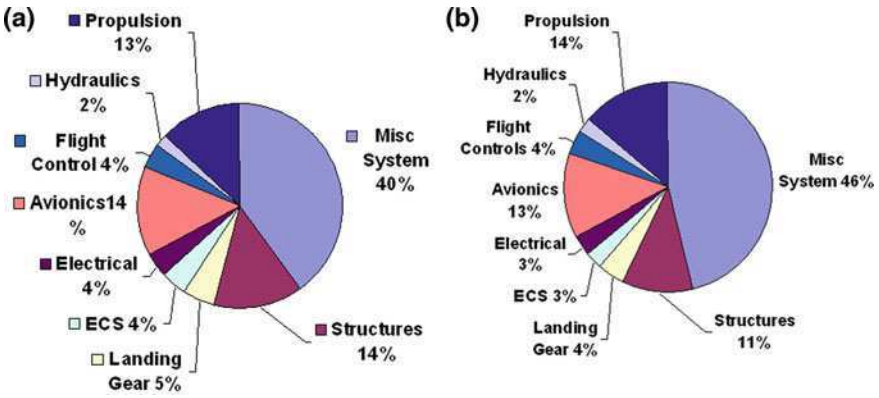

Fig. 1.4 Aircraft System wise maintenance costs: (**a**) maintenance action distribution (**b**) maintenance manpower distribution [3]

development of systems that can trigger such a high frequency content signal is still an open research objective.

More advanced NDE techniques are required for off-line SHM. One of the area that requires development is the pulse-echo eddy current system. Although conventional eddy current methodology is well known, its application is very limited in materials that are conducting. With increased use of composites in aircraft construction, which is a non-conducting material system, development of pulse echo eddy current, which works according to a totally different methodology, will be very helpful. However, such a development should be adaptable to SHM.

From the above discussions, it is clear that in order to incorporate SHM at the design stage itself, certain critical technological needs and challenges are required to be addressed or realized. Some of them are hardware-related, while others are software-related. The entire SHM process depends on how well one understands the measured data. Many times, these data may be incomplete or noise polluted. Hence development of computational tools to analyze the data is the key to the success of SHM.

1.2 Dynamics-Based Structural Health Monitoring

Dynamics-based SHM techniques assess the state of health of a structural component on the basis of the detection and analysis of its dynamic response. Such techniques can be classified on the basis of the type of response being considered for the investigations, on the frequency range of interrogation, and on the modality used to excite the component.

SHM techniques are also classified as “passive” if the component does not need an external source of excitation dedicated to the SHM system, as opposed to

"active" techniques whereby excitation is provided with the purpose of generating a response which can effectively indicate the presence of damage. Passive technique are reviewed in the next sub-section, while this section is devoted to the presentation of various active inspection methods.

1.2.1 Passive SHM

A well known passive technique is Acoustic Emission (AE), which has become a common non-destructive evaluation tool for various structural applications, and has been considered effective particularly for the investigation of damage propagation in composites. AE systems are based on sensors which are designed to detect acoustic events associated with the occurrence and propagation of damage. A typical example of such events is the acoustic signature associate with fiber breakage in composites. The sensors operate at their own resonance frequency to maximize their sensitivity, and generate signals which are subsequently analyzed through a software tool which computes various metrics such as response amplitude, time-of-flight and decay rate, and classifies them to define a recognizable pattern which may be associated with damage. Inspections performed through AE are in general very local in nature, such that AE is generally recognized as an NDE tool, rather than an SHM one. For this reason, and because several books, technical manuals, and scientific papers describe in detail the fundamentals of AE inspection, its drawbacks and advantages, as well as its various fields of application, further discussion of the method is considered as beyond the scope of the current book.

Other passive techniques are based on the analysis of the dynamic response to environment excitation. Typical examples are bridges excited by passing traffic, buildings under wind and ground motion excitation, or airplane wings under aerodynamic loads. Most analysis techniques are based on the extraction of the physical properties of the system, as contained for example in its modal parameters, and in the evaluation of changes and discontinuities caused by damage. Ambient loads are generally non-deterministic, and it is commonly assumed that they can be described as stochastic processes such as a white random noise. This allows the application of signal processing procedures which separate the stochastic part of the response, from the deterministic component associated with the behavior of the structure. One of such technique is the *Random Decrement Technique* (RDT), which is frequently used to estimate cross correlation functions and free response decays [25]. From the cross-correlation functions it is convenient to estimate modal properties such as natural frequencies, damping ratios and mode shapes, through system identification tools and modal analysis procedures. The estimated properties can be then analyzed and monitored to assess the presence, the location and the severity of damage. An overview of such tools is presented later in this book (Chap. 10). Recently, a similar process has been applied for the analysis of elastic diffuse fields, associated with the propagation of elastic waves in

geometrically complex structures. The presence of structurally complex features such as rivets holes and stiffeners in fact causes scattering, multiple reflections and mode conversion of mechanical perturbations propagating within the structure. The resulting elastic diffuse fields, which may be generated either actively or passively by ambient excitation, are characterized by complicated waveforms and randomized elastic energy distribution within the structure, denoted as "diffuse fields". Fully diffuse wavefields are often defined as ones that are globally equipartitioned, with all normal modes having uncorrelated amplitudes with equal mean squares [12, 57, 58]. Diffuse fields in structures have an apparent random nature and are thus generally discarded in conventional SHM systems. However, recent theoretical and experimental studies have demonstrated that the elastic response, as defined for example by the local Green's function or by an equivalent of the impulse response function, can be estimated from the cross-correlation of elastic diffuse fields recorded between a pair of sensors [24, 47, 59], which contains the coherent, that is, not randomized, component of the response. In principle, the cross-correlation of diffuse fields provides the means to perform SHM without a local source, since the extracted coherent responses between the sensors are similar to those obtained from conventional measurements between a source and receiver pair. Several experimental studies have demonstrated the feasibility of extracting estimates of the Green's function (or of the impulse response) from cross-correlations of acoustic or elastic diffuse fields or from ambient noise records in applications relevant to seismology [49], underwater acoustics [43, 45], civil engineering [13], low-frequency (<5 kHz) flexural properties identification of hydrofoils [46], high frequency ultrasonics (Mhz) [22, 59] and guided wave measurements (kHz) [47].

1.2.2 Classification of Inspection Techniques Based on Frequency Range of Analysis

The discussion above makes it apparent how SHM techniques operate over a broad spectrum of frequencies which spans from the low frequency vibrational response of the structure to the ultrasonic regimes in the mega Hertz range. Fatigue and damage generation and progression in fact are processes consisting of a series of interrelated events that span large scales of space and time. Hence, the analysis of damage evolution needs to be accompanied by appropriate interrogation methods capable of monitoring damage progression over these scales, such that the progression of damage starting from the characterization of its precursors, moving ahead to quantifying its location, type and extent, and finally investigating its effects at the component and structural levels can be followed. If dynamics-based monitoring with elastic waves and mechanical vibrations is considered, the spatial and temporal scales can be related to the frequency and time span of interrogation. The obvious relationship is that the sensitivity of detection decreases as the

inspection frequency decreases. Specifically, when the component is excited at frequencies close to its main natural modes of vibration, it will undergo a response which can be considered as "global". As the frequency of inspection is increased, the response becomes more localized around the excitation region, and the recorded behavior becomes more sensitive to small local variations. Such local variations include macroscopic single cracks or clusters, which can be typically detected by low-to-medium frequency guided and bulk ultrasonic waves, and microscopic cracks, material nonlinearities or dislocations pile-ups as detected by nonlinear ultrasonic methods. A global view of SHM envisions the spatial resolution and types of damage which can be detected to span a continuum from the local and microscopic to the global and macroscopic. A schematic representation of the classification of SHM techniques on the basis of frequency range of interrogation and corresponding size of detectable defects is found in Fig. 1.5. Another obvious correlation is between the spatial range of inspection, i.e. the dimensions of the portion of the structure inspected at anyone time, and the frequency of the response to be analyzed.

The broad frequency range covered by the various SHM techniques suggests the challenges associated with the development of proper modeling tools, which in principle should allow simulations and damage interpretation processes to occur over the entire frequency spectrum. As this is clearly not feasible, the need is for dedicated techniques which can be used for high frequency analysis and wave propagation problems up to the MHz regime. Some of these techniques will be presented in this book.

1.2.3 Vibration-Based Techniques

Low-frequency interrogation corresponding to vibration-based techniques typically involves the entire structural component, with its boundary conditions, so

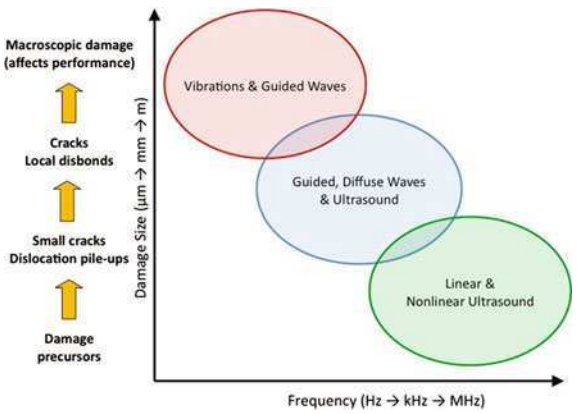

Fig. 1.5 Classification of dynamics-based SHM techniques on the basis of frequency of interrogation of the dynamic behavior of the system

that an indication of damage can be related to the presence of a defect anywhere within the structure. For example, a local reduction in stiffness affects the natural frequencies, and in principle can be detected by a single sensor mounted anywhere on the structure under consideration. For this reason, vibration-based techniques are usually considered as "global" tools. Their global nature, and the relative ease with which modal properties can be extracted through active modal testing or operational modal analysis performed using ambient loads, have promoted the development of several vibration-based techniques for damage identification. Another important aspect associated with the analysis and monitoring of modal parameters is related to their immediate relation to the overall performance of the structure. Knowledge of the modal properties and their relation with the loading configuration is an important step in the design of a component, and significant variations of the modal properties in most circumstances can be directly related to a degradation in performance which dictates the need for maintenance, repair or replacement of the part. An overview of vibration-based techniques for SHM can be found in [10], and is also given later in this book (Chap. 10). The general trend that can be identified from an analysis of the state-of-the-art suggests that natural frequencies in general are not very sensitive damage indicators, and therefore cannot be used for early damage indication. Mode shapes, and more importantly, their spatial derivatives, representing quantities such as modal curvatures and powerflows [50], are instead effective at detecting small damages, and at directly providing their location. The drawback of such an analysis however resides in the need for a large number of sensors to obtain the spatial resolution required to fully characterize the modes and to accurately compute their spatial derivatives. Such a drawback can be partially mitigated by the use of Scanning Laser Doppler Vibrometers (SLDVs), which easily map the dynamic operational shapes of a structure with very favorable spatial resolutions in a timely fashion. The use of SLDVs however does not favor the vision of the implementation of an on-line SHM approach capable of periodic or continuous monitoring of the structure through an embedded system of sensors and actuators as represented schematically in Fig. 1.2. SLDVs are however very valuable tools to support the development of novel SHM techniques as indicated in parts of this book, and, more importantly, to enable the integration of vibration monitoring with inspections performed at higher frequencies such as with guided waves as discussed in the next section. Such integration is essential in order to combine the global nature of vibration-based methods, with the sensitivity of wave-based inspections, and to effectively implement a "global-to-local" (or a "local-to-global") approach to structural health assessment. Merging and integration of various SHM techniques is still an active area of research, which holds many promises towards the practical application of several of the concepts discussed in this book.

1.2.4 Guided Waves Inspection

The application of guided waves (GWs) as inspection tools for SHM is receiving attention of a large number of researchers. The most attractive feature of GWs is their ability to travel long distances in plate and shell-like structures, which makes the inspection of large areas possible. Complicating factors are the multi-modal and dispersive natures of GWs signals, which require the development of proper interpretation tools. The objective is the extraction of relevant features from the recorded response, which may be related to damage. In this regard, proper signal processing algorithms are essential features of GW-based SHM techniques. Overviews of signal processing strategies used for GW interpretation and damage measure formulation can be found in [42, 36, 52]. Time Frequency Transforms (TFTs) are well-suited for the analysis, decomposition and de-noising of GW signals, which are typically non-stationary. Short Time Fourier Transforms (STFT) [31], Wigner–Ville Distributions (WVD) [34, 37], and, more recently, the Hilbert-Huang Transform (HHT) [31, 48] are examples of various techniques used to observe the propagation of various modes, to separate reflections from incident waves and to formulate associated damage measures. The Wavelet Transform (WT) in its various forms is a very important and versatile tool, used extensively for denoising, as well as for feature extraction and selection [52]. The discrete wavelet decomposition is applied for example in [41] as part of a feature extraction and automatic classification framework developed for GW inspection of pipes. The STFT is applied in [19] to select and isolate the first symmetric mode (S_0), known for being particularly sensitive to crack-type damages, and to formulate an associated damage index. In [33], a network of sensors is used to construct GW tomograms for anisoptropic composite plates. The approach accounts for attenuation in the composite material by using the energy of the earliest wave signals as the reconstruction parameter, and by normalizing the wave energy of the defective sample with respect to that of the undamaged one. For quantitative comparisons between tomograms, a parameter β is introduced as the ratio of the considered values in the defect-free region to that of the defective region of a tomogram.

Higher dimensional Fourier Transforms (FTs), transforming the signal in the wavenumber/frequency domain, are also used to identify wave modes and to investigate mode conversion phenomena caused by crack-like damages [1]. Examples of numerical investigations of mode conversion phenomena can be found in [4]. Recently, two-dimensional and three-dimensional FTs have been applied as tools to decouple incident and reflected waves and to filter out the incident component from the recorded signals [44]. The experimental application of this concept is enabled by the application of the SLDV, which easily provides the spatial measurement resolution needed to perform FTs in the spatial domain. A damage measure based on this concept is currently in the works. The SLDV was also used in [53] to investigate maximum amplitudes of low frequency Lamb waves propagating in plate structures. Amplitude reductions and sudden increases across the defect were considered as indicators of damage.

As in [41], signal processing tools are often combined with tools that are able to classify the identified signal features and relate them to damage type and extent. The most common technique for pattern recognition is certainly the use of NNs. Examples of their application for GW in SHM can be found in [54], where spectrographic features from Lamb wave signals in the time-frequency domain were used to construct a damage parameters database, through which a NN was then trained for its successive use for identification of delaminations in quasi-isotropic composite laminates. A multi-layer perceptron (MLP) neural network is used in [29] as part of a novelty detection method. The technique is applied to a thin, isotropic plate, where GWs are sequentially transmitted and captured by eight piezoelectric patches bonded to the plate to act both as sensors and actuators. Scattering waveform responses representing normal and damaged conditions are transformed into a set of novelty indices that are fed as inputs to the NN incorporating the MLP architecture to compute and predict the damage location on the plate.

1.2.5 Ultrasonics and Nonlinear Ultrasound

Ultrasonic inspection is a well-known NDE tool, which provides local, detailed damage information. Its effectiveness to detect a broad range of damage types is well proven by a vast scientific literature and by its broad range of applications. Like AE, ultrasonic inspection as an NDE tool will not be covered in this book. However, it is useful to include it as part of the potential integration with SHM tools such as vibration-based and guided-wave based techniques, which thus far have not shown the same level of accuracy and sensitivity, but which potentially allow more frequent inspections. In this perspective, ultrasonic techniques may be considered for confirmation of damage information obtained from a SHM system, and for its subsequent detailed characterization. This process could lead to significant reductions in time and costs, by limiting the ultrasonic inspections to parts where the indication of the presence of damage derives from information obtained from an on-board SHM system.

An important relation to be made is between the loading history of the part under consideration, damage that can be detected by an SHM system, and its progression from the precursors to its propagation to a detectable level. Such relation can be investigated again through the integration of the SHM approach with an NDE process such as nonlinear ultrasound, which is capable of tracking the accumulation of fatigue and development of defects at the micro-structural level. Nonlinear ultrasound measures elastic and plastic nonlinearities in a material through the analysis of ultrasonic wave distortions in the forms of harmonic generation corresponding to a tonal input. The acoustic nonlinear parameter provides a quantitative measure of wave distortion as its value can be directly related to the amplitude of the harmonics multiples of the input frequency. The magnitude of the nonlinear parameter is also directly dependent on the crystalline structure of

the solid [8, 30], and on the presence of defects. Hence, measurement of the amplitude of higher harmonics' amplitudes allows direct measurement of the nonlinear parameter and the establishment of a direct relation with the accumulation of micro-structural defects such as dislocations pile-up resulting from fatigue loading [8]. The direct relation between amplitude of the higher harmonics, and presence as well as severity of defects at the micro-structural level has made nonlinear ultrasound a very important material characterization tool, which has been widely applied in metals. The transition to an NDE-type application for fatigue tracking as suggested in [20, 30], and its application in conjunction with SHM tools represents a very interesting prospect to gain full understanding of the process of damage growth. The extension of the study to composite materials, with specific relation to allowable defect sizes can be of significant importance towards the optimization of composite structural designs, the understanding of composite structure degradation and fatigue, and the definition of proper acceptance levels for manufacturing defects to avoid overly conservative design specifications.

1.3 Sensing and Actuation Strategies

This section presents an overview of common sensing and actuation strategies for SHM. Focus is placed the techniques devoted to based inspection, where a significant amount of research is being conducted towards the development of efficient excitation of wave modes which are most sensitive to damage, the need for interrogating specific directions in a structure, and the ability to steer elastic waves, so that a large area of a structure can be interrogated. An important aspect of a SHM system is certainly sensing, for which the possibility of having embedded sensors is of great relevance. In this regard, fiber optic sensors are of primary importance: the basic principle of their operation is presented Sect. 1.3.2, together with an overview of piezoelectric actuation and sensing strategies for SHM as described in what immediately follows. Finally, SLDVs as SHM tools will be briefly introduced.

1.3.1 Piezoelectric Actuators and Sensors

Probably the most common approach for the generation and sensing of guided elastic waves is the use of piezoelectric patches. The direct and inverse piezoelectric effects makes piezoelectric materials ideal sensors and actuators, which can be used for guided-wave tomography in a pitch-catch configuration, whereby a receiver captures a signal from a transmitter, or in a pulse-echo mode, where the same component acts both as a transmitter and as a receiver.

Detailed accounts of the application of piezoelectric materials for guided wave excitation are presented in monograph form in [15]. Piezoelectric patches have

been used extensively to excite guided waves by exploiting shear actuation, or a longitudinal actuation mode. Schematic of actuation configurations using piezoelectric patches and stacks in shear and longitudinal mode are shown in Fig. 1.6. The shear actuation mode is very convenient since it simply requires direct bonding of the patch onto the surface, while the longitudinal actuation mode requires a backing to provide enough reaction and facilitate the coupling between the piezo and the underlying structure.

An important issue that needs to be considered is the need for evaluating the optimal matching, or tuning, of the piezo with the excited structure, so that optimal generation of waves is achieved. This aspect is widely discussed in [15]. In here, it is sufficient to indicate that critical parameters define the relation between the dimensions of the patch, the wavelength of the excited wavemode and the corresponding tuning frequency. Figure 1.7 shows the variation of the output amplitude as a function of frequency corresponding to a patch actuated in shear on a plate. The plot clearly shows that the amplitude of the displacement generated by the actuator varies significantly with frequency, and that different maxima are achieved for the A_0 and the S_0 mode, indicating the possibility of tuning the frequency of excitation to preferentially generate one mode or the other.

Another important parameter is the actuator/sensor shape which can lead to directional excitation and sensing. Solid, individual patches typically do not lead to strong directivity, however, it is well known that arrays of patches [14, 16], as well as properly shaped piezoelectric actuators can lead to strong directional characteristics and can provide the ability to direct waves in specific directions through electronic or spatial phasing of the array components. Some of these aspects are discussed in Chap. 8.

Recently, more complex piezoelectric configurations have been considered to improve the coupling conditions, to optimize tuning and to obtain directivity. The application of piezo-composites of the kind shown in Fig. 1.8, can lead to novel actuation and sensing configurations, and could be exploited for directional sensing and actuation.

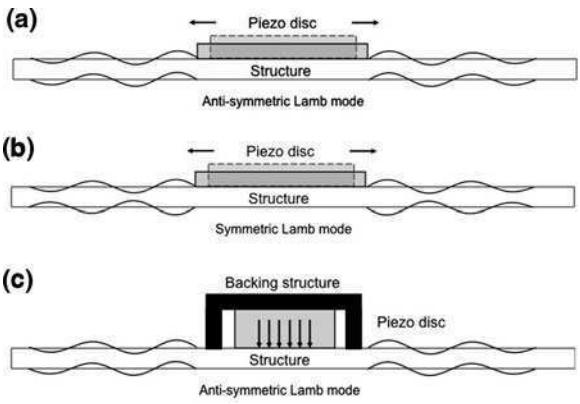

Fig. 1.6 Lamb wave generation using shear mode: anti-symmetric (**a**), and symmetric mode (**b**), and using longitudinal mode (**c**)

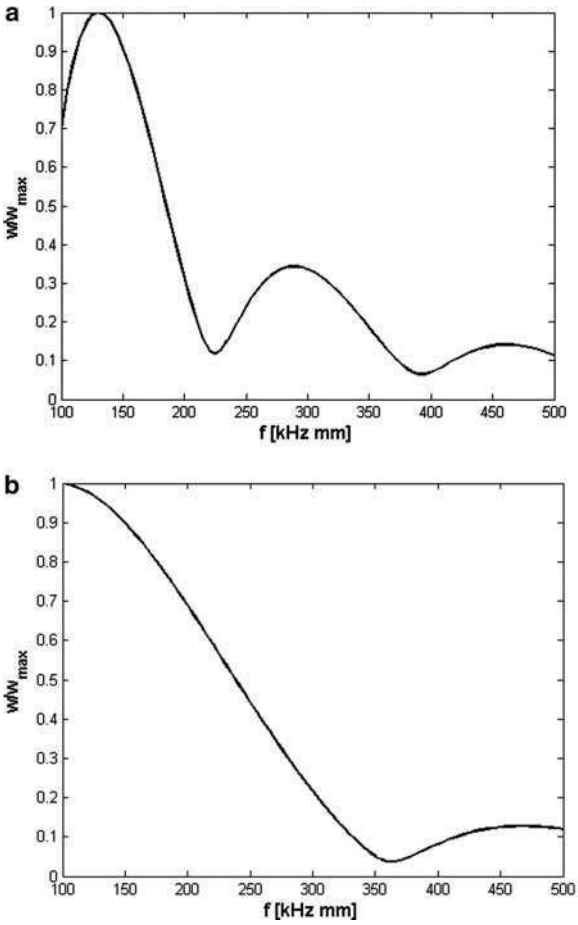

Fig. 1.7 Normalized amplitude of plate response versus frequency for shear mode excitation: A_0 mode (**a**), and S_0 mode (**b**)

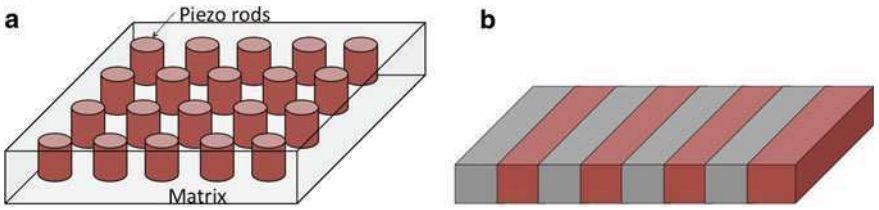

Fig. 1.8 Examples of piezoelectric composites: 1-3 piezoelectric composites feature piezoelectric rods embedded in a polymer matrix (**a**), 2-2 piezoelectric composites feature piezoelectric sheets laminated between polymer sheets (**b**)

Significant attention has been devoted to the use of Macro Fiber Composite (MFC) patches for various applications including SHM. The MFC patch is an innovative actuator produced by Smart Material Corporation and originally

developed at NASA Langley Research Center. The design consists of rectangular piezo ceramic rods sandwiched between layers of adhesive and electroded polyimide film as shown in Fig. 1.9. The film contains interdigitated electrodes that transfer the applied voltage directly to and from the ribbon shaped rods. This assembly enables in-plane poling, actuation, as well as sensing in a sealed, durable, ready-to-use package. When embedded in a surface or attached to flexible structures, the MFC provides distributed solid-state deflection and vibration control capabilities as well as the ability to measure strains. Two types of MFC transducer exist. A first types uses the 31 piezoelectric effect in the ceramic rods by applying a through-the thickness voltage as described in Fig. 1.9. The second configuration exploits the 33 piezoelectric effect by applying a longitudinal voltage through interdigitated electrodes (Fig. 1.10).

In light of the introduction of actuators/sensors of complex shapes and functionalities of particular importance is the accurate estimation of guided wave generation through surface mounted or embedded piezoelectric patches or wafer transducers [14–16]. Accurate models can provide the basis for the selection of geometry, dimensions, and excitation bandwidth suitable for the excitation of specific modes and the detection of specific damage types. A common approach is based on the solution of the wave equation in the spatial Fourier domain [56]. This technique is applied to the analysis of waves generated by several actuator configurations generating plane and crested waves in isotropic structures in [14, 15], where it is shown how the size of the actuator is a very important parameter for tuning the excitation to a specific frequency and wave mode. These results, which are limited to one-dimensional (1D) wave propagation, are extended to the 2D analysis of crested waves propagation in plates in [35], where an analytical model allows the investigation of the effects of the in-plane shape of the piezo-patch. The formulation of [35] relies on the solution of the 3D equations of elasticity with the

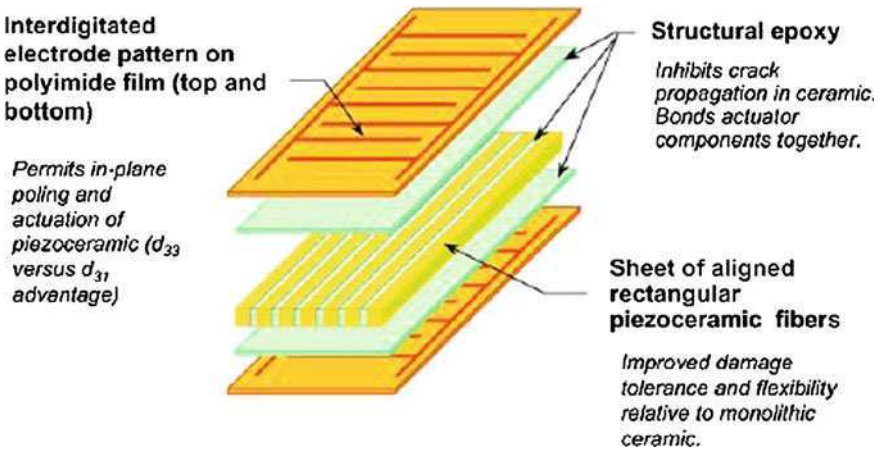

Fig. 1.9 Macro fiber composite (MFC) transducers (Smart Material Corporation)

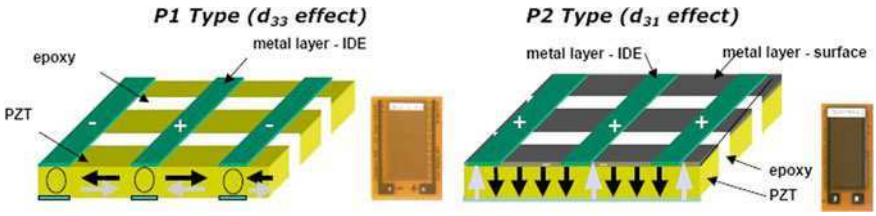

Fig. 1.10 Smart Material Corporation

stress field generated by the surface bonded piezo as boundary conditions. The analytical derivations assume simplified expressions for such stress distributions, which allow the analytical derivations of the plate response, but may lead to inaccurate estimations of tuning frequencies and directionality, specifically at high frequencies. In particular, the approximation that piezoelectric stresses are concentrated on the boundaries of the patch leads to neglecting the shear lag phenomena associated with the presence of a bonding layer [26], which results in the inaccurate estimation of the tuning conditions for actuation [23]. The development of general procedures to couple actuation through surface mounted piezo-patches and underlying structure and to accurately capture the generated wavefield still represents a significant challenge to the SHM research community. Capturing details of the actuation, while being able to simulate the propagating wavefield can easily lead to FE models that are very large and computationally costly. Semi-analytical solutions of the kind proposed in [35] are very convenient, but rely on simplifying assumptions, which may reduce the accuracy of the simulations. Proper coupling between a coarser FE model of the structure and a locally refined model of the actuator is certainly a goal to be achieved in the near future to provide the accuracy required for model-based design of a guided wave-based SHM system.

1.3.2 Fiber Optics Sensors

Fiber Optic Sensors (FOS) are one of the most widely used sensors in the context of SHM due to the simplicity of their use. In fiber optic sensing, the response to external influence is deliberately enhanced so that the resulting change in optical radiation can be used as a measure of the external perturbation. In the area of communication, the signal passing through a fiber is already modulated, while in sensing, the fiber acts as a modulator. It also serves as a transducer and converts measurands like temperature, stress, strain, rotation or electric and magnetic currents into a corresponding change in the optical radiation. Since light is characterized by amplitude (intensity), phase, frequency and polarization, any one or more of these parameters may undergo a change. The usefulness of the fiber optic

sensor therefore depends upon the magnitude of this change and the ability to measure and quantify the same reliably and accurately.

The advantages of fiber optic sensors are freedom from EMI, wide bandwidth, compactness, geometric versatility and economy. In general, FOS is characterized by high sensitivity when compared to other types of sensors. It is also passive in nature due to the dielectric construction. Specially prepared fibers can withstand high temperature and other harsh environments. In telemetry and remote sensing applications, it is possible to use a segment of the fiber as a sensor gauge while a long length of the same or another fiber can convey the sensed information to a remote station. Deployment of distributed and array sensors covering extensive structures and geographical locations is also feasible. Many signal processing devices (splitter, combiner, multiplexer, filter, delay line etc.) can also be made of fiber elements thus enabling the realization of an all-fiber measuring system.

1.3.2.1 FOS Classification

There are a variety of ways the FOS can be classified. These are as follows:

- *Classification based on Modulation and Demodulation process:* Based on modulation or demodulation, an FOS can be called as an *intensity* (amplitude), *phase*, or *frequency* or *a polarization* sensor. Since detection of phase or frequency in optics calls for interferometric techniques, the latter are also termed as interferometric sensors. From a detection point of view, the interferometric technique implies heterodyne detection/coherent detection. On the other hand intensity sensors are basically incoherent in nature. Intensity or incoherent sensors are simple in construction, while coherent detection (interferometric) sensors are more complex in design, however they offer better sensitivity and resolution.
- *Classification based on the application of FOS:* FOS can also be classified on the basis of their application such as *physical sensors* (e.g. measurement of temperature, stress, etc.), *chemical sensors* (e.g. measurement of PH content, gas analysis, spectroscopic studies, etc.), and *bio-medical sensors* (inserted via catheters or endoscopes which measure blood flow, glucose content and so on). Both the intensity types and the interferometric types of sensors can be considered in any of the above applications.
- *Classification based on mode of sensing:* In this classification there are two types of FOS, namely *Extrinsic* and *Intrinsic* sensors . In the former, sensing takes place in a region outside of the fiber and the fiber essentially serves as a conduit for the to-and-fro transmission of light to the sensing region efficiently and in a desired form. On the other hand, in an intrinsic sensor, one or more of the physical properties of the fiber undergo a change as mentioned in the first item above.

1.3.2.2 Basic Components of a FOS

A fiber optic sensor in general will consist of a source of light, a length of sensing (and transmission) fiber, a photo detector, demodulator, processing and display optics and the required electronics. In a fiber-optic sensing system, the emitter and the receiver share a single housing. The fiber-optic cable that is connected to the amplifier allows the sensor to reach areas inaccessible to standard photoelectric sensors. The sensor emits, receives, and converts the light energy into an electrical signal. Fiber-optic cable consists of a plastic or glass fiber surrounded by a layer of cladding material (see Fig. 1.11). The difference in densities between these two components enables the cables to act in accordance with the principle of total internal reflection.

1.3.2.3 Principle of Operation

The FOS works on the principle of total internal reflection, which states that all the light striking a boundary between two media will be totally reflected. That is, no light energy will ever be lost across the boundary. This principle pertains only when the following two conditions are met:

- The critical angle is less than the angle of incidence for the particular combination of materials. The materials in this case are the core and the cladding of the optical fiber.
- The light is in the denser medium and approaching the less dense medium. The cladding material is less dense than the core material, and as a result has a lower refractive index.

As long as these two conditions are satisfied, the principle of total internal reflection applies whether the fiber-optic cable is bent or straight (within a defined minimum bend radius). The amount of literature pertaining to FOS is quite large. In this section, we will describe only two important Extrinsic FOS that find extensive applications in SHM, that is, *Extrinsic Fabry-Perot interferometric* (EPFI) FOSand *Fiber Bragg Grating* (FBG) FOS.

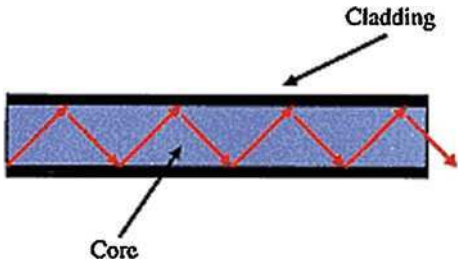

Fig. 1.11 Schematic of a typical optical fiber used in FOS

1.3.2.4 Fabry-Perot Interferometric FOS

A schematic of the EFPI sensor is shown in Fig. 1.12. EPFI is an extrinsic sensor that works on the principle of multi reflection Fabry-Perot interference between the two reflected mirror as shown in Fig. 1.12. This sensor is made using single mode optical fiber and a multi mode fiber as reflectors. These two fibers are inserted and fused into a quartz capillary tube of larger diameter. The ends of the capillary tube is glued with epoxy to avoid weak fusion points.

In this FOS, a cavity is created between two parallel reflectors and this cavity is perpendicular to the optical fibers. When an external load is applied, the cavity length changes, which can be measured using CCD spectrometer. If Δd is the change in the cavity length, and L is the gauge length (or the length between two fusion points in a capillary), then the strain on the sensor is given by $\varepsilon = \Delta d/L$. The strains change in the presence of the crack or change in the loading and hence this measure can be used effectively used in SHM studies.

1.3.2.5 Fiber Bragg Grating FOS

Some optical fibers, especially those made by doping germanium are highly photosensitive when a light of a specific wavelength are incident on them. That is, the refractive index of the fiber change permanently when these fibres are exposed to light of a specific wavelength. A uniform FBG has a segment of optical fiber containing periodic modulation of refractive index. The principle of operation of FBG sensor is shown in Fig. 1.13.

Normally FBG is fabricated on a germanium doped single mode optical fiber using ultraviolet laser source of range 240–248 nm. Many fabrication method can be adopted, such as interferometric method, phase mask method etc. The length of gratings are normally in the range of 1–20 nm. When the input light is incident on the grating, some parts of it is reflected, while the others are transmitted. The principle on which the FBG works is based on the changes in the measured reflective signal, which is the center wavelength of the back reflected light from the Bragg Grating. This depends on the effective refractive index of the core and the periodicity of the grating. Knowing the grating periodic spacing δ and effective refractive indexr_{eff}, the Bragg wavelength is given by

$$\lambda_b = r_{\text{eff}}\delta \tag{1.1}$$

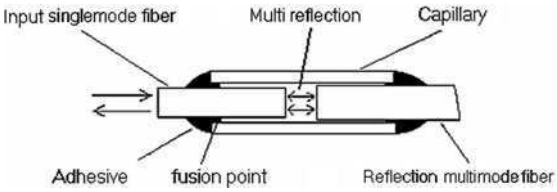

Fig. 1.12 Schematic of a Fabry–Perot interferometric FOS

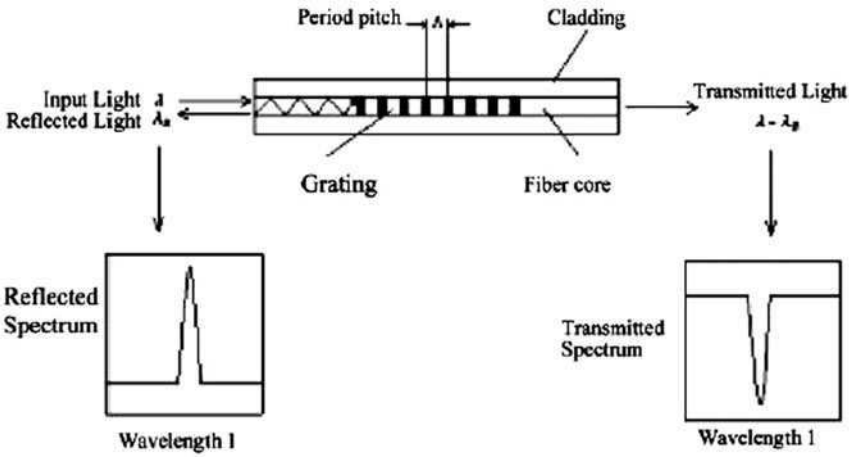

Fig. 1.13 Principle of operation of fiber bragg grating of FOS

Hence the wavelength will shift with the change in the effective refractive index or the spacing of the grating. Such changes can be caused when the grating area is subjected to mechanical or thermal load. If $\Delta\varepsilon$ is the change in mechanical strain due to a mechanical load, and ΔT is the change in temperature due to thermal load, then these changes can be related to the Bragg wavelength change as

$$\Delta\lambda_b = \alpha\Delta\varepsilon + \beta\Delta T \quad \alpha = \lambda_b(1 - p_c) \quad \beta = \lambda_b(\alpha_A + \alpha_B) \tag{1.2}$$

where p_c is the strain-optic constant, α_A is the thermal expansion coefficient of the fiber and α_B is the thermal optic coefficient of the fiber. Measurement of the changes in the Bragg wavelength is paramount in the SHM studies for either load monitoring or damage detection.

1.3.3 Laser Vibrometer

Scanning Laser Doppler Vibrometers are convenient tools for the detailed measurement of dynamic deformed shapes of structures. Based on the evaluation of the doppler shift between a reference and a reflected Laser beam, SLDVs can conveniently measure the response over a fine grid of measurement points. The grid can be selected and modified by the user such that global operational shapes, or local vibration patterns in a region of interest can be captured. The non-contact nature of the measurement is a very important feature, together with the extremely large bandwidth over which dynamic measurements can be performed. Current SLDVs can detect motion at frequencies which span the 0.1 Hz up to 20 MHz regimes, a bandwidth that cannot be achieved with sensing devices such as accelerometers.

The use of SLDV has initially been dedicated to modal analysis purposes, while more recently it has been extended to SHM. The fine spatial resolution of the measurements in fact allows the accurate application of vibration-based techniques relying on the evaluation of the modal curvatures of panel structures, as discussed in [50]. As previously mentioned, the SLDV was also employed in [53] to investigate maximum amplitudes of low frequency Lamb waves propagating in plate structures. Amplitude reductions and sudden increases across the defect were considered as indicators of damage. The high frequency capabilities of SLDVs have also made the detection and analysis of propagating wavefield a practical and viable procedure for damage detection and characterization [28, 44, 50]. Time-domain measurements of transient wavefield using the SLDV require the generation of a pulse at each grid point in order to record the corresponding response. Phase information is retained by triggering the excitation signal through a low frequency signal, which also defines the scanning rate. A schematic of a typical set-up considered for wavefield measurement is shown in Fig. 1.14.

Upon completion of measurements at all grid points, the recorded responses are post-processed to obtain full images of the propagating wavefield within the region of inspection. The data are organized in 3D arrays $u(x, y, t)$, which define the velocity component aligned with the Laser beam at the considered location and time instant. Examples of snapshots of recorded wavefield images in an aluminum plate with several artificial defects are presented in Fig. 3.28. The visualization of the detected wavefields clearly shows waveforms propagating out from the source, and interacting with structural discontinuities, where they are converted, reflected and diffracted. Signals scattered from defects however are typically much smaller

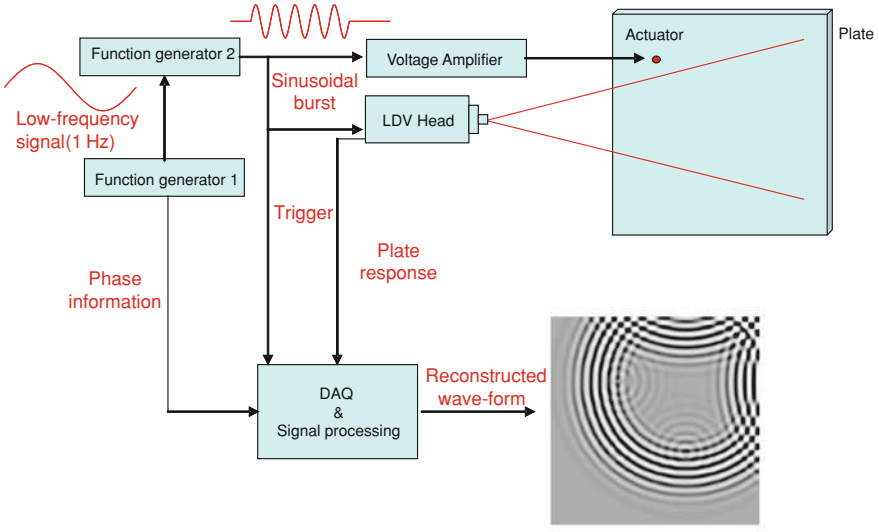

Fig. 1.14 Schematic of experimental set-up for wavefield detection using a SLDV system

in amplitude than incident waves, and additional processing is required to effectively identify, localize and possibly characterize damage. To this end, several procedures for incident wave removal have been proposed in recent years [27, 44]. Such procedures, which operate either in the time domain [27], or in the frequency/wavenumber domain [44] have the objective of removing the wave generated by the transducer to obtain a residual wavefield which contains only the contributions of small scatterers such as defects. Some of these techniques will be presented in detail later in this book (Chaps. 3 and 10) (Fig. 1.15).

1.4 Modeling and Simulation Techniques for SHM

The focus of this book is to address the computational aspects related to SHM. Hence, it is appropriate at this point of time to discuss the importance of modeling and the various available simulation techniques in the context of SHM.

1.4.1 The Importance of Modeling in Structural Health Monitoring

Section 1.1.2 discussed how modeling forms the major part of the SHM process. In this respect, SHM can be thought out as a system identification problem. It is well known that the solution of the system identification problem is not straight forward and often very difficult. In many cases, these problems do not have a unique solution. This is because the solutions depend on a large number of parameters whose effects on output is not known. Most system identification problem requires determination of the System Transfer Function or Frequency Response Function (FRF), which requires sound mathematical models for its determination. In the context of SHM, the damage modes of metallic structures are quite different when compared to that of composites. In fact, damage in composites is an order of magnitude more complex and difficult to understand than in metallic

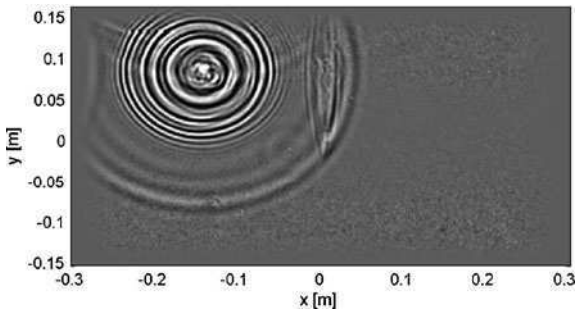

Fig. 1.15 Snapshot of guided wavefield measured on a bonded aluminum plate using a SLDV system

structures. Hence, it is necessary to develop computational models for various damage types in structures. The choice of appropriate computational mathematical models depends on the size of damage that needs to be predicted. If the damage sizes are quite large compared to the dimension of the structure, then models based on Finite Element Method, Finite Difference method etc. may be sufficient. However, when the damage sizes are very small, one needs very small duration input pulse (of the order of $\mu secs$ or lower) having very high frequency content. For such cases, wave propagation based method, that never imposes any constraint on the frequency content, is required. Spectral Finite Element (SFE) is one of those methods that falls under this category. Next important aspect is the damage detections algorithms to predict and locate the damage and determine its orientation and extent. These are the first two levels of SHM that we discussed earlier in Sect. 1.1.3. The damage prediction algorithm should be able to complement the chosen mathematical model and must be able to predict the damage location with incomplete and noisy measured data. In addition to these, in many large structures, the number of measured data will be enormously large and all of these data may not be useful for damage prediction. Hence, methods to reduce the data to a suitable set that can give meaningful information is required. This requires significant mathematical and regressional analysis of the measured signals. Hence, from the above discussion, the importance of modeling in SHM is quite clear.

All mathematical models are represented by Partial Differential Equations (PDEs), which are derived based on assumptions on the behavior of the field variables. Most PDE's encountered in SHM are either of hyberbolic or elliptic type. In both cases, analytical solutions are quite difficult to obtain, therefore numerical techniques need to be applied. Some of the numerical techniques transform the governing PDE's into a *weak form*, which is the integral representation of the governing equation and it is obtained using *Variational Principles*. In the weak form, the dependent field variable is weighted with a function and the resulting expression, when integrated by parts over the domain, will convert the PDE's into an integral form that is amenable to numerical solution. The choice of the weights determines the type of the numerical method. This procedure is called the *Weighted Residual Technique* (WRT) and more details of this method can be found in [55]. In the next few subsections, we will describe a few numerical techniques, many of which can be derived from WRT, for the solution of PDE's.

1.4.2 Finite Difference Techniques

This method can be directly derived from the weak form of the governing equation and using WRT, where the dependent variable is weighted by a weighting function represented by *Dirac Delta* function. This will convert the governing PDE to a *difference equation* in terms of the values of the dependent variable over a domain called the *cell*. The essential and natural boundary conditions at the cell interface with the other cells are enforced, which gives a set of algebraic equations, using

which the unknown nodal values are obtained. This method is extensively used in the solution of fluid dynamic problems and the details of this method can be found in [2].

The above explained procedure, which results in the *Central Difference Finite Difference Scheme* that is only second order accurate. Higher order accurate difference schemes are also highly reported in the literature. The details of some of these methods are given in [5]. The method has two sub categories, namely *method* and *implicit methods*. In explicit method, the size of cell (also called the *step size*) is very critical for the solution accuracy. That is, the explicit methods such as central difference scheme, have a constraint placed on the step size. When the step sizes are larger than the critical value, the solution diverges. However, the solution process mandates that the value at the present step is dependent only on the values preceding the current step and hence at every step, we need to solve only an algebraic equation. In the implicit method, the value of an unknown dependent variable also depends on the value preceding the current step and also values ahead of the current step. Hence, we need to solve matrix system of equations at every step. The main advantage is that this method does not have a constraint on the step size.

In the context of SHM, cell sizes are very critical. If the size of the damage is very small, then the SHM process requires a signal having very high frequency content to be applied to the system. At these high frequencies, the wavelengths are very small and hence the cell sizes need to be compatible to the wavelength of the response of the structure. Typically 8–20 cells should span each wavelength.

1.4.3 Finite Element Method

The Finite Element Method is the most versatile of all the available modeling methods because of its ability to model complex geometries by piecing together the information available over a small domain called an "element". Hence, FEM needs a mesh (which is the collection of elements) of the domain of interest and over each element, the variation of the field variable (say displacements) is assumed. These assumed variation are then converted to the nodal quantities (nodal displacements). These are then substituted into the weak form of the differential equation and a system of matrix algebraic equations are obtained in the case of static analysis or ordinary differential equations in the case of time-dependent problems. This process gives the stiffness matrix for static analysis problems and the stiffness and mass matrices for time dependent problems. The static system of equations are solved using the standard algebraic equation solver, while the time dependent equations are solved by converting the coupled set of differential equations into difference equations using the procedures outlined in Sect. 1.4.2. More details are available in many classic text books on FEM [5, 9, 40] can also be derived directly from the WRT, wherein the weight function and

the displacement variation over each element, are same. This aspect is discussed in [55].

From the SHM point of view, the approach has the same limitations of the finite difference method, that is, mesh sizes have to be very small for modeling small damages. The relationship between the mesh sizes and the frequency content of excitation and the effects of choosing large mesh sizes are discussed in [17]. The details of the application of this method to SHM problems is discussed in Chap. 4.

1.4.4 Boundary Element Method

In the Boundary Element method (BEM), the governing PDEs over the domain of interest are converted into two components, one containing the integral over the domain surface and the second component is a volume integral over the domain. Such a splitting is possible using the Stokes Theorem [21]. The solution of the second component comprising of the volume integral is obtained considering the Green's function for a point load on an infinite space, which is standard for most problems. This solution is called the *Fundamental Solutions*. The first component of the PDE, namely the boundary integral on the surface of the domain are solved via standard FEM. This process reduces the dimensionality of the problem by one, that is a 2D problem become 1D and a 3D problem becomes a 2D problem. However, the main disadvantage of this method is that the fundamental solutions are available only to some select problems. Analyzing non-linear problems are very difficult. The details of this method can be found in [6].

There is a great advantage of using BEM to SHM problems. This is because, the internal part of the domain of interest need not be modeled. However, if a crack or some damage is present in the structure, they form the part of the boundary. As in the other two methods, the mesh sizes for the boundary should be small enough to be comparable to the wavelength of the input signal. As such there is not much reported in the literature on the application of BEM to SHM problems.

1.4.5 Spectral Finite Element Method

The Spectral Finite Element Method (SFEM) was initially conceived by Beskos and Narayan [7]. This was later popularized by Doyle and co-workers [11]. The spectral element method is essentially a finite element method formulated in the frequency domain. However, their methods of implementation are quite different. The basic differences between SFEM and FEM are highlighted in the following paragraph.

FEM is based on an assumed polynomial for displacements. These assumed displacement polynomials are forced to satisfy the weak form of the governing differential equation, which yields two different matrices, namely the stiffness

matrix and the mass matrix. These elemental matrices are assembled to obtain global stiffness and mass matrices. The assembly process ensures equilibrium of forces between adjacent elements. This procedure will give the discretized form of the governing equation, given by $[M]\{\ddot{u}\} + [C]\{\dot{u}\} + [K]\{u\} = \{F(t)\}$, where $[M]$ and $[K]$ are the global mass and stiffness matrix and $\{\ddot{u}\}$, $\{\dot{u}\}$ and $\{u\}$ are the acceleration, the velocity and the displacement vector, respectively. Matrix $[C]$ is the damping matrix, which is normally obtained from the combination stiffness and mass matrix as $[C] = \alpha[K] + \beta[M]$, where α and β are the stiffness and the mass proportional damping factors, and the damping scheme is called the proportional damping scheme. There are two methods of solving the above matrix differential equation, namely the *Direct Time Integration* and the *Mode Superposition Method*. The mode superposition method of solution cannot be used for wave propagation analysis. This is because, the solution requires extraction of all the higher order eigen modes, which is computationally prohibitive. The preferred solution method is the time marching scheme, where two different strategies are available, namely the explicit methods and the implicit methods. These were discussed in Sect. 1.4.2. For wave propagation and highly transient dynamics problems, explicit methods are normally preferred. In the time marching scheme, the solution process takes place over a small time step ΔT. The solution of the dynamic equations will give displacement, velocity and acceleration histories. The solution process is repeated for N time steps until the total time $T = N\Delta T$ is reached. The solution time is directly proportional to the number of degrees of freedom in the model, which is usually very high for wave propagation problems.

SFEM on the other hand uses in most cases the exact solution to the wave equation in the frequency domain as its interpolating function. One can see, unlike the polynomials in the case of FEM, here, we need to deal with complex exponentials as the interpolating functions. The exact solution will have wave coefficients corresponding to the incident and reflected wave components. If one wants to model an infinite domain, then the reflected components can be dropped from the interpolating functions. This gives what is called the *throw-off elements*formulation. This is a great advantage that SFEM has over FEM. Using the interpolating functions for the displacement, the dynamic element stiffness matrix is formulated. One can formulate this stiffness matrix as in the case of conventional FEM, using the weak form of the governing equations. This approach will involve complex integration. Alternatively, one can formulate the dynamic stiffness matrix using stress or force resultant expressions. This method is normally suitable since it does not involve complex integration. The basic steps involved in the analysis using SFEM are as follows. First, the given forcing function is transformed to the frequency domain using the forward Fast Fourier Transform (FFT). In doing so, we need to choose the time sampling rate and number of FFT points to decide on the analysis time window. Care should be taken to see that the chosen window is good enough to avoid what are called *wraparound* problems [18]. The FFT output will yield the frequency, the real and imaginary part of the forcing function, which are stored separately. Over a big frequency loop, the element dynamic stiffness matrix is generated, assembled and solved as in the case of conventional FEM.

However, these operations have to be performed at each sampled frequency. This does not pose a major computational hurdle since the problem sizes are many orders smaller than conventional FEM. The solution process is first performed for a unit impulse, which directly yields the FRF. The FRF is then convolved with the load to get the required output in the frequency domain. This output is then transformed to the time domain using the inverse FFT.

There are many advantages that SFEM gives over conventional FEM. The SFEM can give results in both the time and frequency domain in a single analysis. Obtaining the FRF is a big advantage of the SFEM. This enables one to solve inverse problems such as the force or the system identification problems in a straightforward manner. Since many damping properties are frequency dependent, damping in structures can be treated more realistically. Visco-elastic analysis can be performed without much alteration of the spectral element code. Since the approach gives the FRF first, responses to different loading can be obtained using a single analysis. In summary, SFEM is a method in which the FFT algorithm is an essential part and gives problem sizes many orders smaller than conventional FEM. SFEM for isotropic waveguides are dealt in [11] and for composites and inhomogeneous structures in [18].

Formulation of the spectral elements requires determination of the spectrum (the variation of wavenumber with frequency) relations and the dispersion relations (speed with frequency). The procedure to determine these for certain waveguides will be given in the next chapter.The complete details of SFEM is discussed in Chap. 5.

1.4.6 Perturbation Techniques

The application of perturbation techniques for the simulation of the dynamic behavior of damaged structure is presented in detail in this book (Chap. 7). The approach leads to efficient computations, which can predict the interaction of propagating waves with damage, or the changes in the modal properties of the structure under consideration. The basic idea consists in expressing damage as a small reduction in thickness, or generally geometry, or a small variations in the mechanical properties (Young's modulus, density). Through a small parameter ε, straightforward expansions are performed so that a set of perturbation equations is obtained. The ε^0 equation corresponds to the undamaged system, while higher order terms introduce the effects of damage as variations with respect to the damage state. Of note is the fact that all the equations in the perturbation set have the same kernel, so that the same solution scheme can be conveniently applied. Damage appears as part of the forcing term in the higher order equations. Various solution methods have been used in conjunction with the perturbation technique, with the SFEM having a predominant role due to the savings in computational times it affords. The application of the perturbation technique has also been used

for the solution of nonlinear problems, as a result of a nonlinear stress–strain relationship as typically considered in nonlinear ultrasound. The expansion in terms of a small parameter leads to a set of linear equations which again can be solved either analytically, or using a discretization tool such as SFEM. Additional details are provided in Chap. 7, together with a number of examples, which show the generality of the perturbation approach for the simulation of wave–damage interaction.

1.5 Organization of the Book

This book is organized in three parts spread over ten chapters. The first part, which has three chapters, introduces the reader to some basic concepts in SHM. The need for SHM, the entire SHM process and the importance of modeling in SHM, is discussed. In Chap. 2, all the necessary theoretical background in theory of elasticity, composites and wave propagation is reviewed. These subjects are necessary to understand the material presented in this book. Chapter 3 presents the signal processing techniques, the understanding of which is crucial in handling many transient signals normally associated with SHM. Part-II of the book focuses on the computational and simulation techniques associated with SHM. This part is spread over six chapters. Both conventional finite element method and spectral finite element method and their associated damage models are reviewed. In Chap. 4, finite element method in the context of SHM is presented. Here, different ways of modeling flaws and the various issues associated with FE modeling are presented. In Chap. 5, spectral finite element method as a modeling tool is presented, wherein the formulation of elements for different 1D waveguides and some 2D waveguides are presented. Chapters 6 and 7 essentially address the formulation of simplified damage models required for SHM simulation. The damage models covered in these chapters include the modeling of different damage modes in composites such as delaminations, fibre breaks, pitting corrosion, material degradation and notch type damages. Chapter 8 addresses the modeling aspects of piezoelectric sensors/actuators used in SHM. Chapter 9 presents a multi-scale method formulated according to the bridging multi-scale technique. The chapter is followed by III, wherein different algorithms for damage detection and quantification are presented. Chapter 10 illustrates some of the damage detection algorithms based on vibration and wave propagation responses, which is followed by Chap. 11, wherein the use of soft computing tools such as the Genetic Algorithm and Artificial Neural Networks and their utility in damage detection are addressed.

The material presented in this book is comprehensive and covers all computational aspects associated with SHM. The book will serve as a useful reference text for graduate students and practicing engineers. The book can also be used to develop a gradate level course in SHM. The reader of the book is expected to have some knowledge in strength of materials, basic finite element method and the first course in Engineering mathematics.

References

1. Alleyne D, Cawley P (1991) A Two-dimensional Fourier transform method for the measurement of propagating multimode signals. J Acoust Soc Am 89:115968
2. Anderson JD (1995) Computational fluid dynamics: basics with applications. McGraw Hill, New York
3. Anderson G (2006) Providing best value IVHM solutions for aging aircraft. In: 9th joint FAA/DOD/NASA conference on aging aircraft, Atlanta, USA
4. Basri R, Chiu WK (2004) Numerical analysis on the interaction of guided lamb waves with a local elastic stiffness reduction in quasi-isotropic composite plate structures. Compos Struct 66:8799
5. Bathe KJ (1997) Finite element procedures. Printice Hall, Englewood Cliffs
6. Becker AA (1990) Boundary element method. Mcgraw Hill, New York
7. Beskos DE, Narayanan GV (1983) Dynamic response of frameworks by numerical laplace transform. Comput Methods Appl Mech Eng 37:289–307
8. Cantrell JH, Yost WT (2001) Nonlinear ultrasonic characterization of fatigue microstructures. Int J Fatigue 23(1):487–490
9. Cook RD, Malkus DS, Plesha ME, Witt RJ (2001) Concepts and applications of finite element analysis, 4th edn. Wiley, New York
10. Doebling SW, Farrar C, Prime MB, Daniel WS (1996) Damage identification and health monitoring of structural and mechanical systems from changes in their vibration characteristics: a literature review. LA-13070-MS, May
11. Doyle JF (1997) Wave propagation in structures. Springer, New York
12. Evans MJ, Cawley P (1999) Measurement and prediction of diffuse fields in structures. J Acoust Soc Am 106:3348–3360
13. Farrar C, James G (1987) System identification from ambient vibration measurements on a bridge. J Sound Vib 205:118
14. Giurgiutiu V (2005) Tuned lamb wave excitation and detection with piezoelectric wafer active sensors for structural health monitoring. J Intell Mater Syst Struct 16(4):291305
15. Giurgiutiu V (2007) Structural health monitoring: with piezoelectric wafer active sensors. Academic Press, New York
16. Giurgiutiu V, Bao J, Zhao W (2003) Piezoelectric wafer active sensor embedded ultrasonics in beams and plates. Exp Mech 43(4):428449
17. Gopalakrishnan S (2009) Modeling aspects in finite elements for structural health monitoring, encyclopedia on structural health monitoring, vol 2. Wiley, Chichester, pp 811–831, Chap. 43
18. Gopalakrishnan S, Chakraborty A, Roy Mahapatra D (2008) Spectral finite element method. Springer, London
19. Ihn J-B, Chang FK (2003) Detection and monitoring of hidden fatigue crack growth using a built-in piezoelectric sensor/actuator network: I. Diagnostics, 2004. Smart Mater Struct 13:609620
20. Kim JY, Jacobs LJ, Qu J, Littles JW (2006) Experimental characterization of fatigue damage in a nickel-base superalloy using nonlinear ultrasonic waves. J Acoust Soc Am 120(3):1266–1273
21. Krezig E (1992) Advanced engineering mathematics, 9th edn. McGraw Hill, New York
22. Langley RS (2007) On the diffuse field reciprocity relationship and vibrational energy variance in a random subsystem at high frequencies. J Acoust Soc Am 121:913921
23. Lanza Di Scalea F, Salamone S (2008) Temperature effects in ultrasonic lamb wave structural health monitoring systems. J Acoust Soc Am 124(1):161–174
24. Larose E, Roux P, Campillo M, Derode A (2008) Fluctuations of correlations and greens function reconstruction: role of scattering. Am Inst Phys 103:114907-1
25. Lee JW, Kim JD, Yun CB, Yi JH, Shim JM (2002) Health-monitoring method for bridges under ordinary traffic loadings. J Sound Vib 257(2):247–264

26. de Luis J, Crawley EF (1987) Use of piezoelectric actuators as elements of intelligent structures. AIAA J 25:13731385
27. Master ZM, Michaels TE, Michaels JE (2007) Incident wave removal for defect enhancement in acoustic wavefield imaging. In: AIP conference Proceedings vol 894, pp 665–672
28. Michaels TE, Michaels JE, Mi B, Ruzzene M (2005) Damage detection in plate structures using sparse transducer arrays and acoustic wavefield imaging. In: Thompson DO, Chimenti DE (eds) Review of progress in quantitative nondestructive evaluation, AIP 24A, 2005
29. Mustapha F, Manson G, Worden K, Pierce SG (2006) Damage location in an isotropic plate using a vector of novelty indices. Mech Syst Signal Process 21:18851906
30. Nagy PB (1998) Fatigue damage assessment by nonlinear ultrasonic materials characterization. Ultrasonics 36:375–381
31. Oseguda R, Kreinovich V, Nazarian S, Roldan E (2003) Detection of cracks at rivet holes in thin plates using Lamb wave scanning. Proc SPIE 5047:55–66
32. Prasad MS et al (2003) Imaging of defects in composite structures using guided ultrasonics. Proc SPIE 5062:700–703
33. Prasad SM, Balasubramaniam K, Krishnamurthy CV (2004) Structural health monitoring of composite structures using lamb wave tomography. Smart Mater Struct 13:7379
34. Prosser WH, Seale MD, Smith BT (1999) Time-frequency analysis of the dispersion of lamb modes. J Acoust Soc Am 105(5):26692676
35. Raghavan A, Cesnik CES (2005) Finite-dimensional piezoelectric transducers modeling for guided wave based structural health monitoring. Smart Mater Struct 14:4481461
36. Raghavan A, Cesnik CES (2007) Review of guided-wave structural health monitoring. Shock Vib Dig 39(2):91114
37. Raghavan A, Cesnik CES (2007) Guided-wave signal processing using chirplet matching pursuits and mode correlation for structural health monitoring. Smart Mater Struct 16(2):355366
38. Randall BR (2004) State of the art in monitoring rotating machinerypart 1. J Sound Vib 38:1421
39. Randall BR (2004) State of the art in monitoring rotating machinerypart 2. J Sound Vib 38:1017
40. Reddy JN (1985) Finite element method. McGraw Hill, New York
41. Rizzo P, Bartoli I, Marzani A, Lanzadi Scalea F (2005) Defect classification in pipes by neural network using multiple guided ultrasonic wave features extracted after wavelet processing. Trans ASME J Press Vessel Technol 127:294303
42. Rose JL (2002) A baseline and vision of ultrasonic guided wave inspection potential. J Press Vessel Technol 124:273–282
43. Roux P, Sabra KG, Kuperman W, Roux A (2005) Ambient noise cross correlation in free space: theoretical approach. J Acoust Soc Am 117:79–84
44. Ruzzene M (2007) Frequency/wavenumber filtering for improved damage visualization. Smart Mater Struct 16:21162129
45. Sabra KG, Roux P, Kuperman WA (2005) Arrival-time structure of the time-averaged ambient noise cross-correlation function in an oceanic waveguide. J Acoust Soc Am 117:164–174
46. Sabra KG, Winkel ES, Bourgoyne DA, Elbing BR, Ceccio SL, Perlin M, Dowling DR (2007) Using cross correlations of turbulent flow-induced ambient vibrations to estimate the structural impulse response. Application to structural health monitoring. J Acoust Soc Am 121:19872005
47. Sabra KG, Srivastava A, Lanzadi Scalea F, Bartoli I, Rizzo P, Conti S (2008) Structural health monitoring by extraction of coherent guided waves from diffuse fields. J Acoust Soc Am 123:EL8–EL13
48. Salvino L, Purekar A, Pines DJ (2005) Health monitoring of 2-D plates using EMD and hilbert phase. In: Proceedings of the 4th international workshop on structural health monitoring, Stanford University, CA

49. Shapiro NM, Campillo M, Stehly L, Ritzwoller M (2005) High resolution surface-wave tomography from ambient seismic noise. Science 29:1615–1617
50. Sharma V, Ruzzene M, Hanagud S (2006) Damage index estimation in beams and plates using laser vibrometry. AIAA J 44:919923
51. Sohn H, Farrar CR, Hemez FM, Czarnecki JJ, Shunk DD, Stinemates DW, Nadler BR (2003) A review of structural health monitoring literature: 19962001. Los Alamos National Laboratory Report, LA-13976-MS
52. Staszewski WJ, Boller C, Tomlinson G (2004) Health monitoring of aerospace structures. Smart sensors and signal processing. Wiley, Chichester
53. Staszewski WJ, Lee BC, Mallet L, Scarpa F (2004) Structural health monitoring using laser vibrometry. Part I and II. Smart Mater Struct 13:251269
54. Su Z, Ye L (2004) An intelligent signal processing and pattern recognition technique for defect identification using an active sensor network. Smart Mater Struct 13(4):957969
55. Varadan VK, Vinoy KJ, Gopalakrishnan S (2006) Smart material systems and MEMS. Wiley, Chichester
56. Viktorov IA (1967) Rayleigh and lamb waves. Plenum, New York
57. Weaver RL (1982) On diffuse waves in solid media. J Acoust Soc Am 71:1608–1609
58. Weaver RL (1984) Diffuse waves in finite plates. J Sound Vib 94:319335
59. Weaver RL, Lobkis OI (2001) Ultrasonics without a source: thermal fluctuation correlations at MHz frequencies. Phys Rev Lett 87:134301
60. Worden K, Dulieu-Barton JM (2004) An overview of intelligent fault detection in systems and structures. Int J Struct Health Monit 3:8598

Chapter 2
Fundamentals Concepts in Elasticity, Mechanics and Wave Propagation

2.1 Introduction

One of the fundamental concepts involved in the mathematical modeling is to first generate the governing differential equation of the system. There are two general ways of doing this. In the first method, the system is broken at the continuum level and the 3D state of stress acting on block are written. Writing the equilibrium equation of this free body essentially gives the equation governing the system. 2D and 1D approximations can further be obtained from the 3D equations of motion by converting the stresses into stress resultants through integration of the equation of motion in the directions where the condensation of the dimension is desired. The method described above is the theory of elasticity procedure of obtaining the governing equation. One can see that, in this method, one has to deal with tensors and vectors. This chapter will give the complete bird's eye view on this subject.

An alternate way of generating the governing equations is by energy methods, wherein the minimization of an energy functional yields the desired governing equations along with the associated boundary conditions. This is the most widely used method in techniques (see Chap. 4), where obtaining an approximate solution to the governing equation is the main goal.

2.2 Basic Concepts in Elasticity

2.2.1 Description of Motion

Consider a body undergoing deformation to some applied loading (see Fig. 2.1). Let $\boldsymbol{u}^0$ be its position at time $t = 0$ (undeformed configuration) and $\boldsymbol{u}^t$ its position at time t. The motion of the body can be expressed in terms of the Eulerian coordinates

$$\boldsymbol{u} = \boldsymbol{u}(x^0, y^0, z^0, t) \tag{2.1}$$

S. Gopalakrishnan et al., *Computational Techniques for Structural Health Monitoring*, Springer Series in Reliability Engineering, DOI: 10.1007/978-0-85729-284-1_2,

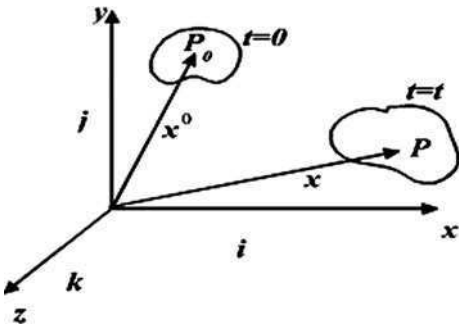

Fig. 2.1 Undeformed and deformed configuration of a body

which is normally used to represent fluid in motion, or the Lagrangian coordinates:

$$\boldsymbol{u}^0 = \boldsymbol{u}^0(x, y, z, t) \tag{2.2}$$

where quantities are expressed in terms of the initial position vector $\boldsymbol{u}^0$ and time t.

In here and in the following, bold lower case letters denote vectors, while bold capitals denote matrices.

Due to the above definitions, the evaluation of material derivative differ. In the Eulerian frame of reference, the derivative of $\boldsymbol{u}(x^0, y^0, z^0, t)$ is given by

$$\frac{d\boldsymbol{u}}{dt} = \frac{\partial \boldsymbol{u}}{\partial t} \tag{2.3}$$

while in the Lagrangian frame, the derivative of $\boldsymbol{u}^0(x, y, z, t)$ is given by

$$\frac{d\boldsymbol{u}}{dt} = \frac{\partial \boldsymbol{u}}{\partial t} + \frac{\partial \boldsymbol{u} dx}{\partial x\, dt} + \frac{\partial \boldsymbol{u} dy}{\partial y\, dt} + \frac{\partial \boldsymbol{u} dz}{\partial z\, dt} = \frac{\partial \boldsymbol{u}}{\partial t} + v_x \frac{\partial \boldsymbol{u}}{\partial x} + v_y \frac{\partial \boldsymbol{u}}{\partial y} + v_z \frac{\partial \boldsymbol{u}}{\partial z} \tag{2.4}$$

where v_x, v_y, and v_z are the convective velocity in the three material directions.

The motion of a particle is defined in terms of its coordinates attached to the particle. Displacement is for example defined as the shortest distance traveled when a particle moves from one location to the other. If the position vectors of two points are $\boldsymbol{r}_1$ and $\boldsymbol{r}_2$, the displacement vector $\boldsymbol{u}$ is given by

$$\boldsymbol{u} = \boldsymbol{r}_2 - \boldsymbol{r}_1 = (x_2\boldsymbol{i} + y_2\boldsymbol{j} + z_2\boldsymbol{k}) - (x_1\boldsymbol{i} + y_1\boldsymbol{j} + z_2\boldsymbol{k})$$

In other words, the displacement vector can be written as

$$\boldsymbol{u} = (x_2 - x_1)\boldsymbol{i} + (y_2 - y_1)\boldsymbol{j} + (z_2 - z_1)\boldsymbol{k} \tag{2.5}$$

Deformation is defined as the comparison of two states, namely the initial and the final configuration. The deformation gradient is a concept extensively used in the theory of elasticity, which relates the behavior of the neighboring particles. Consider

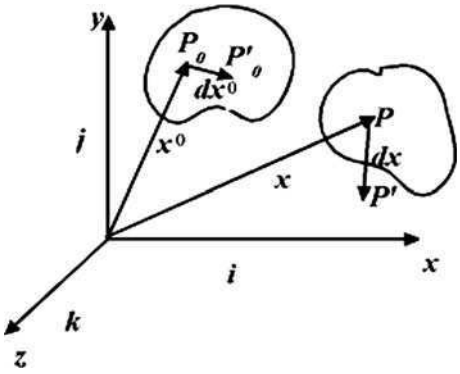

Fig. 2.2 Deformation of neighboring points

points P_0 and P'_0, which at time $t = 0$ are at a distance $d\boldsymbol{r}^0 = dx^0\boldsymbol{i} + dy^0\boldsymbol{j} + dz^0\boldsymbol{k}$ (Fig. 2.2). At time t, the two points move to locations P and P', so that the new distance is denoted $d\boldsymbol{r} = dx\boldsymbol{i} + dy\boldsymbol{j} + dz\boldsymbol{k}$. The location of P' with respect to P is given by $\boldsymbol{r} + d\boldsymbol{r} = (x + dx)\boldsymbol{i} + (y + dy)\boldsymbol{j} + (z + dz)\boldsymbol{k}$.

Consider the first term in the vector, namely $(x + dx)$. Expanding this term in Taylor series with respect to variables corresponding at time $t = 0$, gives

$$x + dx = x + \frac{\partial x}{\partial x^0}dx^0 + \frac{\partial x}{\partial y^0}dy^0 + \frac{\partial x}{\partial z^0}dz^0 \cdots \tag{2.6}$$

which gives the following relation along with analogues for the other components:

$$\begin{aligned} dx &= \frac{\partial x}{\partial x^0}dx^0 + \frac{\partial x}{\partial y^0}dy^0 + \frac{\partial x}{\partial z^0}dz^0 \\ dy &= \frac{\partial y}{\partial x^0}dx^0 + \frac{\partial y}{\partial y^0}dy^0 + \frac{\partial y}{\partial z^0}dz^0 \\ dz &= \frac{\partial z}{\partial x^0}dx^0 + \frac{\partial z}{\partial y^0}dy^0 + \frac{\partial z}{\partial z^0}dz^0 \end{aligned}$$

In tensorial notation, these expressions can be written as:

$$dx_i = \frac{\partial x_i}{\partial x_j^0}dx_j^0 \quad i,j = 1,2,3 \tag{2.7}$$

where $x_1 = x, x_2 = y, x_3 = z$.

Similarly, the motion of particles at time $t = 0$ can be expressed in terms of the current time t as

$$dx_i^0 = \frac{\partial x_i^0}{\partial x_j}dx_j \quad i,j = 1,2,3 \tag{2.8}$$

The quantities $\partial x_i/\partial x_j^0$ and $\partial x_i^0/\partial x_j$ are the *deformation gradients* and they form the basis of description of any deformation state.

When expanded and written in the matrix form Eqs. 2.7 and 2.8 become

$$d\boldsymbol{r} = \boldsymbol{J}_0 d\boldsymbol{r}^0$$
$$\begin{Bmatrix} dx \\ dy \\ dz \end{Bmatrix} = \begin{bmatrix} \frac{\partial x}{\partial x^0} & \frac{\partial x}{\partial y^0} & \frac{\partial x}{\partial z^0} \\ \frac{\partial y}{\partial x^0} & \frac{\partial y}{\partial y^0} & \frac{\partial y}{\partial z^0} \\ \frac{\partial z}{\partial x^0} & \frac{\partial z}{\partial y^0} & \frac{\partial z}{\partial z^0} \end{bmatrix} \begin{Bmatrix} dx^0 \\ dy^0 \\ dz^0 \end{Bmatrix} \tag{2.9}$$

and,

$$d\boldsymbol{r}^0 = \boldsymbol{J} d\boldsymbol{r}$$
$$\begin{Bmatrix} dx^0 \\ dy^0 \\ dz^0 \end{Bmatrix} = \begin{bmatrix} \frac{\partial x^0}{\partial x} & \frac{\partial x^0}{\partial y} & \frac{\partial x^0}{\partial z} \\ \frac{\partial y^0}{\partial x} & \frac{\partial y^0}{\partial y} & \frac{\partial y^0}{\partial z} \\ \frac{\partial z^0}{\partial x} & \frac{\partial z^0}{\partial y} & \frac{\partial z^0}{\partial z} \end{bmatrix} \begin{Bmatrix} dx \\ dy \\ dz \end{Bmatrix} \tag{2.10}$$

The matrices $\boldsymbol{J}$ and $\boldsymbol{J}_0$ are the *Jacobian* matrices. Since the deformation is continuous, the determinant of the Jacobian matrices must not equal to zero. Since no region of finite volume can be deformed into a region of zero or infinite volume, it is required that the following conditions are satisfied

$$0 < J_0 < \infty, \quad 0 < J < \infty \tag{2.11}$$

where $J = \det[\boldsymbol{J}], J_0 = \det[\boldsymbol{J}_0]$. The above condition is very useful to verify that the deformation is physically possible. The above relations, allow the expression of the deformation of a line, an area or a volume in a straightforward manner.

2.2.2 Strain

Strain is a measure of relative displacement among particles within a body, which is essential ingredient for the description of the constitutive behavior of materials. There are three different measures of strain, which can be described on a specimen of initial and final length L_0 and L according to the following three definitions:

1. Engineering Strain:

$$\varepsilon = \frac{L - L_0}{L_0} = \frac{\Delta L}{L_0}$$

2. True Strain:

$$\varepsilon^t = \frac{\Delta L}{L} = \frac{\Delta L}{L_0 + \Delta L}$$

3. Logarithmic Strain:

$$\varepsilon^n = \int_{L_0}^{L} \frac{dl}{l} = \ln\left(\frac{L}{L_0}\right)$$

According to three definitions above, the final Length L can be written in terms of the engineering strain:

$$L = L_0 + \Delta L = L_0 + L_0\varepsilon = L_0(1+\varepsilon)$$

the true strain:

$$L = L_0 + \Delta L = L_0 + \frac{\varepsilon^t L_0}{(1-\varepsilon^t)} = \frac{L_0}{(1-\varepsilon^t)}$$

and the logarithmic strain:

$$L = L_0 \exp(\varepsilon^n)$$

The three strain measures are related by the following expressions

$$\varepsilon^t = \frac{\varepsilon}{1+\varepsilon}, \quad \varepsilon^n = \ln(1+\varepsilon)$$

Strain measures are normally established by considering the change in the distance between two neighboring material particles. Consider two material particles having coordinates (x^0, y^0, z^0) and $(x^0 + dx^0, y^0 + dy^0, z^0 + dz^0)$. After the motion, these particles will have the coordinates (x, y, z) and $(x + dx, y + dy, z + dz)$. The initial and final distances between these neighboring particles are given by

$$(dr^0)^2 = (dx^0)^2 + (dy^0)^2 + (dz^0)^2 \tag{2.12}$$

$$dr^2 = (dx)^2 + (dy)^2 + (dz)^2 \tag{2.13}$$

Substituting Eq. 2.9 in Eq. 2.13 gives:

$$dr^2 = d\boldsymbol{r}^T d\boldsymbol{r} = d\boldsymbol{r}^{0^T} \boldsymbol{J}_0^T \boldsymbol{J}_0 d\boldsymbol{r}^0 \tag{2.14}$$

In the event that deformation, dr^2 is different from $(dr^0)^2$. That is

$$dr^2 - dr_0^2 = d\boldsymbol{r}^{0^T} \boldsymbol{J}_0^T \boldsymbol{J}_0 d\boldsymbol{r}_0 - d\boldsymbol{r}^{0^T} d\boldsymbol{r}^0 = 2d\boldsymbol{r}^{0^T} \boldsymbol{E}_0 d\boldsymbol{r}^0 \tag{2.15}$$

where $\boldsymbol{E}_0 = \boldsymbol{J}_0^T \boldsymbol{J}_0 - \boldsymbol{I}$.

The above measure gives the relative displacements between the two material particles, which is insensitive to rotations. If the Eulerian frame of reference is used, then the relative displacement is given by

$$\begin{aligned} dr^2 - (dr^0)^2 &= d\boldsymbol{r}^T d\boldsymbol{r} - d\boldsymbol{r}^T \boldsymbol{J}^T \boldsymbol{J} d\boldsymbol{r} \\ &= 2d\boldsymbol{r}^T \boldsymbol{E} d\boldsymbol{r} \end{aligned} \tag{2.16}$$

where $\boldsymbol{E} = \boldsymbol{I} - \boldsymbol{J}^T \boldsymbol{J}$.

In Eqs. 2.15 and 2.16, the matrices $\boldsymbol{E}_0$ and $\boldsymbol{E}$ are the Lagrangian and Eulerian strain tensors. In tensorial form, they are given by

$$E_{0_{ij}} = \frac{1}{2}\left(\frac{\partial x_m}{\partial x_i^0}\frac{\partial x_m}{\partial x_j^0} - \delta_{ij}\right) \tag{2.17}$$

$$E_{ij} = \frac{1}{2}\left(\delta_{ij} - \frac{\partial x_m^0}{\partial x_i}\frac{\partial x_m^0}{\partial x_j}\right) \tag{2.18}$$

The physical significance of $E_{0_{ij}}$ and E_{ij} can be established by considering a line element of length $dr^0 = dx^0$. The extension of the line element per unit length E_{0_1} is given by

$$\begin{aligned} &E_{0_1} = \frac{dr - dr^0}{dr^0} \quad \text{or} \quad dr = (1 + E_{0_1})dr^0 \\ &dr^2 - dr^{0^2} = 2E_{0_{11}} dr^{0^2} \end{aligned} \tag{2.19}$$

Combining the above, we can establish the relationship between E_{0_1} and $E_{0_{11}}$ as

$$E_{0_{11}} = E_{0_1} + \frac{1}{2}E_{0_1}^2 \quad \text{or} \quad E_{0_1} = \sqrt{1 + 2E_{0_{11}}} - 1 \tag{2.20}$$

Expanding the right hand term by binomial expansion, we get

$$E = (1 + E_{0_{11}} - \frac{1}{2}E_{0_{11}}^2 + \cdots) - 1 \approx E_{0_{11}} - \frac{1}{2}E_{0_{11}}^2 \tag{2.21}$$

For small $E_{0_{11}}, E_{0_1} = E_{0_{11}}$, so that $E_{0_{11}}$ can be interpreted as an elongation per unit length only when the extension is very small. Similarly, we can write

$$E_{0_2} = \sqrt{1 + 2E_{0_{22}}} - 1, \quad E_{0_3} = \sqrt{1 + 2E_{0_{33}}} - 1 \tag{2.22}$$

2.2.3 Strain–Displacement Relations

In most of the analysis methods to follow, it is customary to deal with the displacement and displacement gradients rather than deformation gradients. If u, v and w are the three displacements in the three coordinate directions. Hence, we can write

$$x = x^0 + u, \quad y = y^0 + v, \quad z = z^0 + w \tag{2.23}$$

The derivatives of these can be written as

$$\begin{aligned}
\frac{\partial x}{\partial x^0} &= 1 + \frac{\partial u}{\partial x^0}, \quad \frac{\partial y}{\partial x^0} = \frac{\partial v}{\partial x^0}, \quad \frac{\partial z}{\partial x^0} = \frac{\partial w}{\partial x^0} \\
\frac{\partial x}{\partial y^0} &= \frac{\partial u}{\partial y^0}, \quad \frac{\partial y}{\partial y^0} = 1 + \frac{\partial v}{\partial y^0}, \quad \frac{\partial z}{\partial y^0} = \frac{\partial w}{\partial y^0} \\
\frac{\partial x}{\partial z^0} &= \frac{\partial u}{\partial z^0}, \quad \frac{\partial y}{\partial z^0} = \frac{\partial v}{\partial z^0}, \quad \frac{\partial z}{\partial z^0} = 1 + \frac{\partial w}{\partial z^0}
\end{aligned}$$

In tensorial form, we can write the above equations as

$$\frac{\partial x_m}{\partial x_i^0} = \frac{\partial u_m}{\partial x_i^0} + \delta_{im} \tag{2.24}$$

Similarly, one can write

$$\begin{aligned}
\frac{\partial x^0}{\partial x} &= 1 - \frac{\partial u}{\partial x}, \quad \frac{\partial y^0}{\partial x} = -\frac{\partial v}{\partial x}, \quad \frac{\partial z^0}{\partial x} = -\frac{\partial w}{\partial x} \\
\frac{\partial x^0}{\partial y} &= -\frac{\partial u}{\partial y}, \quad \frac{\partial y^0}{\partial y} = 1 - \frac{\partial v}{\partial y}, \quad \frac{\partial z^0}{\partial y} = \frac{\partial w}{\partial y} \\
\frac{\partial x^0}{\partial z} &= -\frac{\partial u}{\partial z}, \quad \frac{\partial y^0}{\partial z} = -\frac{\partial v}{\partial z}, \quad \frac{\partial z^0}{\partial z} = 1 - \frac{\partial w}{\partial z}
\end{aligned}$$

In tensorial form, the above equations become

$$\frac{\partial x_m^0}{\partial x_i} = \delta_{im} - \frac{\partial u_m}{\partial x_i} \tag{2.25}$$

where, δ_{ij} is the kronecker delta. Substituting Eqs. 2.24 and 2.25 in the Lagrangian and Eulerian strain tensors (Eq. 2.18), we get after some simplification

$$\begin{aligned}
E_{0_{ij}} &= \frac{1}{2}\left[\frac{\partial u_i}{\partial x_j^0} + \frac{\partial u_j}{\partial x_i^0} + \frac{\partial u_m}{\partial x_i^0}\frac{\partial u_m}{\partial x_j^0}\right] \\
E_{ij} &= \frac{1}{2}\left[\frac{\partial u_i}{\partial x_j} + \frac{\partial u_j}{\partial x_i} + \frac{\partial u_m}{\partial x_i}\frac{\partial u_m}{\partial x_j}\right]
\end{aligned} \tag{2.26}$$

The first two terms in the above two equations represent the linear part of the strain tensors, while the last term represents the nonlinear part. Both these tensors are symmetric. When the displacement gradients are very small, we can neglect the nonlinear part of in above tensors. Thus, infinitesimal strain components have direct interpretations as extensions or change of angles. Further, the magnitudes of the strains are very small compared to unity, which means that deformations are very small.

In this book, we will mostly consider the linear part of the strain–displacement relations and in addition, we will assume that the deformations are very small compared to the characteristic dimension of the structure. This will make $x_i^0 = x_i$. In other words, all the problems in this text book will be formulated in the Lagrangian frame of reference.

2.2.4 Stress

Strains (deformations) are normally caused by forces or moments exerted on the continuum or through contacts. Contact forces are normally referred to as surface tractions as they occur on the surface of the continuum. The different types of forces or moments can be *extrinsic, mutual or contact* type, depending upon the way these act on a body. Extrinsic forces act outside the body under consideration. Examples are gravity load, magnetic loads etc. Mutual forces arise within the body. The most general type of forces is of contact type which generate stress or pressure.

To explain the concept of stress, let us consider a small surface element of area ΔA in the deformed configuration (Fig. 2.3). The forces and moments should be acting in this small elemental area such that they cancel each other, or in other words, the elemental area should be in equilibrium. These forces can be thought of as contact forces although they act inside a body. Let $\boldsymbol{n}$ be a unit vector perpendicular to the surface of the elemental area and let $\Delta \boldsymbol{f}$ be the resultant force exerted on the surface element ΔA. In the limiting case of ΔA becoming very small, one can define the traction as follows:

$$\boldsymbol{t}^{(n)} = \frac{d\boldsymbol{f}}{dA} = \lim_{\Delta A \to 0} \frac{\Delta \boldsymbol{f}}{\Delta A} \tag{2.27}$$

The above limit is possible due to the assumption that the material is continuous. This traction vector describes a unit of force per unit area acting on the surface. The superscript (n) remind the reader that the traction vector is dependent on the orientation of the area. To give explicit representation of traction vector, let us consider the elementary cube shown in Fig. 2.4 showing the components of the traction vector on the three faces of the cube. Considering $\boldsymbol{n} = \boldsymbol{i}$:

$$\boldsymbol{t}^{(i)} = t_x^{(i)}\boldsymbol{i} + t_y^{(i)}\boldsymbol{j} + t_z^{(i)}\boldsymbol{k}$$

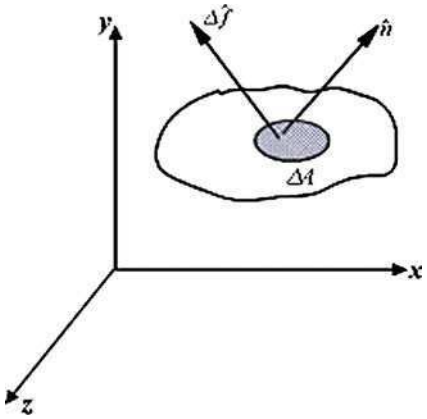

Fig. 2.3 A section of an arbitrary continuum

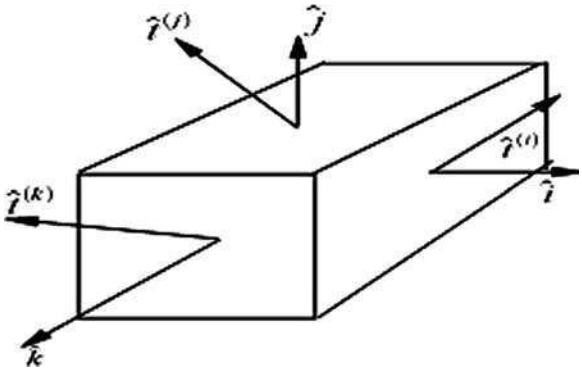

Fig. 2.4 Stress cube with stress vectors and outward unit normal

Similarly for $\boldsymbol{n} = \boldsymbol{j}$ and $\boldsymbol{n} = \boldsymbol{k}$:

$$\boldsymbol{t}^{(j)} = t_x^{(j)}\boldsymbol{i} + t_y^{(j)}\boldsymbol{j} + t_z^{(j)}\boldsymbol{k}$$
$$\boldsymbol{t}^{(k)} = t_x^{(k)}\boldsymbol{i} + t_y^{(k)}\boldsymbol{j} + t_z^{(k)}\boldsymbol{k}$$

The above definition can be simplified by introducing a second order tensor $\sigma_{ij} = t_j^{(i)}$, which describes the direction of traction and its plane of application. That is, in the $x - z$ plane, $\sigma_{xx} = t_x^{(i)}, \sigma_{xz} = t_z^{(i)}, \sigma_{zx} = t_x^{(k)}$. Hence, the projections of the traction vector $\boldsymbol{t}^{(n)}$ on the faces are the normal stress components σ_{xx}, σ_{yy} and σ_{zz}, while projections perpendicular to outward normal $\boldsymbol{n}$ are the shear stress components $\sigma_{xy}, \sigma_{yz}, \sigma_{zx}, \sigma_{yx}, \sigma_{zy}$ and σ_{xz}.

The matrix containing all the nine stress components σ_{ij} is called the *Cauchy's Stress Tensor*, which is a symmetric tensor, i.e. $\sigma_{ij} = \sigma_{ji}$.

Next, we can establish the relation between the traction vector $\boldsymbol{t}$ and the outward normal $\boldsymbol{n}$. For this purpose, consider the arbitrary surface of a tetrahedron shown in Fig. 2.5.

On the faces perpendicular to the reference axes, the components of the three stress vectors are denoted by the corresponding stress components σ_{ij} on the

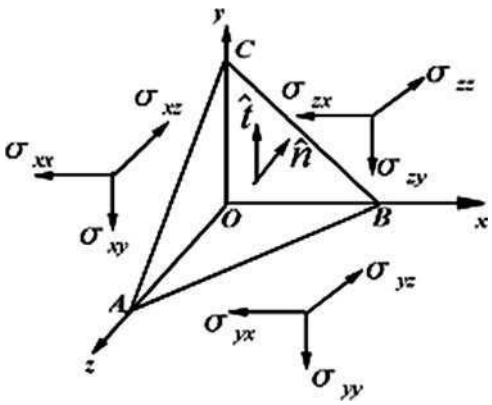

Fig. 2.5 Stresses acting on an arbitrary surface of a tetrahedron

plane on which they are acting. For example, the stresses acting on the face normal to x-axis are denoted as $\sigma xx, \sigma xy$ and σxz.

The equilibrium of the tetrahedron requires that the resultant force acting on it vanishes. Imposing equilibrium along the x-direction gives

$$t_x dA - \sigma_{xx} dA_x - \sigma_{yx} dA_y - \sigma_{zx} dA_z + b_x \rho dV = 0 \tag{2.28}$$

where b_x is the x-component of the body force vector $\boldsymbol{b}$. Here t_x is the x-component of the traction vector, dA_x, dA_y, and dA_z are the areas of the face perpendicular to the coordinate axes x, y, and z axes, while dA is the area of the inclined surface ABC. Also, $dV = (1/3)hdA$ is the volume of the tetrahedron, where h is the smallest distance from any point to the inclined surface ABC. The outward normal vector can be written in terms of unit vectors along the three reference directions as $\boldsymbol{n} = n_x\boldsymbol{i} + n_y\boldsymbol{j} + n_z\boldsymbol{k}$. The elemental areas dA_i can now be written in terms of components of unit normal vector as

$$dA_x = n_x dA, \quad dA_y = n_y dA, \quad dA_z = n_z dA \tag{2.29}$$

Substituting Eq. 2.28 in Eq. 2.29 and letting $dA \to 0$, we get the traction–stress relation in the x-direction as

$$t_x = \sigma_{xx} n_x + \sigma_{yx} n_y + \sigma_{zx} n_z \tag{2.30}$$

Similarly, traction–stress relation in the y and z directions can be written as

$$t_y = \sigma_{xy} n_x + \sigma_{yy} n_y + \sigma_{zy} n_z$$
$$t_z = \sigma_{xz} n_x + \sigma_{yz} n_y + \sigma_{zz} n_z$$

The above equations can be written in tensorial form as

$$t_i = \sigma_{ij} n_j \tag{2.31}$$

which is valid for any outward normal vector and in any coordinate system. Hence, it can be concluded that the state of stress in a body is completely known if the stress tensor σ_{ij} is given. In other words, given any surface and associated unit normal vector $\boldsymbol{n}$, it is possible to determine a traction vector acting on that surface if the stress tensor is known.

2.2.5 Constitutive Relations

Constitutive relations relate the stresses developed with the strains through a material matrix. The constitutive relations are normally established under certain assumptions. These can be summarized as the following:

1. The stress at a point depends on geometric changes that take place in the immediate vicinity.
2. There are no history effects. The present state of stress will give the strain. Hence the presence of material nonlinearity is generally assumed negligible.

3. The structure under loading will bounce back to its original shape upon load removal.
4. Temperature changes only cause a change in shape or volume but otherwise do not directly affect the stresses.
5. The material is homogeneous. That is, the material properties are not a function of spatial coordinates.
6. Displacements and strains are small.

The constitutive model is normally referred to as *Hooke's Law*. It is based on the assumption that for an elastic body, the stress depends only on deformation and not on the history of deformation. This can be mathematically expressed as

$$\sigma_{ij} = f_{ij}(\varepsilon_{ij}) \tag{2.32}$$

Expanding the above term by Taylor series about the initial configuration ($t = 0$), we get

$$\sigma_{ij} = f_{ij}(0) + \left[\frac{\partial f_{ij}(0)}{\partial \varepsilon_{kl}}\right]\varepsilon_{kl} + \frac{1}{2}\left[\frac{\partial^2 f_{ij}(0)}{\partial \varepsilon_{kl}\varepsilon_{mn}}\right]\varepsilon_{kl}\varepsilon_{mn} + \cdots \tag{2.33}$$

If the assumption of zero initial stress is true, then we require $\sigma_{ij} = 0$ when $\varepsilon_{ij} = 0$. This condition leads to $f_{ij} = 0$. The second term in Eq. 2.33 is the linear term and all other terms in the expression are nonlinear. Retaining only the linear term due to small strain assumption, we can write Eq. 2.33 as

$$\sigma_{ij} = C_{ijkl}\varepsilon_{kl} \quad \text{with} \quad C_{ijkl} = \left[\frac{\partial f_{ij}(0)}{\partial \varepsilon_{kl}}\right] \tag{2.34}$$

The Eq. 2.34 is called the *Hooke's Law*, which states that the stress tensor is linearly related to the strain tensor through a fourth order tensor called the *Constitutive Matrix*.

The term in Eq. 2.34 C_{ijkl} is a fourth order tensor of elastic constants, which are independent of either stress or strain. The tensorial quality of the constants C_{ijkl} follows the quotient rule, according to which for a fourth order tensor, it should have $3^4 = 81$ elements. Due to symmetry of the stress tensor ($\sigma_{ij} = \sigma_{ji}$), we should have $C_{ijkl} = C_{jikl}$. Further more, since the strain tensor is also symmetric ($\varepsilon_{kl} = \varepsilon_{lk}$), we have $C_{ijkl} = C_{ijlk}$. Under these conditions, the fourth order tensor C_{ijkl} will have only 36 independent constants. Hence, the total number of elastic constants cannot exceed 36, since the maximum independent elements in the stress and strain tensors are only six each. With these reductions, the generalized Hook's law can be written in the matrix form as

$$\begin{Bmatrix} \sigma_{xx} \\ \sigma_{yy} \\ \sigma_{zz} \\ \tau_{yz} \\ \tau_{xz} \\ \tau_{xy} \end{Bmatrix} = \begin{bmatrix} C_{11} & C_{12} & C_{13} & C_{14} & C_{15} & C_{16} \\ C_{21} & C_{22} & C_{23} & C_{24} & C_{25} & C_{26} \\ C_{31} & C_{32} & C_{33} & C_{34} & C_{35} & C_{36} \\ C_{41} & C_{42} & C_{43} & C_{44} & C_{45} & C_{46} \\ C_{51} & C_{52} & C_{53} & C_{54} & C_{55} & C_{56} \\ C_{61} & C_{62} & C_{63} & C_{64} & C_{65} & C_{66} \end{bmatrix} \begin{Bmatrix} \varepsilon_{xx} \\ \varepsilon_{yy} \\ \varepsilon_{zz} \\ \gamma_{yz} \\ \gamma_{xz} \\ \gamma_{xy} \end{Bmatrix} \tag{2.35}$$

where all the τ's represent the shear stresses in their respective planes, while all the γ's are the corresponding shear strains. For most elastic solids, the number of elastic constants can further be reduced by exploiting the material symmetry about different reference planes.

2.2.6 Elastic Symmetry

A material having all the 36 unknown material constant is said to be *anisotropic* (*Triclinic System*). However, if the internal composition of a material possesses symmetry of any kind, then symmetry can also be observed in the elastic properties. The presence of symmetry reduces the number of independent constants. Such simplification in the generalized Hooke's law can be obtained as follows. Let x, y, and z define the original coordinate system of the body. Let x', y' and z' be a second coordinate system, which is symmetric to the first system in accordance with the form of elastic symmetry. Since the directions of similar axes of both systems are equivalent with respect to elastic properties, the equations of the generalized Hooke's law will have the same form in both coordinate systems and the corresponding constants should be identical.

2.2.6.1 Monoclinic System: One Elastic Symmetric Plane

Suppose the material system is symmetric about the z-axis, the second coordinate system x', y' and z' can be described by the following base unit vectors.

$$\boldsymbol{e}_1 = \{1, 0, 0\}, \quad \boldsymbol{e}_2 = \{0, 1, 0\}, \quad \boldsymbol{e}_3 = \{0, 0, -1\}$$

Using this, we can construct a transformation matrix with base vectors as columns of the transformation matrix. For the above case, the transformation matrix and the stress tensor in primed coordinate system becomes

$$\boldsymbol{T} = \begin{bmatrix} 1 & 0 & 0 \\ 0 & 1 & 0 \\ 0 & 0 & -1 \end{bmatrix}$$

which gives:

$$\boldsymbol{\sigma}' = \boldsymbol{T}^T \boldsymbol{\sigma} \boldsymbol{T} = \begin{bmatrix} \sigma_{xx} & \tau_{xy} & -\sigma_{xz} \\ \tau_{yx} & \sigma_{yy} & -\tau_{yx} \\ -\sigma_{zx} & -\tau_{zy} & \sigma_{zz} \end{bmatrix}$$

Similarly, transforming the strains in the primed coordinate gives

$$\boldsymbol{\varepsilon}' = \begin{bmatrix} \varepsilon_{xx} & \gamma_{xy} & -\varepsilon_{xz} \\ \gamma_{yx} & \varepsilon_{yy} & -\gamma_{yz} \\ -\varepsilon_{zx} & -\gamma_{zy} & \varepsilon_{zz} \end{bmatrix}$$

so that:

$$\boldsymbol{\sigma}' = \boldsymbol{C}\boldsymbol{\varepsilon}'$$

Using the above relations, the constitutive law in the original coordinate system becomes

$$\begin{Bmatrix} \sigma_{xx} \\ \sigma_{yy} \\ \sigma_{zz} \\ \tau_{yz} \\ \tau_{xz} \\ \tau_{xy} \end{Bmatrix} = \begin{bmatrix} C_{11} & C_{12} & C_{13} & -C_{14} & -C_{15} & C_{16} \\ C_{21} & C_{22} & C_{23} & -C_{24} & -C_{25} & C_{26} \\ C_{31} & C_{32} & C_{33} & -C_{34} & -C_{35} & C_{36} \\ -C_{41} & -C_{42} & -C_{43} & C_{44} & C_{45} & -C_{46} \\ -C_{51} & -C_{52} & -C_{53} & C_{54} & C_{55} & -C_{56} \\ C_{61} & C_{62} & C_{63} & -C_{64} & -C_{65} & C_{66} \end{bmatrix} \begin{Bmatrix} \varepsilon_{xx} \\ \varepsilon_{yy} \\ \varepsilon_{zz} \\ \gamma_{yz} \\ \gamma_{xz} \\ \gamma_{xy} \end{Bmatrix}$$

Comparing the above matrix with the general matrix (Eq. 2.35) leads to the conclusion $C_{14} = C_{15} = C_{24} = C_{25} = C_{34} = C_{35} = C_{46} = C_{56} = 0$. Hence, the material matrix for a monoclinic system becomes

$$\begin{bmatrix} C_{11} & C_{12} & C_{13} & 0 & 0 & C_{16} \\ C_{12} & C_{22} & C_{23} & 0 & 0 & C_{26} \\ C_{13} & C_{23} & C_{33} & 0 & 0 & C_{36} \\ 0 & 0 & 0 & C_{44} & C_{45} & 0 \\ 0 & 0 & 0 & C_{45} & C_{55} & 0 \\ C_{16} & C_{26} & C_{36} & 0 & 0 & C_{66} \end{bmatrix} \tag{2.36}$$

Hence, in the case of monoclinic system, 13 independent constants requires to be determined to define the material matrix.

2.2.6.2 Orthotropic System: Three Orthogonal Planes of Symmetry

The most common example of the orthotropic system is the lamina of a laminated composite structure, which is dealt in a later part of this chapter.

Here, the original coordinate system of the body is perpendicular to the three planes. The orthotropy assures that no change in mechanical behavior will be incurred when the coordinate directions are reversed. Following the procedure described for the monoclinic system, the material matrix for an orthotropic system is given by

$$\begin{bmatrix} C_{11} & C_{12} & C_{13} & 0 & 0 & 0 \\ C_{12} & C_{22} & C_{23} & 0 & 0 & 0 \\ C_{13} & C_{23} & C_{33} & 0 & 0 & 0 \\ 0 & 0 & 0 & C_{44} & 0 & 0 \\ 0 & 0 & 0 & 0 & C_{55} & 0 \\ 0 & 0 & 0 & 0 & 0 & C_{66} \end{bmatrix} \tag{2.37}$$

The number of elastic constants that requires to be determined is 9. The relationship of these constants with the elastic constants can be found in [6].

2.2.6.3 Isotropic System: Infinite Plane of Symmetry

This is the most commonly occurring material system for structural materials. For this case, every plane is a plane of symmetry and every axis is an axis of symmetry. It turns out, there are only two elastic constants that requires to be determined and the material matrix is given by

$$\begin{bmatrix} C_{11} & C_{12} & C_{12} & 0 & 0 & 0 \\ C_{12} & C_{11} & C_{12} & 0 & 0 & 0 \\ C_{12} & C_{12} & C_{11} & 0 & 0 & 0 \\ 0 & 0 & 0 & \frac{1}{2}(C_{11}-C_{12}) & 0 & 0 \\ 0 & 0 & 0 & 0 & \frac{1}{2}(C_{11}-C_{12}) & 0 \\ 0 & 0 & 0 & 0 & 0 & \frac{1}{2}(C_{11}-C_{12}) \end{bmatrix} \tag{2.38}$$

where

$$C_{11} = \lambda + 2G, \quad C_{12} = \lambda$$

The constants λ and G are the Lam*é* constants. The stress–strain relations for isotropic materials are usually expressed in the form

$$\sigma_{ij} = \lambda \varepsilon_{kk}\delta_{ij} + 2G\varepsilon_{ij}, \quad 2G\varepsilon_{ij} = \sigma_{ij} - \frac{\lambda}{3\lambda + 2G}\sigma_{kk}\delta_{ij} \tag{2.39}$$

Note that except for isotropic materials, the coefficients are given with respect to a particular coordinate system.

In practice, the elastic constants for an isotropic material are the *Bulk Modulus K*, *Young's Modulus E*, and *Poisson's ratio v*. They are related to the Lam*é* constants and are defined as follows:

$$K = \frac{1}{3}(3\lambda + 2G), \quad v = \frac{\lambda}{2(\lambda + 2\mathrm{G})} \tag{2.40}$$

other relationships among the constants are:

$$\lambda = \frac{vE}{(1+v)(1-2v)}, \quad G = \frac{E}{2(1+v)}, \quad K = \frac{E}{3(1-2v)} \tag{2.41}$$

2.3 Governing Equations of Motion and the Solution Methods

There are a number of ways to derive the governing differential equation of a continuum. The most common method is to draw the free body diagram of an isolated volume of the continuum and establish the equilibrium of forces in all the three coordinate directions to get the required governing equations. However, here we will use Newton's second law of motion for not only deriving the governing equation, but also establish the symmetry of the Cauchy's stress tensor.

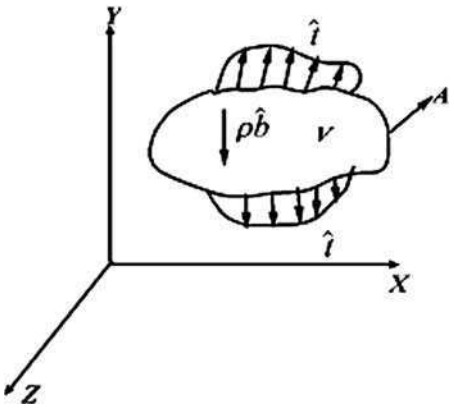

Fig. 2.6 Arbitrary small volume under the action of forces

Consider a body of density ρ and volume V as shown in Fig. 2.6. Let the body be subjected to a surface traction $\boldsymbol{t} = t_x\boldsymbol{i} + t_y\boldsymbol{j} + t_z\boldsymbol{k}$ and the body force $\boldsymbol{b} = b_x\boldsymbol{i} + b_y\boldsymbol{j} + b_z\boldsymbol{k}$.

Applying Newton's laws to the elemental volume shown in Fig. 2.6 gives:

$$\int_A \boldsymbol{t}dA + \int_V \rho\boldsymbol{b}dV = \int_V \rho\ddot{\boldsymbol{u}}dV \tag{2.42}$$

$$\int_A \boldsymbol{x} \times \boldsymbol{t}dA + \int_V \boldsymbol{x} \times \rho\boldsymbol{b}dV = \int_V \boldsymbol{x} \times \rho\ddot{\boldsymbol{u}}dV \tag{2.43}$$

Here, $\boldsymbol{t}$ is the traction vector on the boundary surface of area A. In tensor notation, these equations can be rewritten as

$$\begin{aligned} &\int_A t_i dA + \int_V \rho b_i dV = \int_V \rho\ddot{u}_i dV \\ &\int_A \varepsilon_{ijk}x_j t_k dA + \int_V \varepsilon_{ijk}x_j b_k \rho dV = \int_V \varepsilon_{ijk}x_j \rho\ddot{u}_k dV \end{aligned} \tag{2.44}$$

Here, ε_{ijk} is the permutation tensor used to represent a cross product of any two vectors. Using Eq. 2.31 in Eqs. 2.44, and using the Divergence theorem [7]

$$\int_A t_i dA = \int_A \sigma_{pi}n_p dA = \int_V \frac{\partial\sigma_{pi}}{\partial x_p}dV$$

we get

$$\begin{aligned} &\int_V \left[\frac{\partial\sigma_{pi}}{\partial x_p} + \rho b_i - \rho\ddot{u}_i\right]dV \\ &\int_V \left[\frac{\partial}{\partial x_k}(\varepsilon_{ijk}x_j\sigma_{pk}) + \rho\varepsilon_{ijk}x_j b_k - \rho\varepsilon_{ijk}x_j\ddot{u}_k\right]dV \end{aligned} \tag{2.45}$$

The first term in the second equation can be written as

$$\frac{\partial}{\partial x_p}(x_j \sigma_{pk}) = \sigma_{jk} + x_j \frac{\partial \sigma_{pk}}{\partial x_p}$$

Using the above equation in Eq. 2.45, we can get the governing equilibrium equation as

$$\frac{\partial \sigma_{pi}}{\partial x_p} + \rho b_i = \rho \ddot{u}, \quad \text{with} \quad \varepsilon_{ijk}\sigma_{jk} = 0 \tag{2.46}$$

While the first equation gives the governing differential equation of a continuum in terms of stresses, the second equation states that Cauchy's stress tensor σ_{ij} is symmetric, that is $\sigma_{ij} = \sigma_{ji}$. The above equations will form the heart of many analysis, which will be reported later in this book. It is also worth mentioning that out of nine stress components in the Cauchy's stress tensor, only 6 are independent, which is the result of the symmetry of the tensor. The derived equations of equilibrium are valid for both small and large deformation analysis.

2.3.1 Solution Procedures in Linear Theory of Elasticity

The theory developed in the last subsections form the basis of the field equations in theory of elasticity. In this subsection, these are reformulated to make them convenient for solving boundary value problems. The fundamental assumptions adopted here are the following:

1. All the deformations are small
2. The constitutive relations are linear. For metallic structures, the material behavior can be idealized as isotropic. However, for composite structures, the material behavior is assumed anisotropic

In 3D elasticity, there are 15 unknowns, namely six stress components, six strain components and three displacements. Hence, for a complete solution, we require 15 equations, which come from three equations of equilibrium (Eq. 2.46), six stress–strain relations (Eq. 2.34) and six strain–displacement relations (Eq. 2.26). In addition, boundary conditions on the surface S must be satisfied. Such conditions can be in the form of prescribed displacements u_i and prescribed surface tractions $t_i = \sigma_{ij} n_j$.

Historically, there are two different solution philosophies, one based on assuming displacement as basic unknown, while the other approach considers stresses as unknowns. In the former, the compatibility of displacements is ensured as we begin the analysis with displacement as basic unknowns. However, the equilibrium is not ensured and hence they are enforced in the solution process. In the latter, since the stresses are basic unknowns, the equilibrium is ensured and the compatibility is not ensured and must be hence enforced during the solution process.

2.3.1.1 Displacement Formulation: Navier's Equation

In this approach, the displacements are taken as the basic unknowns, that is, at each point, there are three unknown functions u, v, and w. These must be determined under the constraint that the stresses corresponding to them are equilibrated, or in other words, by enforcing equilibrium. For this, the stresses are first expressed in terms of displacements. That is, first the strains are expressed in terms of displacements using strain–displacement relations (Eq. 2.26) and these are later converted to stresses. For isotropic solids, these can be written as

$$\sigma_{ij} = G\left(\frac{\partial u_i}{\partial x_j} + \frac{\partial u_j}{\partial x_i}\right) + \lambda \frac{\partial u_k}{\partial x_k}\delta_{ij} \tag{2.47}$$

Substituting this in the equilibrium equation (Eq. 2.46), we get

$$G\frac{\partial^2 u_i}{\partial x_k \partial x_k} + (\lambda + G)\frac{\partial^2 u_k}{\partial x_i \partial x_k} + \rho b_i = 0 \tag{2.48}$$

These are the *Navier's equations* with three displacements as unknowns. The equations must satisfy the following boundary conditions in terms of displacements.

$$\begin{array}{llll} \text{On} & S_u: & u_i & \text{Specified} \\ \text{On} & S_t: & \lambda\frac{\partial u_k}{\partial x_k}n_i + G\left(\frac{\partial u_i}{\partial x_j} + \frac{\partial u_j}{\partial x_i}\right)n_j = t_i & \text{Specified} \end{array}$$

Note that the traction boundary conditions are a set of inhomogeneous differential equations. These are very difficult to solve directly. The most common way to solve the above equation is to express the displacement field into scalar potential (ϕ) and vector potential (**H**) using Helmholz's theorem [3]. The displacement field, take the following form

$$u_i = \frac{\partial \Phi}{\partial x_i} + \varepsilon_{ijk}\frac{\partial H_k}{\partial x_j}, \quad \frac{\partial H_k}{\partial x_k} = 0 \tag{2.49}$$

where, ε_{ijk} is the permutation symbol. If the body force is absent, then the Navier's equations can be expressed as

$$(\lambda + 2G)\frac{\partial}{\partial x_i}\nabla^2\Phi + G\varepsilon_{ijk}\nabla^2 H = 0 \tag{2.50}$$

This equation will be satisfied if

$$\nabla^2\Phi = \text{constant}, \quad \nabla^2 H = \text{constant} \tag{2.51}$$

Thus the problem reduces to solving a set of Poisson's equations in terms of potentials, which are easier to solve than the original Eq. 2.48. The displacements are later obtained from Eq. 2.49. Note that the above procedure of solving using Helmholtz decomposition is valid only for structures with Isotropic material

properties. For anisotropic materials, a different approach is required, which is explained in the later part of this chapter.

2.3.1.2 Stress Formulation: Beltrami–Mitchell Equations

In this approach, the stresses are assumed as basic unknowns. That is, at each point in a body, there are six unknown functions, namely $\sigma_{xx}, \sigma_{yy}, \sigma_{zz}, \tau_{xy}, \tau_{yz}$ and τ_{zx}. These stresses obviously have to satisfy the equilibrium equations. However, there are only three equations of equilibrium. The rest of the conditions come from the requirement that the strains must be *compatible*.

The assumed stress field can be converted into strain using the generalized Hooke's law, which in turn can be converted to the displacement field using strain–displacement relationships. In doing so, we get six independent partial differential equations for displacements with prescribed strains ε_{ij}. For arbitrary values of ε_{ij}, there may not exist a unique solution for the displacement field. Hence, for getting the unique solution for displacements, it is necessary to place some restriction on the strains ε_{ij}. By differentiating twice the strain displacement relations (Eq. 2.26), we get

$$\frac{\partial^2 \varepsilon_{ij}}{\partial x_k \partial x_l} = \frac{1}{2}\left(\frac{\partial^3 u_i}{\partial x_j \partial x_k \partial x_l} + \frac{\partial^3 u_j}{\partial x_i \partial x_k \partial x_l}\right) \tag{2.52}$$

Interchanging the subscripts and some manipulation lead to the following relation

$$\frac{\partial^2 \varepsilon_{ij}}{\partial x_k \partial x_l} + \frac{\partial^2 \varepsilon_{kl}}{\partial x_i \partial x_j} - \frac{\partial^2 \varepsilon_{ik}}{\partial x_j \partial x_l} - \frac{\partial^2 \varepsilon_{jl}}{\partial x_i \partial x_k} = 0 \tag{2.53}$$

There are 81 equations in the above relation, out of which some are identically satisfied and some of them are repetitions. Only six equations are nontrivial and independent in expanded notation, these equations are the following

$$\begin{aligned}
&\frac{\partial^2 \varepsilon_{xx}}{\partial y \partial z} = \frac{\partial}{\partial x}\left(-\frac{\partial \varepsilon_{yz}}{\partial x} + \frac{\partial \varepsilon_{zx}}{\partial y} + \frac{\partial \varepsilon_{xy}}{\partial z}\right) \quad \frac{\partial^2 \varepsilon_{xy}}{\partial x \partial y} = \frac{\partial^2 \varepsilon_{xx}}{\partial y^2} + \frac{\partial^2 \varepsilon_{yy}}{\partial x^2} \\
&\frac{\partial^2 \varepsilon_{yy}}{\partial z \partial x} = \frac{\partial}{\partial y}\left(-\frac{\partial \varepsilon_{xz}}{\partial y} + \frac{\partial \varepsilon_{xy}}{\partial z} + \frac{\partial \varepsilon_{yz}}{\partial x}\right) \quad \frac{\partial^2 \varepsilon_{yz}}{\partial y \partial z} = \frac{\partial^2 \varepsilon_{yy}}{\partial z^2} + \frac{\partial^2 \varepsilon_{zz}}{\partial y^2} \\
&\frac{\partial^2 \varepsilon_{zz}}{\partial x \partial y} = \frac{\partial}{\partial z}\left(-\frac{\partial \varepsilon_{xy}}{\partial z} + \frac{\partial \varepsilon_{yz}}{\partial x} + \frac{\partial \varepsilon_{xz}}{\partial y}\right) \quad \frac{\partial^2 \varepsilon_{zx}}{\partial z \partial x} = \frac{\partial^2 \varepsilon_{zz}}{\partial x^2} + \frac{\partial^2 \varepsilon_{yy}}{\partial z^2}
\end{aligned} \tag{2.54}$$

These six relations are collectively known as *compatibility equations*.

The general solution procedure in stress formulation is as follows. We first transform the strains into stresses using Hooke's law (for isotropic solids), which is of the form

$$\varepsilon_{ij} = \frac{1+\nu}{E}\sigma_{ij} - \frac{\nu}{E}\sigma_{kk}\delta_{ij}$$

By substituting for strains in the compatibility equation (Eq. 2.55) and with some simplification (that is by using equations of equilibrium), we get

$$\frac{\partial^2 \sigma_{ij}}{\partial x_k \partial x_k} + \left(\frac{1}{1+v}\right)\frac{\partial^2 \sigma_{kk}}{\partial x_i \partial x_j} + \left(\frac{v}{1-v}\right)\rho\frac{\partial b_k}{\partial x_k}\delta_{ij} + \rho\left(\frac{\partial b_i}{\partial x_j} + \frac{\partial b_j}{\partial x_i}\right) = 0 \qquad (2.55)$$

The stress field should satisfy the above equation along with the equilibrium equations in order to be admissible. In addition, it has to satisfy the traction and displacement boundary conditions.

2.3.2 Plane Problems in Elasticity

The 3D equations and their associated boundary conditions are extremely difficult to solve and solution exists only for very few problems. Hence, in most cases some approximations are made to reduce the complexity of the problem. One such simplification is to reduce the dimensions of the problem from three to two. This can be made for *plane stress* and *plane strain* problems, respectively.

If a plate in $x-y$ plane is thin along the z-direction, then the stress perpendicular to the plane of the plate (σ_{zz}) can be neglected. In addition, the corresponding shear in x–z and y–z planes (τ_{yz} and τ_{xz}) can also be assumed zero. In the process, the equations get simplified considerably. Following are the equations required for the solution of plane stress problem:

- *Equations of equilibrium*:

$$\frac{\partial \sigma_{xx}}{\partial x} + \frac{\partial \tau_{xy}}{\partial y} + b_x = \rho\frac{\partial^2 u}{\partial t^2}, \quad \frac{\partial \tau_{xy}}{\partial x} + \frac{\partial \sigma_{yy}}{\partial y} + b_y = \rho\frac{\partial^2 v}{\partial t^2}$$

- *Strain–displacement relations*:

$$\varepsilon_{xx} = \frac{\partial u}{\partial x}, \quad \varepsilon_{yy} = \frac{\partial v}{\partial y}, \quad \gamma_{xy} = \frac{\partial u}{\partial y} + \frac{\partial v}{\partial x}$$

- *Stress–Strain relations*: This is obtained by inserting $\sigma_{zz} = 0, \tau_{xz} = 0, \tau_{yz} = 0$ in the generalized Hooke's law (Eq. 2.34) and solving the resulting equation after substituting for strains in terms of displacements. After substitution, we get

$$\sigma_{xx} = \frac{E}{(1-v^2)}\left(\frac{\partial u}{\partial x} + v\frac{\partial v}{\partial y}\right), \quad \sigma_{yy} = \frac{E}{(1-v^2)}\left(\frac{\partial v}{\partial y} + v\frac{\partial u}{\partial x}\right), \quad \tau_{xy} = G\gamma_{xy}$$

- *Compatibility Condition*: If one has to use stress based approach for the solution, then only one compatibility equation requires to be enforced, which is given by

$$2\frac{\partial^2 \gamma_{xy}}{\partial x \partial y} = \frac{\partial^2 \varepsilon_{xx}}{\partial y^2} + \frac{\partial^2 \varepsilon_{yy}}{\partial x^2}$$

Note that, although the normal stress σ_{zz} is zero in the plane stress case, the normal strain ε_{zz} is non zero and its value can be computed from the 3D constitutive law.

The second type of reduction is called the plane strain reduction, where the body is assumed rigid in the perpendicular to the plane of loading, that is the strains $\varepsilon_{zz} = \varepsilon_{xz} = \varepsilon_{yz} = 0$. The resulting simplified 3D constitutive model and equations can be solved to get the stress–strain relations, as was done for the plane stress case.

2.4 Introduction to Theory of Composites

Composite materials are obtained by combining two or more materials at the macro scale to obtain a useful structural material. Although these materials at the microscopic scale can be inhomogeneous, they can be considered homogeneous at the macroscopic level. These materials possess the qualities of each of the constituents and the choice of constituents depends on the specific application. These materials are normally preferred due to their light weight, high strength, and high corrosion resistance properties. The two normal constituents of a composite material are the *fiber* and the *matrix*. Depending upon how they are bound together, different types of composite materials can be obtained. Owing to the difference in the constitutive behavior of these two constituent materials, the constitutive model of the compound material is normally anisotropic. Composites can be classified into three different categories, namely *fibrous composites*, *particulate composites* and *laminated composites*. In this book, we will mainly deal with laminated composites and hence will be discussed below.

2.4.1 Theory of Laminated Composites

Laminated composites have found extensive use as aircraft structural materials due to their high strength-to-weight and stiffness-to-weight ratios. Their popularity stems from the fact that they are extremely light-weight and the laminate construction enables the designer to tailor the strength of the structure in any required direction depending upon the loading directions to which the structure is subjected. In addition to aircraft structures, they have found their way into many automobile and building structures. Apart from having better strength, stiffness and lower weight, they have better corrosion resistance, and sometimes thermal and acoustic insulation properties than metallic structures.

The laminated composite structure consists of many laminas (plies) stacked together to form the structure. The number of plies or laminas depends on the strength that the structure is required to sustain. Each lamina contains fibers oriented in the direction where maximum strength is required. These fibers are bound

together by a matrix material. The laminated composite structure derives its strength from the fibers. The commonly used fibers are made of Carbon, Glass, Kevlar and Boron. The most commonly used matrix material is the epoxy resin. These materials are orthotropic at the lamina level while at the laminate level, they exhibit highly anisotropic properties. The anisotropic behavior results in stiffness coupling, such as bending–axial–shear coupling in beams and plates, bending–axial–torsion coupling in aircraft thin-walled structures, etc. These coupling effects make the analysis of laminated composite structures very complex.

2.4.1.1 Micromechanical Analysis of a Lamina

A lamina is a basic element of a laminated composite structure, constructed from fibers that are bound together by the matrix resin. The strength of the lamina, and hence the laminate, depends on the type of fiber, their orientation and also the volume fraction of fiber in relation to the overall volume of lamina. Since the lamina is a heterogeneous mixture of fibers dispersed in a matrix, determination of the material properties of the lamina, which is assumed to be orthotropic in character, is a very involved process. The method used in the determination of lamina material properties is called the micromechanical analysis [6].

Hence, the objective of micromechanics is to determine the elastic moduli of a composite material in terms of the elastic moduli of the constituent materials, namely the fibers and the matrix. Thus, the property of a lamina can be expressed as

$$Q_{ij} = Q_{ij}(E_f, E_m, \nu_f, \nu_m, V_f, V_m), \tag{2.56}$$

where E, ν and V are the elastic moduli, Poisson's ratio and the volume fraction respectively, and f and m subscripts denote the fiber and the matrix, respectively. The volume fraction of fiber is determined from the expression: V_f = (volume of fiber)/(total volume of lamina) and the volume fraction of the matrix is given by $V_m = 1 - V_f$.

There are two basic approaches for the determination of material properties of the lamina. They can be grouped under the following heads: (1) the strength of materials approach and (2) the theory of elasticity approach. The first method gives an experimental way of determining the elastic moduli. The second method gives upper and lower bounds on the elastic moduli and not their actual values. In fact, there are many papers available in the literature that deal with the theory of elasticity approach to determine the elastic moduli of a composite. In this section, only the first method is presented. There are many classic textbooks on composites such as [6, 17] that cover these approaches in detail.

2.4.1.2 Determination of Material Properties of a Lamina

The material properties of a lamina are determined by making some assumptions concerning the behavior of its constituents. The fundamental assumption is that the

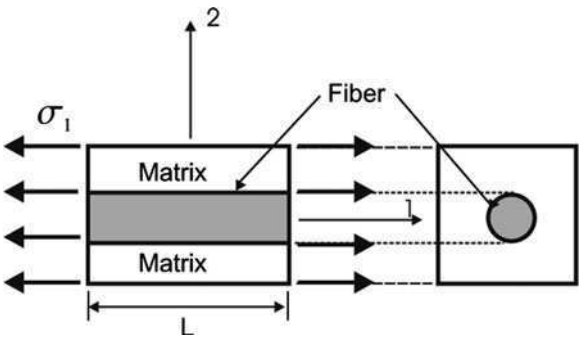

Fig. 2.7 RV for the determination of longitudinal material properties

fibers are strong and hence are the main load bearing member, and the matrix is weak and its main function is to protect the fibers from severe environmental effects. Also, the strains in the matrix and the fiber are assumed to be the same. Hence, a plane section before the application of bending stress remains plane after bending. In the present analysis, we consider a unidirectional, orthotropic composite lamina to derive expressions for the elastic moduli. In doing so, we limit our analysis to a small volume element, small enough to show the microscopic structural details, yet large enough to represent the overall behavior of the composite lamina. Such a volume is called the *representative volume* (*RV*). A simple RV is a fiber surrounded by matrix as shown in Fig. 2.7. First, the procedure for determining the elastic modulus E_1 is given. In Fig. 2.7, the strain in the one-direction is given by $\varepsilon_1 = \Delta L/L$, where this strain is felt both by the matrix and the fiber, according to the assumption stated earlier. The corresponding stresses in the fiber and the matrix are given by

$$\sigma_f = E_f \varepsilon_1, \quad \sigma_m = E_m \varepsilon_1. \tag{2.57}$$

Here E_f and E_m are the elastic modulus of the fiber and the matrix respectively. The cross-sectional area A of the RV is made up of the area of the fiber A_f and the area of the matrix A_m. If the total stress acting on the cross-section of the RV is σ_1, then the total load acting on the cross-section is

$$P = \sigma_1 A = E_1 \varepsilon_1 A = \sigma_f A_f + \sigma_m A_m. \tag{2.58}$$

From the above expression, we can write the elastic moduli in the one-direction as

$$E_1 = E_f \frac{A_f}{A} + E_m \frac{A_m}{A}. \tag{2.59}$$

The volume fraction of the fiber and the matrix can be expressed in terms of areas of the fiber and the matrix as

$$V_f = A_f/A, \quad V_m = A_m/A. \tag{2.60}$$

Using Eq. 2.60 in Eq. 2.59, we can write the modulus in the one-direction as

$$E_1 = E_f V_f + E_m V_m. \tag{2.61}$$

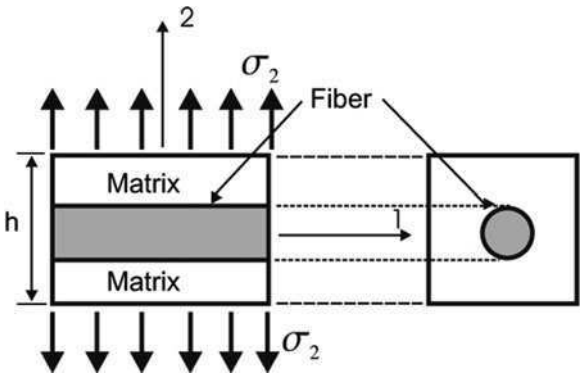

Fig. 2.8 RV for the determination of transverse material properties

Equation 2.61 is the well known *rule of mixtures* for the equivalent modulus of the lamina in the direction of the fibers.

The equivalent modulus E_2 of the lamina is determined by subjecting the RV to a stress σ_2 perpendicular to the direction of the fiber as shown in Fig. 2.8. This stress is assumed to be the same in both the matrix and the fiber. The strains in the fiber and matrix due to this stress are given by

$$\varepsilon_f = \sigma_2/E_f, \quad \varepsilon_m = \sigma_2/E_m. \tag{2.62}$$

If h is the depth of the RV (see Fig. 2.8), then this total strain ε_2 is distributed as a function of the volume fraction as

$$\varepsilon_2 h = (V_f \varepsilon_f + V_m \varepsilon_m)h. \tag{2.63}$$

Substituting Eq. 2.62 in Eq. 2.63, we get

$$\varepsilon_2 = V_f \frac{\sigma_2}{E_f} + V_m \frac{\sigma_2}{E_m}. \tag{2.64}$$

However, we have

$$\sigma_2 = E_2 \varepsilon_2 = E_2 \left(V_f \frac{\sigma_2}{E_f} + V_m \frac{\sigma_2}{E_m} \right). \tag{2.65}$$

From the above relation, the equivalent modulus in the transverse direction is given by

$$E_2 = \frac{E_f E_m}{V_f E_m + V_m E_f}. \tag{2.66}$$

The major Poisson's ratio ν_{12} is determined next as follows. If the RV of width W and depth h is loaded in the direction of the fiber, then both strains ε_1 and ε_2 will be induced in the 1 and 2 directions. The total transverse deformation δ_h is the sum of the transverse deformation in the matrix and the fiber and is given by

$$\delta_h = \delta_{hf} + \delta_{hm}. \tag{2.67}$$

The major Poisson's ratio is also defined as the ratio of the transverse strain to the longitudinal strain and expressed as

$$v_{12} = -\varepsilon_2/\varepsilon_1. \tag{2.68}$$

The total transverse deformation can also be expressed in terms of the depth h as

$$\delta_h = -h\varepsilon_2 = hv_{12}\varepsilon_1. \tag{2.69}$$

Following the procedure adopted for the determination of the transverse modulus, the transverse displacement in the matrix and the fiber can be expressed in terms of its respective volume fraction and the Poisson's ratio as

$$\delta_{hf} = hV_f v_f \varepsilon_1, \quad \delta_{hm} = hV_m v_m \varepsilon_1. \tag{2.70}$$

Using Eqs. 2.69 and 2.70 in Eq. 2.67, we can write the expression for the major Poisson's ratio as

$$v_{12} = v_f V_f + v_m V_m. \tag{2.71}$$

By adopting a similar procedure to that used in the determination of the transverse modulus, we can write the shear modulus in terms of the constituent properties as

$$G_{12} = \frac{G_f G_m}{V_f G_m + V_m G_f}. \tag{2.72}$$

The next important property of the composite that requires determination is the density. For this, we begin with the total mass of the lamina, which is the sum of the masses of the fiber and the matrix. That is, the total mass M can be expressed in terms of the densities (ρ_f and ρ_m) and the volume fractions (V_f and V_m) as

$$M = M_f + M_m = \rho_f V_f + \rho_m V_m. \tag{2.73}$$

The density of the composite lamina can then be expressed as

$$\rho = \frac{M}{V} = \frac{\rho_f V_f + \rho_m V_m}{V}. \tag{2.74}$$

Once the properties of the lamina are determined, then one can proceed to perform a macro mechanical analysis of the lamina to characterize the constitutive model of the laminate.

2.4.1.3 Stress–Strain Relations for a Lamina

Determination of the overall constitutive model for a lamina of a laminated composite constitutes the macro mechanical analysis of composites. Unlike the micro-mechanical study, where the composite is treated as a heterogeneous mixture, here the composite is presumed to be homogeneous and the effects of the

constituent materials are accounted for only as an averaged apparent property of the composite. The following are the basic assumptions used in deriving the constitutive relations:

- The composite material is assumed to behave in a linear (elastic) manner. That is, Hooke's law and the principle of superposition are valid.
- At the lamina level, the composite material is assumed to be homogeneous and orthotropic. Hence the material has two planes of symmetry, one coinciding with the fiber direction and the other perpendicular to the fiber direction.
- The state of the stress in a lamina is predominantly plane stress.

Consider the lamina shown in Fig. 2.9 and its principal axes, denoted as 1−2−3. Axis 1 corresponds to the direction of the fiber and axis 2 is the axis transverse to the fiber. The lamina is assumed to be in a 3D state of stress with six stress components given by $\{\sigma_{11}, \sigma_{22}, \sigma_{33}, \tau_{23}, \tau_{13}, \tau_{12}\}$. For an orthotropic material in a 3D state of stress, nine engineering constants require to be determined. The macromechanical analysis will begin from here. The stress–strain relationship for an orthotropic material is given by [6]

$$\begin{Bmatrix} \varepsilon_{11} \\ \varepsilon_{22} \\ \varepsilon_{33} \\ \gamma_{23} \\ \gamma_{13} \\ \gamma_{12} \end{Bmatrix} = \begin{bmatrix} S_{11} & S_{12} & S_{13} & 0 & 0 & 0 \\ S_{12} & S_{22} & S_{23} & 0 & 0 & 0 \\ S_{13} & S_{23} & S_{33} & 0 & 0 & 0 \\ 0 & 0 & 0 & S_{44} & 0 & 0 \\ 0 & 0 & 0 & 0 & S_{55} & 0 \\ 0 & 0 & 0 & 0 & 0 & S_{66} \end{bmatrix} \begin{Bmatrix} \sigma_{11} \\ \sigma_{22} \\ \sigma_{33} \\ \tau_{23} \\ \tau_{13} \\ \tau_{12} \end{Bmatrix}. \tag{2.75}$$

Here, S_{ij} are the material compliances. Their relationship with the engineering constants is given in [6]. The Poisson's ratio v_{ij} for the transverse strain in the jth direction when the stress is applied in the ith direction is given by

$$v_{ij} = -\varepsilon_{jj}/\varepsilon ii. \tag{2.76}$$

The above condition is for $\sigma_{jj} = \sigma$ and all other stresses equal to zero. The complaint matrix is symmetric, that is, $S_{ij} = S_{ji}$. This condition enforces the following relationship among Poisson's ratios:

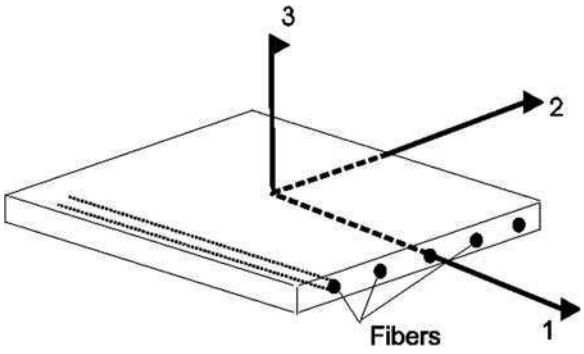

Fig. 2.9 Principal axes of a lamina

$$\frac{v_{ij}}{E_i} = \frac{v_{ji}}{E_j}. \tag{2.77}$$

Hence, for a lamina under a 3D state of stress, only three Poisson's ratios namely v_{12}, v_{23} and v_{31}, need to be determined. Other Poisson's ratio can be obtained from Eq. 2.77.

For most of our analysis, we assume the condition of plane stress. Here, we derive the equations assuming that conditions of plane stress exist in the $1-2$ plane (see Fig. 2.9). However, if one has to do an analysis of a laminated composite beam, which is essentially a 1D member, the condition of plane stress will exist in the $1-3$ plane and a similar procedure to derive the constitutive relation may be followed as outlined below.

For the plane stress condition in the 1–2 plane, we set the following stresses equal to zero in Eq. 2.75, $\sigma_{33} = \tau_{23} = \tau_{13} = 0$. The resulting constitutive model under plane stress conditions can be written as

$$\begin{Bmatrix} \varepsilon_{11} \\ \varepsilon_{22} \\ \gamma_{12} \end{Bmatrix} = \begin{bmatrix} 1/E_1 & -v_{12}/E_1 & 0 \\ -v_{21}/E_2 & 1/E_2 & 0 \\ 0 & 0 & 1/G_{12} \end{bmatrix} \begin{Bmatrix} \sigma_{11} \\ \sigma_{22} \\ \tau_{12} \end{Bmatrix}. \tag{2.78}$$

Note that the strain ε_{33} also exists, which can be obtained from the third constitutive equation

$$\varepsilon_{33} = S_{13}\sigma_{11} + S_{23}\sigma_{22}. \tag{2.79}$$

This equation indicates that Poisson's ratios v_{13} and v_{23} should also exist. Inverting Eq. 2.78, we can express the stresses in terms of the strains:

$$\begin{Bmatrix} \sigma_{11} \\ \sigma_{22} \\ \tau_{12} \end{Bmatrix} = \begin{bmatrix} Q_{11} & Q_{12} & 0 \\ Q_{12} & Q_{22} & 0 \\ 0 & 0 & Q_{66} \end{bmatrix} \begin{Bmatrix} \varepsilon_{11} \\ \varepsilon_{22} \\ \gamma_{12} \end{Bmatrix}, \tag{2.80}$$

where Q_{ij} are the reduced stiffness coefficients, which can be expressed in terms of the elastic constants as

$$Q_{11} = \frac{E_1}{1 - v_{12}v_{21}}, \quad Q_{12} = v_{21}Q_{11}, \quad Q_{22} = \frac{E_2}{1 - v_{12}v_{21}}, \quad Q_{66} = G_{12} \tag{2.81}$$

2.4.2 Stress–Strain Relation for a Lamina with Arbitrary Orientation of Fibers

In most cases, the orientation of the global axes $x-y$ which are geometrically natural for the solution of the problem, do not coincide with the lamina principal axes, previously designated as $1-2$ axes. The lamina principal axes and the global axes are shown in Fig. 2.10. A small element in the lamina of area dA is taken and the free body diagram is shown in Fig. 2.11.

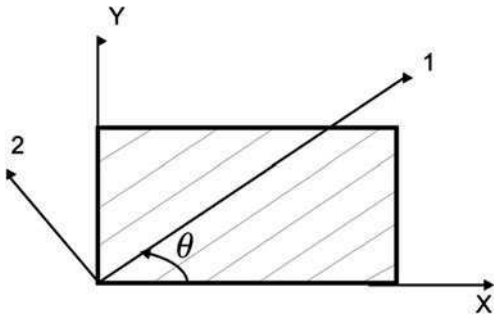

Fig. 2.10 Principal material axes of a lamina and the global $x-y$ axes

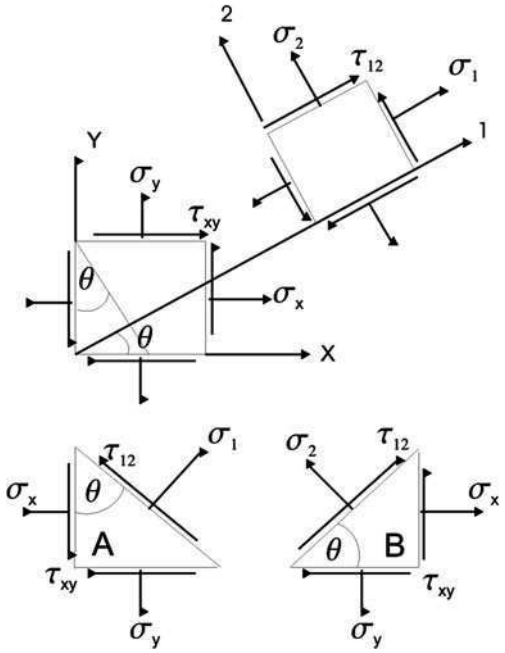

Fig. 2.11 FBD of a stressed element: lamina and laminate coordinate system and FBD of a stressed element

Consider the free body A. Summing all the forces in the 1-axis direction, we get

$$\begin{aligned}\sigma_{11}dA - \sigma_{xx}(\cos\,\theta dA)(\cos\,\theta) - \sigma_{yy}(\sin\,\theta dA)(\sin\,\theta)\\ - \tau_{xy}(\sin\,\theta dA)(\cos\,\theta) - \tau_{xy}(\cos\,\theta dA)(\sin\,\theta) = 0.\end{aligned} \tag{2.82}$$

On simplification, the above equation can be written as

$$\sigma_{11} = \sigma_{xx}\cos^2\theta + \sigma_{yy}\sin^2\theta + 2\tau_{xy}\sin\,\theta\cos\,\theta. \tag{2.83}$$

Similarly, summing all the forces along the 2-axis (free body A) gives

$$\begin{aligned}\tau_{12}dA - \sigma_{xx}(\cos\,\theta dA)(\sin\,\theta) - \sigma_{yy}(\sin\,\theta dA)(\cos\,\theta)\\ - \tau_{xy}(\sin\,\theta dA)(\sin\,\theta) - \tau_{xy}(\cos\,\theta dA)(\cos\,\theta) = 0.\end{aligned} \tag{2.84}$$

Simplifying the above equation, we get

$$\tau_{12} = -\sigma_{xx} \sin\theta \cos\theta + \sigma_{yy} \sin\theta \cos\theta + \tau_{xy}(\cos^2\theta - \sin^2\theta). \tag{2.85}$$

Following the same procedure and summing all the forces in the two-direction in the free body B, one can write

$$\sigma_{22} = \sigma_{xx} \sin^2\theta + \sigma_{yy} \cos^2\theta - 2\tau_{xy} \sin\theta \cos\theta. \tag{2.86}$$

Equations 2.83, 2.85 and 2.86 can be written in matrix form as

$$\begin{Bmatrix} \sigma_{11} \\ \sigma_{22} \\ \tau_{12} \end{Bmatrix} = \begin{bmatrix} C^2 & S^2 & 2CS \\ S^2 & C^2 & -2CS \\ -CS & CS & (C^2 - S^2) \end{bmatrix} \begin{Bmatrix} \sigma_{xx} \\ \sigma_{yy} \\ \tau_{xy} \end{Bmatrix} \tag{2.87}$$

where $C = \cos\theta, S = \sin\theta$. The equation above can be rewritten as:

$$\boldsymbol{\sigma}_{1-2} = \boldsymbol{T}\boldsymbol{\sigma}_{x-y}$$

The strains in the $1-2$ axis, can be transformed to the $x-y$ axis by a similar transformation. Note that for the same transformation to hold, the shear strains are divided by 2. Accordingly:

$$\begin{Bmatrix} \varepsilon_{11} \\ \varepsilon_{22} \\ \frac{\gamma_{12}}{2} \end{Bmatrix} = \begin{bmatrix} C^2 & S^2 & 2CS \\ S^2 & C^2 & -2CS \\ -CS & CS & (C^2 - S^2) \end{bmatrix} \begin{Bmatrix} \varepsilon_{xx} \\ \varepsilon_{yy} \\ \frac{\gamma_{xy}}{2} \end{Bmatrix} \tag{2.88}$$

or

$$\boldsymbol{\varepsilon}_{1-2} = \boldsymbol{T}\boldsymbol{\varepsilon}_{x-y}$$

Inverting Eqs. 2.87 and 2.88, we can express the stresses and strains in global coordinates as

$$\boldsymbol{\sigma}_{x-y} = \boldsymbol{T}^{-1}\boldsymbol{\sigma}_{1-2} \tag{2.89}$$

and

$$\boldsymbol{\varepsilon}_{x-y} = \boldsymbol{T}^{-1}\boldsymbol{\varepsilon}_{1-2} \tag{2.90}$$

The actual strain vectors in both $1-2$ and $x-y$ axes $\boldsymbol{\varepsilon}_{1-2}$ and $\boldsymbol{\varepsilon}_{x-y}$ are related to $\boldsymbol{\varepsilon}_{1-2}$ and $\boldsymbol{\varepsilon}_{x-y}$ through a transformation matrix:

$$\boldsymbol{\varepsilon}_{1-2} = \boldsymbol{R}\boldsymbol{\varepsilon}_{1-2}$$
$$\boldsymbol{\varepsilon}_{x-y} = \boldsymbol{R}\boldsymbol{\varepsilon}_{x-y}$$

where

$$\boldsymbol{R} = \begin{bmatrix} 1 & 0 & 0 \\ 0 & 1 & 0 \\ 0 & 0 & 2 \end{bmatrix} \tag{2.91}$$

The constitutive equation of a lamina in its principal directions (Eq. 2.80) can be written as

$$\boldsymbol{\sigma}_{1-2} = \boldsymbol{Q}\boldsymbol{\varepsilon}_{1-2}. \tag{2.92}$$

Substituting Eqs. 2.87, 2.88 and 2.91 in Eq. 2.92, gives

$$\boldsymbol{T}\boldsymbol{\sigma}_{x-y} = \boldsymbol{Q}\boldsymbol{R}\bar{\boldsymbol{\varepsilon}}_{1-2} = \boldsymbol{Q}\boldsymbol{R}\boldsymbol{T}\bar{\boldsymbol{\varepsilon}}_{x-y} = \boldsymbol{Q}\boldsymbol{R}\boldsymbol{T}\boldsymbol{R}^{-1}\boldsymbol{\varepsilon}_{\boldsymbol{x}-\boldsymbol{y}} \tag{2.93}$$

The constitutive relation in the global x–y axes can now be written as

$$\boldsymbol{\sigma}_{x-y} = \bar{\boldsymbol{Q}}\boldsymbol{\varepsilon}_{x-y} = \boldsymbol{T}^{-1}\boldsymbol{Q}\boldsymbol{R}\boldsymbol{T}\boldsymbol{R}^{-1}\boldsymbol{\varepsilon}_{x-y} \tag{2.94}$$

Here the matrix $\bar{\boldsymbol{Q}}$ is fully populated. Hence, although the lamina in its own principal direction is orthotropic, in the transformed coordinate, it represents a completely anisotropic behavior, that is the normal stresses are coupled to the shear strains and viceversa. The elements of $\bar{\boldsymbol{Q}}$ are given by

$$\begin{aligned}
\bar{Q}_{11} &= Q_{11}C^4 + 2(Q_{12} + 2Q_{66})S^2C^2 + Q_{22}S^4,\\
\bar{Q}_{12} &= (Q_{11} + Q_{22} - 4Q_{66})S^2C^2 + Q_{12}(S^4 + C^4),\\
\bar{Q}_{16} &= (Q_{11} - Q_{12} - 2Q_{66})SC^3 + (Q_{12} - Q_{22} + 2Q_{66})S^3C,\\
\bar{Q}_{22} &= Q_{11}S^4 + 2(Q_{12} + 2Q_{66})S^2C^2 + Q_{22}C^4,\\
\bar{Q}_{26} &= (Q_{11} - Q_{12} - 2Q_{66})S^3C + (Q_{12} - Q_{22} + 2Q_{66})SC^3,\\
\bar{Q}_{66} &= (Q_{11} + Q_{22} - 2Q_{12} - 2Q_{66})S^2C^2 + Q_{66}(S^4 + C^4)
\end{aligned} \tag{2.95}$$

which gives the constitutive equation of a lamina under plane stress in the 1–2 plane.

2.5 Introduction to Wave Propagation in Structures

A structure, when subjected to dynamic loads, will experience stresses of varying degree of severity depending upon the load magnitude and its duration. If the temporal variation of load is of long duration , the intensity of the load felt by the structure will usually be of lower severity and such problems falls under the category of *structural dynamics*. For these problems, there are two parameters which are of paramount importance in the determination of its response, namely the natural frequency of the system and its normal modes (mode shapes). The total response of structure is obtained by the superposition of the normal modes. Large duration of the load makes it low on the frequency content, and hence the load will excite only the first few modes. Hence, the structure could be idealized with fewer unknowns (which we call as degrees of freedom, a terminology which is normally used in structural dynamics). However, when the duration of the load is small, stress waves are set up, which starts propagating in the medium with a certain velocity. Hence, the response is necessarily transient in nature and in the process,

many normal modes will get excited. Hence, the model sizes will be many orders bigger than what is required for structural dynamics problem. Such problems come under the category of *wave propagation*. The key factor in wave propagation is the velocity, level of attenuation of the response and its wavelength. In addition, phase information is one of the important parameters.

Since wave propagation is a multi-modal phenomenon, the analysis becomes quite complex when the problem is solved in the time domain. This is because the problem by its very nature is associated with high frequency content. Hence, analysis methods based on the frequency domain highly suited for such problems. That is, all the governing equations, boundary conditions and the variables are transformed to the frequency domain using any of the integral transforms available. The most common transformation for transforming the problem to the frequency domain is the Fourier Transforms, although, more recently Wavelet Transform is also becoming popular. This transform has the discrete representation and hence it is amenable to numerical implementation, which makes its use attractive in wave propagation analysis. By transforming the problem into frequency domain, the complexity of the governing partial differential equation is reduced by removing the time variable out of the formulation, thus making the solution of the resulting ODE (in the 1D case) much simpler than the original PDE. In wave propagation problems, two parameters are very important, namely the wavenumber and the speeds of the propagation.

2.5.1 Spectral Analysis

Spectral analysis is a means to ascertain the wave type and its behavior in a system represented by a governing PDE by obtaining its local wave behavior, which is different for different *waveguides*. The spectral analysis give two important wave characteristics, namely the *spectrum* and the *dispersion* relation. Spectral analysis uses Discrete Fourier Transform (DFT), to represent a field variable (say displacement) as a finite series involving a set of coefficients, which require to be determined. Spectral analysis enables the determination of two important wave parameters, namely the *wavenumbers* and the *group speeds*. These parameters are required to understand wave propagation in a given medium or waveguide. These parameters enable us to know whether the wave mode is a propagating or evanescent (attenuated) mode. If the wave is propagating, the wavenumber expression will let us know whether the wave is *non-dispersive* (that is, the wave retains its shape as it propagates) or *dispersive* (when the wave changes its shape as it propagates). In this sub section, we give a brief outline of spectral analysis for second- and fourth-order systems. Additional details can be found in [3].

The starting point of spectral analysis is the governing differential equation. Consider a second-order partial differential equation given by

$$a\frac{\partial^2 u}{\partial x^2} + b\frac{\partial u}{\partial x} = c\frac{\partial^2 u}{\partial t^2} \tag{2.96}$$

where, *a, b, c* are known constants and $u(x,t)$ is the dependent field variable, x is the spatial variable and t is the temporal variable. We first approximate or transform the above PDE to frequency domain using the DFT, which gives

$$u(x,t) = \sum_{n=0}^{N-1} \hat{u}_n(x,\omega_n)e^{j\omega_n t} \tag{2.97}$$

where, ω_n is the circular frequency and N is the total number of frequency points used in the approximation. Here $\hat{u}$ is the frequency-dependent Fourier transform of the field variable. Substituting Eq. 2.97 into Eq. 2.96, gives:

$$a\frac{d^2\hat{u}_n}{dx^2} + b\frac{d\hat{u}_n}{dx} + c\omega_n^2\hat{u}_n = 0, n = 0,\ldots,N-1. \tag{2.98}$$

From the above equation, we see that a partial differential equation is reduced to a set of ordinary differential equation (ODE) with the time variation removed and frequency introduced as a parameter. The summation is omitted in the above equation for brevity. Equation 2.98 is a constant coefficient ODE, which has a solution of the type $\hat{u}_n(x,\omega) = A_n e^{jkx}$, where A_n is some unknown constant and k is called the *wavenumber*. Substituting the above solution in Eq. 2.98, we get the following characteristic equation to determine k

$$\left(k^2 - \frac{bj}{a}k + \frac{c\omega_n^2}{a}\right)A_n = 0. \tag{2.99}$$

The above equation is quadratic in k and has two roots corresponding to two modes of wave propagation. These two modes correspond to the incident and reflected waves. If the wavenumbers are real, then the wave modes are called *propagating modes*. On the other hand, if the wavenumbers are complex, then the wave modes are *evanescent modes*. These are given by

$$k_{1,2} = \frac{bj}{2a} \pm \sqrt{\frac{-b^2}{4a^2} + \frac{c\omega_n^2}{a}}. \tag{2.100}$$

Different wave behavior is possible depending upon the values of *a, b*, and *c*. The behavior also depends on the numerical value of the radical $\sqrt{c\omega_n^2/a - b^2/4a^2}$. Let us consider a simple case of $b = 0$. The two wavenumbers are given by

$$k_1 = \omega_n\frac{c}{a}, \quad k_2 = -\omega_n\frac{c}{a}. \tag{2.101}$$

From the above expression, we find that the wavenumbers are real and hence they are propagating modes. The wavenumbers are linear functions of frequency ω. At this point, we would like to introduce two important wave parameters that will

determine the wave characteristics, namely the *phase speed* c_p and *group speed* c_g. They are defined as

$$c_p = \frac{\omega_n}{\text{Real}(k)}, \quad c_g = \frac{d\omega_n}{dk}. \tag{2.102}$$

For the wavenumbers given in Eq. 2.101, the speeds are given by

$$c_p = c_g = \frac{a}{c}. \tag{2.103}$$

We find that both group and phase speed are constant and equal. When wavenumbers vary linearly with frequency ω and the phase speed and the group speed are constant and equal, then the wave, as it propagates, retains its shape. Such waves are called *Non-dispersive waves*. Longitudinal waves in elementary rods are of this type. If the wavenumber varies in a non-linear manner with respect to frequency, the phase and group speeds will not be constant with frequency. That is, each frequency component travels with different speed and as a result, the wave changes its shape as it propagates. Such waves are called *dispersive waves*.

Next, let us again consider Eq. 2.100 with all the constants nonzero. The wavenumber no longer varies linearly with frequency. Hence, one can expect dispersive behavior of the waves and the level of dispersion depends upon the numerical value of the radical. We will investigate this aspect in a little more detail. There can be the following three situations:

1. $b^2/4a^2 > c\omega_n^2/a$
2. $b^2/4a^2 < c\omega_n^2/a$ and
3. $b^2/4a^2 = c\omega_n^2/a$

Let us now consider Case 1. When $b^2/4a^2 > c\omega_n^2/a$, then the radical is a complex number and hence all the wavenumbers are complex. This implies that the wave modes are non-propagating and they attenuated rapidly in space. For Case 2, where $b^2/4a^2 < c\omega_n^2/a$, the value of the radical will be positive and real. Hence the wavenumber has both real and imaginary parts. Waves having this feature are attenuated as they propagate. The phase and group speeds for this case are respectively given by

$$c_p = \frac{\omega_n}{k} = \frac{\omega_n}{\sqrt{c\omega_n^2/a - b^2/4a^2}}, \tag{2.104}$$

$$c_g = \frac{d\omega_n}{dk} = \frac{a\sqrt{c\omega_n^2/a - b^2/4a^2}}{c\omega_n}. \tag{2.105}$$

It is quite obvious that these are not the same and hence the waves could be dispersive in nature. One can get back the non-dispersive solution by substituting $b = 0$ in Eq. 2.105. Now, let us see Case 3 where the value of the radical will be zero and hence the wavenumber is purely imaginary indicating that the wave mode is a damping mode. The interesting point here is to find the frequency of transition at

which the propagating mode becomes evanescent or a damping mode. This can be obtained by equating the radical to zero. Thus the transition frequency ω_t is given by

$$\omega_t = \frac{b}{2\sqrt{ac}}.$$

Once the wavenumbers are determined, the solution to the governing wave equation (Eq. 2.98) in the frequency domain can be written as (for $b = 0$)

$$\hat{u_n}(x, \omega_n) = A_n e^{-jk_n x} + B_n e^{jk_n x}, \quad k_n = \omega_n \sqrt{\frac{c}{a}}. \tag{2.106}$$

In the above equation A_n represents the incident wave coefficient while B_n represents the reflected wave coefficient.

It is clearly seen how the values of the constants in the governing differential equation play an important part in dictating the type of wave propagation in a given medium. Now let us consider a fourth-order system and study the wave behavior in such systems. Consider the following governing partial differential equation of motion:

$$A\frac{\partial^4 w}{\partial x^4} + Bw + C\frac{\partial^2 w}{\partial t^2} = 0. \tag{2.107}$$

Here w is the field variable, and A, B, C are known constants. The above equation is similar to the equation of motion of a beam on elastic foundations. Let us now assume the spectral form of solution for the field variable, which is given by

$$w(x, t) = \sum_{n=0}^{N} \hat{w_n}(x, \omega_n) e^{j\omega_n t}. \tag{2.108}$$

Using Eq. 2.108 in Eq. 2.107, the PDE is transformed to an ODE as

$$A\frac{d^4 \hat{w_n}}{dx^4} - (C\omega_n^2 - B)\hat{w_n} = 0. \tag{2.109}$$

Again, this equation is an ODE with constant coefficients and it has solutions of the form $\hat{w}_n = A_n e^{jkx}$. Using this solution in Eq. 2.109, we get the characteristic equation for the wavenumber, which is given by

$$k^4 - \beta^4 = 0, \quad \beta^4 = \left(\frac{C}{A}\omega_n^2 - \frac{B}{A}\right). \tag{2.110}$$

The above is a fourth-order equation corresponding to four wave modes, two of which are for the incident wave and the other two are for the reflected wave. Also, the type of wave is dependent upon the numerical value of $C\omega_n^2/A - B/A$. Let us now assume that $C\omega_n^2/A > B/A$. For this case, the solution of Eq. 2.110 will give the following wavenumbers:

$$k_1 = \beta, \quad k_2 = -\beta, \quad k_3 = j\beta, \quad k_4 = -j\beta \tag{2.111}$$

In the above equation, k_1 and k_2 are propagating modes while k_3 and k_4 are the evanescent modes. From the above equations, we find that the wavenumbers are non-linear functions of frequency and hence waves are expected to be dispersive in nature. Also, using the above expression, we can find the phase and group speeds for the propagating modes using Eqs. 2.102 and 2.103, respectively.

Next, consider the case when $C\omega_n^2/A < B/A$. For this case, the characteristic equation and hence the wavenumbers are given by

$$k^4 + \beta^4 = 0 \tag{2.112}$$

$$k_1 = \left[\frac{1}{\sqrt{2}} + j\frac{1}{\sqrt{2}}\right]\beta, \quad k_2 = -\left[\frac{1}{\sqrt{2}} + j\frac{1}{\sqrt{2}}\right]\beta, \tag{2.113}$$

$$k_3 = \left[-\frac{1}{\sqrt{2}} + j\frac{1}{\sqrt{2}}\right]\beta, \quad k_4 = -\left[-\frac{1}{\sqrt{2}} + j\frac{1}{\sqrt{2}}\right]\beta. \tag{2.114}$$

From the above equation, we see a completely different wave behavior. The wavenumbers have both real and the imaginary parts and hence all the modes will attenuate as they propagate. Also, the initial evanescent mode, after a certain frequency, becomes a propagating mode, giving a completely different wave behavior. The frequency at which this transition takes place is called the *cut-off frequency*. The expression for the cut-off frequency can be obtained if we equate $C\omega_n^2/A - B/A$ to zero, giving $\omega_{\text{cut-off}} = \sqrt{B/C}$. We can see that when $B = 0$, the cut-off frequency vanishes and the wave behavior is similar to the first case, i.e., it will have two propagating and two evanescent modes.

The solution of the fourth-order governing equation in the frequency domain (Eq. 2.109) can be written as

$$\hat{w_n}(x, \omega_n) = A_n e^{-j\beta x} + B_n e^{-\beta x} + C_n e^{j\beta x} + D e^{\beta x}. \tag{2.115}$$

As in the previous case, A_n and B_n are the incident wave coefficients and C_n and D_n are the reflected wave coefficients. These can be determined based on the boundary conditions of the problem.

From the above discussion, we see that spectral analysis gives us a deep insight into the wave mechanics of a system defined by its governing differential equation. The direct output of spectral analysis are the *spectrum relations*, which define the wavenumber variation with frequency, and the *dispersion relations*, which relate phase and group speed and frequency. The determination of spectrum relations is required for the development of spectral finite elements for different waveguides, which is explained in Chap. 5.

2.6 Characteristics of Waves in Anisotropic Media

An important characteristic that separates waves in anisotropic media from the isotropic media counterpart is the direction of energy flow i.e. group velocity [11].

For isotropic material, the incident and reflected waves are purely longitudinal, which are called (P) or (S)waves. In two-dimensional (2D) media, for example, if the wave vector is given by $\boldsymbol{k} = (k_x, k_y)$, the direction cosines of the normal to the wavefront would be (k_x, k_y) and $(-k_y, k_x)$ for P and S wave, respectively. However, the situation is much more complex in the anisotropic case, where the wave directions are material property dependent and they can no longer be thought of as purely P or S waves. They are called the quasi-P wave and the quasi-S wave (Waves in vertical direction is called QSV waves and the waves in the horizontal direction is called QSH waves). In this case, the three waves (in three Cartesian coordinate directions) are coupled, and in order to identify them, one needs to solve a sixth-order characteristic polynomial equation. Thus, the simplified analysis for the isotropic case based on the Helmholtz decomposition (possible by virtue of uncoupled P and S motions), is not practical in the anisotropic case. The wave velocity and direction in anisotropic material can be obtained from the governing equation and the plane wave assumption. The governing equation for a general homogeneous anisotropic media is

$$\frac{\partial \sigma_{ik}}{\partial x_k} = \rho \ddot{u}_i, \quad \sigma_{ik} = C_{ik\ell m}\varepsilon_{\ell m}, \tag{2.116}$$

where the constitutive matrix $C_{ik\ell m}$ is symmetric with respect to ℓ and m. For the plane wave assumption, the displacement field is given by

$$u_i = A\alpha_i e^{jk(n_m x_m - ct)}, \tag{2.117}$$

where n_m are the direction cosines of the normal to the wavefront and α_i are the direction cosines of particle displacement. Substitution of the assumed form in the governing equation results in an eigenvalue problem for the phase velocity c as

$$(\Gamma_{im} - \rho c^2 \delta_{im})\alpha_m = 0, \quad \Gamma_{im} = C_{ik\ell m} n_k n_\ell, \tag{2.118}$$

where Γ_{im} is called the Christoffel symbol, and Eq. 2.118 is the Chirstoffel equation. Solving Eq. 2.118, the wave phase velocity and the wave directions are obtained.

2.7 Governing Equations for Beams and Plates

There are different methods of obtaining the governing wave equation for a given waveguide. Here, we resort to using energy methods. This is because, energy methods through Hamilton's principle, will not only give the required wave equation, but also the associated force boundary conditions. We make the following assumptions:

1. The structure is assumed to behave linearly and the deformations are assumed to be small.
2. The structural material is assumed to behave linearly.
3. Material is homogenous.

Developing the governing equations from Hamilton's Principle requires the energy associated with the motion, namely the strain energy and the kinetic energy to be expressed in terms of displacements. For this, some assumptions on the displacement field are made based on the physics of the problem.

In this section, we derive the governing equations for beams and plates using Hamilton's theorem [2, 18]. The governing equations are derived assuming structures are laminated composites. The equations for their isotopic counter parts can be deduced from the composites equations by substituting the appropriate reduction in the composites constitutive model.

2.7.1 Governing Equation for an Elementary Beam

The Elementary Beam Theory (EBT) is also called Euler–Bernoulli Beam Theory. The predominant motions are the transverse displacement, $w(x,t)$, the axial displacement $u^0(x,t)$ and the slope $\phi(x,t)$, which is derived from the transverse displacement as $\phi(x,t) = dw/dx$. Note that in the laminated composites, the axial motion and transverse motions are coupled due to the unsymmetric ply sequence. However, in the case of isotropic beams, the axial and bending motions are uncoupled. The deformation field for EBT is given by

$$u(x,y,z,t) = u^o(x,t) - zw(x,t)_{,x}\,, \quad w(x,y,z,t) = w(x,t) \tag{2.119}$$

where u^o and w are the axial and transverse displacement of the reference plane. In the above equation z is the distance measured in the thickness direction from the reference plane. The layer-wise constitutive law is defined as

$$\sigma_{xx} = \bar{Q}_{11}\varepsilon_{xx}, \tag{2.120}$$

where σ_{xx} and ε_{xx} are the stress and strain in the X direction. The expression for $\bar{Q}_{11}$ as a function of ply fiber angle θ is given by the first of Eq. 2.95. That is

$$\bar{Q}_{11} = Q_{11}\cos^4\theta + Q_{22}\sin^4\theta + 2\big(Q_{12} + 2Q_{66}\sin^2\theta\cos^2\theta\big), \tag{2.121}$$

where Q_{ij} are the orthotropic elastic coefficients for the individual composite ply and these values in terms of lamina properties are given in Eq. 2.81 The strain energy and the kinetic energy are defined as

$$S = \frac{1}{2}\int \sigma_{xx}\varepsilon_{xx}d\upsilon, \quad \Gamma = \frac{1}{2}\int \rho(\dot{u^o}^2 + \dot{w}^2)d\upsilon, \tag{2.122}$$

where $\dot{(\,)}$ denotes derivative with respect to time and ρ is the layer-wise density.

Applying Hamilton's principle, the governing differential equations are obtained, and can be expressed as

$$\rho A\ddot{u^o} - A_{11}u^o{}_{,xx} + B_{11}w_{,xxx} = 0, \tag{2.123}$$

$$\rho A\ddot{w} - B_{11}u^o{}_{,xxx} + D_{11}w_{,xxxx} = 0 \tag{2.124}$$

and the force boundary conditions are obtained as

$$A_{11}u^o{}_{,x} - B_{11}w_{,xx} = N_x, \tag{2.125}$$

$$B_{11}u^o{}_{,xx} - D_{11}w_{,xxx} = V_x, \tag{2.126}$$

$$-B_{11}u^o{}_{,x} + D_{11}w_{,xx} = M_x, \tag{2.127}$$

where

$$[A_{11}, B_{11}, D_{11}] = \int_{-h/2}^{+h/2} \bar{Q}_{11}\left[1, z, z^2\right] b dz, \tag{2.128}$$

h is the depth of the beam, b is the layer width and A is the cross-sectional area of the beam. N_x, V_x and M_x are the axial force, shear force and bending moment, respectively. The governing differential Eqs. 2.123 and 2.124 represent a system of coupled linear PDEs. Note that when B_{11} is zero, that is when the ply stacking sequence is symmetric, the axial and transverse motion gets uncoupled.

2.7.2 Governing Differential Equation for a Higher Order Beam

In higher order beams, higher order effects are introduced by considering the shear deformation and lateral contraction. If shear deformation alone is considered, then such a theory is called the *First Order Shear Deformation Theory* (FSDT) as first introduced in [15]. In FSDT, the *plane sections remain plane* assumption of the elementary beam is violated and as a result the slopes are not derived from the transverse displacements. This also introduces a shear strain in the model. The introduction of lateral contraction in the isotropic rod model was first done by Mindlin and Herreman [10]. Introduction of lateral contraction introduces an additional motion in the form of transverse displacement. The direction of motion of the lateral contraction is shown in Fig. 2.12. The displacement field for the axial and transverse motion based on FSDT and lateral contraction is given by

$$u(x, y, z, t) = u^o(x, t) - z\phi(x, t), \quad w(x, y, z, t) = w(x, t) + z\psi(x, t) \tag{2.129}$$

where u and w are, respectively, the axial and transverse displacements at a material point. u^o and w^o are the beam axial and transverse displacement of the reference plane. ϕ is the curvature-independent rotation of the beam cross-section about the Y-axis. $\psi = \varepsilon_{zz}$ is the contraction/elongation parallel to the Z-axis.

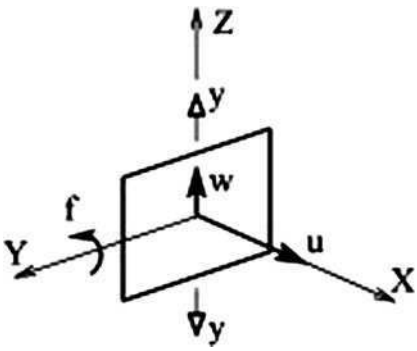

Fig. 2.12 Beam cross-section in the *YZ* plane and degrees of freedom

Following conventional notation [12], the constitutive model for an orthotropic laminated composite beam can be expressed as

$$\begin{Bmatrix} \sigma_{xx} \\ \sigma_{zz} \\ \tau_{xz} \end{Bmatrix} = \begin{bmatrix} \bar{Q}_{11} & \bar{Q}_{13} & 0 \\ \bar{Q}_{13} & \bar{Q}_{33} & 0 \\ 0 & 0 & \bar{Q}_{55} \end{bmatrix} \begin{Bmatrix} \varepsilon_{xx} \\ \varepsilon_{zz} \\ \gamma_{xz} \end{Bmatrix}. \tag{2.130}$$

Using Hamilton's principle and Eqs. 2.129 and 2.130, the governing wave equations can be obtained as

$$\delta u : I_0 \ddot{u}^o - I_1 \ddot{\phi} - A_{11} u^o{}_{,xx} + B_{11} \phi_{,xx} - A_{13} \psi_{,x} = 0, \tag{2.131}$$

$$\delta \psi : I_2 \ddot{\psi} + I_1 \ddot{w} + A_{13} u^o{}_{,x} - B_{13} \phi_{,x} + A_{33} \psi - B_{55}(w_{,xx} - \phi_{,x}) - D_{55} \psi_{,xx} = 0, \tag{2.132}$$

$$\delta w : I_0 \ddot{w} + I_1 \ddot{\psi} - A_{55}(w_{,xx} - \phi_x) - B_{55} \psi_{,xx} = 0, \tag{2.133}$$

$$\delta \phi : I_2 \ddot{\phi} - I_1 \ddot{u}^o - A_{55}(w_{,x} - \phi) - B_{55} \psi_{,x} + B_{11} u^o{}_{,xx} - D_{11} \phi_{,xx} + B_{13} \psi_{,x} = 0. \tag{2.134}$$

The four associated force boundary conditions are

$$A_{11} u^\circ{}_{,x} - B_{11} \phi_{,x} + A_{13} \psi = N_x, \quad B_{55}\left(w_{,x} - \phi\right) + D_{55} \psi_{,x} = Q_x, \tag{2.135}$$

$$A_{55}(w_{,x} - \phi) + B_{55} \psi_{,x} = V_x, \quad -B_{11} u^\circ{}_{,x} + D_{11} \phi_{,x} - B_{13} \psi = M_x. \tag{2.136}$$

The stiffness coefficients which are functions of individual ply properties, ply orientation etc. and integrated over the beam cross-section, can be expressed as

$$\left[A_{ij}, B_{ij}, D_{ij}\right] = \sum_i \int_{z_i}^{z_{i+1}} \bar{Q}_{ij}\left[1, z, z^2\right] b dz, \tag{2.137}$$

which is a slightly generalized form of Eq. 2.128. The coefficients associated with the inertial terms can be expressed as

$$[I_0, I_1, I_2] = \sum_i \int_{z_i}^{z_{i+1}} \rho\left[1, z, z^2\right] b dz. \tag{2.138}$$

In Eqs. 2.137 and 2.138, z_i and z_{i+1} are the Z-coordinate of bottom and top surfaces of the ith layer and b is the overall width of the beam. It can be noticed that for asymmetric ply stacking, all four modes; axial, flexural, shear and thickness contraction, are coupled with each other. This makes the problem cumbersome to solve accurately using an analytical approach for all boundary conditions. Note that we can recover the elementary beam equations by substituting $A_{55} \Longrightarrow \infty$ and $I_2 \Rightarrow 0$.

2.7.3 Governing Equations for a Composite Plate

Here, we will use the Classical Plate Theory (CLPT) to derive the equation of motion for a laminated composite plate. The plate is symbolized with three motions, namely the in-plane motions $u(x, y, t)$ and $v(x, y, t)$ and the out-of-plane motion $w(x, y, t)$. In addition, the plate can support two slopes in the in-plane directions, namely ϕ_x and ϕ_y, which as in the case of elementary beam, are derived from transverse displacement.

The assumed displacement field for a plate as per CLPT, is given by

$$\begin{aligned} U(x, y, z, t) &= u(x, y, t) - z\partial w/\partial x, \\ V(x, y, z, t) &= v(x, y, t) - z\partial w/\partial y, \\ W(x, y, z, t) &= w(x, y, t), \end{aligned}$$

where, u, v and w are the displacement components of the reference plane in the X, Y and Z directions, respectively and z is measured downward positive along the out-of-plane direction.

The associated non-zero strains are

$$\begin{Bmatrix} \varepsilon_{xx} \\ \varepsilon_{yy} \\ \varepsilon_{xy} \end{Bmatrix} = \begin{Bmatrix} \partial u/\partial x \\ \partial v/\partial y \\ \partial u/\partial y + \partial v/\partial x \end{Bmatrix} + \begin{Bmatrix} -z\partial^2 w/\partial x^2 \\ -z\partial^2 w/\partial y^2 \\ -2z\partial^2 w/\partial x \partial y \end{Bmatrix} = \{\varepsilon_\circ\} + \{\varepsilon_1\}, \tag{2.139}$$

where ε_{xx} and ε_{yy} are the normal strains in the X and the Y directions, respectively and ε_{xy} is the in-plane shear strain. The corresponding normal and shear stresses are related to these strains by the relation

$$\begin{Bmatrix} \sigma_{xx} \\ \sigma_{yy} \\ \sigma_{xy} \end{Bmatrix} = \begin{bmatrix} \bar{Q}_{11} & \bar{Q}_{12} & 0 \\ \bar{Q}_{12} & \bar{Q}_{22} & 0 \\ 0 & 0 & \bar{Q}_{66} \end{bmatrix} \begin{Bmatrix} \varepsilon_{xx} \\ \varepsilon_{yy} \\ \varepsilon_{xy} \end{Bmatrix}, \tag{2.140}$$

where $\bar{Q}_{ij}$ are the elements of the anisotropic constitutive matrix. As before, the expressions for $\bar{Q}_{ij}$ in terms of the elastic constants and ply-angles are given by Eq. 2.81. The force resultants are defined in terms of these stresses as

$$\begin{Bmatrix} N_{xx} \\ N_{yy} \\ N_{xy} \end{Bmatrix} = \int_A \begin{Bmatrix} \sigma_{xx} \\ \sigma_{yy} \\ \sigma_{xy} \end{Bmatrix} dA, \quad \begin{Bmatrix} M_{xx} \\ M_{yy} \\ M_{xy} \end{Bmatrix} = \int_A z \begin{Bmatrix} \sigma_{xx} \\ \sigma_{yy} \\ \sigma_{xy} \end{Bmatrix} dA. \tag{2.141}$$

Substituting Eqs 2.140 and 2.139 in Eq. 2.141, the relation between the force resultants and the displacement field is obtained as

$$\begin{Bmatrix} N_{xx} \\ N_{yy} \\ N_{xy} \end{Bmatrix} = \begin{bmatrix} A_{11} & A_{12} & 0 \\ A_{12} & A_{22} & 0 \\ 0 & 0 & A_{66} \end{bmatrix} \{\varepsilon_\circ\} + \begin{bmatrix} B_{11} & B_{12} & 0 \\ B_{12} & B_{22} & 0 \\ 0 & 0 & B_{66} \end{bmatrix} \{\varepsilon_1\}, \tag{2.142}$$

$$\begin{Bmatrix} M_{xx} \\ M_{yy} \\ M_{xy} \end{Bmatrix} = \begin{bmatrix} B_{11} & B_{12} & 0 \\ B_{12} & B_{22} & 0 \\ 0 & 0 & B_{66} \end{bmatrix} \{\varepsilon_\circ\} + \begin{bmatrix} D_{11} & D_{12} & 0 \\ D_{12} & D_{22} & 0 \\ 0 & 0 & D_{66} \end{bmatrix} \{\varepsilon_1\}, \tag{2.143}$$

where the elements A_{ij}, B_{ij} and D_{ij} are defined by Eq. 2.137.

The kinetic energy (T) and the strain energy (U) are defined in terms of the displacement field and stresses as

$$T = (1/2) \int_V \rho(\dot{U}^2 + \dot{V}^2 + \dot{W}^2) dV, \tag{2.144}$$

$$U = (1/2) \int_V (\sigma_{xx}\varepsilon_{xx} + \sigma_{yy}\varepsilon_{yy} + \sigma_{xy}\varepsilon_{xy}) dV. \tag{2.145}$$

Applying Hamilton's principle, the governing equations can be written in terms of these force resultants as

$$\partial N_{xx}/\partial x + \partial N_{xy}/\partial y = I_\circ \ddot{u} - I_1 \partial \ddot{w}/\partial x, \tag{2.146}$$

$$\partial N_{xy}/\partial x + \partial N_{yy}/\partial y = I_\circ \ddot{v} - I_1 \partial \ddot{w}/\partial y, \tag{2.147}$$

$$\begin{aligned} \partial^2 M_{xx}/\partial xx + 2\partial^2 M_{xy}/\partial xy + \partial^2 M_{yy}/\partial yy = I_\circ \ddot{w} - I_2(\partial^2 \ddot{w}/\partial xx + \partial^2 \ddot{w}/\partial yy) \\ + I_1(\partial \dot{u}/\partial x + \partial \dot{v}/\partial y), \end{aligned} \tag{2.148}$$

where the mass moments I_0, I_1 and I_2 are given by Eq. 2.138.

The governing equations can be further expanded in terms of the displacement components. However, because of their complexity, they are not given here and can be found in [12]. The associated boundary conditions are

$$\bar{N}_{xx} = N_{xx}n_x + N_{xy}n_y, \quad \bar{N}_{yy} = N_{xy}n_x + N_{yy}n_y, \tag{2.149}$$

$$\bar{M}_{xx} = -M_{xx}n_x - M_{xy}n_y, \tag{2.150}$$

$$\begin{aligned} \bar{V}_x = &(\partial M_{xx}/\partial x + 2\partial M_{xy}/\partial y - I_1 \ddot{u} + I_2 \partial \ddot{w}/\partial x) n_x \\ &+ (\partial M_{xy}/\partial x + 2\partial M_{yy}/\partial y - I_1 \ddot{v} + I_2 \partial \ddot{w}/\partial y) n_y, \end{aligned} \tag{2.151}$$

where $\bar{N}_{xx}$ and $\bar{N}_{yy}$ are the applied normal forces in the X and Y direction, $\bar{M}_{xx}$ and $\bar{M}_{yy}$ are the applied moments about the Y and X axes and $\bar{V}_x$ is the applied shear force in the Z direction. By expressing the strains and curvature in terms of displacements, we can write the governing equations for a plate.

2.8 Spectrum and Dispersion Relations

As mentioned earlier, the two important characteristics of wave propagation that are very significant from the SHM point of view are the spectrum and dispersion relations, respectively. Spectrum relations are obtained by plotting the different wavenumbers of the system with frequency. If the variation is a straight line, then the wavenumbers are linearly related to the frequency signifying that the waves are non dispersive and the group speeds do not depend on the frequency. Non dispersive waves do not change their shape as they propagate. This property is very useful in SHM since the reflections, if any coming from the damage of the structure, can be clearly identified from the time history plots if the group wave speeds are known. On the other hand, if the wavenumber has a nonlinear relation with frequency, then such waves are called dispersive waves and for these waves, at each frequency, their group speeds are different. These waves change their wave profiles as they propagate. Handling dispersive signals is more difficult. The wavenumber and group speeds for different 1D general waveguides were discussed earlier in Sect. 2.5.1.

In this section, we derive the spectrum and dispersion relations for a few specific waveguides. We saw in Sect. 2.5.1 that the wavenumber characteristic equation of one dimensional (1D) waveguides is a polynomial expression, the order of which is defined by the type of motion the waveguide can support. These equations can get more complicated due to the presence of stiffness or inertial coupling as is found in laminated composite structures. Hence, to solve such polynomial equation of very high order, we explain two different methods in this section.

2.8.1 Efficient Computation of the Wavenumber and Wave Amplitude

The constitutive relation and the displacement field in an laminated composite material give rise to both stiffness and inertial coupling, which poses great difficulty in wavenumber and wave vector computation. This is due to the increased order of the polynomial of the characteristic equation. The conventional method of wavenumber and coefficient computation (see Sect. 2.5.1) is not adequate to tackle this situation and there is a need to improve the existing formalism. The development towards this end started with the elementary composite beam [13], which needs a sixth-order polynomial to be solved for wavenumber computation. The wavenumbers were computed numerically, where the Newton–Raphson method

was used. The rest of the roots were expressed in terms of this real wavenumber. The coefficient vectors were evaluated analytically. The situation becomes complicated in the first-order shear deformable beam [14], where the wave matrix has a size of 3×3, although the spectrum relation is still a sixth-order polynomial. As was done before, the spectrum relation was solved numerically by tracking the real roots first using the NR algorithm, and wave amplitude vectors were evaluated analytically. It must be noted that computation of the wave vectors requires the solution of a system of matrices of size $N_v - 1 \times N_v - 1$, where N_v is the number of different motions the waveguide can support. The situation becomes too difficult to handle in the 3D beam model, where $N_v = 6$. This model gives rise to 6×6 wave matrix and as a result, it generates a 12th-order polynomial, which is required to be solved at each frequency. The solution of this equation is not possible using conventional quadratic solvers that was reported earlier in Sect. 2.5.1 or using the Newton–Raphson algorithm. As mentioned earlier, the characteristic equation is a polynomial in the wavenumber k and the problem can be formulated as a standard polynomial eigenvalue problem (PEP) of finding nonzero $\boldsymbol{v}$ and k such that

$$\boldsymbol{W}(k)\boldsymbol{v} = \left(\sum_{i=0}^{p} k^i \boldsymbol{A}_i\right)\boldsymbol{v} = 0 \tag{2.152}$$

where

$$\boldsymbol{A}_i \in C^{N_v \times N_v} \boldsymbol{v} \in C^{N_v \times 1}$$

and where p is the order of the PEP. Each $\boldsymbol{A}_i$ depends upon the material properties, frequency and wavenumber. Two different strategies are given here to solve the PEP.

2.8.1.1 Method 1: The Companion Matrix and the SVD Technique

In the first method, it is noted that the desired eigenvalues are the latent roots, which satisfy the condition $\det(\boldsymbol{W}(k)) = 0$ [8]. Further, if k_i is any such root, then there is at least one non-trivial solution for $\boldsymbol{v}$, which is known as the *latent eigenvector*. To find the latent root, the determinant is expanded in a polynomial $p(k)$, and solved by the companion matrix method, where the following matrix is formed:

$$L(p) = \begin{bmatrix} 0 & 1 & 0 & \cdots & 0 \\ 0 & 0 & 1 & & . \\ \vdots & \vdots & \vdots & \ddots & \vdots \\ 0 & 0 & & 0 & 1 \\ -\alpha_m & -\alpha_{m-1} & \cdots & -\alpha_2 & -\alpha_1 \end{bmatrix} \tag{2.153}$$

where $p(\lambda)$ is given by

$$p(\lambda) = \lambda^m + \alpha_1 \lambda^{m-1} + \cdots + \alpha_m. \tag{2.154}$$

One of the many important properties of the companion matrix is that the characteristic polynomial of $L(p)$ is $p(k)$ itself [9]. Thus, the eigenvalues of $L(p)$ are the roots of $p(k)$, which are obtained readily using any standard subroutine, e.g., LAPACK (xGEEV group).

Once the eigenvalues are obtained, they can be used to obtain the eigenvectors. To do so, it is to be noted that the eigenvectors are the elements of the null space of $\boldsymbol{W}(k)$ and the eigenvalues make this null space non-trivial by rendering $\boldsymbol{W}(k)$ singular. Hence, computation of the eigenvectors is equivalent to computation of the null space of a matrix. To this end, the singular value decomposition (SVD) method is most effective. Any matrix $\boldsymbol{A} \in C^{m \times n}$ can be decomposed in terms of unitary matrices $\boldsymbol{U}$ and $\boldsymbol{V}$ and diagonal matrix $\boldsymbol{S}$ as $\boldsymbol{A} = \boldsymbol{U}\boldsymbol{S}\boldsymbol{V}^H$, where H denotes the Hermitian conjugate [4]. Also, $\boldsymbol{S}$ is the matrix of singular values. The columns of the unitary matrix $\boldsymbol{V}$ that correspond to zero singular values (zero diagonal elements of $\boldsymbol{S}$) are the elements of the null space of $\boldsymbol{A}$. The SVD again can be performed by any standard subroutine (e.g. xGESVD group of LAPACK)

2.8.1.2 Method 2: Linearization of PEP

In this method, the PEP is linearized as

$$\boldsymbol{A}z = \lambda \boldsymbol{B}z \tag{2.155}$$

with

$$\boldsymbol{A}, \boldsymbol{B} \in C^{pN_v \times pN_v}$$

and where

$$\boldsymbol{A} = \begin{bmatrix} 0 & \boldsymbol{I} & 0 & \cdots & 0 \\ 0 & 0 & \boldsymbol{I} & \cdots & 0 \\ \vdots & \vdots & \ddots & \ddots & \vdots \\ \vdots & \vdots & \ddots & \ddots & \boldsymbol{I} \\ -\boldsymbol{A}_0 & -\boldsymbol{A}_1 & \boldsymbol{A}_2 & \cdots & -\boldsymbol{A}_{p-1} \end{bmatrix}, \quad \boldsymbol{B} = \begin{bmatrix} \boldsymbol{I} & & & & \\ & \boldsymbol{I} & & & \\ & & \ddots & & \\ & & & \boldsymbol{I} & \\ & & & & -\boldsymbol{A}_p \end{bmatrix}, \tag{2.156}$$

The relation between x and z is given by $z = (x^T, \lambda x^T, \ldots, \lambda^{p-1} x^T)^T$, while $\boldsymbol{B}^{-1}\boldsymbol{A}$ is a block companion matrix of the PEP. The generalized eigenvalue problem of Eq. 2.155 can be solved by the QZ algorithm, the iterative method, the Jacobi–Davidson method or the rational Krylov method. Each one of these has its own advantages and deficiencies, however, the QZ algorithm is the most powerful method for small to moderate sized problems, and is employed in the subroutines available in LAPACK (xGGEV and xGGES group).

In both of these methods, an eigenvalue solver is employed, where for the QZ algorithm, the cost of computation is $\sim 30n^3$ and an extra $\sim 16n^3$ for eigenvector computation (n is the order of the matrix). Since, the order of the companion matrix in the second method is three times that of the first method, the cost is 27 times more, which is significant as this computation is to be performed $N \times M$ times.

The PEP admits $N_v \times p$ eigenvalues and p eigenvectors. If both $\boldsymbol{A}_0$ and $\boldsymbol{A}_p$ are singular, the problem is potentially ill-posed. Theoretically, the solutions might not exist or might not be unique. Computationally, the computed solutions may be inaccurate. If one, but not both, $\boldsymbol{A}_0$ and $\boldsymbol{A}_p$ is singular, the problem is well posed, but some of the eigenvalues may be zero or infinite, and caution should be exercised in rejecting those roots.

There are advantages and disadvantages of both methods. In the first method, the determinant of the wave matrix needs to be formed, which for large N_v is too difficult to obtain. In this case, resorting to the second method is advantageous as it obviates the necessity for obtaining the lengthy expressions for α_i in Eq. 2.154. However, in the second method, there is no control over the eigenvalues, as we might be interested sometimes in separating the forward propagating wavenumbers (for the formulation of throw-off elements). In this case, the first method is the only option.

2.8.2 Spectrum and Dispersion Relation for an Elementary Beam

The first step in constructing the spectrum and dispersion relation is to transform the governing differential equation to the frequency domain using DFT, which would normally lead to an ordinary differential equation with constant coefficient. In the present case, the governing differential equations are given by Eqs. 2.123 and 2.124. The DFT on the field variables u^0 and w is given by

$$u^o(x,t) = \sum_{n=1}^{N} \hat{u}(x,\omega_n) e^{j\omega_n t} = \sum_{n=1}^{N} \left(\tilde{u}_p e^{-jk_p x}\right) e^{j\omega_n t}, \tag{2.157}$$

$$w(x,t) = \sum_{n=1}^{N} \hat{w}(x,\omega_n) e^{j\omega_n t} = \sum_{n=1}^{N} \left(\tilde{w}_p e^{-jk_p x}\right) e^{j\omega_n t}, \tag{2.158}$$

When the above transform is substituted in the governing equation, the governing PDE's will become a set of ODE's with the time t removed from the governing equation and the frequency ω introduced as a parameter. The resulting ODE's are of constant coefficients type and have complex exponentials as solutions. When the exponential solutions are substituted in the transformed ODE's, we get a characteristic equation for the computation of wavenumber k, which can be transformed into PEP, which is given by

$$k_p^4\begin{bmatrix}0 & 0\\ 0 & D_{11}\end{bmatrix}+k_p^3\begin{bmatrix}0 & -jB_{11}\\ jB_{11} & 0\end{bmatrix}+k_p^2\begin{bmatrix}A_{11} & 0\\ 0 & 0\end{bmatrix}+\begin{bmatrix}-\rho A\omega^2 & 0\\ 0 & -\rho A\omega^2\end{bmatrix}\begin{Bmatrix}\tilde{u}_p\\ \tilde{w}_p\end{Bmatrix}=\begin{Bmatrix}0\\ 0\end{Bmatrix} \tag{2.159}$$

This equation is of the form given in Eq. 2.152, which can be recast in the form given by Eq. 2.153 or 2.155. Using the companion matrix method outlined in Sect. 2.8.1.1, we can determine the wavenumbers and the group speeds. Once the solutions k_p and the pairs $\{\tilde{u}_p, \tilde{w}_p\}$ are obtained for each p, the explicit form of the solution is

$$\begin{Bmatrix}\hat{u}(x,\omega_n)\\ \hat{w}(x,\omega_n)\end{Bmatrix}=\sum_{m=1}^{6}C_m\begin{Bmatrix}R_{1m}\\ R_{2m}\end{Bmatrix}e^{-jk_m x}. \tag{2.160}$$

We will now plot the spectrum and dispersion relations. The main objective here is to bring out the effect of coupling on wave behavior. The maximum axial–flexural coupling that one gets from such natural ply-stacking is when the cross-plies and 0^o plies are stacked in separate groups. A generalization of the effect of axial–flexural coupling gives some valuable insights, when the spectrum relation (Fig. 2.13) and dispersion relation (Fig. 2.14) are studied. The bending–axial coupling is characterized by a factor $r = B_{11}^2/D_{11}A_{11}$. An AS/3501-6 graphite–epoxy plies (thickness of each layer 1.0 mm) with three stacking sequences $[0_{10}](r = 0.0), [0_5/30_2/60_3](r = 0.312)$ and $[0_5/90_5](r = 0.574)$ are considered. In Fig. 2.13, it can be observed that, corresponding to axial mode (Mode 1) and flexural modes (Mode 2 and 3), the wavenumbers increase in magnitude for increasing coupling. However, this increase in Mode 2 (propagating component) is more than that in Mode 3 (evanescent component). Fig. 2.14 also shows the variation of group speed $C_g = d\omega/dk_j$ normalized with the parameter

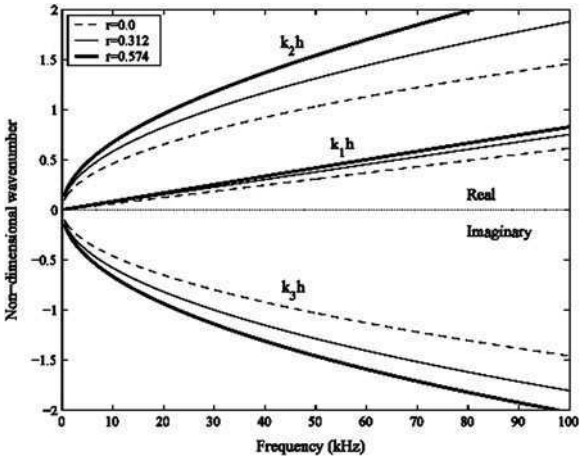

Fig. 2.13 Spectrum relation for various axial–flexural couplings

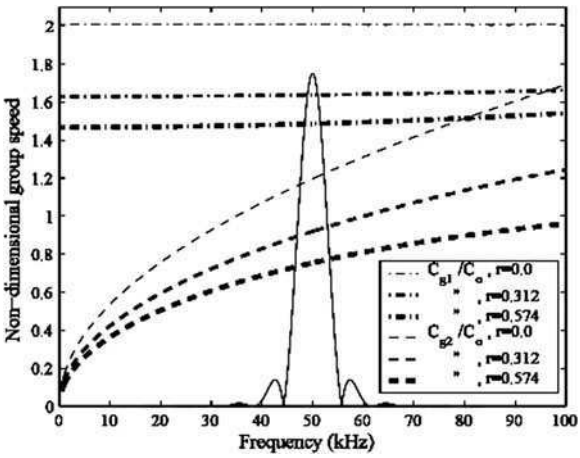

Fig. 2.14 Dispersion relation for various axial–flexural couplings—frequency amplitude spectrum of a modulated sinusoidal pulse

$c_o = \sqrt{E/\rho}$. From these plots, it is clear that the axial speed is reduced by more than 26% due to the presence of asymmetry arising from cross-ply stacking in groups. Also at around 50 kHz, the flexural speed of propagation is reduced by 42% for maximum coupling.

2.8.3 *Spectrum and Dispersion Relation for a Higher Order Beam*

The governing Equation for a higher order beam is given by Eqs. 2.131–2.134. As before, the governing equations are transformed to frequency domain using DFT, where the displacement field, $\{\mathbf{u}\} = \{u^o, \psi, w, \phi\}(x,t)$, can be written as

$$\boldsymbol{u} = \sum_{n=1}^{N} \{\tilde{u}, \tilde{\psi}, \tilde{w}, \tilde{\phi}\}(x) e^{-j\omega_n t} = \sum_{n=1}^{N} \tilde{\boldsymbol{u}}(x) e^{-j\omega_n t}, \tag{2.161}$$

where ω_n is the circular frequency at the nth sampling point and N is the frequency index corresponding to the Nyquist frequency in DFT.

Substituting the assumed solution of the field variables in Eqs. 2.131–2.134, a set of ODEs is obtained for $\tilde{\mathbf{u}}(x)$. Since, the ODEs have constant coefficients, the solution is of the form $\tilde{\boldsymbol{u}}_0 e^{-jkx}$, where k is the wavenumber and $\tilde{\boldsymbol{u}}_0$ is a vector of unknown constants, i.e., $\tilde{\boldsymbol{u}}_0 = \{u_\circ, \psi_\circ, w_\circ, \phi_\circ\}$. Substituting the assumed form in the set of ODEs, a matrix–vector relation is obtained which gives the following characteristic equation

$$\boldsymbol{W}\tilde{\boldsymbol{u}}_0 = \boldsymbol{0} \tag{2.162}$$

where $\boldsymbol{W}$ is

$$\begin{bmatrix} A_{11}k^2 - I_\circ\omega_n^2 & jA_{13}k & 0 & I_1\omega_n^2 - B_{11}k^2 \\ -jA_{13}k & -k_I I_2\omega_n^2 + A_{33} + D_{55}k^2 & -I_1\omega_n^2 + B_{55}k^2 & -jB_{55}k + jB_{13}k \\ 0 & -I_1\omega_n^2 + B_{55}k^2 & A_{55}k^2 - I_\circ\omega_n^2 & -jA_{55}k \\ I_1\omega_n^2 - B_{11}k^2 & jB_{55}k - jB_{13}k & jA_{55}k & -I_2\omega_n^2 + D_{11}k^2 + A_{55} \end{bmatrix}. \tag{2.163}$$

In this case, we use the method based on linearization of PEP outlined in Sect. 2.8.1.2. According to the previous discussion, in this case, the order of the PEP, $p = 2$ and N_v (size of the $\boldsymbol{W}$) is 4. Thus, there are eight eigenvalues altogether, which are the roots of the polynomial (called the spectrum relation obtained from the singularity condition of $\boldsymbol{W}$ as

$$Q_1k^8 + Q_2k^6 + Q_3k^4 + Q_4k^2 + Q_5 = 0. \tag{2.164}$$

The spectrum relation suggests that the roots can be written as $\pm k_1, \pm k_2, \pm k_3$ and $\pm k_4$.

Before solving this eighth-order characteristic equation (obtained by setting the determinant of the PEP equal to zero), one can obtain an overview of the number of propagating and evanescent modes as follows. By substituting $\omega_n = 0$ in the characteristic equation and solving for k_j, it can be shown that for the uncoupled case ($B_{ij} = 0$)

$$k(0)_{1,\ldots,6} = 0, \quad k(0)_{7,8} = \pm\sqrt{\frac{A_{13}^2 - A_{11}A_{33}}{A_{55}D_{55}}}. \tag{2.165}$$

This implies that six zero roots starting at $\omega_n = 0$ correspond to the axial, flexural and shear modes, whereas the two nonzero roots must be the wavenumbers associated with the contractional mode. Here, it is to be noted that $\sigma_{zz} = 0$ for elementary Beam theory and FSDT for the 3D orthotropic constitutive model is reduced to plane stress model with respect to the XY plane. However, in the presence of thickness contraction, $\sigma_{zz} \neq 0$, which requires a plane-stress model in the XZ plane reduced from a 3D constitutive model. This produces a slight difference in the values of A_{55} compared to that in FSDT. However, almost all the conventional fiber reinforced composites used as structural material have $Q_{11} > Q_{13}, Q_{33} > Q_{13}$, which implies that the nonzero roots in Eq. 2.165 must be imaginary at and near $\omega_n = 0$. Therefore, we have two evanescent (one forward and one backward) components in the contractional mode in the low frequency regime. Next, by substituting $k_j = 0$ in Eq. 2.164 and solving for ω_n, we get the cut-off frequencies as

$$\omega_{\text{cut-off}} = 0, 0, 0, 0, \sqrt{\frac{A_{55}}{I_2(1 - s_2^2)}}, \sqrt{\frac{A_{33}}{I_2(1 - s_2^2)}}. \tag{2.166}$$

This shows that initially there are two forward propagating modes(one axial, one flexural), two backward propagating modes (one axial and one flexural), two evanescent flexural modes (forward and backward) and two additional evanescent

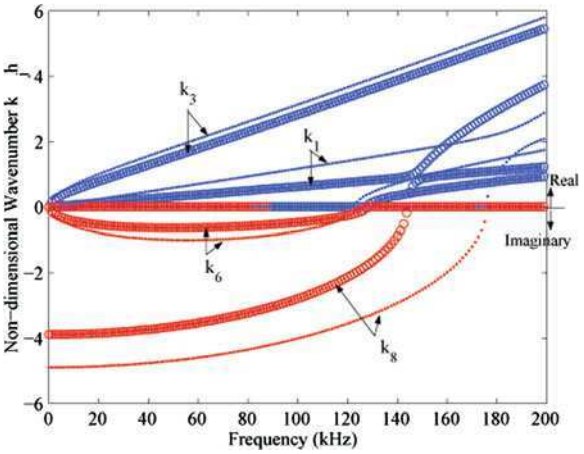

Fig. 2.15 Nature of wavenumber dispersion in axial (k_1), flexural (k_3), and shear (k_6) with cut-off and contraction (k_8) with cut-off; 'o', graphite–epoxy AS/3501 $[0]_{10}$ composite; …, glass–epoxy $[0]_{10}$ composite; Total thickness $h = 0.01$ m

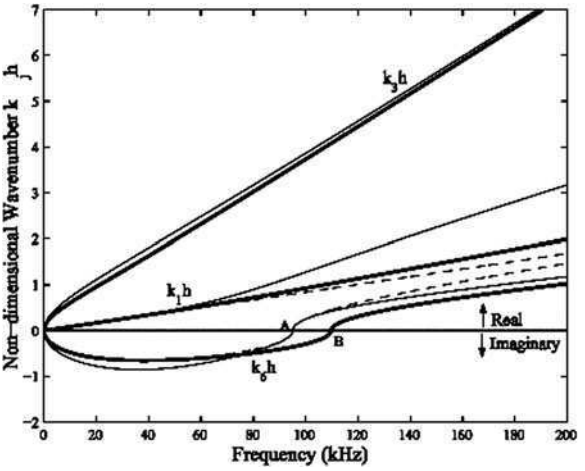

Fig. 2.16 Nature of wavenumber dispersion in axial, flexural and shear modes for different stiffness and material asymmetries; - - -, $r = 0.0, s2 = 0.0$; —, $r = 0.757, s2 = 0.0$; —, $r = 0.0, s2 = 0.5$. The locations of cut-off frequency are marked by A and B

contractional modes (forward and backward) for $\omega_n > 0$. The shear mode starts propagating after the cut-off frequency corresponding to A_{55} in Eq. 2.166. The contractional mode starts propagating later, since $A_{33} \geq A_{55}$.

In Fig. 2.15, the wavenumber dispersion is plotted for AS/3501 graphite–epoxy and glass–epoxy $[0]_{10}$ composite beam with total thickness $h = 0.01$ m. Material properties are taken from [12]. Note that the graphite–epoxy has very high ratio E_{11}/G_{13} ($\approx$20) and moderate stiffness $E_{11} \approx 144$ GPa. On the other hand, the glass–epoxy has very low ratio E_{11}/G_{13} ($\approx$6) and very low stiffness $E_{11} \approx 54$ GPa. For both of these materials, the plot in Fig. 2.15 shows that the propagating components before the cut-off frequency in contraction are similar to those in Fig. 2.16 in the absence of the variable ψ. Also the wavenumber associated with the evanescent components in contractional mode before the cut-off frequency is much higher than that due to shear, and therefore decays rapidly.

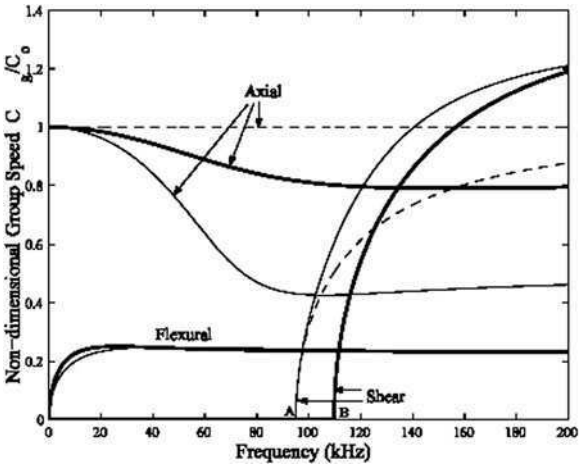

Fig. 2.17 Dispersion of group speeds in axial, flexural and shear modes for different stiffness and material asymmetries; - - -, $r = 0.0, s2 = 0.0$; —, $r = 0.757, s2 = 0.0$; —, $r = 0.0, s2 = 0.5$. The locations of cut-off frequency are marked by A and B

Hence, below the cut-off frequency in contraction (which is always much higher than shear cut-off since $A_{33} > A_{55}$ for a composite), change in the response due to addition of the contractional mode is negligible.

When the thickness contraction term ψ is neglected in the displacement field, and subsequently in the wave equations, the characteristic equation is a sixth-order polynomial in k. Again, the PEP framework is used to obtain the wavenumber and hence, the group speeds.

In Fig. 2.16, the dispersion of wavenumbers corresponding to axial, flexural and shear modes are shown. An AS/3501-6 graphite–epoxy beam cross-section with depth $h = 0.01$ m is considered. Beside this, to study how the wave packets travel at different frequencies, the group speeds $c_g = Re[d\omega_n/dk_j]$ in the axial, flexural and shear modes are plotted in Fig. 2.17, where $c_0 = \sqrt{A_{11}/I_0}$ is the constant phase speed in axial mode. From these two plots, only one cut-off frequency appears, above which the shear mode starts propagating, which is otherwise an evanescent component contributing to the flexural wave. Figure 2.17 shows that the higher the stiffness coupling (higher value of r) the higher the group speed of the shear wave above the cut-off frequency. At the same time, the group speed of the longitudinal wave drastically falls well before the cut-off frequency. The flexural mode remains least affected by both stiffness and mass coupling, and remains almost non-dispersive above the cut-off frequency.

2.8.4 Spectrum and Dispersion Relation for an Anisotropic Plate

Here, we begin with the governing differential equation, derived earlier (Eqs. 2.146–2.148). These force resultant differential equations are first written in terms of displacement using force resultant displacement relationship. These differential equations are functions of two spatial variables x and y. By assuming that

the second spatial variable, that is, y extends to infinity, we eliminate this variable from the governing equation by taking an additional transform in this direction. This process introduces an additional wavenumber in the horizontal direction. Instead of using DFT for the second transform in the y directions, Fourier Series can be conveniently employed for the ease of applying the loading boundary conditions [5]. Hence, the solution for the three dependent variables (displacements $u(x,y,t), v(x,y,t)$ and $w(x,y,t)$) is given by

$$u(x,y,t) = \sum_{n=0}^{N-1}\sum_{m=1}^{M} \hat{u}(x)\begin{Bmatrix}\cos(\eta_m y)\\ \sin(\eta_m y)\end{Bmatrix} e^{-j\omega_n t}, \tag{2.167}$$

$$v(x,y,t) = \sum_{n=0}^{N-1}\sum_{m=1}^{M} \hat{v}(x)\begin{Bmatrix}\sin(\eta_m y)\\ \cos(\eta_m y)\end{Bmatrix} e^{-j\omega_n t}, \tag{2.168}$$

$$w(x,y,t) = \sum_{n=0}^{N-1}\sum_{m=1}^{M} \hat{w}(x)\begin{Bmatrix}\cos(\eta_m y)\\ \sin(\eta_m y)\end{Bmatrix} e^{-j\omega_n t}, \tag{2.169}$$

where again the cosine or sine dependency is chosen based on the symmetry or anti-symmetry of the applied load about the X axis and η_m is the horizontal wavenumber corresponding to mth spatial mode. Substituting Eqs. 2.167–2.169 in the governing differential equations, a set of ODEs is obtained for the unknowns $\hat{u}(x), \hat{v}(x)$ and $\hat{w}(x)$. Since these ODEs have constant coefficients, their solutions can be written as $\tilde{u}e^{-jkx}, \tilde{v}e^{-jkx}$ and $\tilde{w}e^{-jkx}$, where k is the wavenumber in the X direction, yet to be determined and $\tilde{u}, \tilde{v}$ and $\tilde{w}$ are the unknown constants. Substituting these assumed forms in the set of ODEs, a PEP is posed to find $(\boldsymbol{v}, k)$, such that,

$$\boldsymbol{\Psi}(k)\boldsymbol{v} = (k^4\boldsymbol{A}_4 + k^3\boldsymbol{A}_3 + k^2\boldsymbol{A}_2 + k\boldsymbol{A}_1 + \boldsymbol{A}_0)\boldsymbol{v} = 0, \quad \boldsymbol{v} \neq 0, \tag{2.170}$$

where $\boldsymbol{A}_i \in \boldsymbol{C}^{3\times 3}$, k is an eigenvalue and $\boldsymbol{v}$ is the corresponding right eigenvector. The matrices $\boldsymbol{A}_i$ are

$$\boldsymbol{A}_0 = \begin{bmatrix} -A_{66}\eta_m^2 + I_\circ\omega_n^2 & 0 & 0 \\ 0 & -A_{22}\eta_m^2 + I_\circ\omega_n^2 & -B_{22}\eta_m^3 + I_1\omega_n^2\eta_m \\ 0 & -B_{22}\eta_m^3 + I_1\omega_n^2\eta_m & -D_{22}\eta_m^4 + I_\circ\omega_n^2 + I_2\omega_n^2\eta_m^2 \end{bmatrix}, \tag{2.171}$$

$$\boldsymbol{A}_1 = \begin{bmatrix} 0 & -j\eta_m(A_{12}+A_{66}) & -j\eta_m^2(B_{12}+2B_{66}) + jI_1\omega_n^2 \\ j\eta_m(A_{12}+A_{66}) & 0 & 0 \\ j\eta_m^2(B_{12}+2B_{66}) - jI_1\omega_n^2 & 0 & 0 \end{bmatrix}, \tag{2.172}$$

$$\boldsymbol{A}_2 = \begin{bmatrix} -A_{11} & 0 & 0 \\ 0 & -A_{66} & -\eta_m(B_{12}+2B_{66}) \\ 0 & -\eta_m(B_{12}+2B_{66}) & -\eta_m^2(2D_{12}+4D_{66})+I_2\omega_n^2 \end{bmatrix}, \tag{2.173}$$

$$\boldsymbol{A}_3 = \begin{bmatrix} 0 & 0 & -jB_{11} \\ 0 & 0 & 0 \\ jB_{11} & 0 & 0 \end{bmatrix}, \tag{2.174}$$

$$\boldsymbol{A}_4 = \begin{bmatrix} 0 & 0 & 0 \\ 0 & 0 & 0 \\ 0 & 0 & -D_{11} \end{bmatrix}. \tag{2.175}$$

It can be noticed that $\boldsymbol{A}_4$ is singular, thus the lambda matrix $\Psi(k)$ is not regular [9] and admits infinite eigenvalues [16].

The PEP is solved by the methods described before. In this case, the spectrum relation is a quartic polynomial in m, where $m = k^2$,

$$p(m) = m^4 + C_1 m^3 + C_2 m^2 + C_3 m + C_4, \quad C_i \in \boldsymbol{C}, \tag{2.176}$$

which generates a companion matrix of order 4. In both the methods of wavenumber computation described earlier, an eigenvalue solver based on QZ algorithm is employed. The polynomial governing the wavenumbers (Eq. 2.176) is solved by considering a graphite–epoxy (AS/3501) plate of 10 mm thickness. Two different ply-stacking sequences are considered, one symmetric $[0_{10}]$ and the other asymmetric $[0_5/90_5]$. The Y wavenumber, η_m is fixed at 50 for all the wavenumber computations. The real and imaginary part of the wavenumbers are shown in Figs. 2.18 and 2.19, respectively. The points in the abscissa marked 1, 2 and 3 denote the cut-off frequencies and they are at 3, 13.7 and 21 kHz. Two roots are equal before point 1, and they are denoted by $k_{1,2}$. Thus, before point 1, there are only four non-zero real roots ($\pm k_{1,2}$) and eight non-zero imaginary roots

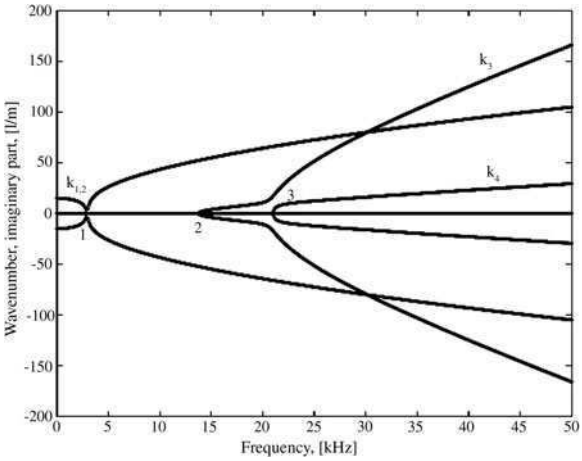

Fig. 2.18 Real part of wavenumbers, symmetric sequence

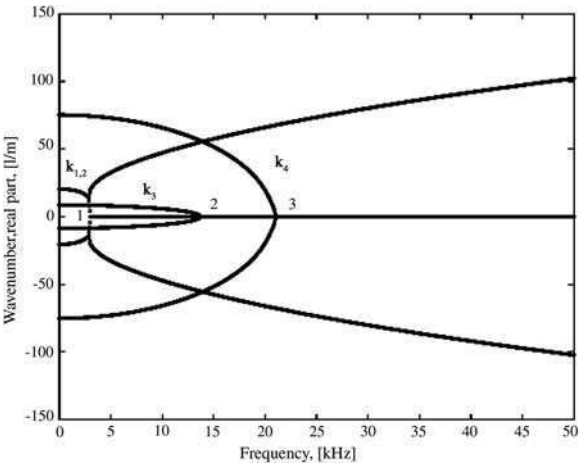

Fig. 2.19 Imaginary part of wavenumbers, symmetric sequence

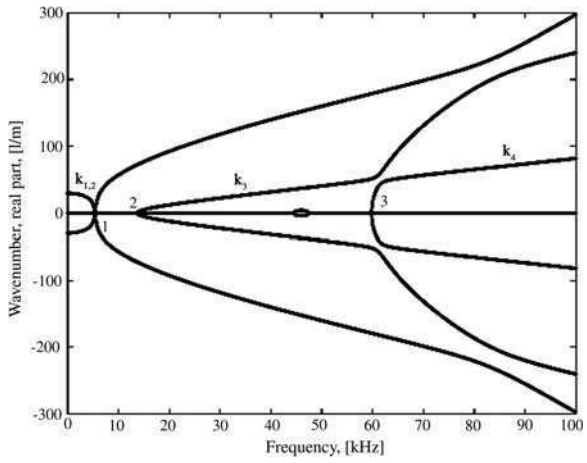

Fig. 2.20 Real part of wavenumbers, asymmetric sequence

($\pm k_{1,2}, \pm k_3$ and $\pm k_4$). After point 1, one of the $k_{1,2}$ becomes pure real and another one becomes pure imaginary and there is only an imaginary root at high frequency. These roots correspond to the bending mode, w. It can be further noticed that before point 1, these wavenumbers ($k_{1,2}$) simultaneously possess both real and imaginary parts, which implies these modes are attenuated while propagating. Thus, there exist inhomogeneous waves in anisotropic composite plate [1]. The points marked 2 and 3 are the two cut-off frequencies, since the roots k_3 and k_4 become real at this point from their imaginary values. These roots correspond to the in plane motion, i.e., u and v displacements.

Next, the asymmetric ply-sequence is considered (Figs. 2.20 and 2.21), for which the wavenumber pattern remains qualitatively the same. The cut-off frequencies are at 5.3, 13.8 and 60 kHz, where the first one corresponds to the bending mode and the last two correspond to the in-plane motion. In comparison to

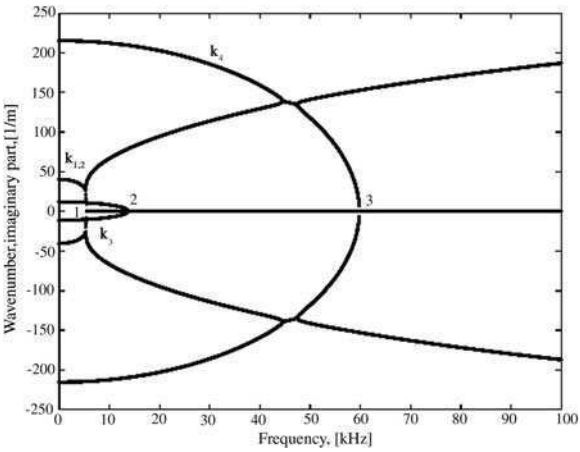

Fig. 2.21 Imaginary part of wavenumbers, asymmetric sequence

symmetric ply-stacking, it can be said that the first and the third cut-off frequencies are of higher magnitude than their symmetric counterparts and the rate of increment is higher in the third cut-off frequency. Further, the magnitudes of all wavenumbers are increased. Significantly, at higher frequency, the third wavenumber k_3 has lower magnitude than the bending wavenumbers (one of $k_{1,2}$) as opposed to the symmetric case. Similar trends are visible in the imaginary part of the wavenumbers, where the magnitude is higher in all cases (almost double) than the imaginary wavenumbers of the symmetric sequence. Thus attenuation of the propagating modes is comparatively higher in the asymmetric case.

The cut-off frequencies can be obtained from Eq. 2.176 by letting $k = 0$ and solving for ω_n. The governing equation for the cut-off frequency becomes

$$a_0\omega_n^6 + a_1\omega_n^4 + a_2\omega_n^2 + a_3 = 0, \tag{2.177}$$

where a_i are material property and wavenumber η_m dependent coefficients given as

$$a_0 = I_\circ^2 I_2\eta^2 + I_\circ^3 - I_\circ I_1^2 I_2, \tag{2.178}$$

$$a_1 = -I_\circ^2 D_{22}\eta^4 - I_\circ^2(A_{22} + A_{66})\eta^2 - I_\circ I_2\eta^4(A_{66} + A_{22}) + A_{66}\eta^4 I_1^2 + 2I_\circ B_{22}\eta_4 I_1, \tag{2.179}$$

$$\begin{aligned} a_2 = {} & -I_\circ B_{22}^2\eta^6 + A_{66}\eta^4 A_{22} I_\circ + A_{66}\eta^6 I_\circ D_{22} - 2A_{66}\eta^6 B_{22} I_1 \\ & + I_\circ A_{22}\eta^6 D_{22} + A_{66}\eta^6 A_{22} I_2, \end{aligned} \tag{2.180}$$

$$a_3 = A_{66}\eta^8(-A_{22}D_{22} + B_{22}^2). \tag{2.181}$$

When Eq. 2.177 is solved for different η_m, the variation of the cut-off frequencies with η_m can be obtained. This variation is given in Fig. 2.22. As shown in the figure, variation of the cut-off frequency for the bending mode $\omega_{1,2}$ follows a non-linear pattern, whereas the other two increase linearly. Although not evident

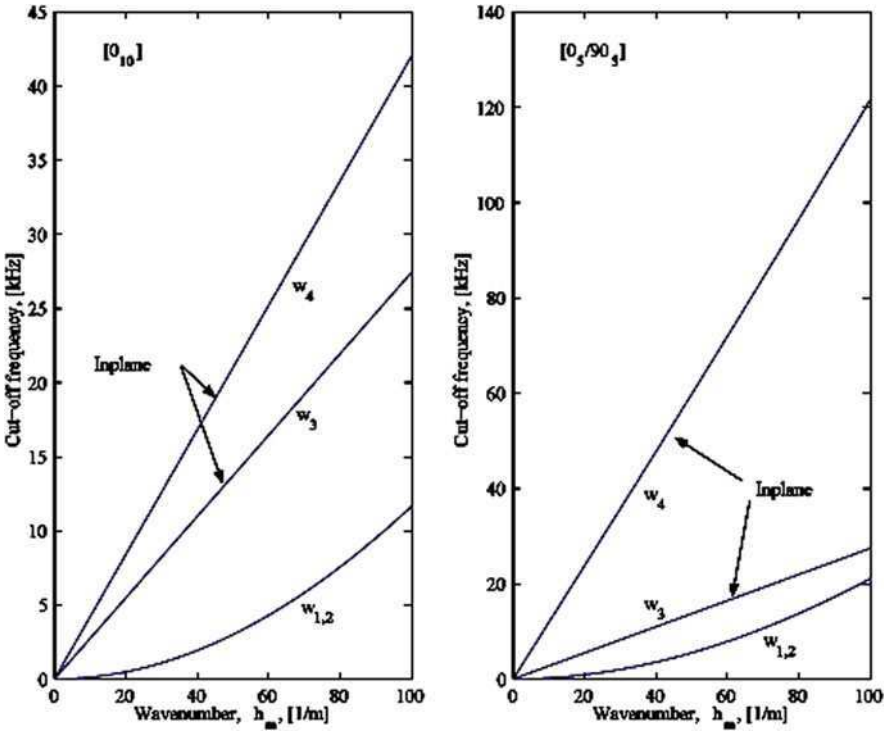

Fig. 2.22 Variation of cut-off frequency with η_m

from this figure, close inspection reveals that the pattern for ω_3 is the same for both symmetric and asymmetric cases. Since it is the magnitude of A_{12} that has not changed with ply-angle, it can be concluded that ω_3 is proportional to the ratio of $\sqrt{A_{12}/\rho}$. Further, there is no variation in $\omega_{1,2}$ for changing ply-stacking, whereas, for ω_4, the effect is maximum. Thus, with the help of this figure, the location of the points 1–3 in Fig. 2.18, 2.19, 2.20 and 2.21 can be explained.

References

1. Caviglia G, Morro A (1992) Inhomogeneous waves in solids and fluids. World Scientific, Singapore
2. Clough RW, Penzin J (1975) Dynamics of structures. Printice-Hall, New York
3. Doyle JF (1997) Wave propagation in structures. Springer, New York
4. Golub G, Van Loan C (1989) Matrix computations. Johns Hopkins University Press, Baltimore
5. Gopalakrishnan S, Chakraborty A, Roy Mahapatra D (2008) Spectral finite element method. Springer, London

6. Jones RM (1975) Mechanics of composites material. McGraw Hill, New York
7. Krezig E (1992) Advanced engineering mathematics, 9th edn. McGraw Hill, New York
8. Lancaster P (1966) Lambda matrices and vibrating systems. Pergamon Press, Oxford
9. Lancaster P (1969) Theory of matrices. Acaxdemic Press, New York
10. Mindlin RD, Herrmann G (1950) A one dimensional theory of compressional waves in an elastic rod. In: Proceedings of first U.S. national congress of applied mechanics, pp 187–191
11. Nayfeh AH (1995) Wave propagation in layered anisotropic media. North Holland, Amsterdam
12. Reddy JN (1997) Mechanics of laminated composite plates. CRC Press, Boca Raton
13. Roy Mahapatra D, Gopalakrishnan S, Sankar TS (2000) Spectral-element-based solutions for wave propagation analysis of multiply connected laminated composite beams. J Sound Vib 237(5):819–836
14. Roy Mahapatra D, Gopalakrishnan S (2002) A spectral finite element model for analysis of axial–flexural–shear coupled wave propagation in laminated composite beams. Compos Struct 59(1):57–88
15. Timoshenko SP (1921) On the correction factor for shear of the differential equation for transverse vibrations of bars of uniform cross-section. Philosophical Magazine, p 744
16. Tisseur F, Meerbergen K (2001) The quadratic eigenvalue problem. SIAM Rev 43(2):235–286
17. Tsai SW, Hahn HT (1980) Introduction to composite materials. Technomic, Westport
18. Varadan VK, Vinoy KJ, Gopalakrishnan S (2006) Smart material systems and MEMS. Wiley, Chichester

Chapter 3
Signal Processing Techniques

3.1 Integral Transforms

It is customary in SHM studies to handle time signals of varying complexity, which requires manipulation and fine tuning for their use in damage prediction. In many cases, these actions are effective if performed in the frequency domain. In addition, SHM studies involve using signals of high frequency content and require methods for wave propagation analysis. There are a number of different methods available to transform a time signal into the frequency domain. Advantages and disadvantages as well as issues concerning these different transforms are described in the following sections.

3.1.1 Fourier Transforms

A time signal can be represented in the Fourier (frequency) domain in three possible ways, namely the *Continuous Fourier Transform* (CFT), the *Fourier Series* (FS) and the *Discrete Fourier Transform* (DFT). In this section, only brief descriptions of the above transforms are given. The reader is encouraged to refer to [13] for more details.

3.1.1.1 Continuous Fourier Transforms

Consider any time signal $F(t)$. The inverse and the forward CFTs, normally referred to as the transform pair, are given by

S. Gopalakrishnan et al., *Computational Techniques for Structural Health Monitoring*, Springer Series in Reliability Engineering, DOI: 10.1007/978-0-85729-284-1_3,

$$F(t) = \frac{1}{2\pi} \int_{-\infty}^{\infty} \hat{F}(\omega) e^{j\omega t} d\omega, \quad \hat{F}(\omega) = \int_{-\infty}^{\infty} F(t) e^{-j\omega t} dt, \tag{3.1}$$

where ω is the angular frequency and j ($j^2 = -1$) is the complex number. $\hat{F}(\omega)$ is necessarily complex and a plot of the amplitude of this function against frequency will represent the frequency content of the time signal. As an example, consider a rectangular time signal of pulse width d. Mathematically, this function can be represented as

$$\begin{aligned} F(t) &= F_0 \quad -d/2 \le t \le d/2 \\ &= 0 \quad \text{otherwise.} \end{aligned} \tag{3.2}$$

This time signal is symmetrical about the origin. If this expression is substituted in Eq. 3.1, we get

$$\hat{F}(\omega) = F_0 d \left\{ \frac{\sin(\omega d/2)}{\omega d/2} \right\}. \tag{3.3}$$

The CFT for this function is real only and symmetric about $\omega = 0$. The term inside the curly brace is called the *sinc* function. Also, the value of the CFT at $\omega = 0$ is equal to the area under the time signal.

Now the pulse is allowed to propagate in the time domain by an amount t_0. Mathematically such a signal can be written as

$$\begin{aligned} F(t) &= F_0 \quad t_0 \le t \le t_0 + d \\ &= 0 \quad \text{otherwise.} \end{aligned} \tag{3.4}$$

Substituting the above function in Eq. 3.1 and integrating, gives

$$\hat{F}(\omega) = F_0 d \left\{ \frac{\sin(\omega d/2)}{\omega d/2} \right\} e^{-j\omega(t_0 + d/2)}. \tag{3.5}$$

The above CFT has both real and imaginary parts. These are plotted in Fig. 3.1. From Eqs. 3.3 and 3.5, we see that the magnitude of both these transforms are the same, however, the second transform has phase information built in it. That is, we see that the propagation of the signal in the time domain is associated with the change of phase in the frequency domain. Wave propagation problems are always associated with phase changes, which occur as the signal propagates. Based on the CFT, one can also determine the spread of the signal in both the time and frequency domain. For this, one has to look at the frequencies at which the CFT is zero. This occurs when

$$\sin\left(\frac{\omega_n d}{2}\right) = 0, \quad \frac{\omega_n d}{2} = n\pi, \quad \text{or} \quad \omega_n = \frac{2n\pi}{d} \; \omega_2 - \omega_1 = \Delta\omega = \frac{4\pi}{d}$$

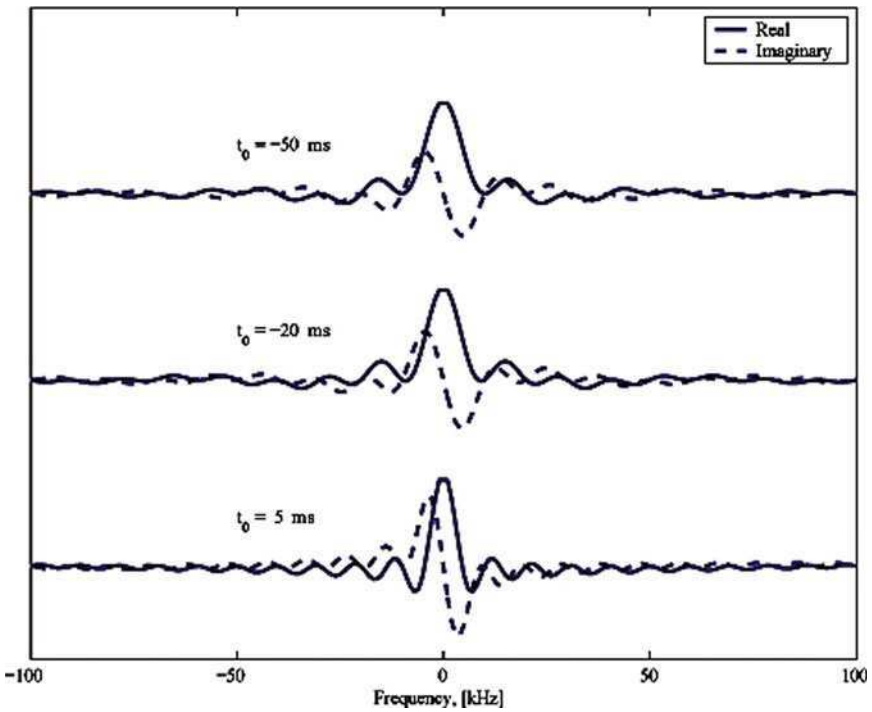

Fig. 3.1 Continuous Fourier transforms for various pulse width

That is, if the spread of the signal in the time domain is d then the spread in the frequency domain is $\Delta\omega = 4\pi/d$. Here, $\Delta\omega$ represents the frequency bandwidth. Hence, a Dirac delta function, which has infinitesimal width in the time domain, will have infinite bandwidth in the frequency domain.

3.1.2 Fourier Series

Both the forward and the inverse CFT require mathematical description of the time signal as well as their integration. In most cases, the time signals are point data acquired during experimentation. Hence, what we require is the numerical representation for the transform pair (Eq. 3.1), which is called the DFT. The DFT is introduced in detail in the next section. The Fourier Series (FS) is in between the CFT and the DFT, wherein the inverse transform is represented by a series, while the forward transform is still in the integral form as in CFT. That is, one still needs the mathematical description of the time signal to obtain the transforms.

The FS of a given time signal can be represented as

$$F(t) = \frac{a_0}{2} + \sum_{n=1}^{\infty} \left[a_n \cos\left(2\pi n \frac{t}{T}\right) + b_n \sin\left(2\pi n \frac{t}{T}\right) \right] \tag{3.6}$$

where

$$a_n = \frac{2}{T} \int_0^T F(t) \cos\left(\frac{2}{T}\right) dt, \quad b_n = \frac{2}{T} \int_0^T F(t) \sin\left(\frac{2\pi nt}{T}\right) dt. \tag{3.7}$$

Equation 3.6 corresponds to the inverse transform of the CFT, while Eq. 3.7 corresponds to the forward transforms of the CFT. Here T is the period of the time signal, i.e., the discrete representation of a continuous time signal $F(t)$, introduces periodicity of the time signal. The FS given in Eq. 3.6 can also be written in terms of complex exponentials, which can give one-to-one comparison with CFT. That is, Eqs. 3.6 and 3.7 can be rewritten as

$$\begin{aligned} F(t) &= \frac{1}{2} \sum_{-\infty}^{\infty} (a_n - b_n) e^{j\omega_n t} = \sum_{-\infty}^{\infty} \hat{F}_n e^{j\omega_n t} \\ \hat{F}_n &= \frac{1}{2}(a_n - b_n) = \frac{1}{T} \int_0^T F(t) e^{-j\omega_n t} dt, \quad \omega_n = \frac{2\pi n}{T}. \end{aligned} \tag{3.8}$$

Because of enforced periodicity, the signal repeats itself after every T seconds. We can now express the time signal in terms of the fundamental frequency as

$$F(t) = \sum_{-\infty}^{\infty} \hat{F}_n e^{j2\pi n f_0 t} = \sum_{-\infty}^{\infty} \hat{F}_n e^{jn\omega_0 t}. \tag{3.9}$$

From Eq. 3.9, it is clear that, unlike in CFT, the transform given by FS is discrete in frequency. To understand the behavior of FS as opposed to the CFT, the same rectangular time signal used earlier is again considered here. The FS coefficients (or transform) are obtained by substituting the time signal variation in Eq. 3.8. This is given by

$$\hat{F}_n = \frac{F_0}{T} \left[\frac{\sin(n\pi d/T)}{(n\pi d/T)} \right] e^{-j(t_0 + d/2)2\pi n/T}. \tag{3.10}$$

The plot of the transform amplitude obtained from the CFT and the FS are shown in Fig. 3.2. The figure shows that the values of the transform obtained by FS at discrete frequencies fall exactly on the transform obtained by CFT. The figure also shows the transform values for different time periods T. We see from the figure that the larger the time period, the closer are the frequency spacings. Hence, if the period tends to infinity, the transform obtained by FS will be exactly equal to the transform obtained by CFT.

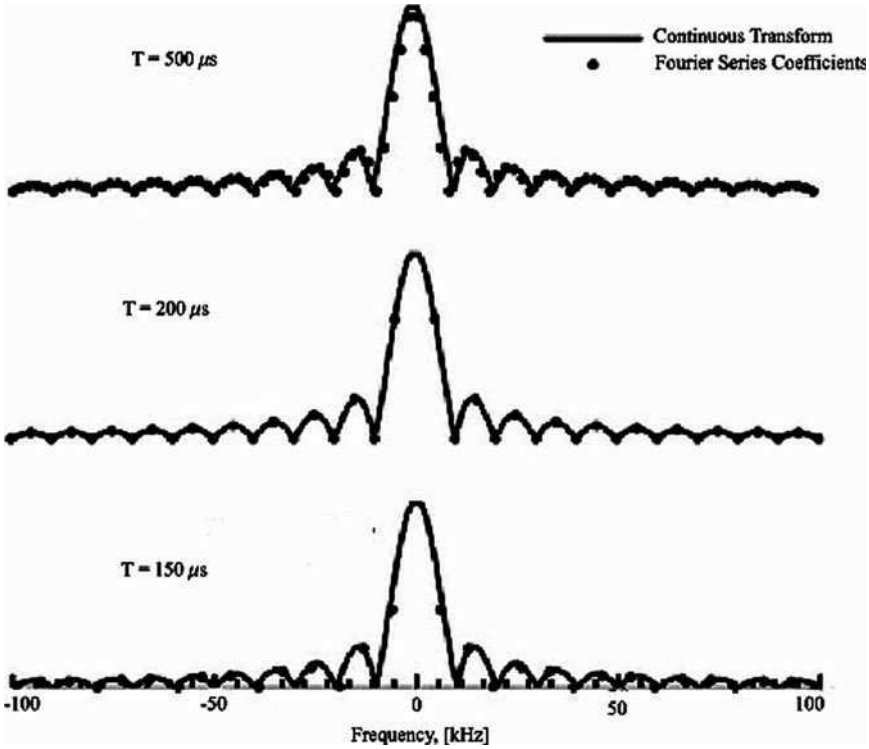

Fig. 3.2 Comparison of Fourier series with continuous Fourier transforms

3.1.3 Discrete Fourier Transform

The DFT is an alternative way of mathematically representing the CFT in terms of summations. Here, both the forward and inverse CFT given in Eq. 3.1 are represented by summations. This will completely do away with all complex integration involved in the computation of CFT. In addition, it is not necessary to represent the time signals mathematically and the great advantage of this is that one can use the time data obtained from experiments. Numerical implementation of the DFT is done using the well-known FFT algorithm.

We begin here with Eq. 3.8, which is the FS representation of the time signal. The main objective here is to replace the integral involved in the computation of the Fourier coefficients by summation. For this, the plot of time signal shown in Fig. 3.3 is considered.

The time signal is divided into M piecewise constant rectangles, whose height is given by F_m, while the width is $\Delta T = T/M$. We derived earlier that the continuous transform of a rectangle is a *sinc* function. By rectangular idealization of the signal, the DFT of the signal will be the summation of M *sinc* functions of width ΔT. Hence the second integral in Eq. 3.8 can be written as

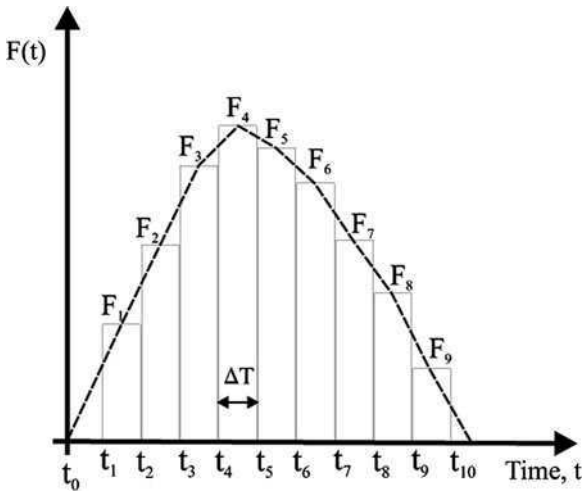

Fig. 3.3 Time signal discretization for DFT

$$\hat{F}_n = \Delta T \left[\frac{\sin(\omega_n \Delta T/2)}{(\omega_n \Delta T/2)}\right] \sum_{m=0}^{M} F_m e^{-j\omega_n t_m} \tag{3.11}$$

Let us now look at the *sinc* function in Eq. 3.11. Its value depends on the width of the rectangle ΔT. That is, as the width of the rectangle becomes smaller, the term inside the bracket of Eq. 3.11 tends to unity. This happens for all values of $n < M$. It can easily be shown that for values of $n \geq M$, the values of the transform is approximately equal to zero. Hence, the DFT transform pairs can now be written as

$$\begin{aligned} F_m &= F(t_m) = \frac{1}{T}\sum_{n=0}^{N-1} \hat{F}_m e^{j\omega_n t_m} = \frac{1}{T}\sum_{n=0}^{N-1} \hat{F}_m e^{j2/N} \\ \hat{F}_n &= \hat{F}(\omega_n) = \sum_{n} = 0^{N-1} F_m e^{-j\omega_n t_m} = \sum_{n=0}^{N-1} F_m e^{-j2\pi nm/N} \end{aligned} \tag{3.12}$$

The periodicity of the time signal is necessary for DFT as we begin from the FS representation of the time signal. Now, we can probe a little further to see whether the signal has any periodicity in the frequency domain. For this, we can look at the summation term in Eq. 3.11. Hypothetically, let us assume $n > M$. Hence, we can write $n = M + \bar{n}$. Then, the exponential term in the equation becomes

$$e^{-j\omega_n t_m} = e^{-jn\omega_0 t_m} = e^{-jM\omega_0 t_m} e^{-j\bar{n}\omega_0 t_m} = e^{-j2\pi m} e^{-j\bar{n}\omega_0 t_m} = e^{-j\bar{n}\omega_0 t_m}.$$

Hence, the summation term in Eq. 3.11 becomes

$$\Delta T \sum_{m=0}^{M-1} F_m e^{-j\bar{n}\omega_0 t_m}.$$

This term shows that the above summation has the same value when $n = \bar{n}$. For example, if $M = 6$, then the value of the summation for $n = 9$, 11, 17 is same as the value for $n = 3$, 5, and 11, respectively. Two aspects are very clear from this analysis. First, $n > M$ is not important, and second, there is forced periodicity in both the time and frequency domain in using DFT. This periodicity occurs about a frequency where the transform goes to zero. This frequency can be obtained if one looks at the *sinc* function given in Eq. 3.11. That is, the argument of the *sinc* function is given by

$$\frac{\omega_n \Delta T}{2} = \pi n \Delta T = \frac{\pi n}{M}$$

where, we have used the relation $\Delta T = T/M$.

Here, we see that the *sinc* function goes to zero when $n = M$. It is at this value of n that the periodicity is enforced and the frequency corresponding to this value is called the *Nyquist* frequency. As mentioned earlier, this happens due to the time signal being real only and the transform beyond the Nyquist frequency is the complex conjugate of the transform before this frequency. Thus, N real points are transformed to $N/2$ complex points. Knowing the sampling rate ΔT, we can compute the Nyquist frequency from the expression

$$f_{\text{Nyquist}} = \frac{1}{2\Delta T}. \tag{3.13}$$

There are a number of issues in the numerical implementation of the DFT, which are not discussed here. However, the reader is encouraged to consult [13] to get more information on these aspects.

In order to see the difference in different transform representation, the same rectangular pulse is again used here. There are two parameters on which the accuracy of the transforms obtained by the DFT depends, namely the sampling rate ΔT and the time window parameter N. Figures 3.4 and 3.5 show the transform obtained for various sampling rates ΔT and time window parameter N.

From the figures, we can clearly see the periodicity about the Nyquist frequency. For a given time window N, the figure shows that the frequency spacing increases with decreasing sampling rate. Also, the Nyquist frequency shifts to a higher value. Next, for a given sampling rate ΔT, the time window is varied through the parameter N. In this case, the Nyquist frequency does not change. However, for larger N, the frequency spacing becomes smaller and hence we get denser frequency distribution.

3.1.4 Wavelet Transforms

The concept of the existence of wavelet-like functions, for example, functions like the Haar wavelet and Littlewood–Paley wavelet, have been known since the early

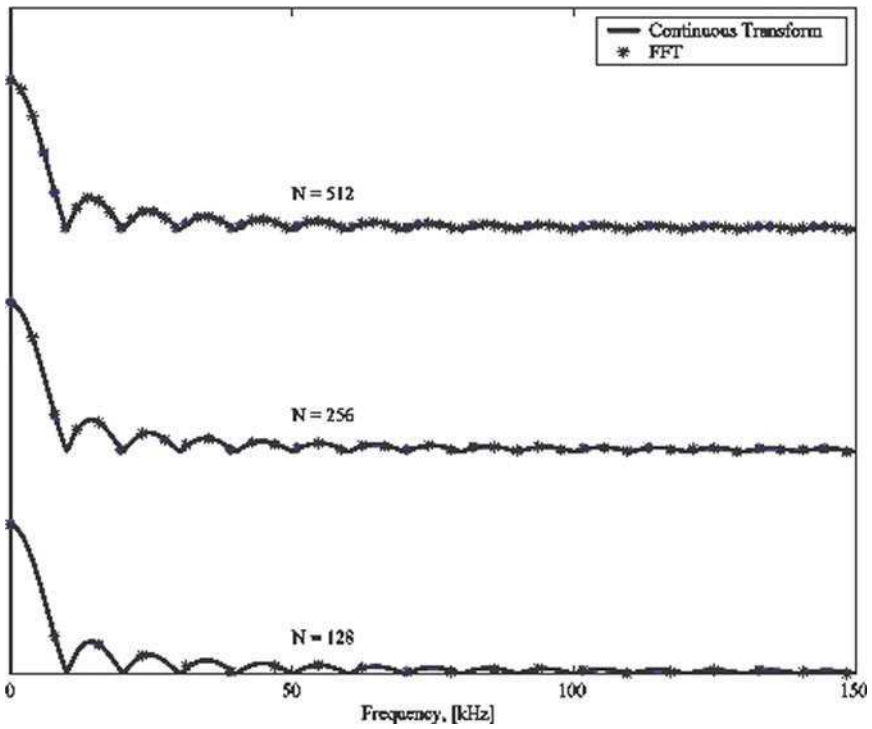

Fig. 3.4 Comparison of FFT and continuous transform for a sampling rate $\Delta T = 1\,\mu s$

part of the century. The present form of wavelets is obtained only after an effort by many researchers [10, 24] to unify the existing concepts and their development for general understanding of mathematics of wavelets. Since then, an enormous amount of work has been devoted to the use of wavelets in various applications such the solution of PDE's, approximation theories, signal processing and other related fields.

The wavelet transform is a tool that cuts up data, functions or operators into different frequency components with a resolution matched to its scale [11]. In signal analysis, the wavelet transform allows to study the time history in terms of its frequency content. In this respect, the Fourier transform extracts from the signals, the details of the frequency content but loses all information on the location of a particular frequency within the signal. Time localization can be achieved by windowing the signal and then by taking its Fourier transform. However, the problem with windowed Fourier transform is that the window lengths are always the same, irrespective of the frequency components. In contrast, wavelet transforms allow multiple time resolutions according to the frequency components. Thus, a signal after windowed Fourier transform is as follows:

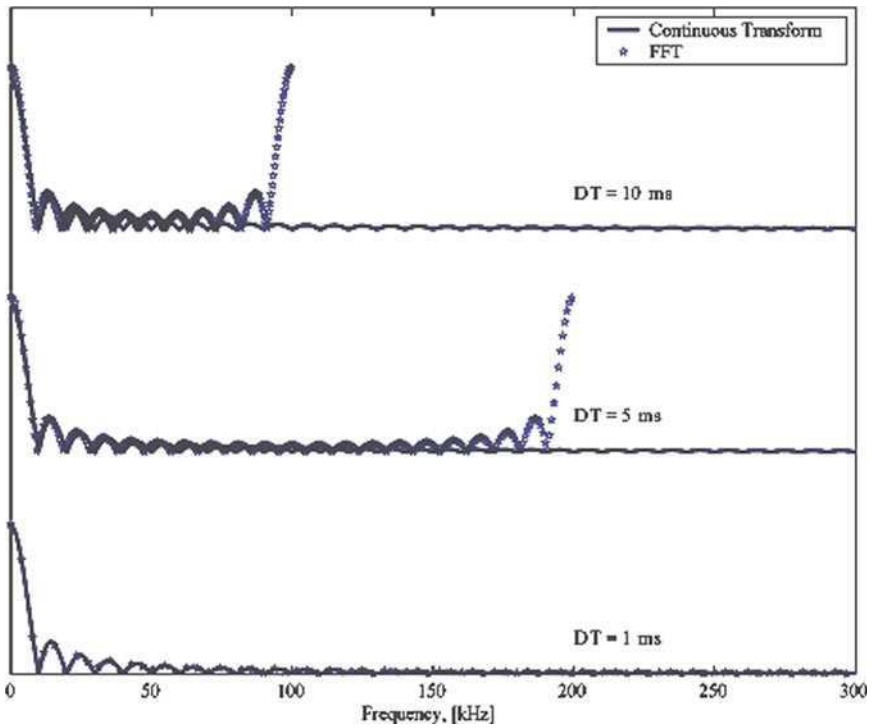

Fig. 3.5 Comparison of FFT and continuous transform for different sampling rates

$$\left(T^{\mathrm{wf}} f\right)(\omega, t) = \int f(s) g(s-t) e^{-t\omega t} ds \tag{3.14}$$

The corresponding wavelet transform is given as

$$\left(T^{\mathrm{wav}} f\right)(a, b) = \int f(t) \psi\left(\frac{t-b}{a}\right) dt \tag{3.15}$$

where the position of the time window is controlled by b and its length is determined by the scaling parameter a.

Wavelets are a family of functions which are characterized by the translation and dilation of a single function $\psi(t)$. This family of functions is denoted by $\psi_{j,k}(t)$ and is given by

$$\psi_{j,k}(t) = 2^{m/2} \psi(2^j t - k), \quad j, k \in Z \tag{3.16}$$

where, k is the translation or shift index and j the dilation or scaling index. They form the basis for the space of square integrable functions $L^2(R)$, given by

$$f(t) = \sum_j \sum_k d_{j,k} \psi_{j,k}(t) \in L^2(R) \tag{3.17}$$

The wavelets are derived from scaling function $\varphi(t)$ which are obtained by solving the recursive equation, called dilation or scaling equation given as

$$\varphi(t) = \sum_k a_k \varphi(2t - k) \tag{3.18}$$

The constant coefficients a_k are called the filter coefficients and often, like in Daubechies wavelets, only a finite number of them are non-zero. Similar to the wavelets, $\psi_{j,k}(t)$, the scaling functions $\varphi_{j,k}(t)$ are also obtained from translation and dilation of $\varphi(t)$ as,

$$\varphi_{j,k}(t) = 2^{m/2} \varphi(2^j t - k), \quad j, k \in Z \tag{3.19}$$

The scaling function and its translates are orthogonal,

$$\int \varphi(t)\varphi(t + l)dt = \delta_{0,l} \quad l \in Z \tag{3.20}$$

where,

$$\delta_{0,l} = \begin{cases} 1, & l = 0 \\ 0, & \text{otherwise} \end{cases} \tag{3.21}$$

A wavelet $\psi(t)$, is orthogonal to the scaling function and is defined by

$$\psi(t) = \sum_k (-1)^k a_{1-k} \varphi(2t - k) \tag{3.22}$$

This definition satisfies orthogonality, since

$$\begin{aligned} \langle \varphi(t), \psi(t) \rangle &= \int \sum_k a_k \varphi(2t - k) \sum_l (-1)^l a_{1-l} \varphi(2t - l) \\ &= \frac{1}{2} \sum_k (-1)^k a_k a_{1-k} \\ &= 0 \end{aligned} \tag{3.23}$$

The set of coefficients a_k and $(-1)^k a_{1-k}$ are a pair of quadrature mirror filters.

The filter coefficients a_k defined in Eq. 3.18 are derived by imposing certain constraints on the scaling functions as follows:

1. In order to uniquely define all scaling functions of a given shape, the area under the scaling function is normalized to unity,

$$\int \varphi(t)dt = 1 \tag{3.24}$$

The above constraint on the scaling function leads to the following condition on the filter coefficients

$$\sum_k a_k = 2 \tag{3.25}$$

2. For the scaling function and its translate to be orthogonal given by Eq. 3.20, the filter coefficients have to satisfy the condition

$$\sum_k a_k a_{k+2l} = 2\delta_{0,l} \quad l \in Z \tag{3.26}$$

3. Equations 3.25 and 3.26 are insufficient to determine a unique set of filter coefficients. In an N coefficient system, they yield a total of $N/2 + 1$ equations. The other $N/2 - 1$ equations are therefore required for a unique solution. For constructing Daubechies compactly supported wavelets [11], the scaling functions are required to be able to exactly represent polynomials of order up to, but not greater than, M. This M determines the order of the Daubechies scaling function, referred as N, where it is given as $N = 2M$. The requirement for approximation of order M is that any function of the form

$$f(t) = \alpha_0 + \alpha_1 t + \alpha_2 t^2 + \cdots + \alpha_{M-1} t^M \tag{3.27}$$

can be exactly represented by an expansion of the form

$$f(t) = \sum_k c_k \varphi(t - k) \tag{3.28}$$

where, c_k are the approximation coefficients. The above equation may be translated into a condition on the wavelet. Taking the inner product of Eq. 3.28 with $\psi(t)$ gives

$$\langle f(t), \psi(t) \rangle = \sum_k \langle \varphi(t - k), \psi(t) \rangle \equiv 0 \tag{3.29}$$

Thus from Eq. 3.27 we get,

$$\alpha_0 \int \psi(t)dt + \alpha_1 \int \psi(t)tdt + \cdots + \alpha_{M-1} \int \psi(t)t^{M-1}dt \equiv 0 \tag{3.30}$$

This identity is valid for all α_j $(j = 0, 1, 2, \ldots, M - 1)$. Considering $\alpha_{M-1} = 1$ and all other $\alpha_j = 0$ gives

$$\int \psi(t)t^l dt = 0, \quad l = 0, 1, 2, \ldots, M - 1 \tag{3.31}$$

Thus, the first p moments of the wavelet must be zero. Substituting Eq. 3.22 in Eq. 3.31 and following certain modifications give

$$\sum_k (-1)^k a_k k^l = 0 \quad l = 0, 1, 2, \ldots, M-1 \tag{3.32}$$

Thus the filter coefficients a_k, $k = 1, 2, \ldots, N-1$ can be determined uniquely from Eqs. 3.25, 3.26 and 3.32 and are sufficient to construct Daubechies compactly supported wavelets of different orders N.

Apart from advantages of being capable to perform time–frequency analysis, possessing orthogonal basis functions with localized supports, which allows finite domain analysis and imposition of initial/boundary conditions, the most important property of wavelets is multi-resolution representation of a function. The translates of the scaling and wavelet functions on each fixed scale j form the orthogonal subspaces, which given by

$$V_j = \left\{ 2^{j/2} \varphi(2^j t - k);\, j \in \mathbf{Z} \right\} \tag{3.33}$$

$$W_j = \left\{ 2^{j/2} \psi(2^j t - k);\, j \in \mathbf{Z} \right\} \tag{3.34}$$

such that V_j form a sequence of embedded subspaces

$$\{0\}, \ldots, \subset V_{-1}, \subset V_0, \subset V_1, \ldots, \subset \mathbf{L^2}(\mathbf{R}) \tag{3.35}$$

and

$$V_{j+1} = V_j \oplus W_j \tag{3.36}$$

Let $P_j(f)(t)$ be approximation of a function $f(t)$ in $\mathbf{L^2}(\mathbf{R})$ using $\varphi_{j,k}(t)$ as basis, at a certain level (resolution) j, then

$$P_j(f)(t) = \sum_k c_{j,k} \varphi_{j,k}(t), \quad k \in \mathbf{Z} \tag{3.37}$$

where, $c_{j,k}$ are the approximation coefficients. Let $Q_j(f)(t)$ be the approximation of the function using $\psi_{j,k}(t)$ as basis, at the same level j.

$$Q_j(f)(t) = \sum_k d_{j,k} \psi_{j,k}(t), \quad k \in \mathbf{Z} \tag{3.38}$$

where, $d_{j,k}$ are the detail coefficients. The approximation $P_{j+1}(f)(t)$ to the next finer level of resolution $j+1$ is given by

$$P_{j+1}(f)(t) = P_j(f)(t) + Q_j(f)(t) \tag{3.39}$$

This forms the basis of multi resolution analysis associated with wavelet approximation.

3.1.5 Wavelet-Based Numerical Solutions of Wave Equations

Interest in wavelets historically grew from the fact that they are effective tools for numerical solutions of PDEs [4, 14]. The wavelet-based methods can give not only high accuracy in numerical differentiation but also flexible implementation of physical boundary conditions. Wavelets are also a great candidate for adaptive and multi-resolution schemes which help in large computational savings. Dahmen [9] has provided a review of wavelet techniques for solution of PDEs.

Here, we will review some of the works in wavelets that addresses the solution of wave equation. Among the several wavelet-based numerical schemes for the solution of PDEs, quite a large number of such techniques have been developed specially for solution of wave equations. Wavelets have been used for solution of 1D wave equations in [5, 17, 22]. A method for design of optimal stencils for wave propagation problems using an intrinsically explicit Galerkin-wavelet formulation was presented in [22]. Here, the group velocities obtained from the developed wavelet method were compared with traditional finite-difference technique and the former method exhibited gain in accuracy and also large computational savings. In [17], and [7] wavelets with exponential decrease were used for spatial approximation in 1D wave equations for homogeneous and heterogeneous media. Apart from this, a 1D finite element based on Daubechies wavelets [20] has been presented for vibration and wave propagation analysis. In [21], a wavelet-Galerkin solution of bi-harmonic Helmhöltz equation in non-separable two dimensional geometry is presented. Here Daubechies compactly supported wavelets are used for approximation in both the spatial direction and the boundary conditions are imposed through a proposed. wavelet-capacitance matrix method. A wavelet-based method for numerical simulation of acoustic and elastic wave propagation is presented in [16] which uses a displacement–velocity formulation. Here, the linear operators for spatial derivatives are implemented in wavelet bases using an operator projection technique with nonstandard forms of wavelet transform [8]. This wavelet-based method is applied to the acoustic wave equation with rigid boundary conditions at both ends in 1D domain and to the elastic wave equation with a traction-free boundary conditions at a free surface in 2D spatial media.

3.1.6 Comparative Advantages and Disadvantages of Different Transforms

The Fourier transform is extensively used in wave propagation studies due its versatility in going back and forth the time and frequency domain through Fast Fourier Transforms (FFT). Due to induced periodicity both in time and frequency domain, FFT is always associated with time windows. Hence, if the measured signal does not die out within the chosen time window, the remaining part of the signal, will start appearing at the start of the time history, distorting the signal

completely. This problem is quite severe in finite structures where multiple reflections from the boundaries do not die down within the chosen time window even in the presence of damping. Such problem, called *wraparound*, is discussed in greater detail in the next section. In addition, application of FFT to initial value problems is not straight forward. The detailed signal analysis using FFT is given in [13].

Some of the above problems can be effectively solved if one uses compactly supported Daubechies wavelet transforms. These wavelets provide very fine time resolutions as they do not assume any periodicity of the signal. A small time window can provide highly accurate results even for structures of very small dimensions. In addition, imposition of initial conditions is straightforward. However, resolution of the wavelet transform in the frequency domain is poor. The frequency characteristics such as wavenumber and group speeds, are accurate only up to certain fraction of the Nyquist frequency and this fraction depends on the order of the Daubechies basis functions. Beyond this frequency, spurious dispersion is introduced, giving completely inaccurate estimations. A very high order of the basis functions is required to get reasonable frequency resolution, which increases the computational cost. In addition, unlike the Fourier coefficients in FFT, the wavelet coefficients are coupled, which requires an additional step of uncoupling them using the standard eigen analysis to perform wave propagation studies. This also increases the cost of computations. A good account on signal processing using wavelet transforms is given in [19]. All these issues are further elaborated in the next section.

3.2 Signal Processing Issues

SHM studies involves handling different input signals of high frequency content. The measured output signals normally are not readily amenable for direct use in many damage detection algorithms for predicting the damage location, its extent and also its severity. The measured signals are normally highly dispersive in nature, which may be noise polluted. In addition, the complete trace of the signal is usually not available. Many of these problems are transform dependent. Hence, there are several signal processing issues that need to be addressed to obtain decent estimate of damage location. In the next few paragraphs, we discuss a few signal processing issues that may affect SHM studies.

3.2.1 Wraparound Problems

Transforming signals to the frequency domain using Fourier transforms was discussed in Sect. 3.1.1 where it was shown that there are three variants of Fourier Transforms, namely the Continuous Fourier Transform, the Fourier Series, and the

Discrete Fourier Transforms, respectively. The numerical implementation of DFT is the Fast Fourier Transform (FFT), which is an extremely powerful technique to go back and forth time and frequency domain. The FFT implicitly assumes that the signal is periodic both in the time and frequency domain. Hence, the signal is associated with a finite time window, that is dictated by the number of FFT points chosen to sample the signal or by the time sampling rate. It is quite well known that the dispersive signal traveling in a medium with small attenuation normally does not die down within the chosen window, no matter how long the time window is. The trace of the signal beyond the chosen time window will start appearing in the initial part of the time history thereby completely distorting the time response. This problem is referred to as *wraparound*. This is normally noticed when one uses FFT to sample signals. Such problems do not exist if one uses wavelet transforms. To understand this problem better, we consider a 1D cantilever bar undergoing axial motion $u(x,t)$ (Fig. 3.6a) and subjected to a time dependent load $P(x,t)$.

The governing equation for this problem is given by [13]

$$EA\frac{\partial^2 u}{\partial x^2} = \rho A\frac{\partial^2 u}{\partial x^2} \tag{3.40}$$

In the above equation, E is the Young's Modulus, A the area of cross section of the beam and ρ is the density of the beam. The above equation is transformed into frequency domain using DFT, which is given by

$$\sum_{n=1}^{N} \hat{u}_n(x,\omega)e^{j\omega t} \tag{3.41}$$

Substituting Eq. 3.41 in Eq. 3.40, we a set of ordinary differential equation in the transformed frequency domain, which is given by

$$\frac{d^2\hat{u}_n}{dx^2} + k^2\hat{u}_n = 0, \quad k^2 = \omega\frac{\rho A}{EA} \tag{3.42}$$

The exact solution of above equation is given by

$$\hat{u}_n(x,\omega) = Ae^{-jkx} + Be^{jkx} \tag{3.43}$$

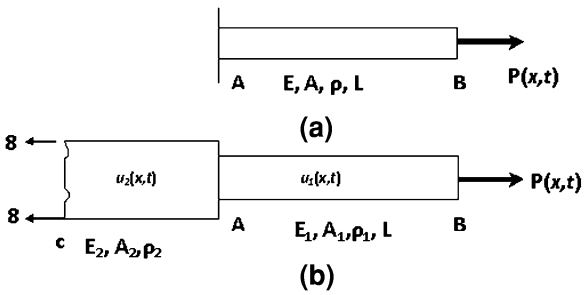

Fig. 3.6 Wraparound problem: **a** a short cantilever bar subjected to axial load **b** a short cantilever bar with an infinite segment attached

where, k is the wavenumber, A is the incident wave coefficient, and B is the reflected wave coefficient, which are to be determined from the two boundary conditions. $\hat{u}_n$ is the FFT of the axial displacement $u(x,t)$ and x is the axial coordinate. The boundary conditions for the cantilever problem are $\hat{u}_n = 0$ at $x = 0$ and $EA\hat{du}_n/dx = \hat{P}$, at $x = L$, where $\hat{P}$ is the FFT of input force $P(x,t)$ and L is the length of the cantilever bar. Substituting these boundary conditions in Eq. 3.43, we get

$$A = -B, \quad A = \frac{\hat{P}}{EA}\frac{Lj}{2kL\cos kL} \tag{3.44}$$

Using the values of A and B in Eq. 3.43, we can write the axial displacement in the transformed Fourier domain as

$$\hat{u}_n(x,\omega) = \mathscr{H}(\omega)\hat{P} \tag{3.45}$$

The above equation can be written as

$$\mathscr{H}(\omega) = \frac{L\sin kx}{EAkL\cos kL} \tag{3.46}$$

The response is obtained by convoluting the transfer function with the input load. For the response to die down within the chosen time window, it is necessary that the transfer function be complex. In the present case, the transfer function is real only as it has *sine* and *cosine* functions of ω which has a finite value for all ω. Hence, no matter how long the rod member is, the response will never die down within the chosen time window. This is one of the severe limitations of FFT in analyzing finite structures.

The total time window $T = N\Delta t$, where N is the number of FFT points, and Δt is the time sampling rate. Hence, the key to avoid wraparound problem is to increase the time window. This can be done either by increasing the number of FFT points, increasing the time sampling rate or a combination of these. Note that, increasing the sampling rate sometime leads to *aliasing* problems, the consequences of which is explained in the next section. Alternatively, one can add a small amount damping to the wavenumber to make it complex as $k = k(i - j\eta)$, where η is a small damping constant. The above methods may still not work for those systems such as the cantilever rod problem, which gives real transfer function. For such problems, the signal wraparound is eliminated by using a different modeling philosophy.

In the finite structure, the energy gets trapped due to repeated reflections from the fixed boundaries, which causes the signal to wraparound. By allowing some leakage of the responses from the fixed boundary, one can add some artificial damping so that good resolution in the time response can be obtained. The modeling philosophy is shown in (Fig. 3.6b), wherein, the fixed boundary is replaced by an infinite rod having axial rigidity EA many times higher than that of the regular rod segment AB. We will now derive the transfer function for this new system.

Let $u_1(x,t)$ be the solution for the actual cantilever rod **AB** and let $u_2(x,t)$ be the solution for the infinite segment **AC**. Let $\hat{u_1}_n$ and $\hat{u_2}_n$ be their respective Fourier transform. As per Eq. 3.43, the solutions in these two segments can be written as

$$\hat{u_1}_n(x,\omega) = Ae^{-jkx} + Be^{jkx}, \quad \text{For Segment AB of Length } L \tag{3.47}$$

where

$$k^2 = \omega \frac{\rho_1 A_1}{E_1 A_1}$$

$$\hat{u_2}_n(x,\omega) = \bar{A}e^{-j\bar{k}x}, \quad \text{For Segment AC} \tag{3.48}$$

where

$$\bar{k}^2 = \omega \frac{\rho_2 A_2}{E_2 A_2}$$

Note that the solution of the infinite bar (Segment AC) does not have any expression corresponding to the reflected wave. Hence, there are three wave coefficients that needs to be determined. The three conditions that are necessary for their determination are obtained as follows. Considering point **A** as the origin, we have the following three conditions:

- At $x = 0$, we have, $\hat{u_1}_n = \hat{u_2}_n$
- At $x = 0$, we have the total force, that is $E_1 A_1 d\hat{u_1}_n/dx + E_2 A_2 d\hat{u_2}_n/dx = 0$, and
- At $x = L$, $E_2 A_2 d\hat{u_2}_n/dx = \hat{P}$, where $\hat{P}$ is the FFT of the axial force.

Using these conditions in Eqs. 3.48 and 3.49, after simplification, we get the solution for the finite cantilever bar as

$$\hat{u_1}_n(x,\omega) = \hat{P}\left[\frac{-jL((1-\beta)e^{-jkx} + (1+\beta)e^{jkx})}{2E_1A_1kL(\beta\cos kL + jsinkl)}\right], \quad \beta = \frac{A_2}{A_1}\sqrt{\frac{E_2\rho_2}{E_1\rho_1}} \tag{3.49}$$

The term in the brackets in Eq. 3.49 is the transfer function, which has both the real part as well as imaginary part, indicating that the wave as it propagates, it also attenuates. That is, if the time window is large enough, the wraparound problems can be avoided. The level of attenuation can be manipulated by appropriately choosing β, or in other words the axial regidity E_2A_2 such that the response dies out within the chosen window. If $\beta = \infty$, we recover back the fixed bar solution, which was derived in Eq. 3.45. Also, if we substitute $\beta = 0$, we simulate a free-free bar, whose solution is given by

$$\hat{u_1}_n(x,\omega) = \hat{P}\left[\frac{L\cos kx}{2E_1A_1kL\sin kL}\right] \tag{3.50}$$

In this equation, the term inside the brackets is the transfer function, which is again real, indicating that severe wraparound problems will be encountered if one uses

FFT to solve the problem. From the above discussion it is clear that if FFT is used in the wave analysis, then, in order to avoid signal wraparound and have good time resolution, it is necessary to have an infinite segment of appropriate material properties be attached to the short finite segment.

It was mentioned earlier that the wavelet transform does not suffer from wraparound problems since the periodicity assumption is not used in constructing the transform. Here, we will solve some examples to show the severity of wraparound problems in some finite structures. In all these examples, we will use the results obtained from wavelet transform for comparison. The analysis is performed using Spectral Finite Element simulation (explained in detail in Chap. 5).

In the first example, we will consider a cantilever beam with a length $L = 20$ in., width $b = 1.0$ in., and thickness $h = 0.01$ in. The beam is made of aluminum having a Young's Modulus of $E = 70$ GPa and a density $\rho = 2.7 \times 10^3$ kg/m^3. The beam is loaded by a force $P(x,t)$, whose time history and its FFT are shown in Fig. 3.7.

The input signal is sampled using a FFT time sampling rate of 1 μs. In order to bring out the effects of time window on the signal wraparound, the results are plotted for three different time windows, namely 1,024, 2,048 and 4,096 μs, respectively. The wavelet response is obtained using only 512 points with a time sampling rate of 1 μs. The order of wavelet basis function used is equal to 8. The axial velocity response is shown in Fig. 3.8.

Here, the wavenumber is heavily damped by $k = k(1 + j\eta)$, where a value of $\eta = 0.5$ is used. We see from (Fig. 3.8a), even with such a heavy damping, signal wraps around for a time window of 1,024 μs. However, when the time window is increased to 4,096 μs, the wraparound is completely eliminated. Note that the response obtained via wavelet transform does not suffer from this problem and a time window of 512 μs is sufficient to get an accurate response.

Next the same beam with similar properties is considered, however,the length of the beam is further reduced to 10 in. and the load $P(x,t)$ shown in Fig. 3.7 is

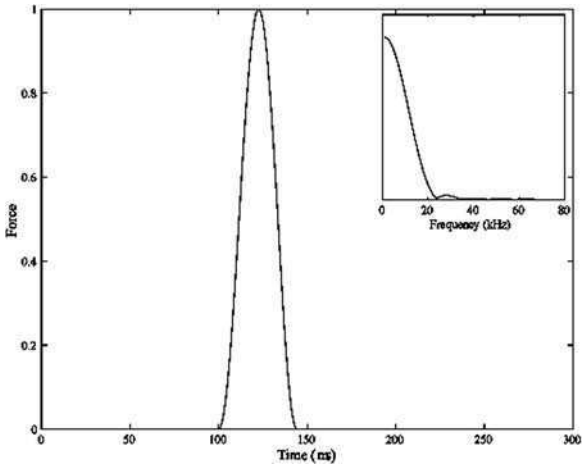

Fig. 3.7 Impact load and Fourier transform of the load (*inset*)

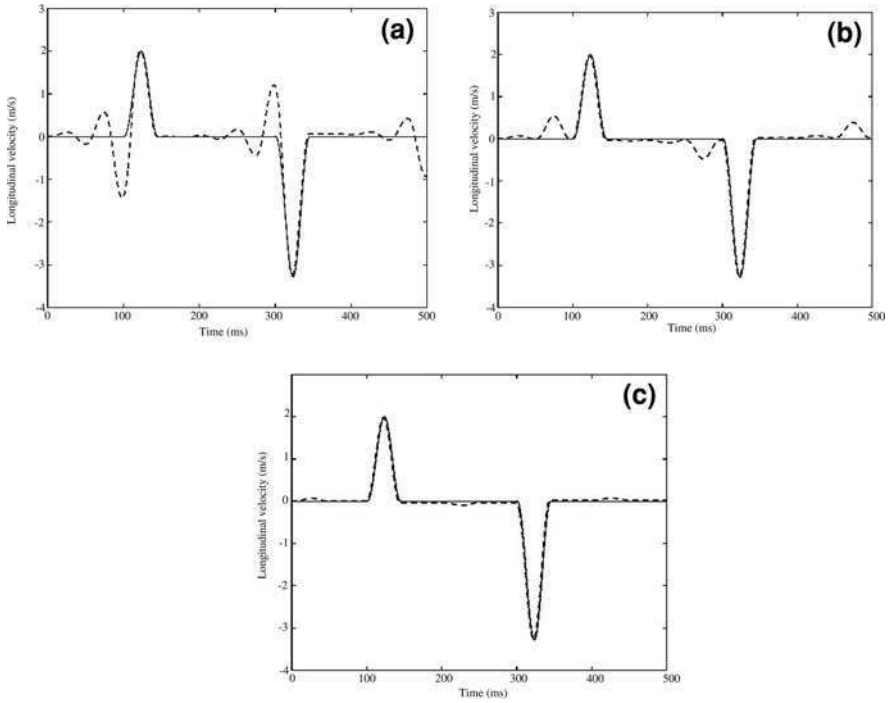

Fig. 3.8 Longitudinal tip velocity in rod due to tip axial load fortime window T_w **a** $T_w = 1{,}024\,\mu s$, **b** $T_w = 2{,}048\,\mu s$ and **c** $T_w = 4{,}096\,\mu s$ *dotted lines* Wavelet Response, *continuous lines* FFT Response

applied transversely. The aim of reducing the length is to amplify the effect of signal wraparound. In this case the waves generated are dispersive innature and identifying the wraparound becomes very difficult. The responses are generated using the spectral finite element formulation. As before, the responses based on FFT are obtained for three different time windows, namely 1,024, 2,048 and 4,096 μs, respectively. The FFT responses are compared with wavelet responses, which use a time window of 512 μs, withan order of wavelet basis function of $N = 8$. the responses are shown in Fig. 3.9. Unlike the axial response case, the wraparound causes the response to appear right from the initial time. This is the characteristic of all dispersive systems, where at each frequency, the wave speeds are different. It is possible to identify the signal wraparound in this example since we had provided a zero header in our input pulse, which is a necessity if one uses the FFT to perform wave analysis. As in the axial input case, signal wraparound vanishes if we use a large time window.

In summary, the following conclusions can be drawn from this study:

1. Wavelet transform based wave analysis does not suffer from signal wraparound problems. A small time window is sufficient to capture the response and the wavelet transform provides good time resolution.

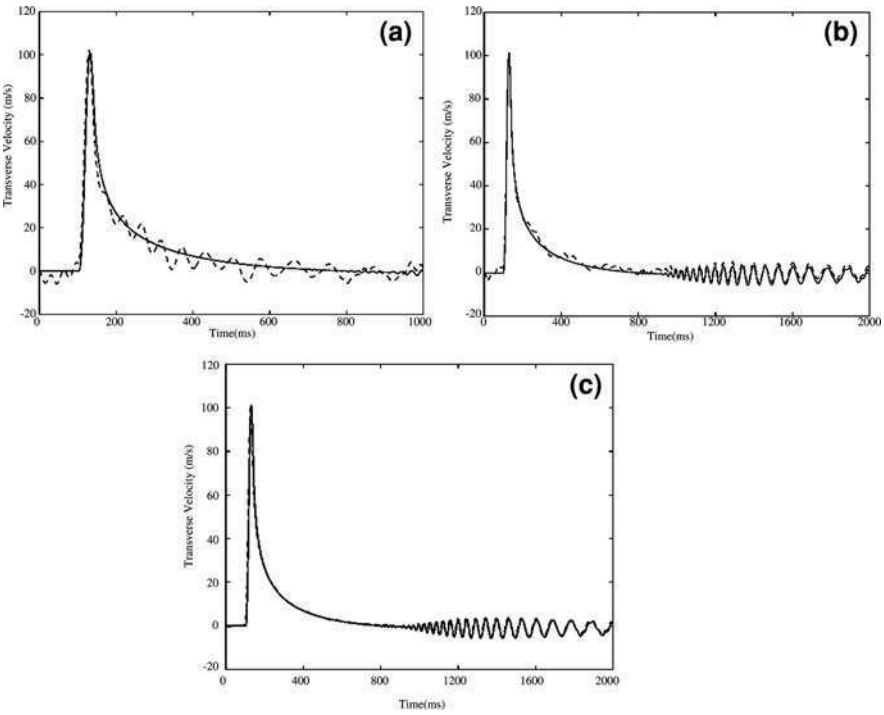

Fig. 3.9 Transverse tip velocity in rod due to tip Transverse load for time window T_w **a** $T_w = 1{,}024\,\mu s$, **b** $T_w = 2{,}048\,\mu s$ and **c** $T_w = 4{,}096\,\mu s$ *dotted lines* Wavelet Response, *continues line* FFT Response

2. The time resolution in FFT-based analysis is poor due to severe wraparound problems caused by the associated finite window size.
3. Signal wraparound in FFT analysis can be removed to certain extent by increasing the time window, which can be done either by increasing the signal sampling rate or by increasing the number of FFT points.
4. In analyzing finite structures of small dimensions using FFT, it is required to add a infinite segment to remove the signal wraparound. In addition, it may be required to add damping.

3.2.2 Signal Processing of Sampled Waveforms

This section discusses some common problems encountered in handling experimentally measured signals. Experimentally obtained signals are truncated and then used to perform the Fourier analysis. The quality of the sampled signal depends on two factors, that is, the signal itself and its time sampling rate. If the time sampling

rate is not high enough then all high frequency wave components will appear as low frequency waves as a result of *aliasing*. If ΔT is the time sampling rate, the highest detectable frequency is given by $f = 1/2\Delta T$. That is, if the highest frequency component of the signal is known, then the sample rate is chosen from the above expression.

Another problem normally encountered while sampling signals is the *Leakage* of the response. This normally happens when the sampled signals have many spectral peaks. For example, if a spectral peak occurs at say 11, 19 and 23 kHz and the sampling rate of the signal chosen is such that frequency sampling is only at every 3 kHz, then these spectral peaks will not be captured. The energy associated with these peak leaks into neighboring frequencies distorting the spectral estimates.

FFT of a signal is always associated with a finite time window. The leakage problem can be avoided if the signal is contained well within the chosen time window. In most cases leakage cannot be avoided, that is, it is very difficult to contain the entire signal within the time window. The type of window determines the amount of signal leakage. For example, if the window is of rectangular type, and if the size of the time window is more than $(N-1)\Delta T$, then leakage will certainly be present. If the signal is nearly periodic within the chosen window, leakage can be minimized and hence the type of window should be such that it makes the signal nearly periodic in the chosen time window, This can be done by using a window that will smoothly attenuate the signal at the end of the sampled time record. However, many windows minimizing leakage also introduce amplitude and frequency error. Some of the commonly used windows are the Hanning and Gaussian windows.

3.2.3 Artificial Dispersion in Wavelet Transform

It was mentioned earlier that use of wavelet transform for solving wave equation results in good time resolution and very poor frequency resolution. Due to poor frequency resolution, the spectrum and dispersion relations derived using wavelet transform are generally valid only up to a fraction of the Nyquist frequency, beyond which artificial dispersion is introduced. In this section, we show this phenomenon for an axial rod. However, this is true for all other waveguides. More details on this aspect is found in [19].

The governing differential wave equation of an isotropic rod is given as [15]

$$EA\frac{\partial^2 u}{\partial x^2} - \eta A\frac{\partial u}{\partial t} = \rho A\frac{\partial^2 u}{\partial t^2} \tag{3.51}$$

where, E, A, η and ρ are the Young's modulus, cross sectional area, damping ratio and density, respectively. Note here that the second term is the force due to viscous damping and it is added to the formulation to make the rod model more realistic. Here, $u(x,t)$ is the axial deformation, which is discretized at N points in the time window $[0\, t_f]$. Let $\tau = 0, 1, \ldots, n-1$ be the sampling points, then

$$t = \triangle t\tau \tag{3.52}$$

where, $\triangle t$ is the time interval between two sampling points. The function $u(x,t)$ can be approximated by scaling function $\varphi(\tau)$ at an arbitrary scale as (see Sect. 3.1.4 for more details on Wavelet transforms)

$$u(x,t) = u(x,\tau) = \sum_k u_k(x)\varphi(\tau - k), \quad k \in \mathbf{Z} \tag{3.53}$$

where, $u_k(x)$ (referred as u_k hereafter) are the approximation coefficients at a certain spatial location x. Substituting Eqs. 3.52 and 3.53 in Eq. 3.51 we get,

$$EA\sum_k \frac{d^2u_k}{dx^2}\varphi(\tau - k) - \frac{\eta A}{\triangle t}\sum_k u_k\varphi'(\tau - k) = \frac{\rho A}{\triangle t^2}\sum_k u_k\varphi''(\tau - k) \tag{3.54}$$

Taking inner product on both sides of Eq. 3.54 with $\varphi(\tau - j)$, where $j = 0, 1, \ldots, n-1$ we get,

$$EA\sum_k \frac{d^2u_k}{dx^2}\int \varphi(\tau - k)\varphi(\tau - j)d\tau - \frac{\eta A}{\triangle t}\sum_k u_k \int \varphi'(\tau - k)\varphi(\tau - j)d\tau$$
$$= \frac{\rho A}{\triangle t^2}\sum_k u_k \int \varphi''(\tau - k)\varphi(\tau - j)d\tau \tag{3.55}$$

Since the translates of scaling functions are orthogonal, we get

$$\int \varphi(\tau - k)\varphi(\tau - j)d\tau = 0 \quad \text{for} \quad j \neq k \tag{3.56}$$

Using Eq. 3.56, Eq. 3.55 can be written as n simultaneous ODEs

$$EA\frac{d^2u_j}{dx^2} = \sum_{k=j-N+2}^{j+N-2}\left(\frac{\eta A}{\triangle t}\Omega^1_{j-k} + \frac{\rho A}{\triangle t^2}\Omega^2_{j-k}\right)u_k \quad j = 0, 1, \ldots, n-1 \tag{3.57}$$

where, N is the order of the Daubechies wavelet as discussed in Sect. 3.1.4. Here, Ω^1_{j-k} and Ω^2_{j-k} are the connection coefficients defined as

$$\Omega^1_{j-k} = \int \varphi'(\tau - k)\varphi(\tau - j)d\tau \tag{3.58}$$

$$\Omega^2_{j-k} = \int \varphi''(\tau - k)\varphi(\tau - j)d\tau \tag{3.59}$$

For compactly supported wavelets, Ω^1_{j-k}, Ω^2_{j-k} are nonzero only in the interval $k = j - N + 2$ to $k = j + N - 2$. The details for evaluation of connection coefficients for different orders of derivative are given in [8].

The forced boundary condition associated with the governing differential equation given by Eq. 3.51 is

$$EA\frac{\partial u}{\partial x} = F \tag{3.60}$$

where, $F(x,t)$ is the axial force applied. $F(x,t)$ can be approximated similarly as $u(x,t)$ in Eq. 3.53

$$F(x,t) = F(x,\tau) = \sum_k F_k(x)\varphi(\tau - k), \quad k \in \mathbf{Z} \tag{3.61}$$

Substituting Eqs. 3.53 and 3.61 in Eq. 3.60 and taking the inner product with $\varphi(\tau - j)$ we get,

$$EA\frac{du_j}{dx} = F_j \quad j = 0, 1, \ldots, n-1 \tag{3.62}$$

While dealing with finite length data sequence, problems arise at the boundaries. It can be observed from the governing equations given by Eq. 3.57 that certain coefficients u_j near the vicinity of the boundaries ($j = 0$ and $j = n-1$) lie outside the time window $[0\, t_f]$ defined by $j = 0, 1, \ldots, n-1$. Several approaches like capacitance matrix methods [21], penalty function methods for treating boundaries are reported in the literature. Here, a circular convolution method is first adopted assuming periodicity of the solution. The solutions obtained by this method are exactly similar to those obtained using FFT. Next, a wavelet-based extrapolation scheme proposed by Amaratunga and Williams [2], is implemented for solution of boundary value problems. This approach allows treatment of finite length data and uses polynomial to extrapolate wavelet coefficients at boundaries either from interior coefficients or boundary values. The method is particularly suitable for approximation in time for the ease to impose initial values.

Next, we see how we can treat the finite boundaries in wavelets. From Eq. 3.57, we get n coupled Ordinary Differential Equations (ODEs), which are to be solved for u_j. For numerical implementation, we can deal with only finite sequence. In other words, $u(x,t)$ and hence u_j are only known in the interval $[0,\ t_f]$ and $j = 0$ to $j = n-1$. In Eq. 3.57 the ODEs corresponding to $j = 0$ to $j = N-2$, contain coefficients u_j that lie outside the $[0,\ t_f]$. Similarly, on the other boundary, for $j = (n-1) - N + 2$ to $j = (n-1)$ same problem exists.

3.2.3.1 Periodic Boundary Condition

In this approach, the function $u(x,t)$ is assumed to be periodic in time, with time period t_f. Thus, the unknown coefficients on left end are taken as

$$\begin{aligned} u_{-1} &= u_{n-1} \\ u_{-2} &= u_{n-2} \\ \vdots &\qquad \vdots \\ u_{-N+2} &= u_{n-N+2} \end{aligned} \tag{3.63}$$

Similarly the unknown coefficients on right end, that is, u_n, $u_{n+1}, \ldots, u_{n+N-2}$ are equal to u_0, $u_1, \ldots, u_{N-2}$, respectively. With the above assumption, the coupled ODEs given by Eq. 3.57 can be written in matrix form as

$$\left\{\frac{d^2u_j}{dx^2}\right\} = \left(\frac{\eta A}{EA}\Lambda^1 + \frac{\rho A}{EA}\Lambda^2\right)\{u_j\} \tag{3.64}$$

where, Λ^1 and Λ^2 are $n \times n$ circulant connection coefficient matrices and have the form

$$\Lambda^1 = \frac{1}{\triangle t}\begin{bmatrix} \Omega_0^1 & \Omega_{-1}^1 & \ldots & \Omega_{-N+2}^1 & \ldots & \Omega_{N-2}^1 & \ldots & \Omega_1^1 \\ \Omega_1^1 & \Omega_0^1 & \ldots & \Omega_{-N+3}^1 & \ldots & 0 & \ldots & \Omega_2^1 \\ \vdots & \vdots & \ldots & \vdots & \ldots & \vdots & \ldots & \vdots \\ \Omega_{-1}^1 & \Omega_{-2}^1 & \ldots & 0 & \ldots & \Omega_{N-3}^1 & \ldots & \Omega_0^1 \end{bmatrix} \tag{3.65}$$

Λ^2 for second order derivative has a similar form. For a circulant matrix Λ^1 [12], the eigenvalues α_j are

$$\alpha_j = \sum_{k=-N+2}^{N-2} \Omega_k^1 e^{-2\pi ijk/n} \quad j = 0,\ 1, \ldots, n-1 \tag{3.66}$$

and the corresponding orthonormal eigenvectors v_j, $j = 0, 1, \ldots, n-1$ are

$$(v_j)_k = \frac{1}{\sqrt{n}} e^{-2\pi ijk/n}, \quad k = 0,\ 1, \ldots, n-1 \tag{3.67}$$

For Λ^1, $\Omega_p^1 = -\Omega_{-p}^1$ for $p = 1, 2, \ldots, N-2$ and $\Omega_0^1 = 0$ and we can write $\alpha_j = i\lambda_j$ where

$$\lambda_j = -\frac{2}{\triangle t}\sum_{k=1}^{N-2} \Omega_k^1 \sin\left[\frac{2\pi kj}{n}\right] \quad j = 0,\ 1, \ldots, n-1 \tag{3.68}$$

The spectral element formulation involves eigenvalue analysis. This is done to diagonalize the matrix in Eq. 3.64 and decouple the ODEs. For periodic boundary condition, the eigenvalues are known analytically which decreases the computational cost. The solutions obtained through this scheme are the same as those obtained using FFT and possess several problems such as signal wraparound due to the assumed periodicity of the solution.

3.2.3.2 Non-Periodic Boundary Condition

Here, the boundaries are treated using wavelet extrapolation method for Daubechies compactly supported wavelets. The detail of the formulation is given in [2]. Here, a brief outline is presented.

In this method, a polynomial of order $p-1$, $(p = N/2)$ is assumed to extrapolate the values at the boundaries. Since wavelets are here used in time, the unknown coefficients on the left end $(u_{-1}, u_{-2}, \ldots, u_{-N+2})$ are extrapolated from the initial values. The coefficients $u_n, u_{n+1}, \ldots, u_{n+N-2}$ on the right end are extrapolated from the known coefficients $u_{(n-1)-p+1}, u_{(n-1)-p+2}, \ldots, u_{n-1}$.

Assuming polynomial representation of order $p-1$ for u in the vicinity of $t = 0$ and using Eq. 3.53 gives

$$u(x,\tau) = \sum_k u_k(x)\varphi(\tau - k) = \sum_{l=0}^{p-1} c_l \tau^l \tag{3.69}$$

where c_l are constant coefficients. Taking inner product of both sides of Eq. 3.69 and using Eq. 3.56, we get

$$u_j = \sum_{l=0}^{p-1} c_l \mu_j^l \quad j = -1, -2, \ldots, -N+2 \tag{3.70}$$

where, μ_j^l are the moments of the scaling function defined as

$$\mu_j^l = \int_{-\infty}^{\infty} \tau^l \varphi(\tau - j) d\tau \tag{3.71}$$

and are derived by solving a recursive equation [18].

Solution of Eq. 3.69 to obtain c_l requires $p-1$ initial values of $u(x,\tau)$ at $\tau = 0, 1, \ldots, p-1$ which may be obtained using finite difference schemes.

Next, the values of c_l obtained in terms of the initial values are substituted back into Eq. 3.70. Thus the unknown coefficients u_j, $j = -1, -2, \ldots, -N+2$ are obtained as

$$\begin{bmatrix} u_{-1} \\ u_{-2} \\ \vdots \\ u_{-N+2} \end{bmatrix} = \begin{bmatrix} \mu_{-1}^0 & \mu_{-1}^1 & \cdots & \mu_{-1}^{p-1} \\ \mu_{-2}^0 & \mu_{-2}^1 & \cdots & \mu_{-2}^{p-1} \\ \vdots & \vdots & \cdots & \vdots \\ \mu_{-N+2}^0 & \mu_{-N+2}^1 & \cdots & \mu_{-N+2}^{p-1} \end{bmatrix} \begin{bmatrix} c_0 \\ c_1 \\ \vdots \\ c_{p-1} \end{bmatrix} \tag{3.72}$$

The unknown coefficients at the right end boundary are evaluated assuming the same polynomial representation and

$$u_j = \sum_{l=0}^{p-1} c_l \mu_{j-n}^{l} \quad j = (n-1) - p + 1,\ (n-1) - p + 2, \ldots, n-1 \tag{3.73}$$

Equation 3.73 can be written in matrix form as

$$\begin{bmatrix} \mu_{-p}^{0} & \mu_{-p}^{1} & \cdots & \mu_{-p}^{p-1} \\ \mu_{-p+1}^{0} & \mu_{-p+1}^{1} & \cdots & \mu_{-p+1}^{p-1} \\ \vdots & \vdots & \cdots & \vdots \\ \mu_{-1}^{0} & \mu_{-1}^{1} & \cdots & \mu_{-1}^{p-1} \end{bmatrix} \begin{bmatrix} c_0 \\ c_1 \\ \vdots \\ c_{p-1} \end{bmatrix} = \begin{bmatrix} u_{(n-1)-p+1} \\ u_{(n-1)-p+2} \\ \vdots \\ u_{(n-1)} \end{bmatrix} \tag{3.74}$$

The c_l obtained are then substituted into Eq. 3.73 for $j = n, n+1, \ldots, n+N-2$ to derive $u_{(n-1)-p+1}, u_{(n-1)-p+2}, \ldots, u_{n-1}$ as

$$\begin{bmatrix} u_n \\ u_{n+1} \\ \vdots \\ u_{n-1+N-2} \end{bmatrix} = \begin{bmatrix} \mu_0^0 & \mu_0^1 & \cdots & \mu_0^{p-1} \\ \mu_1^0 & \mu_1^1 & \cdots & \mu_1^{p-1} \\ \vdots & \vdots & \cdots & \vdots \\ \mu_{-N+2}^0 & \mu_{-N+2}^1 & \cdots & \mu_{-N+2}^{p-1} \end{bmatrix} \begin{bmatrix} c_0 \\ c_1 \\ \vdots \\ c_{p-1} \end{bmatrix} \tag{3.75}$$

Finally, these coefficients are substituted in Eq. 3.57 and the system of ODEs can be written in a matrix form similar to Eq. 3.64 as,

$$\left\{ \frac{d^2 u_j}{dx^2} \right\} = \left(\frac{\eta A}{EA} \Gamma^1 + \frac{\rho A}{EA} \Gamma^2 \right) \{u_j\} \tag{3.76}$$

It should be noted that though all the formulations are performed with reference to the governing differential equation for a rod, the connection coefficient matrices Λ^1, Λ^2 and Γ^1, Γ^1 are problem-independent and depend only on the order of wavelet, i.e. N.

We see that the wavelet coefficients are highly coupled with each other. In order to obtain the spectrum and dispersion relations, we need to decouple the equations. This can be done by performing an eigenvalue analysis. It can be seen from the above derivations that the wavelet coefficients of first and second derivatives can be obtained as

$$\{\dot{u}_j\} = \Gamma^1 \{u_j\} \tag{3.77}$$

$$\{\ddot{u}_j\} = \Gamma^2 \{u_j\} \tag{3.78}$$

The second derivative can also be written as

$$\{\ddot{u}_j\} = \Gamma^1 \{\dot{u}_j\} \tag{3.79}$$

Substituting Eq. 3.77 in Eq. 3.79 we get

$$\{\ddot{u}_j\} = [\Gamma^1]^2 \{u_j\} \tag{3.80}$$

Thus though the second order connection coefficient matrices Λ^2 and Γ^2 can be evaluated independently [8], they can also be written as

$$\Lambda^2 = [\Lambda^1]^2 \quad \text{and} \quad \Gamma^2 = [\Gamma^1]^2 \tag{3.81}$$

The above modification is done as this form helps in imposing the initial conditions for non-periodic solution. Thus the Eqs. 3.64 and 3.76 can be written as

$$\left\{\frac{d^2u_j}{dx^2}\right\} = \left(\frac{\eta A}{EA}[\Lambda^1] + \frac{\rho A}{EA}[\Lambda^1]^2\right)\{u_j\} \tag{3.82}$$

$$\left\{\frac{d^2u_j}{dx^2}\right\} = \left(\frac{\eta A}{EA}[\Gamma^1] + \frac{\rho A}{EA}[\Gamma^1]^2\right)\{u_j\} \tag{3.83}$$

In wavelet transforms, for both periodic and non-periodic boundary conditions, the reduced ODEs are coupled unlike those in FFT-based analysis. However, the system of equation can be decoupled by diagonalizing the connection coefficient matrices Γ^1 and Λ^1. This can be done by eigenvalue analysis of the matrix as

$$\Gamma^1 = \Phi\Pi\Phi^{-1} \tag{3.84}$$

where, Φ is the eigenvector matrix of Γ^1 and Π is the diagonal matrix containing corresponding eigenvalues $\imath\gamma_j$. Similar expression holds for Λ^1 where Φ and Π are known analytically (Eqs. 3.67, 3.66). From Eq. 3.81, Γ^2 can be written as

$$\Gamma^2 = \Phi\Pi^2\Phi^{-1} \tag{3.85}$$

where, Π^2 is a diagonal matrix with diagonal terms γ_j^2. This eigenvalue analysis is very costly, however, it can be done only once and stored as it is completely independent of the problem. This makes the computational time comparable to FFT-based analysis.

The ODEs obtained by decoupling the Eqs. 3.82 and 3.83 can be written as

$$\frac{d^2\widehat{u}_j}{dx^2} = \left(\frac{\eta A}{EA}\gamma_j + \frac{\rho A}{EA}\gamma_j^2\right)\widehat{u}_j \quad j = 0,\ 1, \ldots, n-1 \tag{3.86}$$

where

$$\widehat{u}_j = \Phi^{-1}u_j \tag{3.87}$$

Similar steps are followed for decoupling of the coupled ODEs obtained from periodic boundary condition through eigenvalue analysis of Λ^1. The decoupled equations will be similar to Eq. 3.86 except that γ_j has to be replace by λ_j and the eigenvector matrix Φ will be of different form given by Eqs. 3.66, 3.67. Thus, decoupling of the Eq. 3.82 (neglecting damping) and using Eq. 3.68 for the eigenvalues of Λ^1, we get

$$\frac{d^2\widehat{u}_j}{dx^2} = -\frac{\rho A}{EA}\lambda_j^2\widehat{u}_j \quad j = 0,\ 1, \ldots, n-1 \tag{3.88}$$

Similarly, the force boundary condition given by Eq. 3.62 for both periodic and non-periodic boundary conditions can be written as

$$\frac{d\widehat{u}_j}{dx} = \widehat{F}_j \quad j = 0,\ 1, \ldots, n-1 \tag{3.89}$$

where,

$$\widehat{F}_j = \Phi^{-1}F_j \tag{3.90}$$

However, the eigenvector matrix Φ used for transforming u_j to $\widehat{u}_j$, and similarly F_j to $\widehat{F}_j$ will be of different forms for periodic and non-periodic formulations.

Now we are in a position to perform frequency domain analysis, wherein the spectrum and dispersion relations can be obtained. For periodic solution, the wavelet transformation given by Eq. 3.53 can be written as matrix equation [3]

$$\begin{bmatrix} U_0 \\ U_1 \\ U_2 \\ \vdots \\ \vdots \\ \vdots \\ U_{n-1} \end{bmatrix} = \begin{bmatrix} 0 & 0 & 0 & \ldots & \varphi_{N-2} & \ldots & \varphi_2 & \varphi_1 \\ \varphi_1 & 0 & 0 & \ldots & 0 & \ldots & \varphi_3 & \varphi_2 \\ \varphi_2 & \varphi_1 & 0 & \ldots & 0 & \ldots & \varphi_4 & \varphi_3 \\ \vdots & \vdots & \vdots & \ldots & \vdots & \ldots & \vdots & \vdots \\ \varphi_{N-2} & \varphi_{N-3} & \varphi_{N-4} & \ldots & \ldots & \ldots & 0 & 0 \\ \vdots & \vdots & \vdots & \ldots & \vdots & \ldots & \vdots & \vdots \\ 0 & 0 & 0 & \ldots & \varphi_{N-3} & \ldots & \varphi_1 & 0 \end{bmatrix} \begin{bmatrix} u_0 \\ u_1 \\ u_2 \\ \vdots \\ \vdots \\ \vdots \\ u_{n-1} \end{bmatrix} \tag{3.91}$$

where U_j, φ_j are the values of $u(x, \tau)$ and $\varphi(\tau)$ at $\tau = j$. For such circulant matrix, Eq. 3.91 can be replaced by a convolution relation, which can be written as

$$\{\widetilde{U}_j\} = \{\widetilde{K}_j\} \tag{3.92}$$

where, $\{\widetilde{U}_j\}$, $\{\widetilde{u}_j\}$ are the FFTs of $\{U_j\}$ and $\{u_j\}$ respectively, and $\{\widetilde{K}_{\varphi j}\}$ is the FFT of $\{K_\varphi\} = \{0\, \varphi_1\, \varphi_2, \ldots, \varphi_{N-2}, \ldots, 0\}$, which is the first column of the scaling function matrix given in Eq. 3.91. Similarly, in Eq. 3.82, the matrix Λ^1 is also the circulant matrix and it can be written as (neglecting the damping)

$$\left\{\frac{d^2\widetilde{u}_j}{dx^2}\right\} = \frac{\rho A}{EA}\{\widetilde{K}_{\Omega j}{}^2 . \widetilde{u}_j\} \tag{3.93}$$

where, $\{\widetilde{K}_{\Omega j}\}$ are the FFT of $K_\Omega = \{\Omega_0^1\, \Omega_{-1}^1, \ldots, \Omega_{-N+2}^1, \ldots, \Omega_{N-2}^1, \ldots, \Omega_1^1\}$, which is the first column of the connection coefficient matrix Λ^1. Substituting Eq. 3.92 in Eq. 3.93 we get

$$\left\{\frac{d^2(\widetilde{U}_j/\widetilde{K}_{\varphi j})}{dx^2}\right\} = \frac{\rho A}{EA}\{\widetilde{K}^2_{\Omega j}.(\widetilde{U}_j/\widetilde{K}_{\varphi j})\} \tag{3.94}$$

or,

$$\left\{\frac{d^2\widetilde{U}_j}{dx^2}\right\} = \frac{\rho A}{EA}\{\widetilde{K}^2_{\Omega j}.\widetilde{U}_j\} \tag{3.95}$$

It can be easily seen that the FFT coefficients $\widetilde{K}_{\Omega j}$ are equal to the eigenvalues $\iota\lambda_j$ of the matrix Λ^1 given by Eq. 3.68. Thus Eq. 3.95 can be written as

$$\frac{d^2\widetilde{U}_j}{dx^2} = -\frac{\rho A}{EA}{\lambda_j}^2\widetilde{U}_j, \quad j = 0, 1, \ldots, n-1 \tag{3.96}$$

It should be mentioned here that, by relating the Eqs. 3.88 and 3.96, it can be observed that the transformation given in Eq. 3.87 is similar to the FFT for periodic wavelet formulation.

In FFT-based analysis, the transformed ODEs are of the form

$$\frac{d^2\widetilde{U}_j}{dx^2} = -\frac{\rho A}{EA}{\omega_j}^2\widetilde{U}_j, \quad j = 0, 1, \ldots, n-1 \tag{3.97}$$

where,

$$\omega_j = \frac{2\Pi j}{n\triangle t} \tag{3.98}$$

It can be seen that for a given sampling rate $\triangle t$, λ_j exactly matches ω_j up to a certain fraction of the Nyquist frequency $f_{nyq} = \frac{1}{2\triangle t}$. Thus similar to FFT-based analysis, the wavelet formulation can be used directly for studying frequency dependent characteristics like spectrum and dispersion relations but up to a certain fraction of f_{nyq}. This fraction is dependent on the order of basis and is more for higher order bases. In Fig. 3.10a, ω_j and λ_j are compared with respect to fraction of f_{nyq}. Unlike λ_j which are real, the eigenvalues γ_j in the non-periodic solution are complex. However, from numerical experiments it is seen that the real part of γ_j matches λ_j which are compared for different order of basis in Fig. 3.10a. The additional imaginary part of γ_j are plotted for different bases in Fig. 3.10b. From this figure, we see that beyond the specified frequency fraction, one can clearly see artificial dispersion. For example, if we use a toneburst signal, sampled at a frequency which falls beyond this specified fraction, one will see unwanted responses. This aspect is very crucial for SHM studies, since such signals are extensively used.This study also helps the determination of the sampling rate required to avoid artificial dispersion.

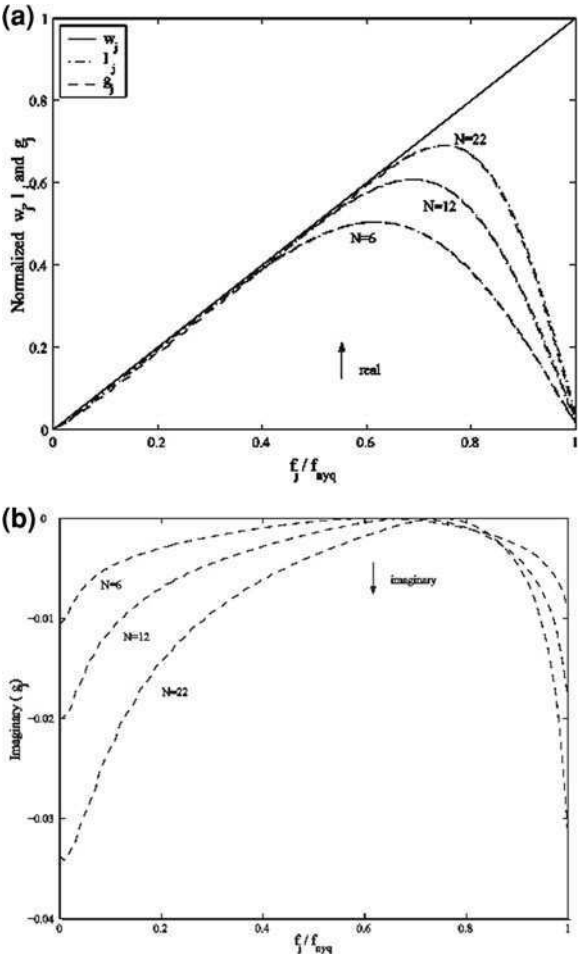

Fig. 3.10 Comparison of ω_j, λ_j and γ_j for different order (N) of basis; **a** real part and **b** imaginary part of γ_j

3.2.4 Excitation Signals and Wave Dispersion

SHM studies for detection of damages in structures normally require predefined dynamic signals that have high frequency content. A common method of detecting damage is to look for the time of arrival of reflections. Knowing the speeds from the dispersion curves and the time of arrival of reflections from the crack, one can predict the location of the crack. The predefined dynamic signal can be triggered using piezoceramic actuators mounted on the structures, which set up the stress waves. The stress wave can be non-dispersive or dispersive depending upon the medium on which it propagates. For example, the stress wave in a bar subjected to axial load is non-dispersive. That is, the waves to not change its shape as it

propagates, which results in reflected wave that have the same shape as the incident wave. This aspect has implications in the SHM studies, as the identification of defects becomes easy if the shape of the reflected pulse is same as the incident pulse. In most second order systems such as rods or membranes, waves are non-dispersive or nearly non dispersive. However, in fourth order systems such as beams and plates, waves are highly dispersive in nature and hence their shape changes significantly as they propagate. Dispersion is the result of a frequency-dependent wave speed, so that typically high frequency components travel very fast and appear early in the response as opposed to low frequency components. In such situations, it is necessary to choose a pulse that travels non dispersively even in a dispersive system. This can happen only when the pulse can inject non zero energy spread over a very small frequency band. In other words, the type of signal plays an important role.

The loading can be *broad band* or *Narrow band* (*Tone Burst*). The broad band loading shown in Fig. 3.7 is a smoothed gaussian pulse having 50 μs pulse width. The frequency content of the pulse, also shown in the same figure, have a significant frequency content up to 25 kHz. Hence, all modes up to this frequency will be excited by this pulse. When this pulse is applied to a axial bar shown in Fig. 3.6, a non dispersive wave is set up. The axial velocity response for this pulse is shown in Fig. 3.8c. We can clearly see two independent pulses, the first is an incident pulse, and the second is a reflected pulse from the fixed boundary, which is of same shape as the incident pulse, but opposite in sign. If the same structure is impacted by the same force transversely, the transverse velocity response obtained is shown in Fig. 3.9c where the dispersive nature of waves is clearly observed. From the figure, it is not possible to clearly identify the reflections coming from the fixed boundary. Such signals are not generally not suitable in SHM studies, especially if the medium is dispersive.

Next we consider a damaged cantilever composite beam with a through width delamination and subjected to the tone burst signal of Fig. 3.11.

The tone burst signal is simulated using a sine wave function of the type $f(t) = \sin\{qt\}$ modulated by a time window such as a Hanning or as Gaussian time window. The number of zeros in the function can be controlled by adjusting the value of q within the selected time interval. The FFT response of such a pulse features a peak at the frequency q, as is seen from Fig. 3.11. This signal is applied to the damaged beam shown in Fig. 3.12a in the transverse direction, wherein the wave is highly dispersive in nature. The transverse response is shown in Fig. 3.12b.

The simulation here is performed using spectral finite element simulations as explained in Chap. 5. From the figure, we see that the reflections both from the crack as well as from the boundary are of the same shape which helps clearly identify the location of the flaw in a dispersive system such as this. Hence, toneburst signals are the preferred signals in SHM studies in highly dispersive media.

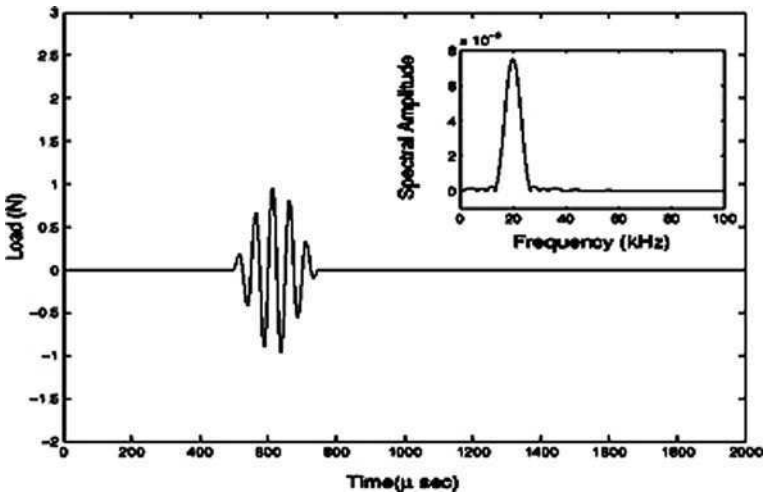

Fig. 3.11 Tone burst load sampled at 20 kHz and its Fourier transform (*inset*)

3.3 Frequency/Wavenumber Analysis

Most of the previous sections in this chapter are devoted to the analysis and representation of response data in the time and frequency domains. Such analysis provides important information in regards to the frequency content of the signal, along with guidelines on the excitation frequencies needed for a specific application or medium. The choice of the excitation frequency, or in general of the type of excitation to be used, has great implications from a practical standpoint, as it is tightly coupled with the choice of the actuation configuration. From the modeling perspective, it dictates important modal parameters such as mesh size and time domain resolution. These aspects are discussed in more detail in Chaps. 4 and 5, which are devoted to the description of common modeling tools for SHM such as the Finite Element and the Spectral Finite Element methods.

Along with the time–frequency analysis of the structural response, recent investigations have relied on the representation of the response in the frequency/wavenumber domain [1]. Such representation requires the application of the FT in the time domain and in the spatial domain. The latter can be performed only if dense measurements along a spatial direction are available. In the following, the two-dimensional Fourier Transform (2D FT) denotes the result of the application of the FT in time and along one spatial direction:

$$\hat{u}(k,\omega) = \mathscr{F}_{2D}[u(x,t)] \tag{3.99}$$

where k denotes the wavenumber. Similarly, the three-dimensional Fourier Transform (3D FT) considers transforms in time and along two spatial directions:

$$\hat{u}(k_x,k_y,\omega) = \mathscr{F}_{2D}[u(x,y,t)] \tag{3.100}$$

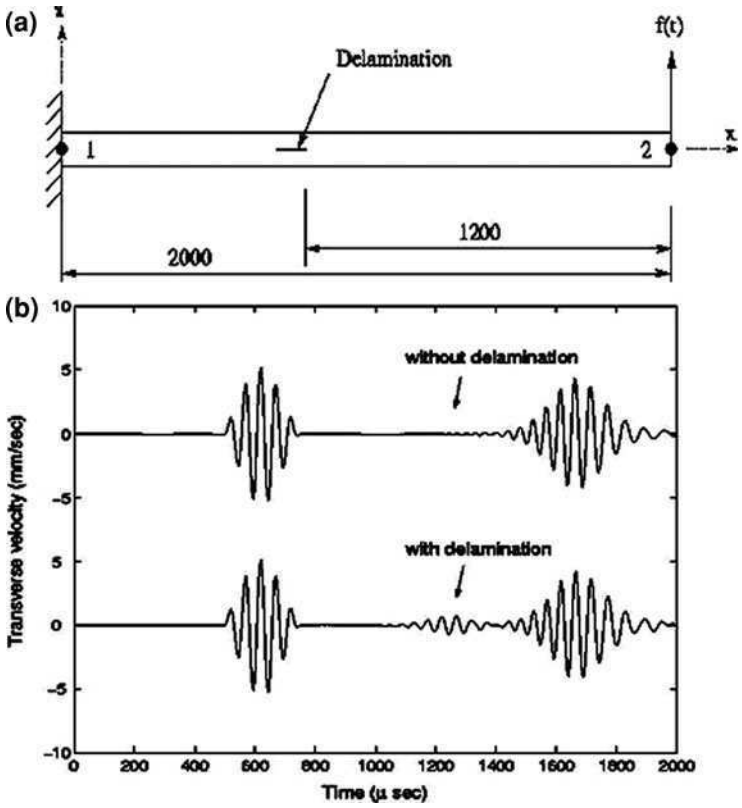

Fig. 3.12 **a** A damaged beam with through width delamination. **b** Transverse tip velocity response

where k_x, k_y are the cartesian components of the wave vector $\mathbf{k} = k_x\mathbf{i} + k_y\mathbf{j}$. Extended definitions and examples of 2D and 3D FTs are provided in the following sections.

The ability to map the signals in the wavenumber space relies on the availability of dense spatial measurements, which are typically denoted as *wavefield data*. Experimental wavefield data can be easily obtained through the use of ultrasonic transducers mounted on scanning stages, or through the application of Scanning Laser Doppler Vibrometers (SLDVs) (see Sect. 1.3.3), which is becoming very popular in the field of SHM. The advantages of frequency/wavenumber representations are numerous as summarized below:

1. They effectively separate all components of the wavefield, so that different wave modes, incident and reflected waves, and mode conversions [6] appear as decoupled and easily recognizable.
2. Their decoupling capabilities can be used to easily remove incident waves from the recorded wavefield, so that only reflected waves can be visualized.

Such visualizations can then be exploited to localize and quantify the damage that is the source of the reflections.

3. They significantly facilitate the analysis of multi-modal signals such as in the case of guided wave-based inspections. Multi-modal signals are the result of the superposition of several modes with different wavenumbers co-existing at the same frequency. Their superposition complicates the analysis of the response and its use for imaging purposes. Given the common frequency content, their separation cannot be performed through filtering procedures operating in the time–frequency domains, and therefore must rely on the information provided by different wavenumbers. Mode separation in the frequency/wavenumber domain is very easily achieved through the application of simple filtering or masking procedures which essentially select portions of the frequency/wavenumber spectrum of the signal.
4. They provide direct visualization of the dispersion properties of the considered medium, and therefore can provide the basis for material characterization and for the estimation of the mechanical properties through the comparison between experimentally observed dispersion properties and analytical predicted ones.

This section is therefore devoted to the analysis of wavefield data in the wavenumber/frequency domain as an effective tool for incident wave removal and mode separation. The concept of incident wave removal is first illustrated on analytical and numerically simulated data, and then tested on experimental results. The application of the 3D FT for mode separation is presented next to complete the overview of this interesting and still rather novel signal processing approach.

3.3.1 Analysis of a One-Dimensional Propagating Wave

The basic concept of frequency/wavenumber analysis is illustrated for a stress wave in a one dimensional (1D) non-dispersive waveguide. The considered configuration is depicted in Fig. 3.13, and assumes the presence of a discontinuity in material at location $x = x_0$. The 1D stress in the region $x < x_0$ can be expressed as a sum of incident and reflected stress waves, according to the following expression:

$$\sigma_x(x,t) = \sigma_x^{(i)}(x,t) + \sigma_x^{(r)}(x,t). \tag{3.101}$$

where

$$\sigma_x^{(i)}(x,t) = f\left(t - \frac{x}{c_{L_1}}\right). \tag{3.102}$$

and

$$\sigma_x^{(r)}(x,t) = g\left(t + \frac{x}{c_{L_1}} - 2\frac{x_0}{c_{L_1}}\right). \tag{3.103}$$

respectively define the incident and the reflected waves. Also in Eqs. 3.102 and 3.103, f, g are the functions defining the waves propagating in the considered media, while c_{L_1} is the phase velocity in region 1 (see Fig. 3.13). Imposing velocity and stress interface conditions:

$$\dot{u}^{(i)}\left(x_0^{(-)}, t\right) + \dot{u}^{(r)}\left(x_0^{(-)}, t\right) = \dot{u}^{(t)}\left(x_0^{(+)}, t\right), \tag{3.104}$$

$$\sigma_x^{(i)}\left(x_0^{(-)}, t\right) + \sigma_x^{(r)}\left(x_0^{(-)}, t\right) = \sigma_x^{(t)}\left(x_0^{(+)}, t\right). \tag{3.105}$$

yields the well-known relationships between the functions f, g:

$$g(\bullet) = \mathscr{R} f(\bullet) \tag{3.106}$$

The reflection coefficient $\mathscr{R}$ is defined in terms of density ρ and wave speed c_L of the two domains composing the waveguide:

$$\mathscr{R} = \frac{\rho_2 c_{L_2}/\rho_1 c_{L_1} - 1}{\rho_2 c_{L_2}/\rho_1 c_{L_1} + 1} \tag{3.107}$$

In Eq. 3.105, the transmitted stress wave $\sigma_x^{(t)}$ is given by:

$$\sigma_x^{(t)}(x, t) = \mathscr{T} f\left(t - \frac{x}{c_{L_2}}\right). \tag{3.108}$$

where the transmission coefficient $\mathscr{T}$ is defined as:

$$\mathscr{T} = \frac{2\rho_2 c_{L_2}/\rho_1 c_{L_1}}{\rho_2 c_{L_2}/\rho_1 c_{L_1} + 1} \tag{3.109}$$

The propagation of a harmonic stress wave of frequency ω_0 and amplitude A_0 is considered such that:

$$f(\tau) = A_0 e^{j\omega_0 \tau}. \tag{3.110}$$

Accordingly, the stress distribution in the $0 \le x \le x_0$ region is given by:

$$\begin{aligned} \sigma_x(x, t) &= A_0 \left[e^{j\omega_0\left(t - \frac{x}{c_{L_1}}\right)} + \mathscr{R} e^{j\omega_0\left(t + \frac{x}{c_{L_1}} - 2\frac{x_0}{c_{L_1}}\right)} \right] \\ &= A_0 \left[e^{j(\omega_0 t - k_0 x)} + \mathscr{R} e^{j(\omega_0 t + k_0 x - 2k_0 x_0)} \right]. \end{aligned} \tag{3.111}$$

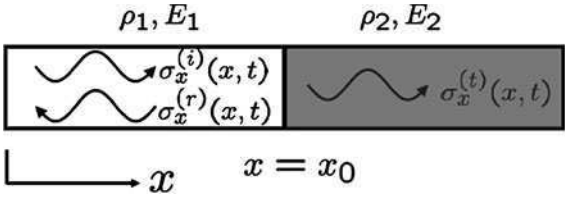

Fig. 3.13 Wave propagation in 1D elastic medium with material discontinuity

where $k_0 = \omega_0/c_{L_1}$ is the wavenumber. It is assumed that both spatial and time information are available for the stress distribution in the domain of interest. Under this assumption, one can evaluate the two-dimensional Fourier Transform (2D FT) of $\sigma_x(x,t)$:

$$\begin{aligned}\Sigma_x(k,\omega) &= \int_{-\infty}^{+\infty}\int_{-\infty}^{+\infty} \sigma_x(x,t)e^{-j(\omega t+kx)}dxdt, \\ &= \mathcal{F}_{2D}[\sigma_x(x,t)].\end{aligned} \tag{3.112}$$

which for the considered propagating wave is given by:

$$\Sigma_x(k,\omega) = A_0\delta(\omega-\omega_0)[\delta(k-k_0) + \mathscr{R}e^{2jk_0x_0}\delta(k+k_0)]. \tag{3.113}$$

where δ denotes the Dirac delta function. The magnitude of the 2D FT expressed in Eq. 113 features two peaks in the frequency/wavenumber domain at $\omega = \omega_0, k = \pm k_0$, corresponding to incident and reflected waves (Fig. 3.14a).

3.3.1.1 Incident Wave Removal

The 2D FT effectively separates the two wave components and allows the application of simple window functions to filter out one of the components. Upon filtering, the residual signal can be transformed back through an inverse FT to the space/time domain for visualization and further processing. This procedure is particularly useful for damage detection purposes, where reflected components carry information regarding the presence and the nature of damage. In many occasions, the reflections are small in amplitude and are often overshadowed by noise or by the incident wave. This makes the identification of damage, and its potential characterization difficult. From this perspective, 2D FT-based filtering represents an attractive approach to separate and highlight the presence of reflections in a given stress wave. Mathematically, the windowing process can be simply expressed as a function product between the wave's 2D FT and a 2D window function:

$$\Sigma_x^{(r)}(k,\omega) \approx [1 - H(k-k_0,\omega-\omega_0)]\Sigma_x(k,\omega) \tag{3.114}$$

where $H(k-k_0,\omega-\omega_0)$ denotes the window centered at k_0,ω_0. The process is depicted graphically in Fig. 3.14b and c, which respectively show a Hanning window overlapped to the signal's 2D spectrum and the residual signal upon filtering. The space/time domain approximation of the reflected wave can be expressed as:

$$\sigma_x^{(r)}(t,x) = \mathscr{F}_{2D}^{-1}[\Sigma_x^{(r)}(k,\omega)] \tag{3.115}$$

where $\mathscr{F}_{2D}^{-1}$ denotes the inverse 2D FT.

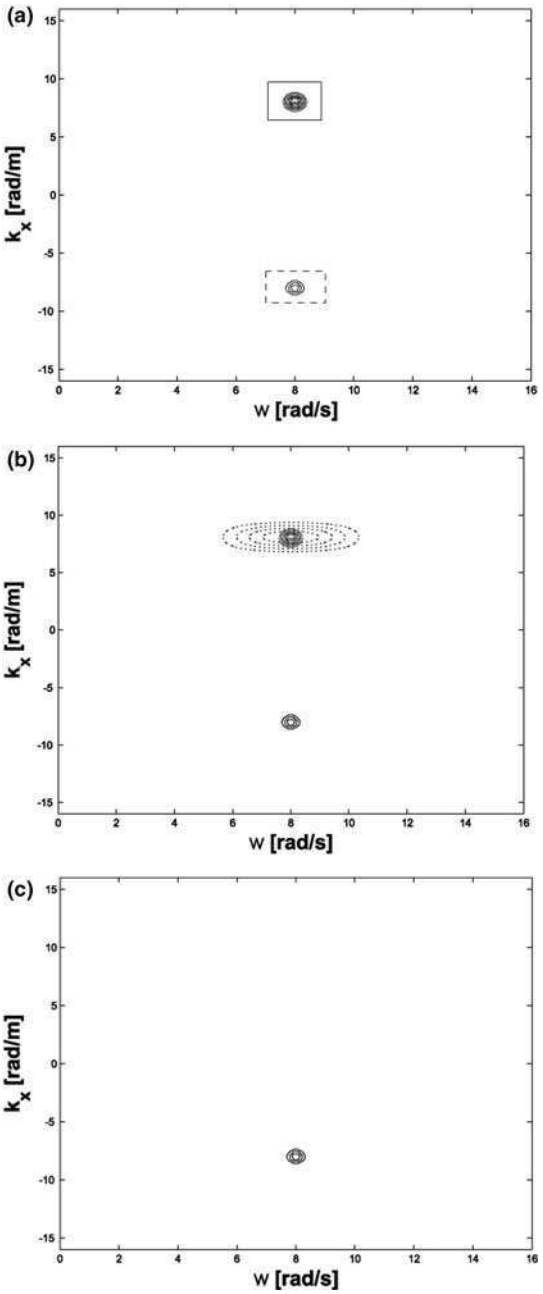

Fig. 3.14 **a** Magnitude of 2D FT of the stress distribution in the $0 < x < x_0$ region: contour plot (*Solid box* highlights incident wave component, *dashed box* highlights reflected wave component), **b** contour plot with overlapped Hanning window applied for filtering, and **c** residual signal spectrum upon filtering

3.3.2 Analysis of 2D Wave Propagation

The previous concept can be extended to the case of waves propagating in a 2D domain. We first consider a signal composed of a plain harmonic wave propagating in the $x > 0$ direction, and of a secondary spherical wave generated at location x_s, y_s as depicted in Fig. 3.15. The wave may be expressed as:

$$\begin{aligned} w(x,y,t) &= w_p(x,y,t) + w_s(x,y,t) \\ &= W_0[e^{-j(k_{x0}x+k_{y0}y-\omega_0 t)} + \mathscr{S}e^{j(k_0 r+\omega_0 t-2k_0 r_s)}] \end{aligned} \tag{3.116}$$

where W_0 is the amplitude, $\mathscr{S}$ is a generic scattering coefficient, and where $k_0 = \omega_0/c_0, k_{x0} = k_0 \cos\theta_0, k_{y0} = k_0 \sin\theta_0, r_s = \sqrt{x_s^2 + y_s^2}$.

The considered waveform can be represented in the frequency/wavenumber domain through the application of the 3D FT, defined as:

$$W(k_x, k_y, \omega) = \mathscr{F}_{3D}[w(x,y,t)] \tag{3.117}$$

$$= \int_{-\infty}^{+\infty}\int_{-\infty}^{+\infty}\int_{-\infty}^{+\infty} w(x,y,t)e^{-j(\omega t+k_x x+k_y y)}dxdydt, \tag{3.118}$$

The 3D FT of the wave signal defined in Eq. 3.123 is given by:

$$W(k_x, k_y, \omega) = W_p(k_x, k_y, \omega) + W_s(k_x, k_y, \omega). \tag{3.119}$$

where

$$W_p(k_x, k_y, \omega) = W_0\delta(\omega - \omega_0)\delta(k_x + k_{x0})\delta(k_y + k_{y0}). \tag{3.120}$$

and

$$W_s(k_x, k_y, \omega) = W_0\mathscr{S}e^{-2ik_0 r_s}\delta(k - k_0)\delta(\omega - \omega_0), \qquad k_x \geq 0 \tag{3.121}$$

Figure 3.16a shows the displacement distribution $w(x,y,t)$ over the considered domain at a specific instant of time, while Fig. 3.16b shows a cross section of the magnitude of the 3D FT evaluated at frequency ω_0. The plane wave component

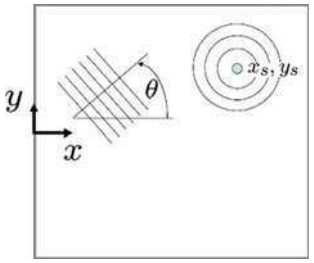

Fig. 3.15 Wave propagation in a 2D elastic medium: interaction between plane and spherical waves

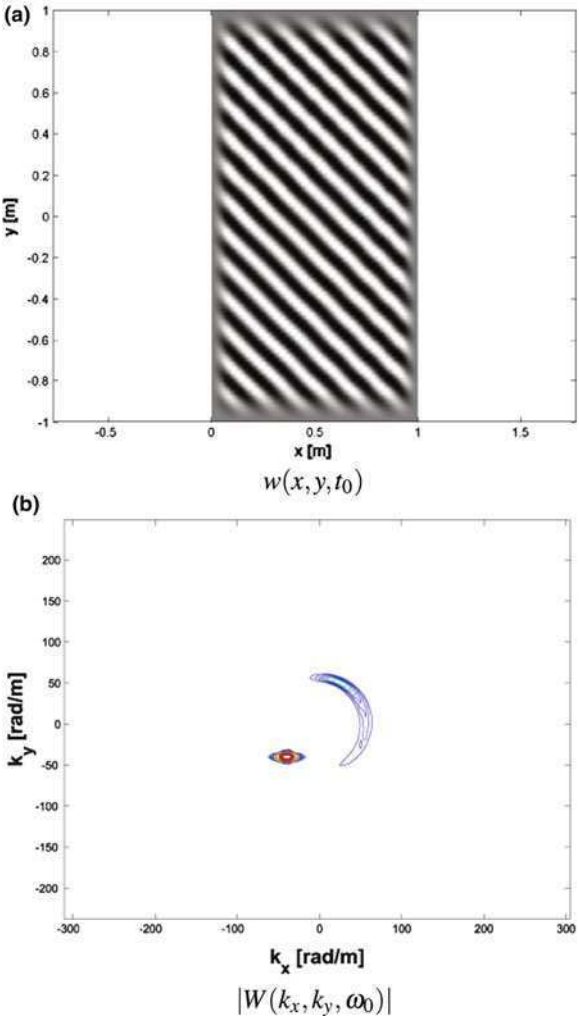

Fig. 3.16 **a** Snapshot of interaction between plane and spherical wave **b** corresponding 3D FT at $\omega = \omega_0$

appears as a peak located at coordinates $k_x = -k_{x0},\ k_y = -k_{y0}$, while the spherical wave appears as a semicircular contour limited to the $k_x > 0$ half-plane. While the presence of the spherical wave as part of the considered displacement distribution is very evident in the wavenumber domain, it appears completely overshadowed by the plane wave component in the spatial displacement distribution of Fig. 3.16a. As discussed in the case of 1D wave propagation, the plane wave component can be conveniently removed through the simple application of a window function centered at the peak corresponding to the wavenumbers $k_x = -k_{x0}, k_y = -k_{y0}$, so that the 3D FT of the spherical wave can be approximated as:

$$W_s(k_x, k_y, \omega) \approx [1 - H(k_x - k_{x0}, k_y - k_{y0}, \omega)]W(k_x, k_y, \omega) \tag{3.122}$$

where $H(k_x - k_{x0}, k_y - k_{y0}, \omega)$ is the considered window function. The result of the filtering process is to isolate the spherical wave, which can then be visualized separately from the overall measured response. The spatial distribution of the filtered signal and the corresponding 3D FT at frequency ω_0 are shown in Fig. 3.17a and b. The analysis of the residual signal displayed in Fig. 3.17a allows the identification of location and potentially the characterization of the characteristics of the secondary wave source.

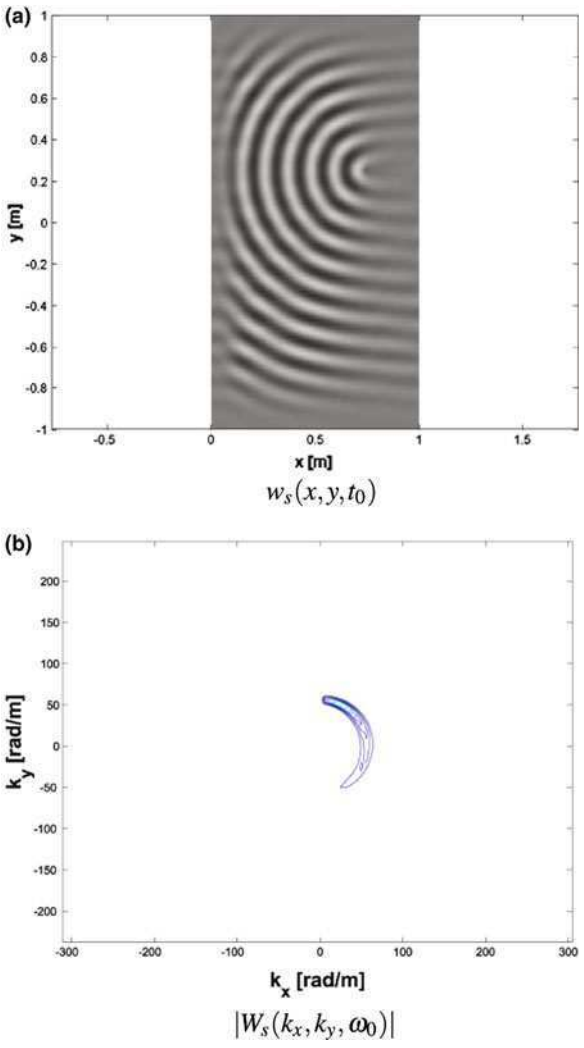

Fig. 3.17 **a** Snapshot of residual spherical wave obtained upon filtering, and **b** corresponding 3D FT

Similar results can be illustrated by considering the interaction between two spherical waves according to the configuration depicted in Fig. 3.18. The wave, in this case can be expressed as:

$$w(x,y,t) = w_{s1}(x,y,t) + w_{s2}(x,y,t), \tag{3.123}$$

$$= W_0[e^{-j(k_0 r - \omega_0 t)} + \mathscr{S} e^{j(k_0 r + \omega_0 t - 2k_0 r_s)}] \tag{3.124}$$

and the corresponding 3D FT is given by:

$$W(k_x,k_y,\omega) = W_{s1}(k_x,k_y,\omega) + W_{s2}(k_x,k_y,\omega). \tag{3.125}$$

where

$$W_{s1}(k_x,k_y,\omega) = W_0\delta(|k| + k_0)\delta(\omega - \omega_0), \quad k_x > 0 \tag{3.126}$$

$$W_{s2}(k_x,k_y,\omega) = W_0\mathscr{S} e^{-2jk_0 r_s}\delta(|k| - k_0)\delta(\omega - \omega_0). \tag{3.127}$$

The spatial distribution at a given instant of time and 3D FT at $\omega = \omega_0$ are shown in Fig. 3.19, for a case where $\mathscr{S} = 0.1$. Again, the presence of the secondary spherical wave is evident from the spectral representation of the signal, but hard to identify from the spatial distribution plot. The application of the window function to eliminate the primary wave can be replaced by the elimination of the part of the 3D spectrum corresponding to $k_x > 0$. This portion of the spectrum in fact contains all information regarding waves propagating in the $x > 0$ direction, and therefore, given the configuration depicted in Fig. 3.18, includes the primary wave.

Removal of the negative part of the spectrum can be done through the evaluation of the Hilbert Transform (HT) of the signal in terms of the x coordinate. This operation can be expressed mathematically as follows:

$$w^{\mathscr{H}_x}(x,y,t) = \mathscr{H}_x[w(x,y,t)]. \tag{3.128}$$

where $\mathscr{H}_x$ denotes the HT performed in terms of the x coordinate. The result of this filtering process is presented in Fig. 3.20a and b, which respectively show the spatial distribution at a given instant of time and the 3D FT spectrum evaluated at ω_0. The residual signal as in the previous case, clearly shows the presence of the secondary wave and the location of its origin. In a practical setting, the excitation

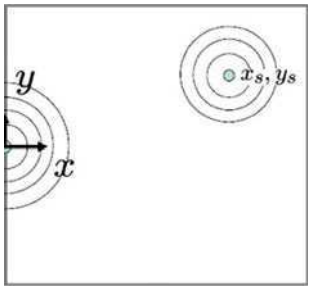

Fig. 3.18 Wave propagation in a 2D elastic medium: interaction between two spherical waves

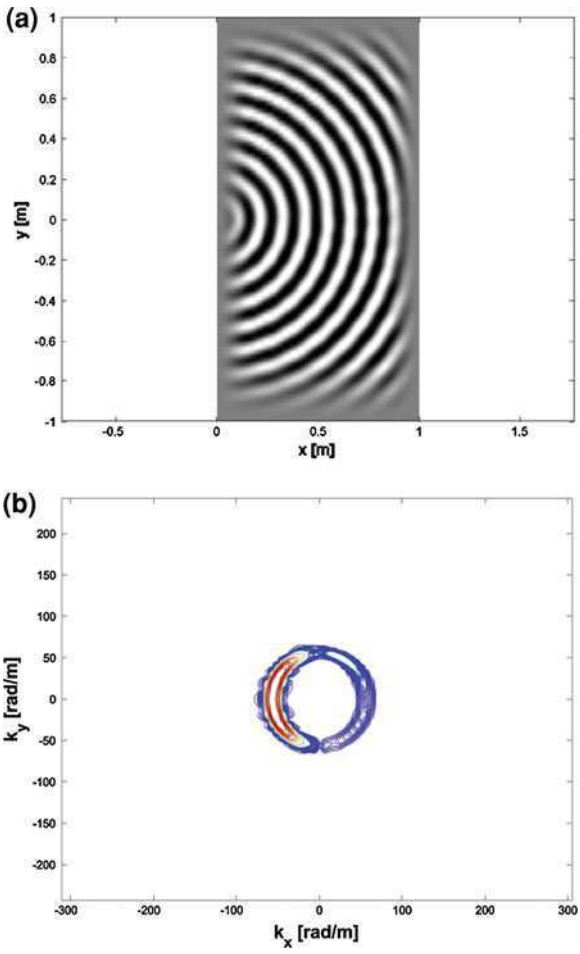

Fig. 3.19 **a** Snapshot of interaction between two spherical waves, **b** corresponding 3D FT at $\omega = \omega_0$

signal generated to interrogate the state of health of the structure can be considered as a primary wave, while the secondary wave can be associated to any damage or in general to any discontinuity in the structure. As the primary wave is selected for optimal excitation of the desired wave modes, one can consider it as fully known. As in the cases considered above, the nature of the filtering procedure can be selected on the basis of the type of excitation signal used for inspection.

3.3.3 Numerical Examples: Wave Propagation in a Damaged Rod

The configuration considered in the first set of simulations is depicted in Fig. 3.21. The rod, which has a length $L = 1$ m, thickness $h = 5$ cm, and it is made of

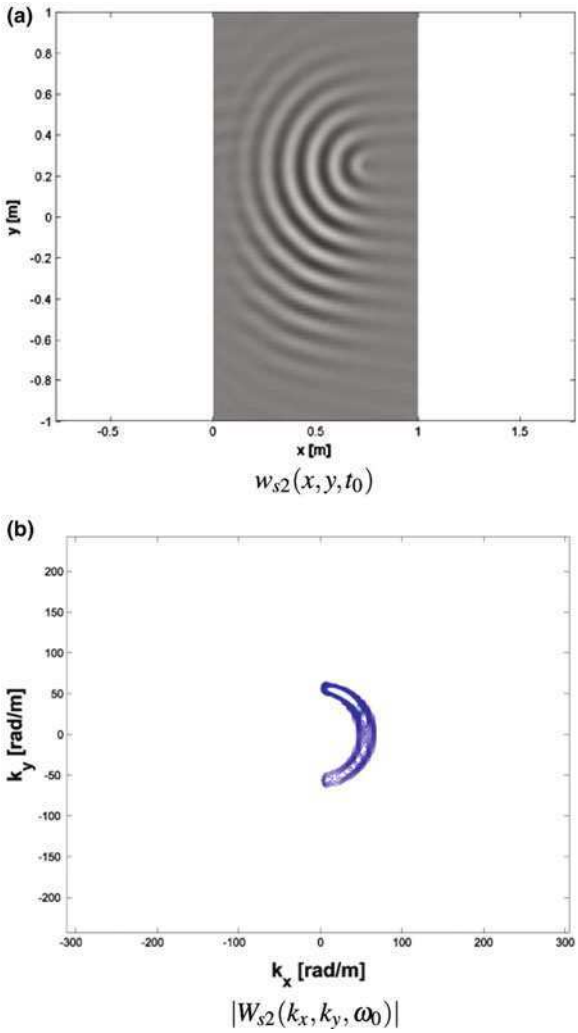

Fig. 3.20 **a** Snapshot of residual spherical wave obtained upon filtering and **b** corresponding 3D FT at $\omega = \omega_0$

aluminum ($E = 7.1 \times 10^{10}$ N/m^2, $\rho = 2,700$ kg/m^3), is excited at its free end by a 5-cycle sinusoidal tone burst at 50 kHz. The rod is discretized using 160 bar finite elements, and its response is computed through numerical integration of the equation of motion using Newmark's method. The simulation is performed over a time interval which corresponds to the time required for the injected pulse to reach the clamped end of the rod. The applied perturbation propagates and interacts with a damage located at $x_D = L/2$, modeled as a thickness reduction corresponding to $h_D/h = 0.9$ occurring over one element of the considered mesh. The response at a specific point ($x = 3/4L$) plotted in (Fig. 3.22a), in which a main pulse, corresponding to the injected wave, and a smaller, secondary, pulse corresponding to the reflection caused by damage. The 2D FT of the rod response is shown in

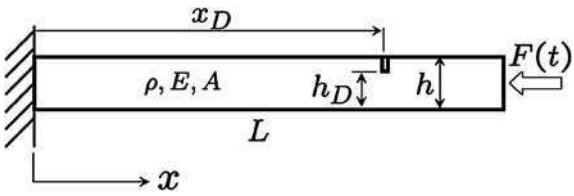

Fig. 3.21 Configuration for simulation of wave propagation in a damaged rod

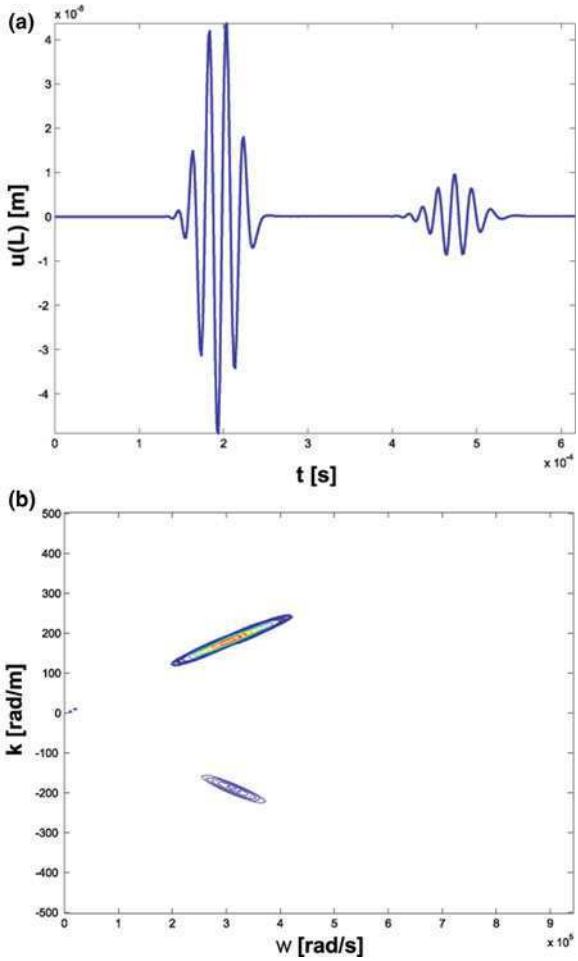

Fig. 3.22 **a** Time response of damaged rod at $x = 3/4L$, and **b** corresponding 2D FT representation

(Fig. 3.22b), which highlights the presence of the main pulse propagating along the $x > 0$ direction, and of the reflected pulse. This pulse has lower amplitude, and it is characterized by the same frequency, and appears in the $k < 0$ region of the wavenumber/frequency domain. Again, the 2D representation effectively separates incident and reflected wave components, and allows effective filtering of the main wave. A 2D Hanning window is applied to isolate the reflected wave, and to

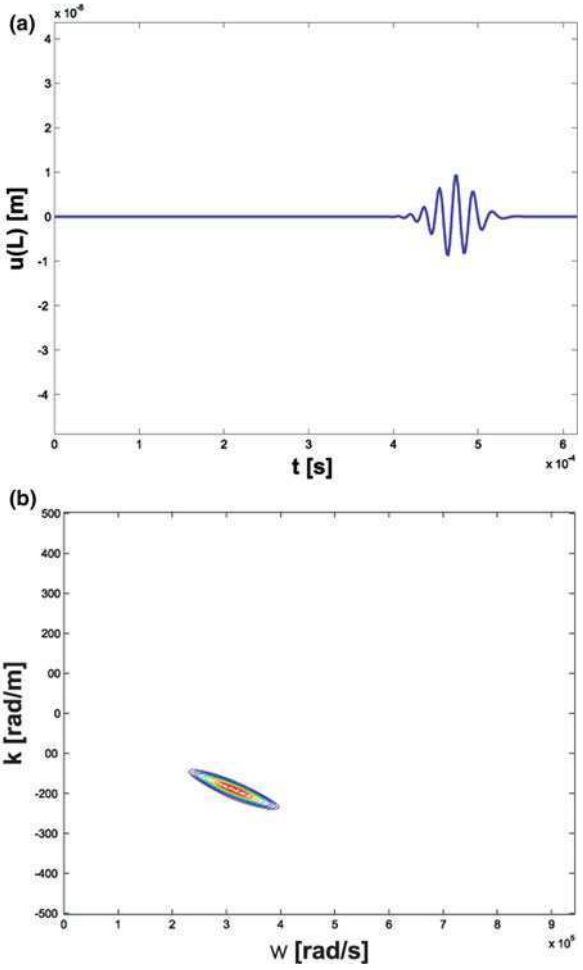

Fig. 3.23 **a** Filtered time response, and **b** 2D FT

obtain the frequency/wavenumber spectrum shown in Fig. 3.23b. The residual space–time domain signal can be then reconstructed through inverse FT transformation, as discussed in the previous section. The residual signal at $x = 3/4L$ shown in (Fig. 3.23) demonstrates the effectiveness of the windowing procedure in removing the main propagating pulse, while leaving the reflected response corresponding to damage.

This filtering procedure can be also applied to reduce the effects of noise in the data. (Fig. 3.24a) shows for example the rod response at the considered location when a random noise is added to the simulated data. The noise, which has an amplitude corresponding to 10% of the signal root mean square (RMS) value, hides almost completely the reflected signal thus making any damage identification very difficult. A narrow band filter can be applied on the filtered signal to eliminate the effect of noise and highlight the reflected signal. A 2D window (Hanning) can

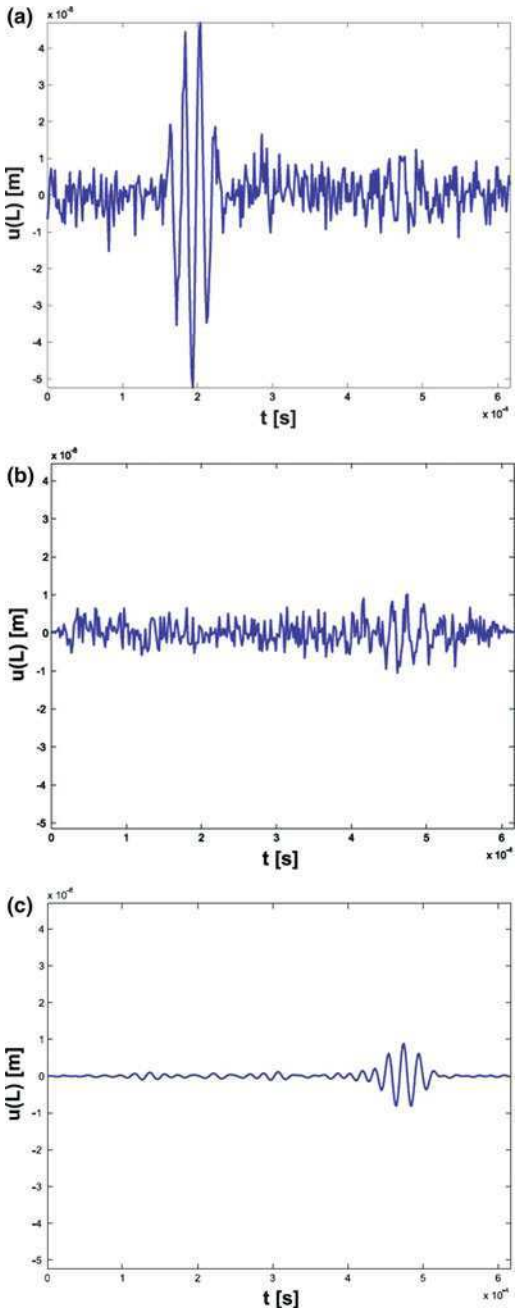

Fig. 3.24 **a** Time response at $x = 3/4L$ with added noise (**b**), residual signal (**c**), and residual signal after narrow band filtering around reflected peak in frequency/wavenumber domain

be easily applied to the frequency/wavenumber spectrum of the residual signal Fig. 3.23b in order to act as a narrow band filter and to mitigate the effects of background noise. The comparison of the estimated residual signal reconstructed with and without narrow band filtering in the frequency/wavenumber domain is presented in Fig. 3.24b and c, to demonstrate how narrow band filtering mitigates the disturbances due to noise and allows visualizing the damage signature.

3.3.4 Numerical Examples: Wave Propagation in a Homogeneous Medium

The propagation of elastic waves in a homogeneous medium is again considered to perform a validation example. The Mass Spring Lattice Model (MSLM) presented in [25] is used to simulate the propagation of elastic waves in the considered homogeneous medium. The goal of the simulations is to test the frequency/wavenumber domain filtering process as applied to simulated 2D wave propagation data. The domain in Fig. 3.25 has dimensions $L_x = 0.5$ m and $L_y = 0.25$ m and it is discretized using a 200×100 lattice. Damage is modeled as a 30% reduction in stiffness over the length L_D of the simulated damage. More sophisticated damage models for such damages is presented in Chap. 6. In the first configuration depicted in (Fig. 3.25a), damage is located at $y_D = 0.125$ m, $x_D = 0.235$ m, and has a length $L_D = 2.5$ cm, while the configuration of Fig. 3.25b features two longitudinal damages respectively located at $y_{D_1} = 0.125$ m, $x_{D_1} = 0.160$ m, and at $y_{D_2} = 0.125$ m, $x_{D_2} = 0.375$ m of length $L_{D_1} = 1.5$ cm and $L_{D_2} = 2.5$ cm. The domain is excited by an imposed displacement applied at $x_E = 0.25$ m, $y_E = 0$, varying as a 5-cycle sinusoidal tone burst of frequency $f_0 = 100$ kHz. Results for the first damage configuration are shown in Fig. 3.26. Specifically Fig. 3.26a, displays a snapshot of the propagating wave at a time instant corresponding to approximately $t_0 = 0.7T_s$, where T_s denotes the total simulation time, here selected as the time required for the induced wave to reach the top edge of the domain. The time snapshot of Fig. 3.26a shows the main pulse with small traces of scattering corresponding to damage. The cross section of the domain response evaluated at $f = f_0$ shown in Fig. 3.26b effectively decomposes the main wave propagating along $y > 0$ from the reflected wave traveling in the opposite direction. In this situation, the negative part of the spectrum can be easily removed to isolate the scattered wave corresponding to damage. This can be effectively done through the application of the Hilbert Transform along one of the spatial directions. Specifically, the reflected wave $w^{(r)}(x, y, t)$ can be estimated as:

$$w^{(r)}(x, y, t) \approx w^{\mathscr{H}_y}(x, y, t) = \mathscr{H}_y[w(x, y, t)]. \tag{3.129}$$

where $\mathscr{H}_y$ denotes the Hilbert Transform evaluated in terms of the y coordinate. The results of this process are shown in Fig. 3.26c and d which respectively present a snapshot at $t = t_0$ of the reconstructed time response upon filtering, and

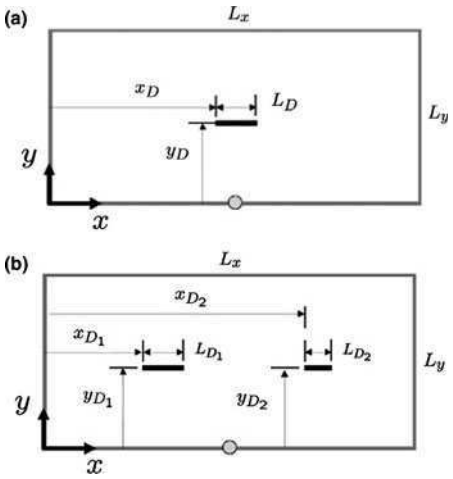

Fig. 3.25 Schematic of **a** 2D elastic domain and **b** simulated damage configurations

the corresponding cross section of the 3D FT at f_0. Given the approximation of the reflected wave $w^{(r)}(x, y, t)$, an effective visualization of presence and location of damage can be obtained through simple means such as the representation of the RMS distribution of the reflected signal defined as:

$$w^{(r)}_{\mathrm{RMS}}(x, y) = \left[\int_0^{T_s} (w^{(r)}(x, y, t))^2 dt \right]^{\frac{1}{2}} \tag{3.130}$$

The RMS distribution corresponding to the filtered response of the domain with a single damage is shown in Fig. 3.26e, while results for the domain with the two damage sites are shown in Fig. 3.27, which indicates how the technique can effectively provide indications of the presence of multiple damages.

3.3.5 Frequency/Wavenumber Filtering for Mode Separation

The frequency/wavenumber analysis of full wavefield data can be also effectively applied for the separation of individual wave modes resulting from guided waves excitation of the structures under consideration. The theory concerning Lamb waves is explained in Chap. 5. This section illustrates the additional information and processing that can be performed through the straightforward application of multi-dimensional FTs, and knowledge of the dispersion properties of the medium.

Experiments performed on a bonded aluminum plate illustrate typical experimental full wavefield data obtained using an SLDV. The SLDV records the time domain response of the structure over a pre-selected grid of points. The data are then organized in 3D arrays $u(x, y, t)$, which define the velocity component aligned

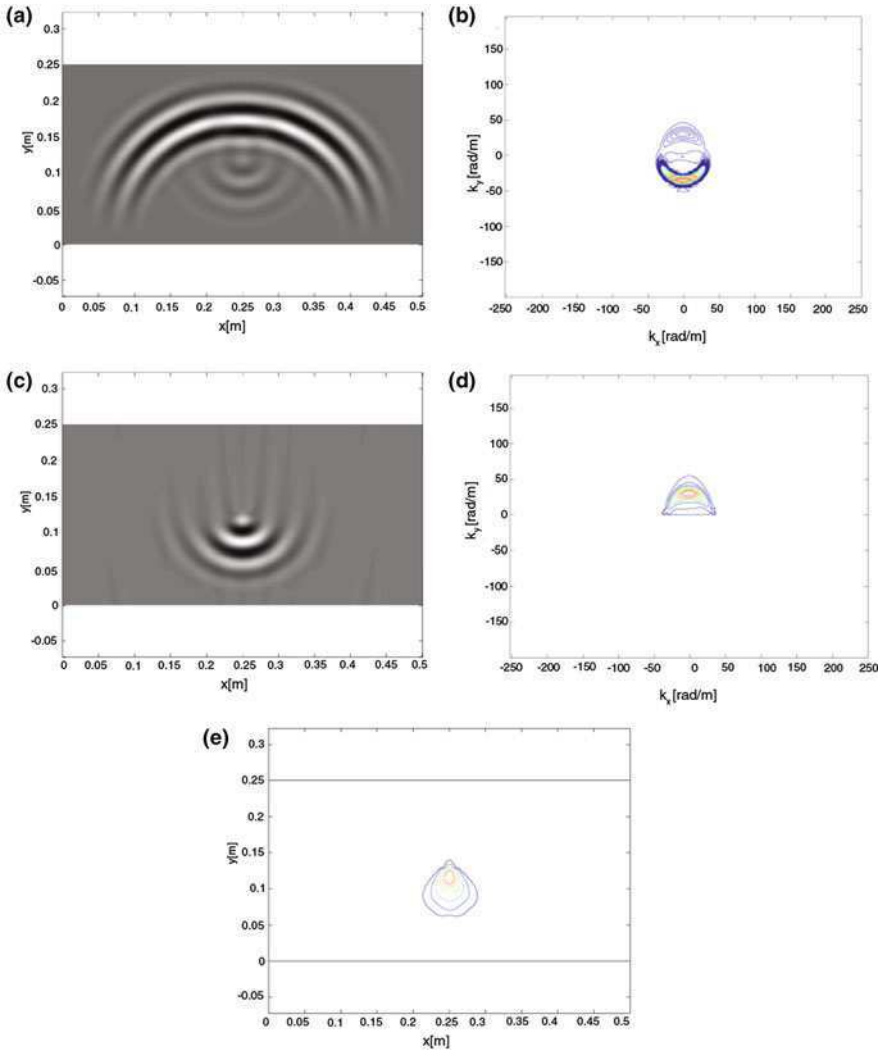

Fig. 3.26 **a** Snapshot of propagating wave in 2D domain with single damage, **b** corresponding 3D FT at the excitation frequency $f_0 = 100$ kHz, **c** snapshot of filtered wave, **d** corresponding 3D FT at $f_0 = 100$ kHz, and **e** RMS distribution of reflected signal

with the laser beam at the considered location. Examples of snapshots of recorded wavefield images are presented in Fig. 3.28. The 3D data arrays $u(x, y, t)$ contain a wealth of information which can be used for structural characterization, and subsequent evaluation of the structural properties of the component under investigation, or for the evaluation of its structural integrity. As indicated earlier, structural characterization and health assessment can be effectively performed by

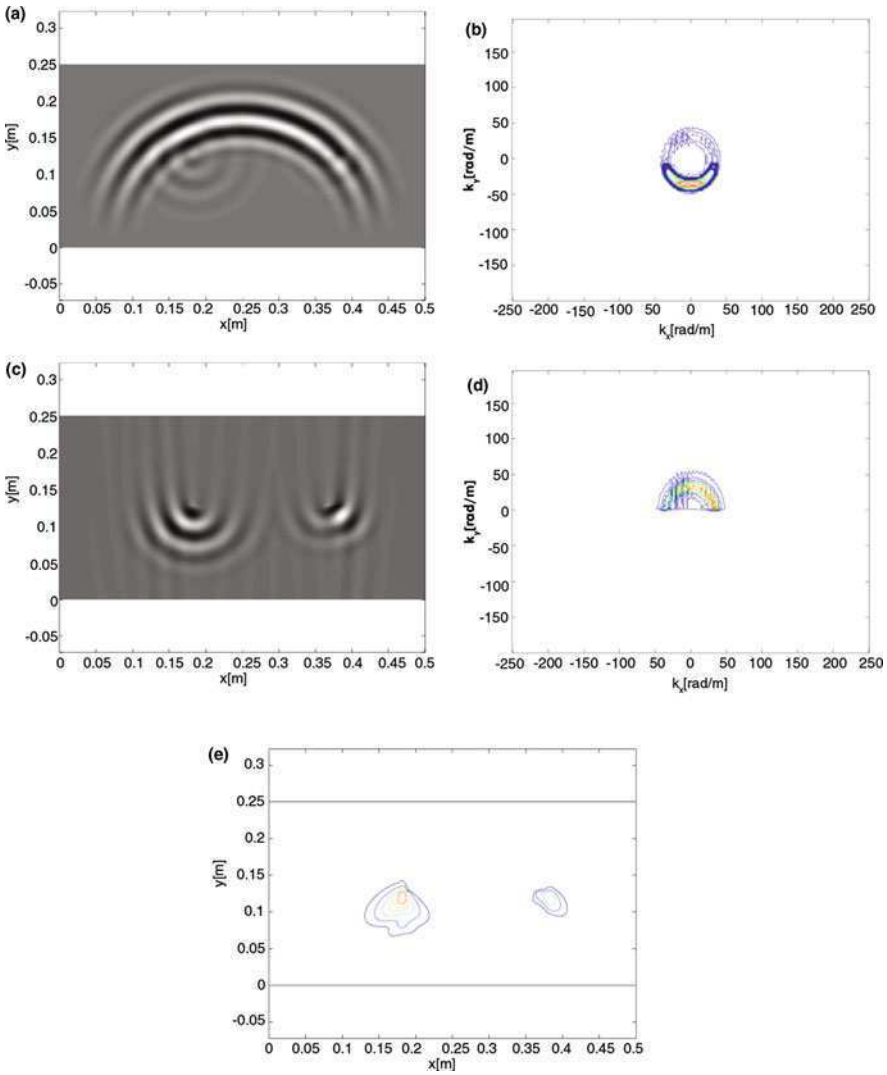

Fig. 3.27 **a** Snapshot of propagating wave in 2D domain with two damages, **b** corresponding 3D FT at the excitation frequency $f_0 = 100$ kHz, **c** snapshot of filtered wave, **d** corresponding 3D FT at $f_0 = 100$ kHz, and **e** RMS distribution of reflected signal **d**

analyzing the response of the specimen in the frequency/wavenumber ($\omega - \mathbf{k}$) domain, where dispersion information on the structure is visualized, and where the separation of multiple wave components and modes is conveniently performed. The wave vector $\mathbf{k} = k_x\mathbf{i} + k_y\mathbf{j}$ is here intended as having two components k_x, k_y, which are resolved along a Cartesian frame defined over the measured surface, and identified by the unit vectors $\mathbf{i}, \mathbf{j}$. Under this hypothesis, a 3D FT can be performed

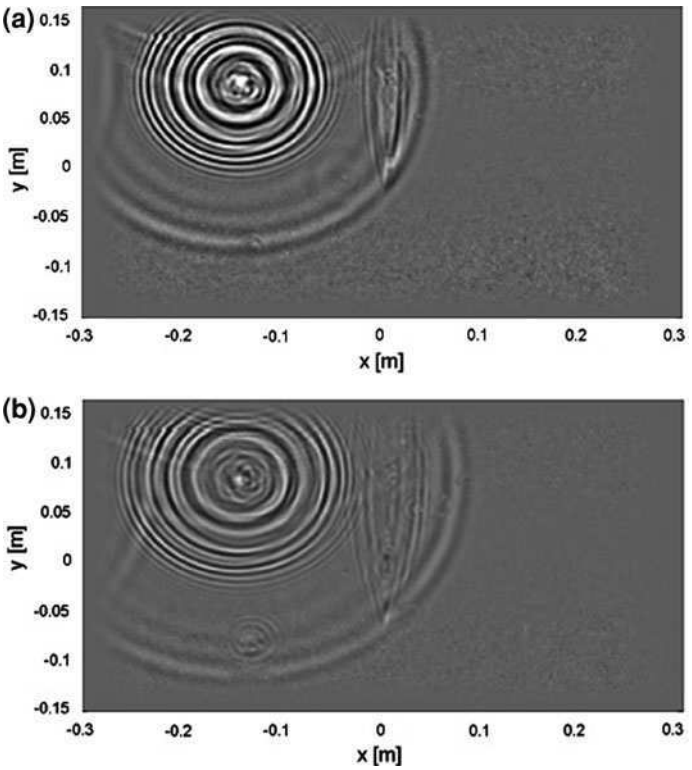

Fig. 3.28 Snapshots of wavefields measured on a bonded aluminum plate using a SLDV system

to represent the response in a 3D domain defined by the wave vector components k_x, k_y and frequency ω.

Frequency/wavenumber analysis of experimentally recorded wavefield data typically requires that the time domain waveform data $u(x,y,t)$ are windowed over a spatial region of interest to obtain:

$$u_w(x, y, t) = u(x, y, t)w_1(x, y, t) \tag{3.131}$$

where $u_w(x, y, t)$ denotes the response of the specimen over a spatial region of interest and time interval defined by the spatial-temporal window $w_1(x, y, t)$. The selection of the region may be driven by practical considerations, as dictated for example by the need to investigate and characterize the wavefield in portions of the structure where structural discontinuities are present by construction or where damage is expected to occur. In addition, the need for spatial windowing is required if incident wave removal through 3D filtering must be performed. In this case, the window must exclude the source from the region under consideration so that the incident wave is associated with a main direction of propagation. It is in

fact important that the incident (outgoing) wave occupies only half of the wavenumber plane, and correspondingly that reflected (incoming) waves are located in the other half. This allows differentiating and decoupling incident and reflected waves in the wavenumber domain when decomposed in terms of the cartesian components of the wave vector k_x, k_y. Temporal windowing prevents the effect of boundary reflections from obscuring other reflections due to the presence of scatterers within the specimen, and minimizes leakage errors.

The windowed waveform data $u_w(x, y, t)$ is transformed to the ω, k_x, k_y domain by

$$U_w(\omega, k_x, k_y) = \mathscr{F}_{3D}[u_w(x, y, t)] \tag{3.132}$$

where $\mathscr{F}_{3D}$ is the 3D FT. Frequency–wavenumber domain data $U_w(\omega, k_x, k_y)$ are subsequently filtered in the frequency/wavenumber domain through a second window function $W_2(\omega, k_x, k_y)$ to obtain:

$$\tilde{U}_w(\omega, k_x, k_y) = U_w(\omega, k_x, k_y) W_2(\omega, k_x, k_y) \tag{3.133}$$

where $\tilde{U}_w(\omega, k_x, k_y)$ is the filtered response. The selection of the frequency/wavenumber window W_2 depends on whether incident wave removal and/or mode separation need to be performed. Referring to the bonded aluminum plate experiments, the analysis considers the region of the plate highlighted in Fig. 3.29, which does not include the source, as discussed above, and where the plate thickness is constant.

The response over the considered region is evaluated through a temporal-spatial window function which is defined by:

$$w_1(x, y, t) = w_x(x) w_y(y) w_t(t) \tag{3.134}$$

where $w_\xi(\xi)$ defines the one-dimensional window applied along the generic coordinate ξ. A tapered-cosine window (Tukey window) is considered for all three directions. Its expression is

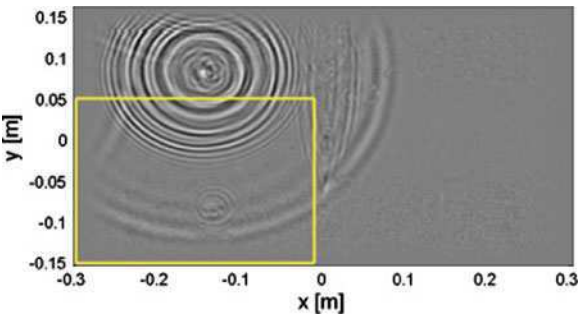

Fig. 3.29 Wavefield $u(x, y, t = t_0)$ at $t_0 = 43\,\mu s$ and detail of the region considered for the subsequent analysis

$$w(\xi) = \begin{cases} 0 & |\xi - \xi_0| > \mathtt{w} \\ 1 & 0 < |\xi - \xi_0| < \alpha\mathtt{w} \\ 0.5 + 0.5\cos[\pi\frac{\xi - \xi_0 - \alpha\mathtt{w}}{2(1-\alpha)\mathtt{w}}] & \alpha\mathtt{w} < |\mathtt{xi} - \xi_0| < \mathtt{w} \end{cases} \tag{3.135}$$

where ξ_0 and $2\mathtt{w}$ respectively denote the center and the width of the window, while α is a parameter that defines the shape of the window. Specifically, for $\alpha = 1$ the window becomes a rectangular window, while $\alpha = 0$ leads to a Hanning window. The Tukey window is particularly convenient in this case as it allows the flexibility needed to avoid that information near the edges of the considered spatial and temporal domains is lost upon windowing, while reducing truncation distortions and leakage errors associated with a sharp triangular window. In this case, a trial and error procedure has led to the selection of $\alpha = 0.25$ for all the three windows defined in Eq. 3.134). The windowed response $u_w(x, y, t)$ is transformed using a 3D FT to obtain $U_w(k_x, k_y, \omega)$.

Cross sections of the resulting three-dimensional function are presented in Fig. 3.30. Specifically, Fig. 3.30. a shows contours of the amplitude of the 3D FT $|U_w(k_x, k_y, \omega)|$ evaluated at the frequency ω_M of maximum response, which in this case is $\omega_M = 1.36 \times 10^6$ rad/s. The map clearly characterizes the modal content of the plate response, as well as the directions of wave propagation of the various modes. In this case, the family of contours associated with smaller wavenumbers corresponds to the first symmetric mode S_0, while a second group of contours is associated with the first asymmetric mode A_0. The generation of A_0 as well as S_0 modes is given in Chap. 5. It is interesting to note how the S_0 mode propagates approximately as a spherical wave, with a stronger wave vector component along the y (vertical) direction. In contrast, the A_0 mode propagates at an angle with respect to the vertical direction, possibly as a result of asymmetry of the transducer which manifests itself mostly on the A_0 mode. Figure 3.30a also shows an arrow which identifies the wave vector $\mathbf{k}_M$ of maximum amplitude, which is expressed as:

$$\mathbf{k}_M = k_{x_M}\mathbf{i} + k_{y_M}\mathbf{j} \tag{3.136}$$

$$\mathbf{k}_M = k_M(\cos\theta_M\mathbf{i} + \sin\theta_M\mathbf{j}) \tag{3.137}$$

where the angle

$$\theta_M = \tan^{-1}\left[\frac{k_{y_M}}{k_{x_M}}\right]$$

identifies the direction of the wave vector associated with the maximum response amplitude. In this case, $k_{x_M} \approx 0$ and $k_{y_M} \approx 284$ rad/m, with $\theta_M = 90°$.

Figure 3.30b shows the cross section of the 3D FT evaluated in the direction of $\mathbf{k}_M$, here denoted denoted as $|U_w(k, \theta_M, \omega)|$. The contour plots of Fig. 3.30b reproduce the dispersion relations of the plate in the frequency/wavenumber range corresponding to the excitation provided by the transducer. This representation therefore provides the means for the experimental evaluation of the dispersion

properties of the specimen, which can be used for structural characterization purposes and for the validation of numerical models. For the case of a flat aluminum plate as here considered, the dispersion properties are well known and can be found through analytical procedures as described for example in [23]. The analytical dispersion relations are superimposed to the experimental ones also in Fig. 3.30b, where they are represented as solid lines. In addition, dashed lines show the upper and lower bounds of the filtering window $W_2(kx, ky, \omega)$ applied to separate the individual modes. The considered window selected to isolate for example the S_0 mode can be expressed as follows:

$$W_2(k_x, k_y, \omega) = \begin{cases} 0 & |k(\omega) - k_{S_0}(\omega)| < 2\mathtt{w}(\omega) \\ 0.5 + 0.5\cos\left[\frac{\pi(k(\omega) - k_{S_0}(\omega))}{\mathtt{w}(\omega)}\right] & |k(\omega) - k_{S_0}(\omega)| > 2\mathtt{w}(\omega) \end{cases} \tag{3.138}$$

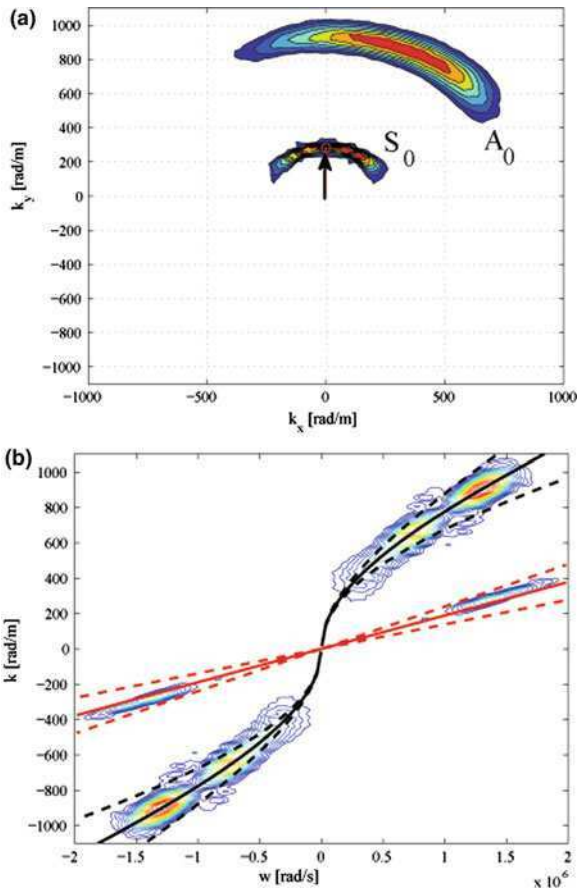

Fig. 3.30 **a** Cross sections of 3D FT of the plate response: wavenumber domain at $\omega_M = 1.38 \times 10^6$ rad/s and **b** frequency/wavenumber plot in the direction of propagation with detail of bounds used for windowing of individual modes (analytical A_0, S_0 modes *solid lines*, upper and lower bounds of windowing functions *dashed lines*)

where $k = [k_x^2 + k_y^2]^{1/2}$. Equation 3.138 defines a Hanning window of width 2w, centered at the wavenumber k_{S_0} corresponding to the mode to be extracted from the overall response. At each value of frequency ω, the center of the window can be estimated analytically from known dispersion relations, or through the evaluation of the ridge of the associated dispersion branch. The width of the window can generally vary as a function of frequency, so that W_2 may be designed to act also as a band-pass filter. The width of the window in this case has been arbitrarily chosen

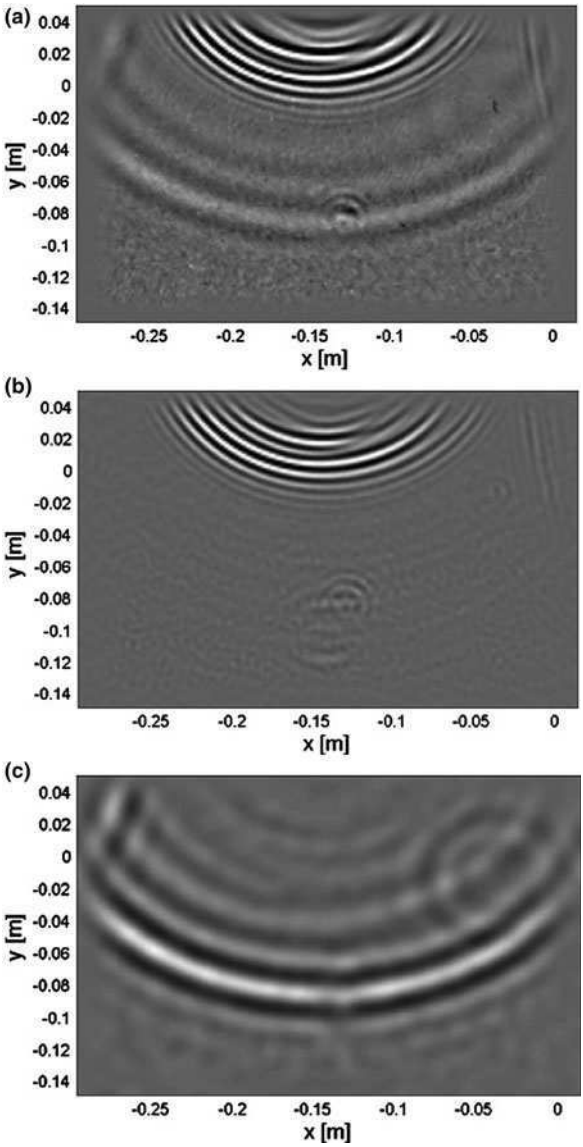

Fig. 3.31 **a** Snapshot of AWI at $t = 37\,\mu s$, **b** corresponding A_0 mode and **c** S_0 mode obtained upon mode separation

to vary linearly with frequency within the $0 - 2 \times 10^6$ rad/s range, thus capturing most of the energy of the recorded response.

Upon mode separation, the response corresponding to the individual modes can be transformed in the spatial/temporal domain so that single-mode propagation can be observed. Examples of results from this procedure are presented in Fig. 3.31 which compare snapshots of the original response, with those corresponding to the isolated A_0 and S_0 modes. The images clearly show the effectiveness of the separation procedure, which allows the selectively investigation of the scattering properties of the individual modes when interacting with defects or structural discontinuities, the estimation of their sensitivities to specific damage types, and the identification of mode conversion phenomena. Of note for example is the fact that in the image for the A_0 mode (Fig. 3.31b), two scatterers appear as secondary sources of A_0 waves as a result of the conversion of the S_0 mode.

A final step in the filtering procedure may involve the removal of the incident wave, according to the procedures outlined in the previous section. A first, simple analysis evaluates the RMS value of the residual response. Results for the plate under consideration are presented in Fig. 3.32, which compares the RMS value corresponding to the scattered A_0 and S_0 modes. The two figures clearly highlight the presence and the location of two scatterers and show their different scattering

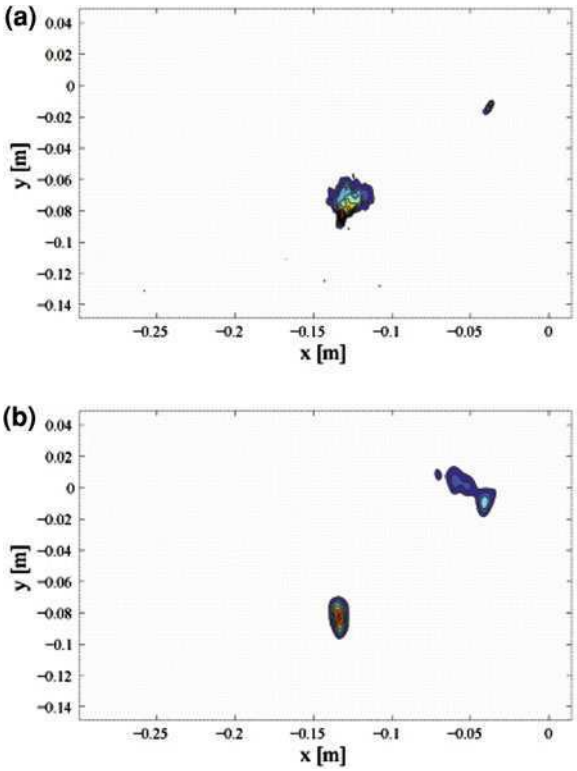

Fig. 3.32 **a** RMS of filtered mode **b** RMS of filtered mode response showing location of scatterers corresponding to locations of artificial damages

behaviors, with the one located at $(-0.05, -0.01)$ clearly producing significant stronger S_0 reflections.

References

1. Alleyne D, Cawley P (1991) A two-dimensional Fourier transform method for the measurement of propagating multimode Signals. J Acoust Soc Am 89:1159–68
2. Amaratunga K, Williams JR (1995) Integration using wavelet. In: Proceedings of SPIE, wavelet application for dual use, vol 2491, pp 894–902
3. Amaratunga K, Williams JR (1997) Wavelet-Galerkin solution of boundary value problems. Arch Comput Meth Eng 4(3):243–285
4. Bacry E, Mallat S, Papanicolac G (1991) A wavelet space–time adaptive numerical method for partial differential equations. Technical report No 591, Robotics report No 257, Courant Institute of Mathematical Sciences, New York University, New York
5. Bacry E, Mallat S, Papanicolac G (1992) A wavelet based space–time adaptive numerical method for partial differential equations. Math Model Numer Anal 26:793–834
6. Basri R, Chiu WK (2004) Numerical analysis on the interaction of guided Lamb waves with a local elastic stiffness reduction in quasi-isotropic composite plate structures. Comp Struct 66:87–99
7. Battle G (1987) A block spin construction of ondelettes. Part I Lemarie functions. Commun Math Phys 110:601–615
8. Beylkin G (1992) On the representation of operators in bases of compactly supported wavelets. SIAM J Numer Anal 6(6):1716–1740
9. Dahmen W (2001) Wavelet methods for PDEs some recent developments. J Computat Appl Math 128(1-):133–85
10. Daubechies I (1988) Orthonormal bases of compactly supported wavelets. Commun Pure Appl Math 41:906–966
11. Daubechies I (1992) Ten lectures on wavelets. Ten lectures on wavelets
12. Davis PJ (1963) Interpolation and approximation. Blaisdell, New York
13. Doyle JF (1997) Wave propagation in structures. Springer, New York
14. Glowinski R, Rieder A, Wells Jr, RO, Zhou X (1993) A Wavelet Multilevel method for Dirichlet boundary value problems in general domains. Technical report 93-06, Computational Mathematics Laboratory, Rice University
15. Gopalakrishnan S, Chakraborty A, Roy Mahapatra D (2008) Spectral finite element method. Springer, UK
16. Hong TK, Kennett BLN (2002) On a wavelet based method for the numerical simulation of wave propagation. J Comput Phys 183:577–622
17. Joly P, Maday Y, Perrier V (1994) Towards a method for solving partial differential equations by using wavelet packet bases. Comp Meth Appl Mech Eng 116:193–202
18. Latto A, Resnikoff H, Tanenbaum E (1991) The evaluation of connection coefficients of compactly supported wavelets. In: Proceedings of French-USA workshop on wavelets and turbulence. Princeton University, Springer, New York
19. Mira Mitra (2006) Wavelet based spectral finite elements for wave propagation analysis in isotropic. Composite and nano composite structures, December, Ph.D., thesis, Indian Institute of Science, Bangalore, India
20. Patton BD, Marks PC (1996) One dimensional finite elements based on the Daubechies family of wavelets. AIAA J 34:1696–1698
21. Qian S, Weis J (1993) Wavelets and the numerical solution of partial differential equations. J Comput Phys 106:155–175

22. Robertsson JOA, Blanch JO, Symes WW, Burrus CS (1994) Galerkin-wavelet modeling of wave propagation: optimal finite-difference stencil design. Math Comput Model 19:31–28
23. Rose JL (2004) Ultrasonic waves in solid media. Cambridge University Press, Cambridge
24. Stromberg JO (1982) A modified Franklin system and higher order spline systems on R^n as unconditional bases for Hardy spaces. Conf. in Honour of A. Zygmund, vol II, Wadsworth Mathematics Series, 475(493), pp 475–493
25. Yim H, Sohn Y (2000) Numerical simulation and visualization of elastic waves using mass-spring lattice model. IEEE Trans Ultrason Ferroelect Freq Control 47((3):549–558

Part II
Computational Simulation Techniques for Structural Health Monitoring

Chapter 4
Application of the Finite Element Method in SHM

4.1 Overview and Basic Principles

Proper mathematical models are required to post-process the measured output to predict the damage location and its extent. Some of the commonly used mathematical models are the finite difference methods (FDM), finite element methods (FEM), spectral finite element methods (SFEM) and boundary element methods (BEM). These were briefly discussed in Chap. 1. Among them, FEM is the most versatile and powerful method due to its ability to model complex geometries.

FEM is a powerful numerical technique to solve problems governed by partial differential equations over complex domains. It is normally adopted to solve forward problems in structures, that is, for a given a loading (input), one can easily determine the deformations the structures undergo (output). Structural health monitoring however requires estimating the state of the structure from the measured output (deformation, velocities, acceleration, voltages etc) for a given predefined input (force) [5]. Hence, SHM falls under the realm of system identification problem. Such problems are also called the inverse problems.

In this chapter, we will not outline the procedure of FEM as such since many classic texts are already available in this area. That is, it is assumed that the reader has enough knowledge of different type elements, generation of stiffness and mass matrices, convergence criteria, modeling for distributed loads etc. We will instead focus on those aspects of FEM that are relevant to SHM, which include creating damaged FE models, choosing the appropriate mesh sizes and its relation to damage size and frequency content of the input etc.

One of the key aspects of performing SHM studies under a FE environment is the modeling of the damages in general, and cracks in particular. Many researchers have used different methods under FE environment to model flaws. For example, Yang et al. [18] used FEM to study the Lamb wave propagation in composite plates. Powar and Ganguli [12] used FEM to model matrix cracks in composites

S. Gopalakrishnan et al., *Computational Techniques for Structural Health Monitoring*, Springer Series in Reliability Engineering, DOI: 10.1007/978-0-85729-284-1_4,

beam and study the performance of a rotating helicopter blade. FEM was used to obtain crack parameters in [4]. A new method to model cracks under FE framework using Heaviside function is proposed in [6]. Many researchers have used FEs to model cracks to perform fracture mechanics study and the related literature is too large to be covered here. In this chapter, we instead introduce three different, simplified ways to model damages. The discussed methodologies can be adopted to simulate vibration and wave propagation characteristics of damaged structures with the purpose of generating numerical responses which can then be used in support of the development of SHM techniques. One of the important objectives of such simplified models is primarily to be able to accurately reproduce the effects of damage in the considered frequency range, rather than to precisely model the structure of the damage, its geometry, and its shape from a fracture mechanics perspective. Relevant effects from an SHM standpoint include frequency shifts, mode and curvature shapes distortions, and reflections, diffractions, scattering and mode conversion in wave propagation regimes. The ability to reproduce these observed behaviors with the required accuracy drives the selection of the mesh size and of the simplified models to be used to represent damage. The choice of mesh size and time step are critical to the achievement of such accuracy, as discussed in this chapter. Simplified damage models as here illustrated complement the formulations presented in Chaps. 6, 7, and 8.

Modeling issues and strategies for the simulation of damage are discussed in metallic and composite structures, where different types of damage are encountered. Generally speaking, FE modeling of composites is an order of magnitude more complex than that of isotropic materials, particularly due to the presence of complex stiffness and inertial coupling. In addition, there is a variety of failure modes in composites in contrast to metallic structures. Common failure mechanisms include the delamination of the plies, fiber breakage and matrix cracks. In built-up composite structures, debonds are also a common type of failure. Accurate and efficient modeling of these types of flaws is crucial for the development of proper detection tools. The most common way of modeling flaws such as cracks in FEM is to introduce duplicate nodes along the crack front which have same nodal coordinates but different node number. This procedure ensures discontinuity in the medium arising due to the presence of the crack. One of the important differences in the response behavior of the cracked structure as compared to the uncracked structures is the presence of the phenomenon of mode conversion [2, 16] present in the former. If such a phenomenon can be built using simpler models, one can use such models effectively in SHM studies. One approach is kinematics-based, whereby the cracked structure is considered as a series of multiply connected waveguides. By enforcing kinematic relationship among the nodes of the waveguides, one can eliminate the intermediate nodes of the frame structure, thereby obtaining a FE model with built in damage. References [11, 17] use such models under the spectral finite element environment to study the wave propagation responses in a delaminated beams and in beams with fibre breakage as also explained in detail in Chap. 6.

4.2 Modeling Issues in FEM

Although modeling flaws such as cracks or delamination is well documented in finite elements (which is addressed in the next section), the stress singularity near the crack tip, requires very fine mesh near the crack tip even for a static loading, which makes the model sizes enormously large. If the loading is dynamic, the mesh sizes required will be even and it depends on the frequency content of the predefined input.

Frequency content of the predefined input is yet another parameter that should be carefully chosen depending upon the flaw sizes. When the flaw sizes are larger compared to dimension of the structure, then even static loading is sufficient. However, such flaws will be visible to the naked eye and as such SHM techniques is not needed. However, if the flaws sizes are reasonably small compared to the smallest dimension of the structure, then one requires that the predefined input loading be dynamic in nature and the frequency content could be of the order of few hundred Hertz. Such low frequency content problem comes under the category of structural dynamics. On the other hand, if the flaw sizes are very small, then the frequency content of predefined input signal should be of the order of few hundred kilo Hertz. These problems come under the category of wave propagation. The main difference between these two is that the latter is a multi-modal phenomenon, wherein phase information of the responses becomes very important. Cracks in structures acts like a boundary and results in a very small impedance mismatch at the crack boundary, which will induce reflections for a high frequency input signal. These reflected signals can be effectively used to characterize, predict, and locate the cracks in a structure and also its extent. Hence, the choice between the structural dynamics or wave propagation analysis to be adopted depends upon the frequency content of the input signal, which in turn depends on the flaw size. All these will have a bearing on the mesh sizes to be chosen for the FE analysis.

Now, two questions needs to be answered. That is, *what should be the mesh size for a given input loading?* and *what should be the frequency content of the input signal for a given flaw size?* For a given input loading, the mesh sizes to be chosen such that they are comparable to the wavelength. When the frequency content of the signal is high, the wavelengths are very small and hence the mesh sizes have to be small, which in turn increases the problem sizes enormously. To determine the mesh sizes, first the predefined input signal is transformed into frequency domain using FFT and a plot of the amplitude and the frequency will give the frequency content of the signal. Let us denote this by ω(rad/s). If c_0 is the wave speed of the given wave mode obtained from the dispersion relations of waveguide in question, then the wavelength λ is given by

$$\lambda = \frac{2\pi c_0}{\omega} \tag{4.1}$$

Typically, the mesh sizes should be such that nearly 10 elements should cover a wavelength although in some cases 8–10 elements may be sufficient. In other words it should of the order of $\lambda/10$ [9]. If the mesh sizes are larger than what is given in Eq. 4.1, then, the mesh boundaries will start reflecting the input signal thereby giving erroneous indication of the presence of the crack. Mesh sizes depends on the speeds of the medium in which the signal is propagating. In order to make this statement clear, let us consider two mediums, namely aluminum and composites. The speed of a compressional wave in composites is approximately 3,850 m/s, while in aluminum it is 6,000 m/s. Let these medium be subjected to an input pulse having a frequency content of 50 kHz. From Eq. 4.1, the wavelengths in composites is about 77 mm, while in aluminum, it is about 120 mm. Hence, for a given input, composites require a denser mesh.

Now the second question that needs an answer is related to the frequency content of the predefined input signal for a given flaw size. The requirement here is for the such a signal to induce an impedance mismatch at the crack boundary and a wave reflection. In order for this to happen, wavelengths should be comparable to the flaw sizes. For example, we will again consider the same example considered previously, that is, the aluminum and the composite structure with damage. The wave speeds in composite is approximately 3,850 m/s, while in aluminum it is 6000m/s. Let us assume that both these medium have a small crack of 20 mm size. Eq. 4.1 can be rewritten as

$$f = \frac{c_0}{a} \tag{4.2}$$

where f is the frequency in Hertz and a is the size of the flaw. From Eq. 4.2, substituting the speeds of the composite and aluminum medium, we see that, for inducing a reflection from the damage in composites, the frequency content of the input signal should be 192.5 kHz, while in aluminum medium, the frequency content of the predefined input signal should be 300 kHz. In addition, if the signal needs to travel non-dispersively, then one can create a tone burst signal created using a sine wave of above calculated frequencies. From the above discussion, it is clear that the frequency content of the input pulse and the mesh size is highly dependent upon the medium in which the waves are propagating.

The success of this analysis requires that the speed of the medium is known. Calculation of speeds especially for dispersive system is an involved process. This was discussed in detailed in Sect. 2.8. The procedure outlined in this section can be adopted to obtain the group speeds. Since the dispersive media group speeds are dependent on frequency, a question arises is on the frequency at which speeds need to be calculated in order to determine the mesh size according to Eq. 4.1. To answer this question, let us consider the dispersion plot of a composite beam for different ply orientation shown in Fig. 2.14. The plot shows the group speeds for axial and bending wave for different ply orientation of a laminated composite beam. The parameter r is the bending-axial coupling factor [8] for the beam. The speeds are normalized with the axial speed in an isotropic rod ($c_0 = \sqrt{E/\rho}$).

The three horizontal lines are the axial wave speeds for three different ply orientations. One can clearly see that the axial speeds are constant for all frequencies and hence they are non-dispersive. The figure also shows three non linear curves for bending waves for three different ply orientations. These waves are highly dispersive in nature and hence their speeds are different at different frequencies. If the input signal is broadband, then the choice of wave speed to be used in Eq. 4.1 becomes difficult. In such cases, modulated signals are very useful since their active energies are band limited over a small frequency band. One such modulated signal also called the tone burst signals is shown in Fig. 4.1. This signal is created using a sine wave of frequency 50 kHz and modulated using a Hanning window. The FFT amplitude of this signal is superimposed in Fig. 2.14 along with the dispersion plots. Through this superposition, the wave speeds corresponding to 50 kHz can be easily computed for various propagating modes and this value can be used in Eq. 4.1 for calculating the wave speeds. It can be seen from Fig. 2.14. that the frequency spectrum of the input signal also peaks at 50 kHz, which is its modulated frequency. That is, such a pulse will excite modes only those lying very close to 50 kHz, while all other modes do not participate in the response. As a result, the group speeds of the wave is a function of only a small set of frequencies close to the modulated frequency, which forces the response to be non-dispersive even in a dispersive medium.

An alternative way of fixing the mesh sizes is by looking at the stiffness of the structure. It is well known that the presence of a flaw reduces the stiffness of the structure. This stiffness reduction depends on the size of the flaw. If the flaw size is small, it causes insignificant change of the stiffness of the structure and hence insignificant change in the first few natural frequencies of the structure. However, for large flaw sizes, stiffness change is significant and hence the modal frequencies. This is shown in Fig. 4.2. for a laminated composite beam of 20 cm length with two different delamination sizes, where the bending stiffness is plotted as a function of frequency. For a delamination of 1 cm, one can hardly notice any

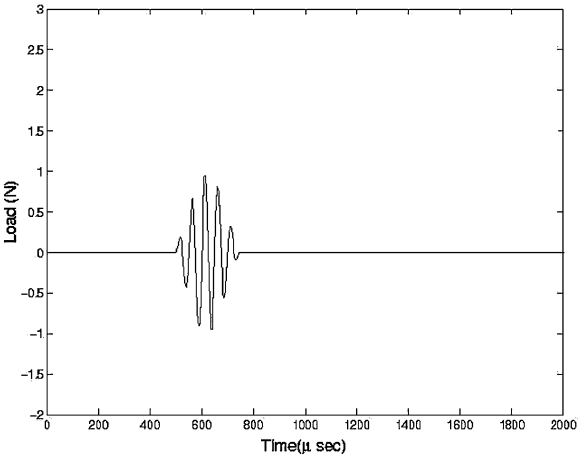

Fig. 4.1 A tone burst signal modulated at 50 kHz frequency

changes up to 20 kHz frequency and only modes beyond this frequency may get excited for the given loading, while for a delamination of 5 cm, one can see that the frequency change happens at 3 kHz. That is, for small flaw sizes, only higher modes get excited and hence to capture all higher modes accurately, one needs very fine mesh. Hence, for such small flaw sizes, modal methods are not suitable, and one needs wave propagation analysis.

Accuracy of the response to high frequency input depends on the density of the FE mesh. For a reasonably dense mesh, the wave response predicted may be accurate, however may show period error. To reinforce these ideas better, let us consider a simple aluminum rod of 2.0 m length and 0.01 m^2 cross section, with Young's Modulus $E = 70$ GPa and a density $\rho = 2600$ kg/m^3. The wave speeds in the aluminum can be calculated from the formula $c_0 = \sqrt{E/\rho} = 5189$ m/s. This rod is subjected to the input signal shown in Fig. 4.3. (inset), which has a frequency content of 46 kHz. From Eq. 4.1, the wavelength can be calculated, which is equal to 0.11 m. In order to capture the wave behavior accurately, at least 10 elements per wavelength are required, that is an element length of 10.0 mm. Hence, for a length of 1.0 m, at least 100 1D finite elements are required for modeling. Fig. 4.4, shows the axial wave responses at the cantilever tip for different number of elements. We have used 250 1D rod elements to get a fully

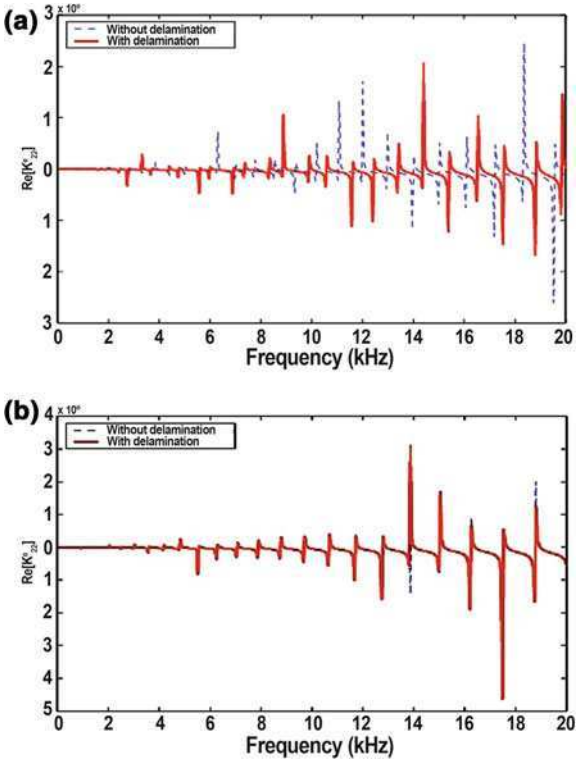

Fig. 4.2 Stiffness changes as a function of frequency for different delamination sizes: **a** delamination length 5 cm, **b** delamination length 1 cm

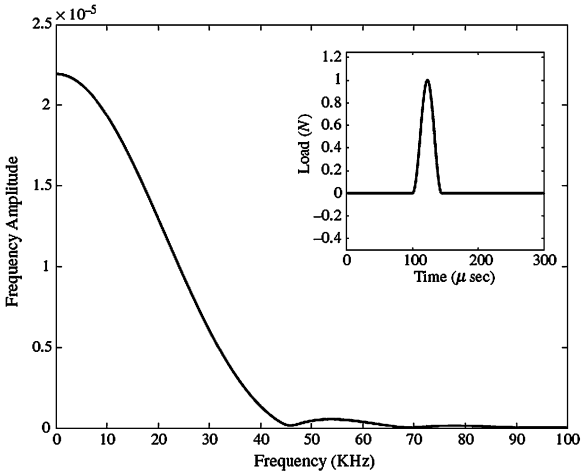

Fig. 4.3 High frequency input load with its Fourier transform

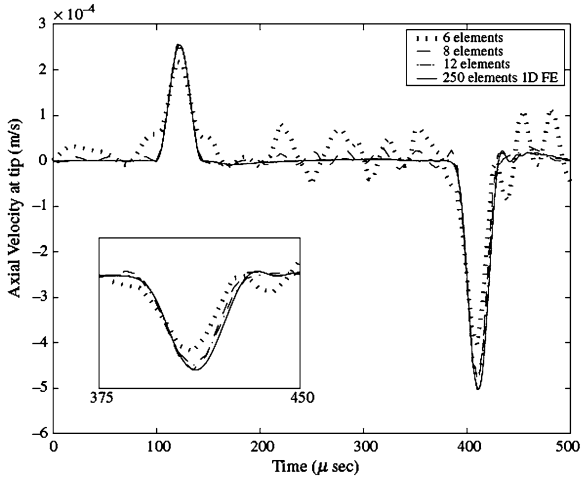

Fig. 4.4 Longitudinal wave responses in a rod for different element discritizations

converged solution, which shows an initial pulse at round 100 μs and a reflected pulse from the boundary at around 420 μs. Fig. 4.4. also shows (in the inset) the period error when the mesh sizes are inadequate. Inadequate FE mesh for a high frequency input pulse results in mass or inertial distribution not being accurate. As a result, the wave speeds predicted by FE analysis will be highly inaccurate resulting in period error. In addition, if the mesh sizes are much smaller than what is required, then the mesh boundaries will act as a fixed boundary and start reflecting responses from these boundaries. These are clearly seen in Fig. 4.4. for very coarse mesh density. Hence, for very high frequency content input pulse, which is normally the case for most SHM problems, fine mesh is an absolute necessity.

4.3 Damage Modeling Using FEM

Materials such as composites have many modes of failures. Among the different failure modes, delaminations, and fibre breakages are important modes of failure. These failure modes correspond to horizontal and vertical cracks in metallic structures. This section outlines some of the methods adopted to model the above failure modes in composites and metallic structures under FE environment. These methods can be classified as

1. Stiffness Reduction Method (SRM)
2. Duplicate Node Method (DNM), and
3. Kinematics Based Method (KBM) A description of each method is provided below

4.3.1 Stiffness Reduction Method

It is quite well known that the presence of flaw causes a reduction of stiffness in a structure. A simple way of modeling flaws is to incorporate the stiffness loss in the region of the flaw by modifying the materials properties P (where P can signify, Young's modulus, shear modulus, density etc.) to αP where $\alpha < 1$. The concept is demonstrated in Fig. 4.5, where Fig. 4.5a shows the actual model of a laminated beam with a through width delamination and Fig. 4.5b presents the equivalent stiffness-reduced model. This procedure can be adopted to model any number of flaws in the structure. One main drawback of this approach is its inability to predict mode conversion. In [9], such a model was however used to perform SHM studies on large civil structures.

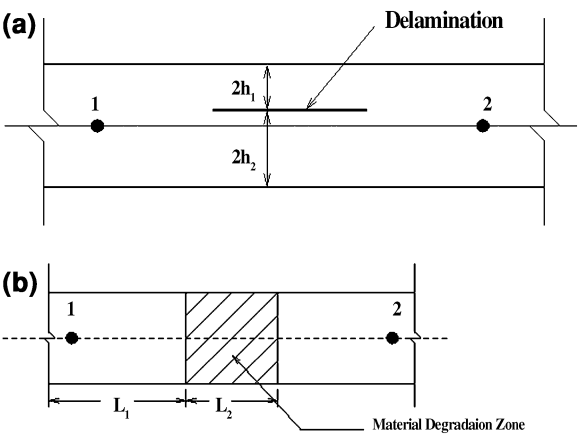

Fig. 4.5 Modeling of flaws using stiffness reduction method: **a** delaminated beam, **b** stiffness reduced beam

4.3.2 Duplicate Node Method

A better way of modeling cracks in FE is to completely model the entire crack front. This can be performed in the following way. Modeling can be done using either the 1D beam element or with the 2D plane stress/strain finite elements using the concept of duplicate nodes. In the case of beams, the modeling of a flaw such as a delamination is done by keeping the two nodes in same place, one for the elements above the flaw and other below it. This is shown in Fig. 4.6a. Here, elements 1 and 2 are at the left part of the flaw, while elements 8 and 9 are to the right part of the flaw. All other elements are in the flawed zone, either above or below the flaw. The zone below the flaw is modeled with elements 3–7 and above by elements 10–14. The flaw is modeled through proper nodal connectivity of these elements. That is, for a healthy zone, element 1 is connected with nodes 1 and 2; and element 9 is connected with nodes 9 and 10. All of these nodes are in the mid-plane of the corresponding beam elements. For element below the flaw, say, element 3, is connected with nodes 3 and 4, where nodes 3 and 4 are not on the mid plane of the element. This may create high bending-stretching coupling, which is the objective of the modeling process to induce mode conversion. Similarly, for element above the delamination, element 10 is connected through nodes 3 and 11, where nodes 3 and 11 are not in the mid plane of this element. As mentioned earlier, nodes 4 and 11 are in the same place and not connected with any direct element. These are termed as duplicate nodes. Similarly, (nodes 5 and 12), (nodes 6 and 13) and (nodes 7 and 14) nodes are the duplicate nodes. In the flaw zone, the lower part of the elements connects with nodes 4, 5–7 and upper parts of the elements connect nodes 11–14. If these nodes are merged with their corresponding duplicate nodes, the beam will be healthy. In addition, with these

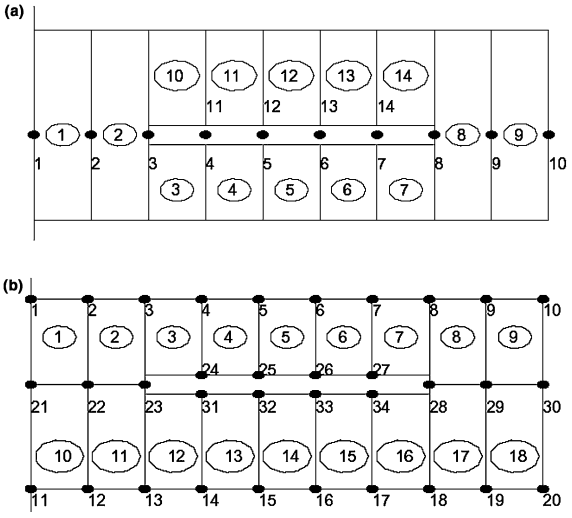

Fig. 4.6 Modeling of flaws using duplicate node method: **a** modeling of flaw using beam elements **b** modeling of flaw using plane stress/strain elements

duplicate nodes, different kinds of contact or gap elements can be used in finite element analysis to prevent inter penetration of the crack front.

Similar procedures can be adopted in modeling a flaw using 2D plane stress (or strain) elements, which are shown in Fig. 4.6b using duplicate nodes. The figure is self explanatory. Extending of this procedure to model fibre breakages and multiple delaminations in composites is quite similar and straightforward.

4.3.3 Kinematics Based Method

This method is very useful for modeling delaminations, fibre breakage, and multiple delaminations in 1D beam type of structures and has lot of similarities to DNM method explained in the previous subsection. More details can be found in Chap. 6 and in references [11, 17, 14]. The approach involves enforcing kinematics to the nodes surrounding the flaw through two techniques: rigid links between the FE nodes that share flaw are used, or enforcing actual displacement constraints corresponding to the beam displacement field. Thus far, the KBM method has only been applied to model delaminations and fibre breakages in 1D laminated composite structures, and it is limited to through-width straight-line cracks.

The main idea behind this modeling approach is to cut the beam structure into multiple elements (domains) along the crack front. The stiffness and mass matrices for each of the sub domains is generated. The intermediate nodes away from the crack front arising due to this splitting are then connected to the nodes along the crack front through rigid links in order create a coupling between the axial and transverse displacements. The procedure for modeling delaminations and fibre breakage are quite different and hence described separately.

4.3.3.1 Modeling of Horizontal Crack or Delamination

Here, let us consider a composite beam with a through width delamination, the dimensions of which are shown in Fig. 4.7a. This delaminated beam is split into base laminates and sub-laminates as shown in Fig. 4.7b. The equivalent beam model with eight nodes, make up this delaminated beam. Each sub-domain (element) is indicated by a number within a circle. Let each node support three degrees of freedom namely the axial deformation u, the transverse deformation w and the slope ϕ and they are represented by a vector u_i, where i represents the domain (element) of interest. Note that between nodes 4 and 7 lies the through width delamination. It is assumed that there is no contact action between the sub-laminates at the plane of delaminations and the cross sections are perfectly straight at the interfaces. The connections between the nodes 3–4, 4–5, 6–7 and 7–8 are made with the help of the *rigid links* to simulate the bending-axial coupling. This model does not take care of crack tip stress singularity as it is not of importance in

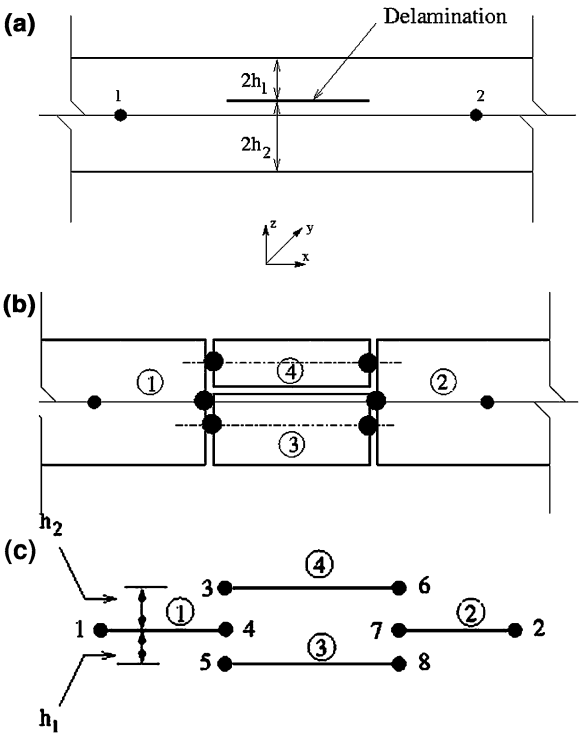

Fig. 4.7 **a** Original delaminated beam, **b** Splitting of the damaged beam into base and sub laminates and **c** equivalent beam models

the context of damage detection. A similar approach can be adopted when the laminated composite structures has multiple delaminations. Some examples on use of this model in the context of SHM, is given in the next section.

4.3.3.2 Modeling of Vertical Crack or Fibre Breakage

Let us consider a beam with a fibre breakage represented in Fig. 4.8a. The split up model is shown in Fig. 4.8b and the beam model representation is shown in Fig. 4.8c. We assume that there exists a distributed dynamic contact at the crack surfaces and the crack surface remains perfectly straight. The nodes along the left and right side of the crack are connected by rigid links to simulate bending-axial coupling behavior. That is, nodes 9–8, 8–5, 5–7, 10–6, 6–11 and 11–12 are connected by rigid link. Unlike the previous case of delamination, there is a hanging interface between nodes 3 and 4, which are connected by a non-linear spring to simulate the distributed dynamic contact. The spring constant has to be chosen in such a manner that this simplified beam model simulates the actual waveguide behavior at high frequencies. As before, the effects of crack tip stress singularity is here ignored. Examples of applications of this model are given in the next section.

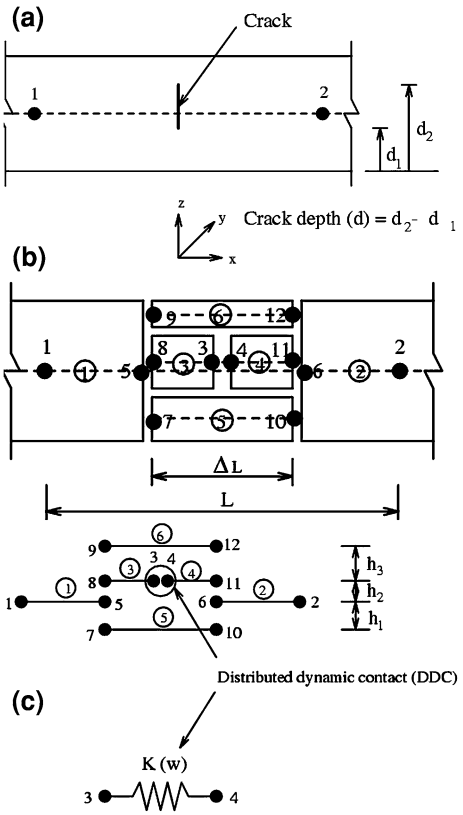

Fig. 4.8 **a** Original beam with fibre breakage, **b** splitting of the damaged beam into base and sub laminates and **c** equivalent beam models

4.4 Numerical Examples

The choice of the model entirely depends upon the level of sophistication required for the analysis. The next sub-sections describe numerical examples related to static, free vibration and wave propagation analysis in the context of SHM using the models described above.

4.4.1 Static and Free Vibration Analysis of a Damaged Cantilever Beam Using DNM

Here two different studies are performed. In the first case, the results from the two different DNM models (1D beam and 2D plane stress models) are compared to see the effectiveness of each of these models for SHM studies. In the next case, the results from the DNM and the KBM based models are compared.

A unidirectional 12-layer laminated composite beam of total depth of 1.8 mm and a length of 500 mm is considered. A through width delamination is

symmetrically placed with respect to both top and bottom and the sides. The lamina is assumed to be orthotropic with the Young's Modulus in the two perpendicular directions being equal to 181 and 10.3 GPa, respectively. The shear modulus G_{12} is assumed equal to 28 GPa. The FE model details are as shown in Fig. 4.6, while Table 4.1 gives the percentage increase in the tip deflection due to the damage for a tip unit load. From the results, we find that the agreement between the two DNM models is closer for large delaminations.

Next, free vibration study is performed to assess the performance of the two different DNM models and these are plotted in Fig. 4.9. Both the models (beam and 2D) show more or less similar results. When the delamination is 10% of the length of the cantilever, the 15th natural frequency reduces 20% compared to the corresponding frequency of the healthy beam. Similarly, for 90% delamination, the first natural frequency reduces 29%, second natural frequency reduces 40% and third natural frequency reduces 72%. From these studies, it is quite clear that beam DNM beam models can give comparable results with the plane stress DNM models. This has implications in SHM studies as beam models can give substantially smaller problem sizes, which is one of the key requirements for SHM simulations.

In the next exercise, the static analysis is performed using DNM (plane stress model) and KBM model on a metallic cantilever beam of length 635 mm, width 25.4 mm, depth 25.4 mm, with Young's Modulus of beam assumed to be 70 GPa, and Shear Modulus of 27 GPa. The results are generated for a given crack length of L/10 located at different location along and across the beam. The DNM model has 100 elements with due care taken to have finer mesh near the crack tip. The KBM model has only four elements as shown in Fig. 4.7c. The beam is subjected to a load of 5,000 N. The results of these two models are tabulated in Table 4.2.

From Table 4.2, it is clear that the four element KBM model is able to capture quite accurately the damaged behavior of the cantilever metallic beam. This again results in substantial reduction in problem sizes. However, most SHM problem requires high frequency content loads for damage detection, which needs wave propagation analysis. This is addressed in the next subsection.

Table 4.1 Comparison of static results for two different DNM models

Delamination (%)	Beam DNM model (% increase in tip deflection)	Plane stress DNM model (% increase in tip deflection)
10	0.39	0.08
20	0.91	0.61
30	2.35	2.03
40	5.15	4.80
50	9.77	9.37
60	16.63	16.24
70	26.13	25.75
80	38.90	38.32

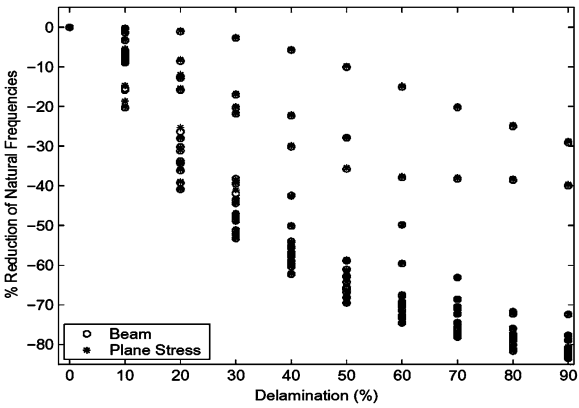

Fig. 4.9 Comparison of free vibration results for two different DNM models

Table 4.2 Comparison of static results for DNM and KBM models for different crack locations

Location of the crack of size L/10 in the cantilever beam	Tip deflection based on Plane stress DNM Model (mm)	Tip deflection based on 4 element KBM (mm)	% difference
Crack located symmetrically both length wise and depth wise	1.78×10^{-4}	1.804×10^{-4}	1.37
Crack located symmetrically lengthwise and 17.78 mm from the bottom	1.778×10^{-4}	1.90×10^{-4}	5.92
Crack located symmetrically depth wise and 228.6mm from the fixed end	1.786×10^{-4}	1.77×10^{-4}	1.02
Crack located symmetrically depth wise and 342.9 mm from the fixed end	1.773×10^{-4}	1.84×10^{-4}	3.78

4.4.2 Response Analysis of a Cantilever Composite Beam with Different Damage Types

The aim of this numerical example is to bring out the differences in the responses predicted by the three different damage models, namely DNM 2D plane stress model, SRM and KBM model, respectively. Here, we consider a delaminated AS/3505-6 graphite epoxy composite cantilever beam of length 800 mm and the beam is subjected to an impact load shown in Fig. 4.3.

Two different damage types, namely the delamination and fiber breakage, both of which are of 20 mm size is considered on this beam, which are symmetrically placed as shown in Fig. 4.10. The beam with 20 mm delamination is modeled by DNM model, while the beam with 20 mm fiber breakage is modeled using KBM model. The results from these are compared with the 1D beam FE model with stiffness reduced by 50% in the small region close to the damage. The main objective of this example is to not only to compare the responses predicted by

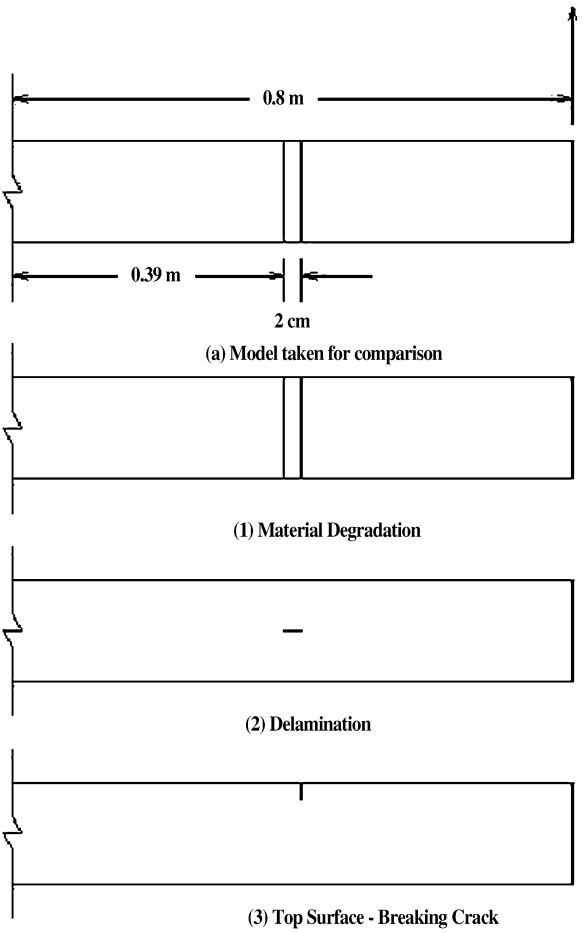

Fig. 4.10 **a** Basic model showing the damage 1. SRM model with 50% stiffness reduction in the cracked region, 2. Delamination modeled using DNM, 3. vertical surface breaking crack modeled using KBM with a spring constant of 1×10^{-3} of $\bar{Q}_{11}$

these models, but also to look at the possibility of substituting the detailed KBM model with SRM model for SHM analysis.

The damage is modeled as a horizontal crack (delamination) using DNM model, where in a total of 3500 2D triangular elements are used. The vertical crack or the fiber breakage is modeled using KBN method, while the SRM model is obtained from the healthy beam 2D model by reducing the stiffness (composite modulus $\bar{Q}_{11}$) by around 50%. The input force has a frequency content of 44 kHz. For this force, with a wave speed of 3850 m/s, it requires nearly 320 beam elements. However, this simulation is performed using 500 elements for the SRM and DNM models, respectively. The hanging interface in case of the KBM model of the spring is simulated with a spring constant of 1×10^{-3} times the $\bar{Q}_{11}$, where $\bar{Q}_{11}$ is the composite stiffness property (See Chap. 2, Sect. 2.4.1.3 for details). The different beam configuration with the associated damages is shown in Fig. 4.10 and the transverse response histories is shown in Fig. 4.11. From the figure, we can

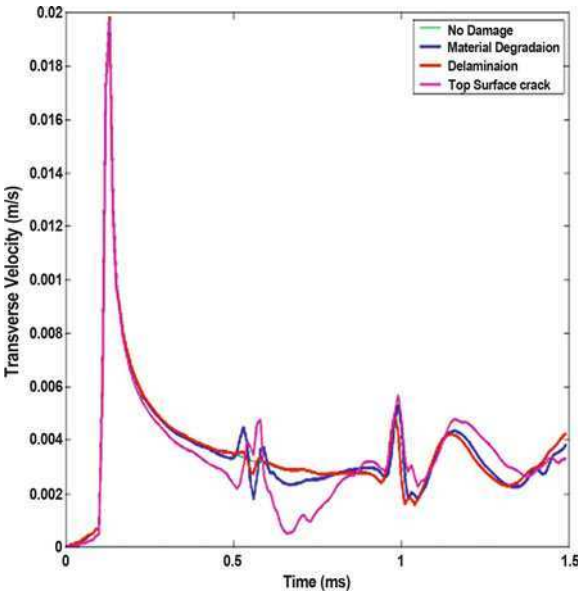

Fig. 4.11 Comparison of wave propagation responses for different models

clearly see that each of these models pick up the reflection from the damage at around 0.5 ms and the responses show very little change between different damage types for same size and location. Hence, it can be concluded that SRM model, which is the easiest to model, can indeed be used to get the response estimates on a damages structure. However, if one needs to further predict the location and extend of damage, more local models such as the DNM method may be required.

4.5 Finite Element Modeling Suggestions

All the examples shown in this chapter dealt with 1D waveguides. This is because, the modeling concepts outlined are better understood with 1D waveguides. However, most practical structures are either two or three dimensional in nature. Here we outline some suggestions for modeling flaws in a general 3D structure.

1. The procedure for deciding mesh sizes and the frequency content of the input signal for 2 and 3D structures outlined in this chapter. However, as mesh size obtained from Eq. 4.1 should be applied for all the dimension of the structure.
2. For modeling 1D, straight line cracks for SHM studies, KBM method is sufficient for damage detection purpose. However, a more detailed DNM models will be required if one needs to perform life estimation studies.
3. Deriving finite elements based on KBM is not straightforward and hence this method is seldom used in 2 or 3D structures with flaws. However, for certain

crack orientations, some cracks functions are derived, which captures the mode coupling aspects in 2D structures. These functions can be readily incorporated into the finite element formulation, to obtain a simplified damage model. This is outlined in [1].

4. If the frequency content of the signal is large, that is if the mesh sizes are very small, then we seldom use a graded mesh as used in static analysis of a cracked structure. We normally choose very small but equal mesh sizes as dictated by Eq. 4.1.
5. All the examples demonstrated the use of various modeling methods for either perfectly horizontal or perfectly vertical cracks, which are normally the case in composites. However, in metals, the commonly occurring cracks are inclined in nature. For such structures with inclined cracks, normally DNM method is used, although SRM method can also be employed. However, for matrix cracking type in damages, where the determination of the location is not that important, SRM method is ideally suited

4.6 Modeling Pitfalls in FEM for SHM and Their Remedies

One of the fundamental objectives of SHM is to rapidly obtain the state of the structure. It was mentioned earlier that the FE model sizes depend on the size of the flaw. For very small flaw sizes, the frequency content of the signal should be large, which leads to enormously large problem, which take many hours to obtain the solution. This is one of the bottlenecks in SHM modeling.

Unlike in a beam, wherein most damages are through width, single dimension crack, in most 2 and 3D structures, the damages will have an area. For modeling these type flaws, DNM method is ideal, although the mesh sizes will be very large. One way to reduce the size of model is to adopt, reduced order FE models. Reduced order FE models will have only few nodes retained, which correspond to either sensor locations or the locations where forces are applied, while all other nodes are condensed out. For static analysis, simple static condensation as outlined in [3] is sufficient. For dynamic loading, there are many reduced order models are available, which are outlined in [15]. Procedure to model and its application to SHM studies are reported in [13].

Spectral FEM [8] can model very long structure with very limited model sizes irrespective of the frequency content of the input signal. However, modeling arbitrary geometries in Spectral FEM is practically not possible. The solution to such problems is to marry these two methods. For example, in the region very close to the crack, FE modeling can be used and in the region far away from the crack, spectral FEM could be used. This is because, SFEM can model long and straight edge surface with only one element. Such an approach was adopted [7] to model cracks in isotropic beams. Alternatively, a new finite element formulation based on partition of unity [10], which can be used to model the zone near the

crack and far away, one can use spectral element enrichment functions. Such a method will be very useful for SHM analysis of large scale structures.

A complete SHM analysis requires modeling of flaws, their detection from the measured responses, its location, its extent and its severity. Today, many general purpose modeling tools such as NASTRAN, ANSYS, ABAQUES, ALGOR, etc. are available for modeling cracks using any of the above methods described in this chapter and also for assessing its severity. Some of these software can also perform optimization studies to decide on the number of sensors required and their locations. However, most of these tools cannot perform SHM centric analysis as these do not have the other components of SHM, namely the damage detection algorithms and the signal processing algorithms. Since SHM concepts are built in the design of today's civil, aerospace, mechanical, and ship structures, the need of the hour is to develop SHM centric FE software that integrates many different modules and new modeling concepts. Such an effort will go a long way towards taking SHM development to a higher level.

References

1. Chakraborty A, Gopalakrishnan S (2006) A spectral finite element model for wave propagation analysis in laminated composite plate. ASME J Vib Acoust 128(4):477–488
2. Chakraborty A, Gopalakrishnan S (2004) A spectrally formulated finite element for wave propagation analysis in layered composite media. Int J Solids Str 41(18):5155–5183
3. Cook RD, Malkus RD, Plesha ME (1989) Concepts and applications of finite element analysis. John Wiley, New York
4. Dado MHF, Shpli OA (2003) Crack parameter estimation in structures using finite element modeling. Int J Solids Str 40(20):5389–5408
5. Doebling SW, Farrar CR, Prime MB, Shevitz DW (1998) A review of damage identification methods that examine changes in dynamic properties. Shock Vib Dig 30(2):91–105
6. Ghoshal A, Kim HS, Kim J, Choi SB, Prosser WH, Tai H (2006) Modeling delamination in composite structures by incorporating the Fermi-Dirac distribution function and hybrid damage indicators. Finite elem Anal Des 42(8-9):715–725
7. Gopalakrishnan S, Doyle JF (1995) Spectral super-elements for wave propagation in structures with local non-uniformities. Comput Methods Appl Mech Eng 121:77–90
8. Gopalakrishnana S, Roy Mahapatra D, Chakraborty A (2008) Spectral finite element methods. Springer, London
9. Hu XF, Shenton HW (2007) Dead load based damage identification method for long-term structural health monitoring. J Mater Syst Str 18(9):923–938
10. Hu N, Fukunaga H, Kameyama M, Roy Mahapatra D, Gopalakrishnan S (2007) Analysis of wave propagation in beams with transverse and lateral cracks using a weakly formulated spectral method. ASME J Appl Mech 74(1):119–127
11. Nag A, Roy Mahapatra D, Gopalakrishnan S, Sankar TS (2003) A spectral finite element with embedded delamination for modeling of wave scattering in composite beams. Compos Sci Technol 63:2187–2200
12. Powar PM, Ganguli R (2005) On the effect of matrix cracks in composite helicopter rotor blade. Compos Sci Technol 65(3-4):581–594
13. Priyank Gupta Gridhara G, Gopalakrishnan S (2008) Damage detection based on damage force indicator, using reduced order fe models. Int J Comput Eng Mech 9(3):154–170

14. Roy Mahapatra D, Gopalakrishnan S (2004) Spectral finite element analysis of coupled wave propagation in composite beams with multiple delaminations and strip inclusions. Int J Solids Str 41:1173–1208
15. Sastry CVS, Roy-Mahapatra D, Gopalakrishnan S, Ramamurthy TS (2003) An iterative system equivalent reduction process for extraction of high frequency response from reduced order finite element model. Comput Methods Appl Mech Eng 192(15):1821–1840
16. Sharma V, Ruzzene M, Hanagud S (2006) Damage index estimation in beams and plates using laser vibrometry. AIAA J 44:919–923
17. Sreekanth Kumar D, Roy Mahapatra D, Gopalakrishnan S (2004) A Spectral finite element for wave propagation and structural diagnostic analysis in a composite beam with transverse cracks. Finite elem Anal Des 40:1729–1751
18. Yang CH, Ye L, Su Z, Bannister M (2006) Some aspects of numerical simulation for Lamb wave propagation in composite laminates. Compos Str 75(1–4):267–275

Chapter 5
Spectral Finite Element Method

5.1 The Need for Spectral FEM in SHM

Spectral Finite Element Method (SFEM) is an effective tool to solve wave propagation problems. In essence, it can be considered as a FE method formulated in the frequency domain. Before we explain what this method is all about, the question that need to be answered is on the relevance of SFEM as an effective computational tool for SHM.

Previous chapters have widely documented how the assessment of the presence of small size damage requires the support of mathematical models that can efficiently capture the high frequency response of damaged structures. In other words, the development of a wave propagation-based is essential to the development of diagnostic tools for SHM.

The history of the study of wave propagation dates back several centuries. An account of these developments can be found in [13]. However, analysis of wave propagation by SFEM is a relatively new approach. The SFEM is based on the application of integral transforms [22]. Examples are the extensive use of Fourier or Wavelet transforms. For instance, the application of the continuous Fourier transform (CFT) to the solution of wave propagation problems is a standard approach as seen in early work [21]. Similarly, for certain boundary and initial value problems, Wavelet transforms (WT) are very useful [3].

We will now briefly outline the procedures involved in the formulation of SFEs based on FFT and WT, respectively. Following are two references that give details on Fourier transform based SFEM. While the initial development of this method is given in [9], the reader is advised to refer to [12] to get more advanced applications of SFEM in wave propagation analysis, SHM and active control of structures.

S. Gopalakrishnan et al., *Computational Techniques for Structural Health Monitoring*, Springer Series in Reliability Engineering, DOI: 10.1007/978-0-85729-284-1_5,

5.1.1 General Formulation Procedure: Fourier Transform Based SFEM

The use of integral transforms involves performing an inverse transform (reconstructing the signal), which is very difficult to do in an exact analytical manner. Consequently, many approximate and asymptotic schemes have been developed. These are quite adequate for studying the far-field behavior, e.g. for seismological studies. However, for structural wave propagation in general and SHM in particular, these schemes are not sufficient because of heavy loss of information caused by the reflection of the interacting stress waves at numerous boundaries. Further, analytical transforms are feasible only if the functions to be transformed are relatively simple, which is not the case for most practical problems. Thus, the absence of a suitable inversion technique arrested the growth of CFT based methods and paved the way for the DFT, which is an approximation of the integral involved in CFT. These aspects were discussed in Chap. 3.

The development of SFEM had to wait for the re-invention [14] and publication of a FFT algorithm, popularly known as the Cooley Tukey algorithm [7], which revolutionized signal processing. The SFEM, conceived by Doyle [9], is a DFT based wave propagation analysis tool, where the DFT is performed by a FFT algorithm. The unknown variable, a scalar or a vector, can be a function of space and time, and is approximated as

$$\boldsymbol{u}(x,y,z,t) = \sum_{n=0}^{N-1} \hat{\boldsymbol{u}}(x,y,z,\omega_n) e^{-j\omega_n t}, \quad j^2 = -1, \tag{5.1}$$

where N is the number of FFT points. ω_n is the discrete circular frequency, which is related to the time window T by

$$\omega_n = n\Delta\omega = \frac{n\omega_f}{N} = \frac{n}{N\Delta t} = \frac{n}{T}, \tag{5.2}$$

In the equations above, Δt is the sampling rate and ω_f is the highest frequency captured by Δt. The frequency content of the load decides N and consideration of the wrap-around problem or aliasing problem decides $\Delta\omega$. More details on the associated problems were discussed in Chap. 3.

Representation of the unknown variable in Eq. 5.1, removes one dimension from the system, i.e., the time t so that frequency enters as a parameter. If the structure is a 1D idealization, then the governing PDE reduces to an ODE. The ODE has constant coefficients for most cases where the material properties does not vary spatially. Variable coefficients ODE's arise for cases when the material inhomogeneity in the structure is in the direction of wave propagation and also for circular waveguides. For a constant coefficient ODE, the exact solution can be found for any order of the equation. SFEM employs this exact solution as an interpolating function for element formulation. The constants of integration are made to satisfy the boundary conditions in the frequency domain and thus all the requirements are satisfied at each discrete frequency, ω_n. Using the IFFT, the time domain data are obtained.

However, there is more to SFEM than just solving PDEs in frequency domain using FFT. As the name suggests, the method has a resemblance to the FEM. As in FEM, in SFEM, the Ritz method [18, 24] can be employed in frequency domain to obtain the structural stiffness matrix, known as the dynamic stiffness matrix $\hat{\boldsymbol{K}}_n$. The matrix vector equation (much like the FEM) that is solved at each frequency ω_n is

$$\hat{\boldsymbol{K}}_n \hat{\boldsymbol{u}}_n = \hat{\boldsymbol{f}}_n, \tag{5.3}$$

where $\hat{\boldsymbol{u}}_n$ and $\hat{\boldsymbol{f}}_n$ respectively are the vectors of unknown displacements and known forces at frequency ω_n. The dynamic stiffness matrix can also be obtained using regular FEM by taking the Fourier transform of the governing equation, using the stiffness matrix $\boldsymbol{K}$ and the consistent mass matrix $\boldsymbol{M}$ as

$$\hat{\boldsymbol{K}}_n = \boldsymbol{K} - \omega_n^2 \boldsymbol{M}, \tag{5.4}$$

where n in the suffix indicates the formation at ω_n. However, in most cases $\hat{\boldsymbol{K}}_n$ in SFEM is obtained using the exact solution to the governing in the transformed domain as interpolating functions, whereas $\hat{\boldsymbol{K}}_n$ from FEM is just an approximation. The $\hat{\boldsymbol{K}}_n$ in FEM approaches the $\hat{\boldsymbol{K}}_n$ from SFEM in the limiting process of taking the number of FEs to infinity. Further, the matrix–vector structure of the SFEM gives the flexibility of FE modeling, where large structures can be assembled in terms of many spectral waveguides. The assemblage and imposition of boundary condition in SFEM is the same as in FEM, which makes the method attractive. With the use of Ritz method and the theorem of Minimum Potential Energy in frequency domain, many approximate spectral elements can be formulated. Examples of these are reported in [5, 10]. Furthermore, there is the possibility of coupling SFE and FE in complex structures as reported in [11].

The formulation of SFEs for 2D structural waveguides poses extra complexity. The reduced equation in the frequency domain is no longer an ODE, but remains a PDE in terms of the space variables. This PDE is not readily solvable and another transform is necessary to reduce the equation to one spatial dimension. A possibility consists in moving to the frequency/wavenumber domain, through a 2D FT as defined in Chap. 3. Thus, the unknown variable is further decomposed, normally using a Fourier series (FS) representation as

$$\hat{\boldsymbol{u}}(x, y, \omega_n) = \sum_{m=0}^{M-1} \tilde{\boldsymbol{u}}(x, \eta_m, \omega_n) \begin{Bmatrix} \sin(\eta_m y) \\ \cos(\eta_m y) \end{Bmatrix}, \tag{5.5}$$

where M is the number of FS points, and η_m is the discrete wavenumber related to the spatial window Y by

$$\eta_m = m\Delta\eta = \frac{m\eta_f}{M} = \frac{m}{M\Delta y} = \frac{m}{Y}, \tag{5.6}$$

with Δy denoting the spatial sampling rate and η_f is the highest wavenumber captured by Δy. The spatial variation of the load determines M. Using this representation, the governing equation becomes an ODE in x and again can be solved exactly for some cases. This exact solution is again used as the interpolating

function for the unknown in the spectral element formulation. Thus, for each frequency ω_n and wavenumber η_m the dynamic stiffness matrix is formed and assembled and the unknown variable is solved for its FWD amplitude $\tilde{\boldsymbol{u}}_{n,m}$ as

$$\tilde{\boldsymbol{K}}_{n,m}\tilde{\boldsymbol{u}}_{n,m} = \tilde{\boldsymbol{f}}_{n,m}, \tag{5.7}$$

where $\tilde{\boldsymbol{f}}_{n,m}$ is the FWD amplitude of applied load. First $\tilde{\boldsymbol{u}}_{n,m} = \tilde{\boldsymbol{u}}(x, \eta_m, \omega_n)$, and $\hat{\boldsymbol{u}}(x, y, \omega_n)$ is recovered by the FS and $\boldsymbol{u}(x, y, t)$ is recovered by the IFFT algorithm.

To obtain the exact solution of the ODE in frequency domain (for 1D analysis) or FWD (for 2D analysis), it is assumed that the solution of $\hat{\boldsymbol{u}}(x, \omega_n)$ or $\tilde{\boldsymbol{u}}(x, \eta_m, \omega_n)$ is in the form $u_\circ e^{-jkx}$, where $\boldsymbol{u}_\circ$ is an unknown constant and k is the unknown wavenumber in the direction of propagation, say x. This assumption is valid for a constant coefficient ODE only. However, the above assumption may sometimes yield good approximate solutions even for variable coefficient equations, if we formulate SFE through a Ritz approach. Substitution of the solution in the reduced ODE results in a single homogeneous linear algebraic equation for $\boldsymbol{u}_\circ$ (in the case of a single ODE) or a system of linear homogeneous algebraic equations for $\boldsymbol{u}_\circ$ (for a system of ODEs) as

$$\boldsymbol{W}(k, \omega_n, \eta_m)\boldsymbol{u}_\circ = 0, \quad \boldsymbol{W} \in \boldsymbol{C}^{N_v \times N_v}, \boldsymbol{u}_\circ \in \boldsymbol{C}^{N_v \times 1}. \tag{5.8}$$

In this equation, $\boldsymbol{W}$ is called the wave matrix, which is of the order $N_v \times N_v$, where N_v is the number of independent variables. For a non-trivial solution of $\boldsymbol{u}_\circ$, the wave matrix must be singular, i.e., its determinant must be zero. This condition generates the required equation for the solution of the wavenumber k, which will be a polynomial in k, called the spectrum relation. Wavenumbers essentially determine the type of wave, i.e., dispersive or non-dispersive. The form of wave matrix for different waveguides is described in Chap. 2.

If there are N_k roots of the characteristic equation then the complete solution is

$$\tilde{\boldsymbol{u}}(x, \eta_m, \omega_n) = \sum_{i=1}^{N_k} \boldsymbol{u}_{\circ,i}(\eta_m, \omega_n) \exp(-jk_i x) \tag{5.9}$$

where k_i is the ith wavenumber and $\boldsymbol{u}_{\circ,i}$ is the ith coefficient vector, called the wave amplitude vector. Thus at the heart of the SFE formulation is the computation of wavenumber k and wave vectors $\boldsymbol{u}_{\circ,i}$, which determines the efficiency of the SFEM. This is done by posing the problem as Polynomial Eigenvalue Problem (PEP), the details of which were explained in Sect. 2.8. In this book, we call the spectral element formulated through FFT as FSFEM.

5.1.2 General Formulation Procedure: Wavelet Transform Based SFEM

Formulating SFEM under Wavelet transform (WT) is slightly different. Unlike Fourier transforms, there are a number of different wavelets to represent the given

field variable. For solution of wave equation in general, the most desirable wavelet is the *Daubechies* wavelet [8]. It is compactly supported and allows multi-resolution analysis. We call the element formulated using WT as WSFEM.

In WSFEM formulation, the dependent variable $u(x,t)$ can be approximated by scaling function $\varphi(\tau)$ at an arbitrary scale as

$$u(x,\tau) = \sum_k u_k(x)\varphi(\tau - k), \quad k \in \boldsymbol{Z} \tag{5.10}$$

where, $u_k(x)$ are the approximation coefficients at a certain spatial location x. The first task involves the reduction of the governing differential equation to a form that is amenable for solution. Hence, Eq. 5.10 is first substituted in a governing differential equation $L(u) - q = 0$ and multiplied by the scaling function throughout. Using the orthogonality of the scaling functions, we can simplify certain terms in the governing equations. The resulting equation is ready to be solved in the transformed domain. However, unlike the FFT based method, the wavelet coefficients are highly coupled. Using the relationship between the first and the second derivatives of the wavelet coefficients, one can setup an eigenvalue problem that uncouples the governing differential equations. Although performing eigen analysis is time consuming, this can be computed and stored only once as it is not related to the particular problem. Next, an extrapolation technique proposed by Amaratunga and Williams [1, 2, 28] is used for adapting wavelet in a finite domain and imposing the initial values. The latter approach is expected to remove the problems associated with wrap around due to the assumed periodicity of solutions in FSFEM and thus may result in smaller time window for a same problem. The procedure of formulation of WSFEM is very similar to FSFEM explained in the last subsection and hence not repeated here. The method of reducing the governing differential equation and the uncoupling of wavelet coefficients for a non-dispersive rod was discussed in Sect. 3.2.3.

The steps followed in 2D WSFEM formulation are quite similar to those for 2D FSFEM. First Daubechies scaling functions are used for approximation in time and this reduces the governing partial differential equation to a set of coupled PDEs in the spatial variables. Wavelet extrapolation technique [28] is used for adapting wavelet to finite domains and imposing the initial conditions. The coupled transformed PDEs are decoupled through an eigen analysis. Next, each of these decoupled PDEs are further reduced to a set of coupled ODEs by using the same Daubechies scaling functions for approximation of the spatial dimension. Unlike the temporal approximation, here, the scaling function coefficients lying outside the finite domain are not extrapolated but obtained through periodic extension for free lateral edges. The other boundary conditions, such as fixed-fixed, free-fixed etc, are imposed through a restrain matrix [6]. Each set of ODEs is also coupled, but here, decoupling can only be done for unrestrained boundary condition i.e. free–free boundary condition.

In the next few sections we will outline the formulation of spectral elements for a few 1D and 2D waveguides under both Fourier and Wavelet transform environment.

5.2 Spectral Elements for Rods and Beams

5.2.1 Non-dispersive Isotropic Rod: FFT Based Spectral Element Formulation

The rod element of length L model has two degrees of freedom $\hat{u}_1$ and $\hat{u_2}$ which define the axial displacement of two nodes at $x = 0$ and $x = L$. The corresponding forces at these two nodes are the $\hat{F}_1$ and $\hat{F}_2$, respectively.

The spectral element formulation requires the strong form of the governing differential equation. The homogeneous form of the governing equation for an isotropic homogeneous rod of density ρ and Young's modulus E is

$$\frac{\partial^2 u}{\partial t^2} = c^2 \frac{\partial^2 u}{\partial x^2} \tag{5.11}$$

where $u = u(x, t)$ is the axial displacement and $c^2 = E/\rho$ is the square of the wave speed in the material. The governing equation is supplemented by the force (natural) boundary condition

$$F(x, t) = AE \frac{\partial u}{\partial x} \tag{5.12}$$

where A is the cross-sectional area of the rod and $F(x, t)$ is the axial force. The displacement (essential) boundary condition is the specification of the displacement u at the boundaries. It should be noted that only homogeneous initial conditions can be tackled with the present method.

Assuming a solution of the form

$$u(x, t) = \sum_{n=1}^{N} \hat{u}(x, \omega_n) e^{-j\omega_n t} \tag{5.13}$$

allows replacing the time dependency with the parameter ω_n. The summation is carried out up to the Nyquist frequency ω_N. Substituting Eq. 5.13 in Eq. 5.11, the reduced governing ordinary differential equation becomes

$$c^2 \frac{d^2 \hat{u}}{dx^2} + \omega_n^2 \hat{u} = 0 \tag{5.14}$$

whose solution is of the form $u_\circ e^{-jkx}$. Upon substitution in Eq. 5.14, the discretized form of the governing equation becomes

$$(-c^2 k^2 + \omega_n^2) u_\circ = 0 \tag{5.15}$$

which is the PEP (see Sect. 2.8) for this model. As the equation suggests, in this case the number of modes is $N_v = 1$ while $p = 1$. The wavenumber can be computed trivially in this case as $k_n = \pm\omega_n/c$ and for both modes, wave amplitude can be taken as 1. Thus, the complete solution is

$$\hat{u}(x,\omega_n) = c_1 e^{-jk_n x} + c_2 e^{-jk_n(L-x)} \tag{5.16}$$

where c_1 and c_2 are coefficients to be determined, with L being the length of the element. These coefficients are dependent on the displacement and/or force boundary conditions. Specifically, they can be expressed in terms of the nodal displacements $\hat{u}_1 = \hat{u}(x_1,\omega_n)$ and $\hat{u}_2 = \hat{u}(x_2,\omega_n)$ as

$$\begin{Bmatrix} \hat{u}_1 \\ u \end{Bmatrix} = \begin{bmatrix} e^{-jk_n x_1} & -e^{+jk_n x_1} \\ -e^{-jk_n x_1} & e^{+jk_n x_1} \end{bmatrix} \begin{Bmatrix} c_1 \\ c_2 \end{Bmatrix} = [T_1] \begin{Bmatrix} c_1 \\ c_2 \end{Bmatrix}, \tag{5.17}$$

where the matrix involved is represented as $\boldsymbol{T}_1$.

Similarly, the force in the frequency domain, $\hat{F}(x,\omega_n)$ can be evaluated at x_1 and x_2 to relate the nodal forces to the unknown coefficients

$$\begin{Bmatrix} \hat{F}_1 \\ \hat{F}_2 \end{Bmatrix} = AE(jk_n) \begin{bmatrix} e^{-jk_n x_1} & -e^{+jk_n x_1} \\ -e^{-jk_n x_1} & e^{+jk_n x_1} \end{bmatrix} \begin{Bmatrix} c_1 \\ c_2 \end{Bmatrix} = [T_2] \begin{Bmatrix} c_1 \\ c_2 \end{Bmatrix}, \tag{5.18}$$

where the matrix involved is represented as $\boldsymbol{T}_2$. Thus, the nodal forces are related to the nodal displacements by

$$\begin{Bmatrix} \hat{F}_1 \\ \hat{F}_2 \end{Bmatrix} = \boldsymbol{T}_2 \boldsymbol{T}_1{}^{-1} \begin{Bmatrix} \hat{u}_1 \\ \hat{u}_2 \end{Bmatrix}, \tag{5.19}$$

Hence, the dynamic stiffness matrix (DSM) for the rod at frequency ω_n is

$$\boldsymbol{D}_{\text{SFEM}} = \boldsymbol{T}_2 \boldsymbol{T}_1{}^{-1}$$

In comparison, the DSM for conventional FEM will be $\boldsymbol{D}_{\text{FEM}} = \boldsymbol{K} - \omega_n{}^2 \boldsymbol{M}$, where $\boldsymbol{K}$ and $\boldsymbol{M}$ are the stiffness and mass matrices, respectively. If these two DSMs are compared, it is found that in the limit of infinitely many finite elements $\boldsymbol{D}_{\text{FEM}} \rightarrow \boldsymbol{D}_{\text{SFEM}}$ [9].

FFT based SFEM requires the formulation of one-noded infinite segment called the *throw-off* element for good time resolution. This is obtained by removing the reflected coefficients from the solution given in Eq. 5.16. Hence, the solution to the throw-off elements become

$$\hat{u}(x,\omega_n) = c_1 e^{-jk_n x} \tag{5.20}$$

Following the same procedure followed for two noded elements, we consider the force expression given in Eq. 5.12 and using $\hat{F}_1 = -\hat{F}(x_1,\omega_n)$, we obtain the following dynamic stiffness for the throw-off elements

$$\hat{F}_1 = EAjk_n \hat{u}_1 \tag{5.21}$$

Note that the throw-off stiffness (in the brackets) is complex and it is this factor that adds damping to the structure resulting in good time resolution. Such a stiffness formulation is not possible in conventional FEM.

5.2.2 Non-dispersive Isotropic Rod: Wavelet Transform Based Spectral Element Formulation

As in the case of FSFEM, we begin with the governing differential equation (Eq. 5.11). After substituting the wavelet transform given by Eq. 3.53, the equation needs further reduction. That is, after applying the initial conditions, the coefficients are uncoupled according to the procedure given in Sect. 3.2.3.

The set of uncoupled equation in the transformed wavelet domain is given by (refer to Sect. 3.2.3 for more details)

$$\frac{d^2\widehat{u}_j}{dx^2} = \left(\frac{\rho A}{EA}\gamma_j^2\right)\widehat{u}_j \quad j = 0, 1, \ldots, n-1 \tag{5.22}$$

where, γ_j^2 is the element of the diagonal matrix Π^2 containing the eigenvalues of Eq. 3.85. However, if the boundary conditions are periodic, γ_j in Eq. 5.22 should be replace by λ_j, which are the eigenvalues obtained using Λ^2 matrix given in Eq. 3.81.

The solution of Eq. 5.22 is the same as that obtained through FSFEM (Eq. 5.16). However, the wavenumber in this case is given by $k_n = \gamma_n\sqrt{\rho/E}$. Note that the real part of γ_n is not accurate for the entire frequency spectrum and it is valid only up to certain fraction of Nyquist frequency, which is a function of the order of the wavelet basis function N. These aspects were discussed in Sect. 3.2.3. From this point on, the procedure to formulate the WSFEM is very similar to the FSFEM and hence not repeated here.

5.2.3 Dispersive Isotropic Timoshenko Beams-FFT Based Spectral Element Formulation

In this section, we will only outline the FFT based spectral FEM formulation. As seen from the last subsection, the formulation of WSFEM is exactly same as that of FSFEM once the transformed governing equation is reduced and all the wavelet coefficients are uncoupled. The procedure to reduce the transformed equation is similar for all waveguides of known governing equation, and follows the steps outlined in Sect. 3.2.3. Hence, for the Timoshenko beam and for other waveguides to follow in this chapter, only the FSFEM formulation is discussed.

The FSFEM formulation begins with the strong form of the differential equation. According to the first-order shear deformation (Timoshenko beam) theory, the governing equations are

$$\begin{aligned} GAK\frac{\partial}{\partial x}\left[\frac{\partial w}{\partial x} - \phi\right] &= \rho A\ddot{w}, \\ EI\frac{\partial^2\phi}{\partial x^2} + GAK\left[\frac{\partial w}{\partial x} - \phi\right] &= \rho I\ddot{\phi} \end{aligned} \tag{5.23}$$

where $w(x,t)$ and $\phi(x,t)$ are the transverse displacement and rotation of the mid-plane of the beam, G is the shear modulus, I and A are the moment of inertia and area of the cross-section, and K is the shape factor, which is introduced to compensate for the approximation in the shear stress distribution. These equations are supplemented by the expressions for the stress resultants which are

$$V = GAK\left[\frac{\partial w}{\partial x} - \phi\right] \quad \text{and} \quad M = EI\frac{\partial \phi}{\partial x} \tag{5.24}$$

where V is the shear force and M is the bending moment.

Assuming a solution of the form

$$w(x,t) = w_\circ e^{j(kx-\omega_n t)}, \quad \phi = \phi_\circ e^{j(kx-\omega_n t)} \tag{5.25}$$

and substituting in Eq. 5.23, gives the following PEP becomes

$$\left\{k^2\begin{bmatrix} GAK & 0 \\ 0 & EI \end{bmatrix} + k\begin{bmatrix} 0 & -jGAK \\ jGAK & 0 \end{bmatrix} + \begin{bmatrix} -\rho A{\omega_n}^2 & 0 \\ 0 & GAK - \rho I{\omega_n}^2 \end{bmatrix}\right\}\begin{Bmatrix} w_\circ \\ \phi_\circ \end{Bmatrix} = 0 \tag{5.26}$$

where the unknowns are $k, w_\circ$ and $\phi_\circ$. Thus, in this case, the order of the matrix polynomial p is 2 and $N_v = 2$. Thus, there are four eigenvalues (k) and eigenvectors $(\{w_\circ\ \phi_\circ\})$. The determinant of the matrix polynomial suggests that the roots are complex conjugate. After solving the eigenvalue problem, the eigenvectors are arranged in a matrix $\boldsymbol{R}$, so that

$$\left\{{k_p}^2\boldsymbol{A}_2 + k_p\boldsymbol{A}_1 + \boldsymbol{A}_\circ\right\}\begin{Bmatrix} R_{1p} \\ R_{2p} \end{Bmatrix} = 0. \tag{5.27}$$

The complete solution at frequency ω_n is now written as

$$\begin{Bmatrix} \hat{w}(x,\omega_n) \\ \hat{\phi}(x,\omega_n) \end{Bmatrix} = \sum_{m=1}^{4} C_m \begin{Bmatrix} R_{1m} \\ R_{2m} \end{Bmatrix} e^{-jk_m x} \tag{5.28}$$

where C_m are the unknown coefficients to be determined from the boundary conditions. Evaluating Eq. 5.28 at the nodes, $x = x_1$ and $x = x_2$, the $\boldsymbol{T}_1$ matrix is formed as

$$\boldsymbol{T}_1 = \begin{bmatrix} R_{11}e^{-jk_1x_1} & R_{12}e^{-jk_2x_1} & R_{13}e^{-jk_3x_1} & R_{14}e^{-jk_4x_1} \\ R_{21}e^{-jk_1x_1} & R_{22}e^{-jk_2x_1} & R_{23}e^{-jk_3x_1} & R_{24}e^{-jk_4x_1} \\ R_{11}e^{-jk_1x_2} & R_{12}e^{-jk_2x_2} & R_{13}e^{-jk_3x_2} & R_{14}e^{-jk_4x_2} \\ R_{21}e^{-jk_1x_2} & R_{22}e^{-jk_2x_2} & R_{23}e^{-jk_3x_2} & R_{24}e^{-jk_4x_2} \end{bmatrix}. \tag{5.29}$$

Similarly, the forces and moments are evaluated at the nodes as

$$\hat{V}_1 = -V(x_1), \hat{V}_2 = +V(x_2), \hat{M}_1 = -M(x_1), \hat{M}_2 = +M(x_2), \tag{5.30}$$

which can be expressed in terms of C_m by the $\boldsymbol{T}_2$ matrix where

$$\begin{aligned} T_2(1,m) &= -GA(-jk_mR(1,m) - R(2,m)) \\ T_2(2,m) &= -EI(-jk_m)R(2,m) \\ T_2(3,m) &= +GA(-jk_mR(1,m) - R(2,m)) \\ T_2(4,m) &= +EI(-jk_m)R(2,m). \end{aligned} \tag{5.31}$$

Once these two matrices are obtained, $\boldsymbol{D}_{\text{SFEM}}$, the dynamic stiffness matrix for the Timoshenko beam is formed as $\boldsymbol{T}_2\boldsymbol{T}_1{}^{-1}$.

5.2.4 Composite Beams-FFT Based Spectral Element Formulation

The basic theory of composites was introduced in Chap. 2 (Sect. 2.4). The behavior of laminated composite beam is dictated by its ply stacking sequence. A general ply stacking results in bending and axial motion coupling, which is not the case in the isotropic structures. This coupled motion results in both inertial as well as the stiffness coupling. Hence, the formulated element will have three degrees of freedom at each node, namely the axial degree of freedom $u(x,t)$, the transverse degree of freedom $w(x,t)$ and the beam rotation $\phi(x,t)$. The stress resultants and their corresponding degrees of freedom are shown in Fig. 5.1 FSFEM formulation begins with the solutions to strong form of the governing equations in the transformed frequency domain. The Governing PDE for an elementary composite beam was derived in Sect. 2.7.1. They are given by Eqs. 2.123–2.124. The associated force conditions are given by Eq. 2.125–2.127. Next, need to perform spectral analysis to obtain the wavenumbers. The wavenumbers were obtained and wave behavior were thoroughly discussed in Sect. 2.8.2. These wavenumbers will be required for the spectral element formulation. The solutions to the strong form the governing equation in the transformed frequency domain is given by

$$\left\{ \begin{matrix} \hat{u}(x,\omega_n) \\ \hat{w}(x,\omega_n) \end{matrix} \right\} = \sum_{m=1}^{6} C_m \left\{ \begin{matrix} R_{1m} \\ R_{2m} \end{matrix} \right\} e^{-jk_m x}. \tag{5.32}$$

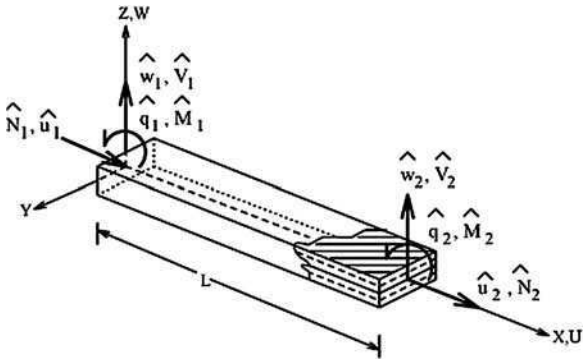

Fig. 5.1 Coordinate system and degrees of freedom for the spectral element

As mentioned earlier, two cases arise in the dynamics of connected beams, namely the finite length element and throw-off elements, respectively. The behavior of these are fundamentally different and hence will be treated separately.

5.2.4.1 Finite Length Element

A 2-node finite element of length L with nodal displacements and forces as shown in Fig. 5.1 is considered. Using the explicit expression for displacement field given by Eq. 5.32, the element nodal displacement vector $\hat{\boldsymbol{u}}^{\mathrm{e}}$ with entries $\hat{u}_1 = \hat{u}(0,\omega_n)$, $\hat{w}_1 = \hat{w}(0,\omega_n)$, $\hat{\theta}_1 = \hat{w}_{,x}(0,\omega_n)$, $\hat{u}_2 = \hat{u}(L,\omega_n)$, $\hat{w}_2 = \hat{w}(L,\omega_n)$ and $\hat{\theta}_2 = \hat{w}_{,x}(L,\omega_n)$ is expressed in terms of the wave coefficient vector $\tilde{\boldsymbol{u}}$ with entries $\tilde{u}_j$, $\tilde{w}_j$ as

$$\hat{\boldsymbol{u}}^{\mathrm{e}} = \hat{\boldsymbol{T}}_1 \tilde{\boldsymbol{u}}, \tag{5.33}$$

where $\hat{\boldsymbol{u}}^{\mathrm{e}} = \{\hat{u}_1\ \hat{w}_1\ \hat{\theta}_1\ \hat{u}_2\ \hat{w}_2\ \hat{\theta}_2\}^T$ and $\tilde{\boldsymbol{u}} = \{\tilde{u}_1\ \tilde{u}_2\ \tilde{w}_3\ \tilde{w}_4\ \tilde{w}_5\ \tilde{w}_6\}^T \cdot \hat{\boldsymbol{T}}_1$ is a 6×6 non-symmetric, non-singular matrix, which is a function of frequency, material properties and dimensions of the element. This matrix represents the local wave characteristic of the displacements.

Next, using the expressions for force boundary condition from Eqs. 2.125–2.127, the nodal forces are related to the wave coefficients $\tilde{u}_j$ and $\tilde{w}_j$ through the following force boundary equations:

$$\begin{array}{lll} \hat{N}_1 = -\hat{N}_x(0,\omega_n), & \hat{V}_1 = -\hat{V}_x(0,\omega_n), & \hat{M}_1 = -\hat{M}_x(0,\omega_n), \\ \hat{N}_1 = \hat{N}_x(L,\omega_n), & \hat{V}_1 = \hat{V}_x(L,\omega_n), & \hat{M}_1 = \hat{M}_x(L,\omega_n). \end{array} \tag{5.34}$$

In matrix notation, this can be written as

$$\hat{\boldsymbol{f}}^{\mathrm{e}} = \hat{\boldsymbol{T}}_2 \tilde{\boldsymbol{u}}, \tag{5.35}$$

where the element nodal force vector $\hat{\boldsymbol{f}} = \{\hat{N}_1\ \hat{V}_1\ \hat{M}_1\ \hat{N}_2\ \hat{V}_2\ \hat{M}_2\}^T$. The matrix $\hat{\boldsymbol{T}}_2$ has properties that are similar to $\hat{\boldsymbol{T}}_1$, and it represents the local wave characteristic of forces. Combining Eqs. 5.33 and 5.35, the equilibrium equation is obtained as

$$\hat{\boldsymbol{f}}^{\mathrm{e}} = \hat{\boldsymbol{T}}_2 \hat{\boldsymbol{T}}_1{}^{-1} \hat{\boldsymbol{u}}^{\mathrm{e}} = \hat{\boldsymbol{K}}^{\mathrm{e}} \hat{\boldsymbol{u}}^{\mathrm{e}}, \tag{5.36}$$

where $\hat{\boldsymbol{K}}^{\mathrm{e}}$ is the symmetric dynamic stiffness matrix for an unsymmetric composite beam element as a complex function of frequency.

5.2.4.2 Throw-Off Element

As mentioned in Sect. 5.2.1, throw-off elements are essentially used in FSFEM formulation to obtain good resolution of response in time domain. In other words, these elements are used to eliminate signal wraparound by artificially introducing damping, while analyzing short waveguide structures. This was explained in Chap. 3 (Sect. 3.2.1).

Throw-off elements simulates a condition wherein the boundaries are at such a distance that the effect of reflected waves becomes negligible due to attenuation throughout their long traversal, and do not reach the location under consideration within the time of observation. In other words, a throw-off element is a non-resonant single node element that acts as a conduit to allow the propagation of trapped energy out of the system. Considering only the incident part of the displacement field given by Eq. 5.32, the field variables for the throw-off element can be written as

$$\left\{ \begin{array}{c} \hat{u}(x,\omega_n) \\ \hat{w}(x,\omega_n) \end{array} \right\} = \begin{bmatrix} R_{11} & R_{13} & R_{15} \\ R_{21} & R_{23} & R_{25} \end{bmatrix} \left\{ \begin{array}{c} \tilde{u}_1 e^{-ik_1 x} \\ \tilde{w}_3 e^{-ik_2 x} \\ \tilde{w}_5 e^{-ik_3 x} \end{array} \right\}. \tag{5.37}$$

Using the same procedure as followed in the case of finite length element formulation in the previous subsection, a 3×3 symmetric dynamic stiffness matrix $\hat{\boldsymbol{K}}^{\mathrm{e}}$ as a complex function of frequency can be derived. An important property of the dynamic stiffness matrix is that the elements are always complex.

5.2.5 *Higher Order Composite Beam-FFT Based Spectral Element Formulation*

The spectral and dispersion relations for a higher order composite beam, which are very essential for the spectral formulation was discussed in Sect. 2.8.3. The governing equations were derived in Sect. 2.7.2. We see that the higher order assumption introduces additional degrees of freedom in the form of lateral contraction $\psi(x,t)$ (see Fig. 2.12), in addition to the axial, transverse and rotational degrees of freedom. As before, we will derive two sets of spectral element, one is a two-noded finite length element and the other is a one-noded semi infinite throw-off element.

5.2.5.1 Finite Length Element

The displacement field for the two-noded finite element is the result of four forward moving and four backward moving wave components. Hence, the displacement field contains eight wave coefficients, which need to be determined from eight boundary conditions imposed at the two nodes. The displacement at any point $x\,(x \in [0,L])$ and at frequency ω_n is

$$\tilde{\mathbf{u}}_n = \left\{ \begin{array}{c} \hat{u}(x,\omega_n) \\ \hat{\psi}(x,\omega_n) \\ \hat{w}(x,\omega_n) \\ \hat{\phi}(x,\omega_n) \end{array} \right\} = \begin{bmatrix} R_{11} & \dots & R_{18} \\ R_{21} & \dots & R_{28} \\ R_{31} & \dots & R_{38} \\ R_{41} & \dots & R_{48} \end{bmatrix} \begin{bmatrix} e^{-jk_1 x} & 0 & \dots & 0 \\ 0 & e^{-jk_2 x} & \dots & 0 \\ \vdots & \ddots & \ddots & \vdots \\ 0 & \dots & \dots & e^{-jk_8 x} \end{bmatrix} \mathbf{a}_n \tag{5.38}$$

with $k_{p+4} = -k_p, p = 1, \dots, 4$.

The above equation in concise form can be written

$$\{\tilde{\mathbf{u}}\}_n = \boldsymbol{R}_n \boldsymbol{D}_n(x) \boldsymbol{a}_n \tag{5.39}$$

where $\boldsymbol{D}_n(x)$ is a diagonal matrix of size 8×8 whose ith element is $e^{-jk_i x}$, and $\boldsymbol{R}_n$ is the amplitude ratio matrix and is of size 4×8. This matrix needs to be known beforehand for the element formulation. There are several ways to compute the elements of this matrix. In this formulation the SVD method, explained in Chap. 2 Sect. 2.8.1.1, is followed, which is suitable for structural models with a large number of degrees of freedom.

Here, $\boldsymbol{a}_n$ is a vector of eight unknown constants to be determined. These unknown constants are expressed in terms of the nodal displacements by evaluating Eq. 5.38 at the two nodes, i.e., at $x = 0$ and $x = L$. In doing so, we get

$$\hat{\mathbf{u}}_n = \begin{Bmatrix} \tilde{\mathbf{u}}_1 \\ \tilde{\mathbf{u}}_2 \end{Bmatrix}_n = \begin{bmatrix} R \\ R \end{bmatrix}_n \begin{bmatrix} D(0) \\ D(L) \end{bmatrix}_n \boldsymbol{a}_n = \boldsymbol{T}_{1_n} \boldsymbol{a}_n \tag{5.40}$$

where $\tilde{\mathbf{u}}_1$ and $\tilde{\mathbf{u}}_2$ are the nodal displacements of node 1 and node 2, respectively.

Using the force boundary conditions Eqs. 2.135 and 2.136, the force vector $\{\mathbf{f}\}_n = \{N_x,\ Q_x,\ V_x,\ M_x\}_n$ can be written in terms of the unknown constants $\boldsymbol{a}_n$ as $\{\mathbf{f}\}_n = \boldsymbol{P}_n \boldsymbol{a}_n$. When the force vector is evaluated at node 1 and node 2, nodal force vector, $\{\hat{\mathbf{f}}\}_n$, is obtained and can be related to $\boldsymbol{a}_n$ by

$$\{\hat{\mathbf{f}}\}_n = \begin{Bmatrix} \tilde{\mathbf{f}}_1 \\ \tilde{\mathbf{f}}_2 \end{Bmatrix}_n = \begin{bmatrix} P(0) \\ P(L) \end{bmatrix}_n \boldsymbol{a}_n = \boldsymbol{T}_{2_n} \boldsymbol{a}_n \tag{5.41}$$

Equations 5.40 and 5.41 together yield the relation between the nodal force and the nodal displacement vector at frequency ω_n:

$$\{\hat{\mathbf{f}}\}_n = \boldsymbol{T}_{2_n} \boldsymbol{T}_{1_n}^{-1} \{\hat{\mathbf{u}}\}_n = \boldsymbol{K}_n \{\hat{\mathbf{u}}\}_n \tag{5.42}$$

where $\boldsymbol{K}_n$ is the dynamic stiffness matrix at frequency ω_n of dimension 8×8. Explicit forms of the matrix $\boldsymbol{T}_1$ and $\boldsymbol{T}_2$ are given below.

$$T_1(1:4, 1:8) = R(1:4, 1:8) \tag{5.43}$$

$$T_1(l, m) = R(l-4, m) e^{-jk_m L}, \quad l = 5\ldots8, m = 1, \ldots, 8. \tag{5.44}$$

Similarly,

$$\begin{aligned}
T_2(1, i) &= j(A_{11} R(1, i) - B_{11} R(4, i)) k_i - A_{13} R(2, i) \\
T_2(2, i) &= -B_{55}(-jR(3, i) k_i - R(4, i)) + jk_d D_{55} R(2, i) k_i \\
T_2(3, i) &= -A_{55}(-jR(3, i) k_i - R(4, i)) + jB_{55} R(2, i) k_i \\
T_2(4, i) &= -j(B_{11} R(1, i) - D_{11} R(4, i)) k_i + B_{13} R(2, i) \\
T_2(5:8, i) &= -T_2(1:4, i) e^{-jk_i L}, \quad i = 1, \ldots, 8.
\end{aligned} \tag{5.45}$$

5.2.5.2 Throw-Off Element

For the infinite length element, only the forward propagating modes are considered. The displacement field (at frequency ω_n) becomes

$$\tilde{\mathbf{u}}_n = \sum_{m=1}^{4} R_n^m e^{-jk_{m_n}x} a_m^n = \boldsymbol{R}_n \boldsymbol{D}_n(x) \boldsymbol{a}_n, \tag{5.46}$$

where $\boldsymbol{R}_n$ and $\boldsymbol{D}_n(x)$ is now of size 4×4. The $\boldsymbol{a_n}$ is a vector of four unknown constants. Evaluating the above expression at node 1 $(x = 0)$, the nodal displacements are related to these constants through the matrix $\boldsymbol{T}_1$ as

$$\hat{\mathbf{u}}_n = \{\tilde{\mathbf{u}}_1\}_n = \boldsymbol{R}_n \boldsymbol{D}_n(0) \boldsymbol{a}_n = \boldsymbol{T}_{1_n} \boldsymbol{a}_n \tag{5.47}$$

where $\boldsymbol{T}_1$ is now a matrix of dimension 4×4. Similarly, the nodal forces at node 1 can be related to the unknown constants

$$\{\hat{\mathbf{f}}\}_n = \{\tilde{\mathbf{f}}_1\}_n = \boldsymbol{P}_n(0) \boldsymbol{a}_n = \boldsymbol{T}_{2_n} \boldsymbol{a}_n \tag{5.48}$$

Using Eqs. 5.47 and 5.48, the nodal forces at node 1 are related to the corresponding nodal displacements at node 1

$$\{\hat{\mathbf{f}}\}_n = \boldsymbol{T}_{2_n} \boldsymbol{T}_{1_n}^{-1} \{\hat{\mathbf{u}}\}_n = \boldsymbol{K}_n \{\hat{\mathbf{u}}\}_n \tag{5.49}$$

where $\boldsymbol{K}_n$ is the element dynamic stiffness matrix of dimension 4×4 at frequency ω_n. The submatrices $T_1(1:4, 1:4)$ and $T_2(1:4, i)$ are the same as for the finite length element $i = 1 \ldots 4$, and as in the elementary case, the dynamic stiffness is complex.

5.3 Spectral Elements for 2D Composite Layers-FFT Based Spectral Element Formulation

In the previous section, the SFE formulation for 1D waveguides was outlined in detail. In this section, we present the formulation of SFE formulation for 2D waveguides. As mentioned in Chap. 2, 2D SFE formulation requires a second transform in one of the spatial directions in order to transform the governing PDE to a set of ODE's. In this process, an additional parameter called "*horizontal wavenumber*" is introduced in the formulation, which is coupled to the propagating wavenumber. These aspects were explained in the context of 2D plates in Sect. 2.8.4.

The Partial Wave Technique (PWT) is a suitable option [4] for the formulation of SFEM for layered media which includes anisotropic and inhomogeneous materials. The SVD method described in Sect. 2.8.1.1 is specifically utilized to obtain the wave amplitudes, which are essential for constructing the partial waves.

In the PWT method, once the partial waves are found, the wave coefficients are made to satisfy the prescribed boundary conditions, i.e., two non-zero tractions specified at the top and bottom of each layer. In our case, the formulation is slightly different, as no specific problem oriented boundary conditions are imposed. Thus a system matrix is established, which relates the tractions at the interfaces to the interfacial displacements. This generalization enables the use of the system matrix as a finite element dynamic stiffness matrix, although formulated in the frequency/wavenumber domain. These matrices can be assembled to model different layers of different ply-orientation, which obviates to the necessity of cumbersome computations associated with multilayer analysis (e.g., see [20]). The only shortcoming of the method is that each spectral layer element can accommodate only one fiber angle, thus for different ply-stacking sequences the number of elements will be at least equal to the number of different ply-angles in the stacking.

One advantage of the present formulation is the ease in capturing Lamb wave [27] propagation in anisotropic plates. By definition, Lamb waves are guided waves propagating in a domain bounded by two parallel, traction-free surfaces. The importance of Lamb waves in structural inspection lies in their ability to propagate long distances which enables the inspection of large areas. Hence, these waves are very attractive for SHM.

Historically, the dispersion relation for anisotropic materials was given first by Solie and Auld [23], where PWT were used. However, the relation was obtained for a (001)-cut copper plate. Subsequent investigations on modeling aspects of Lamb waves were carried out by several researchers [16]. Finite element modeling of Lamb waves was performed by Verdict et al. [26]. On the basis of discrete layer theory and a multiple integral transform, an analytical–numerical approach was given by Veidt et al. [25]. A coupled FE-normal mode expansion method is given by Moulin et al. [15]. Similarly a boundary element normal mode expansion method is given by Zhao and Rose [29].

The present formulation by virtue of the frequency wavenumber domain representation of the solution is an inexpensive way of estimating Lamb wave modes as well as predicting time domain signals. The formulation is based on the assumption that there is no heat conduction in and out of the system, that displacements are small, the material is homogeneous and anisotropic and the domain is a 2D Euclidean space. The general elastodynamic equation of motion for 3D elastic medium is given by

$$\sigma_{ij,j} = \rho(x_1, x_2, x_3)\ddot{u}_i \tag{5.50}$$

which is applied in conjunction with the associated constitutive equations and strain–displacement relations:

$$\sigma_{ij} = C_{ijkl}(x_1, x_2, x_3)\varepsilon_{kl}, \quad \varepsilon_{ij} = (u_{i,j} + u_{j,i})/2 \tag{5.51}$$

where comma (,) and dot $\dot{()}$ denote partial differentiation with respect to the spatial variables and time, respectively.

For a 2D model with orthotropic material construction, the complexity of the above equation can be further reduced by the following assumptions. The non-zero displacements are $u_1 = u$ and $u_3 = w$ in the direction $x_1 = x$ and $x_3 = z$, respectively (see Fig. 5.2). The non-zero strains are related to these displacements by

$$\varepsilon_{xx} = u_x, \quad \varepsilon_{zz} = w_z, \quad \varepsilon_{xz} = u_z + w_x. \tag{5.52}$$

The non-zero stresses are then related to the strains by

$$\sigma_{xx} = Q_{11}\varepsilon_{xx} + Q_{13}\varepsilon_{zz}, \quad \sigma_{zz} = Q_{13}\varepsilon_{xx} + Q_{33}\varepsilon_{zz}, \quad \sigma_{xz} = Q_{55}\varepsilon_{xz}, \tag{5.53}$$

where Q_{ij} are the stiffness coefficients, which depend on the ply lay-up, its orientation and the z coordinate within the layer. Substituting Eq. 5.53 in Eq. 5.50 and imposing the assumptions above yields the following elastodynamic equation for 2D homogeneous orthotropic:

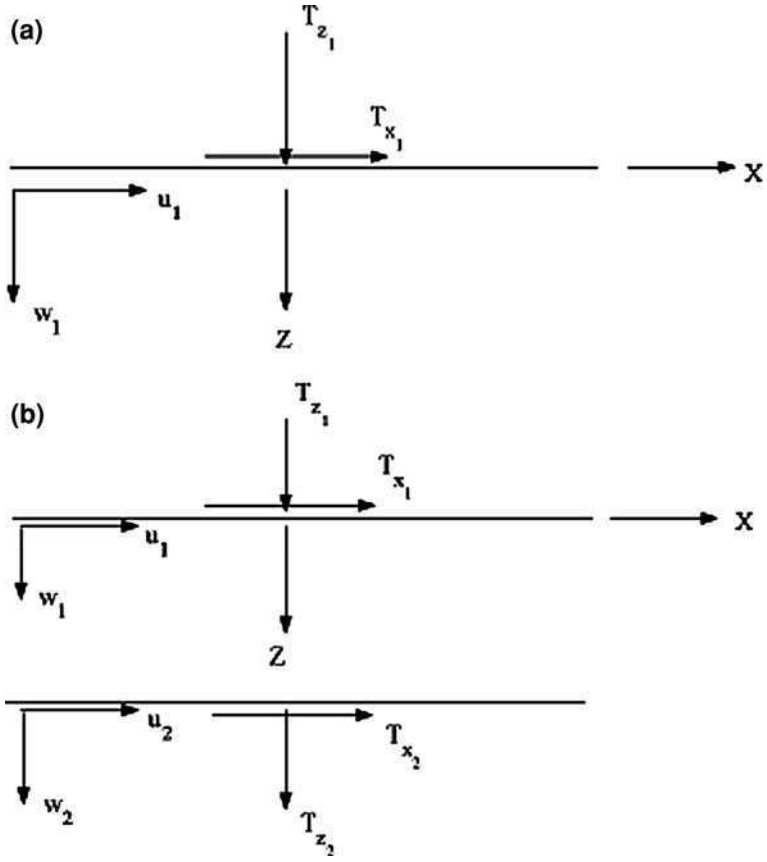

Fig. 5.2 Sign conventions of **a** throw-off spectral element **b** layer element

$$\begin{aligned} Q_{11}u_{xx} + (Q_{13} + Q_{55})w_{xz} + Q_{55}u_{zz} &= \rho\ddot{u}, \\ Q_{55}w_{xx} + (Q_{13} + Q_{55})u_{xz} + Q_{33}w_{zz} &= \rho\ddot{w}. \end{aligned} \tag{5.54}$$

Here, we attempt to reduce the governing PDEs to a set of ODEs. Two variables are replaced by two new parameters through the application of the Fourier transform in time and in space. With this assumption, the spectral form of the displacement field becomes

$$u(x,z,t) = \sum_{n=1}^{N-1}\sum_{m=1}^{M-1} \hat{u}(z,\eta_m,\omega_n)\begin{Bmatrix} \sin(\eta_m x) \\ \cos(\eta_m x) \end{Bmatrix} e^{-j\omega_n t} \tag{5.55}$$

$$w(x,z,t) = \sum_{n=1}^{N-1}\sum_{m=1}^{M-1} \hat{w}(z,\eta_m,\omega_n)\begin{Bmatrix} \cos(\eta_m x) \\ \sin(\eta_m x) \end{Bmatrix} e^{-j\omega_n t} \tag{5.56}$$

where ω_n is the discrete angular frequency and η_m is the discrete horizontal wavenumber. As the assumed field suggests, for $M \to \infty$, the model has infinite extent in the positive and negative x direction, although the domain is finite in the z direction, according the layered configuration considered. In particular, the domain can be written as $\Omega = [-\infty, +\infty] \times [0, L]$, where L is the thickness of the layer. The boundaries of any layer will be specified by a fixed value of z. The x dependency of the displacement field (sine or cosine) will be determined based upon the loading pattern. In all subsequent formulation and computation, a symmetric load pattern will be considered, i.e., $\sin(\eta_m x)$ for u and $\cos(\eta_m x)$ for w. The real computational domain is $\Omega_c = [-X_L/2, +X_L/2] \times [0, L]$, where x_L is the x window length. Discrete values of η_m depend upon x_L and the number of mode shapes (M) chosen.

This displacement field reduces the governing equations to a set of ODEs

$$\boldsymbol{A}\hat{\boldsymbol{u}}'' + \boldsymbol{B}\hat{\boldsymbol{u}}' + \boldsymbol{C}\hat{\boldsymbol{u}} = \boldsymbol{0} \tag{5.57}$$

where $\hat{\boldsymbol{u}} = \{\hat{u}\hat{w}\}$, and the prime denotes differentiation with respect to z. The matrices $\boldsymbol{A}$, $\boldsymbol{B}$ and $\boldsymbol{C}$ are

$$\boldsymbol{A} = \begin{bmatrix} Q_{55} & 0 \\ 0 & Q_{33} \end{bmatrix}, \quad \boldsymbol{B} = \begin{bmatrix} 0 & -(Q_{13} + Q_{55})\eta_m \\ (Q_{13} + Q_{55})\eta_m & 0 \end{bmatrix}, \tag{5.58}$$

$$\boldsymbol{C} = \begin{bmatrix} -\eta_m^2 Q_{11} + \rho\omega_n^2 & 0 \\ 0 & -\eta_m^2 Q_{55} + \rho\omega_n^2 \end{bmatrix}. \tag{5.59}$$

The associated boundary conditions specify the stresses σ_{zz} and σ_{xz} at the layer interfaces. From Eq. 5.53, the stresses are related to the unknowns by

$$\hat{\boldsymbol{s}} = \boldsymbol{D}\hat{\boldsymbol{u}}' + \boldsymbol{E}\hat{\boldsymbol{u}}, \tag{5.60}$$

where

$$\hat{\boldsymbol{s}} = \{\sigma_{zz}\ \sigma_{xz}\}$$
$$\boldsymbol{D} = \begin{bmatrix} 0 & Q_{33} \\ Q_{55} & 0 \end{bmatrix}$$
$$\boldsymbol{E} = \begin{bmatrix} \eta_m Q_{13} & 0 \\ 0 & -\eta_m Q_{55} \end{bmatrix}$$

The original boundary value problem reduces to finding $\hat{\boldsymbol{u}}$, which satisfies Eq. 5.57 for all $z \in \Omega_c$, and the specification of $\hat{\boldsymbol{u}}$ or $\hat{\boldsymbol{s}}$ at $z = 0$ or $z = L$. Once the solution is obtained for different values of z in the $z - \eta - \omega$ domain, for given values of ω_n and η_m, the summation over η_m will bring the solution back to the $z - x - \omega$ domain and the inverse FFT will bring the solution back to the $z - x - t$ domain.

The solutions to these ODEs are of the form $u_\circ e^{-jkz}$ and $w_\circ e^{-jkz}$, which yields the PEP

$$\begin{aligned} \boldsymbol{W}\boldsymbol{u}_\circ &= \boldsymbol{0} \\ \boldsymbol{W} &= -k^2\boldsymbol{A} - jk\boldsymbol{B} + \boldsymbol{C} \end{aligned} \tag{5.61}$$

where $\boldsymbol{u}_\circ = \{u_\circ w_\circ\}$ and $\boldsymbol{W}$ is the wave matrix given by

$$\boldsymbol{W} = \begin{bmatrix} -k^2 Q_{55} - \eta_m^2 Q_{11} + \rho\omega_n^2 & jk\eta_m(Q_{13} + Q_{55}) \\ -jk\eta_m(Q_{13} + Q_{55}) & -k^2 Q_{33} - \eta_m^2 Q_{55} + \rho\omega_n^2 \end{bmatrix}. \tag{5.62}$$

The singularity condition of $\boldsymbol{W}$ yields the following spectral equation

$$\begin{aligned} Q_{33}Q_{55}k^4 + \{(Q_{11}Q_{33} - 2Q_{13}Q_{55} - Q_{13}^2)\eta_m^2 - \rho\omega_n^2(Q_{33} + Q_{55})\}k^2 \\ + \{Q_{11}Q_{55}\eta_m^4 - \rho\omega_n^2\eta_m^2(Q_{11} + Q_{55}) + \rho^2\omega_n^4\} = 0. \end{aligned} \tag{5.63}$$

It is to be noted that for each value of η_m and ω_n, there are four values of k, denoted by k_{lmn} $(l = 1, \ldots, 4)$, which will be obtained by solving Eq. 5.63. The explicit wavenumber solution $k_{lnm} = \pm\sqrt{-b \pm \sqrt{b^2 - 4ac}}$, where a, b and c are the coefficients of k^4, k^2 and k^0, respectively, in Eq. 5.63.

There are certain properties of the wavenumbers which will be explored now. As can be seen from Eq. 5.63, for $\eta_m = 0$, the equation is readily solvable to give the roots $\pm\omega\sqrt{\rho/Q_{33}}$ and $\pm\omega\sqrt{\rho/Q_{55}}$. Since none of the ρ, Q_{33} or Q_{55} can be negative or zero, these roots are always real and linear with ω. When η_m is not zero, k becomes zero for ω satisfying

$$\begin{aligned} & Q_{11}Q_{55}\eta_m^4 - \rho\omega_n^2\eta_m^2(Q_{11} + Q_{55}) + \rho^2\omega_n^4 = 0 \\ \text{i.e.,} \quad & (Q_{11}\eta_m^2 - \rho\omega^2)(Q_{55}\eta_m^2 - \rho\omega^2) = 0 \\ \text{i.e.,} \quad & \omega = \eta_m\sqrt{Q_{11}/\rho}, \quad \eta_m\sqrt{Q_{55}/\rho} \end{aligned} \tag{5.64}$$

which identify the cut-off frequencies. For frequencies lower than the cut-off frequencies, the roots are imaginary which correspond to non-propagating waves,

while above these frequencies, the roots are real and define propagating waves. For isotropic materials the cut-off frequencies are given by $c_p\eta$ and $c_s\eta$ [19]. The current expressions for the cut-off frequencies are also reducible to that of isotropic materials if we identify Q_{11} and Q_{55} with $\lambda + 2\mu$ and μ, respectively, where λ and μ are the Lamé parameters. If we identify the QP wave with Q_{33} (or Q_{11}) and the QSV wave with Q_{55}, then as the cut-off frequencies suggest, for the same value of η_m, it is the QSV wave that becomes propagating first, since $Q_{11} > Q_{55}$.

Once, the required wavenumbers k are obtained, the solution $\boldsymbol{u}_\circ$ at frequency ω_n and wavenumber η_m is

$$u_{nm} = R_{11}C_1e^{-jk_1x} + R_{12}C_2e^{-jk_2x} + R_{13}C_3e^{-jk_3x} + R_{14}C_4e^{-jk_4x} \tag{5.65}$$

$$w_{nm} = R_{21}C_1e^{-jk_1x} + R_{22}C_2e^{-jk_2x} + R_{23}C_3e^{-jk_3x} + R_{24}C_4e^{-jk_4x} \tag{5.66}$$

where R_{ij} are the amplitude coefficients to be determined and are called wave amplitudes. As outlined in Chap. 2, following the method of SVD (Sect. 2.8.1.1), R_{ij} are obtained from the wave matrix $\boldsymbol{W}$ evaluated at wavenumber k_i.

Once the four wavenumbers and wave amplitudes are known, the four partial waves can be constructed and the displacement field can be written as a linear combination of the partial waves. Each partial wave is given by

$$\boldsymbol{a}_i = \begin{Bmatrix} u_i \\ w_i \end{Bmatrix} = \begin{Bmatrix} R_{1i} \\ R_{2i} \end{Bmatrix} e^{-jk_iz} \begin{Bmatrix} \sin(\eta_m x) \\ \cos(\eta_m x) \end{Bmatrix} e^{-j\omega_n t}, \quad i = 1\ldots4, \tag{5.67}$$

and the total solution is

$$\boldsymbol{u} = \sum_{i=1}^{4} C_i\boldsymbol{a}_i. \tag{5.68}$$

5.3.1 Finite Layer Element (FLE)

Once the solutions of u and w are obtained in the form of Eqs. 5.65 and 5.66 for each value of ω_n and η_m, the same procedure as outlined in the 1D element formulation is employed to obtain the element dynamic stiffness matrix as a function of ω_n and η_m. Thus, the nodal displacements are related to the unknown constants by

$$\{u_{1nm}\ v_{1nm}\ u_{2nm}\ v_{2nm}\}^T = \boldsymbol{T}_{1nm}\{c_1\ \ c_2\ \ c_3\ \ c_4\}^T, \tag{5.69}$$

i.e.,

$$\hat{\boldsymbol{u}}_{nm} = \boldsymbol{T}_{1nm}\boldsymbol{c}_{nm} \tag{5.70}$$

Using Eq. 5.53, nodal tractions are related to the constants by

$$\hat{\boldsymbol{t}}_{nm} = \boldsymbol{T}_{2nm}\boldsymbol{c}_{nm} \tag{5.71}$$

where $\hat{\boldsymbol{t}}_{nm} = \{\sigma_{zz1}, \sigma_{xz1}, \sigma_{zz2}, \sigma_{xz2}\}$.

Explicit forms of $\boldsymbol{T}_{2nm}$ and $\boldsymbol{T}_{1nm}$ are

$$\boldsymbol{T}_1 = \begin{bmatrix} R_{11} & R_{12} & R_{13} & R_{14} \\ R_{21} & R_{22} & R_{23} & R_{24} \\ R_{11}e^{(-jk_1L)} & R_{12}e^{(-jk_2L)} & R_{13}e^{(+jk_1L)} & R_{14}e^{(+jk_2L)} \\ R_{21}e^{(-jk_1L)} & R_{22}e^{(-jk_2L)} & R_{23}e^{(+jk_1L)} & R_{24}e^{(+jk_2L)} \end{bmatrix}, \tag{5.72}$$

$$\begin{aligned} T_2(1,p) &= -Q_{55}(-jR_{1p}k_p - \eta R_{2p}), \\ T_2(2,p) &= jQ_{33}R_{2p}k_p - Q_{13}\eta R_{1p}, \\ T_2(3,p) &= Q_{55}(-jR_{1p}k_p - \eta R_{2p})e^{(-jk_pL)} \\ T_2(4,p) &= \{-jQ_{33}R_{2p}k_p + Q_{13}\eta R_{1p}\}e^{(-jk_pL)}, \end{aligned}$$

where p ranges from 1 to 4.

Thus, the dynamic stiffness matrix becomes

$$\hat{\boldsymbol{K}}_{nm} = \boldsymbol{T}_{2nm}\boldsymbol{T}_{1nm}^{-1} \tag{5.73}$$

which is of size 4×4 having ω_n and η_m as parameters. This matrix represents the dynamics of an entire layer of any length L at frequency ω_n and horizontal wavenumber η_m. Consequently, this matrix acts as a substitute for the global stiffness matrix of FE modeling, whose size, depending upon the thickness of the layer, will be many orders larger.

5.3.2 Infinite Layer (Throw-Off) Element (ILE)

This is the 2D counter part of the 1D throw-off element. The element is formulated by considering only the forward moving components, which means no reflection will come back from the boundary. This element, as mentioned earlier, acts as a conduit to throw away energy from the system and is very effective in modeling the infinite domain in the z direction. This element is also used to impose absorbing boundary conditions or to introduce maximum damping in the structure. The element has only one edge where the displacements are to be measured and tractions are to be specified. The displacement field for this element (at ω_n and η_m) is

$$u_{nm} = R_{11}c_{1nm}e^{-jk_1z} + R_{12}c_{2nm}e^{-jk_2z}, \tag{5.74}$$

$$w_{nm} = R_{21}c_{1nm}e^{-jk_1z} + R_{22}c_{2nm}e^{-jk_2z}, \tag{5.75}$$

where it is assumed that k_1 and k_2 have positive real parts. Following the same procedure as before, displacement at node 1 can be related to the constants C_i, $i = 1, 2$ as

$$\hat{\boldsymbol{u}}_{nm} = \boldsymbol{T}_{1nm}\boldsymbol{c}_{nm} \tag{5.76}$$

Similarly, nodal tractions can be related to the constants $\boldsymbol{c}$ as

$$\hat{\boldsymbol{t}}_{nm} = \boldsymbol{T}_{2nm}\boldsymbol{c}_{nm} \tag{5.77}$$

Explicit forms of the matrix $\boldsymbol{T}_1$ and $\boldsymbol{T}_2$ are

$$\boldsymbol{T}_{1(\mathrm{ILE})} = \boldsymbol{T}_{1(\mathrm{FLE})}(1:2,1:2), \quad \boldsymbol{T}_{2(\mathrm{ILE})} = \boldsymbol{T}_{2(\mathrm{FLE})}(1:2,1:2). \tag{5.78}$$

The dynamic stiffness for the homogeneous infinite half space becomes

$$\hat{\boldsymbol{K}}_{nm} = \boldsymbol{T}_{2nm}\boldsymbol{T}_{1nm}^{-1}, \tag{5.79}$$

which is a 2×2 complex matrix.

5.3.3 Expressions for Stresses and Strains

From the displacement field (Eqs. 5.65 and 5.66), the strain–displacement and stress–strain relations, the matrix of strain nodal displacement relation and the stress nodal displacement relation can be established as

$$\begin{aligned} \boldsymbol{\varepsilon} &= \boldsymbol{B}\boldsymbol{T}_1^{-1}\hat{\boldsymbol{u}} \\ \boldsymbol{\sigma} &= \boldsymbol{Q}\boldsymbol{B}\boldsymbol{T}_1^{-1}\hat{\boldsymbol{u}} \end{aligned} \tag{5.80}$$

where $\boldsymbol{\varepsilon} = \{\varepsilon_{xx}, \varepsilon_{zz}, \varepsilon_{xz}\}, \boldsymbol{\sigma} = \{\sigma_{xx}, \sigma_{zz}, \sigma_{xz}\}$, while the elements of $\boldsymbol{B}$ (size 3×4) are described in terms of the wave amplitude matrix $\boldsymbol{R}$ as

$$\begin{aligned} B(1,p) &= R_{1p}\eta e^{-jk_p z}, \quad B(2,p) = -jR_{2p}k_p e^{-jk_p z}, \\ B(3,p) &= -(jR_{1p}k_p + R_{2p}\eta)e^{-jk_p z} \end{aligned} \tag{5.81}$$

where $p = 1, \ldots, 4$ and z is the point of strain measurement.

The elasticity matrix $\boldsymbol{Q}$ is

$$\boldsymbol{Q} = \begin{bmatrix} Q_{11} & Q_{13} & 0 \\ Q_{13} & Q_{33} & 0 \\ 0 & 0 & Q_{55} \end{bmatrix} \tag{5.82}$$

5.3.4 Prescription of Force Boundary Conditions

Essential boundary conditions are prescribed as in FE methods, where the nodal displacements are constrained or released depending upon the nature of the boundary conditions. The applied tractions are prescribed at the nodes. Assuming symmetric loading, the loading function can be written as

$$F(x,z,t) = \delta(z - z_j)\left(\sum_{m=1}^{M} a_m \cos(\eta_m x)\right)\left(\sum_{n=0}^{N-1} \hat{f}_n e^{(-j\omega_n t)}\right), \tag{5.83}$$

where δ denotes the Dirac delta function, z_j is the z coordinate of the point where the load is applied and the z dependency is fixed by suitably choosing the node where the load is prescribed. No variation of load along the z direction is allowed in this analysis. Also, $\hat{f}_n$ are the Fourier transform coefficients of the time dependent part of the load, which are computed by FFT, and a_m are the Fourier series coefficients of the x dependent part of the load.

There are two summations involved in the solution and two associated windows, one in time t and the other in space x_L. The discrete frequencies ω_n and the discrete horizontal wavenumbers η_m are related to these windows by the number of data points N and M chosen in each summation, that is,

$$\omega_n = 2n\pi/T = 2n\pi/(N\Delta t), \quad \eta_m = 2(m-1)\pi/x_L = 2(m-1)\pi/(M\Delta x), \quad (5.84)$$

where Δt and Δx are the temporal and spatial sample rate, respectively.

5.3.5 Determination of Lamb Wave Modes

Lamb waves are guided waves (Fig. 5.3), propagating in a plate with traction free surfaces. There are two main approaches to the analysis of Lamb waves. The first one is the method of potentials, where Helmholtz decomposition of the displacement field decouples the governing equations written in terms of potentials. Solutions are sought for the potentials, which contain four arbitrary constants. The displacement field and the stresses are expressed in terms of the potentials and the imposition of traction-free upper and lower surfaces generates the necessary condition for finding the unknown constants and the dispersion equation [20]. The advantage of this method is that the symmetric and anti-symmetric modes can be analyzed separately (Fig. 5.3a, b). However, the method is applicable only to the isotropic waveguides.

The second approach is based on the PWT, which was introduced previously and is further discussed below. In the formulation, the solution is expressed in terms of summations over the discrete frequencies and the horizontal wavenumbers. Each partial wave of Eq. 5.68 satisfies the governing PDEs (Eq. 5.54), while the coefficients c_i satisfy any prescribed boundary conditions. As long as the prescribed natural boundary conditions are non-homogeneous, no restriction upon

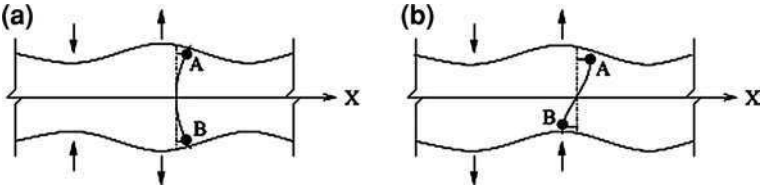

Fig. 5.3 **a** Symmetric Lamb wave propagation; **b** anti-symmetric Lamb wave propagation

the horizontal wavenumber η is imposed which leads to a double summation solution of the displacement field. However, that is not the case for traction-free boundary conditions on the two surfaces, which are the necessary condition for generating Lamb waves. The governing discrete equation for a finite layer (Eq. 5.73) in this case becomes

$$\hat{\boldsymbol{K}}(\eta_m, \omega_n)_{nm}\hat{\boldsymbol{u}}_{nm} = 0 \tag{5.85}$$

and we are interested in a non-trivial $\hat{\boldsymbol{u}}$. Hence, the stiffness matrix $\hat{\boldsymbol{K}}$ must be singular, i.e., $\det(\hat{\boldsymbol{K}}(\eta_m, \omega_n)) = 0$, which gives the required relation between η_m and ω_n. Since, ω_n is made to vary independently, the above relation must be solved for η_m to render the stiffness matrix singular. More precisely, for each value of ω_n there is a set of values of horizontal wavenumber η_m (one for each mode) and for each value of ω_n and η_m there are four vertical wavenumbers k_{nm}. The difference in this case is in the value of η_m, which is to be solved for, as opposed to its expression in Eq. 5.84, in the fact that M denotes the number of Lamb modes considered rather than Fourier modes. Now, for each set of $(\omega_n, \eta_m, k_{nml})(l = 1, \ldots, 4), \hat{\boldsymbol{K}}$ is singular and $c_l(l = 1, \ldots, 4)$ define the null space of $\hat{\boldsymbol{K}}$. The total solution can finally be reconstructed using Eq. 5.68. Following normal practice, the traction-free boundary conditions $(\sigma_{zz}, \sigma_{xz} = 0)$ are prescribed at $z = \mp h/2$. Using Eq. 5.80, the governing equation for c_i and η_m becomes

$$\boldsymbol{W}_2(\eta_m, \omega_n)\boldsymbol{c}_{nm} = \boldsymbol{0} \tag{5.86}$$

where $\boldsymbol{c} = \{c_1, c_2, c_3, c_4\}$, while $\boldsymbol{W}_2$ is another form of the stiffness matrix $\hat{\boldsymbol{K}}$ and is given by

$$\begin{aligned}
W_2(1,p) &= (Q_{11\circ}R(1,p)\eta - jQ_{13\circ}R(2,p)k_p)e^{jk_p h/2},\\
W_2(2,p) &= (Q_{11\circ}R(1,p)\eta - jQ_{13\circ}R(2,p)k_p)e^{-jk_p h/2},\\
W_2(3,p) &= Q_{55\circ}(-R(1,p)k_p + jR(2,p)\eta)e^{jk_p h/2},\\
W_2(4,p) &= Q_{55\circ}(-R(1,p)k_p + jR(2,p)\eta)e^{-jk_p h/2}.
\end{aligned}$$

The dispersion relation is $\det\{\boldsymbol{W}_2\} = 0$, which yields $\eta_m(\omega_n)$, while the phase speed for Lamb waves c_{nm} is given by ω_n/η_m. Once the values of η_m are known for the desired number of modes, the elements of $\boldsymbol{c}$ are obtained by the SVD technique as described earlier to find the elements of $\boldsymbol{R}$. Summing over all the Lamb modes provides the solution at each frequency.

5.4 Anisotropic Plate-FFT Based Spectral Element Formulation

The governing equation derivation and the wavenumber computation through spectral analysis were reported in Sects. 2.7.3 and 2.8.4. Here we directly go to the spectral element formulation.

5.4.1 Finite Plate Element

The geometry of the semi-bounded plate element is shown in Fig. 5.4. It has four degrees of freedom per node, three displacements in three coordinate directions and one rotational degree of freedom about the y axis. Thus, there are a total of eight degrees of freedom per element, which are the unknowns. The displacement at any x coordinate of the plate in the frequency/wavenumber domain can be written as a linear combination of all its solution given by

$$\tilde{\boldsymbol{u}} = \sum_{i=1}^{8} a_i \boldsymbol{\phi}_i e^{-jk_i x}, \tag{5.87}$$

where $\tilde{\boldsymbol{u}} = \{\tilde{u}, \tilde{v}, \tilde{w}\}^T$, and $\boldsymbol{\phi}_i \in \boldsymbol{C}^{3\times 1}$ are the columns of the wave matrix. The a_i are the unknown constants, which must be expressed in terms of the nodal variables. This step can be viewed as a transformation from the generalized coordinates to the physical coordinates. To do so, we can write the displacement field in a matrix vector multiplication form as

$$\tilde{\mathbf{u}} = \begin{Bmatrix} \hat{u}(x,\omega_n) \\ \hat{v}(x,\omega_n) \\ \hat{w}(x,\omega_n) \end{Bmatrix} = \begin{bmatrix} \phi_{11} & \dots & \phi_{18} \\ \phi_{21} & \dots & \phi_{28} \\ \phi_{31} & \dots & \phi_{38} \end{bmatrix} \begin{bmatrix} e^{-jk_1 x} & 0 & \dots & 0 \\ 0 & e^{-jk_2 x} & \dots & 0 \\ \vdots & \ddots & \ddots & \vdots \\ 0 & \dots & \dots & e^{-jk_8 x} \end{bmatrix} \boldsymbol{a} \tag{5.88}$$

where $k_{p+4} = -k_p, (p = 1, \dots, 4)$ and the elements of $\boldsymbol{\phi}_i$ are written as $\phi_{pi} (p = 1, \dots, 3)$. In concise notation the above equation becomes

$$\tilde{\mathbf{u}}_{n,m} = \boldsymbol{\Phi}_{n,m} \boldsymbol{\Lambda}(x)_{n,m} \boldsymbol{a}_{n,m} \tag{5.89}$$

where n, m is introduced in the subscript to remind that all these expressions are evaluated at a particular value of ω_n and η_m, $\boldsymbol{\Lambda}(x)_{nm}$ is a diagonal matrix of order 8×8 whose ith element is $e^{-jk_i x}$, $\boldsymbol{\Phi}_{n,m} = [\phi_1 \dots \phi_8]$ is the wave amplitude matrix, and $\boldsymbol{a}_{n,m}$ is the vector of eight unknown constants to be determined. These unknowns are expressed in terms of the nodal displacements by evaluating Eq. 5.89 at the two nodes, i.e., at $x = 0$ and $x = L$. In doing so, we get

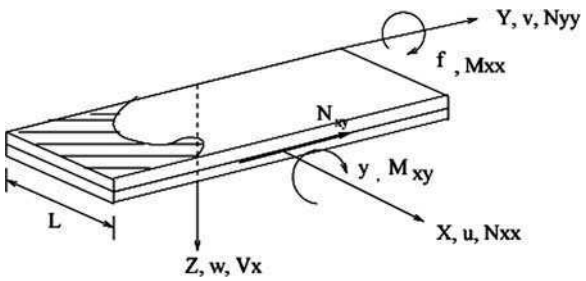

Fig. 5.4 Displacements and stress resultants of the spectral plate element (CLPT and FLPT): for CLPT $\phi = \partial w/\partial x$ and ψ is absent

$$\{\hat{\mathbf{u}}\}_{n,m} = \left\{ \begin{matrix} \tilde{\mathbf{u}}_1 \\ \tilde{\mathbf{u}}_2 \end{matrix} \right\}_n = \boldsymbol{T}_{1_{n,m}} \boldsymbol{a}_{n,m} \tag{5.90}$$

where $\tilde{\mathbf{u}}_i = \{u_i, v_i, w_i, (\partial w/\partial x)_i\}$, and $\tilde{\mathbf{u}}_1$ and $\tilde{\mathbf{u}}_2$ are the nodal displacements of node 1 and node 2, respectively. The elements of $\boldsymbol{T}_{1_{n,m}}$ are

$$\begin{aligned}
T_1(m,n) &= \Phi(m,n), \quad m = 1,\ldots,3, n = 1,\ldots,8 \\
T_1(m,n) &= -jk_p\Phi(m-4,p)e^{-jk_nL}, \quad m = 5,\ldots,7, n = 1,\ldots,8 \\
T_1(4,n) &= -jk_n\Phi(3,n), \quad n = 1,\ldots,8 \\
T_1(8,n) &= -jk_n\Phi(7,n), \quad n = 1,\ldots,8.
\end{aligned}$$

Before advancing further, it is to be noted that the element has edges parallel to the y axis, hence at the plate boundary $n_x = \pm 1$ and $n_y = 0$. These relations are to be utilized in the force–displacement relation. Using the force boundary conditions Eqs. 2.149–2.151, the force vector $\mathbf{f}_{nm} = \{\bar{N}_{xx},\ \bar{N}_{yy},\ \bar{V}_x,\ \bar{M}_{xx}\}_{n,m}$ can be written in terms of the unknown constants $\boldsymbol{a}_{n,m}$ as $\mathbf{f}_{n,m} = \boldsymbol{P}_{n,m}\boldsymbol{a}_{n,m}$. When the force vector is evaluated at node 1 and node 2 (substituting $n_x = \pm 1$) nodal force vectors are obtained and can be related to $\boldsymbol{a}_{n,m}$ by

$$\hat{\mathbf{f}}_{n,m} = \left\{ \begin{matrix} \tilde{\mathbf{f}}_1 \\ \tilde{\mathbf{f}}_2 \end{matrix} \right\}_{n,m} = \begin{bmatrix} \boldsymbol{P}(0) \\ \boldsymbol{P}(L) \end{bmatrix}_{n,m} \boldsymbol{a}_{n,m} = [\boldsymbol{T}_2]_{n,m}\boldsymbol{a}_{n,m}. \tag{5.91}$$

Equations 5.90 and 5.91 together yield the relation between the nodal force and nodal displacement vector at frequency ω_n and wavenumber η_m as

$$\hat{\mathbf{f}}_{n,m} = \boldsymbol{T}_{2_{n,m}}\boldsymbol{T}_{1_{n,m}}^{-1}\hat{\mathbf{u}}_{n,m} = \boldsymbol{K}_{n,m}\hat{\mathbf{u}}_{n,m}, \tag{5.92}$$

where $\boldsymbol{K}_{n,m}$ is the dynamic stiffness matrix at frequency ω_n and wavenumber η_m of order 8×8. The explicit form of the matrix $\boldsymbol{T}_{2_{n,m}}$ for $n = 1,\ldots,8$ is

$$\begin{aligned}
T_2(1,n) &= jk_nA_{11}\Phi(1,n) - \eta A_{12}\Phi(2,n) - k_n^2B_{11}\Phi(3,n) - \eta^2B_{12}\Phi(3,n), \\
T_2(2,n) &= \eta A_{66}\Phi(1,n) + jk_nA_{66}\Phi(2,n) + 2jB_{66}k_n\eta\Phi(3,n), \\
T_2(3,n) &= k_n^2B_{11}\Phi(1,n) + jB_{12}k_n\eta\Phi(2,n) + jk_n^3D_{11}\Phi(3,n) + jD_{12}k_n\eta^2\Phi(3,n) \\
&\quad + 2\eta^2B_{66}\Phi(1,n) + 2jk_n\eta B_{66}\Phi(2,n) + 4jk_n\eta^2D_{66}\Phi(3,n), \\
T_2(4,n) &= -jk_nB_{11}\Phi(1,n) + \eta B_{12}\Phi(2,n) + k_n^2D_{11}\Phi(3,n) + \eta^2D_{12}\Phi(3,n), \\
T_2(m,n) &= -T_2(m-4,n)e^{-jk_nL}, m = 5,\ldots,8.
\end{aligned}$$

5.4.2 Semi-infinite or Throw-Off Plate Element

As mentioned earlier, for the infinite domain element, only the forward propagating modes are considered. The displacement field at frequency ω_n and wavenumber η_m is given by

$$\tilde{\mathbf{u}}_{n,m} = \sum_{m=1}^{4} \phi_m e^{-jk_m x} a_m = \mathbf{\Phi}_{n,m} \mathbf{\Lambda}_{n,m}(x) \boldsymbol{a}_{n,m}, \tag{5.93}$$

where $\mathbf{\Phi}_{n,m}$ and $\mathbf{\Lambda}_{n,m}(x)$ is now of order 4×4. The $\boldsymbol{a}_{n,m}$ is a vector of four unknown constants. Evaluating the above expression at node 1 $(x = 0)$, the nodal displacements are related to these constants through the matrix $\boldsymbol{T}_{1_{n,m}}$ as

$$\begin{aligned} \hat{\mathbf{u}}_{n,m} &= \tilde{\mathbf{u}}_{1_{n,m}} = \mathbf{\Phi}_{n,m} \mathbf{\Lambda}_{n,m}(0) \boldsymbol{a}_{n,m} \\ \hat{\mathbf{u}}_{n,m} &= \boldsymbol{T}_{1_{n,m}} \boldsymbol{a}_{n,m} \end{aligned} \tag{5.94}$$

where $\boldsymbol{T}_{1_{n,m}}$ is now a matrix of dimension 4×4. Similarly, the nodal forces at node 1 can be related to the unknown constants as

$$\hat{\mathbf{f}}_{n,m} = \tilde{\mathbf{f}}_{1_{n,m}} = \boldsymbol{P}_n(0) \boldsymbol{a}_{n,m} = \boldsymbol{T}_{2_{n,m}} \boldsymbol{a}_{n,m}. \tag{5.95}$$

Using Eqs. 5.94 and 5.95, nodal forces at node 1 are related to the nodal displacements at node 1 as

$$\hat{\mathbf{f}}_{n,m} = \boldsymbol{T}_{2_{n,m}} \boldsymbol{T}_{1_{n,m}}^{-1} \hat{\mathbf{u}}_{n,m} = \boldsymbol{K}_{n,m} \hat{\mathbf{u}}_{n,m} \tag{5.96}$$

where $\boldsymbol{K}_{n,m}$ is the element dynamic stiffness matrix of dimension 4×4 at frequency ω_n and wavenumber η_m. The matrices $\boldsymbol{T}_{1_{n,m}}$ and $\boldsymbol{T}_{2_{n,m}}$ are the first 4×4 truncated part of the corresponding matrices for the finite plate element.

5.5 Numerical Examples

In this section, we provide some interesting examples of wave propagation in both 1D and 2D connected waveguides using the formulated spectral elements. In some examples, the results of both FSFEM and WSFEM are provided to understand the relative merits and demerits of both formulations.

5.5.1 Wave Transmission and Scattering Through an Angle-Joint

Often in practice, we come across planar frame structures with complex geometry. Such structures are commonly used for space applications such as solar panels, antennas etc., wherein a number of skeletal members are connected by rigid or flexible joints, thereby creating a complex structural network. Both FSFEM and WSFEM formulation can account for such situations with relative ease. In this section, the problem is solved by FSFEM formulation. In this example, we consider a rigid angle-joint with three composite members (Fig. 5.5) to analyze the

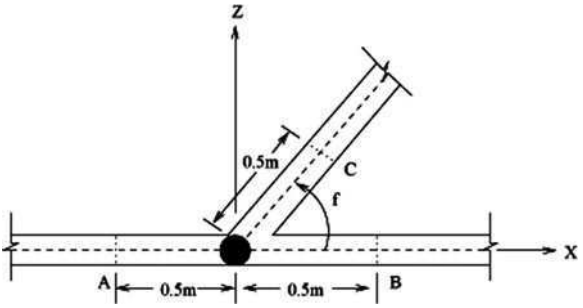

Fig. 5.5 Rigid angle-joint with AS/3501-6 graphite–epoxy composite members

nature of reflected and transmitted waves through the joint. In particular, it will be interesting to observe how the dynamics of the system change with the change in joint angle. In addition, it is also important to investigate the effects of axial–flexural coupling on the overall response.

The FSFEM model features 0.5 m long segments on both sides of the joint along the x-axis, which are modeled with two finite length spectral elements. The rest of the semi-infinite segments are modeled with three throw-off elements.

The responses obtained from FSFEM model are compared with the responses obtained from conventional FE formulation, where the three semi-infinite segments are modeled with 950 elements each, while the segment AB is modeled with 100 elements. The length of each element is 1.0 cm. This gives an overall system size of 8994×9 in banded form.

Each member connected to the joint is made up of AS/3501-6 graphite–epoxy composite members with ply stacking sequence $[0_5/45_5]$. Here, the coupling between bending and axial motions are quantified by a coupling factor defined as $r = B_{11}^2/D_{11}A_{11}$, which can be altered by modifying the ply stacking sequence. In the present example, we consider the coupling factor of $r = 0.213$.

First of all, to validate the accuracy of the response obtained from SFEM, an impact load as considered earlier (Fig. 4.3) is applied axially at A for joint angle $\phi = 30^\circ$. The axial velocity history at the same point A, is computed and compared with the FEM result, which is shown in Fig. 5.6a. Similarly, the same load is applied transversely at A. The axial velocity history at A is computed, and compared with the FEM results. Such comparison is shown in Fig. 5.6b. In the two cases, the results show good agreement. To study the effect of axial–flexural coupling on the dynamic response, the same rigid joint (Fig. 5.5) with an axial loading at point A, is considered as in the previous case. The angle of the rigid joint ϕ is fixed as 45°. The non-dimensional coupling parameter r is varied by using different ply-stacking sequences. In Fig. 5.7a, the axial velocity (normalized with $P_{\max}c_L/A_{11}$ with $P_{\max}$ being the maximum load amplitude and c_L, the longitudinal wave speed in a rod) response at A and B (both at a distance of 0.5 m from the joint) is plotted. The figure shows that the reflected axial response at A, as well as the transmitted axial response at B, occur at the same time for a particular value of r. However, due to the decrease in the values of A_{11}, for increasing values of r, the axial speed of propagation decreases. As a result, both responses occur at

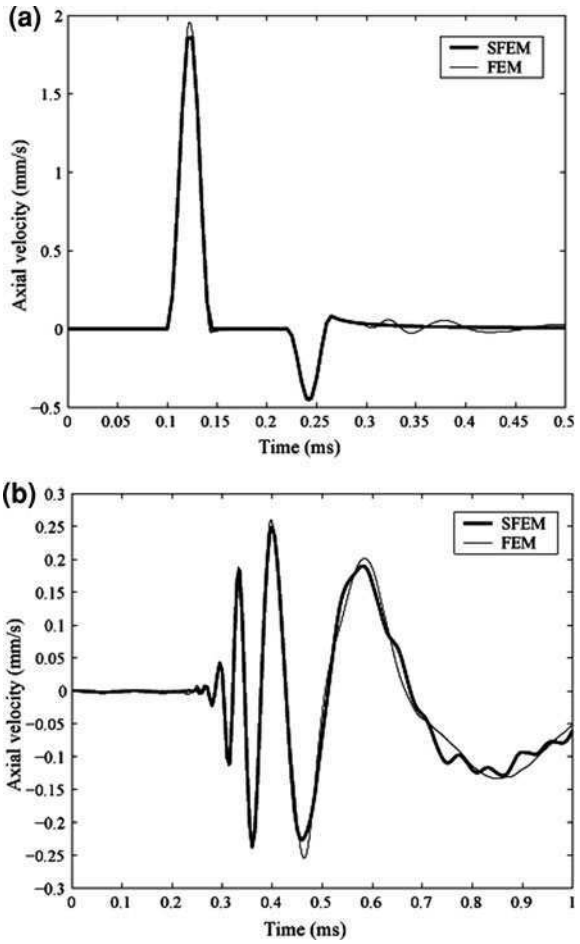

Fig. 5.6 **a** Comparison of axial response at A, due to axial impact load applied at A. **b** Comparison of axial response at A, due to transverse impact load applied at A

a later stage. A separation of 0.24 ms can be observed between responses due to unsymmetric cross-plies and the symmetric 0° ply configurations. Also, the dispersive behavior becomes dominant after the initial peak, which can be considered as a contribution from Mode 2 and Mode 3, as discussed earlier. Fig. 5.7b shows the plot of transverse velocity (normalized with $P_{\max} c_L h^2 / D_{11}$) response at A and B. Other than a similar time lag in the arrival of reflected and transmitted responses as observed in the case of axial propagation, the smoothness in the response curves disappears and their transient nature becomes significant for increasing values of r. This example has shown the ease with which FSFEM allows simulating the dynamics of complicated networks of connected beams. Unlike the conventional FE formulation, however, the length of the spectral element is not a limiting factor; each element is formulated exactly, irrespective of its length. This leads to a substantial reduction in the number of equations that are to be solved.

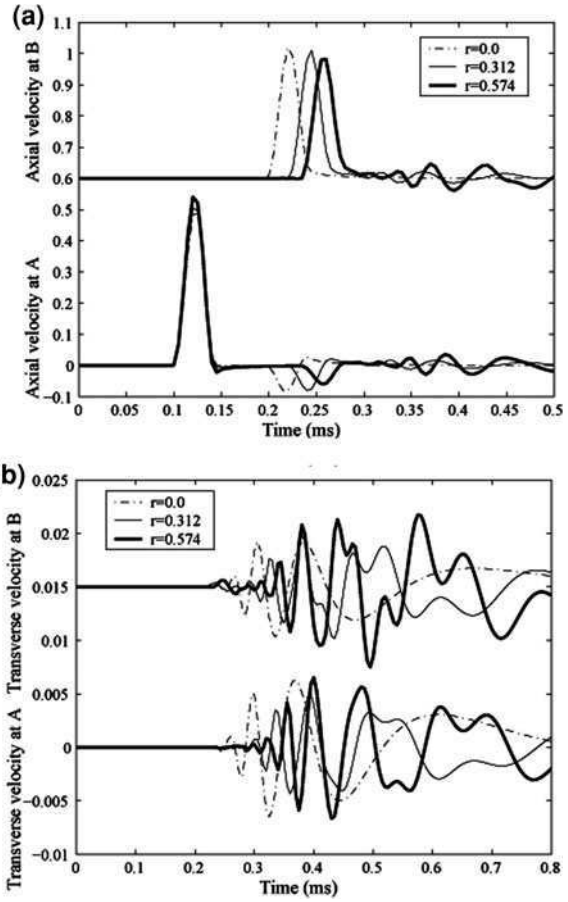

Fig. 5.7 **a** Normalized axial velocity history and **b** normalized transverse velocity history at A and B (Fig. 5.5), showing the reflection and transmission response through the rigid joint ($\phi = 45^\circ$) due to an axial impact load at A

5.5.2 *Wave Propagation in 2D Portal Frame*

The aim of this example is to demonstrate the ability of FSFEM and WSFEM to handle multiple reflections arising out of finite domain structures such as a 2D portal frame.

The considered frame is subjected to the impact load shown in Fig. 3.7 at the location indicated in Fig. 5.8. This example is more complicated than the previous example of the angle joint, as multiple reflections occur from the joints and supports. For the analysis of this structure, three spectral elements for the three members are used and the elemental dynamic stiffness matrices of these members are assembled using standard FE procedures.

In Fig. 5.9, the transverse wave velocity obtained using WSFEM formulation at point A in Fig. 5.8 is presented and compared with conventional FE response obtained using 2-noded 1D beam element with axial, transverse and rotational degrees of freedom at each node. Each of the three members of the frame is discretized with 5000 elements.

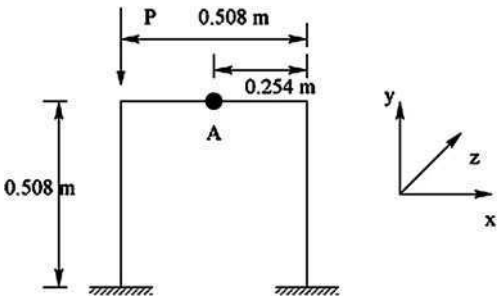

Fig. 5.8 2D frame structure

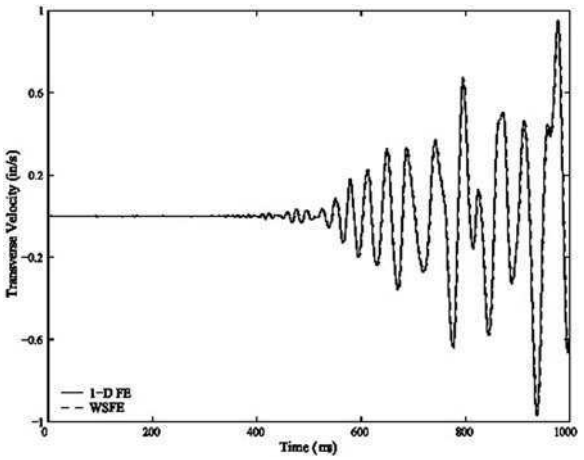

Fig. 5.9 Transverse velocity at A of 2D frame in Fig. 5.8 due to the applied load P.

Results show very good agreement between the two solutions. Since FSFE cannot be used for similar analysis of undamped finite length structures, the wave velocities are plotted in Figs. 5.10a–c for a damping of $\eta = 0.5$. In the above mentioned figures for all the plots obtained using wavelet, a time window T_w of 1024 μs is used. For FSFE, T_w is increased from 1024 μs to 4096 μs in Fig. 5.10a–c to remove signal wraparound. It can be seen that for $T_w = 1024$ μs, the results are highly distorted which gradually decreases with an increase in T_w. From Fig. 5.10c, we see that increasing T_w to 4096 μs is not sufficient to completely eliminate the response distortion. It further requires higher resolution. The above numerical experiment is performed using basis function of order $N = 8$ and sampling rate $\triangle t = 1$ μs. The problem of wraparound in FSFEM and the ability of WSFEM to accurately predict response in finite structures is clearly demonstrated. Also, the example shows need for large time windows in FSFEM formulation, and signal wraparound problems, present in FSFEM formulation, are completely eliminated in the WSFEM formulation.

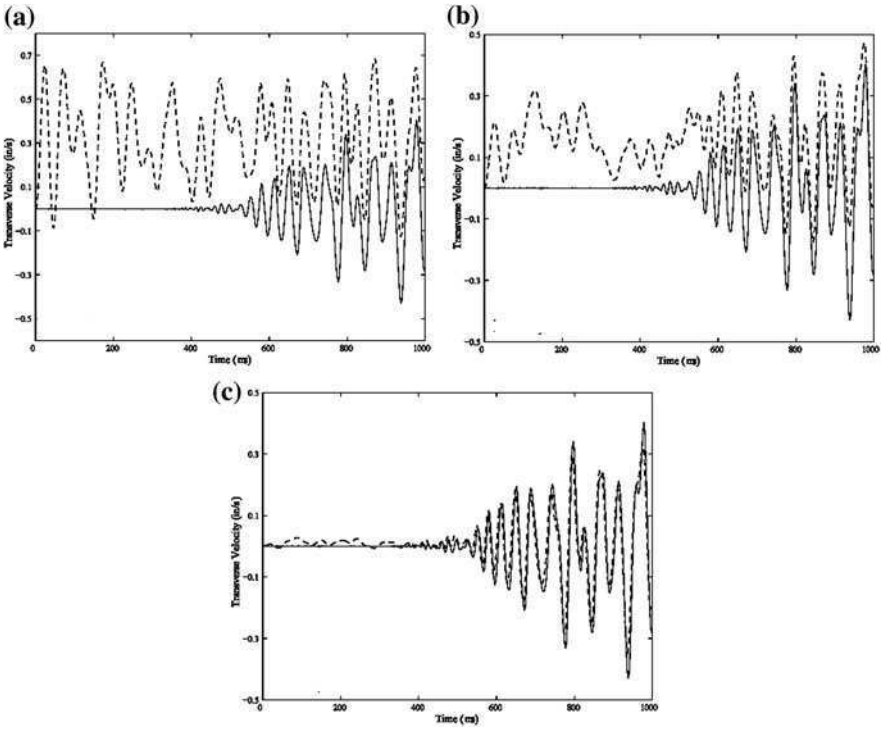

Fig. 5.10 Transverse tip velocity at A of 2D frame in Fig. 5.8 due to the applied load P, for time windows T_w **a** $T_w = 1024\,\mu s$, **b** $T_w = 2048\,\mu s$ and **c** $T_w = 4096\,\mu s$.

5.5.3 *Propagation of Surface and Interfacial Waves in a Composite Layer*

In this section, wave propagation in 2D composite layers is presented by comparing FSFEM results with those obtained from a 2D FE formulation. The material used is GFRP composite whose material properties are as follows: $E_1 = 144.48\,\text{GPa}$, $E_3 = 9.63\,\text{GPa}$, $G_{13} = 4.13\,\text{GPa}$, $v_{13} = 0.3$, $v_{12} = 0.02$ and $\rho = 1389\,\text{kg/m}^3$. The ply-sequence considered is $[0^\circ{}_{10}/90^\circ{}_{10}/0^\circ{}_{10}]$, where each lamina is 0.01 m thick. This large thickness is chosen to differentiate between the incident and the reflected pulse, although any layer thickness can be chosen and easily handled by the considered approach. The layered system, shown in Fig. 5.11, is impacted by a high frequency loading, where the bottom of the layer is fixed. The time history of the high frequency load along with its spectrum are shown in Fig. 3.7.

The load is applied at the center of the top layer first in the z direction, which generates primarily QP waves, and then in the x direction, which generates primarily QSV waves. The response of the structure is measured at several locations along the surface and interfaces. For FE analysis, the layer is modeled with 3600,

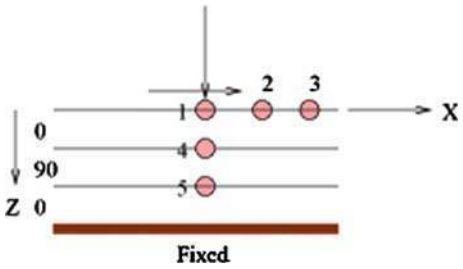

Fig. 5.11 Layer model for verification

three-noded plane-strain FEs. In comparison, there are only three FLEs in the spectral model. The FE formulation results in a global system matrix of size 3656×126 (where 126 is the bandwidth of the matrices), whereas the spectral model features a global system matrix (dynamic stiffness matrix) of size 6×6. While solving via FE analysis, Newmark's time integration is adopted with a time step $\Delta t = 1\,\mu s$. For the spectral analysis, the load is sampled at 48.83 Hz with $N = 2048$ (in Eq. 5.83) FFT points. Further, for the spatial variation 32 Fourier series coefficients (i.e. M in Eq. 5.83) are considered. For the concentrated load, all the a_m are equal to $2/x_L$, where x_L is the window length in the x direction, here taken as 1.0 m, as per the FE model. Since, the time domain response is real, the computation of displacements (or velocities) needs to be carried out only upto the Nyquist frequency. Hence, the global stiffness matrix needs to be inverted 1024×32 times. This computational requirement is many orders smaller than the requirement of the FE analysis. Further, a typical simulation in FE takes 110 s of CPU time, whereas, a SE run takes 14 s on a Compaq Alpha Server ES40 with DEC compiler.

Before discussing the velocity histories, a few points need to be considered. When a velocity wave encounters a stiffer zone, the reflected wave has an opposite sign to that of the incident wave. In contrast, when the wave encounters a zone of comparatively lower stiffness, the reflected wave has the same phase as the incident wave. These phenomena are best visible in the reflections from the fixed end (infinite stiffness) and the free end (zero stiffness) of a structure. However, reflected waves are also generated at the interfaces of laminates because of the mismatch in the impedance. In the present model, propagation is considered in the direction of ply-stacking and there is a nominal change in stiffness in that direction due to the change in laminae angle. Hence, the magnitude of the reflected waves from the interface will not be large enough to be visible, in comparison to the boundary generated waves. Thus whatever reflections are present in the velocity history are solely due to reflections from the boundary.

For the load applied in the z direction at point 1, the z directional velocity $\dot{w}$, is measured at points marked 1, 4, and 5 (see Fig. 5.11). The velocity histories at these nodes are plotted in Figs. 5.12, 5.13, 5.14, and 5.15. In Fig. 5.12, where the peak at 100 μs is the direct effect of the load. For this kind of loading, the propagating wave is essentially a QP wave. In this case, the inverted peak at around 3.2×10^{-4} s corresponds to the reflection from the fixed end i.e., at $z = 0.3$ m.

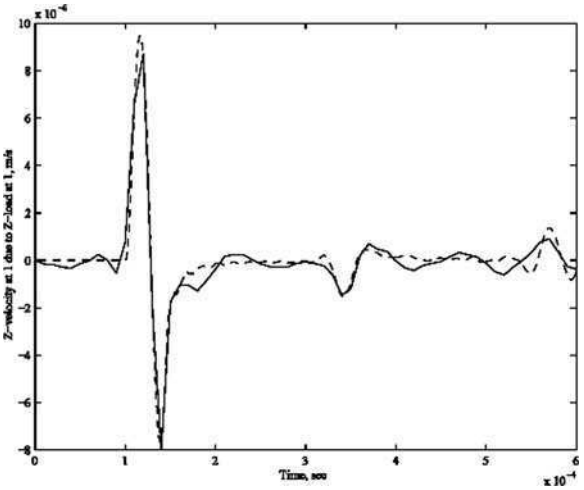

Fig. 5.12 QP wave at the surface (point 1); *solid line*, SE; *dashed line*, 2D FE

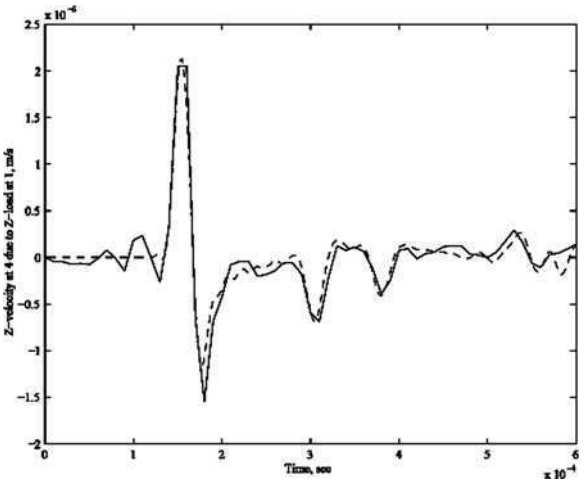

Fig. 5.13 QP wave at the interface (point 4); *solid line*, SE; *dashed line*, 2D FE

Again at the fixed end, the wave is inverted and shows up at around 5.4×10^{-4} s. This figure also shows the excellent agreement between the FE and Spectral Layer Element responses.

Next, the $\dot{w}$ history at the first interface ($z = 0.1$ m, point marked 4) is plotted in Fig. 5.13. The response in this case does not start at 100 μs as before, but at 130 μs. This is due to the time taken for propagation in the first layer, i.e., 0° laminate. Subsequent reflections at around 2.9×10^{-4} s and 3.6×10^{-4} s are due to the reflections from the fixed edge ($z = 0.3$ m) and free edge ($z = 0.0$ m), respectively. Further, the peak at around 5.0×10^{-4} s is the second reflection from the fixed edge.

For the $\dot{w}$ history measured at the second interface ($z = 0.2$ m, point marked 5) and the response plotted in Fig. 5.14 the main peak comes down to 1.67×10^{-4} s because of the large travel distance. The QP wave velocity at 90° laminate is less

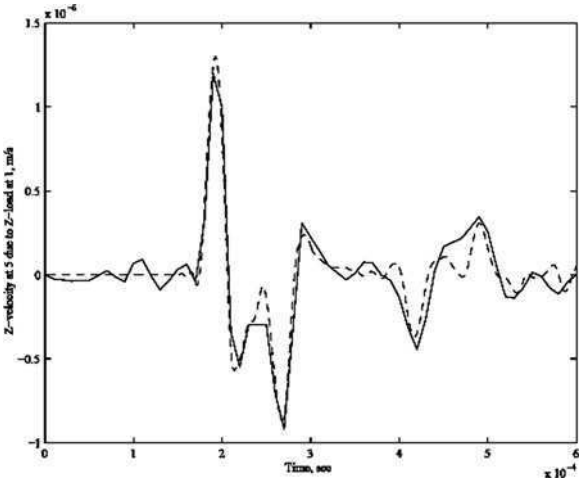

Fig. 5.14 QP wave at the interface (point 5); *solid line*, SE; *dashed line*, 2D FE

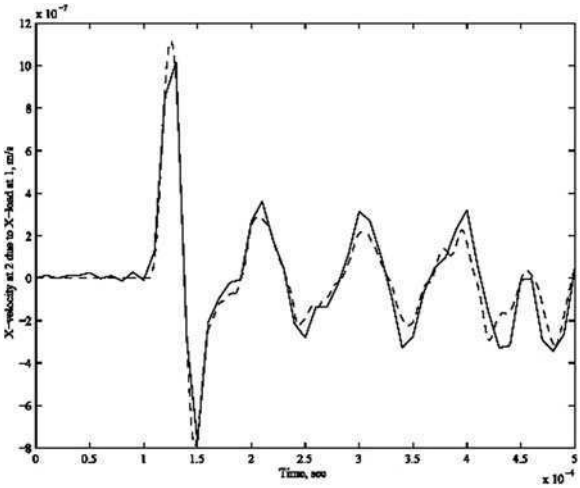

Fig. 5.15 QSV wave at the surface (point 2); *solid line*, SE; *dashed line*, 2D FE

than that in the 0° laminate and hence the increase (above 1.6×10^{-4} s) in propagation time. There are reflections from the fixed end (inverted peak at around 2.46×10^{-4} s), reflections from the free end (inverted peak at 4.0×10^{-4} s) and second reflections from the fixed end (peak at around 4.7×10^{-4} s). The spectral element formulation captures these reflections quite well, and except for the last reflection, the response matches satisfactorily with the FE response.

Next, the same load is applied at point 1 in the x direction. For this load, primarily QSV waves are generated. There will be no wave at the impact point and the x directional velocity $\dot{u}$ is measured at the surface points 2 and 3 and plotted in Figs. 5.15 and 5.16, respectively. In both cases, several reflections from the fixed ends are visible. As before, good agreement between the FE and the SLE responses

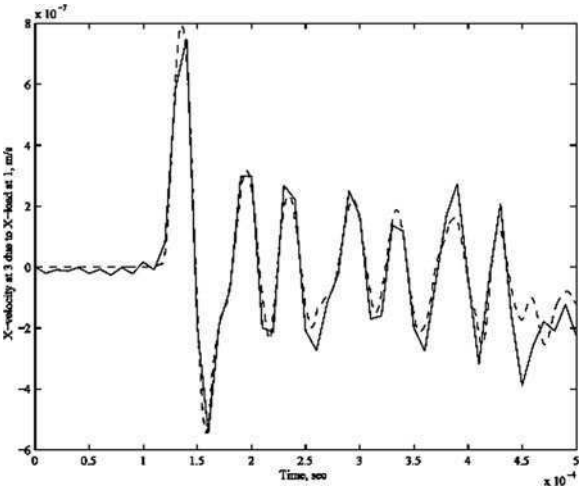

Fig. 5.16 QSV wave at the surface (point 5); *solid line*, SE; *dashed line*, 2D FE

can be observed. These responses establish the developed SLE in terms of accuracy, efficiency and cheap cost of computation.

5.5.4 Propagation of Lamb Wave

The importance of Lamb wave in the context of SHM was earlier discussed. In this section, we derive the dispersion relations for Lamb waves in composite plates and illustrate the changes of ply angle and thickness on its wave propagation characteristics. We also illustrate the propagation of Lamb wave modes through a numerical example.

A unidirectional lamina of 2 mm thickness is considered, with the material properties of AS/3501-6 graphite–epoxy composites.

The solution of the dispersion relations in cases such as this requires particular care as it is multi-valued, unbounded and complex (although the real part is of interest). One way to solve these equations is to appeal to the strategies of non-linear optimization, which are based on non-linear least square methods. There are several choices of algorithms, like the trust-region dogleg method, Gauss Newton method with a line search, or Levenberg Merquardt method with line search. Here, the MATLAB function *fsolve* is used and for the default option for medium scale optimization, the trust-region dogleg method is adopted, which is a variant of Powell's dogleg method [17].

Apart from the choice of algorithm, there are other subtle issues in root capturing for the solution of wavenumbers. For instance, except the first one or two modes, all the roots escape to infinity at low frequency. For isotropic materials, these cut-off frequencies are known a priori. However, no expressions can be found for anisotropic materials and generally, the solutions need to be tracked backwards, from the high frequency to the low frequency region. In general two

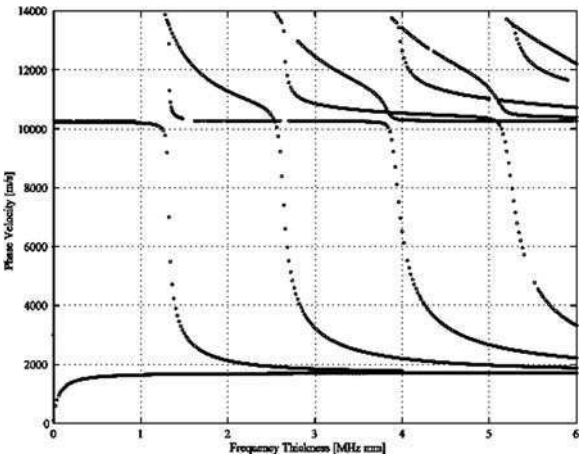

Fig. 5.17 Lamb wave dispersion relations for 0° ply-angle layer

strategies are essential in capturing all the modes within a given frequency band. Initially, the whole region should be scanned for different values of the initial guess, where the initial guess should remain constant for the whole frequency range. These sweeps open up all the modes in that region, although they are not completely traced. Subsequently, each individual mode should be followed to the end of the domain or to a pre-set value. For this case, the initial guess should be updated to the solution of the previous frequency step. Also, sometimes it is necessary to reduce the frequency step in the vicinity of high gradients. Once the Lamb modes are generated they are fed back into the frequency loop to produce the frequency domain solution for Lamb wave propagation, which through IFFT produces the time domain signal. As the Lamb modes are generated first, they need to be stored separately. To this end, data are collected from the generated modes at several discrete points over the considered frequency range. Next, a cubic spline interpolation is performed for a very fine frequency step within the same range. While generating the time domain data, interpolation is performed from these finely graded data to get the phase speeds (hence, η).

In the considered example, Lamb waves are generated through a modulated pulse of 200 kHz center frequency applied at one end of an infinite plate. Velocities components in the x and z directions are recorded at a propagating distance of $320h$, where h is the thickness of the plate. While studying the time domain representation, the thickness of the plate is taken as 10 mm, which amounts to a frequency-thickness value of 2. The thickness values is chosen so that at least three modes are excited according to the dispersion curve shown in Fig. 5.17.

Figure 5.17 shows the first 10 Lamb modes for fiber angle 0°. The first anti-symmetric mode (Mode 1) converges to a value of 1719 m/s in a range of 1 MHz-mm, where all the other modes also converge. In analogy to the isotropic case, this is the velocity of the Rayleigh surface waves in 0° fiber laminae. The first

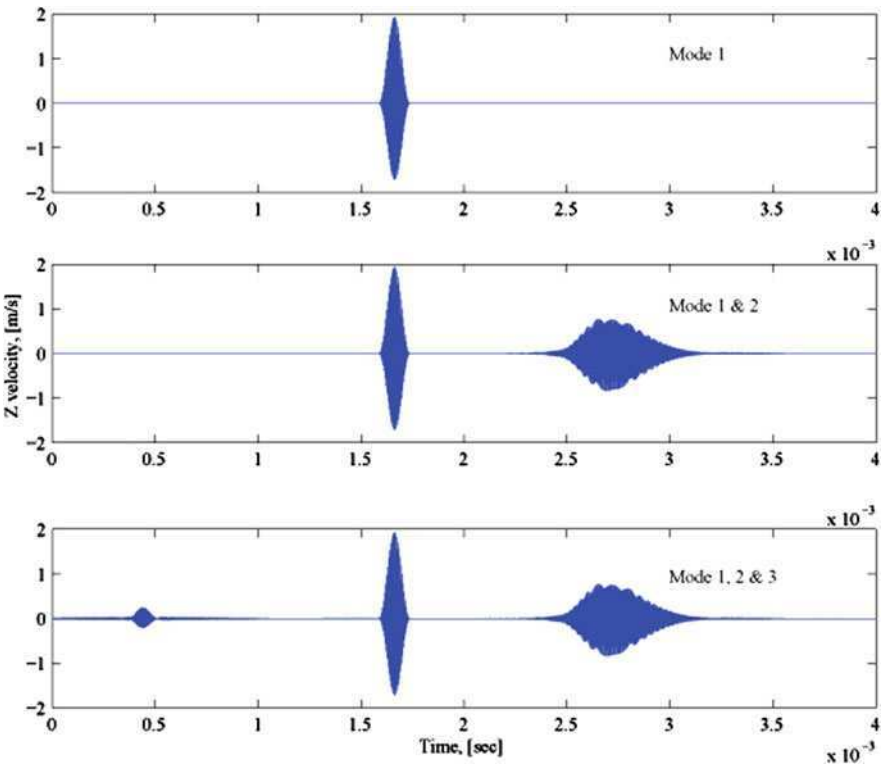

Fig. 5.18 Lamb wave propagation for 0° ply-angle, Z direction velocity history, $L = 320\,\text{h}$

symmetric mode (Mode 2) starts above 10000 m/s and drops suddenly at around 1.3 MHz-mm to converge to 1719 m/s, before which it has a fairly constant value. All the other higher order modes escape to infinity at various points in the frequency range. Also the symmetric and the anti-symmetric pair of each mode escape almost at the same frequency.

Propagation of these modes are plotted in Figs. 5.18 and 5.19 for the first three modes $(a_\circ, s_\circ$ and $a_1)$, here referred to as Mode 1, 2 and 3 respectively. In Fig. 5.18, the z velocity history is plotted, whereas in Fig. 5.19 the x velocity history is plotted. These figures readily show the different propagating modes, each corresponds to one wave packet propagating at the group speed (and not the phase speed). Hence, Fig. 5.17 is not helpful at predicting the arrivals of the different modes. However, as Figs. 5.18 and 5.19 suggest, mode 2 has a lower group speed than mode 1, and mode 3 has a group speed much higher than both mode 1 and 2. One difference in the $\dot{u}$ and $\dot{w}$ history can be observed. That is, for $\dot{u}$ history plot, the higher mode generates velocity of comparatively less magnitude, whereas, for $\dot{w}$ history plot, the magnitude is highest.

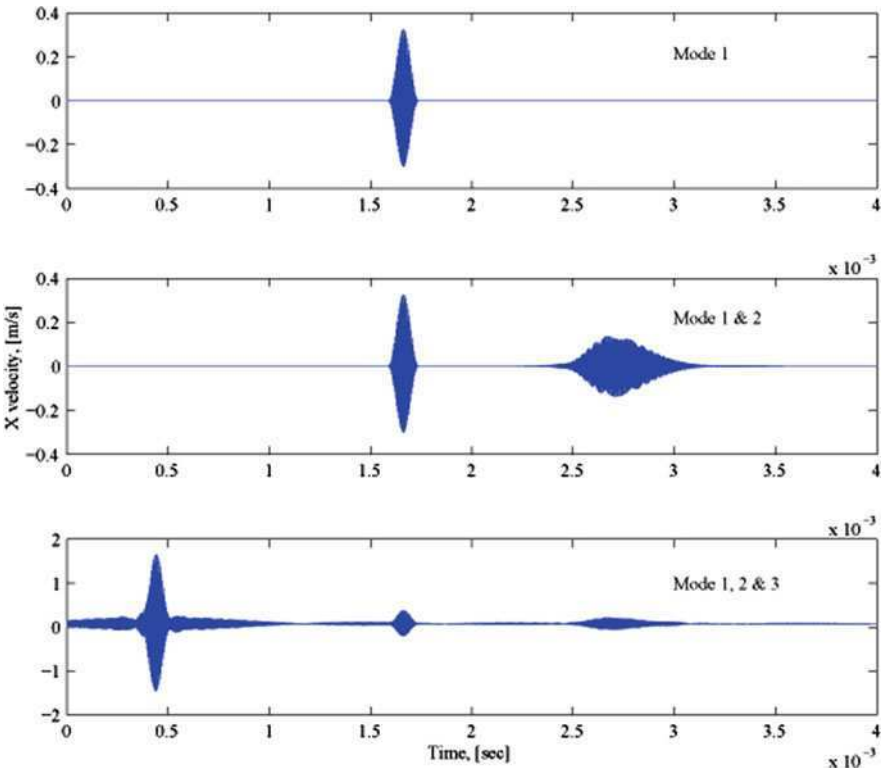

Fig. 5.19 Lamb wave propagation for 0° ply-angle, X direction velocity history, $L = 320\,\mathrm{h}$

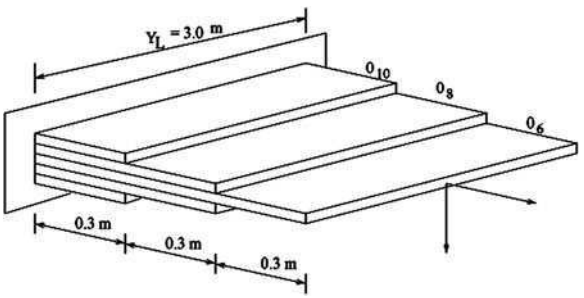

Fig. 5.20 Plate with ply-drop

5.5.5 *Wave Propagation in a Composite Plate with Ply-Drop*

Next, we consider the case of composite structures with ply drops. Ply drops are common in composite construction and are commonly employed to reduce the thickness of a laminated composite structural member. From the wave propagation point of view, they introduce geometrical discontinuity, which

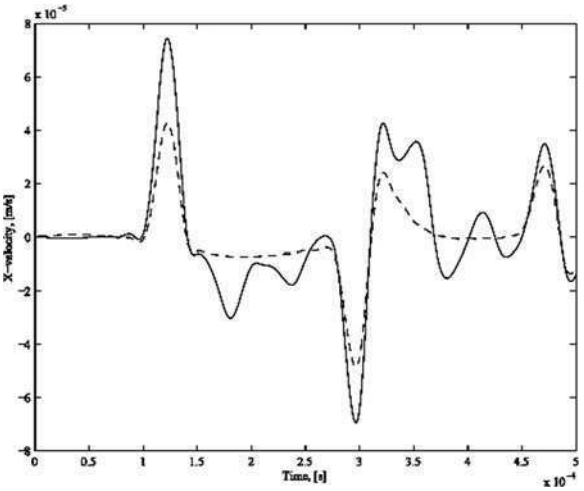

Fig. 5.21 Variation of axial velocity: *solid line*—ply-drop, *dashed line*—uniform plate

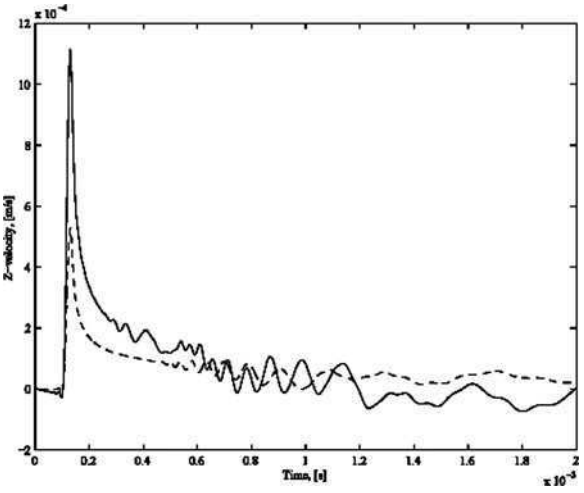

Fig. 5.22 Variation of transverse velocity: *solid line*—ply-drop, *dashed line*—uniform plate

results in impendence mismatch at the ply drop junction causing repeated reflections, which may eventually cause failure of the structure in the form delamination.

We consider the ply dropped plate shown in Fig. 5.20. The plate is impacted at the mid-point of the free end by a concentrated load whose time dependency is the same as taken previously (Fig. 3.7). The load is first applied in the x direction and the x velocity is measured at the impact point. The measured velocity history is plotted in Fig. 5.21. The same structure is also analyzed for uniform ply-stacking

(10 layers) and the result is superimposed in the same figure. It is evident from the figure that the ply drop affects the stiffness of the plate considerably, as there is an increment in the maximum amplitude of about 90%. This reduction of stiffness is also visible in the reflection from the boundary. The reflection from the boundary appears at the same instant in both the cases, which indicates that there is not much alteration in the group speed due to the ply-drop. However, there are two extra reflections, corresponding to the inverted peaks at around 175 μs and 240 μs, in the response from the ply-drop plate before the arrival of the boundary reflection, which originate at the ply-drop junctions due to the mismatch in impedance.

Next, the plate is impacted at the same point in the z direction and the z velocity is measured at the same point (Fig. 5.22). For reference, the response of the uniform plate is also plotted in the same figure. As noticed before, there is a considerable difference in the peak amplitudes (almost of a factor of 2), which follows the same pattern of axial velocity history. The extra reflections originated at the interfaces are also visible (starting at around 250 μs), which are not present in the uniform plate response. However, there is no deviation in the arrival time of the boundary reflection, which denotes the closeness of the bending group speed in both cases. Overall, this example shows the efficiency of the present element in modeling structures with discontinuity and bringing out its essential dynamic characteristics.

5.6 Conclusions

In this chapter, various spectral finite element models were formulated and their ability to perform wave propagation analysis were demonstrated on a healthy structure. In the next chapter, we will extend the spectral element approach to model waveguides with flaws such as horizontal cracks or delamination, vertical cracks or fibre breaks etc.

References

1. Amaratunga K, Williams JR (1995) Time integration using wavelet. In: Proceedings of SPIE, wavelet application for dual use, 2491, Orlando, FL, pp 894–902
2. Amaratunga K, Williams JR (1997) Wavelet-Galerkin solution of boundary value problems. Arch Comput Methods Eng 4(3):243–285
3. Belykin G (1992) On wavelet based algorithms for solving differential equations. Department of Mathematics, University of Colorado, Boulder
4. Chakroborty A (2004) Wave propagation in anisotropic and inhomogeneous medium, October 2004. Ph.D. thesis, Indian Institute of Science, Bangalore
5. Chakraborty A, Gopalakrishnan S (2006) An approximate spectral element for the analysis of wave propagation in inhomogeneous layered media. AIAA J 44(7):1676–1685
6. Chen MQ, Hwang C, Shih YP (1996) The computation of wavelet-Galerkin approximation on a bounded interval. Int J Numer Methods Eng 39:2921–2944

7. Cooley JW, Tukey JW (1965) An algorithm for the machine calculation of complex Fourier series. Math Comput 19:297–301
8. Daubechies I (1988) Orthonormal bases of compactly supported wavelets. Commun Pure Appl Math 41:906–966
9. Doyle JF (1997) Wave propagation in structures. Springer, New York
10. Gopalakrishnan S, Doyle JF (1994) Wave propagation in connected waveguides of varying cross-section. J Sound Vib 175(3):347–363
11. Gopalakrishnan S, Doyle JF (1995) Spectral super-elements for wave propagation in structures with local non-uniformities. Comput Methods Appl Mech Eng 121:77–90
12. Gopalakrishnan S, Chakraborty A, Roy Mahapatra D (2008) Spectral finite element method. Springer, London
13. Graff KF (1975) Wave motion in elastic solids. Dover Publications Inc., New York
14. Heideman MT, Johnson DH, Burrus CS (1984) Gauss and the history of the fast Fourier transform. IEEE ASSP Mag 1(4):14–21
15. Moulin E, Assaad J, Delebarre C, Grondel S, Balageas D (2000) Modeling of integrated Lamb waves generation systems using a coupled finite element normal mode expansion method. Ultrasonics 38:522–526
16. Nayfeh AH (1995) Wave propagation in layered anisotropic media. North Holland, Amsterdam
17. Powel MJD (1970) A Fortran subroutine for solving systems of nonlinear. Numerical methods for nonlinear algebraic equations. Rabinowitz P (ed) Ch. 7, pp 115–161, Algebraic Equations
18. Reddy JN (1985) Finite element method. McGraw Hill, New York
19. Rizzi SA (1989) A spectral analysis approach to wave propagation in layered solids potential in a wave guide. PhD thesis, Purdue University
20. Rose JL (1999) Ultrasonic waves in solid media. Cambridge University Press, Cambridge
21. Sneddon IN (1951) Fourier transforms. McGraw-Hill, New York
22. Sneddon IN (1964) Partial differential equations. McGraw-Hill, New York
23. Solie LP, Auld BA (1973) Elastic waves in free anisotropic plates. J Acoust Soc Am 54(1):50–65
24. Varadan VK, Vinoy KJ, Gopalakrishnan S (2006) Smart material systems and MEMS. Wiley, Chichester
25. Veidt M, Liub T, Kitipornchai S (2002) Modelling of Lamb waves in composite laminated plates excited by interdigital transducers. NDT E Int 35(7):437–447
26. Verdict GS, Gien PH, Burge CP (1996) Finite element study of Lamb wave interactions with holes and through thickness defects in thin metal plates. NDT E Int 29(4):248
27. Viktorov IA (1967) Rayleigh and Lamb wave. Plenum Press, New York
28. Williams JR, Amaratunga K (1997) A discrete wavelet transform without edge effects using wavelet extrapolation. J Fourier Anal Appl 3(4):435–449
29. Zhao G, Rose JL (2003) Boundary element modeling for defect characterization. Int J Solids Struct 40(11):2645–2658

Chapter 6
Simplified Spectral Models for Damaged Waveguides

6.1 Need for Spectral Element Damage Models in Structural Health Monitoring

Composite structures provide opportunities for weight reduction, tailoring of the material properties, integrating control surfaces in the form of embedded transducers, etc. Since very few such high-importance composite structures have completed significant number of years of design life, the damage tolerance of these structures is yet to be explored. Unlike the design of metal structures, this information has not been incorporated into the design process. Therefore, a potential barrier at present is that composite structures can have internal defects that are difficult to detect and therefore need frequent monitoring to assess their vulnerability. Although matrix cracking, fiber breakage, fiber debonding, etc., initiate the damage that occurs in laminated composites, inter-laminar cracking or delamination is most important and can easily grow to reduce the life of the structure. This is because, in contrast to their in-plane properties, transverse tensile and inter-laminar shear strengths are quite low. Furthermore, material degradation defects due to porosity and moisture absorption are common in composite structures. As widely discussed in the previous chapters, meaningful damage detection analysis needs to be supported by efficient models which can simulate the presence of defects and most importantly can replicate their effects on the dynamic response of the structure. Finite element modeling of some of the above defects were addressed in Chap. 4. Although, FEM is versatile in modeling most defects, the FE model sizes places severe restriction on its use for the simulation of wave-based inspections. This aspect was discussed in Chap. 4. The main requirements of models in support of SHM are their ability to develop simplified damage models. This aspect is addressed in this chapter, while the damage detection aspect is dealt with in Chaps. 10 and 11. This chapter presents the formulation of simplified spectral element models for single and multiple delaminations, fibre breakage,

S. Gopalakrishnan et al., *Computational Techniques for Structural Health Monitoring*, Springer Series in Reliability Engineering, DOI: 10.1007/978-0-85729-284-1_6,

corrosion in metals and material degradation in composites. In the next chapter, damage models for notched type structures are presented through formulations based on perturbation techniques.

6.2 Review of Simplified Models for Structural Defects

There are a number of damage models for metallic and composite structures reported in the literature. Modeling flaws using conventional FEM is simple and straightforward and this aspect was discussed in detail in Chap. 4. Kinematics based models have received significant attention by the researchers. Some of such models use simple springs to represent damage by fine tuning the value of the spring constant until the response from the model matches experimental/FEM responses. Such models do not represent the physics of the problem accurately. That is, the presence of cracks in the structure introduces mode conversion, which is a phenomenon by which a purely axial input give rise to bending response and vice versa. In terms of Lamb wave terminology, an A_0 mode generates an S_0 mode and vice versa in the presence of damage. Simple spring models cannot capture this physics. Hence, different researchers have proposed different methods to capture mode conversion phenomena and some of these are found in [1, 6, 8, 19, 22, 23, 38, 42]. Each of these models make varying assumptions, the result of which is the increasing complexity in the formulated models. We are not discussing each of these models here. Models based on constant shear kinematics are found to be very useful in capturing accurately the dynamics of the cracked beams [1, 6]. Most of these works are ad hoc in nature and are not suitable for automation to tackle practical problems. In this chapter, a new modeling methodology under SFEM environment is outlined to model defects in beam and plates. Since SFEM is based on FE procedures, the scheme is highly suited for automation. That is, the formulated spectral damage elements can be inserted in the region of suspected damage without the need for fine meshing, normally required in the conventional FEM to capture the stress singularity at the crack tip. The utility of these formulated elements to capture the mode conversion phenomenon is also demonstrated in this chapter.

Most of damage modeling in 2D waveguides are performed using conventional FEM using the concepts outlined in Chap. 4. Some of these, especially the delamination models for composite structures are reported in [8, 15, 29, 34, 35]. However, a few researchers have used Layerwise Theories (LT) to accurately capture the response of a damaged structure. There are many variants of the LT modeling reported in the literature some of which can be found in [2, 5, 12, 30, 43, 44]. All these LT models require enormous model sizes to accurately capture the response features of a delaminated structures. One simple method to model delamination using LT or alternatively the Equivalent single layer Theory (ESLT) is to measure slope discontinuity at the crack (delamination) front. It is shown in the work of Rice and Levy [31] that the slope discontinuity at both sides of the crack location due to bending moments is proportional to bending compliance of

the crack and nominal bending stress. Using the expressions given in this paper, Khadem and Rezaee [17] obtained slope discontinuity at both sides of a hypothetical boundary along the crack in terms of the characteristics of the crack. This expression is used to introduce delamination in the spectral plate element developed in Chap. 5 (see Sect. 5.4). Similar work can be found in [18], where the delamination is modeled using isotropic spectral plate elements. In the next few subsections, simplified spectral element damage models for both 1D and 2D composite waveguides are described.

6.3 Modeling of Single Delamination or Horizontal Cracks

This model was described under the FE environment in Sect. 4.3.3 where the kinematics between the nodes of the base laminate and sub-laminates were imposed through rigid links. In this section, the system kinematics is enforced through a transformation matrix that is constructed using assumed displacement field of a 1D composite waveguide. The simplified damaged model presented in this section can be used to model single through-width delamination in composites or a through-width horizontal cracks in metals. This model can be formulated both under Fourier or Wavelet transform environment.

The location of the nodes of the spectral elements for a delaminated beam is shown in Fig. 4.7. In the absence of delamination, one spectral element between node 1 and node 2 is sufficient for the analysis. The presence of a delamination when treated as a structural discontinuity by neglecting the effect of stress singularity at the delamination tip, increases the number of elements from 1 to 4. Six more nodes are introduced to model individual base laminates and sub-laminates. For the sub-laminate elements (elements 3 and 4) the nodes are located at the mid-plane of the sub-laminates and element lengths are equal to the length of the delamination.

The kinematic assumption for the interface of base laminate and sub-laminates is that the cross-section remains straight, i.e., the slope is continuous and constant at the interface. Under this assumption, one can obtain the following equations:

$$\hat{\mathbf{u}}_{\mathbf{3}} = \begin{Bmatrix} \hat{u}_3^0 \\ \hat{\omega}_3 \\ \hat{\phi}_3 \end{Bmatrix} = \begin{Bmatrix} \hat{u}_4^0 + h_2\hat{\phi}_4 \\ \hat{\omega}_4 \\ \hat{\phi}_4 \end{Bmatrix} = \mathbf{S_1}\hat{\mathbf{u}}_{\mathbf{4}} \tag{6.1}$$

$$\hat{\mathbf{u}}_{\mathbf{5}} = \begin{Bmatrix} \hat{u}_5^0 \\ \hat{\omega}_5 \\ \hat{\phi}_5 \end{Bmatrix} = \begin{Bmatrix} \hat{u}_4^0 - h_1\hat{\phi}_4 \\ \hat{\omega}_4 \\ \hat{\phi}_4 \end{Bmatrix} = \mathbf{S_2}\hat{\mathbf{u}}_{\mathbf{4}} \tag{6.2}$$

and similarly,

$$\hat{\mathbf{u}}_{\mathbf{6}} = \mathbf{S_1}\hat{\mathbf{u}}_{\mathbf{7}}, \quad \hat{\mathbf{u}}_{\mathbf{8}} = \mathbf{S_2}\hat{\mathbf{u}}_{\mathbf{7}}. \tag{6.3}$$

Here all the vectors are marked with overhead hat to indicate that the variables are discretized in the frequency domain. Using these we can map the displacements at sub-laminate element nodes 3, 5 (on the left interface) and 6, 8 (on the right interface) in terms of displacements of base laminate nodes 4 (on the left interface) and 7 (on the right interface), respectively (see Fig. 4.7c). Also, $\mathbf{S_1}$ and $\mathbf{S_2}$ are the 3×3 transformation matrices given by

$$\mathbf{S_1} = \begin{bmatrix} 1 & 0 & h_2 \\ 0 & 1 & 0 \\ 0 & 0 & 1 \end{bmatrix}, \quad \mathbf{S_2} = \begin{bmatrix} 1 & 0 & -h_1 \\ 0 & 1 & 0 \\ 0 & 0 & 1 \end{bmatrix}. \tag{6.4}$$

From the equilibrium of the left interface *AB* (Fig. 6.1), we can draw the following force balance equation:

$$\begin{Bmatrix} \hat{N}_4 \\ \hat{V}_4 \\ \hat{M}_4 \end{Bmatrix} + \begin{Bmatrix} \hat{N}_3 \\ \hat{V}_3 \\ \hat{M}_3 \end{Bmatrix} + \begin{Bmatrix} 0 \\ 0 \\ h_2\hat{N}_3 \end{Bmatrix} + \begin{Bmatrix} \hat{N}_5 \\ \hat{V}_5 \\ \hat{M}_5 \end{Bmatrix} + \begin{Bmatrix} 0 \\ 0 \\ -h_1\hat{N}_5 \end{Bmatrix} = \begin{Bmatrix} 0 \\ 0 \\ 0 \end{Bmatrix} \tag{6.5}$$

which, in matrix form can be written as

$$\hat{\mathbf{f}}_\mathbf{4} + \mathbf{S}_\mathbf{1}^T\hat{\mathbf{f}}_\mathbf{3} + \mathbf{S}_\mathbf{2}^T\hat{\mathbf{f}}_\mathbf{5} = \mathbf{0}. \tag{6.6}$$

Similarly, from the equilibrium of the right interface *CD*, we can get

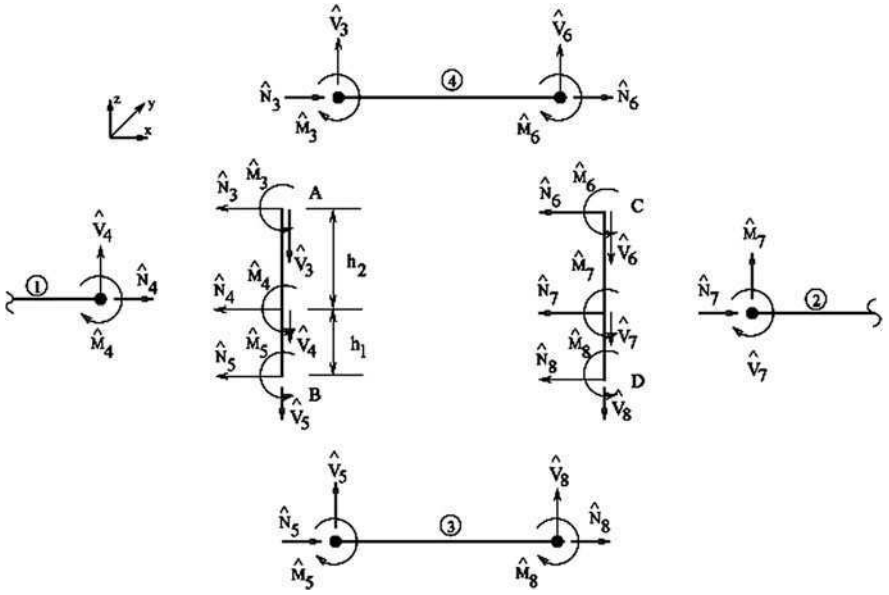

Fig. 6.1 Force balance at the interface between base laminate and sub-laminate elements

$$\hat{\mathbf{f}}_7 + \mathbf{S}_1^T \hat{\mathbf{f}}_6 + \mathbf{S}_2^T \hat{\mathbf{f}}_8 = \mathbf{0}. \tag{6.7}$$

The element equilibrium equation for the jth element ($j = 1, 2$ for base laminates, $j = 3, 4$ for sub-laminates) with nodes p and q can be written as

$$\hat{\mathbf{K}}^{(j)}_{(6\times6)} \begin{Bmatrix} \hat{\mathbf{u}}_\mathbf{p} \\ \hat{\mathbf{u}}_\mathbf{q} \end{Bmatrix} = \begin{Bmatrix} \hat{\mathbf{f}}_\mathbf{p} \\ \hat{\mathbf{f}}_\mathbf{q} \end{Bmatrix}. \tag{6.8}$$

This equation can be rewritten using 3×3 sub-matrices of the stiffness matrix as

$$\begin{bmatrix} \hat{\mathbf{K}}^{(\mathbf{j})}_{\mathbf{11}} & \hat{\mathbf{K}}^{(\mathbf{j})}_{\mathbf{12}} \\ \hat{\mathbf{K}}^{(\mathbf{j})}_{\mathbf{21}} & \hat{\mathbf{K}}^{(\mathbf{j})}_{\mathbf{22}} \end{bmatrix}_{(6\times6)} \begin{Bmatrix} \hat{\mathbf{u}}_\mathbf{p} \\ \hat{\mathbf{u}}_\mathbf{q} \end{Bmatrix} = \begin{Bmatrix} \hat{\mathbf{f}}_\mathbf{p} \\ \hat{\mathbf{f}}_\mathbf{q} \end{Bmatrix}. \tag{6.9}$$

The above equation for the local element 1 can be written as

$$\begin{bmatrix} \hat{\mathbf{K}}^{(1)}_{\mathbf{11}} & \hat{\mathbf{K}}^{(1)}_{\mathbf{12}} \\ \hat{\mathbf{K}}^{(1)}_{\mathbf{21}} & \hat{\mathbf{K}}^{(1)}_{\mathbf{22}} \end{bmatrix}_{(6\times6)} \begin{Bmatrix} \hat{\mathbf{u}}_\mathbf{1} \\ \hat{\mathbf{u}}_\mathbf{4} \end{Bmatrix} = \begin{Bmatrix} \hat{\mathbf{f}}_\mathbf{1} \\ \hat{\mathbf{f}}_\mathbf{4} \end{Bmatrix}. \tag{6.10}$$

For local element 2, we have

$$\begin{bmatrix} \hat{\mathbf{K}}^{(2)}_{\mathbf{11}} & \hat{\mathbf{K}}^{(2)}_{\mathbf{12}} \\ \hat{\mathbf{K}}^{(2)}_{\mathbf{21}} & \hat{\mathbf{K}}^{(2)}_{\mathbf{22}} \end{bmatrix}_{(6\times6)} \begin{Bmatrix} \hat{\mathbf{u}}_\mathbf{7} \\ \hat{\mathbf{u}}_\mathbf{2} \end{Bmatrix} = \begin{Bmatrix} \hat{\mathbf{f}}_\mathbf{7} \\ \hat{\mathbf{f}}_\mathbf{2} \end{Bmatrix}. \tag{6.11}$$

For local element 3, we have

$$\begin{bmatrix} \hat{\mathbf{K}}^{(3)}_{\mathbf{11}} & \hat{\mathbf{K}}^{(3)}_{\mathbf{12}} \\ \hat{\mathbf{K}}^{(3)}_{\mathbf{21}} & \hat{\mathbf{K}}^{(3)}_{\mathbf{22}} \end{bmatrix}_{(6\times6)} \begin{Bmatrix} \hat{\mathbf{u}}_\mathbf{5} \\ \hat{\mathbf{u}}_\mathbf{8} \end{Bmatrix} = \begin{Bmatrix} \hat{\mathbf{f}}_\mathbf{5} \\ \hat{\mathbf{f}}_\mathbf{8} \end{Bmatrix}. \tag{6.12}$$

Expressing $\hat{\mathbf{u}}_\mathbf{5}$ and $\hat{\mathbf{u}}_\mathbf{8}$ in terms of $\hat{\mathbf{u}}_\mathbf{4}$ and $\hat{\mathbf{u}}_\mathbf{7}$ respectively (Eqs. 6.2 and 6.3) and pre-multiplying both sides by $\mathbf{S}_2^T$, we get

$$\begin{bmatrix} \mathbf{S}_2^T \hat{\mathbf{K}}^{(3)}_{\mathbf{11}} \mathbf{S}_2 & \mathbf{S}_2^T \hat{\mathbf{K}}^{(3)}_{\mathbf{12}} \mathbf{S}_2 \\ \mathbf{S}_2^T \hat{\mathbf{K}}^{(3)}_{\mathbf{21}} \mathbf{S}_2 & \mathbf{S}_2^T \hat{\mathbf{K}}^{(3)}_{\mathbf{22}} \mathbf{S}_2 \end{bmatrix}_{(6\times6)} \begin{Bmatrix} \hat{\mathbf{u}}_\mathbf{4} \\ \hat{\mathbf{u}}_\mathbf{7} \end{Bmatrix} = \begin{Bmatrix} \mathbf{S}_2^T \hat{\mathbf{f}}_\mathbf{5} \\ \mathbf{S}_2^T \hat{\mathbf{f}}_\mathbf{8} \end{Bmatrix}. \tag{6.13}$$

For the local element 4, we have

$$\begin{bmatrix} \hat{\mathbf{K}}^{(4)}_{\mathbf{11}} & \hat{\mathbf{K}}^{(4)}_{\mathbf{12}} \\ \hat{\mathbf{K}}^{(4)}_{\mathbf{21}} & \hat{\mathbf{K}}^{(4)}_{\mathbf{22}} \end{bmatrix}_{(6\times6)} \begin{Bmatrix} \hat{\mathbf{u}}_\mathbf{3} \\ \hat{\mathbf{u}}_\mathbf{6} \end{Bmatrix} = \begin{Bmatrix} \hat{\mathbf{f}}_\mathbf{3} \\ \hat{\mathbf{f}}_\mathbf{6} \end{Bmatrix}. \tag{6.14}$$

Similarly expressing $\hat{\mathbf{u}}_\mathbf{3}$ and $\hat{\mathbf{u}}_\mathbf{6}$ in terms of $\hat{\mathbf{u}}_\mathbf{4}$ and $\hat{\mathbf{u}}_\mathbf{7}$ respectively (Eqs. 6.1–6.3) and pre-multiplying both sides by $\mathbf{S}_1^T$, we get

$$\begin{bmatrix} \mathbf{S}_1^T \hat{\mathbf{K}}^{(4)}_{\mathbf{11}} \mathbf{S}_1 & \mathbf{S}_1^T \hat{\mathbf{K}}^{(4)}_{\mathbf{12}} \mathbf{S}_1 \\ \mathbf{S}_1^T \hat{\mathbf{K}}^{(4)}_{\mathbf{21}} \mathbf{S}_1 & \mathbf{S}_1^T \hat{\mathbf{K}}^{(4)}_{\mathbf{22}} \mathbf{S}_1 \end{bmatrix}_{(6\times6)} \begin{Bmatrix} \hat{\mathbf{u}}_\mathbf{4} \\ \hat{\mathbf{u}}_\mathbf{7} \end{Bmatrix} = \begin{Bmatrix} \mathbf{S}_1^T \hat{\mathbf{f}}_\mathbf{3} \\ \mathbf{S}_1^T \hat{\mathbf{f}}_\mathbf{6} \end{Bmatrix}. \tag{6.15}$$

After assembly of the above equations for the four local elements (two base laminates and two sub-laminates) and subsequent use of Eqs. 6.6 and 6.7 yield the following matrix equation:

$$\hat{\hat{\mathbf{K}}}\begin{Bmatrix}\hat{\mathbf{u}}_1\\ \hat{\mathbf{u}}_4\\ \hat{\mathbf{u}}_7\\ \hat{\mathbf{u}}_2\end{Bmatrix} = \begin{Bmatrix}\hat{\mathbf{f}}_1\\ \mathbf{0}\\ \mathbf{0}\\ \hat{\mathbf{f}}_2\end{Bmatrix}, \tag{6.16}$$

where $\hat{\hat{\mathbf{K}}}$ is

$$\begin{bmatrix} \hat{\mathbf{K}}_{11}^{(1)} & \hat{\mathbf{K}}_{12}^{(1)} & \mathbf{0} & \mathbf{0} \\ \hat{\mathbf{K}}_{21}^{(1)} & \hat{\mathbf{K}}_{22}^{(1)} + \mathbf{S}_1^T\hat{\mathbf{K}}_{11}^{(4)}\mathbf{S}_1 + \mathbf{S}_2^T\hat{\mathbf{K}}_{11}^{(3)}\mathbf{S}_2 & \mathbf{S}_1^T\hat{\mathbf{K}}_{12}^{(4)}\mathbf{S}_1 + \mathbf{S}_2^T\hat{\mathbf{K}}_{12}^{(3)}\mathbf{S}_2 & \mathbf{0} \\ \mathbf{0} & \mathbf{S}_1^T\hat{\mathbf{K}}_{21}^{(4)}\mathbf{S}_1 + \mathbf{S}_2^T\hat{\mathbf{K}}_{21}^{(3)}\mathbf{S}_2 & \mathbf{S}_1^T\hat{\mathbf{K}}_{22}^{(4)}\mathbf{S}_1 + \mathbf{S}_2^T\hat{\mathbf{K}}_{22}^{(3)}\mathbf{S}_2 + \hat{\mathbf{K}}_{11}^{(2)} & \hat{\mathbf{K}}_{12}^{(2)} \\ \mathbf{0} & \mathbf{0} & \hat{\mathbf{K}}_{21}^{(2)} & \hat{\mathbf{K}}_{22}^{(2)} \end{bmatrix}.$$

Upon condensation of the degrees of freedom at the internal nodes 4 and 7, the final form of the equilibrium equation is obtained as

$$\hat{\hat{\mathbf{K}}}_{(6\times6)}\begin{Bmatrix}\hat{\mathbf{u}}_1\\ \hat{\mathbf{u}}_2\end{Bmatrix} = \begin{Bmatrix}\hat{\mathbf{f}}_1\\ \hat{\mathbf{f}}_2\end{Bmatrix}, \tag{6.17}$$

where $\hat{\hat{\mathbf{K}}}$ is the reconstructed stiffness matrix for the *spectral element with embedded delamination*. Now, one only needs to replace the usual spectral element with this spectral element wherever a possible delamination may exist in composite beams and frame structures, keeping the original nodes unaltered. Hence, it is evident that insertion of this element in a modular approach is suitable for faster modeling and accurate prediction of delaminations in composite beams and frames with partial measurement of sensor signals.

In the above formulation, we have not considered the effect of distributed contact between the delaminated surfaces, at the top from the sub-laminate (4) and at the bottom from the sub-laminate (3) (Fig. 6.2). In the present study, this is modeled as a viscoelastic layer between the delaminated surfaces. This model not only includes the effect of interfacial frictional slip under Mode-II fracture but also can be used as a linearized model to restrict the interpenetration and frictional contact under Mode-I fracture. However, more complex models considering a non-linear spring to restrict the occurrence of the incompatible modes due to interpenetration can be developed. Such aspects have been studied semi-analytically in [22].

Figure 6.2 shows the delaminated zone between two delaminated surfaces. Let us consider the distributed spring constants K_x and K_z, and the distributed viscous damping coefficients C_x and C_z. The spectral amplitude of the distributed contact force vectors $\hat{\Gamma}_t$ acting on the top surface of sub-laminate (3) and $\hat{\Gamma}_b$ acting on the

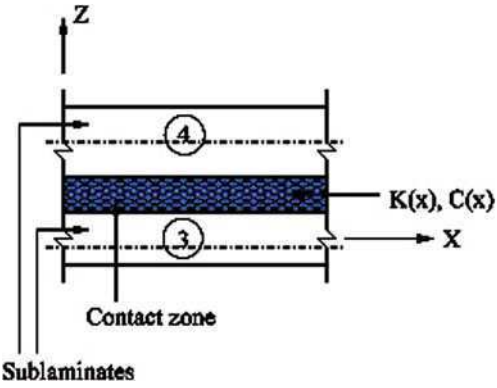

Fig. 6.2 Distributed contact idealized through distributed linear spring **K** and distributed linear viscous damper **C** between the delaminated surfaces. The waveguides (4) and (3) represents the top and bottom sub-laminates respectively as shown in Fig. 4.7a

bottom surface sub-laminate (4) and consisting of longitudinal force along x, transverse force along z and moment about y due to relative motion between the top and bottom surfaces can be expressed as

$$\hat{\mathbf{\Gamma}}_t = \begin{bmatrix} K_x + i\omega_n C_x & 0 \\ 0 & K_z + i\omega_n C_z \\ z_{bt}(K_x + i\omega_n C_x) & 0 \end{bmatrix} \begin{Bmatrix} \hat{u}_b - \hat{u}_t \\ \hat{w}_b - \hat{w}_t \end{Bmatrix} = \mathbf{K}^*(\hat{\mathbf{u}}_\mathbf{b} - \hat{\mathbf{u}}_\mathbf{t}), \tag{6.18}$$

$$\hat{\mathbf{\Gamma}}_b = -\hat{\mathbf{\Gamma}}_t \tag{6.19}$$

where the subscripts t and b respectively indicate the quantities associated with the top surface of the sub-laminate (3) and the bottom surface of the sub-laminate (4). In Eq. 6.18, z_{bt} is the depth of separation between the delaminated surfaces. Considering the displacement field according to the Timoshenko beam theory in Eq. 2.129, the top surface displacement vector $\hat{\mathbf{u}}_\mathbf{t}$ for sub-laminate (3) can be expressed as

$$\hat{\mathbf{u}}_\mathbf{t} = \begin{Bmatrix} \hat{u}_t \\ \hat{w}_t \end{Bmatrix} = \begin{bmatrix} 1 & 0 & z_t^{(3)} \\ 0 & 1 & 0 \end{bmatrix} \hat{\mathbf{u}}(x, \omega_n)^{(3)} = \bar{\mathbf{S}}_\mathbf{1} \hat{\mathbf{u}}(x, \omega_n)^{(3)} \tag{6.20}$$

and similarly, the bottom surface displacement vector $\hat{\mathbf{u}}_\mathbf{b}$ for sub-laminate (4) can be expressed as

$$\hat{\mathbf{u}}_\mathbf{b} = \begin{Bmatrix} \hat{u}_b \\ \hat{w}_b \end{Bmatrix} = \begin{bmatrix} 1 & 0 & z_b^{(4)} \\ 0 & 1 & 0 \end{bmatrix} \hat{\mathbf{u}}(x, \omega_n)^{(4)} = \bar{\mathbf{S}}_\mathbf{2} \hat{\mathbf{u}}(x, \omega_n)^{(4)} \tag{6.21}$$

where $z_t^{(3)}$ denotes the depth of the top surface measured from the local reference plane of the sub-laminate (3) and $z_b^{(4)}$ denotes the depth of the bottom surface measured from the local reference plane of the sub-laminate (4). Using the generic displacement vector $\hat{\mathbf{u}}(x, \omega_n)^{(3)}$ and $\hat{\mathbf{u}}(x, \omega_n)^{(4)}$ in terms of the spectral element shape function matrices and nodal displacement vectors, a consistent nodal force vector can be formed. Thus, for sub-laminate (3), the consistent nodal force vector is $\hat{\mathbf{f}}^{e_{(3)}} = \int_0^L \mathcal{N}_{(3)}^{e^T} \hat{\mathbf{\Gamma}}_t \, dx.$, where $\mathcal{N}_{(3)}^{e^T}$ is the shape function matrix for element 3. It is

to be noted that the above method of modeling delamination can be incorporated both under Fourier transform or Wavelet transform environment. That is, the respective healthy spectral elements required to model beam segments before and ahead of the crack front could be either WSFEM or FSFEM depending on the transform domain in which the problem is solved.

6.3.1 Wave Scattering in a Delaminated Beam Using Wavelet Spectral Elements

This problem is solved in wavelet domain using the formulated WSFE model of delaminated composite beam. The analysis is performed on different fixed-free delaminated AS4/3501-6 graphite-epoxy beams. The material properties of the beam are given in Table 6.1. The beam configuration is shown in Fig. 6.3, where, L and L_d are the lengths of the beam and delamination respectively and L_1 is the distance of the delamination from the free end of the beam.

The cross-sectional dimension is $0.01 \times 0.01\,m^2$ with depth $2h = 0.01\,m$ and width $2b = 0.01\,m$. Numerical examples are presented for different values of these lengths, ply-lay up sequences and positions of delaminations along the thickness of the beam. In addition, the wave propagation responses are studied for both broad-banded impulse (see Fig. 3.7) and narrow-banded modulated pulse loadings. The unit broadband impulse load used has a duration of 50 μs and a frequency content of 44 kHz. Similarly, the modulated pulse loading with central frequency of 70 kHz is shown in time and frequency domains in Fig. 6.4. The WSFE model is formulated with $N = 22$ and a time sampling rate $\Delta t = 2\,\mu s$. A single spectral element is used to simulate the responses.

First, the WSFE model of delaminated beam is validated with responses simulated using a 2D FE model. The transverse tip velocity of beam shown in Fig. 6.3 with ply-layup $[0]_8, L = 0.5\,m$ and $L_1 = 0.25\,m$ is plotted for centerline delamination length of $L_d = 20\,mm$ and compared with the response obtained using 2D FE in Fig. 6.5a. The FE result is obtained using 400, 4-noded quadrilateral plane stress elements and Newmark's time integration with time step 1 μs. It can be seen that results compare well. However, the small difference in the wave speeds predicted by the two methods can be further reduced by refining the FE mesh.

Table 6.1 Properties of AS4/3501-6 graphite-epoxy beams

Material properties	
E_{11} (GPa)	141.9
E_{22} (GPa)	9.78
$G_{12} = G_{13}$ (GPa)	6.13
G_{23} (GPa)	4.80
ν_{12}	0.42
ρ	$1,449\,kg/m^3$

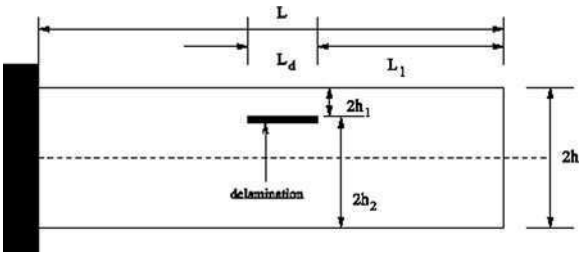

Fig. 6.3 Fixed-free beam configuration with mid-plane delamination

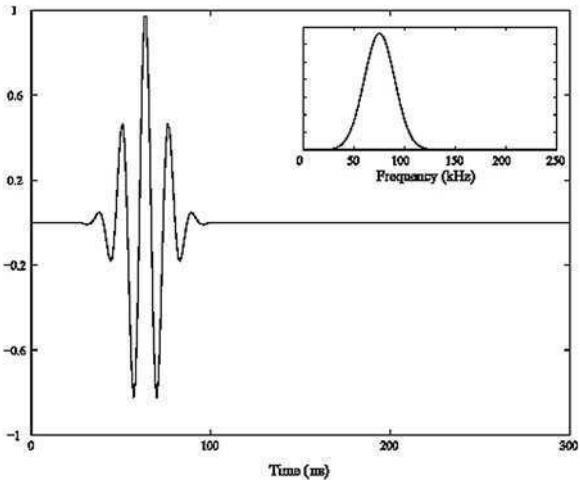

Fig. 6.4 Narrow-banded pulse modulated at 70 kHz in time and frequency (*inset*) domain

In Fig. 6.5b, the transverse tip velocities of same beam configuration are plotted, but, for different lengths, L_d, of delaminations and are compared with the undamaged response. The delaminations are along the centerline of the beam and are of lengths $L_d = 10, 20$ and 30 mm. It can be seen that in addition to the reflection from the fixed end, the damaged responses show early reflections generated from the delaminations and amplitudes of these reflected waves increases with increase in delamination lengths, as expected. Similar tip transverse velocities are presented in Fig. 6.5c, except that, here, the delamination length is kept fixed at $L_d = 20$ mm while the positions along the thickness direction are varied from $h_1 = h, h/2$ and $h/4$ (see Fig. 6.3). As in the previous plot, even here, the damaged responses show reflections from the delaminations and it can be observed that their amplitudes increase as h_1 i.e. depth of the delamination from the top surface of the beam decreases. In Fig. 6.5d, the transverse velocities due to tip transverse impulse load are plotted for beams with different ply orientation sequences. In all the cases, the beam configuration is similar to Fig. 6.3 with $L = 0.5$ m, $L_1 = 0.25$ m and centerline delamination of $L_d = 20$ mm. The three ply-layups used are $[0]_8, [45]_8$ and $[60]_8$. Different ply-layups change the stiffness of the beam and hence the wave speeds also change as seen from Fig. 6.5d, where the responses show different amplitudes and time of arrival of reflections. The $[0]_8$ beam has the

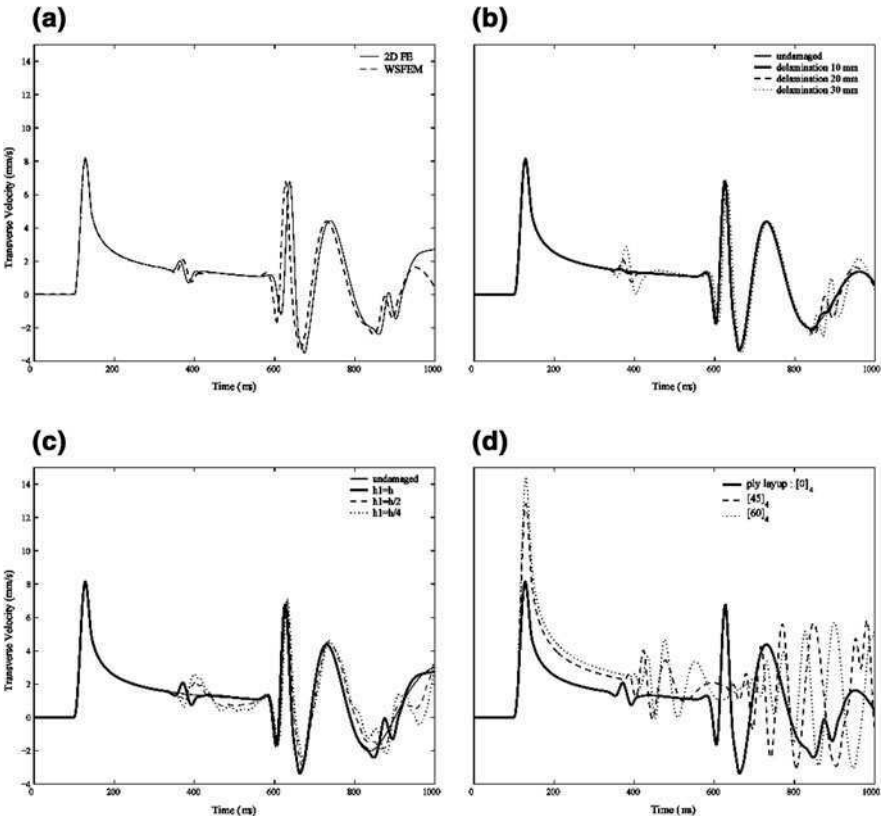

Fig. 6.5 Transverse tip velocity of fixed-free graphite-epoxy beam due to tip impulse load applied in transverse direction with **a** delamination length $L_d = 20$ mm (validated with 2D FE) **b** different delamination lengths $L_d = 10, 20, 30$ mm **c** delaminations at different heights above centreline **d** different ply-lay up $[0]_8, [45]_8, [60]_8$

lowest amplitude and the time of arrival as it has the highest flexural stiffness and hence highest group speed.

Next, numerical experiments are performed using narrow-band sinusoidal load (see Fig. 6.4) with central frequency of 70 kHz as input excitation. For such loading, the waves non-dispersively and used for damage detection. The load is again applied in transverse direction at the tip of a $[0]_8$ beam shown in Fig. 6.3 with $L = 0.5$ m and $L_1 = 0.25$ m. The responses studied are the transverse velocities measured at the tip. In Figs. 6.6a–c, the velocities of undamaged and delaminated beams with $L_d = 10$ and 20 mm are plotted respectively. In either cases, the delamination is along the centerline of the beam. Similar to the responses due to impulse loading in previous example, the damaged responses here show an additional reflection from the delamination and their amplitude increases with increase in the delamination length. From these plots, the

positions of damages can be obtained directly using the time of arrival and wave speed.

6.3.2 *Effect of Wave Scattering Due to Delamination at Ply-Drops*

The formulated damaged spectral element based on Fourier Transform (FSFEM) is used to study wave scattering due to a delamination at the ply drop. These regions are highly susceptible to such damages due to the presence of high stress gradients arising out of thickness loss.

In health monitoring applications, detection of delaminations near ply-drops, composite joints or other structural discontinuities is of great practical relevance. If the delamination length is small, the same modeling strategy used for delamination modeling can be used. A cantilever beam with the same material properties as used

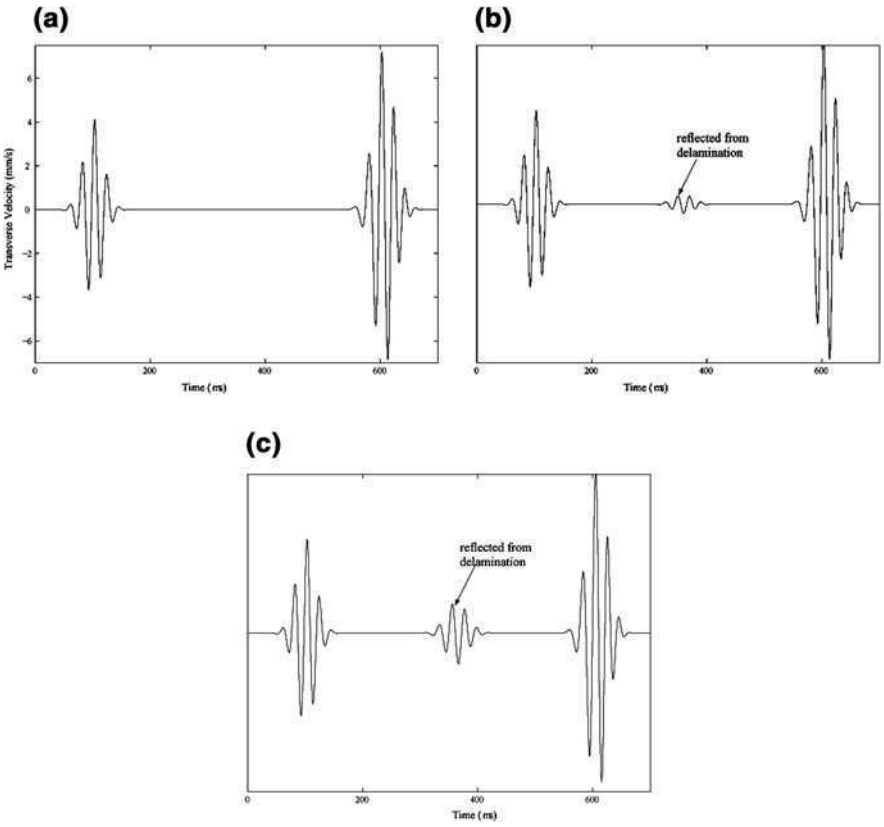

Fig. 6.6 Transverse velocities of fixed-free graphite-epoxy beam due to narrow-banded load at 50 kHz applied in transverse direction **a** undamaged, **b** delaminated $L_d = 10\,\text{mm}$ and **c** $L_d = 20\,\text{mm}$

in the previous illustration and with ply-drops (Fig. 6.7) is considered. The model has five plies dropped from the top, out of 15 plies on the fixed end side of the cantilever. A 20 mm long delamination is considered at the location of the ply-drops. Only two spectral elements are used in the model. Transverse velocity histories at the free end are plotted in Fig. 6.8. For the healthy case, two reflections can be seen; first, one from the ply-drop due to a sudden change in the thickness, and the second one from the fixed end of the beam. For the second case with delamination, the reflection from the ply-drop region is seen to be intensified showing a distinct blob. In actual experimental study, one can use a second transducer pair to generate the incident pulse and also measure the reflected pulse both on the both ends of delamination. Thus, by measuring the reflected waves on both sides of the delamination, it is possible to predict the length of the delamination accurately. Also, the reference structural database can be updated in the presence of any local material degradation by correlating the measured signal and simulated signal using the present spectral element model.

6.4 Modeling of Fiber Breakage and Vertical Cracks

This model was previously described in the context of FEs in Sect. 4.3.3 to model vertical cracks in metals or fibre breaks in composites. Here, we extend the approach to the SFEM environment. For this purpose, we consider Fig. 4.8. As in the case of horizontal cracks, the method was implemented using rigid links (see Chap. 4) for enforcing kinematics between nodes surrounding the damage. In this section, the kinematics is enforced through a transformation matrix constructed using the beam displacement field.

The philosophy behind this approach is the same as that of the horizontal crack model. The cracked member is split into sub-laminates and base laminates, enforcing the kinematics on nodes forming the damage and eliminating the internal nodes through a dynamic condensation procedure. The spectral element model for individual base or sub-laminates could be either FFT based or wavelet based spectral elements.

In the absence of any crack, a single spectral element between node 1 and node 2 (Fig. 4.8a) is sufficient to capture the exact dynamics of the beam. Let us consider a transverse crack in a beam that requires explicit definition by three additional parameters. These three parameters are (1) the span-wise location of the transverse crack ($x = L_1 + \Delta L/2$ as shown in Fig. 4.8a, L_1 and ΔL will be defined later),

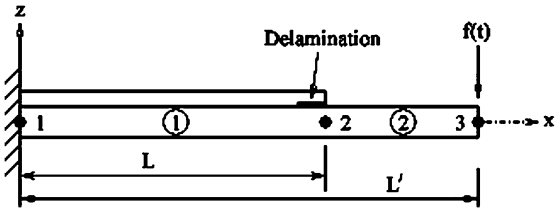

Fig. 6.7 Configuration of the cantilever beam showing a delamination in the region of ply-drops. $L = 1$ m, $L' = 1.5$ m

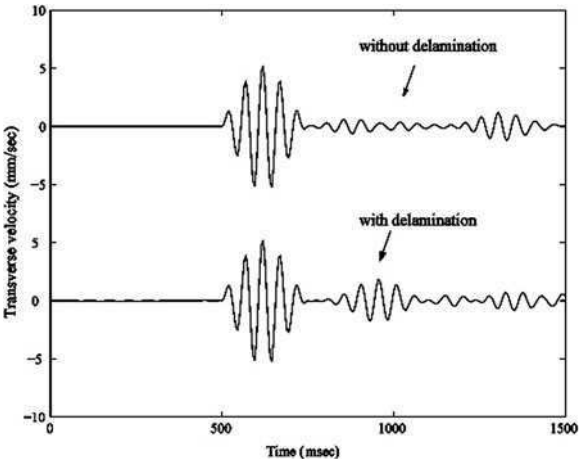

Fig. 6.8 Transverse velocity $\dot{w}$ at the free end due to modulated sine pulse applied transversely at the free end of the cantilever beam with ply-drops

(2) the thickness-wise location of the bottom crack-tip ($z = d_1$), (3) the thickness-wise location of the top crack-tip ($z = d_2, h = d_2 - d_1$ is the crack depth). We assume that the transverse crack is a through-width crack (along the y direction), which allows modeling to be accomplished using one-dimensional waveguides. The element discretization shown in Fig. 4.8b corresponds to six internal waveguides numbered (1)–(6). For all these elements, a total of ten additional nodes apart from node 1 and node 2 will appear in the formulation, and the degrees of freedom associated with them will be condensed out systematically. As a result, a simple two-node element can be used to model the transverse crack in a metallic or composite beam, where faster and repeated analysis with acceptable accuracy will be of prime importance for damage identification studies and various SHM applications in conjunction with a wave-based diagnostic signal.

Since the main objective behind using such a model is to improve upon the various available approximate models based on equivalent flexibility, empirical crack functions, etc., it is essential for the proposed element discretization technique (Fig. 4.8) that any spurious scattering effect is avoided. It can be seen in Fig. 4.8 that the elements (3) and (4) are expected to behave as hanging elements, especially when their lengths become longer. This can be avoided in two ways. Either a bound on the length of the elements (3) and (4) in terms of the incident wavelength can be imposed or appropriate constraints on the top and bottom surfaces of elements (3) and (4) can be imposed by choosing higher lengths.

Calculations for implementing both options are presented below. A bound on the length of the hanging elements is imposed for comparison with standard FE results and other numerical simulations. The constrained equations for unbounded length of the hanging elements are formulated after the basic element formulation.

We consider equal lengths of hanging laminates denoted by $\Delta L/2$ as shown in Fig. 4.8b. For any arbitrary dynamic excitation involving multiple harmonics, the bound on the length of the hanging laminates is imposed in terms of the smallest group wavelength, which is given by

$$\Delta L < \mathrm{Min}(\lambda_g), \quad \lambda_g = c_g/\omega_g \tag{6.22}$$

where c_g is the group wave velocity defined as $c_g = d\omega/dk$, k is the wavenumber, $\omega_g = \omega/2\pi$ is the excitation frequency. As the frequency increases, the group wavelength λ_g decreases. Note that λ_g is the same as the wavelength $\lambda = c/\omega_g$ for single frequency excitation, where c is the phase velocity, but is different from λ for a band-limited excitation about a central frequency. Considering the arrival of the waves through the uncracked base laminates, Eq. 6.22 can now can be used to eliminate any spurious scattering of wave in an approximate manner.

The kinematic assumption adopted in the present formulation is that the cross-sectional interfaces between the base laminate, the sub-laminates and the hanging laminates remain straight, i.e., the slope is continuous and constant at these interfaces. Under this assumption, one can relate the nodal degrees of freedom at the interfaces as follows:

$$\hat{\mathbf{u}}_7 = \begin{Bmatrix} \hat{u}_7^o \\ \hat{\omega}_7 \\ \hat{\phi}_7 \end{Bmatrix} = \begin{Bmatrix} \hat{u}_5^o + h_1\hat{\phi}_5 \\ \hat{\omega}_5 \\ \hat{\phi}_5 \end{Bmatrix} = \mathbf{S_1}\hat{\mathbf{u}}_5 \tag{6.23}$$

$$\hat{\mathbf{u}}_8 = \begin{Bmatrix} \hat{u}_8^o \\ \hat{\omega}_8 \\ \hat{\phi}_8 \end{Bmatrix} = \begin{Bmatrix} \hat{u}_5^o + h_2\hat{\phi}_5 \\ \hat{\omega}_5 \\ \hat{\phi}_5 \end{Bmatrix} = \mathbf{S_2}\hat{\mathbf{u}}_5 \tag{6.24}$$

$$\hat{\mathbf{u}}_9 = \begin{Bmatrix} \hat{u}_9^0 \\ \hat{\omega}_9 \\ \hat{\phi}_9 \end{Bmatrix} = \begin{Bmatrix} \hat{u}_5^0 + h_3\hat{\phi}_5 \\ \hat{\omega}_5 \\ \hat{\phi}_5 \end{Bmatrix} = \mathbf{S_3}\hat{\mathbf{u}}_5 \tag{6.25}$$

and similarly,

$$\hat{\mathbf{u}}_{10} = \mathbf{S_1}\hat{\mathbf{u}}_6, \quad \hat{\mathbf{u}}_{11} = \mathbf{S_2}\hat{\mathbf{u}}_6, \quad \hat{\mathbf{u}}_{12} = \mathbf{S_3}\hat{\mathbf{u}}_6 \tag{6.26}$$

where

$$\mathbf{S_1} = \begin{bmatrix} 1 & 0 & h_1 \\ 0 & 1 & 0 \\ 0 & 0 & 1 \end{bmatrix}, \quad \mathbf{S_2} = \begin{bmatrix} 1 & 0 & h_2 \\ 0 & 1 & 0 \\ 0 & 0 & 1 \end{bmatrix}, \quad \mathbf{S_3} = \begin{bmatrix} 1 & 0 & h_3 \\ 0 & 1 & 0 \\ 0 & 0 & 1 \end{bmatrix}. \tag{6.27}$$

6.4.1 Interface Equilibrium of Forces

Considering the left interface between the base laminate and sub-laminates (Fig. 4.8), the equilibrium of the associated nodal forces can be written as

$$\begin{Bmatrix} \hat{N}_5 \\ \hat{V}_5 \\ \hat{M}_5 \end{Bmatrix} + \begin{Bmatrix} \hat{N}_7 \\ \hat{V}_7 \\ \hat{M}_7 + h_1\hat{N}_7 \end{Bmatrix} + \begin{Bmatrix} \hat{N}_8 \\ \hat{V}_8 \\ \hat{M}_8 + h_2\hat{N}_8 \end{Bmatrix} + \begin{Bmatrix} \hat{N}_9 \\ \hat{V}_9 \\ \hat{M}_9 + h_3\hat{N}_9 \end{Bmatrix} = \begin{Bmatrix} 0 \\ 0 \\ 0 \end{Bmatrix} \tag{6.28}$$

which, in matrix form and with the help of Eq. 6.27, can be expressed as

$$\hat{\mathbf{f}}_5 + \mathbf{S}_1^T\hat{\mathbf{f}}_7 + \mathbf{S}_2^T\hat{\mathbf{f}}_8 + \mathbf{S}_3^T\hat{\mathbf{f}}_9 = \mathbf{0}. \tag{6.29}$$

Similarly, considering the right interface between the base laminate and sub-laminates, the equilibrium of the associated nodal forces can be expressed as

$$\hat{\mathbf{f}}_6 + \mathbf{S}_1^T\hat{\mathbf{f}}_{10} + \mathbf{S}_2^T\hat{\mathbf{f}}_{12} + \mathbf{S}_3^T\hat{\mathbf{f}}_{12} = \mathbf{0}. \tag{6.30}$$

At the crack surface,

$$\hat{\mathbf{f}}_3 + \hat{\mathbf{f}}_4 = \mathbf{0} \tag{6.31}$$

and under the assumption of no contact between the crack surfaces, $\hat{\mathbf{f}}_3 = \mathbf{0}$ and $\hat{\mathbf{f}}_4 = \mathbf{0}$. The effect of contact between the crack surfaces will be dealt with as a separate case in Sect. 6.4.3.

6.4.2 Assembly of the Element Internal Waveguides

The element equilibrium equation for the jth element-internal waveguide ($j = 1, 2$ for base laminates, $j = 5, 6$ for sub-laminates and $j = 3, 4$ for hanging laminates as shown in Fig. 4.8) with nodes p and q can be expressed generically as

$$\begin{bmatrix} \hat{\mathbf{K}}_{11}^{(j)} & \hat{\mathbf{K}}_{12}^{(j)} \\ \hat{\mathbf{K}}_{21}^{(j)} & \hat{\mathbf{K}}_{22}^{(j)} \end{bmatrix}_{(6\times6)} \begin{Bmatrix} \hat{\mathbf{u}}_p \\ \hat{\mathbf{u}}_q \end{Bmatrix} = \begin{Bmatrix} \hat{\mathbf{f}}_p \\ \hat{\mathbf{f}}_q \end{Bmatrix}. \tag{6.32}$$

The above equation, for the internal element (1) is

$$\begin{bmatrix} \hat{\mathbf{K}}_{11}^{(1)} & \hat{\mathbf{K}}_{12}^{(1)} \\ \hat{\mathbf{K}}_{21}^{(1)} & \hat{\mathbf{K}}_{22}^{(1)} \end{bmatrix}_{(6\times6)} \begin{Bmatrix} \hat{\mathbf{u}}_1 \\ \hat{\mathbf{u}}_5 \end{Bmatrix} = \begin{Bmatrix} \hat{\mathbf{f}}_1 \\ \hat{\mathbf{f}}_5 \end{Bmatrix} \tag{6.33}$$

or for the internal element (2),

$$\begin{bmatrix} \hat{\mathbf{K}}_{11}^{(2)} & \hat{\mathbf{K}}_{12}^{(2)} \\ \hat{\mathbf{K}}_{21}^{(2)} & \hat{\mathbf{K}}_{22}^{(2)} \end{bmatrix}_{(6\times6)} \begin{Bmatrix} \hat{\mathbf{u}}_6 \\ \hat{\mathbf{u}}_2 \end{Bmatrix} = \begin{Bmatrix} \hat{\mathbf{f}}_6 \\ \hat{\mathbf{f}}_2 \end{Bmatrix} \tag{6.34}$$

Similarly, for the internal element (3), we have

$$\begin{bmatrix} \hat{\mathbf{K}}_{11}^{(3)} & \hat{\mathbf{K}}_{12}^{(3)} \\ \hat{\mathbf{K}}_{21}^{(3)} & \hat{\mathbf{K}}_{22}^{(3)} \end{bmatrix}_{(6\times6)} \begin{Bmatrix} \hat{\mathbf{u}}_8 \\ \hat{\mathbf{u}}_3 \end{Bmatrix} = \begin{Bmatrix} \hat{\mathbf{f}}_8 \\ \hat{\mathbf{f}}_3 \end{Bmatrix}. \tag{6.35}$$

Expressing $\hat{\mathbf{u}}_8$ in terms of $\hat{\mathbf{u}}_5$ with the help of Eq. 6.24 and pre multiplying both sides of Eq. 6.35 by $\mathbf{S}_2^T$, we get

$$\begin{bmatrix} \mathbf{S}_2^T\hat{\mathbf{K}}_{11}^{(3)}\mathbf{S}_2 & \mathbf{S}_2^T\hat{\mathbf{K}}_{12}^{(3)} \\ \mathbf{S}_2^T\hat{\mathbf{K}}_{21}^{(3)}\mathbf{S}_2 & \mathbf{S}_2^T\hat{\mathbf{K}}_{22}^{(3)} \end{bmatrix}_{(6\times6)} \begin{Bmatrix} \hat{\mathbf{u}}_5 \\ \hat{\mathbf{u}}_3 \end{Bmatrix} = \begin{Bmatrix} \mathbf{S}_2^T\hat{\mathbf{f}}_8 \\ \mathbf{S}_2^T\hat{\mathbf{f}}_3 \end{Bmatrix}. \tag{6.36}$$

The equilibrium equation for the internal element (4) is

$$\begin{bmatrix} \hat{\mathbf{K}}_{11}^{(4)} & \hat{\mathbf{K}}_{12}^{(4)} \\ \hat{\mathbf{K}}_{21}^{(4)} & \hat{\mathbf{K}}_{22}^{(4)} \end{bmatrix}_{(6\times6)} \begin{Bmatrix} \hat{\mathbf{u}}_4 \\ \hat{\mathbf{u}}_{11} \end{Bmatrix} = \begin{Bmatrix} \hat{\mathbf{f}}_4 \\ \hat{\mathbf{f}}_{12} \end{Bmatrix}. \tag{6.37}$$

Expressing $\hat{\mathbf{u}}_{11}$ in terms of $\hat{\mathbf{u}}_6$ with the help of Eq. 6.26 and pre multiplying both sides of Eq. 6.37 by $\mathbf{S}_2^T$, we get

$$\begin{bmatrix} \mathbf{S}_2^T\hat{\mathbf{K}}_{11}^{(4)} & \mathbf{S}_2^T\hat{\mathbf{K}}_{12}^{(4)}\mathbf{S}_2 \\ \mathbf{S}_2^T\hat{\mathbf{K}}_{21}^{(4)} & \mathbf{S}_2^T\hat{\mathbf{K}}_{22}^{(4)}\mathbf{S}_2 \end{bmatrix}_{(6\times6)} \begin{Bmatrix} \hat{\mathbf{u}}_4 \\ \hat{\mathbf{u}}_6 \end{Bmatrix} = \begin{Bmatrix} \mathbf{S}_2^T\hat{\mathbf{f}}_4 \\ \mathbf{S}_2^T\hat{\mathbf{f}}_{12} \end{Bmatrix}. \tag{6.38}$$

The element equilibrium equation for the internal element (5) is

$$\begin{bmatrix} \hat{\mathbf{K}}_{11}^{(5)} & \hat{\mathbf{K}}_{12}^{(5)} \\ \hat{\mathbf{K}}_{21}^{(5)} & \hat{\mathbf{K}}_{22}^{(5)} \end{bmatrix}_{(6\times6)} \begin{Bmatrix} \hat{\mathbf{u}}_7 \\ \hat{\mathbf{u}}_{10} \end{Bmatrix} = \begin{Bmatrix} \hat{\mathbf{f}}_7 \\ \hat{\mathbf{f}}_{10} \end{Bmatrix}. \tag{6.39}$$

Expressing $\hat{\mathbf{u}}_7$ and $\hat{\mathbf{u}}_{10}$ in terms of $\hat{\mathbf{u}}_5$ and $\hat{\mathbf{u}}_6$ respectively with the help of Eqs. 6.23–6.26 and pre multiplying both sides of Eq. 6.39 by $\mathbf{S}_1^T$, we get

$$\begin{bmatrix} \mathbf{S}_1^T\hat{\mathbf{K}}_{11}^{(5)}\mathbf{S}_1 & \mathbf{S}_1^T\hat{\mathbf{K}}_{12}^{(5)}\mathbf{S}_1 \\ \mathbf{S}_1^T\hat{\mathbf{K}}_{21}^{(5)}\mathbf{S}_1 & \mathbf{S}_1^T\hat{\mathbf{K}}_{22}^{(5)}\mathbf{S}_1 \end{bmatrix}_{(6\times6)} \begin{Bmatrix} \hat{\mathbf{u}}_5 \\ \hat{\mathbf{u}}_5 \end{Bmatrix} = \begin{Bmatrix} \mathbf{S}_1^T\hat{\mathbf{f}}_7 \\ \mathbf{S}_1^T\hat{\mathbf{f}}_{10} \end{Bmatrix}. \tag{6.40}$$

The element equilibrium equation for the internal element (6) is

$$\begin{bmatrix} \hat{\mathbf{K}}_{11}^{(6)} & \hat{\mathbf{K}}_{12}^{(6)} \\ \hat{\mathbf{K}}_{21}^{(6)} & \hat{\mathbf{K}}_{22}^{(6)} \end{bmatrix}_{(6\times6)} \begin{Bmatrix} \hat{\mathbf{u}}_9 \\ \hat{\mathbf{u}}_{12} \end{Bmatrix} = \begin{Bmatrix} \hat{\mathbf{f}}_9 \\ \hat{\mathbf{f}}_{12} \end{Bmatrix}. \tag{6.41}$$

Expressing $\hat{\mathbf{u}}_9$ and $\hat{\mathbf{u}}_{12}$ in terms of $\hat{\mathbf{u}}_5$ and $\hat{\mathbf{u}}_6$ respectively with the help of Eqs. 6.25 and 6.26 and pre multiplying both sides of Eq. 6.41 by $\mathbf{S}_3^T$, we get

$$\begin{bmatrix} \mathbf{S}_3^T\hat{\mathbf{K}}_{11}^{(6)}\mathbf{S}_3 & \mathbf{S}_3^T\hat{\mathbf{K}}_{12}^{(6)}\mathbf{S}_3 \\ \mathbf{S}_3^T\hat{\mathbf{K}}_{21}^{(6)}\mathbf{S}_3 & \mathbf{S}_3^T\hat{\mathbf{K}}_{22}^{(6)}\mathbf{S}_3 \end{bmatrix}_{(6\times6)} \begin{Bmatrix} \hat{\mathbf{u}}_5 \\ \hat{\mathbf{u}}_6 \end{Bmatrix} = \begin{Bmatrix} \mathbf{S}_3^T\hat{\mathbf{f}}_9 \\ \mathbf{S}_3^T\hat{\mathbf{f}}_{12} \end{Bmatrix}. \tag{6.42}$$

6.4.3 Modeling Dynamic Contact Between Crack Surfaces

The present SFE with embedded transverse crack can be also formulated to capture the effect of dynamic frictional contact and viscosity due to the polymer matrix grain boundary and broken fiber fragments. Similar models for delamination can

be found in [22, 26]. However, a more complex model includes a non-linear spring to restrict the occurrence of incompatible opening-closing modes due to inter-penetration. This development will not be attempted here. Figure 4.8c shows the transverse crack surfaces and the associated hanging laminates (3) and (4). The motion of the crack surfaces is approximated through the motion of node 3 and node 4. Let us assume that the distributed spring and viscoelastic contact force along the crack surfaces can be lumped on node 3 and node 4 as

$$\begin{Bmatrix} \hat{\mathbf{f}}_3 \\ \hat{\mathbf{f}}_4 \end{Bmatrix} = \begin{bmatrix} \hat{\mathbf{K}}^* & -\hat{\mathbf{K}}^* \\ -\hat{\mathbf{K}}^* & \hat{\mathbf{K}}^* \end{bmatrix}_{(6\times6)} \begin{Bmatrix} \hat{\mathbf{u}}_4 \\ \hat{\mathbf{u}}_3 \end{Bmatrix}, \tag{6.43}$$

where

$$\hat{\mathbf{K}}^* = \begin{bmatrix} (K_u + i\omega C_u) & 0 & 0 \\ 0 & (K_w + i\omega C_w) & 0 \\ 0 & 0 & (K_\phi + i\omega C_\phi) \end{bmatrix}, \tag{6.44}$$

with K_u, K_w, K_ϕ are the spring stiffnesses and C_u, C_w and C_ϕ are the viscous damping coefficients associated with relative longitudinal displacement, transverse displacement and rotation between node 3 and node 4.

After assembling the element equilibrium equations for the six internal elements (Eqs. 6.33–6.41) and subsequently using Eqs. 6.29–6.31 and 6.43, we get

$$\begin{bmatrix} \mathbf{K_{11}} & \mathbf{K_{12}} & \mathbf{0} & \mathbf{0} & \mathbf{0} & \mathbf{0} \\ \mathbf{K_{21}} & \mathbf{K_{22}} & \mathbf{K_{23}} & \mathbf{0} & \mathbf{K_{25}} & \mathbf{0} \\ \mathbf{0} & \mathbf{K_{32}} & \mathbf{K_{33}} & \mathbf{K_{34}} & \mathbf{0} & \mathbf{0} \\ \mathbf{0} & \mathbf{0} & \mathbf{K_{43}} & \mathbf{K_{44}} & \mathbf{K_{45}} & \mathbf{0} \\ \mathbf{0} & \mathbf{K_{52}} & \mathbf{0} & \mathbf{K_{54}} & \mathbf{K_{55}} & \mathbf{K_{56}} \\ \mathbf{0} & \mathbf{0} & \mathbf{0} & \mathbf{0} & \mathbf{K_{65}} & \mathbf{K_{66}} \end{bmatrix}_{(18\times18)} \begin{Bmatrix} \hat{\mathbf{u}}_1 \\ \hat{\mathbf{u}}_5 \\ \hat{\mathbf{u}}_3 \\ \hat{\mathbf{u}}_4 \\ \hat{\mathbf{u}}_6 \\ \hat{\mathbf{u}}_2 \end{Bmatrix} = \begin{Bmatrix} \hat{\mathbf{f}}_1 \\ \mathbf{0} \\ \mathbf{0} \\ \mathbf{0} \\ \mathbf{0} \\ \hat{\mathbf{f}}_2 \end{Bmatrix}, \tag{6.45}$$

where

$$\begin{aligned}
&\mathbf{K_{11}} = \hat{\mathbf{K}}_{\mathbf{11}}^{(1)}, \quad \mathbf{K_{12}} = \hat{\mathbf{K}}_{\mathbf{12}}^{(1)}, \quad \mathbf{K_{21}} = \hat{\mathbf{K}}_{\mathbf{21}}^{(1)}, \\
&\mathbf{K_{22}} = \hat{\mathbf{K}}_{\mathbf{22}}^{(1)} + \mathbf{S}_1^T \hat{\mathbf{K}}_{\mathbf{11}}^{(5)} \mathbf{S_1} + \mathbf{S}_2^T \hat{\mathbf{K}}_{\mathbf{11}}^{(3)} \mathbf{S_2} + \mathbf{S}_3^T \hat{\mathbf{K}}_{\mathbf{11}}^{(6)} \mathbf{S_3}, \\
&\mathbf{K_{23}} = \mathbf{S}_2^T \hat{\mathbf{K}}_{\mathbf{12}}^{(3)}, \quad \mathbf{K_{25}} = \mathbf{S}_1^T \hat{\mathbf{K}}_{\mathbf{12}}^{(5)} \mathbf{S_1} + \mathbf{S}_3^T \hat{\mathbf{K}}_{\mathbf{12}}^{(6)} \mathbf{S_3}, \quad \mathbf{K_{32}} = \hat{\mathbf{K}}_{\mathbf{21}}^{(3)} \mathbf{S_1}, \\
&\mathbf{K_{33}} = \hat{\mathbf{K}}_{\mathbf{22}}^{(3)} + \mathbf{S}_2^T \mathbf{K}^*, \quad \mathbf{K_{34}} = -\mathbf{S}_2^T \mathbf{K}^*, \quad \mathbf{K_{43}} = -\mathbf{S}_2^T \mathbf{K}^*, \\
&\mathbf{K_{44}} = \hat{\mathbf{K}}_{\mathbf{11}}^{(4)} + \mathbf{S}_2^T \mathbf{K}^*, \quad \mathbf{K_{45}} = \hat{\mathbf{K}}_{\mathbf{12}}^{(4)} \mathbf{S_2}, \\
&\mathbf{K_{52}} = \mathbf{S}_1^T \hat{\mathbf{K}}_{\mathbf{21}}^{(5)} \mathbf{S_1} + \mathbf{S}_3^T \hat{\mathbf{K}}_{\mathbf{21}}^{(6)} \mathbf{S_3}, \quad \mathbf{K_{54}} = \mathbf{S}_2^T \hat{\mathbf{K}}_{\mathbf{21}}^{(4)}, \\
&\mathbf{K_{55}} = \hat{\mathbf{K}}_{\mathbf{11}}^{(2)} + \mathbf{S}_1^T \hat{\mathbf{K}}_{\mathbf{22}}^{(5)} \mathbf{S_1} + \mathbf{S}_2^T \hat{\mathbf{K}}_{\mathbf{22}}^{(4)} \mathbf{S_2} + \mathbf{S}_3^T \hat{\mathbf{K}}_{\mathbf{22}}^{(6)} \mathbf{S_3}, \quad \mathbf{K_{56}} = \hat{\mathbf{K}}_{\mathbf{12}}^{(2)}, \\
&\mathbf{K_{65}} = \hat{\mathbf{K}}_{\mathbf{21}}^{(2)}, \quad \mathbf{K_{66}} = \hat{\mathbf{K}}_{\mathbf{22}}^{(2)}.
\end{aligned}$$

6.4.4 Modeling of Surface Breaking Cracks

The surface-breaking cracks can be considered in the same framework as formulated above. Figures 6.9a and b show the internal elements for the top and bottom surface-breaking cracks respectively. The only difference in these cases compared to the embedded transverse crack is that here the number of elements and nodes representing the top sub-laminates (element (6)) and bottom sub-laminates (element 5), which are absent in Fig. 4.8b. Therefore, by removing these element equilibrium equations while assembling, one can obtain the modified form of Eq. 6.45 for the top and bottom surface-breaking cracks.

6.4.4.1 Super Element Level Condensation

We first condense out the degrees of freedom at the crack surfaces (i.e. node 3 and node 4), which reduces Eq. 6.45 to

$$\begin{bmatrix} \bar{\mathbf{K}}_{11} & \bar{\mathbf{K}}_{12} & \mathbf{0} & \mathbf{0} \\ \bar{\mathbf{K}}_{21} & \bar{\mathbf{K}}_{22} & \bar{\mathbf{K}}_{23} & \mathbf{0} \\ \mathbf{0} & \bar{\mathbf{K}}_{32} & \bar{\mathbf{K}}_{33} & \bar{\mathbf{K}}_{34} \\ \mathbf{0} & \mathbf{0} & \bar{\mathbf{K}}_{43} & \bar{\mathbf{K}}_{44} \end{bmatrix}_{(12\times12)} \begin{Bmatrix} \hat{\mathbf{u}}_1 \\ \hat{\mathbf{u}}_5 \\ \hat{\mathbf{u}}_6 \\ \hat{\mathbf{u}}_2 \end{Bmatrix} = \begin{Bmatrix} \hat{\mathbf{f}}_1 \\ \mathbf{0} \\ \mathbf{0} \\ \hat{\mathbf{f}}_2 \end{Bmatrix}, \tag{6.46}$$

where

$$\begin{aligned} &\bar{\mathbf{K}}_{11} = \mathbf{K}_{11}, \quad \bar{\mathbf{K}}_{12} = \mathbf{K}_{12}, \quad \bar{\mathbf{K}}_{21} = \mathbf{K}_{21}, \quad \bar{\mathbf{K}}_{22} = \mathbf{K}_{22} + \mathbf{K}_{23}\mathbf{K}^*_{35}, \\ &\bar{\mathbf{K}}_{23} = \mathbf{K}_{25} + \mathbf{K}_{23}\mathbf{K}^*_{36}, \quad \bar{\mathbf{K}}_{32} = \mathbf{K}_{52} + \mathbf{K}_{54}\mathbf{K}^*_{45}, \\ &\bar{\mathbf{K}}_{33} = \mathbf{K}_{55} + \mathbf{K}_{54}\mathbf{K}^*_{46}, \quad \bar{\mathbf{K}}_{34} = \mathbf{K}_{56}, \quad \bar{\mathbf{K}}_{43} = \mathbf{K}_{65}, \\ &\bar{\mathbf{K}}_{44} = \mathbf{K}_{66}, \quad \mathbf{K}^*_{45} = (\mathbf{K}_{44} - \mathbf{K}_{43}\mathbf{K}_{33}^{-1}\mathbf{K}_{34})^{-1}\mathbf{K}_{43}\mathbf{K}_{33}^{-1}\mathbf{K}_{32}, \end{aligned}$$

In the second step, we condense out the degrees of freedom at node 5 and node 6, which yields the final form of the equilibrium equation representing a two-node element with embedded transverse crack, and can be expressed as

$$\begin{bmatrix} \hat{\bar{\mathbf{K}}}_{11} & \hat{\bar{\mathbf{K}}}_{12} \\ \hat{\bar{\mathbf{K}}}_{21} & \hat{\bar{\mathbf{K}}}_{22} \end{bmatrix}_{(6\times6)} \begin{Bmatrix} \hat{\mathbf{u}}_1 \\ \hat{\mathbf{u}}_2 \end{Bmatrix} = \begin{Bmatrix} \hat{\mathbf{f}}_1 \\ \hat{\mathbf{f}}_2 \end{Bmatrix}, \tag{6.47}$$

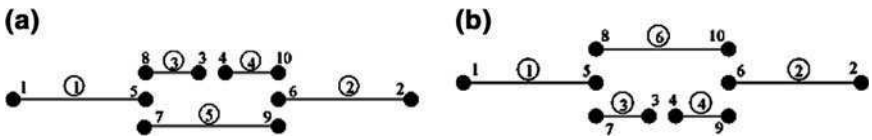

Fig. 6.9 Representation of the base laminates, sub-laminates and hanging laminates by spectral elements for **a** top surface-breaking crack and **b** bottom surface-breaking crack

where

$$\hat{\hat{\mathbf{K}}}_{11} = \mathbf{K}_{11} + \mathbf{K}_{12}\mathbf{K}^*_{51}, \quad \hat{\hat{\mathbf{K}}}_{12} = \mathbf{K}_{12}\mathbf{K}^*_{52}, \quad \hat{\hat{\mathbf{K}}}_{21} = \mathbf{K}_{43}\mathbf{K}^*_{61},$$
$$\hat{\hat{\mathbf{K}}}_{22} = \mathbf{K}_{44} + \mathbf{K}_{43}\mathbf{K}^*_{62}, \quad \mathbf{K}^*_{61} = (\mathbf{K}_{33} - \mathbf{K}_{32}\mathbf{K}^{-1}_{22}\mathbf{K}_{23})^{-1}\mathbf{K}_{32}\mathbf{K}^{-1}_{22}\mathbf{K}_{21},$$
$$\mathbf{K}^*_{62} = -(\mathbf{K}_{33} - \mathbf{K}_{32}\mathbf{K}^{-1}_{22}\mathbf{K}_{23})^{-1}\mathbf{K}_{34},$$
$$\mathbf{K}^*_{51} = -(\mathbf{K}^{-1}_{22}\mathbf{K}_{21} + \mathbf{K}^{-1}_{22}\mathbf{K}_{23}\mathbf{K}^*_{61}), \quad \mathbf{K}^*_{52} = -\mathbf{K}^{-1}_{22}\mathbf{K}_{23}\mathbf{K}^*_{62}.$$

As in the case of delamination modeling, one only needs to replace the spectral element for the healthy beam with this spectral element wherever the presence of a transverse crack is to be accounted for. To emphasize the novel use of this element for applications in SHM, its numerical performance is compared with standard plane-stress finite element simulations in Sect. 6.4.6. Before proceeding further with the numerical studies, the constrained formulation to accommodate longer hanging laminates and the enforcing of displacement continuities, which is an alternative option to Eq. 6.22, is discussed below.

6.4.5 Distributed Constraints at the Interfaces Between Sub-Laminates and Hanging Laminates

For longer lengths of sub-laminates (5) and (6) and intermediate hanging laminates (3) and (4) shown in Fig. 4.8b, especially when $\Delta L > \min(\lambda_g)$ as discussed in the context of Eq. 6.22, interfacial slip and other discontinuities at the horizontal interfaces between the hanging laminates and the top and bottom sub-laminates may become significant for certain wave interactions and to be restricted. This requires displacement continuity between the surface displacements of a hanging laminate and the neighboring sub-laminate, which can be expressed as

$$\hat{\mathbf{u}}(x)^{(j)}_t = \hat{\mathbf{u}}(x)^{(l)}_b, \tag{6.48}$$

where the superscripts (j) and (l) indicates the element numbers and the subscripts t and b indicate the top or bottom surface respectively. While modeling delamination along with fiber fracture, such constraints can be removed. It can be seen from Fig. 4.8a that there are four such horizontal interfaces where constraints need to be imposed otherwise. Considering element (5) and element (3), Eq. 6.48 can be expanded using the generic field variables as

$$\begin{bmatrix} 1 & 0 & z^{(5)}_t \\ 0 & 1 & 0 \\ 0 & 0 & 1 \end{bmatrix} \begin{Bmatrix} \hat{u}^o \\ \hat{\omega} \\ \hat{\phi} \end{Bmatrix}^{(5)} = \begin{bmatrix} 1 & 0 & z^{(3)}_b \\ 0 & 1 & 0 \\ 0 & 0 & 1 \end{bmatrix} \begin{Bmatrix} \hat{u}^o \\ \hat{\omega} \\ \hat{\phi} \end{Bmatrix}^{(3)} \tag{6.49}$$

Further, using element shape functions in Eq. 6.49, we get

$$\mathbf{H}_t^{(5)}\mathbf{N}(x,\omega_n)^{(5)}\hat{\mathbf{u}}^{(5)} = \mathbf{H}_b^{(3)}\mathbf{N}(x,\omega_n)^{(3)}\hat{\mathbf{u}}^{(3)} \tag{6.50}$$

where $\mathbf{N}(x,\omega_n)^{(j)}$ is the shape function matrix of the jth element. Similarly for the other three interfaces, the constraints are

$$\mathbf{H}_t^{(5)}\mathbf{N}(x,\omega_n)^{(5)}\hat{\mathbf{u}}^{(5)} = \mathbf{H}_b^{(4)}\mathbf{N}(x,\omega_n)^{(4)}\hat{\mathbf{u}}^{(4)} \tag{6.51}$$

$$\mathbf{H}_t^{(3)}\mathbf{N}(x,\omega_n)^{(3)}\hat{\mathbf{u}}^{(3)} = \mathbf{H}_b^{(6)}\mathbf{N}(x,\omega_n)^{(6)}\hat{\mathbf{u}}^{(6)} \tag{6.52}$$

$$\mathbf{H}_t^{(4)}\mathbf{N}(x,\omega_n)^{(4)}\hat{\mathbf{u}}^{(4)} = \mathbf{H}_b^{(6)}\mathbf{N}(x,\omega_n)^{(6)}\hat{\mathbf{u}}^{(6)} \tag{6.53}$$

The nodal displacement vectors $\hat{\mathbf{u}}^{(5)^T} = \{\hat{\mathbf{u}}_\mathbf{8}^T\ \hat{\mathbf{u}}_\mathbf{3}^T\}$ and $\hat{\mathbf{u}}^{(4)^T} = \{\hat{\mathbf{u}}_\mathbf{4}^T\ \hat{\mathbf{u}}_\mathbf{11}^T\}$ can now be transformed using Eq. 6.45 in the above equations (6.50)–(6.53) and the internal nodes can be condensed out systematically. To illustrate further, let us consider the constraint for the first interface as given by Eq. 6.50, which can be rewritten after transformation as

$$\begin{bmatrix} \bar{\mathbf{C}}_{\mathbf{11}} & \bar{\mathbf{C}}_{\mathbf{12}} \\ \bar{\mathbf{C}}_{\mathbf{21}} & \bar{\mathbf{C}}_{\mathbf{22}} \end{bmatrix}_{(6\times6)} \begin{Bmatrix} \hat{\mathbf{u}}_\mathbf{5} \\ \hat{\mathbf{u}}_\mathbf{6} \end{Bmatrix} = \begin{Bmatrix} \mathbf{0} \\ \mathbf{0} \end{Bmatrix} \tag{6.54}$$

Since in Eq. 6.54, $\hat{\mathbf{u}}_\mathbf{5}$ and $\hat{\mathbf{u}}_\mathbf{6}$ are the internal nodal vectors, they are mapped onto node 1 and node 2. This second step with the help of Eq. 6.46, gives

$$\begin{bmatrix} \mathbf{C}_{\mathbf{11}} & \mathbf{C}_{\mathbf{12}} \\ \mathbf{C}_{\mathbf{21}} & \mathbf{C}_{\mathbf{22}} \end{bmatrix}_{(6\times6)} \begin{Bmatrix} \hat{\mathbf{u}}_\mathbf{1} \\ \hat{\mathbf{u}}_\mathbf{2} \end{Bmatrix} = \begin{Bmatrix} \mathbf{0} \\ \mathbf{0} \end{Bmatrix} \quad \Rightarrow \mathbf{C}(x,\omega_n)^{(1)}\hat{\mathbf{u}}^e = \mathbf{0} \tag{6.55}$$

Similar constraints for the other three horizontal interfaces can be obtained in the same way, where $\mathbf{C}(x,\omega_n)^{(j)}, j = 1,\ldots,4$ are the matrices of coefficients associated with the multi-point constraints mapped on the degrees of freedom of the two-node element with embedded transverse crack. Introducing a diagonal matrix of penalty parameters $\boldsymbol{\alpha}$ and minimizing the potential in the frequency domain [32], the updated dynamic stiffness matrix for the element with embedded transverse crack incorporating unbounded length of the internal hanging laminates can be expressed as

$$\hat{\hat{\mathbf{K}}}_U = \hat{\hat{\mathbf{K}}} + \hat{\hat{\mathbf{K}}}_C \tag{6.56}$$

where

$$\begin{aligned} \hat{\hat{\mathbf{K}}}_C = &\int_0^{\Delta L/2} \left(\mathbf{C}^{(1)^T}\boldsymbol{\alpha}\mathbf{C}^{(1)} + \mathbf{C}^{(3)^T}\boldsymbol{\alpha}\mathbf{C}^{(3)}\right) dx \\ &+ \int_{/2}^{\Delta L} \left(\mathbf{C}^{(2)^T}\boldsymbol{\alpha}^{(2)} + \mathbf{C}^{(4)^T}\boldsymbol{\alpha}^{(4)}\right) dx \end{aligned} \tag{6.57}$$

6.4.6 Wave Scattering Due to Transverse Cracks

The spectral FEM for modeling transverse cracks requires only three additional input parameters. These additional inputs are span-wise location of the crack ($L_1 + \Delta L/2$), and depth-wise location of the top and bottom crack-tips (d_1, d_2). Although, the effect of crack-tip singularity is not included in the local analysis, it is essential to validate the performance of the proposed element for wave-based diagnostics and SHM applications, where most damage models are approximated by springs or equivalent change in the constitutive model for faster analysis. In the following section, response of a unidirectional composite cantilever beam with mid-span surface-breaking fiber fracture to a high frequency pulse loading is simulated using the developed SFE and the response is compared with a detailed 2D FE model. The analysis is performed using FFT based spectral FEM

A uni-directional graphite-epoxy cantilever beam of length 800 mm and having a cross-section 16 mm (thickness) $\times$10 mm (width) is considered for this study. An 8 mm deep top surface-breaking crack is introduced at mid-span of the beam. The pulse loading shown in Fig. 3.7 is applied at the tip of the cantilever beam in the transverse direction. SFE analysis is carried out using a single SFE with embedded crack. The length of the hanging laminates $\Delta L/2$ is chosen using Eq. 6.22. 16,384 FFT sampling points ($\Delta\omega = 12.2070$ Hz) are used for the forward and inverse transform of the loading and response, respectively. In the detailed FE analysis, the fine mesh consists of 5,120 constant strain triangular elements under plane-stress conditions in the X–Z plane. Newmark time integration with time step $\Delta t = 1$ μs is used. Here the element size is comparable with the wavelength of the applied excitation. The pulse load is applied consistently in the transverse direction at the tip cross-section of the FE model.

Figure 6.10 shows the plots of $\dot{w}$ history at the mid-node of the tip cross-section predicted by SFE and detail 2D FE analysis. After the incident pulse, the effect of the crack due to wave scattering at around 0.55–0.6 ms can be seen. The peak amplitude of the velocity history and its arrival time matches very well with the 2D FE prediction. However, a small additional peak before the main peak amplitude can be seen, which is due to several approximations made in the proposed modeling compared to the actual local crack-tip behavior. Indeed, the overall trend of the response predicted by the proposed spectral element can be seen as reliable, in terms of the arrival time of the broadband wave scattered from the crack, as well as the associated peak amplitude in the signal. Another important aspect we need to mention in this context is that the inter-penetration of the crack surfaces of the breathing crack in the detailed 2D FE analysis (in the absence of contact elements) was found to occur much beyond the time window shown in Fig. 6.10 and had negligible amplitude (relative displacement between the crack surfaces). Hence this can be considered less significant for transient wave-based diagnostics. However, long duration monitoring under sustained loading and associated incremental crack-growth related study need further strategy for FE model-based

identification of frequency dependent dynamic contact forces, which can be used then in the present spectral element model for more accurate analysis.

6.4.7 Sensitivity of the Fiber Breakage Location and Configuration

To identify the location of fiber break from the scattered wave information, the same graphite-epoxy cantilever beam as considered in the previous example is used. Figure 6.11 shows the $\dot{w}$ history at the cantilever tip of the beam with a mid-span 8 mm deep embedded crack introduced symmetrically across the thickness. From the group speed of the flexural wave, the time of arrival of the flexural wave is estimated and is shown by $*$ in Fig. 6.11. Although the time of arrival is the same for both the surface-breaking crack and embedded crack, which is obvious, a smaller wave packet visible at 0.58 ms is due to the presence of the embedded crack.

A 20 kHz tone burst signal is used to perform numerical simulations for varying crack depth and contact stiffnesses. Varying depth and contact stiffnesses of the crack surfaces produce no visible fluctuation in the scattered waves from the embedded crack under the present loading in the flexural shear mode. However, the surface-breaking crack with variation in the crack depth and contact stiffnesses of the crack surfaces shows significant changes in the scattered waves, which are plotted in Figs. 6.12 and 6.13, respectively. As the crack depth becomes more than half the beam thickness (16 mm), additional peaks after the first reflection can be seen in Fig. 6.12. In Fig. 6.13, the contact stiffness between the crack surfaces is varied using a stiffness factor β, where only the surface-normal contact stiffness is considered and is assumed to be $K^* = \beta Q_{11}$, where Q_{11} is the composite material

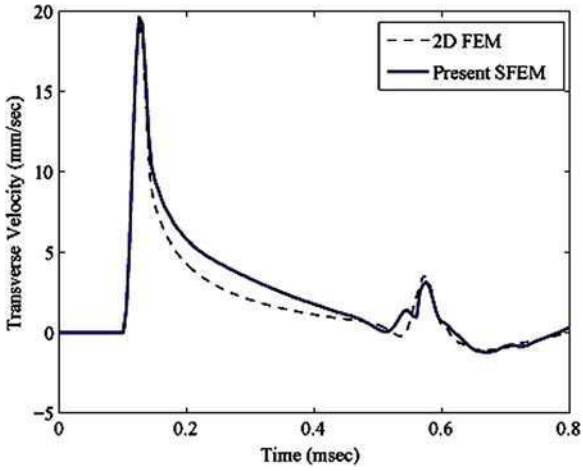

Fig. 6.10 Comparison of the transverse velocity $\dot{w}$ history at the mid-plane of the tip of the cantilever beam predicted by the single spectral element and detailed 2D FE models under high frequency pulse loading (Fig. 3.7)

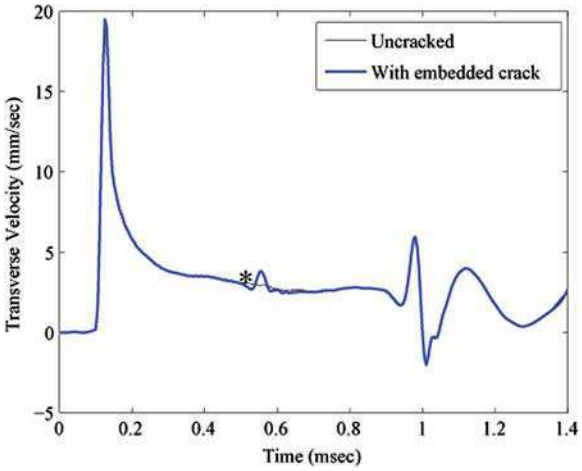

Fig. 6.11 Transverse velocity $\dot{w}$ history at the cantilever tip due to a high frequency pulse (Fig. 3.7) applied at the cantilever tip in the transverse direction for a mid-span 8 mm deep embedded crack placed symmetrically across the beam thickness. $*$ shows the analytical estimate of the arrival time of the reflected wave from the crack

stiffness parameter. Apart from the main reflected wave from the crack at around 1 ms, which indicates the crack location, Fig. 6.13 shows small amplitude of additional scattering for contact stiffness smaller than Q_{11}, and significant amplitude and additional scattering for contact stiffness more than Q_{11}, which can be considered as a stiff inclusion. In the present one-dimensional model, the higher order Lamb wave modes, especially the thickness stretching mode, are not accounted for. From the simulations, it appears that for identification of the crack configuration completely, especially the crack depth and thickness-wise location, a higher-order Lamb wave model based on high frequency excitation in flexural shear thickness stretching modes may be necessary.

6.5 Modeling of Structures with Multiple Horizontal Cracks or Delaminations

Handling of delaminations in composite structures or horizontal cracks in metallic structures can be challenging for standard FE due to the requirements of fine spatial discretization. Generally available FE packages use plate-bending elements or degenerated shell elements, which cannot be used in the interfacial regions where more than one sub-laminate form the base laminate. Moreover, due to the significant difference in the order of the thickness and planar dimensions, planar or solid elements, when used at the interfaces, yield enormous system size. In addition, a high computational cost is required to handle such a large system and to capture highly transient pulse propagation. In the present study, a systematic derivation is presented to model the interfaces between the base laminate and multiple sub-laminates in a general form. When one of the intermediate sub-laminates are of different material configuration, it can be treated as a strip

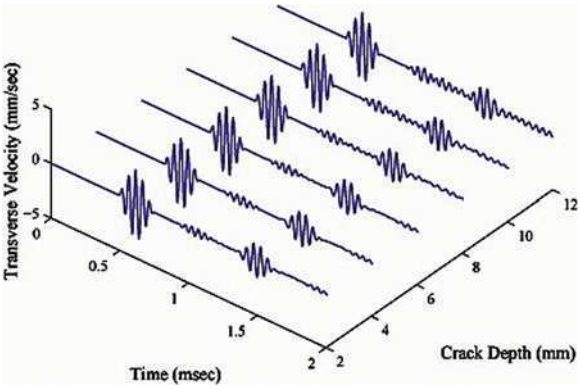

Fig. 6.12 Transverse velocity $\dot{w}$ at the cantilever tip due to modulated sine pulse transversely applied at the tip of the cantilever with a top surface-breaking crack of varying depth. No contact between the surfaces is assumed

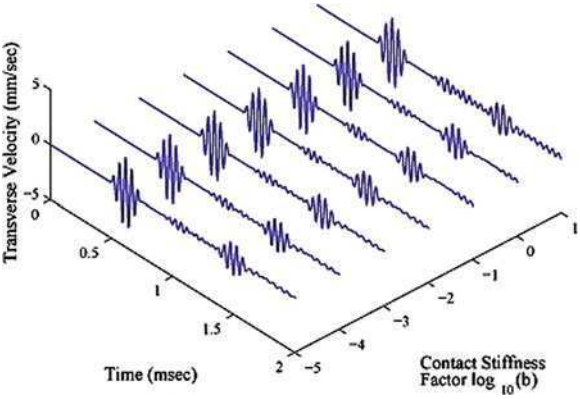

Fig. 6.13 Transverse velocity $\dot{w}$ at the cantilever tip due to modulated sine pulse transversely applied at the tip of the cantilever with a top surface-breaking crack with varying contact stiffnesses ($K^* = \beta Q_{11}$). Crack depth is 8 mm

inclusion. The idea is to capture wave transmission and scattering at these delamination tips or at the interfaces between the inclusions and the host materials using a diagnostic signal. The SFEM (both WSFEM or FSFEM) discussed in Chap. 5 can be used as the basic building block for the spectral interface model.

In this section, our main objective is to construct and solve a set of constrained equations in either the Fourier or Wavelet domain (consistent with the framework of SFEM) for multiple delaminations and inclusions by allowing discontinuity in the rotation θ_y of the cross-sectional plane between two sub-laminates above and below delaminations. The delaminated configuration is shown in Fig. 6.14. This also allows a particular sub-laminate made of different materials to be treated as a strip inclusion debonded from the host material. For simplicity, we assume that the dynamics of the delaminations or the slip between the inclusion and host materials is governed by Mode-II fracture process, excluding any effect of Mode-I fracture corresponding to the opening and closing of delaminations causing interpenetration and incompatibility in the thickness direction.

The formulation is generalized by considering the two cases shown in Fig. 6.15. In case (a) (Fig. 6.15a), two consecutive nodes p and q are considered to connect two elements on opposite sides of the interface. Since, there is no delamination

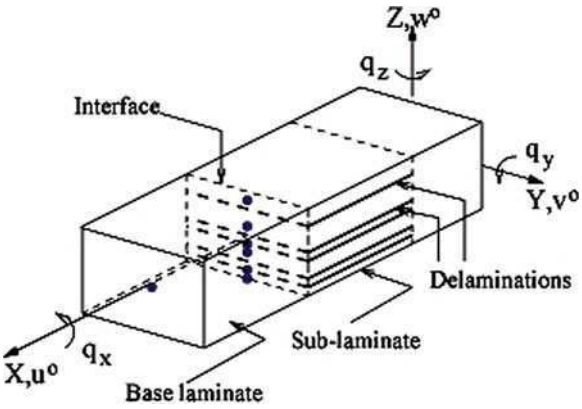

Fig. 6.14 Schematic diagram showing multiple through-width delaminations in a laminated composite beam

between node p and node q, in-plane displacements and rotation of normal planes at these nodes can be constrained as

$$u_p^o + z_{pq}\theta_{y_p} = u_q^o, \quad \theta_{y_p} = \theta_{y_q}, \tag{6.58}$$

where z_{pq} is the distance along the z direction between the node p and node q. In case (b) (Fig. 6.15b), a single delamination is considered between node p and node q, which are on the same face on the interface. Each of these nodes belongs to the element representing one of the sub-laminate above or below the delamination. Node q' on the other side of the interface belongs to the element representing the base laminate. Since, under the assumption of sub-laminate-wise constant shear, the normal plane passing through node q' has to rotate in a rigid body mode, the discontinuous plane passing through node p and node q must rotate in a constrained manner. Such constraint can be imposed as follows. The interface in the region including node p and node q' is already defined in Eq. 6.58 representing the case (a). Now, one needs to construct the constrained equations for interfacing the node p and node q. This can be expressed as

$$u_p^o + z_{p_t}\theta_{y_p} = u_q^o + z_{q_b}\theta_{y_q} \tag{6.59}$$

where z_{pt} is the depth of the top surface of the sub-laminate containing node p and measured from the corresponding element local reference line. Similarly, z_{qb} is the

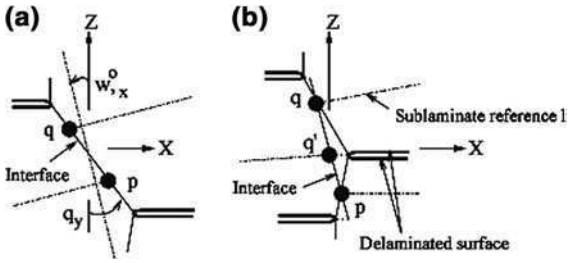

Fig. 6.15 Interfacial nodes taking part in constrained kinematics of base laminate and sub-laminates or debonded strip inclusions with **b** or without **a** a third delaminated surface

depth of the bottom surface of the sub-laminate containing node q and measured from the corresponding element local reference line. For all other nodal displacement components associated with the node p and node q, the equations for constraints can be written as

$$v_p^o = v_q^o, \quad w_p^o = w_q^o, \quad \theta_{xp} = \theta_{xq}, \quad \theta_{zp} = \theta_{zq}. \tag{6.60}$$

Implementation of the above displacement constraints can be automated to model multiple delaminations or inclusions across the thickness as well as for different variations of such configuration at various locations along the length of a beam. Equations 6.58–6.60 can be assembled at the global level with appropriate transformation to form the multi point constraints (MPC) equation in the nodal displacement vector. Let us consider Eq. 6.58 obtained in case (a) along with Eq. 6.60. We can write these six equations in matrix form as

$$\begin{bmatrix} 1 & 0 & 0 & 0 & z_{pq} & 0 & -1 & 0 & 0 & 0 & 0 & 0 \\ 0 & 1 & 0 & 0 & 0 & 0 & 0 & -1 & 0 & 0 & 0 & 0 \\ 0 & 0 & 1 & 0 & 0 & 0 & 0 & 0 & -1 & 0 & 0 & 0 \\ 0 & 0 & 0 & 1 & 0 & 0 & 0 & 0 & 0 & -1 & 0 & 0 \\ 0 & 0 & 0 & 0 & 1 & 0 & 0 & 0 & 0 & 0 & -1 & 0 \\ 0 & 0 & 0 & 0 & 0 & 1 & 0 & 0 & 0 & 0 & 0 & -1 \end{bmatrix} \begin{Bmatrix} \hat{u}_p^o \\ \vdots \\ \hat{\theta}_{zp} \\ \hat{u}_q^o \\ \vdots \\ \hat{\theta}_{zq} \end{Bmatrix} = \mathbf{0}. \tag{6.61}$$

Now, for example, if the node numbering is $p, p+1$ and $q, q+1$ for the two elements connected to the interface, then Eq. 6.61 can be rewritten as

$$\left[\begin{array}{cc|cc} \mathbf{C_{u1}} & \mathbf{0} & \mathbf{C_{u2}} & \mathbf{0} \end{array}\right] \begin{Bmatrix} \mathbf{T}^T \hat{\mathbf{u}}_p^{\mathrm{g}} \\ \mathbf{T}^T \hat{\mathbf{u}}_q^{\mathrm{g}} \end{Bmatrix} = \mathbf{0} \tag{6.62}$$

where $\mathbf{C_{u1}}$ and $\mathbf{C_{u2}}$ are the two 6×6 sub-matrices in Eq. 6.61. A similar form is also obtained for interface in case (b). Finally, all these equations of displacement constraints can be assembled to form a single matrix equation at the global level, which is given by

$$\mathbf{C_u} \hat{\mathbf{u}}^{\mathrm{g}} = \mathbf{0}. \tag{6.63}$$

Next, the equilibrium of the nodal forces at each interface is to be established. This is obtained as

$$\sum_p \mathbf{S'}_p^T \hat{\mathbf{f}}_p^{\mathrm{e}} = \hat{\mathbf{f}}, \tag{6.64}$$

where the summation sign stands for all the nodes in a particular cross-section. Here, $\hat{\mathbf{f}}$ is the applied load vector at the interface under consideration. For an element with nodes numbered p, $p+1$ and the node p on the interface, we have,

$$\mathbf{S}'_p = \left[\begin{array}{cccccc|c} 1 & 0 & 0 & 0 & h_p & 0 & \\ 0 & 1 & 0 & 0 & 0 & 0 & \\ 0 & 0 & 1 & 0 & 0 & 0 & \\ 0 & 0 & 0 & 1 & 0 & 0 & \mathbf{0} \\ 0 & 0 & 0 & 0 & 1 & 0 & \\ 0 & 0 & 0 & 0 & 0 & 1 & \end{array}\right] \tag{6.65}$$

where, h_p is the distance of the node p in the z direction measured from the bottom surface of the beam. Equation 6.65 can be rewritten in terms of the element nodal displacement vector at the global level as

$$\sum_p \mathbf{S}'_p \mathbf{T}^T \hat{\mathbf{K}}^{\mathrm{e}}_p \mathbf{T} \hat{\mathbf{u}}^{\mathrm{g}}_p = \mathbf{T}^T \hat{\mathbf{f}}^{\mathrm{g}}. \tag{6.66}$$

Equation 6.66 can be assembled to form a single matrix equation involving force constraints at the global level, which is given by

$$\mathbf{C_f} \hat{\mathbf{u}}^{\mathrm{g}} = \mathbf{f}'. \tag{6.67}$$

Now, we use two diagonal matrices of penalty parameters $\boldsymbol{\alpha}_\mathbf{u}$ and $\boldsymbol{\alpha}_\mathbf{f}$ to impose displacement constraints in Eq. 6.63 and force constraints in Eq. 6.67 to minimize the stationary potential

$$\begin{aligned} \hat{\prod} = {} & \frac{1}{2} \hat{\mathbf{u}}^{\mathrm{g}^T} \hat{\mathbf{K}}^{\mathrm{g}} \hat{\mathbf{u}}^{\mathrm{g}} - \hat{\mathbf{u}}^{\mathrm{g}^T} \hat{\mathbf{f}}^{\mathrm{g}} + \frac{1}{2} (\mathbf{C_u} \hat{\mathbf{u}}^{\mathrm{g}})^T \boldsymbol{\alpha}_\mathbf{u} (\mathbf{C_u} \hat{\mathbf{u}}^{\mathrm{g}}) \\ & + \frac{1}{2} (\mathbf{C_f} \hat{\mathbf{u}}^{\mathrm{g}} - \mathbf{f}')^T \boldsymbol{\alpha}_\mathbf{u} (\mathbf{C_f} \hat{\mathbf{u}}^{\mathrm{g}} - \mathbf{f}') \end{aligned} \tag{6.68}$$

in the frequency domain for each ω_n. Minimizing the above potential with respect to the global displacement vector $\hat{\mathbf{u}}^{\mathrm{g}}$, we get the spectral finite element equilibrium equation

$$\left(\hat{\mathbf{K}}^{\mathrm{g}} + \mathbf{C}_\mathbf{u}^T \boldsymbol{\alpha}_\mathbf{u} \mathbf{C_u} + \mathbf{C}_\mathbf{f}^T \boldsymbol{\alpha}_\mathbf{f} \mathbf{C_f} \right) \hat{\mathbf{u}}^{\mathrm{g}} = \hat{\mathbf{f}}^{\mathrm{g}} + \mathbf{C}_\mathbf{f}^T \boldsymbol{\alpha}_\mathbf{f} \mathbf{f}'. \tag{6.69}$$

Note that the constraint equations (Eqs. 6.63 and 6.67) involve dissimilar degrees of freedom, whose motion is governed by the dynamic stiffness coefficients $\hat{\mathbf{K}}_{\mathbf{ij}} \mathbf{A}_{\mathbf{jl}}$. Therefore, use of penalty parameters α_u and α_f consistent with the associated degrees of freedom to achieve sufficient numerical accuracy [3] is important. Note the order of the values in the additional entries in the updated dynamic stiffness matrix in Eq. 6.69, that is

$$O\left(\mathbf{C}_\mathbf{u}^T \mathbf{C_u}\right) \approx (-6, 0), \quad O\left(\mathbf{C}_\mathbf{f}^T \mathbf{C_f}\right) \approx O\left(\min\left(\hat{k}^{\mathrm{e}^2}_{jj}\right), \max\left(\hat{k}^{\mathrm{e}^2}_{jj}\right)\right), \tag{6.70}$$

These values are arrived based on the fact that in the matrix $\mathbf{C_u}$, the entries are either 1 or z_{pq} (depth of composite beam sub-laminates are typically in the order of millimeters). These lead to

$$\alpha_{ujj} = \left|\hat{k}^{e}_{jj}\right| \times 10^{9}, \quad \alpha_{fjj} = \left|\hat{k}^{e^{-1}}_{jj}\right| \times 10^{3} \tag{6.71}$$

as a convenient choice of the penalty parameters while solving the constrained system in Eq. 6.69.

6.5.1 Wave Scattering from Delamination: Comparison with 2D FEM

In this section, we consider single and two delaminations using the multiple delamination spectral element model explained in the last section. The main objective here is to validate the FSFEM multiple delamination model through comparisons with conventional FE solutions.

A unidirectional graphite-epoxy $[0^0]_{80}$ composite cantilever beam of length 0.8 m, thickness 16 mm, width 10 mm with a 50 mm mid-plane delamination is considered. The center of the delamination is 0.4 m away from the fixed end of the beam. A single frequency sinusoidal pulse modulated at 20 kHz (Fig. 4.1 is applied transversely at the tip). Issues related to instrumentation and signal generation of such diagnostic wave for integrated SHM systems are discussed in [40, 20, 16]. In the FSFEM model, four elements (two for base-laminates and two for sub-laminates above and below the delamination) with 4,096 FFT sampling points ($\Delta\omega = 48 : 828$ Hz) are used. The 2D plane stress FEM in the xz plane consists of a fine mesh of 2,560 constant strain triangular elements which gives an element size compatible with the wavelength for the applied excitation.

Figure 6.16 shows the comparison of transverse velocity history $\dot{w}$ at the free end mid-plane. The first pulse starting at 0.5 ms is due to the incident load at the tip. After this, the first reflection from the delamination tip arrives at $t = 0.9088$ ms (marked as $*$). The results from FSFEM and FEM match well within the zoomed window. In the FSFEM model, numerical errors due to window distortion during IFFT are avoided by adding a small amount of damping η in the wavenumbers as $k_i \rightarrow k_i(1 - j\eta)$, with $\eta = 1 \times 10^{-3}$. This is done to alleviate the wraparound problems associated with FSFEM model.

A snapshot of the deformed triangular FE mesh at $t = 0.84$ ms is shown in Fig. 6.17, where the relative slip between the delaminated faces can be observed. However, the assumption that this slip is frictionless may lead to erroneous prediction when the delamination length is large.

Next we study the wave scattering due to a broadband load (Fig. 3.7). We consider the same cantilever beam as in the previous example, however two mid-span delaminations, each of length 50 mm, are introduced at $z = \pm 4$ mm. The response of the delaminated beam in Fig. 6.18 shows the first arrival of the wave scattered by the delamination, which along with its resonance behavior, matches well with the FEM. Again here, $\eta = 1 \times 10^{-3}$ is used for damping out the waves. Due to this damping, little amount of decay in the velocity response at time can be

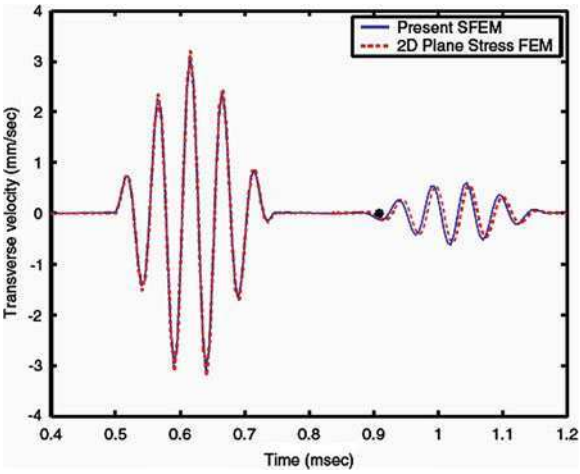

Fig. 6.16 Comparison of velocity history obtained from the present SFEM and a 2D plane stress FEM at the free end of a graphite-epoxy unidirectional composite cantilever beam with single mid-plane delamination. Arrival of the first reflection from the delamination tip is shown by the $*$ mark

observed. However, the nature of the peaks are accurately captured in FSFEM model. The overall performance shows the acceptable accuracy of the multiple delamination FSFEM model.

6.5.2 *Computational Efficiency of FSFEM Compared to FEM*

It was mentioned earlier that both FSFEM or WSFEM are computationally superior to conventional FEM for multi-modal wave propagation problems due to the ability of the former to accurately capture the inertial properties. In this section, we quantify the efficiency of FSFEM model as apposed to FEM by computing the CPU time taken and the memory required by these respective methods to solve the same problem of a waveguide with a delamination.

In FSFEM model, the matrix equation $\hat{\mathbf{K}}\hat{\mathbf{u}} = \hat{\mathbf{f}}$ is solved directly at each frequency sampling point $\omega_n, n = 1, 2, \ldots N$, where N defines the Nyquist frequency. The system size of the present FSFEM depends only on the number of sub-laminates and base-laminates and not on the actual length or thickness of the delaminated beam and therefore it is very small. For example, for a beam with a single delamination, a maximum of four waveguide elements are needed. So, the system size can increase up to (48×48) with 6 degrees of freedom per node. This internally constrained system is formed at each sampling frequency ω_n from the wavenumbers k_i in the shape function and is solved directly. Hence, the main computational cost is in the element formulation only (as seen in the matrix manipulations). Whereas, for conventional FEM, the element size is limited by the smallest wavelength of propagation and the system size increases for increasing span and depth of the beam. For example, if the span of the beam whose existing FEM system size is $(n \times m)$, where m is the bandwidth and n is the number of

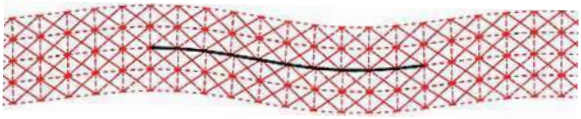

Fig. 6.17 Snap of the deformed FE mesh taken at the region of the delamination at $t = 0.84$ ms. The nodal displacements are magnified by 10^5 times

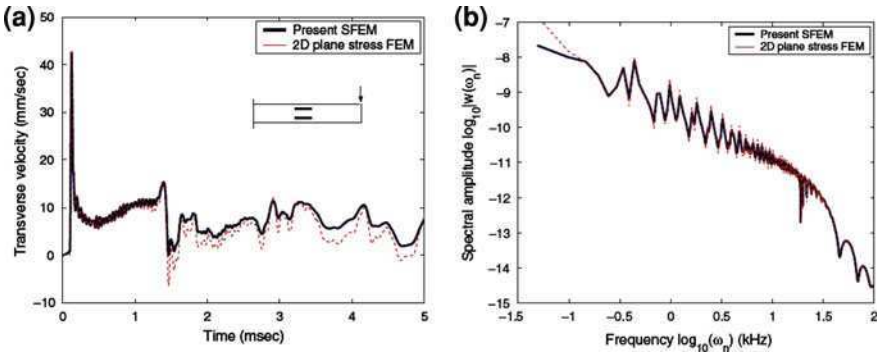

Fig. 6.18 Comparison of **a** transverse velocity history and **b** transverse displacement spectrum obtained from the present SFEM and the 2D plane stress FEM at the free end of a graphite-epoxy unidirectional composite cantilever beam with two symmetric delaminations at the mid-span

degrees of freedom, and the span is increased by length l_1, then the system size will increase to $(\bar{n} \times m)$, where $\bar{n} = \approx n + l_1(n_h + 1)n_d/\Delta l$. Here $\Delta l \approx \lambda/10$, where λ is the smallest wavelength of the propagating waves, n_h is the number of elements across the beam depth and n_d is the number of degrees of freedom per node. Now, such large FE system is to be solved at each time step over the time window of observation while adopting a particular time integration scheme. The time step again has to comply with the high frequency nature of the excitation and is generally of the order of μs. Obviously, the conventional FEM will be always slower and will need more memory compared to FSFEM. The computational costs are given in Table 6.2 for the first comparative study reported in Sect. 6.5.1, which shows nearly three times higher memory requirements and two orders of magnitude higher computation time for FEM. The above numbers are based on computations performed using IBM/RS6000 high performance computer.

6.6 Modeling of Corrosion Pits

In this section, we present techniques for modeling pitting corrosion, which is one of the leading failure types in a metallic structure. It is quite well known that metals corrode in a humid atmosphere. Corrosion is a complex process associated with the release of chemical energy. Although there are many different types of corrosion, we will address only the modeling of pitting corrosion. There are two reasons for this:

Table 6.2 Computational efficiency of FSFEM compared to FEM

Type of model	Total CPU time (s)	Memory (MB)	System size
FEM	365.6	3.364	2,898 × 28
FSFEM	9.2	1.342	42 × 42

(1) the simplified damage models can be most easily generated compared to other types of corrosion and (2) it is the most common type of corrosion occurring in metallic structures.

Pitting is defined as the localized corrosion of a metal surface, confined to a point or a small area, that takes the form of cavities [7]. The combined action of mechanical stresses and corrosion pit severely affect structural integrity. Pitting is one of the most destructive forms of corrosion. Pits can act as a local stress raiser and the sites for crack initiation. It is very difficult to detect the pits owing to its very small size (of the order of microns) and its being covered by corrosion products. Therefore precise structural health monitoring of pre-crack surface corrosion is very important to understand and predict the effect of corrosion on structural integrity and fatigue life.

Several nondestructive techniques are available to detect corrosion [25]. These methods have limited capability and reliability, especially in revealing the conditions beneath paint. The notable nondestructive evaluation (NDE) techniques for corrosion detection include advanced ultrasonic [14], eddy current [37], and thermo-graphic techniques [13]. Both ultrasonic and eddy current techniques are limited in lateral spatial resolution to approximately 1 cm. Thermography systems provide increased spatial resolutions of 10–100 μm, but the environmental noise and difficulties in interpreting results currently restrict widespread use of this technique [13]. Recently structural health monitoring using diagnostic waves is being studied widely for corrosion detection. The high frequency content of the waves helps with the detection of the presence of minute defects, which is otherwise not possible using conventional techniques like modal analysis. Thus damages can be detected at their onset and further propagation can be prevented.

In this section, a spectral finite element beam model based on First order shear deformation theory (FSDT) is developed to model the corrosion pits. The model will depend on the shape of the corrosion pits. Such shape is dependent on the material of the structure and also on the environment to which it is exposed. In aluminum, the pit is generally hemispherical in shape [10, 28] and the rate of corrosion decreases with time when exposed to air. Corrosion pits are normally of arbitrary shape which may require a higher number of elements for their model.

As said earlier, the shape of corrosion pit depends upon the material. For example, in steel its shape is conical with circular at opening, with a ratio of the diameter to the depth in the range between 8 : 1 to 10 : 1 for coal and iron ore carrying cargo, whereas for oil tankers, this ratio is in the range between 4 : 1 to 6 : 1 [27]. In aluminum, the pit tends to be roughly circular at the opening and roughly hemispherical in cross section [10, 28]. For modeling of pits resulting from corrosion in an aluminum beam, we need to know the shape and size of the

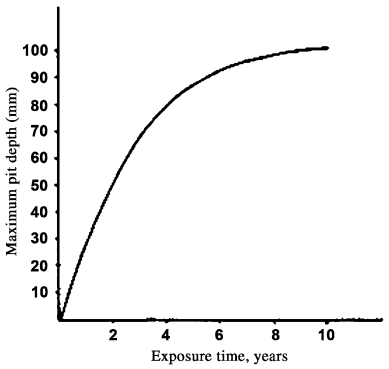

Fig. 6.19 Plot of pit depth as a function of time (in years) [24]

pit, which are function of time of exposure in years. Aluminum has a very high affinity for oxygen resulting in a thin protective layer of aluminum oxide, which is the reason of aluminum being usually very resistant to most atmospheric condition and to a great varieties of chemical agents. In general, the rate of corrosion of aluminum decreases with time baring few cases like in caustic soda, where the rate is nearly linear. In aqueous solutions, at elevated temperature and pressure, corrosion rate increases with time [10]. The growth rate of pit depth is high during early years of exposure and gradually decreases to approach an asymptotical value. The maximum pit depth for 10 years of exposure is about 100 μm after that it is nearly constant as evident from Fig. 6.19. The pit depth rarely exceeds 200 μm after exposure to 20 years [10].

Figure 6.19 shows the variation of pit depth with the number of years of exposure [24]. From this plot, the relationship between the pit depth and time of exposure is established by fitting the curve, which is found to be exponential for aluminum, and can be written as

$$d_{\text{pit}} = 0.1177T^3 - 3.2023T^2 + 30.491T \quad (\mu\text{m}); \tag{6.72}$$

where, d_{pit} is the pit depth (μm), and T is the exposure time (years). In [9], the maximum pit depth of aluminum exposed to various waters is found as the function of the cube root of exposure time, and is of the form:

$$d_{\text{pit}} = kT^{\frac{1}{3}} \tag{6.73}$$

where k is a constant which depends on the composition of water and of the alloy. Here, the corrosion pit is assumed as roughly hemispherical [10, 28] in shape and is modeled as a series of FSDT stepped beams as shown in Fig. 6.20.

6.6.1 Wave Propagation Response Due to Corrosion Pits

It was mentioned earlier that corrosion pits are very small (of the order of few microns). If a wave hits such region, it will encounter a very small impedance

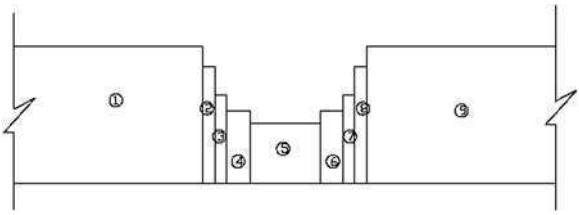

Fig. 6.20 Modeling of hemispherical corrosion pit

mismatch, which will introduce a reflection of magnitude which is many orders smaller than that of the incident wave. The detection of small pit size requires a very high frequency content signal. If this problem is modeled using conventional FEM, it would lead to enormous system size. In this section, the problem is solved using WSFEM, where the beam sections are modeled using FSDT beam element.

The beam used for numerical experiments has a length $L = 0.9\,\text{m}$, width $b = 0.02\,\text{m}$, and depth $h = 0.002\,\text{m}$. The material properties are as follows, Young's modulus $E = 70\,\text{GPa}$; density $\rho = 2{,}700\,\text{kg/m}^3$. For WSFEM formulation, the Daubechies scaling function used has an order of $N = 22$ and the sampling rate is $\Delta t = 1\,\mu\text{s}$. The number of sampling point used is 1,024 which gives a time window of $T_w = 1{,}024\,\mu\text{s}$.

First, a convergence study is performed to select the number of elements required to model the corrosion pit for accurate simulation of response. The hemispherical pit is modeled using 1, 3, 7 and 9 elements, respectively and the discretization of the pit is shown in Fig. 6.21a–d respectively. In the simulation studies, a tone burst signal modulated at a frequency 28.32 kHz is used. From Fig. 6.22 it is evident that there is no significant differences between response obtained from pit modeled using 7 and 9 elements. Hence to save on computational cost, the analysis is performed using 7 elements. In Fig. 6.22, only the portion of the reflected wave is presented, as the changes occur only in the reflected wave responses.

Figure 6.23 shows the tip transverse velocity in the beam due to modulated load applied at the tip. The corrosion is at the middle of the beam and is modeled with seven WSFEM. The responses are plotted for different sizes of the pit at different

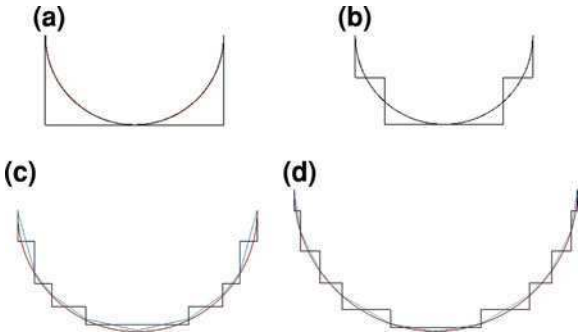

Fig. 6.21 Corrosion pit modeled with **a** 1, **b** 3, **c** 7 and **d** 9 elements

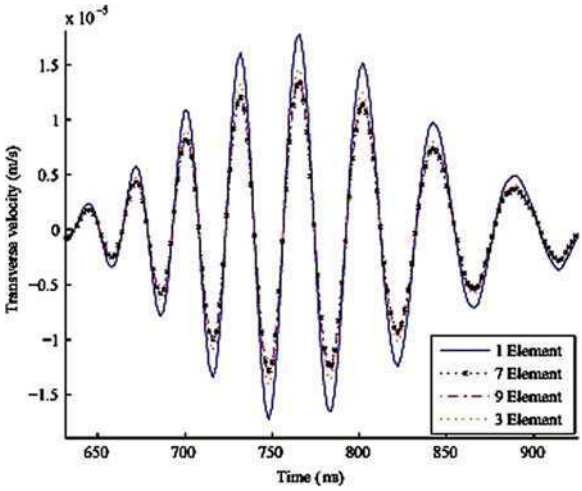

Fig. 6.22 Comparison of reflected responses for various element size

times. These sizes at different times are obtained from Eq. 6.72. It can be seen from the figures that the reflected waves are visible only when magnified. This is due to the very small dimensions of the corrosion pit as compared to the beam dimensions.

Next we will investigate the effect of beam theories on the group speeds. All the examples in this section uses WSFEM formulated using FSDT. It is well known that the beam theory based on Euler–Bernoulli theory predicts higher group speeds compared to FSDT [11]. Note that we can derive the Euler Bernoulli beam element from the FSDT element by setting the shear rigidity to infinity and the rotational inertia to zero. This aspect can be seen from Fig. 6.24 with the early arrival of reflected waves predicted by the Euler–Bernoulli beam case.

Next, we evaluate how the location of the corrosion pits scatter the waves in a beam. The corrosion pits are assumed at three different locations from the fixed end of the beam, namely 0.35, 0.5 and 0.65 m, respectively. The beam length is

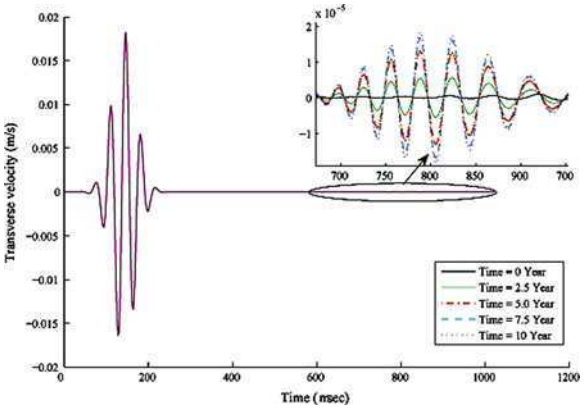

Fig. 6.23 Transverse tip velocity in beam due to tip modulated load

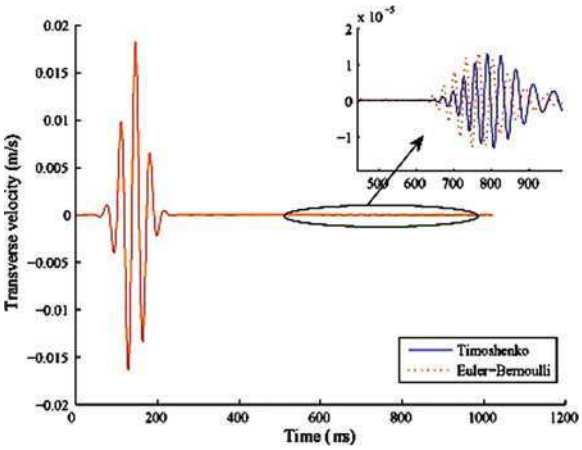

Fig. 6.24 Effect of beam theories on the response of a corroded beam (corrosion pit is at the middle of the beam and time of exposure is equal to 5 years)

assumed to be 0.9 m and has a fixed right end. The time of exposure is assumed equal to 10 years. It is expected that as the corrosion pits moves away from the free end, the reflected waves from the corrosion pits will also shift accordingly, which is clearly seen in Fig. 6.25. Knowing the speed of the medium (from the dispersion curves) and the time of arrival of waves from the time history plots, one can find the flaw location.

This section has shown how a simplified corrosion model can be developed using simplified assumptions. In the next section, we will address the simplified model for degraded zones, which is normally prevalent in composites due to excessive moisture absorption.

6.7 Modeling of Material Degradation

Material degradation occurs commonly in composite structures, especially when exposed to humid environment. Due to the inherent property of the composites and sometimes aided by the manufacturing defects, composite structures are susceptible to being porous. Moisture sits in the pores and reduces the stiffness, and hence the load carrying capacity of these structures. That is, moisture absorption can cause an irreversible hygrothermal deterioration of the material. The change in temperature and moisture absorption changes the mechanical properties. This affects the structure in dimensional stability as well as material degradation due to reduction in mechanical properties. Hence, it becomes necessary to continuously monitor the structure for material degradation and wave based diagnostics can be used for this purpose.

In this section, we develop simplified damage models for composites with degraded zones. The material property reduction due to moisture absorption and temperature can be directly obtained through experimentation and an empirical

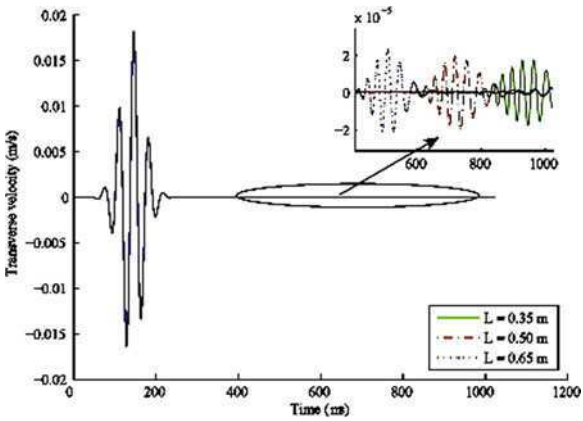

Fig. 6.25 Response of corroded beam for corrosion pit at various location

relation of material properties as a function of moisture and temperature can be obtained. This function can be used in theoretical or spectral FEM model to determine the effects of wave response on the material degradation or determine the degraded zone location from the measured wave response. Alternatively, one can average the material characteristics in the degraded region by determining the ratio of material property of healthy structure to the experimentally obtained property of the degraded region and this ratio, say α will say by how much the moisture has reduced the stiffness of the structure. Such an approach will enable to develop a kinematics based damaged model explained for single delamination in Sect. 6.3. Here we will develop both these damage models for material degradation. The first method based on direct experimentally obtained curves is called the Experimental Degraded (ED) Model while the second method is called the Average Degraded (AD) Model.

6.7.1 Experimental Degraded Model (EDM)

Degradation in composite material causes differential swelling of fiber and the matrix due to moisture absorption and as a result, it causes matrix cracks or/and fiber/matrix debonding. The weakening of bonding between fiber and matrix and softening of matrix material are also the reasons behind decrease in composite strength. In order to utilize the full potential of composite materials for structural applications, the moisture content of composite materials has to be defined well in advance and probably in the design stage. Few researchers have done experiments in standard laboratory conditions to establish the effect of moisture concentration on the elastic modulus of composite materials [39]. The hygrothermal deformation of a unidirectional composite is much higher in the transverse direction than in the longitudinal direction. Such difference in deformation in two directions induces residual stresses in composite laminates, because the multi-directionality of fiber

orientation resists free deformations. Also the change in temperature and moisture absorption changes the mechanical properties. Thus this affects the structure in dimensional stability as well as material degradation due to reduction in mechanical properties. The physical effect of moisture absorption is the reduction in glass transition temperature T_g of the resin. At room temperature, the performance of resin may not change with the reduction in T_g but at elevated temperature, the properties are severely affected. The general observation is that as the composite material degrades after moisture absorption, its tension modulus first slightly increases with relative humidity (RH) up to 50% of RH and then decreases with further increases in RH. Thus the stiffness of the structure varies with the relative humidity.

The moisture concentration increases with time and reaches the saturation level after some prescribed time. The maximum moisture content depends on the environment. In humid air it is a function of relative humidity. It has been found that maximum moisture content, C_m can be related to the relative humidity ϕ by the expression [33]

$$C_m = a\phi^b \tag{6.74}$$

where, a and b are constants which depend on material. The value of these constants can be obtained by fitting the line through the data points obtained experimentally. Table 6.3 gives the values of a and b obtained by various researchers. It has been found that maximum moisture content is insensitive to the ambient temperature but depends on the moisture content of the environment [33]. This is evident from Eq. 6.74. This is a useful approximation and it has been stated also that the maximum moisture concentration C_m varies also with temperature [36].

Figure 6.26 shows the variation of composite modulus E_x, E_y and E_z as a function of moisture content for two different temperatures. These plots are obtained from [33]. From the figure, the expression for modulus as function of moisture concentration can be obtained through curve fitting and can be written in the following forms, which are given in Eqs. 6.75–6.80, where modulus is in GPa and moisture concentration C is in percent.

For temperature, T = 366 K;

$$E_x = 16.344C^6 - 66.161C^5 + 92.479C^4 - 57.29C^3 + 13.769C^2 - 81.049C + 134.39 \tag{6.75}$$

Table 6.3 Values of a and b obtained by various researchers for composite material AS/3501

Investigator	a	b
Springer [21]	0.019	1
DeIasi and Whiteside [4]	0.0186	1.6, $\phi < 60\%$ RH
–	–	1.9, $\phi > 60\%$ RH
Whitney and Browning [41]	0.016	1.1

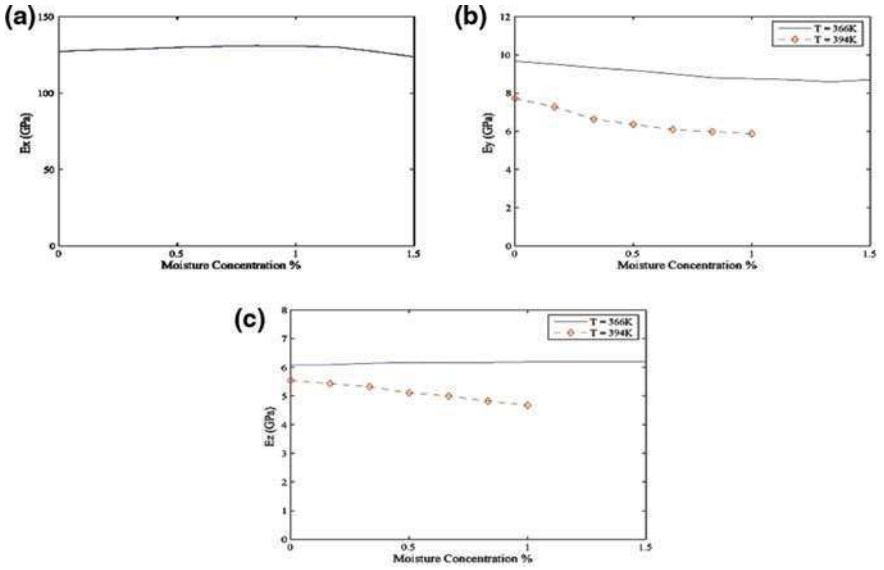

Fig. 6.26 Variation of modulus as a function of moisture content **a** E_x variation **b** E_y variation **c** E_z variation

$$E_y = 4.5804C^6 - 20.11C^5 + 32.943C^4 - 24.297C^3 + 7.7994C^2 - 1.8376C + 9.6732 \tag{6.76}$$

$$E_z = 1.2694C^6 - 6.2108C^5 + 11.629C^4 - 10.281C^3 + 4.129C^2 - 0.4398C + 6.0866 \tag{6.77}$$

For temperature, T = 394 K, we can write the three modulus as

$$E_x = 16.344C^6 - 66.161C^5 + 92.479C^4 - 57.29C^3 + 13.769C^2 - 81.049C + 134.39 \tag{6.78}$$

$$E_y = -5.8703C^4 + 11.744C^3 - 5.3871C^2 - 2.3500C + 7.7277 \tag{6.79}$$

$$E_z = -0.7275C^4 + 1.8871C^3 - 1.6856C^2 - 0.3426C + 5.5415 \tag{6.80}$$

The time required to attain at least 99.9% of its maximum possible moisture content is given by the expression [33].

$$t_m = \frac{0.67s^2}{D} \tag{6.81}$$

where, t_m is maximum time, s is thickness and D is diffusivity. The time required to reach the maximum moisture content is insensitive to the environment, however, it depends on thickness s of the composite material and the temperature T, as diffusivity D_x depends on temperature [33]. The diffusivity, D can be related to the temperature T by the expression [21].

$$D = D_o e^{\left[\frac{-C}{T}\right]} \tag{6.82}$$

where, D_o and C are constants and T is the absolute temperature. Using Eq. 6.82, Eq. 6.81 can be rewritten as follows:

$$t_m = \frac{0.67 s^2}{D_o e^{\left[\frac{-C}{T}\right]}} \tag{6.83}$$

Figure 6.27 shows the graphical representation of Eq. 6.83.

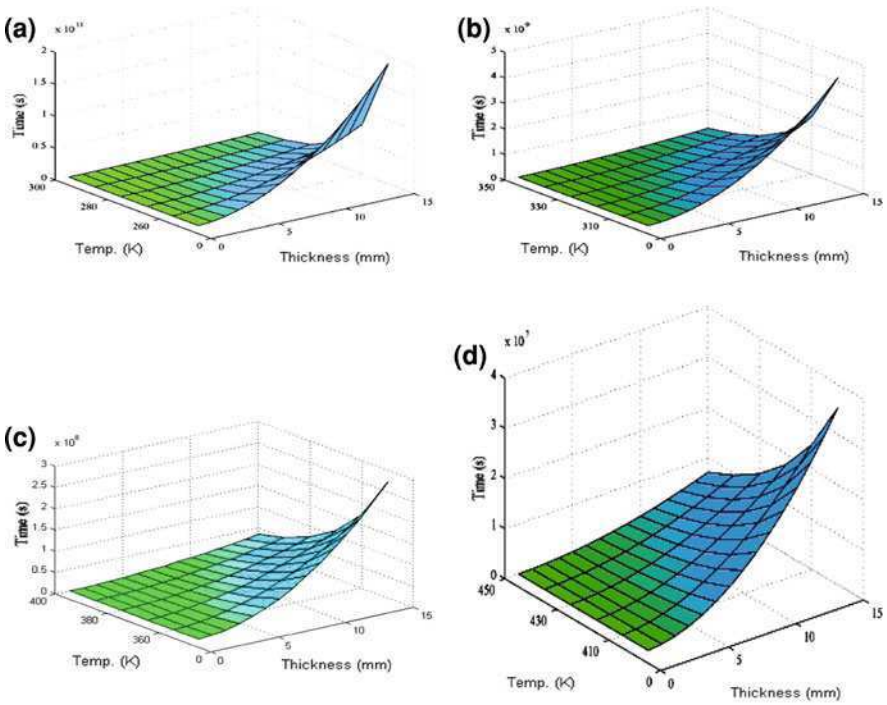

Fig. 6.27 Time required to reach saturation level at various temperature and thickness in mm, **a** at Temp = 250–300 K, **b** at Temp = 300–350 K, **c** at Temp = 350–400 K, **d** at Temp = 400–450 K

6.7.1.1 Wave Propagation in Degraded Composites Using ED Model

A moisture absorbed AS/3501 composite cantilever beam is considered in this numerical experiment solved using the WSFEM formulation. The beam dimensions are as follows: length, $L = 0.75\,\text{m}$, width, $b = 0.05\,\text{m}$, and ply thickness, $t = 0.0013\,\text{m}$. The material properties assumed are as follows, the Young modulus (E) is variable due to moisture absorption and is given in Eqs. 6.75–6.80. In absence of data available for the variation of G with moisture absorption, it is assumed to be constant and its value is taken as, $G_{12} = G_{13} = 6.13\,\text{GPa}; G_{23} = 4.80\,\text{GPa}$; $\nu_{12} = 0.42$; and mass density $= 1{,}449\,\text{kg/m}^3$. The Daubechies scaling function used in these examples has an order of $N = 22$ and the sampling rate is $\Delta t = 1\,\mu\text{s}$. The number of sampling points used is equal to 1,024, which gives a time window is $T_\text{w} = 1{,}024\,\mu\text{s}$. To calculate the moisture concentration Eq. 6.74 is used, where $a = 0.0018$ and $b = 1$ [24].

A sinusoidal pulse modulated at 37.6 kHz is used as input signal. Figure 6.28 shows the tip transverse velocity in the beam due to a modulated load applied at the tip in the transverse direction.

The degraded region is at 0.25 m from the fixed end and is modeled with single WSFEM. The responses are plotted for different values of RH from 0 to 80% in the step of 20%. Figure 6.29 is the magnified view of Fig. 6.28.

On careful observation from Fig. 6.29, it is found that the magnitude of response is increasing from 0% RH to 40% RH after which it is decreasing and at 80% RH, it is found that the phase of the response gets changed. To investigate this further, the response is plotted as shown in Fig. 6.30 at smaller steps of increment.

Again careful observation Fig. 6.30, it is found that the magnitude of response is increasing from 0% RH to 50% RH after which it decreases and the magnitude corresponding to 30% RH and 60% RH are nearly same, which means that

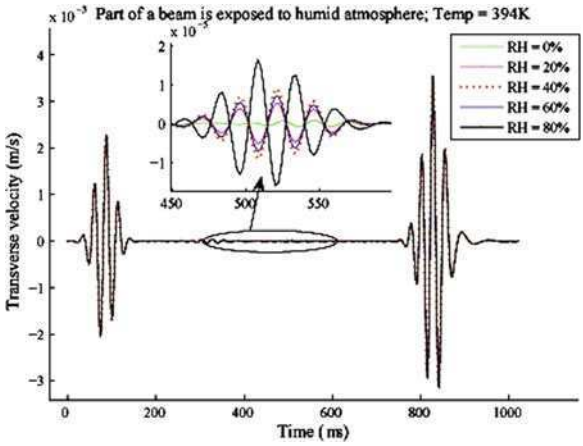

Fig. 6.28 Transverse tip velocity in beam due to tip modulated load

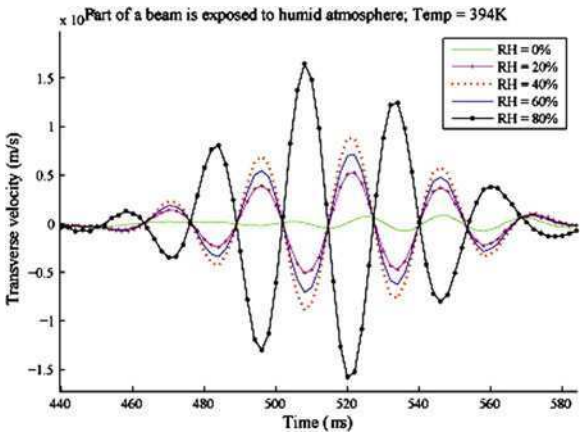

Fig. 6.29 Magnified view of transverse tip velocity shown in Fig. 6.28

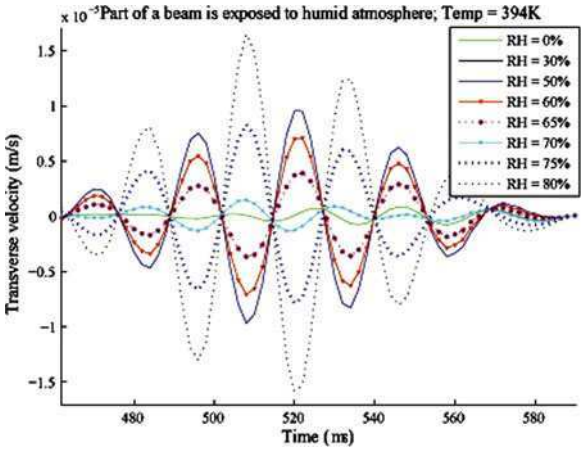

Fig. 6.30 Magnified view of transverse tip velocity shown in Fig. 6.29

stiffnesses at these two values of RH are nearly same. When RH is increased beyond 70%, the phase get changed, which is in accordance with the variation in tension modulus E_X, which first increases up to 50% RH and then decreases. After 70% RH, it decreases rapidly.

We will next treat the same problem slightly differently by using a kinematics based average model, which is explained in the next section.

6.7.2 Average Degraded Model

In the average degraded model (ADM), the characteristic of a degraded region is that the material properties (Young's modulus, density, etc.) gets reduced due to

moisture absorption say by α. Hence, we represent the degraded laminate constitutive property under plane stress or plane strain condition by

$$\begin{Bmatrix} \sigma_{xx} \\ \sigma_{zz} \\ \tau_{xz} \end{Bmatrix} = \begin{bmatrix} \alpha_{11}Q_{11} & \alpha_{13}Q_{13} & 0 \\ \alpha_{13}Q_{13} & \alpha_{33}Q_{33} & 0 \\ 0 & 0 & \alpha_{55}Q_{55} \end{bmatrix} \begin{Bmatrix} \varepsilon_{xx} \\ \varepsilon_{zz} \\ \gamma_{xz} \end{Bmatrix}, \tag{6.84}$$

where z is the laminate thickness direction and x is the longitudinal direction (0° fiber direction). α_{ij} are degradation factors, which are unity for healthy laminates.

We apply the same approach we adopted to model the delamination or vertical cracks (see Sects. 6.3 and 6.4). The element nodal degrees of freedom are condensed after the assembly of two undamaged elements on both sides of the damaged zone. It will then be possible to describe the damage configuration just by prescribing three sets of parameters: (1) the degradation factors (α_{ij}) describing the damaged laminate (Eq. 6.84); (2) the approximate span-wise location of one of the interface between the undamaged and damaged zone; and (3) the length of the damaged zone.

The location of the two nodes of spectral elements with an embedded degraded zone in a beam is shown in Fig. 6.31a. In the absence of degradation, one spectral element between node 1 and node 2 is sufficient for analysis. The presence of degradation, when treated as a structural discontinuity increases the number of elements from one to three as shown in Fig. 6.31b. Four more nodes are introduced to model the degraded zone (element (3)) and the surrounding undamaged zones (elements (1) and (2)). In a practical situation, it may so happen that the matrix crack density in laminates may decrease with some gradation from the damaged zone. In such a case, the elements (1) and (3) can be used with such graded laminate properties, based on the same constitutive model as discussed in Eq. 6.84.

As elsewhere, all variables with "hats" denote that the variables are defined in the frequency domain. The kinematic assumption of continuity of displacements and rotations at the internal element nodes 3, 5 and 4, 6 leads to

$$\hat{\mathbf{u}}_5 = \left\{ \hat{u}_5^0 \ \hat{\omega}_5 \ \hat{\phi}_5 \right\}^T = \hat{\mathbf{u}}_3, \quad \hat{\mathbf{u}}_6 = \left\{ \hat{u}_6^0 \ \hat{\omega}_6 \ \hat{\phi}_6 \right\}^T = \hat{\mathbf{u}}_4. \tag{6.85}$$

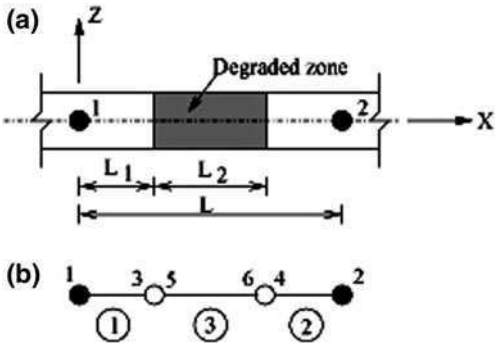

Fig. 6.31 **a** Composite beam segment with degraded zone of size L_2. The whole segment is represented by the end nodes 1 and 2 of the spectral element. **b** Element local configuration showing the internal element numbers (1), (2) and (3) by *circles* and the associated nodes 1–3, 2–4, and 5–6

From equilibrium of the nodal forces and moments at the left interface (between nodes 3 and 5) and at the right interfaces (between nodes 4 and 6), we get respectively

$$\hat{\mathbf{f}}_3 + \hat{\mathbf{f}}_5 = \mathbf{0}, \quad \hat{\mathbf{f}}_4 + \hat{\mathbf{f}}_6 = \mathbf{0}. \tag{6.86}$$

The element equilibrium equation for the jth internal element ($j = 1, 2, 3$) with nodes p and q can be written as

$$\begin{bmatrix} \hat{\mathbf{K}}_{11}^{(j)} & \hat{\mathbf{K}}_{12}^{(j)} \\ \hat{\mathbf{K}}_{21}^{(j)} & \hat{\mathbf{K}}_{22}^{(j)} \end{bmatrix}_{(6\times6)} \begin{Bmatrix} \hat{\mathbf{u}}_\mathbf{p} \\ \hat{\mathbf{u}}_\mathbf{q} \end{Bmatrix} = \begin{Bmatrix} \hat{\mathbf{f}}_\mathbf{p} \\ \hat{\mathbf{f}}_\mathbf{q} \end{Bmatrix}. \tag{6.87}$$

Assembling Eq. 6.87 for the three internal elements (1), (2) and (3), we get

$$\begin{bmatrix} \hat{\mathbf{K}}_{11}^{(1)} & \hat{\mathbf{K}}_{12}^{(1)} & \mathbf{0} & \mathbf{0} \\ \hat{\mathbf{K}}_{21}^{(1)} & \hat{\mathbf{K}}_{22}^{(1)} + \hat{\mathbf{K}}_{11}^{(2)} & \hat{\mathbf{K}}_{12}^{(2)} & \mathbf{0} \\ \mathbf{0} & \hat{\mathbf{K}}_{21}^{(2)} & \hat{\mathbf{K}}_{22}^{(2)} + \hat{\mathbf{K}}_{11}^{(3)} & \hat{\mathbf{K}}_{12}^{(3)} \\ \mathbf{0} & \mathbf{0} & \hat{\mathbf{K}}_{21}^{(3)} & \hat{\mathbf{K}}_{22}^{(3)} \end{bmatrix}_{(12\times12)} \begin{Bmatrix} \hat{\mathbf{u}}_1 \\ \hat{\mathbf{u}}_3 \\ \hat{\mathbf{u}}_4 \\ \hat{\mathbf{u}}_2 \end{Bmatrix} = \begin{Bmatrix} \hat{\mathbf{f}}_1 \\ \mathbf{0} \\ \mathbf{0} \\ \hat{\mathbf{f}}_2 \end{Bmatrix}. \tag{6.88}$$

Upon condensation of the degrees of freedom at the internal nodes 3 and 4 and assuming no load is applied to the damaged zone, Eq. 6.88 becomes

$$\hat{\mathbf{K}}_{(6\times6)} \begin{Bmatrix} \hat{\mathbf{u}}_1 \\ \hat{\mathbf{u}}_2 \end{Bmatrix} = \begin{Bmatrix} \hat{\mathbf{f}}_1 \\ \hat{\mathbf{f}}_2 \end{Bmatrix}, \tag{6.89}$$

where the sub-matrices of the new dynamic stiffness matrix $\hat{\mathbf{K}}$ are defined as

$$\hat{\mathbf{K}}_{11} = \hat{\mathbf{K}}_{11}^{(1)} - \hat{\mathbf{K}}_{12}^{(1)} \left(\hat{\mathbf{K}}_{22}^{(1)} + \hat{\mathbf{K}}_{11}^{(2)} \right)^{-1} \mathbf{X}_2, \tag{6.90}$$

$$\hat{\mathbf{K}}_{12} = \hat{\mathbf{K}}_{12}^{(1)} \left(\hat{\mathbf{K}}_{22}^{(1)} + \hat{\mathbf{K}}_{11}^{(2)} \right)^{-1} \hat{\mathbf{K}}_{12}^{(2)} \mathbf{X}_1^{-1} \hat{\mathbf{K}}_{12}^{(3)}, \tag{6.91}$$

$$\hat{\mathbf{K}}_{21} = \hat{\mathbf{K}}_{21}^{(3)} \mathbf{X}_1^{-1} \hat{\mathbf{K}}_{21}^{(2)} \left(\hat{\mathbf{K}}_{22}^{(1)} + \hat{\mathbf{K}}_{11}^{(2)} \right)^{-1} \hat{\mathbf{K}}_{21}^{(1)} \tag{6.92}$$

$$\hat{\mathbf{K}}_{22} = \hat{\mathbf{K}}_{22}^{(3)} - \hat{\mathbf{K}}_{21}^{(3)} \mathbf{X}_1^{-1} \hat{\mathbf{K}}_{12}^{(3)}, \tag{6.93}$$

$$\mathbf{X}_1 = \left(\hat{\mathbf{K}}_{22}^{(2)} + \hat{\mathbf{K}}_{11}^{(3)} \right) - \hat{\mathbf{K}}_{21}^{(2)} \left(\hat{\mathbf{K}}_{22}^{(1)} + \hat{\mathbf{K}}_{11}^{(2)} \right)^{-1} \hat{\mathbf{K}}_{12}^{(2)}, \tag{6.94}$$

$$\mathbf{X}_2 = \hat{\mathbf{K}}_{21}^{(1)} + \hat{\mathbf{K}}_{12}^{(2)} \mathbf{X}_1^{-1} \hat{\mathbf{K}}_{21}^{(2)} \left(\hat{\mathbf{K}}_{22}^{(1)} + \hat{\mathbf{K}}_{11}^{(2)} \right)^{-1} \hat{\mathbf{K}}_{21}^{(1)}. \tag{6.95}$$

Equation 6.89 is the equilibrium equation for the spectral element with embedded degraded zone, where only the degrees of freedom at the end nodes 1, 2 need to be used while forming the global system of a damaged structure.

6.7.3 Wave Scattering in a Degraded Composite Beam Using ADM

To simulate the effect of stiffness degradation on the diagnostic signal, a graphite-epoxy cantilever beam of length 0.8 m, thickness 16 mm and width 10 mm is considered. All the plies are assumed to be of equal thickness with stacking sequence $(0_{40}/90_{80}/0_{40})$. A 20 mm long degraded zone is introduced at 0.3 mm from the fixed end of the beam. The finite element model of the beam consists of a single damaged spectral element under plane stress conditions in the X–Z plane (Fig. 6.31). It is assumed that all the 90° plies are degraded with the same factor, α_{11} (Eq. 6.84) in the longitudinal mode.

In the transverse and shear modes, the plies are assumed to be undamaged. In a practical situation, however, the transverse and shear moduli will also have degradation but their effect on the damaged structural response under flexural wave excitation (as in the present case) will be negligible compared to that due to degradation in the longitudinal elastic modulus. A sinusoidal pulse modulated at 20 kHz (shown in Fig. 4.1) is applied in the transverse direction (parallel to the z-axis) at the tip. 2,048 FFT sampling points are used in the analysis. Transverse velocity histories at the tip of the beam due to the variation in degradation of cross-ply are shown in Fig. 6.32. As seen in this figure, the first pulse appearing at 0.5–0.75 ms is the incident wave. The next smaller pulses seen at higher degradation (smaller values of α_{11}) are reflections from the two ends of the degraded zone. Here we assume that the plies were degraded uniformly within the degraded zone.

To study the effect of the length of the degraded zone, we consider the same cantilever beam with one of the interfaces fixed at 0.4 m from the tip. However, instead of narrow band load, we will use the broadband signal shown in Fig. 3.7. The length of the degraded zone is varied by moving the other interface towards the fixed end from 0.1 to 0.4 m. The last case represents one-half of the beam on the fixed end side of the beam as degraded. The variation of the transverse velocity histories at the tip of the beam with the variation of the size of the degraded zone is

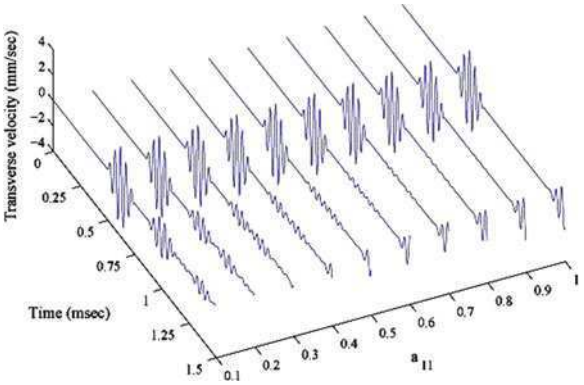

Fig. 6.32 Transverse velocity history due to variation in the degradation factor α_{11} using a narrow-band diagnostic signal (Fig. 4.1). Length of the degraded zone is 20 mm

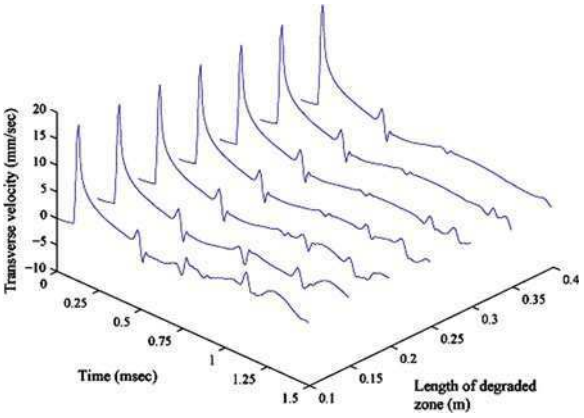

Fig. 6.33 Transverse velocity histories due to variation in the length of the degraded zone with broadband diagnostic signal (Fig. 3.7). Degradation factor $\alpha_{11} = 0.2$

shown in Fig. 6.33 for $\alpha_{11} = 0.2$. From the figure it can be seen that for a smaller size degraded zone with higher degradation (smaller values of α), both reflections from the two interfaces are easily detectable.

6.8 Modeling of Vertical Cracks in 2D Waveguides

Simplified modeling of flaws in 1D waveguides can achieved by imposing kinematics among the nodes that make up the flaw. In 2D waveguides, imposition of kinematics is not straightforward. Alternate ways be adopted for modeling damages in 2D waveguides. One such approach is the use of flexibility functions across the crack front for certain degrees of freedom of the nodes that make up the flaw. Although such approach is limited for very few crack orientation, they are found to be very useful in SHM studies due to their simplicity.

In this section, we will formulate a spectral element based on Fourier transform for a 2D waveguide with through width vertical crack for which flexibility functions are available. This element is an extension of spectral plate element formulated in Sect. 5.4.

A model of the spectral plate element with a transverse open and non-propagating crack is shown in Fig. 6.34. The length of the element in the X direction is L and the plate is infinite in the Y direction (although having a Y window length L_Y). The crack is located at a distance of L_1 from the left edge of the plate and has a length $2c$ in the Y direction.

Following the classical plate theory for symmetric ply-stacking, the displacement field at frequency ω_n is given by

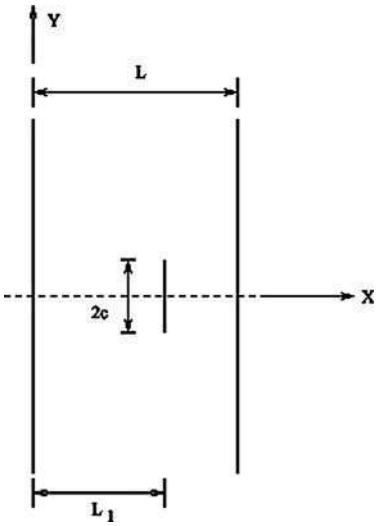

Fig. 6.34 The plate element with transverse and non-propagating crack

$$\hat{w}(x,y) = \sum_{m=1}^{M} \tilde{w}(x) e^{-j\xi_m y}$$
$$= \sum_{m=1}^{M} (A_{mn} e^{-jk_1 x} + B_{mn} e^{-jk_2 x} + C_{mn} e^{-jk_1(L_1 - x)} + D_{mn} e^{-jk_2(L_1 - x)}) e^{-j\xi_m y},$$

where k_1 and k_2 are the wavenumbers, which are the roots of the following dispersion relation:

$$D_{11}k^4 + (2D_{12} + 4D_{66})\xi_m^2 k^2 + (D_{22}\xi_m^4 - I_\circ \omega^2) = 0,$$

with $\xi_m = 2m\pi/L_Y$. Further, expressions of the moment (M_{xx}) and shear force (V_x) according to this theory are

$$M_{xx} = D_{11}\partial^2 \hat{w}(x,y)/\partial x^2 + D_{12}\partial^2 \hat{w}(x,y)/\partial y^2 \tag{6.96}$$

$$V_x = -(D_{11}\partial^3 \hat{w}(x,y)/\partial x^3 + (D_{12} + 4D_{66})\partial^3 \hat{w}(x,y)/\partial x y^2). \tag{6.97}$$

We assume two different displacement fields $\hat{w}_1(x,y)$ and $\hat{w}_2(x,y)$ on the left and right side of the crack, respectively, whose wavenumber domain representations are $\tilde{w}_1(x)$ and $\tilde{w}_2(x)$. These expressions involve a total of eight constants, which will be denoted in subsequent formulation by vector **c**. This vector can be represented as a function of nodal displacements and rotations $\{\tilde{q}_1, \tilde{q}_2, \tilde{q}_3, \tilde{q}_4\} = \{\mathbf{u}_1, \mathbf{u}_2\}$, using the boundary conditions at the left and right edge and a hypothetical boundary along the crack line as:

1. At the left edge of the element ($x = 0$)

$$\tilde{w}_1(x) = \tilde{q}_1, \quad \partial \tilde{w}_1(x)/\partial x = \tilde{q}_2$$

2. At the crack location ($x = L_1$ for $\hat{w}_1$ and $x = 0$ for $\hat{w}_2$)

$$\begin{aligned} \tilde{w}_1(x) &= \tilde{w}_2(x) \quad \text{(continuity of displacement across the crack)} \\ \partial\tilde{w}_1(x)/\partial x - \partial\tilde{w}_2(x)/\partial x &= \tilde{f}_2 \quad \text{(discontinuity of slope across the crack)} \\ M_{xx1} &= M_{xx2} \quad \text{(continuity of bending moment)} \\ V_{x1} &= V_{x2} \quad \text{(continuity of shear force)} \end{aligned}$$

3. At the right edge of the element ($x = L - L_1$):

$$\tilde{w}_2(x) = \tilde{q}_3 \quad \partial\tilde{w}_2(x)/\partial x = \tilde{q}_4$$

where M_{xx1} and V_{x1} are the moment and shear force obtained from $\hat{w}_1(x, y)$ and similarly for M_{xx2} and V_{x2}. The $\tilde{f}_2$ is the wavenumber transform of the slop discontinuity function $\hat{f}_2(y)$ along the crack edge. The way of obtaining $\hat{f}_2(y)$ is given in the next section. These boundary conditions can be written as

$$\begin{bmatrix} \mathbf{M}_1 & \mathbf{0} \\ \mathbf{M}_2 & \mathbf{M}_3 \\ \mathbf{0} & \mathbf{M}_4 \end{bmatrix} \{\mathbf{c}\} = \begin{Bmatrix} \mathbf{u}_1 \\ \mathbf{f} \\ \mathbf{0} \\ \mathbf{u}_2 \end{Bmatrix}, \quad \mathbf{f} = \{0, \tilde{f}_2\}$$

where $\mathbf{c} = \{A_{mn}, B_{mn}, C_{mn}, D_{mn}\}$ and $\mathbf{M}_1, \mathbf{M}_4 \in \mathbf{C}^{2\times 4}$ and $\mathbf{M}_2, \mathbf{M}_3 \in \mathbf{C}^{4\times 4}$. Inverting the matrix $\mathbf{M}$ (and calling it $\mathbf{N}$), the constants $\mathbf{c}$ can be expressed as

$$\mathbf{c} = \mathbf{N} \begin{Bmatrix} \mathbf{u}_1 \\ \mathbf{f} \\ \mathbf{0} \\ \mathbf{u}_2 \end{Bmatrix} = \mathbf{N}(:, [1, 2, 7, 8]) \begin{Bmatrix} \mathbf{u}_1 \\ \mathbf{u}_2 \end{Bmatrix} + \mathbf{N}(:, [3, 4])\mathbf{f} \tag{6.98}$$

Using Eqs. 6.96 and 6.97, the shear forces and bending moments at the left and right edge of the plate can be written as

$$\begin{Bmatrix} V_{x1}(0) \\ M_{xx1}(0) \\ V_{x2}(L) \\ M_{xx2}(L) \end{Bmatrix} = \begin{Bmatrix} \tilde{V}_1 \\ \tilde{M}_1 \\ \tilde{V}_2 \\ \tilde{M}_2 \end{Bmatrix} = \begin{bmatrix} \mathbf{P}_1 & \mathbf{0} \\ \mathbf{0} & \mathbf{P}_2 \end{bmatrix} \mathbf{c}, \quad \mathbf{P}_1, \mathbf{P}_2 \in \mathbf{C}^{2\times 4} \tag{6.99}$$

Combining Eqs. 6.98 and 6.99,

$$\begin{Bmatrix} \tilde{V}_1 \\ \tilde{M}_1 \\ \tilde{V}_2 \\ \tilde{M}_2 \end{Bmatrix} = \tilde{\mathbf{K}} \begin{Bmatrix} \mathbf{u}_1 \\ \mathbf{u}_2 \end{Bmatrix} + \mathbf{b}$$

where $\tilde{\mathbf{K}}$ is the frequency-wavenumber domain element stiffness matrix for the cracked plate and $\tilde{\mathbf{b}}$ is the body force vector due to the presence of the crack. They are given by

$$\tilde{\mathbf{K}} = \begin{bmatrix} \mathbf{P}_1 & \mathbf{0} \\ \mathbf{0} & \mathbf{P}_2 \end{bmatrix} \mathbf{N}(:, [1, 2, 7, 8]), \quad \tilde{\mathbf{b}} = \begin{bmatrix} \mathbf{P}_1 & \mathbf{0} \\ \mathbf{0} & \mathbf{P}_2 \end{bmatrix} \mathbf{N}(:, [3, 4])$$

6.8.1 Flexibility Along the Crack

If $\theta(y)$ denotes the bending flexibility at both sides of the crack, then the slope discontinuity function can be written as

$$\hat{f}_2(y) = \theta(y) M_{xx}(L_1, y). \tag{6.100}$$

The dimensionless form of $\theta(y)$ can be obtained as (see [17])

$$\theta(\bar{y}) = (6H/L_y)\alpha_{bb}(\bar{y})F(\bar{y}), \quad \bar{y} = y/L_y$$

where H is the total thickness of the plate, $\alpha_{bb}(\bar{y})$ is function representing dimensionless bending compliance coefficient and $F(\bar{y})$ is a correction function. The function $\alpha_{bb}(\bar{y})$ is given by the following relation:

$$\alpha_{bb}(\bar{y}) = \alpha^0_{bb} f(\bar{y})$$

with

$$\alpha^0_{bb} = (1/H) \int_0^{h_0} \xi(1.99 - 2.47\xi + 12.97\xi^2 - 23.117\xi^3 + 24.80\xi^4)^2 \, dh,$$
$$\xi = h/H$$

where $h(y)$ is a function representing the shape of the crack and h_0 is the central crack depth. Then

$$f(\bar{y}) = \exp\left[-(\bar{y} - \bar{y}_0)^2 e^2 / 2\bar{c}^2\right]$$

where e is the base of the natural logarithm and $\bar{c}$ is the normalized half-crack length, c/L_y. The correction factor is given as

$$F(\bar{y}) = \frac{2c/H + 3(\nu + 3)(1 - \nu)\alpha^0_{bb}[1 - f(\bar{y})]}{2c/H + 3(\nu + 3)(1 - \nu)\alpha^0_{bb}}$$

Figure 6.35 shows the variation $\theta(y)$ for different values of the crack length c and central crack depth h_0. To obtain $\tilde{f}_2$, it is necessary to take Fourier transform of

$\hat{f}_2(y)$. However, in Eq. 6.100, the expression of $M_{xx}(L_1, y)$, which is the moment at the crack location, is not known beforehand. Thus, to perform the transform, some approximation is necessary. Here, we assume that the moment is not greatly perturbed by the presence of the crack and M_{xx} of the cracked plate can be replaced by the M_{xx} of the undamaged plate, $M_{xx0}f(y)$. Further, if the applied load is concentrated, i.e., its Y dependency is $\delta(y - y_0)$, then so is $f(y)$. Thus, applying the Fourier transform and using the shifting property of the dirac delta function,

$$\tilde{f}_2 = M_{xx0}\theta(y_0)$$

which is a constant. Using this, a first approximation of the displacement and stress field for the cracked plate can be obtained. This new result can be used again to replace M_{xx0} and this iteration can be continued until the convergence is achieved. In the present work, no iteration is performed as the objective is to show the qualitative change induced in the displacement field due to the presence of a crack.

6.8.2 Scattering Due to a Transverse Crack

The effect of a non-propagating transverse crack on the velocity field is studied in this section. A GFRP plate is taken for this purpose, which is 1.0 m long (L, in Fig. 6.34). This large propagating length is taken to distinguish clearly the position of the crack (L_1), where the crack length is taken as 0.1 m. The Y window length, L_Y, is fixed at 10.0 m. In this example symmetric ply-sequence ($[0_{10}]$) is considered, where each ply is 1.0 mm thick. The plate is fixed at one end and is impacted by the same pulse loading (Fig. 3.7) at the other end. The response of the plate (transverse velocity) for various locations of the crack is shown in Fig. 6.36 along with the response of a healthy plate at the bottom. As the figure suggests the presence of crack

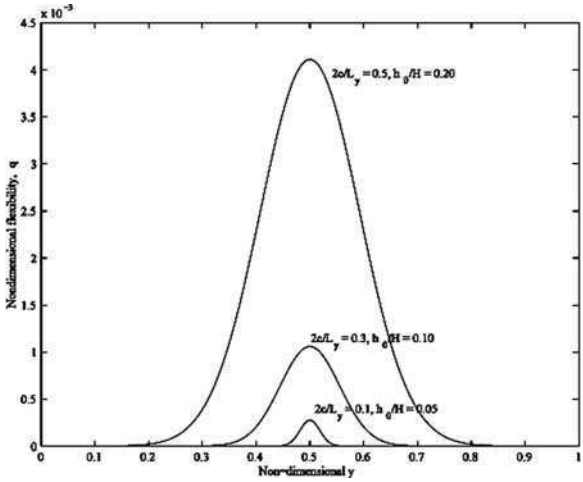

Fig. 6.35 Variation of non-dimensional flexibility at the crack location

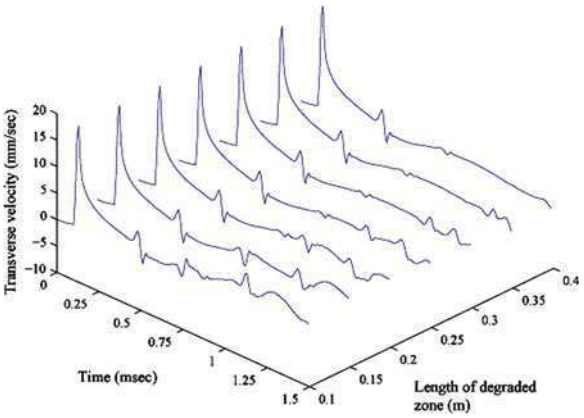

Fig. 6.36 Scattering due to transverse crack: broadband pulse

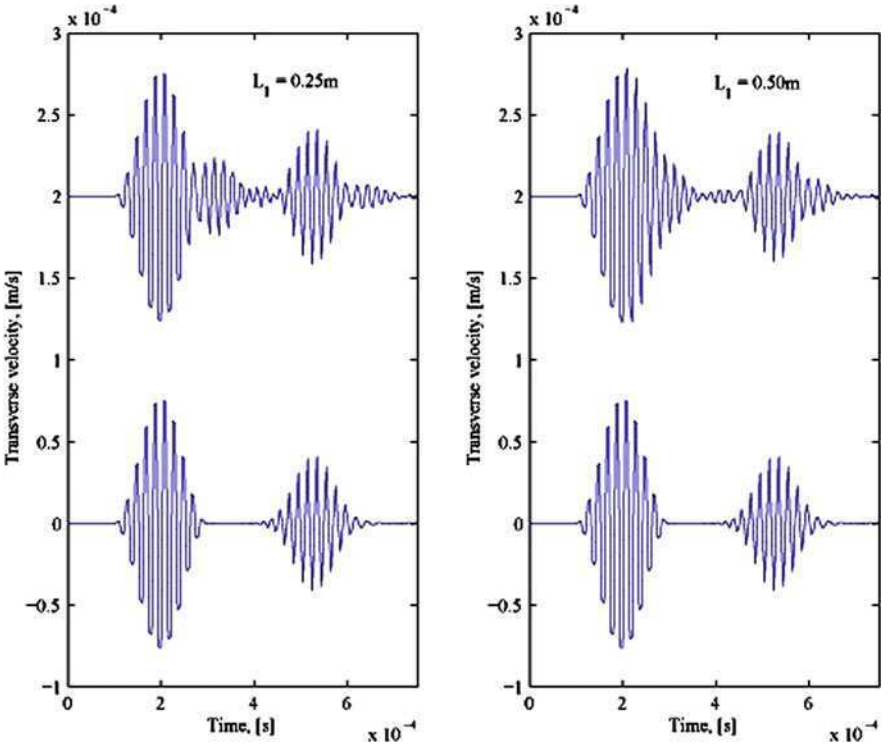

Fig. 6.37 Scattering due to transverse crack: modulated pulse, healthy plate response is also shown below the scattered response

does not alter the peak amplitude and the group velocity of the bending mode significantly, and the reflection from the fixed end arrives at 500 μs in all the cases. However, due to the presence of the crack, there is an extra reflection from the crack front which arrives before the boundary reflection (at around 250, 200 and 150 μs,

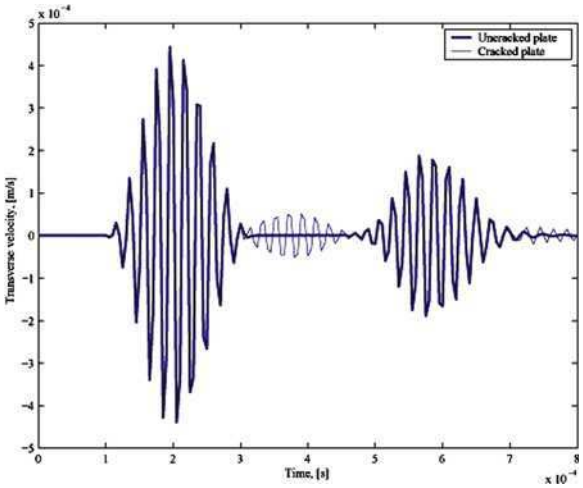

Fig. 6.38 Scattering due to transverse crack: modulated voltage pulse, $L_1 = 0.35$ m

for $L_1 = 0.25, 0.5$ and 0.75 m, respectively). This pattern of wave scattering from a stationary transverse crack is similar to that found in wave scattering due to vertical cracks in beams and this was reported in Sect. 6.4.

Next, a modulated pulse is applied at the free end and the transverse velocity is measured at the same point. Figure 6.37 shows the time histories for both cracked and healthy plate. The extra reflections can be clearly seen in the sub-figures, which change their positions with variation in L_1. Instead of applying mechanical force, the plate can also be subjected to piezoelectric actuation and the measured response will also capture the scattered wave from the crack. This method of actuation has the advantage over mechanical loading in that the center frequency of the modulated pulse can be controlled quite accurately. To demonstrate this, a piezo-patch is placed at the tip of the plate and a pulse voltage of 50 kHz center frequency is applied to this material, which as a result actuates mechanical loading (in terms of bending moment) to the structure. The transverse velocity at the tip is measured and plotted in Fig. 6.38, where the crack is assumed to be at 0.35 m from the fixed end. The thick solid line denotes response of the plate without a crack, which is devoid of the extra waveform. However, for a plate with a damage, we clearly see an extra waveform occurring at 300 μs, which is due to the presence of damage.

6.9 Conclusions

This chapter presented various simplified spectral element damage models for different failure modes in metals and composite in 1D and 2D waveguides. The modeling approach can be easily incorporated in both Fourier and Wavelet spectral FEM environment. Some of these damage models will form the basis for damage detection methodologies, which are outlined in the Part-III of this book.

References

1. Barbero EJ, Reddy JN (1991) Modeling of delamination in composite laminates using a layer-wise plate theory. Int J Solids Struct 28(3):373–388
2. Chattopadhya A, Gu H (1994) New higher order plate theory in modeling delamination buckling of composite laminates. AIAA J 32(8):1709–1716
3. Cook RD, Malkus RD, Plesha ME (1989) Concepts and applications of finite element analysis. Wiley, New York
4. DeIasi R, Whiteside JB (1978) Effect of moisture on epoxy resins and composites. In: Vinson JR (ed) Advanced composite materials—environmental effects. ASTM, STP 658, pp 2–20
5. Finn SR, Springer GR (1993) Delaminations in composite plates under transverse static or impact loads—a model. Composite Struct 23:177–190
6. Gadelrab RM (1996) The effect of delamination on the natural frequencies of a composite beam. J Sound Vib 197(3):283–292
7. Gardner HC, Haynes S, and Baboin R (eds) (1983) Standard recommended practice for examination and evaluation of pitting corrosion. Laboratory Corrosion Tests and standards. ASTM Special Technical Publication 866, pp 552–561
8. Garg A (1988) Delamination—a damage model in composite structures. Eng Fracture Mech 29:557–584
9. Godard HP (1960) The corrosion behavior of aluminium in natural waters. Canadian J Chem Eng 38:1671
10. Godard HP, Jepson WB, Bothwell MR, Kane RL (1967) The corrosion of light metals. Wiley, New York
11. Gopalakrishnana S, Roy Mahapatra D, Chakraborty A (2008) Spectral finite element methods. Springer, London
12. Greco F, Lonetti P, Zinno R (2002) An analytical delamination model for laminated plates including bridging effects. Int J Solids Struct 39(9):2435–2463
13. Han X, Favro L, Li L, Ouyang Z, Sun G, Thomas R, Ashbaugh D (2000) Quantitative thermal wave corrosion measurements on a dc-9 belly skin in the irregular paint thickness variations. In: Thompson D, Chimenti D (eds) Review of progress in quantitative nondestructive evaluation, Ames, Iowa
14. Hansen S, Mossawir B, Ergun A, Degertekin F, and Khuri-Yakub B (1999) Air-coupled nondestructive evaluation using micromachined ultrasonic transducers. In: IEEE ultrasonics symposium
15. Karadomateas GA, Schmueser DW (1988) Buckling and postbuckling of delaminated composites under compressive loads including transverse shear effects. AIAA J 26(3):337–342
16. Kessler SS, Spearing SM, Soutis C (2002) Damage detection in composite materials using Lamb wave methods. Smart Mater Struct 11:269–278
17. Khadem SE, Rezaee M (2000) Introduction of modified comparison functions for vibration analysis of a rectangular cracked plate. J Sound Vib 236(2):245–258
18. Krawczuk M, Palacz M, Ostachowicz W (2004) Wave propagation in plate structures for crack detection. Finite Elem Anal Design 40:991–1004
19. Leo DJ, Smith CA (1997) Performance tradeoffs in active–passive vibration isolation. In: Proceedings of 11th symposium on structural dynamics and control, May 12–14
20. Lin X, Yuan FG (2001) Diagnostic Lamb waves in an integrated piezoelectric sensor/actuator plate: analytical and experimental studies. Smart Mater Struct 10:907–913
21. Loos AC, Springer GS (1979) Moisture absorption of graphite-epoxy composites immersed in liquids and in humid air. J Composite Mater 13:131–147
22. Luo H, Hanagud S (2000) Dynamics of delaminated beams. Int J Solids Struct 37:1501–1519
23. Majumdar PM, Suryanarayan S (1988) Flexural vibration of beams with delamination. J Sound Vib 25(3):441–461

24. Mattsson E, Lindgren S (1968) Metal corrosion in the atmosphere. ASTM STP 435. American Society for Testing and Materials, Philadelphia, p 240
25. Mix P (1987) Introduction to nondestructive testing. Wiley, New York
26. Nag A, Mahapatra DR, Gopalakrishnan S (2003) Identification of delamination in a composite beam using a damaged spectral element. Structural Health Monitoring 1(1):105–126
27. Nakai T, Matsushita H, Yamamoto N, Arai H (2004) Effect of pitting corrosion on local strength of hold frames of bulk carriers. Marine Struct 17:403–432
28. Nam KW, Wei RP, Mal AK (1999) Characteristics of acoustic emission waveforms generated by fatigue crack extension from corrosion sites in aluminium alloys. In: Third FAA/DOE/NASA conference, Chicago
29. Ochoa OO, Reddy JN (1992) Finite element analysis of composite laminates. Kluwer, Dordrecht
30. Point N, Sacco E (1996) A delamination model for laminated composites. Int J Solids Struct 33(4):483–509
31. Rice JR, Levy N (1972) The part-through surface crack in an elastic plate. J Appl Mech 39:183–194
32. Roy Mahapatra D, Gopalakrishnan S (2004) Spectral finite element analysis of coupled wave propagation in composite beams with multiple delaminations and strip inclusions. Int J Solids Struct 41:1173–1208
33. Shen CH, Springer GS (1976) Moisture absorption and desorption of composite materials. J Composite Mater 10:2–20
34. Shivakumar KN, Whitcomb JN (1985) Buckling of a sub-laminate in quasi-isotropic composite laminate. J Composite Mater 19(1):2–18
35. Simitses GJ, Sallam S, Yin WL (1985) Effect of delamination of axially loaded homogeneous laminated plate. AIAA J 23(9):1437–1444
36. Springer GS (1979) Environmental effects on epoxy matrix composites. In: Tsai SW (ed) Composite materials: testing and design (fifth conference), ASTM, STP 674, pp 291–312
37. Sun Y, Ouyang T, Udpa S (2000) Multi-layer aircraft structure inspection using super-sensitive remote-field eddy-current system. In: Thompson D, Chimenti D (eds) Review of progress in quantitative nondestructive evaluation, Ames, Iowa
38. Tracy JJ, Pardoen GC (1989) Effect of delamination on the natural frequencies of composite laminates. J Composite Mater 23:1200–1215
39. Tsai SW, Hahn HT (1980) Introduction to composite materials. Technomics Publishing Company, Westport, pp 329–376
40. Valdez SHD, Soutis C (2001) A structural health monitoring system for laminated composites. In: ASME design engineering technical conference. Proceedings of 18th biennial conference on vibration and noise, Pittsburgh, PA, USA
41. Whitney JM, Browning CE (1978) Some anomalies associated with moisture diffusion in epoxy matrix composite materials. In: Vinson JR (ed) Advanced composite materials—environmental effects. ASTM, STP 658, pp 43–60
42. Williams D (1948) Dynamics loads in aeroplanes under given impulsive loads with particular reference to landing and gust loads on a large flying boat. Aeronautics Research Council, Technical Report No. 2221
43. Williams TO, Addessio FL (1997) A general theory for laminated plates with delaminations. Int J Solids Struct 34(16):2003–2024
44. Williams TO (1999) A generalized multilength scale nonlinear composite plate theory with delamination. Int J Solids Struct 36:3015–3050

Chapter 7
Perturbation Methods for Damaged Structures

7.1 Perturbation Methods for Notched Structures

In this chapter, analysis methods for notch type and line type defects are presented, which are based on perturbation techniques. The line defect could be a horizontal crack (delamination) or vertical crack (fiber breaks). Modeling of some of these defects were addressed in the last chapter and the methods presented here represent another approach to the simplified modeling of these defects.

The effects of cracks on the dynamic behavior of beams and shafts have been studied by many authors. Excellent overviews of the state-of-the-art can be found for example in [23, 3]. Many of the existing formulations are based on the description of damage as an equivalent stiffness at the location of the defect. The dynamic behavior of single-sided cracked beams can for example be found in [5 and 12–14, 19], while the work of [1, 6–7] analyzed the effect of double-sided cracks of equal depth. A different approach of modeling cracked beams consists in using approximated numerical solutions as illustrated in the previous chapter. For example in [2], the variation of the fundamental frequency of a simply supported beam with a mid-span crack is evaluated using a two-term Rayleigh-Ritz solution. In the approximation, an exponentially decaying crack function was used to simulate damage, and the decay rate of the function was estimated from experimental results. The Galerkin approximation is used alternatively in [22] in order to achieve fast convergence rates, while in [20], a Finite Element model is used to predict the behavior of a beam with an edge crack. Finally, [18] and subsequently [17] presented a perturbation method to describe the dynamic behavior and in particular the curvature modes of cracked beams. In these works, the perturbation analysis is based on the assumption of a small crack whose depth is defined by a perturbation parameter. The modal behavior of the cracked beam is evaluated through perturbation of the modal parameters of the undamaged beam, so that approximated analytical expressions for the damaged modes can be obtained. The present chapter extends the formulation presented in [17, 18] to plates with

S. Gopalakrishnan et al., *Computational Techniques for Structural Health Monitoring*, Springer Series in Reliability Engineering, DOI: 10.1007/978-0-85729-284-1_7,

localized defects. Both point defects, or notches, as well as line defects are considered to evaluate their effects on natural frequencies, mode shapes and curvatures. Relatively little work can be found in the literature on the analytical modeling of damaged plates. Among the work considered as reference for this study, the contributions by Ostachowicz, Krawczuk and co-workers are here mentioned as relevant to the present investigations [3, 11, 15]. In addition, the chapter illustrates the application of perturbation techniques in conjunction with FSFEM to investigate the wave propagation characteristics of simple Euler–Bernoulli beams, where damage couples axial and bending behavior so that mode conversion can be captured.

The analytical formulations presented below can be used in support of experimental tests, to analyze data and to supplement the experiments with mechanics-based analysis tools that quantify damage. In particular, the application of scanning laser vibrometry for the detection of dynamic deflection shapes allows unprecedented amounts of information, which can be successively used for the evaluation of curvature shapes. The results presented in this chapter and in [17, 18] in fact indicate how curvatures are extremely sensitive to damage, and can be successfully utilized as part of a damage detection technique.

7.2 Modal Analysis of Damaged Plates

7.2.1 Governing Equations

The free dynamic behavior of isotropic damaged plates can be described by expressions formulated from the general equation of motion for plates of variable thickness, as found in [16]:

$$\nabla^2\left(D\nabla^2 w\right) - (1-\nu)\left(\frac{\partial^2 D}{\partial y^2}\frac{\partial^2 w}{\partial x^2} - 2\frac{\partial^2 D}{\partial y \partial x}\frac{\partial^2 w}{\partial y \partial x} + \frac{\partial^2 D}{\partial x^2}\frac{\partial^2 w}{\partial y^2}\right) + m\frac{\partial^2 w}{\partial t^2} = 0 \quad (7.1)$$

where $w = w(x, y)$ is the out-of-plane displacement of the plate, $h = h(x, y)$ is the plate thickness, $D = D(x, y) = Eh^3/12(1-\nu^2)$ is the plate rigidity, and $m = m(x, y) = \rho h(x, y)$ is the mass per unit area of the plate. Also E, ρ and ν are the Young's modulus, the density and the Poisson's ration of the plate material.

We consider defects described as localized reductions in the plate thickness. Notch-type damage, and line defects along the x and y directions are specifically analyzed according to the configurations presented schematically in Figs. 7.1 and 7.2, respectively. The line loads can be considered as simplified descriptions of a linear crack or of plate delaminations oriented along the reference axis. The extension of the present formulation to line defects of general orientation does not present any theoretical difficulties. However its implementation and related

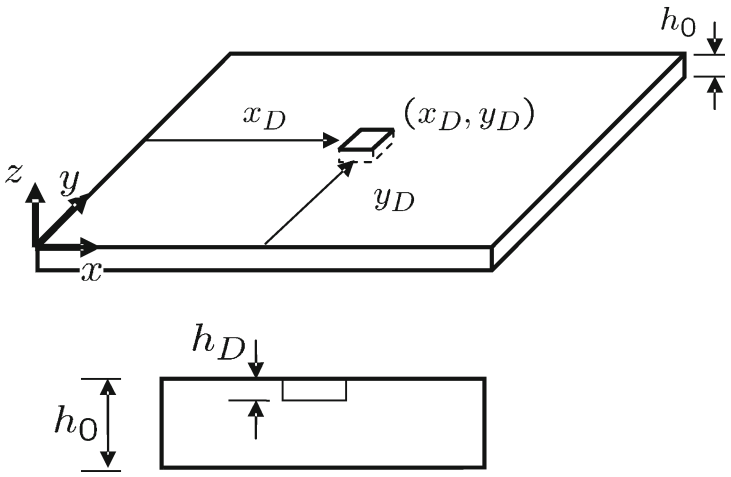

Fig. 7.1 Schematic of plate with notch damage

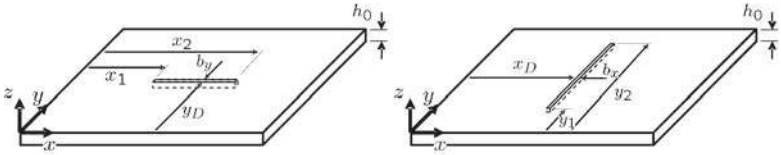

Fig. 7.2 Schematic of plates with considered line defects

analytical derivations are quite involved, and are not reported in this chapter as they do not add significant contributions to the discussion.

Damage is described by expressing the plate thickness at the defect location as:

$$h_d = h_0 - h_D \tag{7.2}$$

where h_0 is the thickness of the undamaged plate and h_D is the thickness of the plate at the damage location. Accordingly, the plate rigidity at the defect site can be expressed as:

$$\begin{aligned} D_d &= \frac{E h_d^3}{12(1-\nu^2)} \\ &= D_0 \left(1 - \frac{h_D}{h_0}\right)^3 \end{aligned} \tag{7.3}$$

where $D_0 = E h_0^3 / 12(1-\nu^2)$ is the rigidity of the undamaged plate. For a small damage, i.e. for $h_D \ll h_0$, Eq. 7.3 can be approximated as:

$$D_d \simeq D_0\left(1 - 3\frac{h_D}{h_0}\right) = D_0(1-\varepsilon) \tag{7.4}$$

where $\varepsilon = 3h_D/h_0$. Similarly, the mass per unit area of the plate at the defect site can be expressed as:

$$m_d = m_0\left(1 - \frac{h_D}{h_0}\right) = m_0\left(1 - \frac{1}{3}\varepsilon\right) \tag{7.5}$$

where $m_0 = \rho h_0$ is the mass per unit area of the undamaged plate. The plate rigidity $D(x,y)$ can in general be described as:

$$D(x,y) = D_0[1 - \varepsilon(H(x-x_1) - H(x-x_2))(H(y-y_1) - H(y-y_2))] \tag{7.6}$$

where x_1, x_2 and y_1, y_2 define the dimensions of the defect in the x, y directions, and where H is the Heaviside step function. Equation 7.6 can be conveniently manipulated to describe both notch-type defects, as well as line loads of the kind shown in Fig. 7.2. Equation 7.6 can in fact be rewritten as:

$$D(x,y) = D_0\left[1 - \varepsilon A_D \frac{(H(x-x_1) - H(x-x_2))}{\Delta l_x}\frac{(H(y-y_1) - H(y-y_2))}{\Delta l_y}\right] \tag{7.7}$$

where $b_x = x_2 - x_1, b_y = y_2 - y_1$, and $A_D = b_x * b_y$. For a notch defect at x_D, y_D (see Fig. 7.1), it is assumed that

$$x_1 \approx x_2 \approx x_D, \quad y_1 \approx y_2 \approx y_D$$

and Eq. 7.6 becomes:

$$D(x,y) = D_0[1 - \varepsilon A_D \delta(x - x_D)\delta(y - y_D)] \tag{7.8}$$

where

$$\delta(x) = \frac{dH(x)}{dx}$$

is the Dirac delta function. Similar expressions can be defined to characterize a line defect. For example, a line defect at location $y = y_D$ and parallel to the x direction (Fig. 7.2a) can be described as:

$$D(x,y) = D_0\left[1 - \varepsilon b_y \delta(y - y_D)\int_{x_1}^{x_2} \delta(x-\xi)d\xi\right] \tag{7.9}$$

while a defect at $x = x_D$ along the y direction (Fig. 7.2b) can be expressed as:

$$D(x,y) = D_0\left[1 - \varepsilon b_x \delta(x - x_D)\int_{y_1}^{y_2} \delta(y-\eta)d\eta\right] \tag{7.10}$$

where x_1, x_2 and y_1, y_2 define the length of the defect, while ξ, η are dummy integration variables. It is worth observing how in Eqs. 7.9 and 7.10, the heaviside function is replaced by the integral of the delta function over the extension of the defect. This substitution is adopted in order to take advantage of properties of the delta function which are very convenient for the the analytical derivations presented below.

A general description of line and notch defects of the kind considered here can be obtained by expressing the plate bending rigidity as:

$$D(x, y) = D_0[1 - \varepsilon\gamma_D(x, y)] \tag{7.11}$$

where $\gamma_D(x, y)$ denotes the function describing the considered damage configuration, which can be particularized to the expressions in Eqs. 7.8–7.10. Similarly, the mass per unit area of the damaged plate can be described as:

$$m(x, y) = m_0\left(1 - \frac{h_d}{h_0}\right) = m_0\left[1 - \frac{1}{3}\varepsilon\gamma_D(x, y)\right] \tag{7.12}$$

The expressions for the plate rigidity and mass given in Eqs. 7.11 and 7.12 can be substituted in Eq. 7.1 to obtain a solution predicting the dynamic behavior of plates with the considered types of damage.

7.2.2 Perturbation Solution

A solution for equation Eq. 7.1 can be obtained through modal superposition by imposing a solution of the kind:

$$w(x, y) = \sum_{i,j} \phi_{i,j}(x, y)e^{\mathrm{j}\omega_{i,j}t} \tag{7.13}$$

where $\phi_{i,j}$, $\omega_{i,j}$ are respectively the i,jth mode shape and natural frequency (eigensolutions) of the plate, while j is the imaginary unit. Considering for simplicity the contributions of a single mode i,j and substituting Eq. 7.13 in Eq. 7.1 gives:

$$\nabla^2\left(D\nabla^2\phi\right) - (1 - \nu)\left(\frac{\partial^2 D}{\partial y^2}\frac{\partial^2\phi}{\partial x^2} - 2\frac{\partial^2 D}{\partial y \partial x}\frac{\partial^2\phi}{\partial y \partial x} + \frac{\partial^2 D}{\partial x^2}\frac{\partial^2\phi}{\partial y^2}\right) - m\lambda\phi = 0 \tag{7.14}$$

where $\lambda = \omega^2$, and the subscripts i,j are omitted for simplicity. In our analysis, ε is assumed to be a small parameter corresponding to a small damage depth h_D. Within this assumption, the eigensolutions for the damaged plate can be expressed as perturbations from the solution for the intact plate, so that the eigenfunctions and eigenvalues of the damaged plate can respectively be expressed as [16]:

$$\phi(x,y) = \phi^{(0)}(x,y) - \varepsilon\phi^{(1)}(x,y) + \mathcal{O}(\varepsilon^2) \tag{7.15}$$

and

$$\lambda = \lambda^{(0)} - \varepsilon\lambda^{(1)} + \mathcal{O}(\varepsilon^2) \tag{7.16}$$

where $\phi^{(0)}(x,y), \lambda^{(0)}$ are the eigensolutions for the undamaged plate, while $\phi^{(1)}(x,y), \lambda^{(1)}$ are the first order perturbations. Substituting the perturbed eigensolutions into Eq. 7.14, and collecting the coefficients of same power of ε gives a set of equations which can be solved in terms of the perturbations coefficients:

ε^0:

$$\nabla^4\phi^{(0)} - \frac{m_0}{D_0}\lambda^{(0)}\phi^{(0)} = 0 \tag{7.17}$$

ε^1:

$$\begin{aligned}&\nabla^4\phi^{(1)} + \nabla^2\left[\gamma_D\left(\phi^{(1)}_{,xx} + \phi^{(1)}_{,yy}\right)\right] = \\ &(1-\nu)\left[\phi^{(0)}_{,xx}\gamma_{D_{,yy}} + \phi^{(0)}_{,yy}\gamma_{D_{,xx}} - 2\phi^{(0)}_{,xy}\gamma_{D_{,xy}}\right] \\ &+\frac{m_0}{D_0}(\lambda^{(0)}\phi^{(1)} + \lambda^{(1)}\phi^{(0)} + \frac{1}{3}\lambda^{(0)}\phi^{(0)}\gamma_D)\end{aligned} \tag{7.18}$$

where $\gamma_D = \gamma_D(x,y)$, and where $(\cdot)_{,\zeta}$ denotes partial derivatives with respect to the variable ζ. Equation 7.17 represents the equation of motion for an undamaged plate, and its solution provides the undamaged modes $\phi^{(0)}(x,y)$ and eigenvalues $\lambda^{(0)}$, which can then be substituted in Eq. 7.18 to obtain a solution in terms of the perturbation modal parameters $\phi^{(1)}(x,y), \lambda^{(1)}$.

7.2.3 Fourier Series Solution of ε^1 Equations

The i,jth eigenfunction and eigenvalue for a plate supported on all edges are respectively given by [16]:

$$\phi^{(0)}_{i,j}(x,y) = \sin\frac{i\pi x}{L_x}\sin\frac{j\pi y}{L_y} \tag{7.19}$$

and

$$\lambda^{(0)}_{i,j} = \frac{D_0}{m_0}\left[\left(\frac{i\pi}{L_x}\right)^2 + \left(\frac{j\pi}{L_y}\right)^2\right]^2 \tag{7.20}$$

where L_x, L_y denote the plate dimensions. An approximate solution for Eq. 7.18 can be found by imposing a solution of the kind:

$$\phi_{i,j}^{(1)}(x,y) = \sum_p \sum_q \eta_{p,q} \sin\frac{p\pi x}{L_x} \sin\frac{q\pi y}{L_y} \tag{7.21}$$

which corresponds to the Fourier series expansion of the perturbed mode. Substituting this expansion in Eq. 7.18 gives:

$$\begin{aligned} &\sum_p \sum_q \left[\left(\left(\frac{p\pi}{L_x}\right)^2 + \left(\frac{q\pi}{L_y}\right)^2 \right)^2 - m_0\lambda_0 \right] \eta_{p,q} \sin\frac{p\pi x}{L_x} \sin\frac{q\pi y}{L_y} = \\ &- \left(\phi_{,xx}^{(0)} + \phi_{,yy}^{(0)}\right) \nabla^2\gamma_D + (1-\nu)\left[\phi_{,xx}^{(0)}\gamma_{D_{,yy}} + \phi_{,yy}^{(0)}\gamma_{D_{,xx}} - 2\phi_{,xy}^{(0)}\gamma_{D_{,xy}}\right] \\ &+ \frac{m_0}{D_0}\left(\lambda^{(1)} + \frac{1}{3}\lambda^{(0)}\gamma_D\right)\phi^{(0)} \end{aligned} \tag{7.22}$$

where $\phi^{(0)} = \phi_{i,j}^{(0)}(x,y), \lambda^{(0)} = \lambda_{i,j}^{(0)}$ are respectively defined in Eqs. 7.19 and 7.20. The complexity of Eq. 7.22 can be substantially reduced by exploiting the orthogonality properties of harmonic functions. Multiplying Eq. 7.22 by $\sin\frac{r\pi x}{L_x}\sin\frac{s\pi y}{L_y}$ and integrating over the plate surface gives:

$$\begin{aligned} &\left[\left(\left(\frac{r\pi}{L_x}\right)^2 + \left(\frac{s\pi}{L_y}\right)^2 \right)^2 - \left(\left(\frac{i\pi}{L_x}\right)^2 + \left(\frac{j\pi}{L_y}\right)^2 \right)^2 \right] \eta_{r,s} \frac{L_x L_y}{4} = \\ &- \kappa_1 + (1-\nu)\kappa_2 + \frac{m_0}{D_0}\lambda^{(1)}\delta_{ri}\delta_{sj}\frac{L_x L_y}{4} \end{aligned} \tag{7.23}$$

where

$$\begin{aligned} \kappa_1 = &\int_0^{L_x}\int_0^{L_y} \left(\left[\left(\frac{i\pi}{L_x}\right)^2 + \left(\frac{j\pi}{L_y}\right)^2 \right] \nabla^2\gamma_D - \frac{1}{3}\frac{m_0}{D_0}\lambda^{(0)}\gamma_D \right) \\ &\sin\frac{i\pi x}{L_x}\sin\frac{j\pi y}{L_y}\sin\frac{r\pi x}{L_x}\sin\frac{s\pi y}{L_y}dxdy \end{aligned}$$

and

$$\begin{aligned} \kappa_2 = &\int_0^{L_x}\int_0^{L_y} \phi_{,xx}^{(0)} \sin\frac{r\pi x_D}{L_x}\sin\frac{s\pi y_D}{L_y}\gamma_{D_{,yy}}dxdy + \\ &+ \int_0^{L_x}\int_0^{L_y} \phi_{,yy}^{(0)} \sin\frac{r\pi x_D}{L_x}\sin\frac{s\pi y_D}{L_y}\gamma_{D_{,xx}}dxdy + \\ &- 2\int_0^{L_x}\int_0^{L_y} \phi_{,xx}^{(0)} \sin\frac{r\pi x_D}{L_x}\sin\frac{s\pi y_D}{L_y}\gamma_{D_{,xy}}dxdy \end{aligned}$$

Also, in Eq. 7.22, $\delta_{k,l}$ is the Kronecker symbol defined as:

$$\delta_{k,l} = \begin{cases} 1 & k = l \\ 0 & k \neq l \end{cases}$$

The summation signs in Eq. 7.22 are eliminated in virtue of the well-known orthogonality property of harmonic functions, which reads:

$$\int_0^{L_x} \int_0^{L_y} \sin\frac{p\pi x}{L_x} \sin\frac{q\pi y}{L_y} \sin\frac{r\pi x}{L_x} \sin\frac{s\pi y}{L_y} dxdy = \frac{L_x L_y}{4} \delta_{r,p} \delta_{s,q}$$

and corresponding versions for cosine functions. Given the considered modes for the undamaged plate, Eq. 7.23 can be solved in terms of the unknowns $\eta_{r,s}, \lambda^{(1)}$. Letting $r = i$ and $s = j$, yields an equation which can be solved in terms of $\lambda_{i,j}^{(1)}$:

$$\lambda_{i,j}^{(1)} = \frac{4D_0}{m_0 L_x L_y} [\kappa_1 - (1 - \nu)\kappa_2] \tag{7.24}$$

It is worth observing how the integrations required for the evaluation of the constants κ_1, κ_2 are significantly simplified by taking advantage of the following properties of the delta function [9]:

$$f(x)\delta(x - x_0) = f(x_0)\delta(x) \tag{7.25}$$

and

$$\int f(x) \frac{\partial^n \delta(x)}{\partial x^n} dx = \int \frac{\partial f(x)}{\partial x} \frac{\partial^{n-1} \delta(x)}{\partial x^{n-1}} dx \tag{7.26}$$

where $f(x)$ is a generic function. A few simple manipulations yield the following expressions:

$$\kappa_1 = \frac{4D_0 \Delta A_D}{L_x L_y} \left(\left[\left(\frac{i\pi}{L_x}\right)^2 + \left(\frac{j\pi}{L_y}\right)^2 \right] - \frac{1}{3}\frac{m_0}{D_0}\lambda^{(0)} \right) \left(\sin\frac{j\pi y_D}{L_y} \right)^2 \left(\sin\frac{i\pi x_D}{L_x} \right)^2,$$

$$\kappa_1 = \frac{4D_0 b_y}{L_x L_y} \left(\left[\left(\frac{i\pi}{L_x}\right)^2 + \left(\frac{j\pi}{L_y}\right)^2 \right] - \frac{1}{3}\frac{m_0}{D_0}\lambda^{(0)} \right) \left(\sin\frac{j\pi y_D}{L_y} \right)^2 \int_{x_1}^{x_2} \left(\sin\frac{i\pi \xi}{L_x} \right)^2 d\xi,$$

and

$$\kappa_1 = \frac{4D_0 b_x}{L_x L_y} \left(\left[\left(\frac{i\pi}{L_x}\right)^2 + \left(\frac{j\pi}{L_y}\right)^2 \right] - \frac{1}{3}\frac{m_0}{D_0}\lambda^{(0)} \right) \left(\sin\frac{i\pi x_D}{L_x} \right)^2 \int_{y_1}^{y_2} \left(\sin\frac{j\pi \eta}{L_y} \right)^2 d\eta.$$

which respectively define the value of κ_1 for a notch damage and for line defects along the x and y directions. Similar expressions, here omitted for the sake of brevity, are obtained for the parameter κ_2.

The amplitude of the Fourier series coefficients $\eta_{r,s}$ can instead by obtained by letting $r \neq i$ and $s \neq j$ in Eq. 7.22. Summation of the various terms of the Fourier series expansion gives an approximate expression for the first order perturbation eigenvalues and eigenvectors, according to Eqs. 7.15 and 7.16.

The results obtained from the formulation presented above are here used to assess the influence of various damage levels, at different locations on the plate surface. Natural frequencies (or eigenvalues), modal deflections, as well as modal curvatures are studied as damage indicators to be used in the development of a modal-based damage detection theory. The modal curvatures can be easily computed from the obtained perturbation solution, and they are given by:

$$\begin{aligned}
\phi_{ij,xx} &= -\left(\frac{i\pi}{L_x}\right)^2 \sin\frac{j\pi x}{L_x}\sin\frac{i\pi x}{L_y} - \sum_r\sum_s \eta_{r,s}\left(\frac{r\pi}{L_x}\right)^2 \sin\frac{r\pi x}{L_x}\sin\frac{s\pi x}{L_y} + \mathcal{O}(\varepsilon^2) \\
\phi_{ij,yy} &= -\left(\frac{i\pi}{L_y}\right)^2 \sin\frac{i\pi x}{L_x}\sin\frac{j\pi x}{L_y} - \sum_r\sum_s \eta_{r,s}\left(\frac{s\pi}{L_y}\right)^2 \sin\frac{r\pi x}{L_x}\sin\frac{s\pi x}{L_y} + \mathcal{O}(\varepsilon^2), \\
\phi_{ij,xy} &= \left(\frac{ij\pi^2}{L_xL_y}\right)\cos\frac{i\pi x}{L_x}\cos\frac{j\pi x}{L_y} + \sum_r\sum_s \eta_{r,s}\frac{rs\pi^2}{L_xL_y}\cos\frac{r\pi x}{L_x}\cos\frac{s\pi x}{L_y} + \mathcal{O}(\varepsilon^2).
\end{aligned} \tag{7.27}$$

7.2.4 Strain Energy Ratio for Damage Localization

The curvature modes evaluated in the previous section can be used directly as damage indicators, and their analytical expressions can be used to evaluate the extent of damage. Alternatively, the curvatures can be used to evaluate the strain energy of the damaged plate. The strain energy for a rectangular plate vibrating according to mode m, n can be expressed as [16]:

$$U_{m,n} = \frac{1}{2}D_0\int_0^{L_x}\int_0^{L_y} \phi^2_{mn,xx} + \phi^2_{mn,yy} + 2\nu\phi_{mn,xx}\phi_{mn,yy} - 2(1-\nu)\phi^2_{mn,xy}\,dxdy \tag{7.28}$$

The evaluation of the strain energy for undamaged and damaged plate can be used as an effective strategy for the identification of damage. Furthermore, the location of the defect can be also evaluated through the estimation of the strain energy over limited regions of the plate corresponding to its subdivision into a grid. The strain energy associated to the i,j area of the plate can be expressed as:

$$U_{m,n}(i,j) = \frac{1}{2}D_0\int_{x_i}^{x_{i+1}}\int_{y_j}^{y_{j+1}} \phi^2_{mn,xx} + \phi^2_{mn,yy} + 2\nu\phi_{mn,xx}\phi_{mn,yy} - 2(1-\nu)\phi^2_{mn,xy}\,dxdy \tag{7.29}$$

We define the modal Strain Energy Ratio (SER) at location i,j as:

$$\sigma_{m,n}(i,j) = \frac{U_{m,n}(i,j)}{U^{(0)}_{m,n}(i,j)} \tag{7.30}$$

where $U, U^{(0)}$ respectively denote the strain energies of the damage and undamaged plate at the considered location. The strain energy for the damage plate can be obtained by using the curvatures obtained from the first order perturbation solution. Imposing Eqs. 7.27 in Eq. 7.32 and neglecting higher powers of ε allows expressing the strain energy for the damaged plate as:

$$U_{m,n}(i,j) = U^{(0)}_{m,n}(i,j) - \varepsilon \Delta U_{m,n}(i,j) \tag{7.31}$$

where:

$$\Delta U_{m,n}(i,j) = 2D_0 \int_{x_i}^{x_{i+1}} \int_{y_j}^{y_{j+1}} \phi^{(1)}_{mn,xx}\phi^{(0)}_{mn,xx} + \phi^{(1)}_{mn,yy}\phi^{(0)}_{mn,yy} + 2(1-v)\phi^{(1)}_{mn,xy}\phi^{(0)}_{mn,xy} + \frac{1}{2}v\left(\phi^{(1)}_{mn,xx}\phi^{(0)}_{mn,yy} + \phi^{(1)}_{mn,yy}\phi^{(0)}_{mn,xx}\right)dxdy$$

The SER can be therefore expressed as:

$$\sigma_{m,n}(i,j) = 1 - \varepsilon \frac{\Delta U_{m,n}(i,j)}{U^{(0)}_{m,n}(i,j)} \tag{7.32}$$

The modal SER provides indications regarding the integrity of the area i,j as any variation from unity indicates a difference between the curvature modes over the particular area. A similar concept has been proposed in the literature in [8, 10]. The analytical framework of the perturbation analysis of the plate provides a theoretical description of the concept. The presented analytical study also offers the opportunity of quantifying the extent of damage through the value of the SER, which is directly related to the level of damage ε.

The definition of strain energy ratio in Eq. 7.32 considers only one mode of the structure. However it is well known that damage mostly affects regions of higher strain energy. It is thus convenient to sum information obtained from the analysis of several modes m,n and therefore to consider a cumulative strain energy ratio, which may be defined as

$$\sigma(i,j) = \sum_{m,n} \sigma_{m,n}(i,j) = 1 - \varepsilon \sum_{m,n} \frac{\Delta U_{m,n}(i,j)}{U^{(0)}_{m,n}(i,j)} \tag{7.33}$$

This cumulative index provides a unique information which combines the results from several modes. Modes not affected by damage because the particular location will not contribute, whereas the index for modes altered by the defect will be combined to provide a robust indication of damage.

7.2.5 Effect of Notch Damage on the Plate Modal Properties

The perturbation analysis presented in the previous section is applied to evaluate natural frequencies, mode shapes and curvature modes of damage plates. Initial results consider the effect of notch damage at various locations, while the investigation of the effects of line defects is presented in the following section. The study is performed on a rectangular plate with $L_x = 1.5$ m and $L_y = 1$ m, supported on all edges as assumed in the analytical derivations. The plate has a thickness $h_0 = 5$ mm and it is made of aluminum ($E = 7.1 \times 10^{10}$ Pa, $\rho = 2700\,\text{kg/m}^3$, $\nu = 0.3$). The extent of damage is varied and it is defined by the parameter ε according to the definition given in the previous section.

The effect of a notch damage on the plate natural frequencies is first investigated. Various damage locations as well as damage extents are considered for the analysis. The results of the investigations are presented in Table 7.1. Damage in general tends to reduce the natural frequencies, as a result of the associated stiffness reduction. It is interesting to observe how frequencies remain unchanged when damage is located at the intersection of the nodal lines of the corresponding mode shape as demonstrated by the frequency of mode (2,2) for damage at $x_D = L_x/2, y_D = L_y/2$. Also frequencies corresponding to higher order modes tend to be more affected by the presence of damage, as demonstrated for example by the comparison of the frequency changes in modes (1,1) and (1,3). Modal deflections and curvatures for plates with notch damage are evaluated through the procedure presented above. The perturbation analysis is limited to the first order based on previous results for beams, which have shown how the second order term gives

Table 7.1 Natural frequencies (rad/s) of plates with notch damage

Mode(i,j)	$h_D/h_0 = 0$	$h_D/h_0 = 1\%$	$h_D/h_0 = 2\%$	$h_D/h_0 = 3\%$	$h_D/h_0 = 4\%$
		$x_D = L_x/2$	$y_D = L_y/2$		
1,1	110.6	110.6	110.4	110.2	109.9
1,2	340.3	340.2	339.6	338.8	337.5
2,1	212.7	212.5	212.0	211.1	209.9
2,2	442.5	442.5	442.5	442.5	442.5
1,3	723.2	722.5	720.1	716.2	710.7
		$x_D = L_x/3$	$y_D = L_y/3$		
1,1	110.6	110.5	110.4	110.0	109.6
1,2	340.3	340.1	339.3	338.0	336.1
2,1	212.7	212.6	212.3	211.7	210.9
2,2	442.5	442.2	441.4	440.2	438.4
1,3	723.2	723.0	722.3	721.2	719.5
		$x_D = L_x/5$	$y_D = L_y/5$		
1,1	110.6	110.6	110.4	110.1	109.6
1,2	340.3	340.1	339.4	338.3	336.7
2,1	212.7	212.6	212.1	211.4	210.4
2,2	442.5	442.2	441.6	440.5	439.0
1,3	723.2	722.8	721.3	718.9	715.5

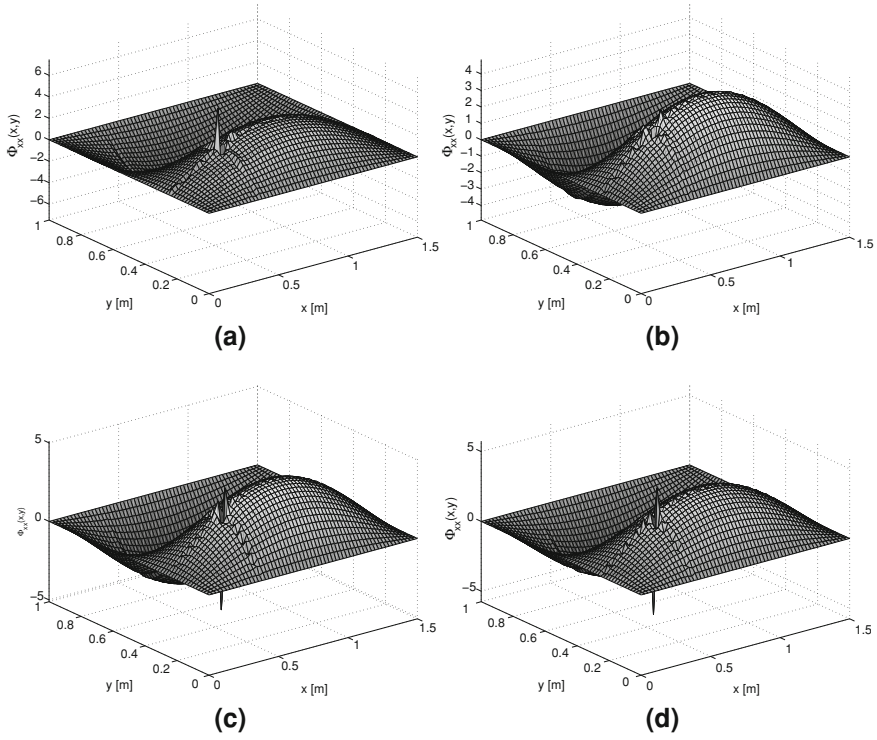

Fig. 7.3 Curvature $\phi_{12,xx}$ estimation using increasing orders of Fourier Series expansion. **a** $r = s = 100$, **b** $r = s = 200$, **c** $r = s = 300$, **d** $r = s = 400$

minor contributions [18]. The Fourier series expansions are performed by considering the superposition of 300 terms. This number has been selected after the qualitative analysis of mode shapes and curvatures predicted with increasing number of expansion terms. A sample of these investigations is shown in Fig. 7.3, which presents the curvature $\phi_{ij,xx}$ for mode (1,2) estimated with increasing number of terms in the expansion. In the plot, the presence of damage is demonstrated by a peak at the corresponding location. It is easy to observe how 300 terms are able to fully capture the peak and that considering higher numbers of terms does not provide additional details on damage. Series expansion with 300 terms are therefore used in our study as a good compromise between accuracy and computational efficiency. Examples of modal deflections and curvatures are shown in Figs. 7.4, 7.5, 7.6, 7.7 and 7.8 for several combinations of damage location and damage extent. The results for modes (1,1) and (1,3) are presented in Figs. 7.4 and 7.5, which clearly demonstrate how for the considered level of damage, the deflection mode shapes are not affected by the presence of the notch, while the curvature modes highlight its presence through a peak at the corresponding locations. The amplitude of the peak is proportional to the extent of damage as shown in Fig. 7.6., which depicts the curvature mode $\phi_{22,xy}$ for increasing damage

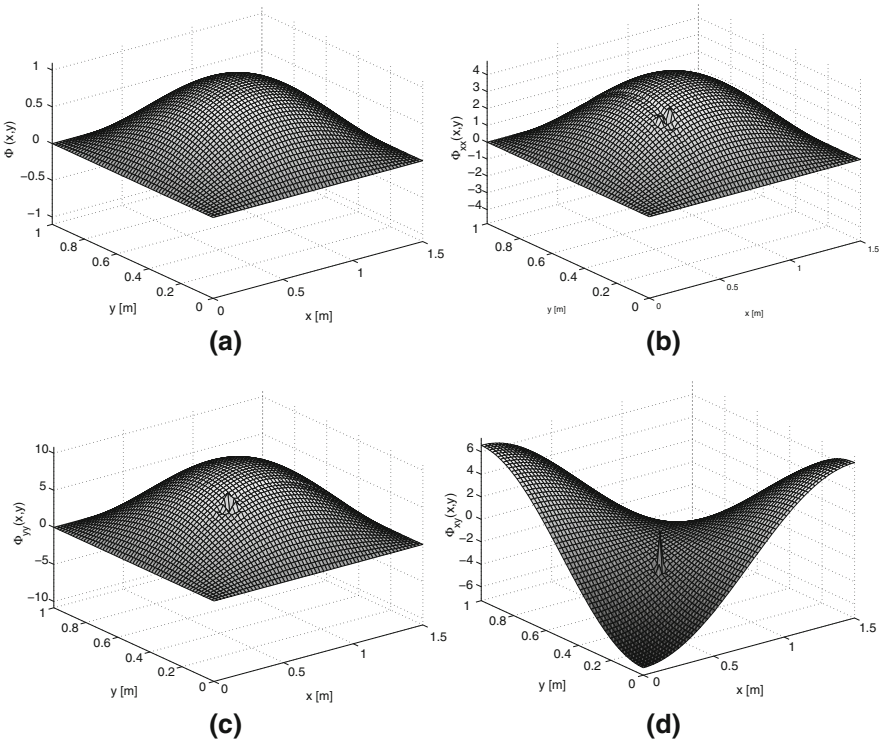

Fig. 7.4 Deflection and curvatures for mode $(1,1)$ with $h_D/h_0 = 2\%$ and damage located at $x_D = L_x/3, y_D = L_y/3$

ratios h_D/h_0. The effect of damage on the curvature modes also depends on its location with respect to the nodal lines of the corresponding mode shapes. Figure 7.7 shows for example how a notch damage with $h_D/h_0 = 2\%$ becomes more evident when it is located close, or at the points of maximum curvature. Finally, Fig. 7.8 compares the effects of a defect of assigned extent on various modes, and demonstrates how the notch tends to affect more significantly higher order modes than lower order modes. This observation confirms the remarks made regarding the natural frequencies of the damaged plates listed in Table 7.1.

7.2.6 Notch Damage Localization Through the Strain Energy Ratio

The SER defined in the previous section is here used for the estimation of damage location and extent. The SER is computed by discretizing the plate surface into a 60×60 grid, over which the strain energy and its variation with respect to the

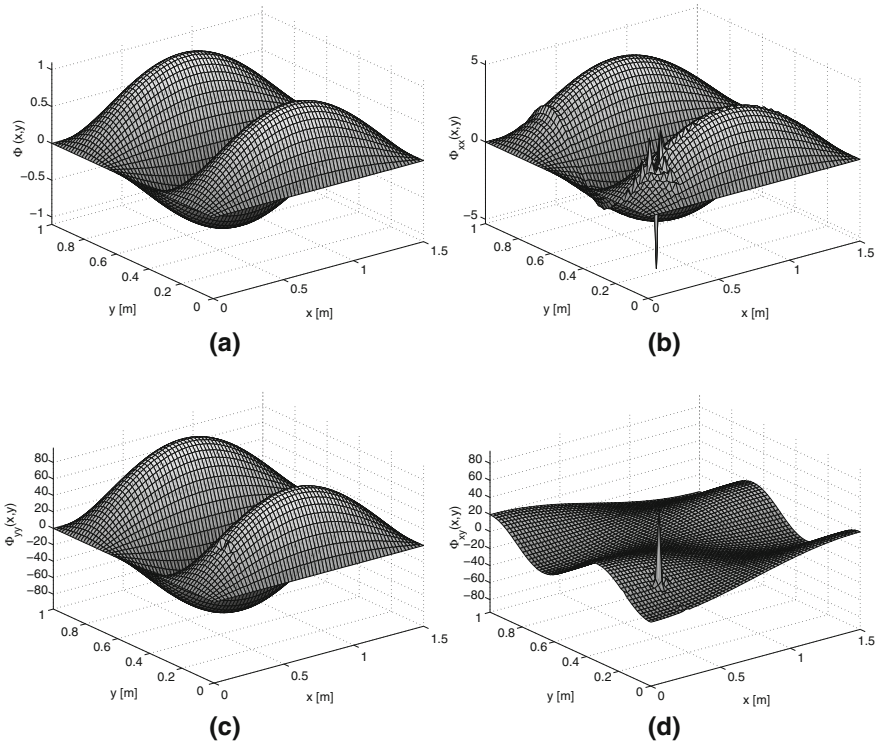

Fig. 7.5 Mode 1,3: Deflection and curvatures for $h_D/h_0 = 2\%$ and damage located at $x_D = L_x/5, y_D = L_y/5$

undamaged configuration are computed. The integration required for the SER evaluation are evaluated analytically, due the convenient formulation for the undamaged and damaged curvature modes obtained through the perturbation analysis. Results for notch defects are presented in Figs. 7.9 and 7.10, where the SER distributions are represented as contour plots. The abscissa and ordinates respectively represent the plate length L_x and width L_y, while the magnitude of the SER is indicated by a gray color scale varying between a minimum of 1.05 (black) to a maximum of 2 (white). The presence of the defect in the presented maps is highlighted by a peak at the corresponding location, which stands out very evidently on the white background imposed on the figure. The extent of the peak and mostly its magnitude are proportional to the damage extent and specifically to the parameter ε or to the ratio h_D/h_0 as predicted by Eqs. 7.32 and 7.33. The correlation between damage extent and magnitude of the SER is shown in Fig. 7.9, which presents modal SER results for notch defects of different extent and location. The application of the superposition of modal SER distributions to obtain a single damage index is instead illustrated in Fig. 7.10, which shows modal SER

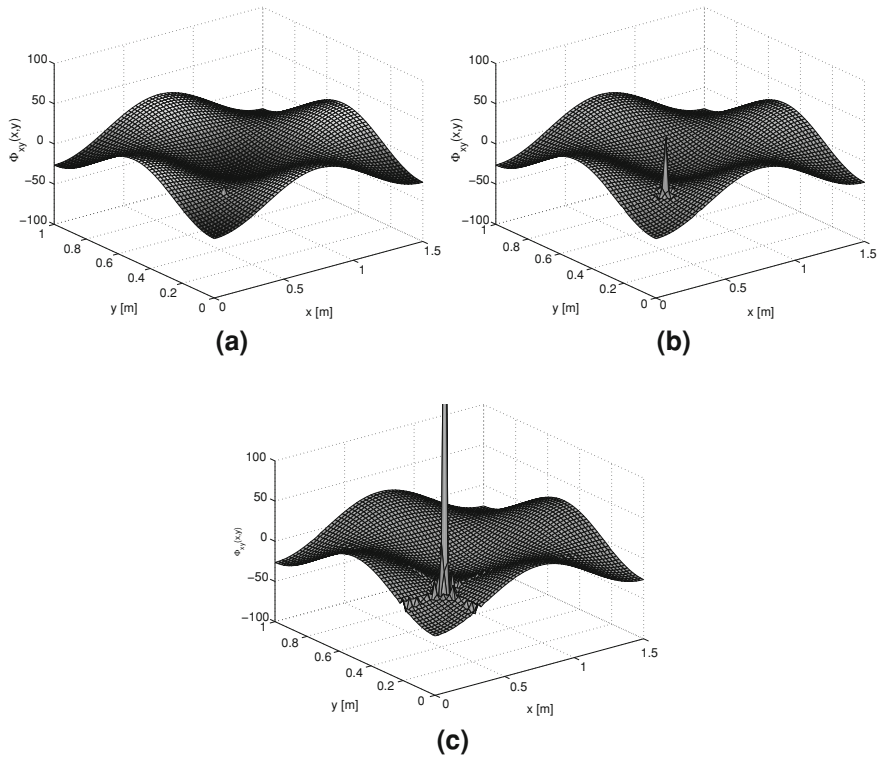

Fig. 7.6 Influence of increasing damage levels on curvature mode $\phi_{22,xy}$ for notch at $x_D = L_x/5, y_D = L_y/5$. **a** $h_D/h_0 = 1\%$, **b** $h_D/h_0 = 2\%$, **c** $h_D/h_0 = 4\%$

values for an assigned damage configuration and the result of the combinations of the modal contributions according to Eq. 7.33. As discussed above, various modes have in fact different sensitivity to damage at a specific location. In here for example, it is clear how the considered damage has very little effect on mode (3,1), as demonstrated by the corresponding modal SER map shown in Fig. 7.10d. The combination of the various modal contributions however is able to capture the presence of the defect by combining the information provided by each mode.

7.2.7 Effect of Line Damage on the Plate Modal Properties

The presented analytical procedure is also applied to the analysis of line defects of the kind depicted in Fig. 7.2. Results for various defect lengths, extensions and orientation are presented in Figs. 7.11 to 7.13. Figure 7.11 for example shows the influence of damage on the curvature mode $\phi_{11,yy}$. Different defect lengths and

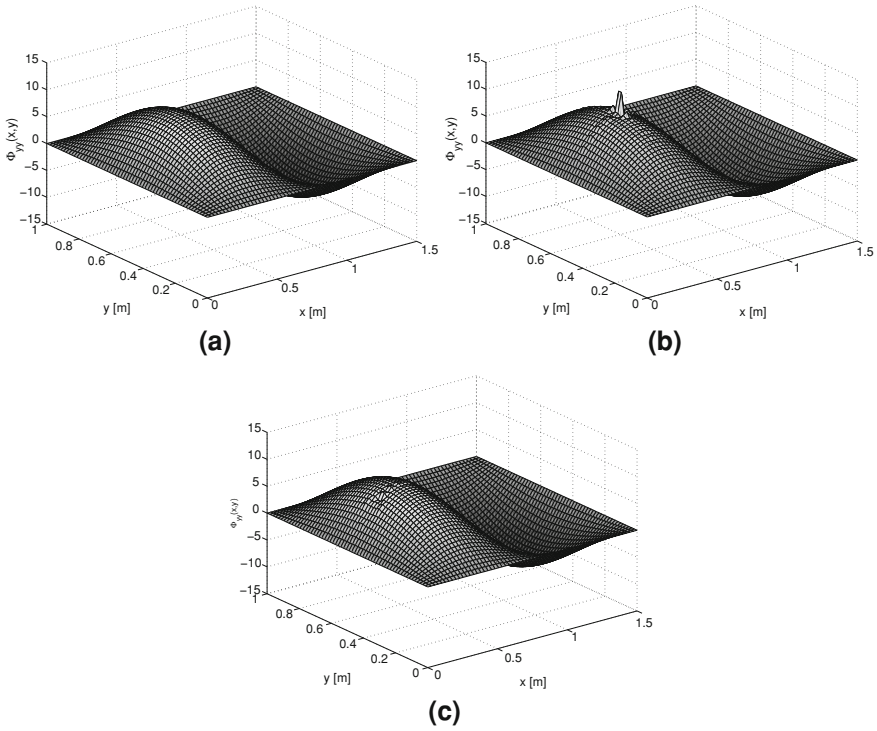

Fig. 7.7 Influence on damage location on curvature mode $\phi_{21,yy}$ for $h_D/h_0 = 2\%$. **a** $xD = Lx/2$, $yD = Ly/2$, **b** $xD = Lx/4$, $yD = Ly/2$, **c** $xD = Lx/8$, $yD = Ly/2$

orientations are considered to demonstrate how the considered curvature mode highlights the presence of damage through an evident discontinuity at the damage location. The length and the orientation of the discontinuity correspond to those of the considered defect. Figure 7.12 presents results for the curvature mode $\phi_{32,xx}$ of a damage plate. The plot in Fig. 7.12a is obtained for the defect located along the nodal line of the curvature mode and therefore no discontinuity can be observed. The same damage at a different location however becomes clearly evident as shown in the case presented in Fig. 7.12b. Moreover, Figs. 7.12b, c compare damage discontinuities corresponding to damage of increasing lengths to demonstrate the increased sensitivity of the curvature modes. In Fig. 7.13 finally, the influence of damage location and extent is demonstrated for mode $\phi_{12,yy}$. Strain Energy Ratios are computed also for line defects. Examples of the results are shown in Figs. 7.14 and 7.15. The maps presented in Fig. 7.14 clearly demonstrate how the SER representation is able to provide information regarding damage extent, length and location. Finally, Fig. 7.15 presents the result of the summation procedure for various modal SER, to obtain a cumulative ratio to be used as a damage index in damage identification routines.

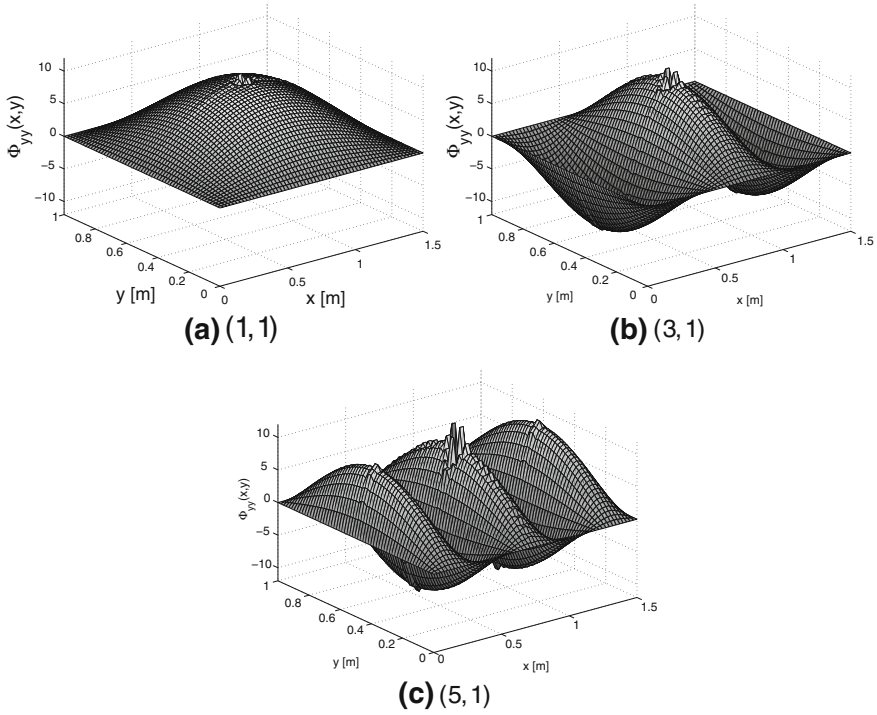

Fig. 7.8 Influence on mode order on curvature mode $\phi_{ij,yy}$ for $h_D/h_0 = 2\%$

7.3 Analysis of Wave Propagation in Notched Beams Through Spectral FE Solution

The perturbation method can be also applied in conjunction with the FSFEM to provide a solution of the perturbed equations in the presence of structures of increasing complexity. The approach is illustrated in this section for the case of beams described according to a elementary beam theory, whereby strain varies linearly across the thickness. This leads to a set of two equations governing bending and axial motion of the beam. In the absence of damage, the two equations are completely uncoupled as predicted by elementary beam theory, whereas damage causes coupling and mode conversion. This is a noteworthy aspect of this approach, which shows how a simple beam formulation can be employed to predict and analyze mode conversions caused by damage. The solution technique is validated by comparing its predictions with those of a model developed in the commercial code ABAQUS, and with solutions from the modal superposition approach. The SFEM was introduced as a general framework in Chap. 5, which combines the advantages of conventional FEs, with the computational efficiency of analytical techniques. The modal superposition technique can easily handle only

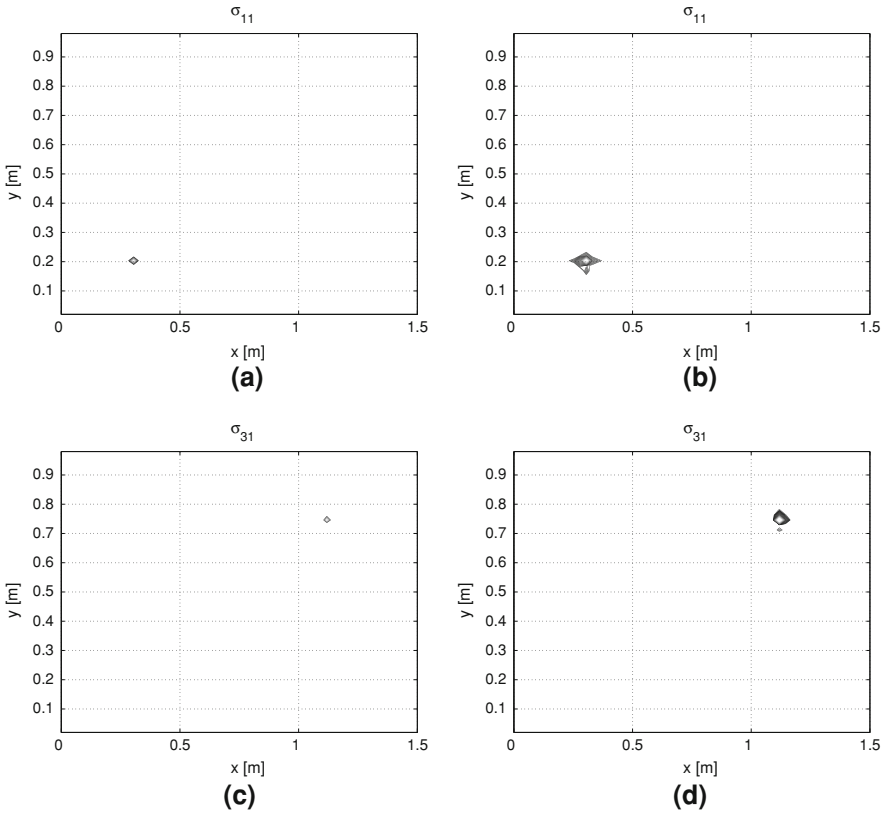

Fig. 7.9 Examples of modal SER for various damage locations and extents. **a** $hD/h0 = 2\%$, $xD = Lx/5$, $yD = Ly/5$, **b** $hD/h0 = 4\%$, $xD = Lx/5$, $yD = Ly/5$, **c** $hD/h0 = 2\%$, $xD = 3Lx/4$, $yD = 3Ly/4$, **d** $hD/h0 = 4\%$, $xD = 3Lx/4$, $yD = 3Ly/4$

simple geometries with reasonable computational costs, which limits its applicability. For this reason it is only used for validation purposes on simple geometries and cannot be considered as a general tool for the simulation of wave propagation in damaged structures. In contrast, the combination of FSFEM and perturbation analysis lends itself to the analysis of complex waveguides affected by small defects.

7.4 Governing Equations

The dynamic behavior of the notched beam shown in Fig. 7.16 is described by a set of governing equations derived through Hamilton principle. The defect is modeled as a reduction in thickness of depth h_d, extending over a length Δl, placed at the distance x_d. According to Fig. 7.16, $x \in [0, L]$ denotes the horizontal coordinate, whereas the vertical coordinate z varies in the following interval:

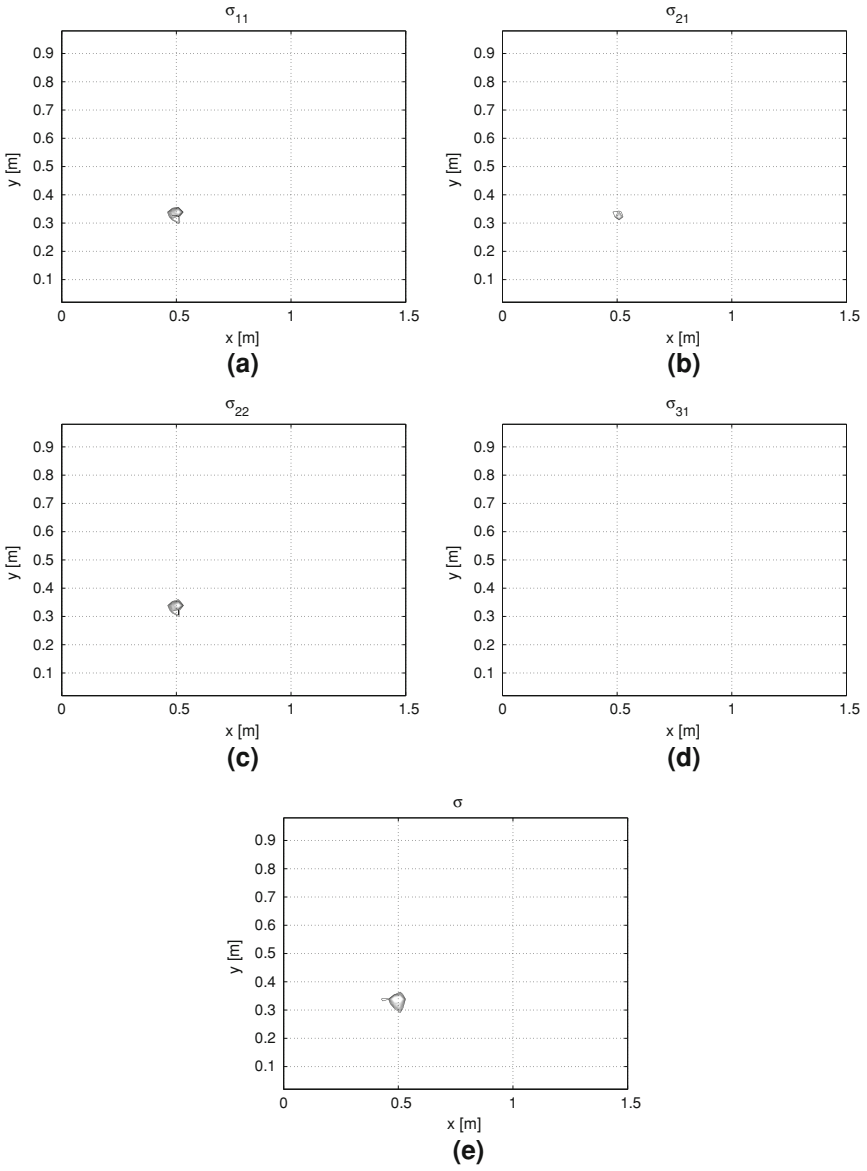

Fig. 7.10 Modal and cumulative SER for $x_D = L_x/3, y_D = L_y/3$ and $h_D/h_0 = 4\%$. **a** $\sigma_{1,1}$, **b** $\sigma_{2,1}$, **c** $\sigma_{2,2}$, **d** $\sigma_{3,1}$, **e** σ

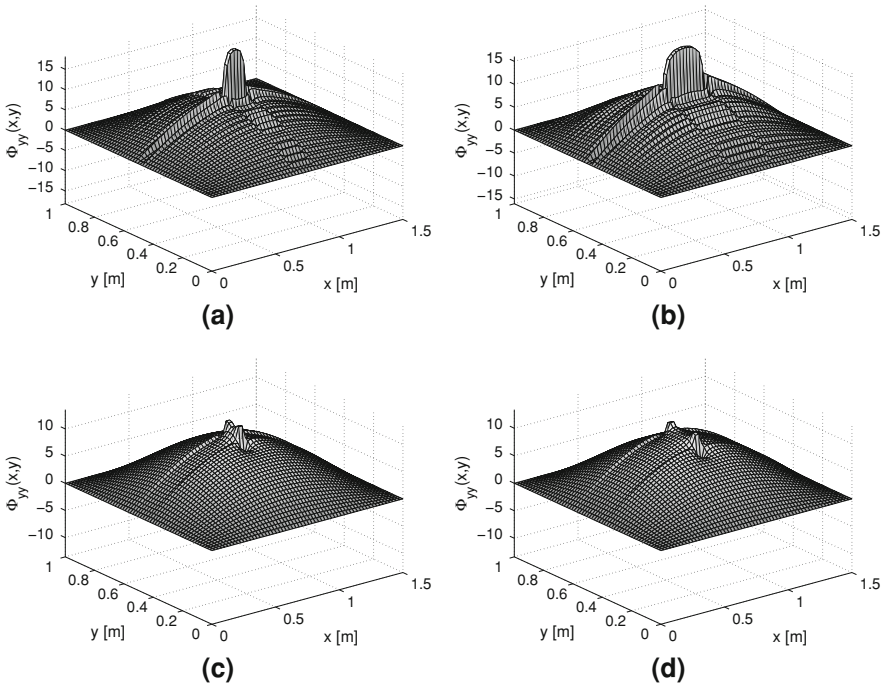

Fig. 7.11 Curvature mode $\phi_{11,yy}$ for $h_D/h_0 = 4\%$ and line defects of various lengths and orientations. **a** x-line defect, $yD = Ly/2$, $x_2 - x_1 = 0.15$ m, **b** x-line defect, $yD = Ly/2$, $x_2 - x_1 = 0.3$ m, **c** y-line defect, $xD = Lx/2$, $y_2 - y_1 = 0.05$ m, **d** y-line defect, $xD = Lx/2$, $y_2 - y_1 = 0.1$ m

$$z \in \left[-\frac{h}{2}, \frac{h}{2}(1 - 2\varepsilon\gamma_d(x)) \right] \tag{7.34}$$

where $\varepsilon = \frac{h_d}{h}$, and where $\gamma_d(x)$ is a damage function defined as:

$$\gamma_d(x) = H(x - (x_d - \Delta l)) - H(x - x_d) \tag{7.35}$$

with H denoting the Heaviside function. The governing equations for the notched beam and the appropriate set of boundary conditions are derived using Hamilton principle. The required kinetic and strain energies, and the work of external forces are formulated using the following kinematic assumptions:

$$\begin{cases} u(x,z,t) = u(x,t) - z\frac{\partial w}{\partial x} \\ w(x,z,t) = w(x,t) \end{cases} \tag{7.36}$$

where $u(x,t)$ and $w(x,t)$ are the axial and transverse displacements in the reference plane $z = 0$, respectively. The linear strain–displacement relations are:

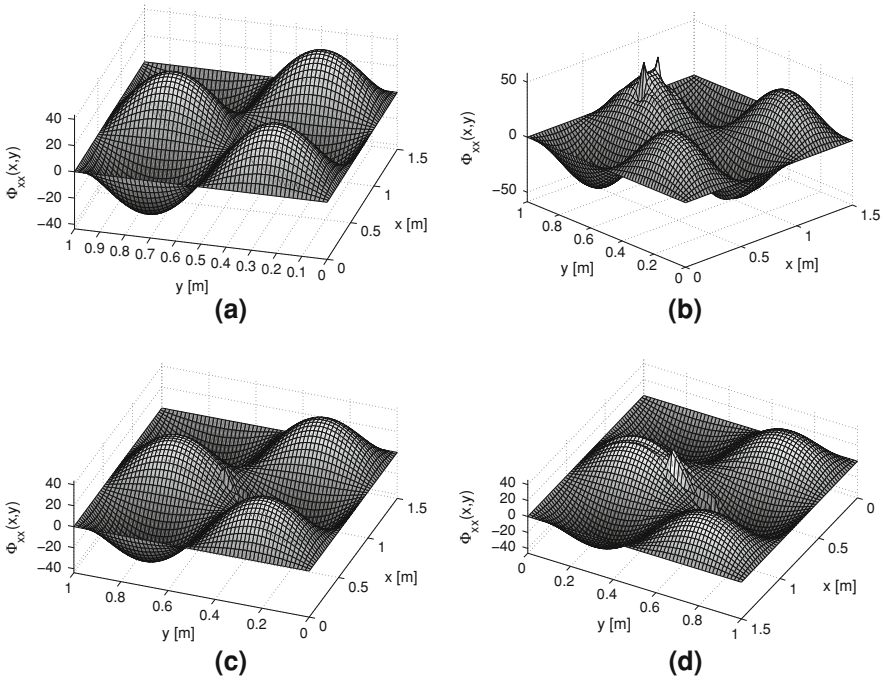

Fig. 7.12 Curvature mode $\phi_{32,xx}$ for $h_D/h_0 = 4\%$ and line defects of various lengths, locations and orientations. **a** x-line defect, $yD = Ly/2$, $x_2 - x_1 = 0.15$ m, **b** x-line defect, $yD = 3Ly/4$, $x_2 - x_1 = 0.3$ m, **c** y-line defect, $xD = Lx/2$, $y_2 - y_1 = 0.05$ m, **d** y-line defect, $xD = Lx/2$, $y_2 - y_1 = 0.1$ m

$$\begin{cases} \varepsilon_{xx}(x,z,t) = u_{,x}(x,t) - z w_{,xx}(x,t) \\ \varepsilon_{zz}(x,z,t) = 0, \quad \gamma_{xz}(x,z,t) = 0 \end{cases} \tag{7.37}$$

where the subscript, $_{,x}$ denotes a partial derivative with respect to x. The constitutive relation is assumed to be of the well known form:

$$\sigma_{xx}(x,z,t) = E\varepsilon_{xx}(x,z,t) \tag{7.38}$$

where σ_{xx} is the normal stress in the x direction and E is the Young's modulus. Accordingly, the axial force resultant and bending moment resultant are expressed as:

$$\begin{aligned} N_{xx}(x,t) &= b \int_{-\frac{h}{2}}^{\frac{h}{2}(1-2\varepsilon\gamma_d(x))} \sigma_{xx}(x,z,t)dz \\ &= Ehbu_{,x} + \left[-u_{,x} + w_{,xx}\frac{h}{2}\right] Ebh\gamma_d(x)\varepsilon \end{aligned} \tag{7.39}$$

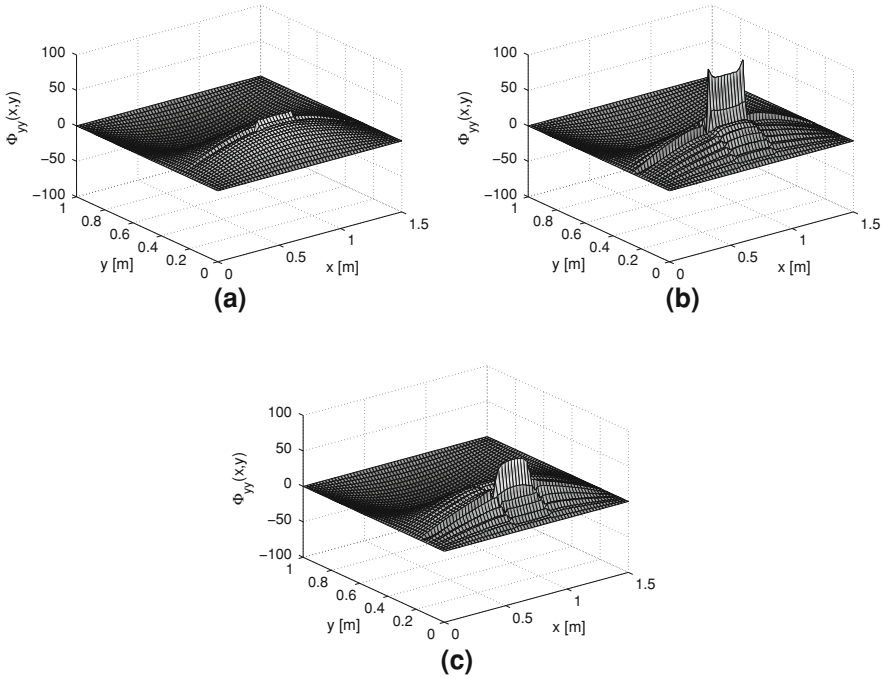

Fig. 7.13 Influence of extent and location of damage on curvature mode $\phi_{12_{yy}}$. **a** x-line defect, $yD = Ly/4$, $x_2 - x_1 = 0.3$ m, $hD/h0 = 2\%$, **b** x-line defect, $yD = Ly/4$, $x_2 - x_1 = 0.3$ m, $hD/h0 = 4\%$, **c** x-line defect, $yD = Ly/6$, $x_2 - x_1 = 0.3$ m, $hD/h0 = 4\%$

$$
\begin{aligned}
M_{xx}(x,t) &= b \int_{-\frac{h}{2}}^{\frac{h}{2}(1-2\varepsilon\gamma_d(x))} z\sigma_{xx}(x,z,t)dz \\
&= -E\frac{bh^3}{12}w_{,xx} + \left[-u_{,x} + w_{,xx}\frac{h}{2}\right]E\frac{bh^2}{2}\gamma_d(x)\varepsilon
\end{aligned}
\tag{7.40}
$$

Hamilton's principle,

$$
\int_{t_1}^{t_2} \delta(U - T + V)dt = 0 \tag{7.41}
$$

requires the derivation of the first variation of the beam's strain and kinetic energies and of the work of the external forces, which in this case are given by:

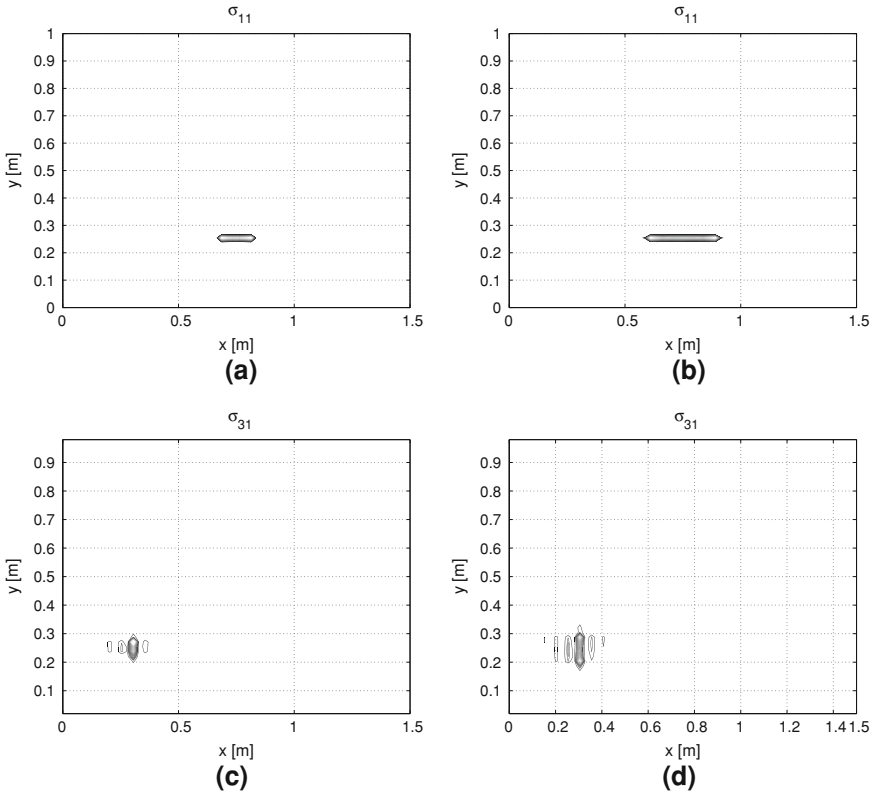

Fig. 7.14 Examples of modal SER for various damage locations and extents. **a** $hD/h0 = 2\%$, $yD = Ly/4$, $x_2 - x_1 = 0.15$ m, **b** $hD/h0 = 4\%$, $yD = Ly/4$, $x_2 - x_1 = 0.3$ m, **c** $hD/h0 = 4\%$, $y_2 - y_1 = 0.05$ m, $xD = Lx/5$, **d** $hD/h0 = 4\%$, $y_2 - y_1 = 0.1$ m, $xD = Lx/5$

$$
\begin{aligned}
\delta T &= b \int_0^L \int_{-\frac{h}{2}}^{\frac{h}{2}(1-2\varepsilon\gamma_d(x))} \rho(u_{,tt}\delta u_{,t} + w_{,t}\delta w_{,t}) dz dx \\
&= -b \int_0^L \int_{-\frac{h}{2}}^{\frac{h}{2}(1-2\varepsilon\gamma_d(x))} \rho(u_{,tt}\delta u + w_{,tt}\delta w) dz dx \\
&= -b\rho \int_0^L \left\{ u_{,t} h[1 - \varepsilon\gamma_d(x)] + w_{,ttx} \frac{h^2}{2} \varepsilon\gamma_d(x) \right\} \delta u dx \\
&\quad - b\rho \int_0^L \left\{ -\left[u_{,tt} \frac{h^2}{2} \varepsilon\gamma_d(x) + w_{,ttx} \frac{h^3}{12} [1 - \varepsilon\gamma_d(x)] \right]_{,x} + w_{,tt} h[1 - \varepsilon\gamma_d(x)] \right\} \delta w dx
\end{aligned}
\tag{7.42}
$$

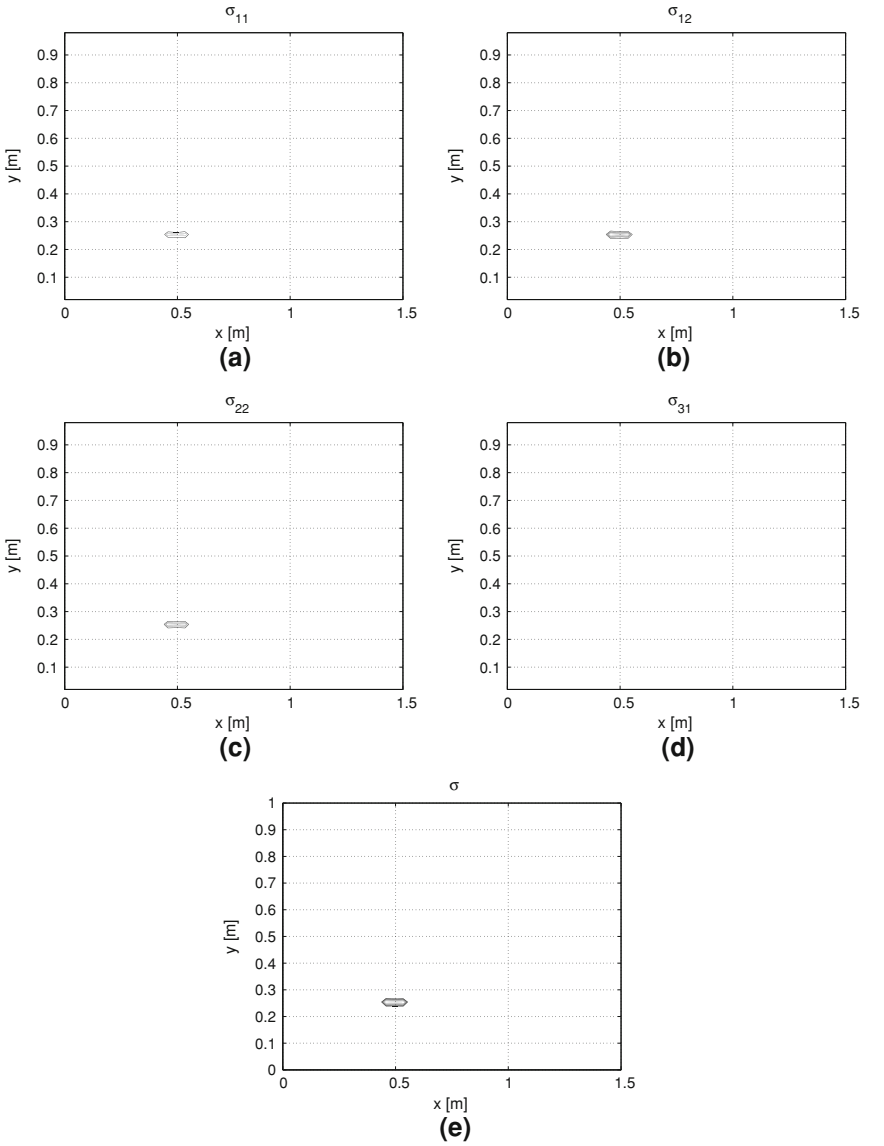

Fig. 7.15 Modal and cumulative SER for line defect with $x_2 - x_1 = 0.15\,\text{m}$, $y_D = L_y/4$ and $h_D/h_0 = 2\%$. **a** $\sigma_{1,1}$, **b** $\sigma_{2,1}$, **c** $\sigma_{2,2}$, **d** $\sigma_{3,1}$, **e** σ

$$-b\rho\left\{u_{,tt}\frac{h^2}{2}\varepsilon\gamma_d(x) + w_{,ttx}\frac{h^3}{12}[1-\varepsilon\gamma_d(x)]\right\}\delta w\Big|_{x=0}^{x=L} \tag{7.43}$$

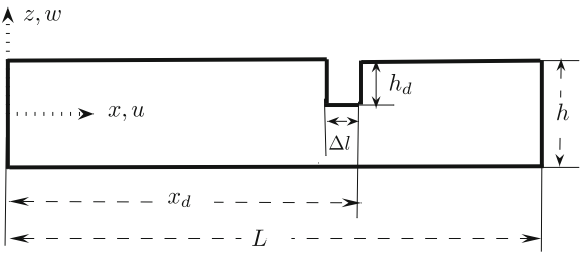

Fig. 7.16 Beam geometry

$$
\begin{aligned}
\delta U &= b\int_0^L \int_{-\frac{h}{2}}^{\frac{h}{2}(1-2\varepsilon\gamma_d(x))} \sigma_{xx}(x,z,t)\delta\varepsilon_{xx}(x,z,t)dzdx \\
&= b\int_0^L \int_{-\frac{h}{2}}^{\frac{h}{2}(1-2\varepsilon\gamma_d(x))} \sigma_{xx}\Big[(\delta u)_{,x} - z(\delta w)_{,xx}\Big]dzdx \\
&= b\int_0^L \Big[N_{xx}(x,t)()_{,x} - M_{xx}(x,t)(\delta w)_{,xx}\Big]dx \\
&= bN_{xx}(x,t)\delta u\big|_{x=0}^{x=L} - b\int_0^L N_{xx,x}(x,t)\delta u dx \\
&\quad - b\Big[M_{xx}(x,t)(\delta w)_{,x} - M_{xx,x}(x,t)\delta w\Big]\Big|_{x=0}^{x=L} - b\int_0^L M_{xx,xx}(x,t)dx
\end{aligned}
\tag{7.44}
$$

and

$$
\begin{aligned}
\delta V &= -\int_0^L \Big[n(x,t)\delta u + q(x,t)\delta w + m(x,t)(\delta w)_{,x}\Big]dx \\
&\quad - \sum_{j=1}^N \int_0^L \Big[N_j(t)\delta u + Q_j(t) + M_j(t)(\delta w)_{,x}\Big]\delta(x-x_j)dx \\
&= -\int_0^L \left[n(x,t) + \sum_{j=1}^N N_j(t)\delta(x-x_j)\right]\delta u dx \\
&\quad - \int_0^L \left[q(x,t) - m_{,x}(x,t) + \sum_{j=1}^N Q_j(t)\delta(x-x_j) - \sum_{j=1}^N M_j(t)(\delta(x-x_j))_{,x}\right]\delta w dx - \\
&\quad - \left[m(x,t) + \sum_{j=1}^N M_j(t)\delta(x-x_j)\right]\delta w\Big|_{x=0}^{x=L}
\end{aligned}
\tag{7.45}
$$

where, for simplicity we assume that the loads are applied along the reference plane $z = 0$. Also in Eq. 7.45 $n(x,t)$ and $q(x,t)$ respectively denote axial and transverse distributed external loads, $m(x,t)$ denotes a distributed bending moment distribution, while $N_j(t), Q_j(t)$ and $M_j(t)$ are external concentrated longitudinal and

vertical loads, and bending moment applied at N locations $x = x_j$. Finally δ is the Dirac delta function.

Application of Hamilton's principle yields the following set of differential equations:

$$\begin{cases} N_{xx,x}(x,t) - \rho h[1 - \varepsilon\gamma_d(x)]\ddot{u} - \rho\frac{h^2}{2}\varepsilon\gamma_d(x)\ddot{w}_{,x} = f_1(x,t) \\ M_{xx,xx}(x,t) + \rho\left\{\ddot{u}\frac{h^2}{2}\varepsilon\gamma_d(x) + \ddot{w}_{,x}\frac{h^3}{12}[1 - \varepsilon\gamma_d(x)]\right\}_{,x} - \rho h[1 - \varepsilon\gamma_d(x)]\ddot{w} = f_2(x,t) \end{cases} \tag{7.46}$$

where $f_1(x,t)$ and $f_2(x,t)$ are respectively defined as:

$$\begin{aligned} f_1(x,t) &= -n(x,t) - \sum_{j=1}^{N} N_j(t)\delta(x - x_j) \\ f_2(x,t) &= -q(x,t) + m_{,x}(x,t) - \sum_{j=1}^{N} Q_j(t)\delta(x - x_j) + \sum_{j=1}^{N} M_j(t)\{\delta(x - x_j)\}_{,x} \end{aligned} \tag{7.47}$$

The associated boundary conditions, at $x = 0$ and $x = L$ are:

$$\begin{cases} N_{xx}(x,t) = 0 \quad \text{or} \quad u(x,t) \text{ given} \\ bM_{xx,x}(x,t) + \rho I_0\ddot{w}_{,x}(x,t) - m(x,t) - \sum_{j=1}^{N} M_j(t)\delta(x - x_j) = 0 \quad \text{or} \quad w(x,t) \text{ given} \\ M_{xx}(x,t) = 0 \quad \text{or} \quad w_{,x}(x,t) \text{given} \end{cases} \tag{7.48}$$

Equations 7.46 can be conveniently expressed in the frequency domain through the Fourier Transform (FT) of the applied generalized loads $f_i(x,t)$ (with $i = 1, 2$), which can be expressed as:

$$f_i(x,t) = \sum_k \hat{f}_{i_k}(x,\omega_k)e^{j\omega_k t} \tag{7.49}$$

where $j = \sqrt{-1}$, and $\hat{f}_{i_k}(x,\omega_k)$ denotes the harmonic component of the generalized load at frequency ω_k [4]. Accordingly, the beam's displacements can be written as:

$$u(x,t) = \sum_k \hat{u}_k(x,\omega_k)e^{j\omega_k t} \tag{7.50}$$

$$w(x,t) = \sum_k \hat{w}_k(x,\omega_k)e^{j\omega_k t} \tag{7.51}$$

where $\hat{u}_k(x,\omega_k), \hat{w}_k(x,\omega_k)$ are the displacements corresponding to the kth harmonic component of the load. For simplicity, in the remainder of the chapter, the subscript k is dropped so that the following notation is adopted $\omega_k = \omega$, $\hat{u}_k(x,\omega_k) = \hat{u}(x,\omega), \hat{w}_k(x,\omega) = \hat{w}(x,\omega)$.

Next, the axial and transverse displacements of the beam in the reference plane are considered as perturbations (over the small parameter ε) of the axial and vertical displacement of the undamaged beam:

$$\left\{ \begin{array}{c} \hat{u}(x,\omega) \\ \hat{w}(x,\omega) \end{array} \right\} = \left\{ \begin{array}{c} \hat{u}^{(0)}(x,\omega) \\ \hat{w}^{(0)}(x,\omega) \end{array} \right\} - \varepsilon \left\{ \begin{array}{c} \hat{u}^{(1)}(x,\omega) \\ \hat{w}^{(1)}(x,\omega) \end{array} \right\} - O(\varepsilon^2) \tag{7.52}$$

Replacing Eqs. 7.39–7.40 and Eq. 7.52 into the differential equation (Eq. 7.46) and collecting the coefficients of ε^0 and ε^1 yields the following set of differential equations:

$$\begin{aligned} \varepsilon^0 : \quad & \left[\begin{array}{cc} m\omega^2 & 0 \\ 0 & m\omega^2 \end{array} \right] \left\{ \begin{array}{c} \hat{u}^{(0)}(x,\omega) \\ \hat{w}^{(0)}(x,\omega) \end{array} \right\} + \left[\begin{array}{cc} EA & 0 \\ 0 & -\rho I_0 \omega^2 \end{array} \right] \left\{ \begin{array}{c} \hat{u}^{(0)}_{,xx}(x,\omega) \\ \hat{w}^{(0)}_{,xx}(x,\omega) \end{array} \right\} \\ & + \left[\begin{array}{cc} 0 & 0 \\ 0 & -EI_0 \end{array} \right] \left\{ \begin{array}{c} \hat{u}^{(0)}_{,4x}(x,\omega) \\ \hat{w}^{(0)}_{,4x}(x,\omega) \end{array} \right\} = \left\{ \begin{array}{c} \hat{f}_1(x,\omega) \\ \hat{f}_2(x,\omega) \end{array} \right\} \end{aligned} \tag{7.53}$$

$$\begin{aligned} \varepsilon^1 : \quad & \left[\begin{array}{cc} m\omega^2 & 0 \\ 0 & m\omega^2 \end{array} \right] \left\{ \begin{array}{c} \hat{u}^{(1)}(x,\omega) \\ \hat{w}^{(1)}(x,\omega) \end{array} \right\} + \left[\begin{array}{cc} EA & 0 \\ 0 & -\rho I_0 \omega^2 \end{array} \right] \left\{ \begin{array}{c} \hat{u}^{(1)}_{,xx}(x,\omega) \\ \hat{w}^{(1)}_{,xx}(x,\omega) \end{array} \right\} \\ & + \left[\begin{array}{cc} 0 & 0 \\ 0 & -EI_0 \end{array} \right] \left\{ \begin{array}{c} \hat{u}^{(1)}_{,4x}(x,\omega) \\ \hat{w}^{(1)}_{,4x}(x,\omega) \end{array} \right\} = \left\{ \begin{array}{c} \hat{g}_1(x,\omega) \\ \hat{g}_2(x,\omega) \end{array} \right\} \end{aligned} \tag{7.54}$$

where $I = bh^3/12, A = bh, \rho$ is the density per unit area, m is the beam mass, and where:

$$\begin{aligned} \left\{ \begin{array}{c} \hat{g}_1(x,\omega) \\ \hat{g}_2(x,\omega) \end{array} \right\} = & \left[\begin{array}{cc} -m\omega^2\gamma_d(x,\omega) & 0 \\ -\frac{mh}{2}\omega^2\gamma_{d,x}(x,\omega) & -m\omega^2\gamma_d(x,\omega) \end{array} \right] \left\{ \begin{array}{c} \hat{u}^{(0)}(x,\omega) \\ \hat{w}^{(0)}(x,\omega) \end{array} \right\} \\ & + \left[\begin{array}{cc} -EA\gamma_{d,x}(x,\omega) & \frac{mh}{2}\omega^2\gamma_d(x,\omega) \\ -EA\frac{h}{2}\gamma_{d,xx}(x,\omega) - \frac{mh}{2}\omega^2\gamma_d(x,\omega) & 3\rho I_0\omega^2\gamma_{d,x}(x,\omega) \end{array} \right] \left\{ \begin{array}{c} \hat{u}^{(0)}_{,x}(x,\omega) \\ \hat{w}^{(0)}_{,x}(x,\omega) \end{array} \right\} \\ & + \left[\begin{array}{cc} -EA\gamma_d(x,\omega) & EA\frac{h}{2}\gamma_{d,x}(x,\omega) \\ -EAh\gamma_{d,x}(x,\omega) & 3EI_0\gamma_{d,xx}(x,\omega) + \rho I_0\omega^2\gamma_d(x,\omega) \end{array} \right] \left\{ \begin{array}{c} \hat{u}^{(0)}_{,xx}(x,\omega) \\ \hat{w}^{(0)}_{,xx}(x,\omega) \end{array} \right\} \\ & + \left[\begin{array}{cc} 0 & EA\frac{h}{2}\gamma_d(x,\omega) \\ -EA\frac{h}{2}\gamma_d(x,\omega) & 6EI_0\gamma_{d,x}(x,\omega) \end{array} \right] \left\{ \begin{array}{c} \hat{u}^{(0)}_{,3x}(x,\omega) \\ \hat{w}^{(0)}_{,3x}(x,\omega) \end{array} \right\} + \left[\begin{array}{cc} 0 & 0 \\ 0 & 3EI_0\gamma_{d,x}(x,\omega) \end{array} \right] \left\{ \begin{array}{c} \hat{u}^{(0)}_{,4x}(x,\omega) \\ \hat{w}^{(0)}_{,4x}(x,\omega) \end{array} \right\} \end{aligned} \tag{7.55}$$

Equations 7.53 and 7.54 can be solved for an assigned set of loads in terms of the unknown displacements $\hat{\mathbf{u}}^{(0)}(x,\omega) = \left[\hat{u}^{(0)}(x,\omega) \quad \hat{w}^{(0)}(x,\omega)\right]^T$ and their first order perturbation $\hat{\mathbf{u}}^{(1)}(x,\omega) = \left[\hat{u}^{(1)}(x,\omega) \quad \hat{w}^{(1)}(x,\omega)\right]^T$.

7.4.1 Spectral Finite Element Discretization

The equation for the ε^0 term corresponds to the governing equation for the undamaged beam, the first order perturbation equation has the same form and features an applied generalized load that is a function of the solution of the ε^0 equation. A common strategy for the solution of the two equations (Eqs. 7.53 and 7.54) derived from the expansion of the beam's displacements in terms of the perturbation parameter can be adopted based on their formally identical form. Each of the equations can in fact be written in the following matrix form:

$$\begin{bmatrix} m\omega^2 & 0 \\ 0 & m\omega^2 \end{bmatrix} \begin{Bmatrix} \hat{u}(x,\omega) \\ \hat{w}(x,\omega) \end{Bmatrix} + \begin{bmatrix} EA & 0 \\ 0 & -\rho I\omega^2 \end{bmatrix} \begin{Bmatrix} \hat{u}_{,xx}(x,\omega) \\ \hat{w}_{,xx}(x,\omega) \end{Bmatrix} + \begin{bmatrix} 0 & 0 \\ 0 & -EI \end{bmatrix} \begin{Bmatrix} \hat{u}_{,4x}(x,\omega) \\ \hat{w}_{,4x}(x,\omega) \end{Bmatrix} = \begin{Bmatrix} q_1(x,\omega) \\ q_2(x,\omega) \end{Bmatrix} \tag{7.56}$$

or

$$\mathbf{M}\hat{\mathbf{u}}(x,\omega) + \mathbf{E}_1\hat{\mathbf{u}}_{,xx}(x,\omega) + \mathbf{E}_2\hat{\mathbf{u}}_{,4x}(x,\omega) = \mathbf{q}(x,\omega) \tag{7.57}$$

The weak form solution of Eq. 7.57 can be sought through multiplication by a suitable test function $\mathbf{v}(x,\omega)^T$:

$$\int_0^{L_j} \mathbf{v}^T(x,\omega)\mathbf{M}\hat{\mathbf{u}}(x,\omega)dx - \int_0^{L_j} \mathbf{v}_{,x}^T(x,\omega)\mathbf{E}_1\hat{\mathbf{u}}_{,x}(x,\omega)dx + \int_0^{L_j} \mathbf{v}_{,xx}^T(x,\omega)\mathbf{E}_2\hat{\mathbf{u}}_{,xx}(x,\omega)dx = \int_0^{L_j} \mathbf{v}^T(x,\omega)\mathbf{q}(x,\omega)dx \tag{7.58}$$

where L_j is the length of an element j that connects two nodes (Fig. 7.17). The behavior of each node is described by three degrees of freedom, so that the element's vector of degrees of freedom is defined as $\mathbf{d}_j = \{\hat{u}_{1j},\ \hat{w}_{1j},\ \hat{w}_{1j,x},\ \hat{u}_{2j},\ \hat{w}_{2j},\ \hat{w}_{2j,x}\}^T$. The displacement $\hat{\mathbf{u}}(x,\omega)$ within element j is obtained as an interpolation of the nodal degrees of freedom $\mathbf{d}_j$:

$$\hat{\mathbf{u}}(x,\omega) = \mathbf{N}_j(x,\omega)\mathbf{d}_j(\omega) \tag{7.59}$$

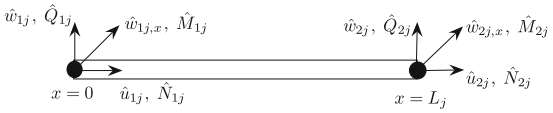

Fig. 7.17 Spectral finite element with nodal displacements and loads

where $\mathbf{N}_j(x,\omega)$ is the matrix of the dynamic shape functions, which is obtained from the solution of the homogeneous governing equation

$$\mathbf{N}_j(x,\omega) = \boldsymbol{\Theta}(\omega)\mathbf{G}_j(x,\omega)\mathbf{T}_j^{-1}(\omega) \tag{7.60}$$

where $\boldsymbol{\Theta}(\omega)$ is an amplitude ratio matrix:

$$\boldsymbol{\Theta}(\omega) = \begin{bmatrix} 1 & 0 & 0 & 1 & 0 & 0 \\ 0 & 1 & 1 & 0 & 1 & 1 \end{bmatrix} \tag{7.61}$$

$\mathbf{G}_j(x,\omega)$ is defined as:

$$\mathbf{G}_j(x,\omega) = \begin{bmatrix} e^{-ikx} & 0 & 0 & 0 & 0 & 0 \\ 0 & e^{-\beta x} & 0 & 0 & 0 & 0 \\ 0 & 0 & e^{-\beta(L_j-x)} & 0 & 0 & 0 \\ 0 & 0 & 0 & e^{-ik(L_j-x)} & 0 & 0 \\ 0 & 0 & 0 & 0 & e^{-i\beta x} & 0 \\ 0 & 0 & 0 & 0 & 0 & e^{-i\beta(L_j-x)} \end{bmatrix} \tag{7.62}$$

whereas $\mathbf{T}_j(\omega)$ is obtained by imposing the displacements at the nodes:

$$\mathbf{T}_j(\omega) = \begin{bmatrix} 1 & 0 & 0 & e^{-ikL_j} & 0 & 0 \\ 0 & 1 & e^{-\beta L_j} & 0 & 1 & e^{-i\beta L_j} \\ 0 & -\beta & -\beta e^{-\beta L_j} & 0 & -i\beta & i\beta e^{-i\beta L_j} \\ e^{-ikL_j} & 0 & 0 & 1 & 0 & 0 \\ 0 & e^{-\beta L_j} & 1 & 0 & e^{-i\beta L_j} & 1 \\ 0 & -\beta e^{-\beta L_j} & \beta & 0 & -i\beta e^{-i\beta L_j} & i\beta \end{bmatrix} \tag{7.63}$$

with $k^2 = \omega^2/c^2 = \omega^2 m/EA$ and $\beta^4 = \omega^2 m/EI_0$.

The dynamic shape functions provide the exact displacement variation along the beam if the external loads are concentrated at the nodal locations [4]. In the case considered here, it can be shown that the generalized load in the first order perturbation equations reduces to a concentrated nodal load if a node is placed at the damage location. Accordingly, the solution of homogeneous beam equations and proper description of nodal loads corresponding to the presence of damage based on the formulation presented above can be used to obtain exact dynamic shape functions and accurate representations of the beam's displacements in the frequency range corresponding to the applied load. This approach can also be applied when loads are generally distributed along the element length. In this case, the dynamic shape functions do not reproduce exactly the displacement field within the element, and some approximation is introduced. The application of nodes at damage and load locations do not cause a dramatic increase in the computational time, and the presented modeling approach still represents an efficient tool for the analysis of wave propagation in the considered class of damaged structures.

The dynamic interpolation functions can be also used for the test function $\mathbf{v}$. Substitution in the weak form of the equation yields the following algebraic equation:

$$\mathbf{K}_j(\omega)\mathbf{d}_j(\omega) = \mathbf{f}_j(\omega) \tag{7.64}$$

where $\mathbf{K}(\omega)_j$ is the element stiffness matrix at frequency ω, defined as:

$$\begin{aligned}\mathbf{K}_j(\omega) = \int_0^{L_j} \Big\{ &\mathbf{N}_j^T(x,\omega)\mathbf{M}_j\mathbf{N}_j(x,\omega) - \mathbf{N}_{j,x}^T(x,\omega)\mathbf{E}_{1_j}\mathbf{N}_{j,x}(x,\omega) \\ &+\mathbf{N}_{j,xx}^T(x,\omega)\mathbf{E}_{1_j}\mathbf{N}_{j,xx}(x,\omega)\Big\}dx\end{aligned} \tag{7.65}$$

and where $\mathbf{f}$ is the vector of applied nodal loads:

$$\mathbf{f}_j(\omega) = \int_0^{L_j} \mathbf{N}_j^T(x,\omega)\boldsymbol{q}(x,\omega)dx \tag{7.66}$$

7.5 Wave Propagation in Notched Beams: Numerical Examples

In this section, the developed technique is applied to evaluate longitudinal and transverse wave propagation in damaged beams. The solution based on FSFEM is first validated through comparisons with the predictions of a model developed in ABAQUS. The case of a simply supported beam solved through the modal superposition approach is then used as a baseline for comparison. Upon assessment of the accuracy of the procedure, simulations in the time and frequency domain are performed for various sets of boundary conditions, excitation configurations, and damage extent and location to show the potential of the technique as a general simulation tool, and to highlight interesting phenomena related to the interaction of propagating waves with damage.

7.5.1 Technique Validation: FSFEM Versus FE Predictions

A detailed finite element model of the damaged beam is developed using the commercial software ABAQUS. The considered beam is assumed in a clamped-free configuration, has length $L = 1\,\text{m}$, thickness $h = 10 \times 10^{-3}\,\text{m}$ and width $b = 50 \times 10^{-3}\,\text{m}$. The beam is made of aluminum (Young's modulus $E = 70\,\text{GPa}$, density $\rho = 2750\,\text{kg/m}^3$), and features a notch of length $\Delta l = 1 \times 10^{-3}\,\text{m}$ and depth $h_d = h/2$ at $x_d = L/2$. The beam is modeled using 10,000 four-node bilinear plane stress quadrilateral elements, and its response is computed through an

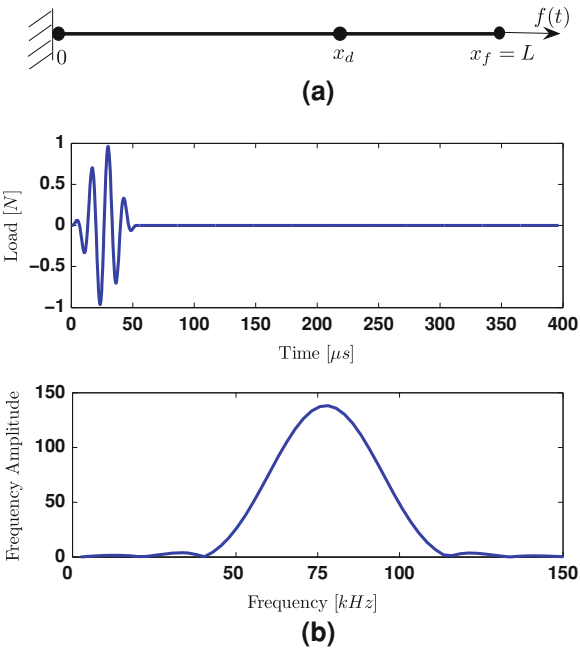

Fig. 7.18 **a** schematic of the clamped-free beam with a longitudinal tip load, modeled using two spectral elements; **b** modulated sinusoidal pulse load in time and frequency domain

explicit dynamic analysis. The same beam is modeled using two spectral finite elements as shown in Fig. 7.18a. The considered excitation is a four-cycles sinusoidal burst at 75 kHz modulated by a Hanning window (Fig. 7.18b), applied at the free end on the beam in the longitudinal direction according to the configuration shown in Fig. 7.18a.

Figures 7.19a, b compare longitudinal and transverse displacements at the free end of the beam as obtained using FSFEM and ABAQUS. The longitudinal responses in Fig. 7.19a show an excellent agreement, both in terms of amplitude of the incident wave and of the reflected wave produced by the damage, and in terms of time of arrival of the reflected waves. Fig. 7.19b presents the comparison between corresponding transverse displacements. Both FSFEM and ABAQUS models predict the generation of a transverse displacement component upon interaction of the longitudinal wave with the defect, which indicates that mode conversion has taken place. The time lag between the models can be explained by the fact that a simple Euler–Bernoulli formulation has been employed for FSFEM. It is well-known that Euler–Bernoulli theory overestimates the wave speeds in comparison with more refined beam theories such as Timoshenko formulation [4]. The ABAQUS model does not rely on beam theory, and can be considered as a more accurate description of the dynamic behavior due to the highly refined mesh employed for the analysis. The discrepancies in terms of wave velocities is estimated from the dispersion relations predicted by the two models. The dispersion relation in FSFEM follows the Euler–Bernoulli relation $k = \left(\frac{\omega^2 EI}{\rho A}\right)^{1/4}$, while that of the ABAQUS model needs to be

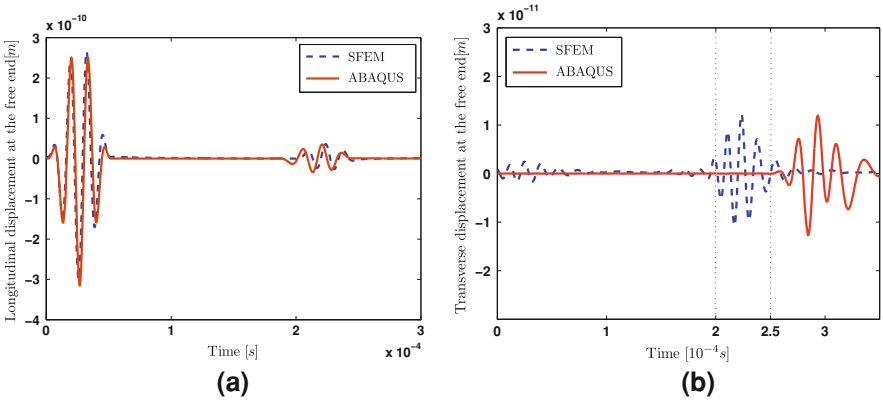

Fig. 7.19 Comparison between FEM and SFEM results: **a** longitudinal and **b** transverse displacement at the free end of notched beam with a defect at $x_d = L/2$

evaluated by means of a numerical experiment. Specifically, the beam is excited by a broadband pulse, and its response in the time domain is recorded at all the nodal points available along the beam span. This allows the computation of two-dimensional FT in space and time, which provides wavenumber and frequency information over the considered frequency range. This data is then used to estimate the group velocity variation in terms of frequency, and compare it with the SFEM one. The result of this analysis is presented in Fig. 7.20: the mismatch in group velocities observed at the excitation frequency of 75 kHz corresponds to the time delay observed in the time plots of Fig. 7.19b.

7.5.2 FSFEM and Modal Superposition Results

A second validation is carried out through comparisons with the modal superposition solution of the perturbation equations Eqs. 7.54 and 7.55. The modes of the

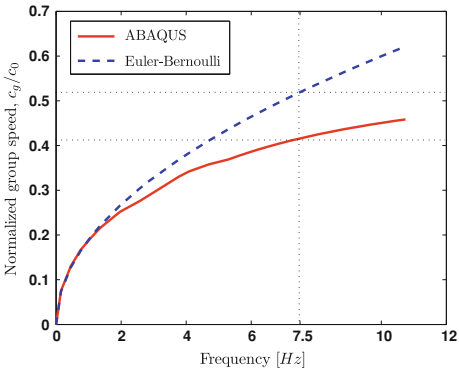

Fig. 7.20 Comparison of ABAQUS and SFEM group velocities

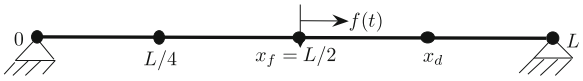

Fig. 7.21 Schematic of the simply-supported beam with a longitudinal load at the middle, used to compare superposition of modes and SFEM results

considered structure are used to decouple the equations of motion and to obtain time-domain ODEs in terms of the modal coordinates. The convolution integral is then employed for the time-domain solution given the assigned excitation time history and the corresponding modal loads. This approach, very well known and established, does not provide the generality of the SFEM and can only be conveniently applied in the case of simple geometries. The considered configuration is that of the beam in Fig. 7.21, which is excited longitudinally at mid span by a four-cycle modulated sinusoidal burst at 500 kHz. The corresponding longitudinal and transverse mid-span displacements in Fig. 7.22 show the agreement between the solutions and confirm that the interaction with the damage partially converts the longitudinal wave into a transverse one.

The second validation example considers a notch placed at $x_d = 3L/8$ and a transverse load at mid-span. Figures 7.23 and 7.24 compare snapshots of the beam deflected configuration (longitudinal and bending component) at various instants of time. The plots show how longitudinal displacements are produced by the interaction of the bending wave with the defect, and confirm the good agreement between FSFEM and mode superposition solutions.

7.5.3 Time Domain Results

The first example in the time domain considers a simply-supported beam with a notch at $x_d = 3L/4$ and a vertical load at $x_f = L/2$. The beam has the same

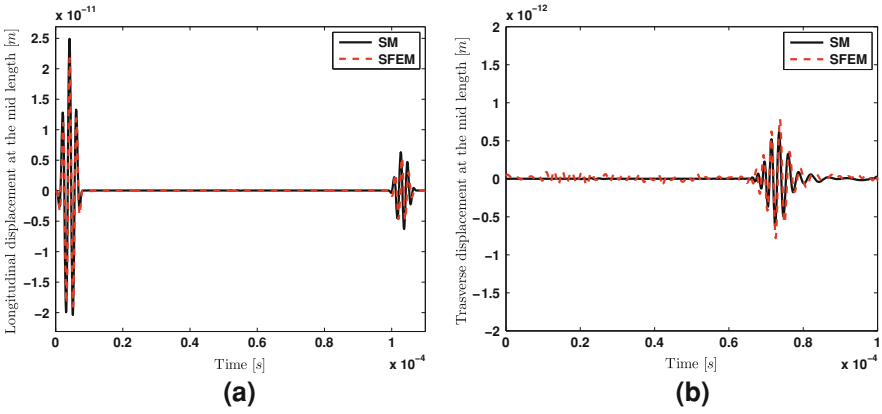

Fig. 7.22 Longitudinal **(a)** and transverse **(b)** displacement at the mid length of notched beams with a defect at $x_d = 3L/4$

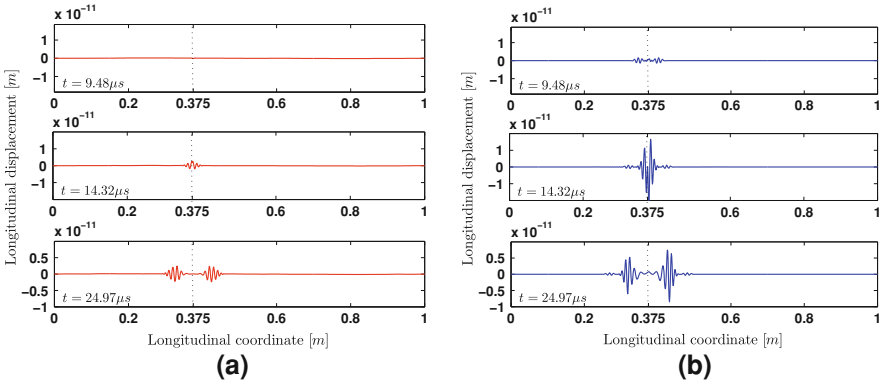

Fig. 7.23 Displacements as function of longitudinal coordinate at the same moments: **a** SFEM longitudinal displacement, **b** SM longitudinal displacement

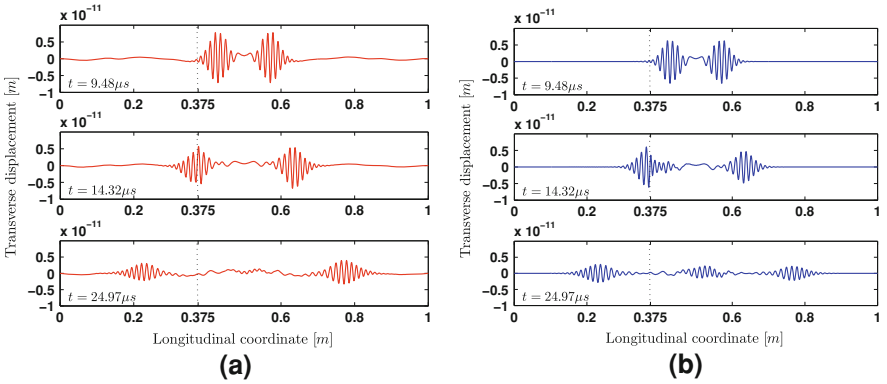

Fig. 7.24 Displacements as function of longitudinal coordinate at the same moments: **a** SFEM transverse displacement, **b** SM transverse displacement

geometry and material properties as described in the previous section. The beam is modeled using four spectral elements as shown in Fig. 7.21. The beam response computed through the FSFEM model is presented in Fig. 7.25 both in time and space as a color map plot, while Fig. 7.26 shows snapshots of the displacements' variation along the beam at three instants of time. In both figures, the axial displacement is plotted in the subplot (a) and the transverse displacement is displayed in subplot (b). The applied transverse load generates a transverse wave which propagates from the middle of the beam in both directions. When the wave reaches the notch, it is partially reflected, and partially gets converted into a longitudinal wave originating at the notch location. Figures 7.27 and 7.28 show the time variation of longitudinal and transverse velocities at the middle of the beam for two

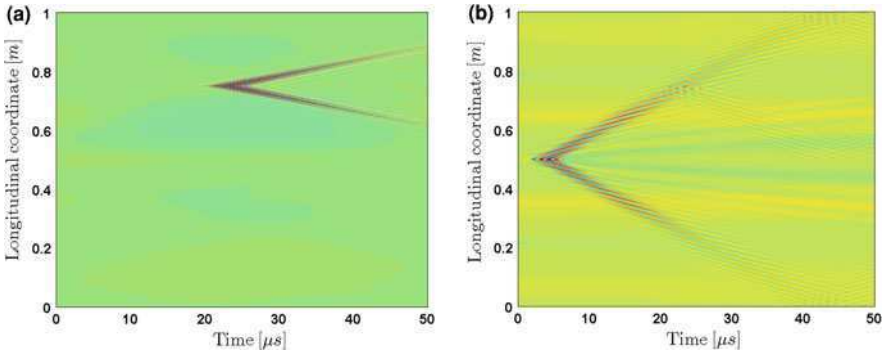

Fig. 7.25 Displacements as function of time and horizontal coordinate **a** longitudinal displacement; **b** transverse displacement. The length of the notch is $\Delta l = 0.001$ m

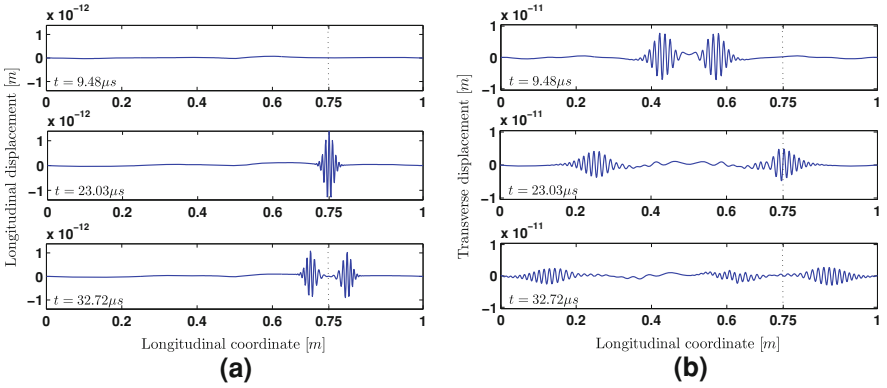

Fig. 7.26 Displacements as function of horizontal coordinate at the same moments **a** longitudinal displacement; **b** transverse displacement

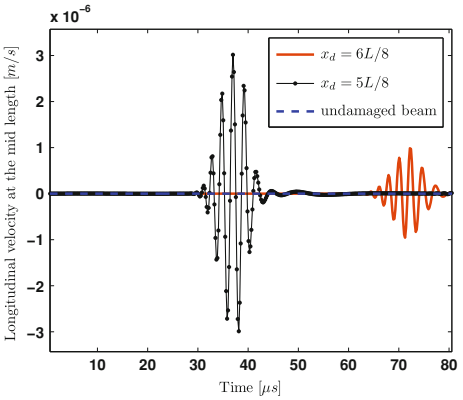

Fig. 7.27 Longitudinal velocity at the mid length for undamaged beam and notched beams with a defect at $x_d = 5L/8$ and $x_d = 6L/8$

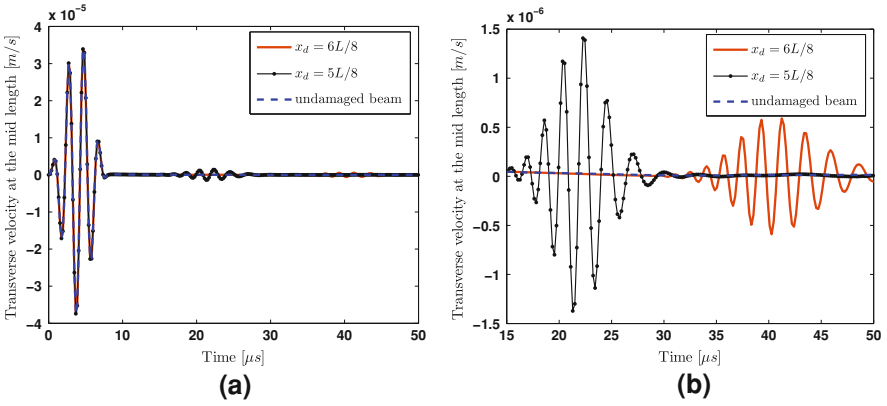

Fig. 7.28 **a** transverse velocity at the mid length of an undamaged beam and notched beams with a defect at $x_d = 5L/8$ and $x_d = 3L/4$; **b** details of reflections caused by damage

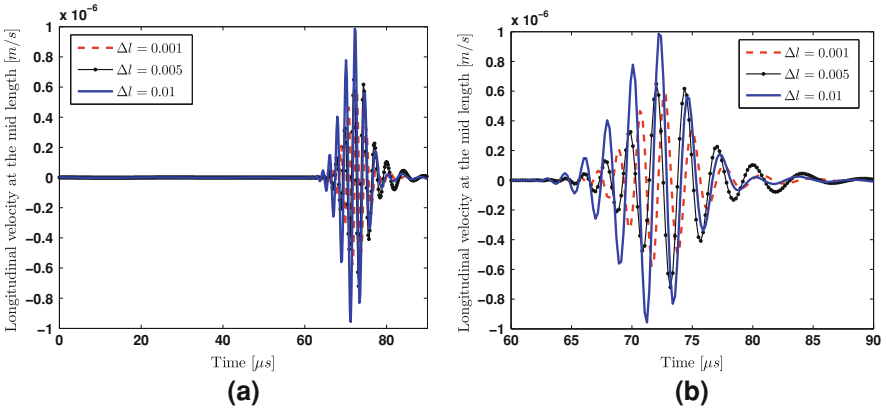

Fig. 7.29 **a** longitudinal velocity at the mid length of notched beams with a defect length, $\Delta l = 0.001, 0.005, 0.01$ m; **b** details of reflections caused by damage

different defect positions ($x_d = 5L/8$ and $x_d = 3L/4$), and compare them directly with the velocity of the undamaged beam. As expected, the arrival time of the wave that is reflected from a defect closer to the applied load is smaller, and the amplitude of the wave is higher due to the dissipation added to the model. Details of the reflected transverse waves for different damage locations are shown in Fig. 7.28b. The influence of the notch length on the axial and transverse velocities is shown in Figs. 7.29 and 7.30, which illustrate how the arrival time of both reflected waves does not change with the damage axial length, and how the amplitude of the waves are instead increasing proportionally with the notch length. A second problem considers a clamped-free beam with a notch at $x_d = 3L/4$ and a

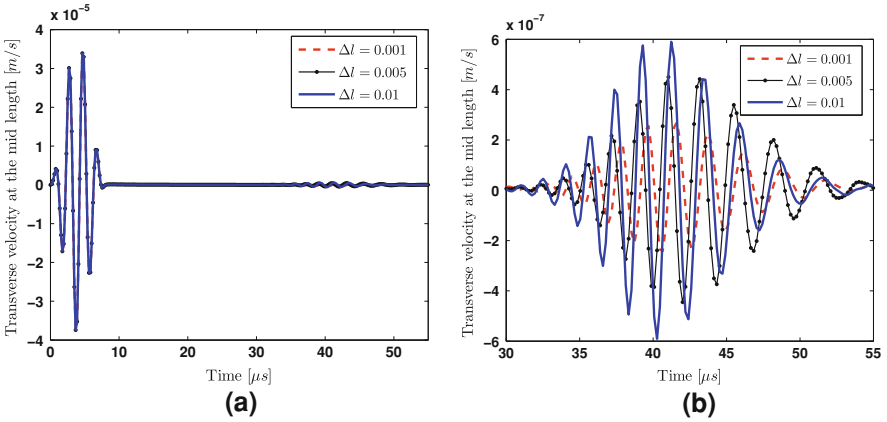

Fig. 7.30 **a** transverse velocity at the middle point of the beam for three values of damage length, $\Delta l = 0.001, 0.005, 0.01$ m; **b** details of reflections caused by damage

horizontal load at $x_f = L$. The beam is modeled using two spectral elements with a total of nine d.o.fs. (Fig. 7.18a). The considered applied load is again a modulated sine burst at 500 kHz. Figure 7.31 presents 3D surfaces of the displacements (as functions of time and longitudinal coordinate) whereas Fig. 7.32 presents snapshots of displacements variations along the beam length at three instants of time. In both cases the axial displacement is plotted in the subplot (a) and the transversal displacement is plotted in subplot (b). A longitudinal load causes a longitudinal wave to propagate from the tip of the beam. When the wave reaches the notch (in this case at $x = 3L/4$), it is partially reflected and partially converted into a transversal wave originating at the notch location.

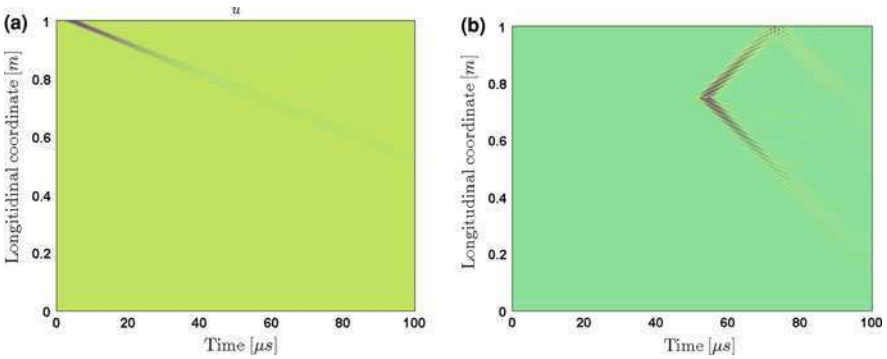

Fig. 7.31 Displacements as function of time and longitudinal coordinate **a** longitudinal displacement; **b** transverse displacement. The length of the notch is $\Delta l = 0.001$ m

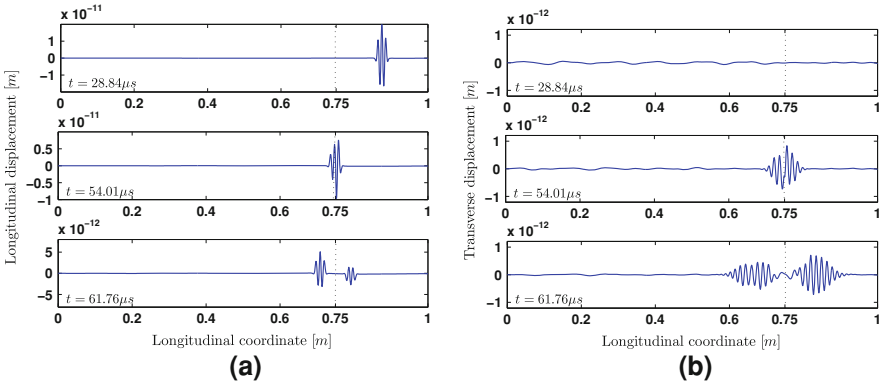

Fig. 7.32 Displacements as function of longitudinal coordinate at the same moments **a** longitudinal displacement; **b** transverse displacement

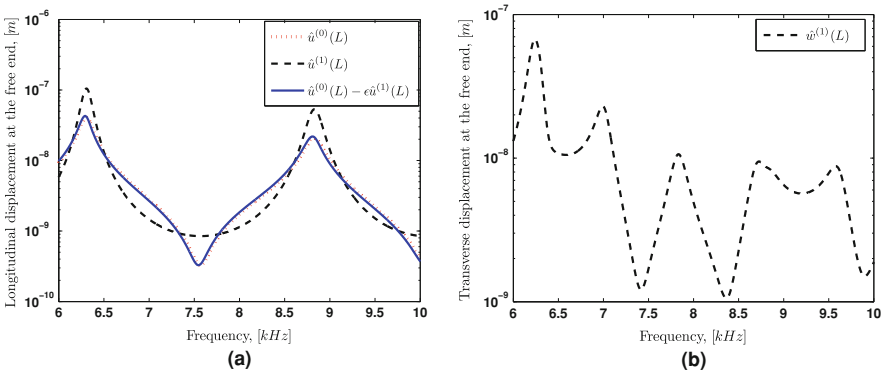

Fig. 7.33 Displacements at the tip of a cantilever beam in the frequency domain. Case I: horizontal load. **a** Longitudinal displacement; **b** transverse displacement

7.5.4 Frequency Domain Results

The FSFEM can be conveniently used to obtain results in the frequency domain, upon transformation of the applied load and direct solution for the nodal amplitudes at each frequency. Frequency sweeps of unit amplitude loads are considered to obtain Frequency Response Function (FRF) predictions. Examples of this kind of analyses are presented in this section.

The frequency response of a clamped-free beam with unit harmonic tip load is evaluated in the presence of a notch at $x_d = 3L/4$, of length $\Delta l = 1 \times 10^{-2}$ m and depth $h_d = h/10$. Figure 7.33 shows FRFs corresponding to a longitudinal load of frequency varying in the 5–10 kHz range. Both longitudinal and transverse response components resulting from a longitudinal load are presented. Specifically, Fig. 7.33a

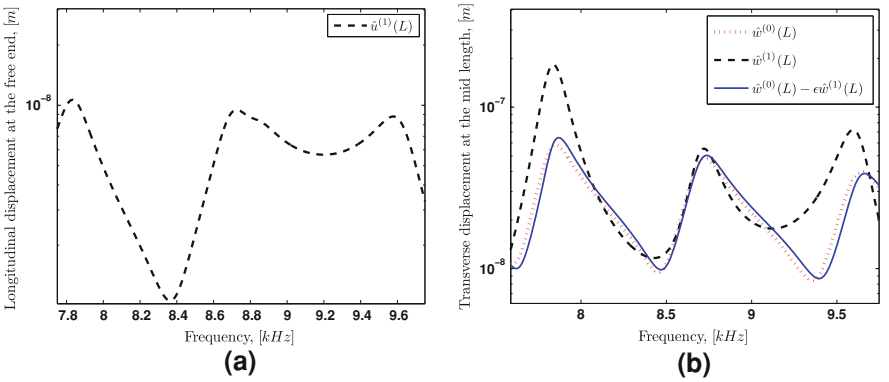

Fig. 7.34 Displacements at the tip of a cantilever beam in the frequency domain. Case II: vertical load. **a** Longitudinal displacement; **b** transverse displacement

compares the responses for damaged and undamaged beams and shows how the small localized notch produces small changes in the frequency domain, and particularly how the location of the resonant peaks is shifted of a negligible amount. This confirms the notion that the considered type of damage does not significantly modify the natural frequencies of the structure, even in a high frequency range as considered here. The changes in natural frequencies due to notch damage in beams and plates are quantified respectively in [17, 21], where it is essentially shown how perturbations $\mathcal{O}(\varepsilon)$ in the mode shapes, correspond to $\mathcal{O}(\varepsilon^2)$ change in the natural frequencies. The transverse response in Fig. 7.33b again demonstrates the intermodal coupling between longitudinal and transverse motion. The peaks in the plot correspond both to the bending frequencies of the beam and to the longitudinal ones, the latter being excited by the considered axial excitation. The results for a transverse tip load shown in Fig. 7.34 lead to similar conclusions and confirm the observations made in commenting the previous figure.

References

1. Atluri SN (1986) Computational methods in the mechanics of fracture. North Holland, Amsterdam
2. Christides S, Barr ADS (1984) One-dimensional theory of cracked Euler–Bernoulli beams. Int J Mech Sci 26(11-12):639–648
3. Doebling SW, Farrar C, Prime MB, Daniel WS (1996) Damage identification and health monitoring of structural and mechanical systems from changes in their vibration characteristics: a literature review, LA-13070-MS, May 1996
4. Doyle JF (1997) Wave propagation in structures. Springer, New York
5. Gudmundson P (1984) The dynamic behavior of slender structures with cross-sectional cracks. J Mech Phys Solids 31: 329–345

6. Haisty BS, Springer WT (1988) A general beam element For use in damage assessment of complex structures. ASME J Vib Acoust Stress Reliab Des 110:356–359
7. Hellan K (1984) Introduction To fracture mechanics. McGraw-Hill, New York
8. Hu N et al (2001) Damage assessment of structures using modal test data. Int J Solids Struct 38:3111–3126
9. Jones DS (1982) The theory of generalized functions. Cambridge University Press, Cambridge
10. Kim JT, Stubbs N (2001) Crack detection in beam type structures using frequency data. J Sound Vib 259(1):146–160
11. Krawczuk M (2002) A rectangular plate finite element with an open crack. Comput. Struct
12. Krawczuk M (2005) Application of spectral beam finite element with a crack and iterative search technique for damage detection. Finite Elem Anal Des 38(6):537–548
13. Krawczuk M, Ostachowicz W (2002) Identification of delamination in composite beams by genetic algorithm. Sci Eng Compos Mater 10(2):147–155
14. Krawczuk M, Ostachowicz W (1995) Modelling and vibration analysis of a cantilever composite beam with a transverse open crack. J Sound Vib 183(1):69–89
15. Krawczuk M, Palacz M, Ostachowicz W (2004) Wave propagation in plate structures for crack detection. Finite Elem Anal Des 40(9–10): 991–1004
16. Leissa A (1993) Vibration of plates Acoustical Society of America, Washington
17. Lestari W (2001) Damage of composite structures: detection technique, Dynamic response and residual strength, Ph.D. Thesis, Georgia Institute of Technology, July 2001
18. Luo H, Hanagud S (1997) An integral equation for changes in the structural characteristics of damaged structures. International Journal of Solids and Structures 34(35-36): 4557–4579
19. Ostachowicz W, Krawczuk M (1990) Analysis of the effect of cracks on the natural frequencies of a cantilever beam. J Sound Vib 138:115–134
20. Qian GL, Gu SN, Jiang JS (1991) The dynamic behavior AN crack detection of a beam with a crack. J Sound Vib 138:233–243
21. Sharma VK, Ruzzene M, Hanagud S (2006) Perturbation methods for the analysis of the dynamic behavior of damaged plates. Inter J Solids Struct 43:4648–4672
22. Shen MH, Pierre C (1990) Natural modes of Euler–Bernoulli beams with symmetric cracks. J Sound Vib 138: 115–134
23. Staszewski WJ, Boller C, Tomlinson G (2004) Health monitoring of aerospace structures smart sensors and signal processing. Wiley, Chichester

Chapter 8
Bridging Scales Analysis of Wave Propagation in Heterogeneous Structures with Imperfections

8.1 Overview

The goal of NDE of SHM techniques is to detect the presence of localized imperfections in the structure. These include, among others, porous regions, voids, sharp discontinuities in material properties of the medium, stiff or soft inclusions, cracks and plastic hinges. Localized damages like cracks or stiff inclusions are of particular interest since they represent points of potential structural weakness. Wave-based inspection methods rely on the common knowledge that waves are reflected by changes in the impedance of the medium. In some cases, the magnitude of the reflective wave can be related to the intensity of the defect. The comparison between reflective and incident waves provides information about location and size of the defect. Inspections are often supported by numerical simulations which can serve two purposes. First, the simulated response of damaged components can be used to test damage detection algorithms under known damage configurations and in the absence of experimental noise. Second, simulations can be employed in support of the interpretation of experimental data, to identify time of arrivals, modes of wave propagation and complex reflection patterns within the domain under consideration.

The main problem that arises during the simulation of wave propagation phenomena is the high computational cost required by the numerical analysis, especially when a very detailed mesh is required to capture the perturbations induced in the wavefield by the presence of a localized defect [7]. The size of the mesh is in fact dictated by the minimum number of elements required to properly model the defect. In a finite element (FE) scenario, the most intuitive way to reduce the computational cost would be to refine the mesh only inside specific regions of the domain where the presence of a discontinuity is simulated. The resulting non-homogeneous mesh, however, will most likely cause spurious numerical phenomena [5, 7], in the form of waves reflected by the boundaries between the meshes. This aspect was also discussed in Chap. 4. These waves have no physical

S. Gopalakrishnan et al., *Computational Techniques for Structural Health Monitoring*, Springer Series in Reliability Engineering, DOI: 10.1007/978-0-85729-284-1_8,

counterpart and potentially interfere with true reflections caused by actual imperfections eventually undermining the validity of the simulations (Fig. 8.1). The occurrence of spurious terms can be partially eliminated through proper transitions of mesh size across the computation domain, which however may produce very large models whose solution requires a very high computational cost. Such cost may be also increase by the requirement that time step and mesh size need to be related and satisfy conditions which ensure the accuracy of the solution. This requires the mesh to be very refined for problems involving high frequency waves, or may impose small time steps for cases where the geometry requires very small elements to proper capture important geometrical features.

One way to address the problem of spurious waves consists in the application of the Bridging Scales Method (BSM) [2, 7, 8], which allows a coarse description of the global behavior of the structure while simultaneously obtaining local information regarding a small region of the domain. Interaction forces at the interfaces between the scales are added in order to bridge the two scales and therefore minimize spurious effects [7]. This method was originally designed for molecular dynamics (MD) applications to address the problem of coupling an atomistic analysis with a continuum representation at the macroscopic level [8], and for problems that are traditionally resistant to theoretical solutions, like fracture and plasticity. However, applications have been presented for the case of two continuum representations projected onto two meshes with different levels of detail [2, 4].

This chapter illustrates the application of the BSM to wave propagation problems in 1D and 2D structures. In addition, the BSM can be applied to the problem of waves in periodic structures in conjunction with an homogenization technique [6]. While a detailed simulation of the actual periodic assembly takes care of the problem inside the fine-scale region, the coarse scale solution is simply sought by solving the homogenized equations of motion for the whole structure with a coarse mesh. One of the examples in this chapter is to explore this kind of application and the limits of the compatibility between the two models.

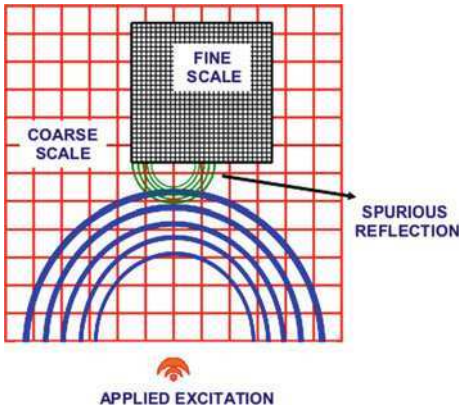

Fig. 8.1 Schematic for the generation of spurious reflective waves at the scale interface

Documented downsides of the BSM consist in the need to carry out a convolution operation at each integration step, and in the two-scale time marching scheme that needs to be implemented to carry out solutions at both coarse and fine scale. The need for a convolution operation in the time domain is significantly simplified through the formulation of the method in the frequency domain, which transforms the convolution into a simple product, thus significantly simplifying the implementation of the technique. In addition, the frequency domain formulation does not need to satisfy the mesh size requirements associated with the time marching scheme, which has the potential to reduce the number of elements needed for proper prediction of the considered phenomena. In the time domain formulation, the need for a two-scale integration scheme can be partially mitigated through a procedure that monitors the total energy in the fine scale region, and therefore identifies when relevant motion is occurring at the fine scales. This reduces the computational time by limiting the fine scale solution to interval of times during which the wave is actually transiting in the fine-scale region. Both of these techniques are presented in this chapter, which first introduces the general concept behind BSM, and subsequently presents its time domain and frequency domain formulations. Examples on 1D and 2D waveguides illustrate the capabilities of the considered formulations.

8.2 Theoretical Background

8.2.1 Coarse and Fine Scale Discretization and Bridging Matrices

Let us consider an elastic domain discretized by both a coarse-scale FE and a fine-scale FE mesh. The underlying assumption is that the resolution of the fine mesh is high enough to capture the localized phenomena under investigation and that of the coarse mesh is such that the computation over the whole domain is possible at a reasonable cost.

For a given discretization of a linear elastic domain, the present multiscale method is based on the decomposition of the displacement field $\boldsymbol{u}$ into coarse and fine scales:

$$\boldsymbol{u} = \bar{\boldsymbol{u}} + \boldsymbol{u}' \tag{8.1}$$

where $\bar{\boldsymbol{u}}$ represents the displacement of the coarse-scale region and $\boldsymbol{u}'$ is a fine-scale displacement whose projection onto the coarse-scale space is zero. In this chapter, the coarse and fine scales respectively include n_c and n_f degrees of freedom as illustrated in Fig. 8.2.

The coarse-scale displacement can be represented in matrix form as:

$$\bar{\boldsymbol{u}} = \mathcal{N}\boldsymbol{d} \tag{8.2}$$

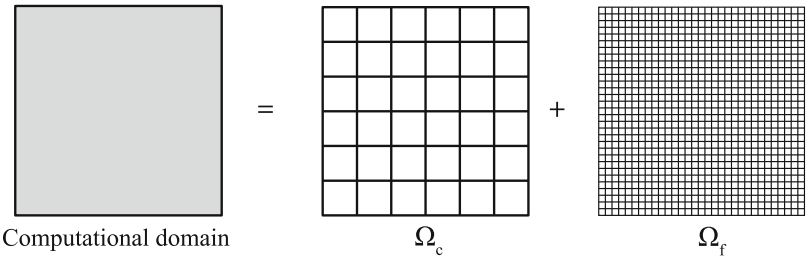

Fig. 8.2 Scale decomposition of the computational domain

where $\boldsymbol{d}$ is the vector of nodal degrees of freedom and $\mathcal{N}$ is an operator of size $n_f \times n_c$ that interpolates the coarse-scale solution on the nodal points of the fine-scale using a proper set of shape functions. In other words, $\bar{\boldsymbol{u}}_i$ represents the coarse-scale interpolation of the nodal values $\boldsymbol{d}_j$ at the fine-scale nodal location $\boldsymbol{x}_i$ through the shape function matrix $\mathcal{N}_j(\boldsymbol{x}_i)$:

$$\bar{\boldsymbol{u}}_i = \sum_{j=1}^{n_c} \mathcal{N}_j(\boldsymbol{x}_i) \boldsymbol{I}_{n_D} \boldsymbol{d}_j \tag{8.3}$$

where $\boldsymbol{I}_{n_D}$ is the identity matrix of size n_D, with n_D denoting the number of degrees of freedom per node. The fine-scale $\boldsymbol{u}'$ defines the part of the total displacement field that cannot be represented by the coarse-scale and that can be derived from the fine solution $\boldsymbol{q}$ as:

$$\boldsymbol{u}' = \mathcal{Q}\boldsymbol{q} \tag{8.4}$$

where $\mathcal{Q}$ is a square operator of size $n_f \times n_f$ whose purpose is to subtract the information shared between the scales. A detailed derivation of the $\mathcal{N}$ and $\mathcal{Q}$ matrices can be found in [2].

8.2.2 Multiscale Lagrangian

The dynamic governing equations of the system are obtained using Lagrange's equations, and the expression of the potential and kinetic energies of the fine-scale discretization:

$$\begin{aligned} V &= \frac{1}{2}\boldsymbol{u}^T \boldsymbol{K}\boldsymbol{u}, \\ T &= \frac{1}{2}\dot{\boldsymbol{u}}^T \boldsymbol{M}\dot{\boldsymbol{u}} \end{aligned} \tag{8.5}$$

where $\boldsymbol{M}$ and $\boldsymbol{K}$ are the lumped mass and stiffness matrices of the fine-scale discretization and can be derived with standard discretization procedures.

The Lagrangian of the system, defined as $\mathscr{L} = T - V$, is used in the general form of Lagrange's equations that for a conservative system subjected to the generalized force vector $\boldsymbol{F}$ can be written as:

$$\frac{d}{dt}\left(\frac{\partial \mathscr{L}}{\partial \dot{\boldsymbol{u}}}\right) - \frac{\partial \mathscr{L}}{\partial \boldsymbol{u}} = \boldsymbol{F} \tag{8.6}$$

Substituting Eq. 8.1 into Eq. 8.5 and imposing Eq. 8.6 gives:

$$\begin{aligned} \boldsymbol{M}\ddot{\boldsymbol{q}} + \boldsymbol{K}(\mathcal{N}\boldsymbol{d} + \mathcal{Q}\boldsymbol{q}) &= \boldsymbol{F} \\ \boldsymbol{M}_c\ddot{\boldsymbol{q}} + \boldsymbol{K}_c\boldsymbol{d} + \mathcal{N}^T\boldsymbol{K}\mathcal{Q}\boldsymbol{q} &= \boldsymbol{F}_c \end{aligned} \tag{8.7}$$

where $\boldsymbol{M}_c, \boldsymbol{K}_c$ and $\boldsymbol{F}_c$ are the consistent mass matrix, stiffness matrix and vector of external forces projected on the coarse grid:

$$\begin{aligned} \boldsymbol{M}_c &= \mathcal{N}^T\boldsymbol{M}\mathcal{N} \\ \boldsymbol{K}_c &= \mathcal{N}^T\boldsymbol{K}\mathcal{N} \\ \boldsymbol{F}_c &= \mathcal{N}^T\boldsymbol{F} \end{aligned} \tag{8.8}$$

Equation 8.7 show how the two governing equations are coupled by the presence of the interpolation and projection operators $\mathcal{N}$ and $\mathcal{Q}$.

8.2.3 Reduction of the Degrees of Freedom

It would be in general interest to explicitly solve for the fine-scale solution only in a small region of the domain, while maintaining a coarse-scale representation in the remaining part of the structure.

The redundant fine-scale degrees of freedom are eliminated by partitioning the fine-scale domain Ω_f into two supplementary regions as illustrated in Fig. 8.3. Specifically, Ω_f^a where the fine-scale solution is computed and coexists with the coarse solution, while Ω_f^b is the sub domain where only the coarse-scale solution is calculated. Accordingly, the fine-scale degrees of freedom $\boldsymbol{q}$ are partitioned as follows:

$$\boldsymbol{q} = [\boldsymbol{q}_a \; \boldsymbol{q}_b]^T \tag{8.9}$$

where $\boldsymbol{q}_a$ are the n_f^a fine-scale degrees of freedom in region Ω_f^a that are to be computed explicitly, and $\boldsymbol{q}^b$, of size n_f^b, the fine-scale degrees of freedom in region Ω_f^b that must be rejected. In this chapter it is assumed that the number of degrees of freedom in the region of interest is much smaller than the degrees of freedom to be condensed out, i.e. $n_f^a \ll n_f^b$, and with $n_f^a + n_f^b = n_f$. The matrices $\boldsymbol{M}$ and $\boldsymbol{K}$ can all be partitioned between the two regions as was done for $\boldsymbol{q}$:

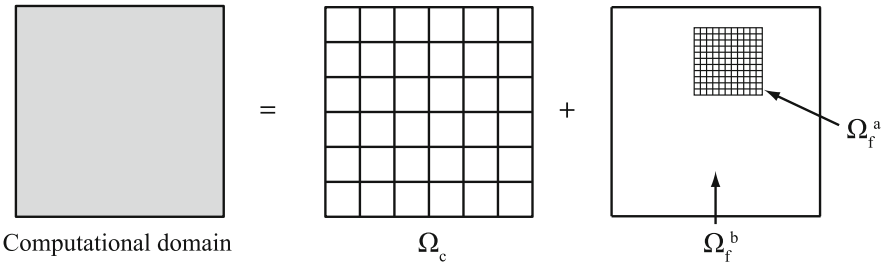

Fig. 8.3 Reduction of the redundant fine-scale degrees of freedom

$$\boldsymbol{M} = \begin{bmatrix} \boldsymbol{M}_{aa} & 0 \\ 0 & \boldsymbol{M}_{bb} \end{bmatrix} \tag{8.10}$$

$$\boldsymbol{K} = \begin{bmatrix} \boldsymbol{K}_{aa} & \boldsymbol{K}_{ab} \\ \boldsymbol{K}_{ba} & \boldsymbol{K}_{bb} \end{bmatrix} \tag{8.11}$$

so that the fine-scale equations of motion can be written as:

$$\boldsymbol{M}_{aa}\ddot{\boldsymbol{q}}_a + \boldsymbol{K}_{aa}\boldsymbol{q}_a + \boldsymbol{K}_{ab}\mathcal{Q}_b\boldsymbol{q}_b = \boldsymbol{F}_a - \boldsymbol{K}_{ab}\mathcal{N}_b\boldsymbol{d} \tag{8.12}$$

$$\boldsymbol{M}_{bb}\ddot{\boldsymbol{q}}_b + \boldsymbol{K}_{bb}\boldsymbol{q}_b + \boldsymbol{K}_{ba}\mathcal{Q}_a\boldsymbol{q}_a = \boldsymbol{F}_b - \boldsymbol{K}_{ba}\mathcal{N}_a\boldsymbol{d} \tag{8.13}$$

Note that the matrix $\boldsymbol{K}_{ab}$ is of size $n_f^a \times n_f^b$ and is nonzero only on the boundary between the two regions, where the two sets of degrees of freedom are directly coupled.

8.2.4 Time Domain Formulation

The fully explicit equations of motion for the fine-scale are expressed as [2]:

$$\boldsymbol{M}_{aa}\ddot{\boldsymbol{q}}_a + \boldsymbol{K}_{aa}\boldsymbol{q}_a = \boldsymbol{F}_a - \boldsymbol{K}_{ab}\mathcal{N}_b\boldsymbol{d} \sum_{m'=m-\frac{M}{2}+1}^{m+\frac{M}{2}} \int_0^t \boldsymbol{\theta}_{m-m'}(t-\tau)\mathbf{u}'_{0,m'}(\tau)d\tau \tag{8.14}$$

Equation 8.14 involves the evaluation at each time step of a convolution integral of the quantity $\boldsymbol{\theta}$ known as the *time kernel history function*. Details about the derivation of kernel functions for various assemblies are discussed thoroughly in [2, 3]. For reference, in the case of a two-dimensional domain with a scale interface placed along a vertical straight line, the kernel history of a node located on the interface at a vertical location m is calculated as:

$$\boldsymbol{\theta}_m(t) = \mathscr{F}^{-1}_{q\longrightarrow m}\mathscr{L}^{-1}\left[\left[\mathscr{F}^{-1}_{p\longrightarrow n}\hat{\mathbf{G}}(p,q,s)\right]_{n=1}\left[\mathscr{F}^{-1}_{p\longrightarrow n}\hat{\mathbf{G}}(p,q,s)\right]^{-1}_{n=0}\right] \tag{8.15}$$

where $n = 0$ and $n = 1$ represent the horizontal locations in the mesh of points sitting respectively on the interface and immediately to its right. Also, the operator $\mathscr{F}^{-1}_{p\longrightarrow n}$ defines the inverse Discrete Fourier Transform in space, with p denoting the discrete variable in the Fourier domain, while n defines the spatial location of the considered boundary cell. In addition, the operator $\mathscr{L}^{-1}$ denotes the inverse Laplace Transform. The quantity $\hat{\mathbf{G}}(p,q,s)$ in Eq. 8.16 is defined as:

$$\hat{\mathbf{G}}(p,q,s) = \left[s^2\mathbf{I} + \mathbf{m}_{\mathbf{A}}^{-1}\hat{\mathbf{K}}^e(p,q)\right]^{-1} \tag{8.16}$$

where s is the Laplace variable and $\mathbf{m}_{\mathbf{A}}, \hat{\mathbf{K}}^e(p,q)$ are respectively the reduced mass matrix and reduce stiffness matrix, expressed in the Fourier domain, of a fine-scale finite element located immediately outside the fine-scale window and sharing one side with the interface line. As pointed out in [2, 8], one of the challenges in the evaluation of Eq. 8.15 consists in the calculation of the inverse Laplace transform, which in most cases needs to be carried out numerically. For the applications presented in what follows, the method of Weeks [9] is implemented by means of the algorithm suggested by Weideman [10].

8.2.5 Frequency Domain Formulation

The complexity associated with the evaluation of the convolution term in Eq. 8.14 can be avoided through the expression of the method in the frequency domain. This alternative approach has also the advantage of limiting requirements on the mesh, whose refinement does not need to be dictated by conditions imposed by the time step size. Some of the drawbacks to be considered however include the computational effort required at each frequency step, along with the restrictions to linear problems. The ability to formulate the BSM in two domains however offers the opportunity to select the approach to be considered on the basis of the specific problem to be analyzed.

For a frequency domain formulation of the BSM, the fine-scale and the coarse-scale governing equations are transformed in the Fourier domain so that differential and integral operators are transformed into algebraic operators. The coarse and fine scale solutions are then found at each frequency step as the solution of a non symmetric complex linear system. The final solution in the time domain is then recovered by means of the inverse Fast Fourier Transform (IFFT).

Equation 8.13 can be used to eliminate the degrees of freedom $\boldsymbol{q}_b$ by solving for them explicitly and then substituting the result into Eq. 8.12. This can be easily accomplished by means of the Fourier transform:

$$\mathscr{F}[f(t)] \equiv F(\omega) = \int_0^\infty e^{-j\omega t} f(t)\, dt \tag{8.17}$$

This allows to rewrite all the differential operators in the equations of motion given by Eqs. 8.12 and 8.13 in terms of algebraic operators and thus leads to a simple expression for the condensed fine-scale degrees of freedom:

$$\boldsymbol{q}_b(\omega) = \left[-\omega^2 \boldsymbol{M}_{bb} + \boldsymbol{K}_{bb}\right]^{-1} (\boldsymbol{F}_b - \boldsymbol{K}_{ba}\mathcal{N}_a \boldsymbol{d}(\omega) - \boldsymbol{K}_{ba}\boldsymbol{Q}_a \boldsymbol{q}_a(\omega)) \tag{8.18}$$

In general, an equation of motion for $\boldsymbol{q}_a$ is found by using the inverse Fourier transform on Eq. 8.18 and substituting the result back into Eq. 8.12 [1, 8]. This approach involves a time history kernel matrix that captures the effects of the removed degrees of freedom and for very simple cases can be derived analytically. However, the evaluation in time of this term is time consuming and for many configurations of practical interest no close form solution exists. An alternative is to conduct the entire analysis in the frequency domain and to post-process the solution to recover the displacements as functions of time. Substituting Eq. 8.18 into Eqs. 8.12 and 8.13 gives the following coupled system of equations in terms of the coarse-scale degrees of freedom $\boldsymbol{d}$ and fine-scale degrees of freedom $\boldsymbol{q}_a$:

$$\left[-\omega^2 \boldsymbol{M}_{aa} + \boldsymbol{K}_{aa} + \boldsymbol{K}_{eq}(\omega)\right]\boldsymbol{q}_a(\omega) + \boldsymbol{K}_{qd}(\omega)\boldsymbol{d}(\omega) = \boldsymbol{F}_{eq}(\omega) \tag{8.19}$$

$$\left[-\omega^2 \boldsymbol{M}_c + \boldsymbol{K}_c\right]\boldsymbol{d}(\omega) + \mathcal{N}^T \boldsymbol{K}\boldsymbol{Q}_a \boldsymbol{q}_a(\omega) = \boldsymbol{F}_c(\omega) \tag{8.20}$$

where the following matrices are introduced to simplify the notation:

$$\boldsymbol{K}_{eq}(\omega) = -\boldsymbol{K}_{ab}\mathcal{Q}_b \left[-\omega^2 \boldsymbol{M}_{bb} + \boldsymbol{K}_{bb}\right]^{-1} \boldsymbol{K}_{ba}\mathcal{Q}_a \tag{8.21}$$

$$\boldsymbol{K}_{qd}(\omega) = \boldsymbol{K}_{ab}\mathcal{N}_b - \boldsymbol{K}_{ab}\mathcal{Q}_b \left[-\omega^2 \boldsymbol{M}_{bb} + \boldsymbol{K}_{bb}\right]^{-1} \boldsymbol{K}_{ba}\mathcal{N}_a \tag{8.22}$$

$$\boldsymbol{F}_{eq}(\omega) = \boldsymbol{F}_a(\omega) - \left[-\omega^2 \boldsymbol{M}_{bb} + \boldsymbol{K}_{bb}\right]^{-1} \boldsymbol{F}_b(\omega) \tag{8.23}$$

Note that the matrices $\boldsymbol{K}_{ab}$ and $\boldsymbol{K}_{ba}$ are characterized by non-zero elements only on the rows corresponding to the nodes belonging to the boundary between regions Ω_f^a and Ω_f^b. This significantly speeds up the computation of $\boldsymbol{K}_{eq}, \boldsymbol{K}_{qd}$ and $\boldsymbol{F}_{eq}$ since only the terms of $\left[-\omega^2 \boldsymbol{M}_{bb} + \boldsymbol{K}_{bb}\right]^{-1}$ adjacent to the interface are actually inverted and contribute to Eq. 8.19. Equations 8.19 and 8.20 can also be effectively written in matrix form as:

$$\begin{bmatrix} -\omega^2 \boldsymbol{M}_c + \boldsymbol{K}_c & \mathcal{N}^T \boldsymbol{K}\boldsymbol{Q}_a \\ \boldsymbol{K}_{qd} & -\omega^2 \boldsymbol{M}_{aa} + \boldsymbol{K}_{aa} + \boldsymbol{K}_{eq}(\omega) \end{bmatrix} \begin{bmatrix} \boldsymbol{d} \\ \boldsymbol{q}_a \end{bmatrix} = \begin{bmatrix} \boldsymbol{F}_{eq} \\ \boldsymbol{F}_c \end{bmatrix} \tag{8.24}$$

The linear system of Eq. 8.24 is solved at each frequency step for the coarse-scale solution in the entire domain and for the fine-scale only in the region Ω_f^a of

interest. Note that this formulation is completely general in the sense that, for a given discretization, it can be applied to any structural element of any spatial dimension without requiring *ad-hoc* expressions for the dynamic coupling conditions.

8.3 Results for Time-Domain Bridging

8.3.1 Application to a One-Dimensional Rod

The first example considers the propagation of axial waves through the one-dimensional (1D) system of Fig. 8.4. The system is a rod whose inertial and stiffness properties are represented by concentrated parameters k and m of an equivalent spring-mass model. For simplicity, free–free boundary conditions are imposed at the ends of the structure. Two meshes are considered: the coarse-scale mesh is defined over the entire length of the rod, while the fine-scale mesh is limited over the central portion of the rod for $x \in [-L_f, L_f]$. The two meshes are selected such that

$$\frac{N_f}{N_c} = 10 \tag{8.25}$$

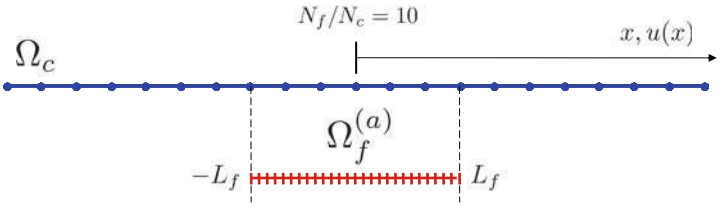

Fig. 8.4 Schematic for one-dimensional case

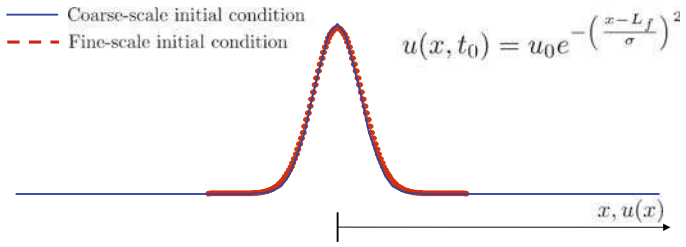

Fig. 8.5 Initial condition expressed in the two scales

where N_c and N_f are the number of coarse-scale elements and fine-scale elements in the whole structure domain, respectively. An initial disturbance is applied in the form of a Gaussian distribution of axial displacement centered at $x = 0$ (see Fig. 8.5):

$$u(x, t = 0) = u_0 e^{-\left(\frac{x-L_f}{\sigma}\right)^2} \tag{8.26}$$

where u_0 is the amplitude of the imposed displacement and σ is the standard deviation of the Gaussian distribution. According to classical wave propagation theory, the disturbance is expected to travel towards the ends of the structure, be reflected at the free ends and travel back towards the source without altering its shape. In this case, the time kernel history function θ can be obtained analytically [8] as:

$$\hat{G}(\xi, s) = \frac{1}{s^2 + \frac{2k}{m}(1 - \cos\xi)} \tag{8.27}$$

where Eq. 8.27 corresponds to Eq. 8.16 for a one-dimensional domain. The time history kernel function for the system is then found as:

$$\theta(t) = \mathcal{L}^{-1}\left[\frac{\tilde{G}_1(s)}{\tilde{G}_0(s)}\right] = \frac{2}{t} J_2(2\omega_n t) \tag{8.28}$$

where J_2 is the second-order Bessel function and

$$\omega_n = \sqrt{\frac{k}{m}} \tag{8.29}$$

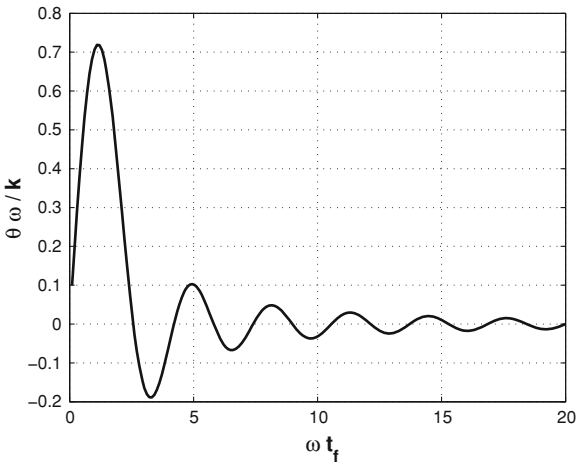

Fig. 8.6 Time history kernel versus normalized fine-scale time

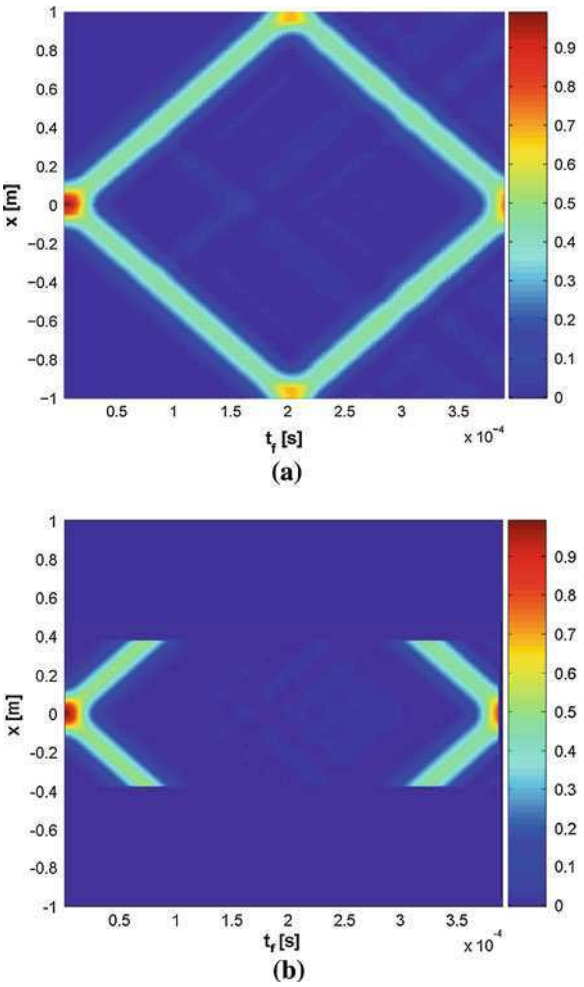

Fig. 8.7 Axial wave propagation in a rod. **a** Coarse-scale simulation. **b** Fine-scale simulation

The kernel history for this system features a transient phase during which it oscillates about the 0 value and its amplitude decays with time. After about $5 \div 10$ time units, the kernel is almost completely damped out [8] (see Fig. 8.6).

The simulation time corresponds to the wave traveling half the length of the bar twice. A second order accurate Newmark scheme is selected as the time integration scheme. The considered rod is 1 m long and is made of aluminum ($E = 7.1 \times 10^{10}\,\mathrm{N/m^2}, \rho = 2700\,\mathrm{kg/m^3}$). The initial disturbance is selected such that $\sigma = 0.1$ and $L_f = 0.375\,\mathrm{m}$. Figure 8.7a, b show the calculated wavefield versus time and space. The coarse-scale representation of Fig. 8.7a shows the applied disturbance moving towards the external regions of the domain being reflected in a non-dispersive manner, within the accuracy limits of the numerical model. When the wave travels across the interface, no spurious reflections due to

the interface between the two meshes are observed. Figure 8.7b, on the other hand, shows the same wave projected onto the fine-scale mesh in the region of the domain where the fine scale is defined. As expected, no reflected waves are observed at the interface: both the outgoing and the incoming waves travel unperturbed through the interfaces without changes in direction or amplitude. One way to quantify the accuracy of the technique consists in comparing the results with those obtained applying a non-uniform mesh over the entire elastic domain. In such a scenario, the only compatibility between the scales that is enforced is the continuity of displacements between two neighboring elements belonging to different scales at the shared node. The results of both methods must then be compared with a reference solution, for instance the one obtained through a full refined discretization of the whole structure. The total mechanical energy of the fine-scale region E_{T_f} is selected as a metric for the comparison and is calculated based on the following expression:

$$E_{T_f} = \frac{1}{2}\dot{\mathbf{q}}_a^{\,T}\mathbf{M}_A^{aa}\dot{\mathbf{q}}_a + \frac{1}{2}\mathbf{q}_a^T\mathbf{K}_f^{aa}\mathbf{q}_a + \mathbf{f}^{I\,T}\mathbf{q}_a \tag{8.30}$$

where $\mathbf{f}^I$ are the interface forces. In Fig. 8.8, the total mechanical energy normalized by its value at $t = 0 (E_n)$ is plotted against the first half of the fine-scale interval for the mesh layouts. It can be observed that, without a proper bridging of the scales, some spurious energy is left inside the system when the wave propagates through the interface. This residual energy is associated with the spurious reflective waves that are generated at the interface when the proper impedance force is not accounted for in the model. On the contrary, the energy curve for the BSM model closely matches the reference one obtained with a detailed FE analysis.

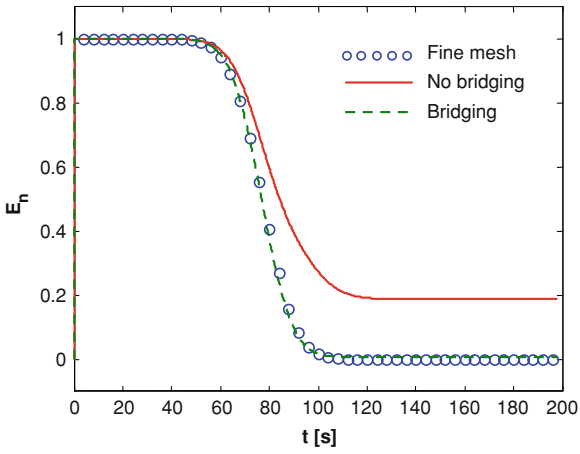

Fig. 8.8 Analysis of the variation of the total mechanical energy of the fine-scale window by means of different models

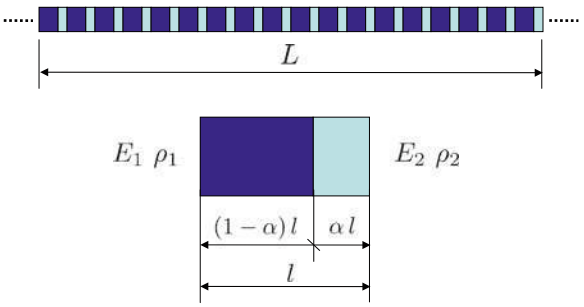

Fig. 8.9 One-dimensional periodic domain

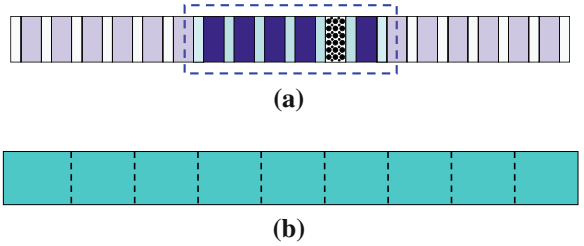

Fig. 8.10 Definition of coarse and fine meshes for a bi-material rod. **a** Fine-scale region. **b** Coarse-scale discretization

8.3.2 Homogenized Bi-material Rod with Imperfections

The structure depicted in Fig. 8.9 consists of a periodic sequence of unit cells with two materials. A first order approximation of the dynamic behavior of the rod can be obtained by considering equivalent properties defined according to the rule of mixtures:

$$\begin{aligned} \rho_H A &= (m_1 + m_2) \\ E_H A &= \frac{k_1 k_2}{k_1 + k_2} \end{aligned} \tag{8.31}$$

where

$$\begin{aligned} k_1 &= \frac{E_1 A}{\alpha}, \quad k_2 = \frac{E_2 A}{(1-\alpha)} \\ m_1 &= \rho_1 A \alpha, \quad m_2 = \rho_2 A (1-\alpha) \end{aligned} \tag{8.32}$$

The definition of the FE meshes used for this problem is shown schematically in Fig. 8.10. A detailed fine-scale mesh is applied to the central region of the rod and accounts for the alternation of material phases over one cell of the structure. The discontinuity is modeled by reducing the Young's modulus associated with one layer in the bi-material pattern ($E_{\text{def}} = 0.025E$), to model a soft inclusion. As shown in the schematic of Fig. 8.10a, the position of the fine-scale window is chosen such that the defect falls within the region where a detailed description of the medium is available. For this example, the discontinuity is introduced at $x = 0.22$. Alongside the detailed

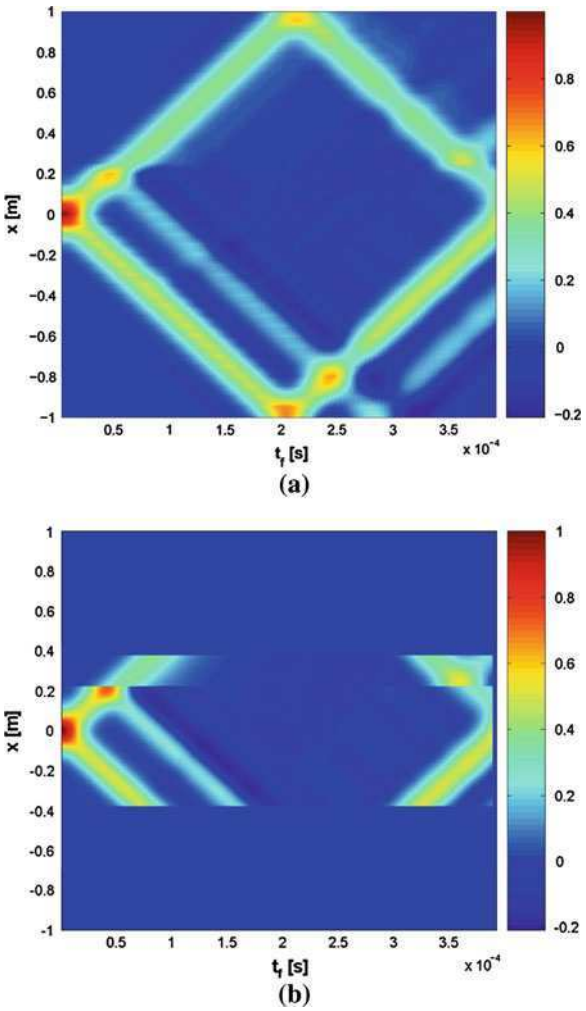

Fig. 8.11 Wave propagation in a homogenized rod with localized defect. **a** Coarse-scale simulation. **b** Fine-scale simulation

problem, an equivalent rod featuring the derived homogeneous properties E_H and ρ_H is discretized with a lower number of bar elements.

Figure 8.11a, b show the propagating wave plotted versus time and space as calculated from the BSM analysis. The presence of the material discontinuity is highlighted by the generation of a reflected wave due to the change in impedance caused by the inclusion. It can be noticed how the imperfection is responsible for a time shift in the incident propagating wave, but does not affect the speed at which the wave propagates past the discontinuity. The same reflection pattern is featured by the returning wave when it hits the imperfection. The absence of spurious reflections at the interfaces between the meshes allows a straightforward interpretation of the wavefield.

Two considerations can be made out of the inspection of Fig. 8.11a, b to underline the effectiveness of the BSM. First, the plots provide two representations of the same propagating wave with different levels of accuracy. The coarse-scale simulation provides a global description of wave motion in the rod while detecting the presence of a defect, but fails to offer a high-resolution representation of the reflection in the neighborhood of the discontinuity. On the contrary, the fine-scale simulation provides an accurate local representation from which details of the reflection generation mechanism can be inferred. Secondly, and most importantly, the size of the damaged area is in most cases (including the example of Fig. 8.11a, b smaller than the size of a single finite element in the coarse scale. Therefore the coarse scale does not model the defect and considers instead the homogeneous properties in Eq. 8.31 applied throughout the rod length.

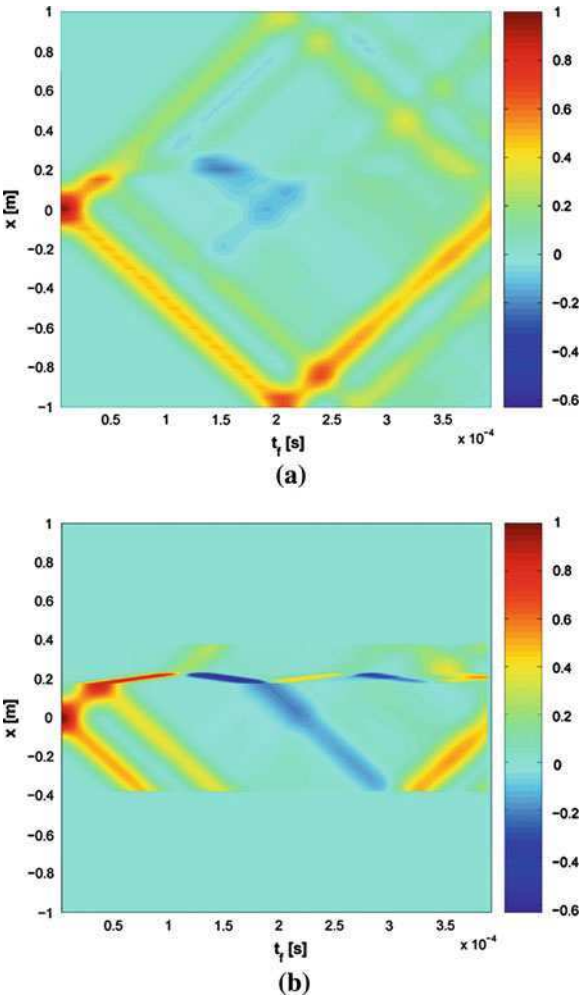

Fig. 8.12 Wave propagation in a homogenized rod with wide damaged region. **a** Coarse-scale simulation. **b** Fine-scale simulation

A slight variation on the previous example is shown in Fig. 8.12a, b. In this case, the region of the rod with reduced stiffness extends over a larger portion of the domain. This configuration results in a more complex wavefield. Like in the previous example, the low-impedance region reflects the incoming wave. In addition, the refracted wave propagates in the damaged region at a lower speed due to the lower stiffness of the material. When the wave leaves the damaged area, a second change in the material impedance occurs, the wave regains its original speed, and another reflection is observed at the damage boundary. A chain of internal reflections can also be observed, which produces a standing wave confined to the discontinuity region. While these additional phenomena are standard features due to the increased complexity of the domain, they allow additional considerations about the method. Unlike the previous example, the succession of consecutive reflections inside the damaged area is here accurately shown only in the fine scale representation, while it is barely visible in the coarse scale. This is due to the fact that the internal reflections span over a small region which is discretized with an insufficient number of coarse elements. A more complicated reflection pattern accentuates the difference in performance between the scales. This example tests the capabilities of the BSM, since it involves many more crossings of the scale interfaces. The inspection of Fig. 8.12b, however, shows that the interface forces are still very effective and no spurious reflections are generated.

It is interesting to note that the fine scale matrices are assembled using the actual material properties of the elements, while the coarse scale considers equivalent or homogenized properties. This results in a certain degree of incompatibility between the two models that is as negligible as the technique used for the homogenization is refined. The mutual transfer of information from one scale to the other generates a contamination of the results that grows with the mismatch between the actual and the homogenized properties of the structure. The impedance mismatch between the materials dominates the validity of the homogenization process and therefore the compatibility between the homogenized model and the original structure. Figure 8.13 shows the results of simulations for bi-material layouts with increasing mismatch between the properties of the two phases. The total mechanical energy of the fine-scale region is again chosen as the metric for the accuracy of the method and compared with the same quantity calculated with a detailed fine-mesh simulation performed over the elastic domain. The results of this comparison are shown in Fig. 8.13. The energy curves feature considerable agreement during the early stages of the simulation, when the fine-scale integration is carried out from a given initial disturbance applied directly to the fine scale. The reconstruction of the wave returning inside the fine-scale window relies instead on values imported from the coarse scale simulation. These values are affected by errors due to the approximation associated with the rule of mixtures approximation, therefore the shortcomings of the homogeneous model used for the coarse scale ultimately affect the refined analysis. As expected, the disagreement between the curves grows with the impedance mismatch.

Let us consider different distributions of the initial applied disturbance $u(x, t = 0)$. The changes are made by controlling the parameter σ in the expression

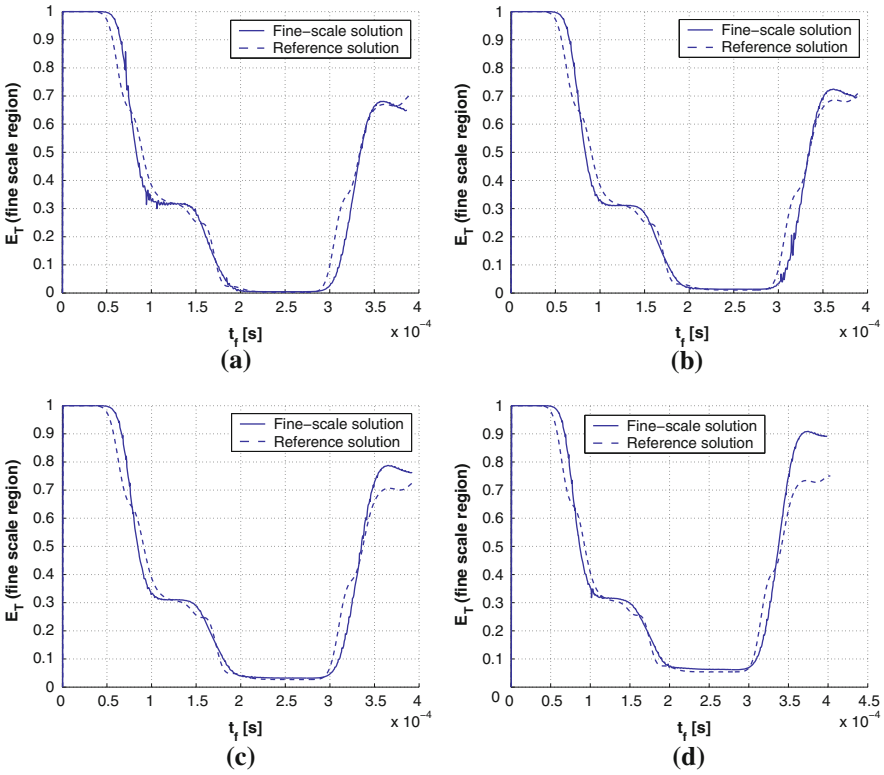

Fig. 8.13 Variation of total mechanical energy for different levels of impedance mismatch: comparison between BSM (*solid line*) and reference solution (*dashed line*). **a** $E_2 = 0.9E_1 - \rho_2 = 0.9\rho_1$. **b** $E_2 = 0.8E_1 - \rho_2 = 0.8\rho_1$. **c** $E_2 = 0.7E_1 - \rho_2 = 0.7\rho_1$. **d** $E_2 = 0.6E_1 - \rho_2 = 0.6\rho_1$

for u that represents the standard deviation of the Gaussian curve. Low values of σ correspond to short wavelength disturbances, as opposed to high values of σ which generate spatially smoother signals. The calculated time histories of the fine-scale energy E_{T_f} are shown in Fig. 8.14 for increasing σ. In the case of high σ, the agreement is good over the whole interval of simulation: the changes occurring because of the internal reflections due to the defects are properly captured and the residual energy level left in the fine scale window at the end of the simulation coincides with the reference value. In contrast, a low σ causes a poor agreement when it comes to the returning wave: for $\sigma = 0.025$, the residual energy is underestimated by almost 80% (Fig. 8.14a. The results of Fig. 8.14 and the comparison with the previous set of results suggest the presence of an incompatibility enhanced by the shape of the excitation. The homogenized model provides in fact a good approximation for the behavior of the bi-material rod only in the low frequency regime. Sharp excitations generate waves whose frequency

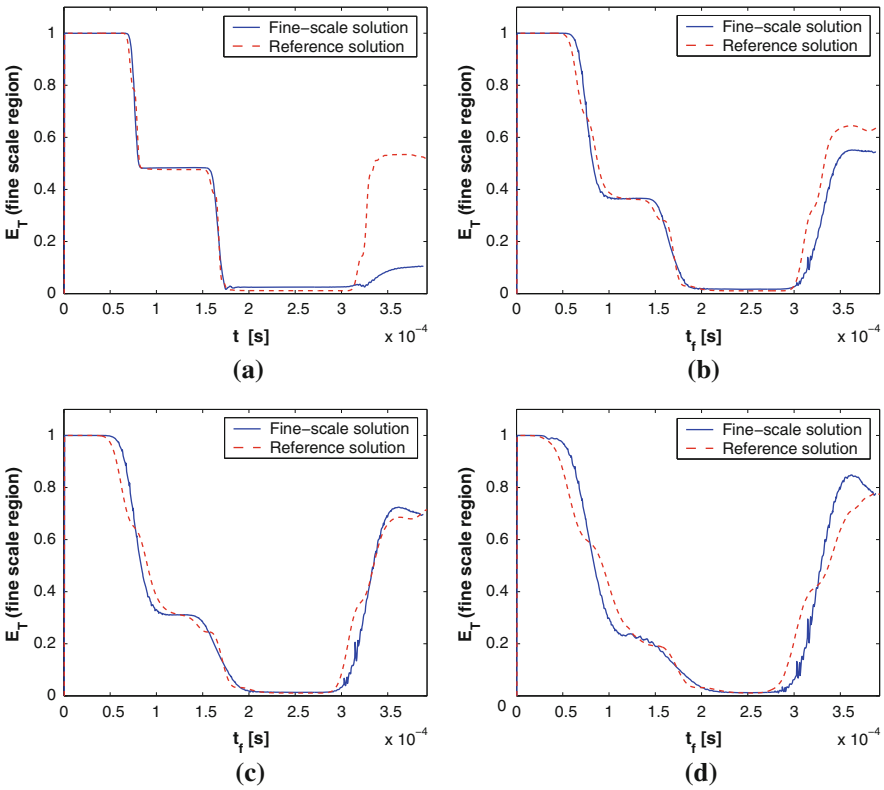

Fig. 8.14 Total mechanical energy for the fine-scale region—BSM method versus full simulation. **a** $\sigma = 0.025$. **b** $\sigma = 0.075$. **c** $\sigma = 0.1$. **d** $\sigma = 0.15$

content is less compatible with the range of applicability of the rule of mixtures. Ultimately sharp excitations induce a shortcoming in the performance of the coarse scale. This is consistent with the trend of Fig. 8.14, but still does not explain why it is the fine scale result to be ultimately so deeply affected by the shortcoming. A possible explanation can be argued by looking at Fig. 8.15 where the calculated wave is shown respectively for the $\sigma = 0.025$ and $\sigma = 0.15$ cases. Figure 8.15a, c show that, when it comes to the incident wave, the fine scale provides an accurate representation of the wavefield for both excitations. However, Fig. 8.15b, d reveal a much better performance of the coarse scale simulation in the $\sigma = 0.15$ scenario, in accordance with the argument made above. For $\sigma = 0.025$, the coarse scale energy deteriorates from the early stages of the integration (Fig. 8.15b), featuring a wavy behavior typical of the dispersive nature of the bi-material rod. Finally, the coarse scale solution eventually contributes to the fine scale simulation of the returning wave. For $\sigma = 0.15$ the fine solution, being based on the good result of the coarse solution, is extremely accurate (Fig. 8.15c),

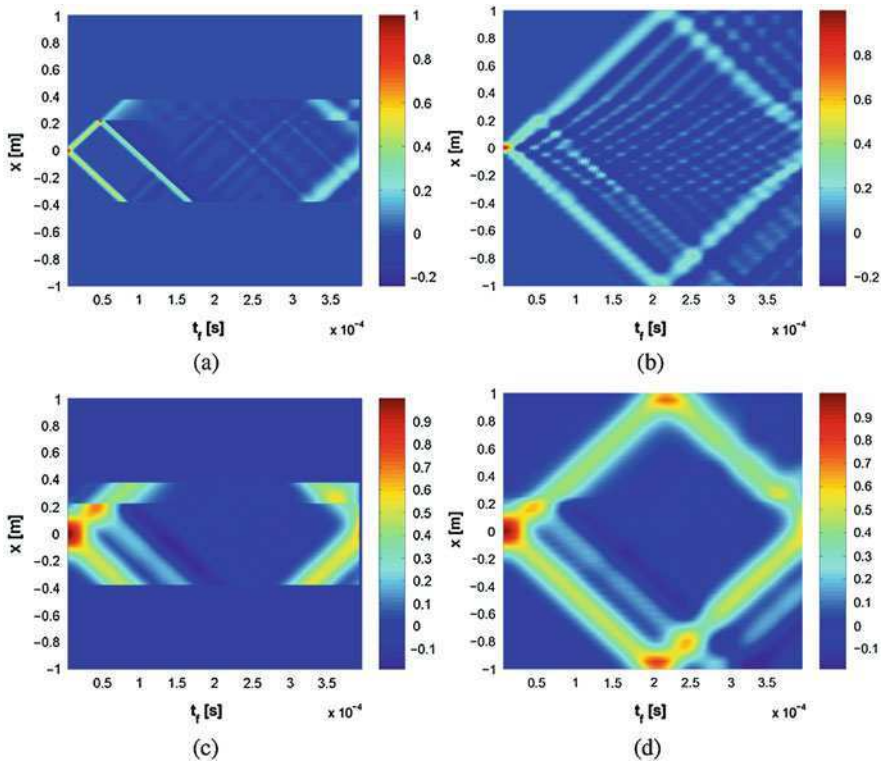

Fig. 8.15 Fine-scale and coarse-scale solutions for different applied excitations. **a** Fine-scale solution $-\sigma = 0.025$. **b** Coarse-scale solution $-\sigma = 0.025$. **c** Fine-scale solution $-\sigma = 0.15$. **d** Coarse-scale solution $-\sigma = 0.15$

while for $\sigma = 0.025$ the incompatibility of the coexisting representations is responsible for the blurry fine scale wave of Fig. 8.15a. All of these effects can also be associated with the interpolation procedure required to project the coarse-scale displacements onto the fine-scale mesh at the coarse-fine scale interface, which is carried out through the shape function matrix **N** introduced above.

8.3.3 Energy-Based Time Integration Scheme

The main motivation for numerical techniques such as the BSM is a reduction in computational cost. The partition of the domain is beneficial since the fine-scale equation of motion involves smaller matrices, which is expected to have dramatic consequences on memory allocation. On the other side, the method has a few downsides that reduce its applicability to a limited number of scenarios. Notably, the interface force generation process involves at each time step a convolution

Table 8.1 CPU Time performance of the BSM on fine meshes of different size

N_f	Full simulation CPU time (s)	Bridging scales CPU time (s)	CPU time saved (%)
400	28.86	25.69	11.0
450	36.61	27.81	24.0
500	45.20	29.97	33.7

integral calculated from the initial instant of the simulation. By its own definition, this operation requires an amount of time that increases at each time step. For long simulations, the process can become time consuming and can cause the simulation time to exceed the time needed to conduct a fully detailed simulation involving a fine scale applied over the entire domain. This limitation becomes critical when the fine-scale window and the entire domain are comparable in size. As soon as the global dimension of the domain increases with respect to that of the fine-scale window, the method begins to pay off. These considerations are summarized in Table 8.1, where the results for the first rod problem presented above are shown for different meshes. For this comparison, an increasing size of the global problem is achieved by varying the number of elements in the detailed fine discretization N_f. The numbers shown in Table 8.1 are relative to a simulation run in *Matlab*® on a PC Dell® Dimension 8250 with a 2.78 GHz CPU, and 1.0 GB RAM. The speed of the method can be enhanced by letting the simulation run on the sole coarse-scale mesh unless the presence of a wave propagating within the fine-scale window is detected. This can be achieved automatically by monitoring the energy level inside the fine-scale window and use it as a threshold to trigger the update of the fine-scale solution. The coarse-scale total mechanical energy calculated inside the fine-scale region is an ideal trigger, since it is updated at each time step even when the wave is outside the fine-scale region. A threshold value E^* is selected such that, when $E_{c_{\text{fine}}} > E^*$, the algorithm interprets it as a wave traveling inside the fine-scale and the coupled integration is conducted. When the wave moves across the scale interface, the value of $E_{c_{\text{fine}}}$ drops below the threshold and only the coarse-scale integration is carried out. When the returning wave traveling back towards the source gets inside the region, the coupled integration is re-established. The procedure is detailed in Fig. 8.16. The performance of the integration with the energy threshold is shown in Table 8.2 for the same set of simulations of Table 8.1. By comparison of the two sets of results, it is clear how the threshold on the energy manages to reduce the CPU time in all the considered cases.

8.3.4 Propagation of In-plane Waves in a 2D Elastic Domain

An additional example considers the propagation of plane waves in a free–free square 2D elastic domain. The plate is 0.5 m long, 0.5 m wide and 0.035 m thick and made of aluminum (Young's modulus $E = 7.1 \times 10^{10}\,\text{N/m}^2$, density $\rho = 2.7 \times 10^3\,\text{Kg/m}^3$ and Poisson's ratio $\nu = 0.3$).

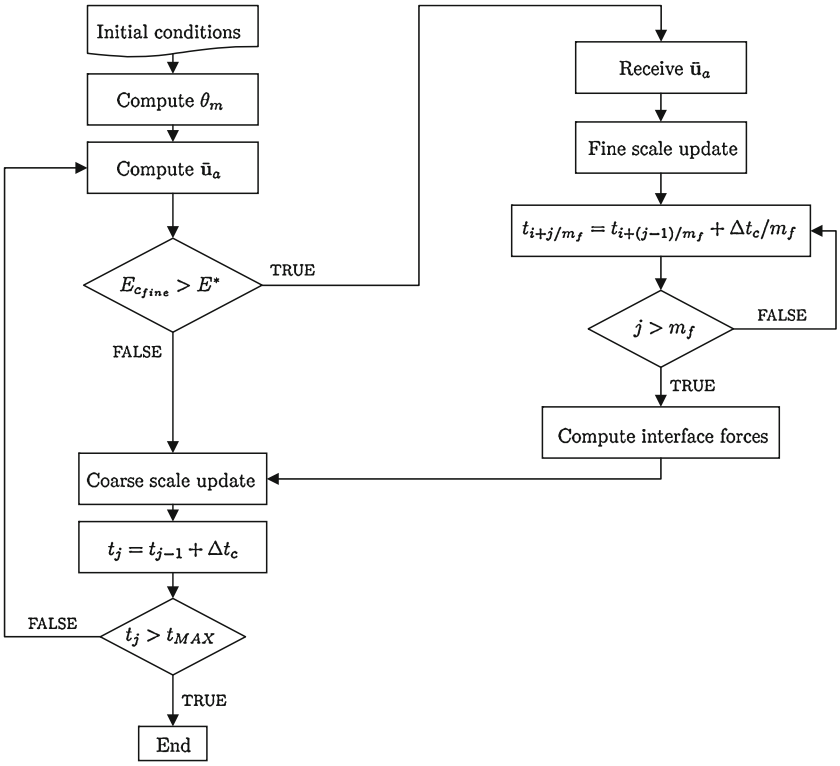

Fig. 8.16 Flow-chart of the energy threshold procedure

Table 8.2 Effect of an energy threshold on the CPU Time

N_f	Full simulation CPU time (s)	Energy threshold CPU time (s)	CPU time saved (%)
400	28.86	14.30	50.5
450	36.61	14.95	52.2
500	45.20	17.58	61.1

The system is initially perturbed by imposing a two-dimensional Gaussian distribution of the displacement along the y coordinate (Fig. 8.17b) defined as:

$$u_y(x,y) = \begin{cases} K\frac{e^{-\left(\frac{d}{\sigma}\right)^2} - u_c}{1-u_c} & d \le L_c \\ 0 & d > L_c \end{cases} \tag{8.33}$$

where d is a radial distance from the origin of the reference frame and u_c is a characteristic parameter of the Gaussian curve, respectively defined as:

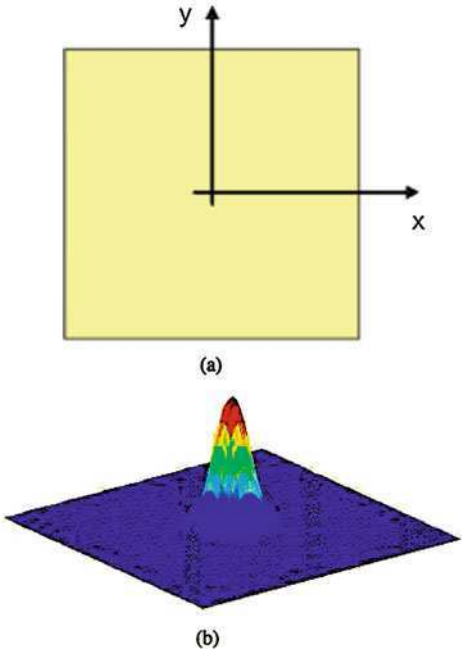

Fig. 8.17 Schematic of a rectangular plate with applied Gaussian in-plane initial disturbance. **a** Geometry. **b** Initial disturbance

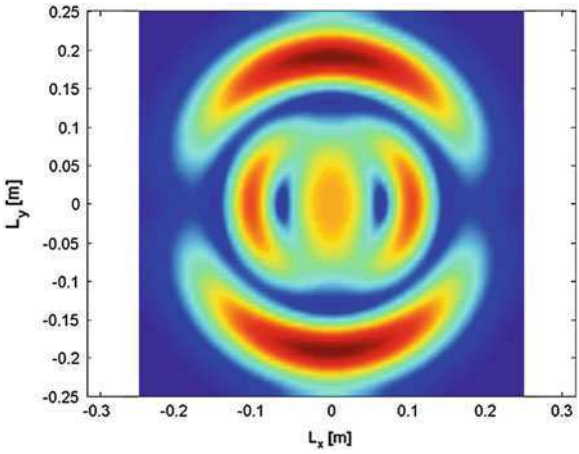

Fig. 8.18 Snapshot of incident travelling wave

$$\begin{aligned} d &= \sqrt{x^2 + y^2} \\ u_c &= e^{-\left(\frac{L_c}{\sigma}\right)^2} \end{aligned} \tag{8.34}$$

K and σ are two additional parameters defining the amplitude and the standard deviation of the Gaussian curve, respectively. A reference solution for this

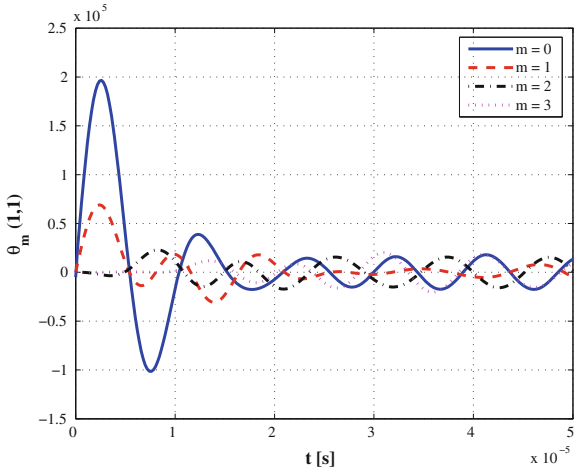

(a)

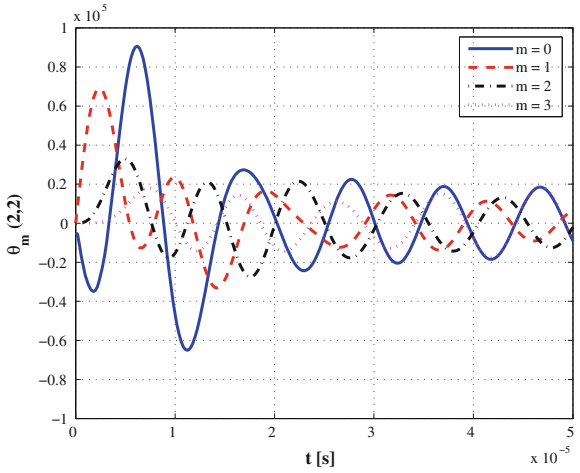

(b)

Fig. 8.19 Behavior of $\boldsymbol{\theta}(t)$ for different m. **a** $\theta(1,1)$. **b** $\theta(2,2)$

example is obtained through a detailed FE analysis conducted by applying a fine mesh over the entire plate domain. Rectangular 4-node bilinear finite elements are used to discretize the plate. Figure 8.18 shows a snapshot of the wavefield after 3×10^{-5} s of simulation. By inspection, it is possible to recognize some characteristic features of in-plane wave motion. A pressure wave is clearly visible traveling along the direction of the disturbance. A shear wave, smaller in amplitude and lagging the pressure wave, can also be observed traveling mostly along the x direction.

Let us now introduce two meshes: a 20×20 coarse mesh applied over the entire square domain and a fine mesh confined to a smaller rectangular window of

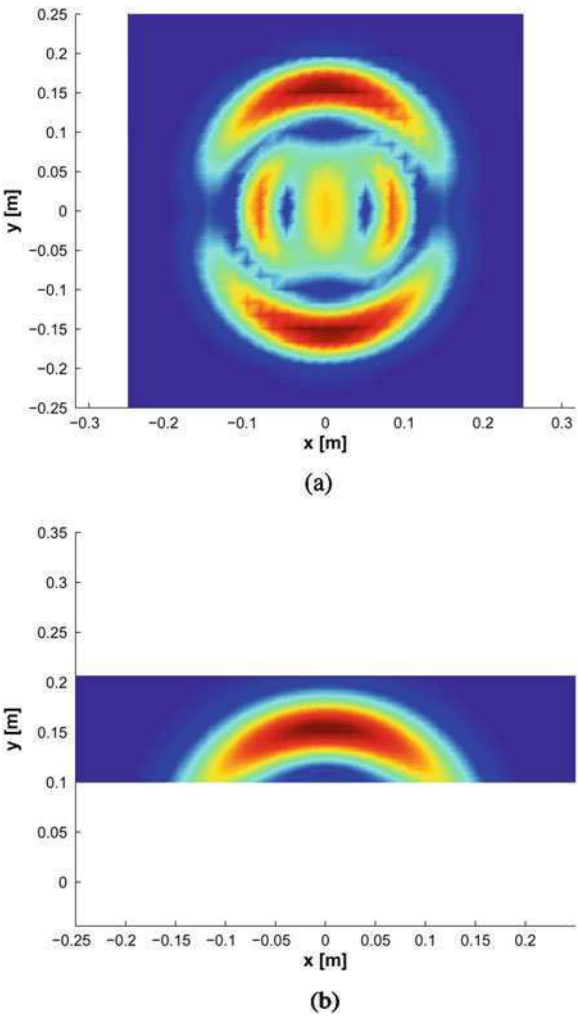

Fig. 8.20 Snapshot of incident travelling wave-Undamaged plate. **a** Coarse-scale simulation. **b** Fine-scale simulation

size 0.5×0.1 m centered about $x = 0, y = 0.15$ m involving elements whose size is such that they would form a 80×80 mesh if applied to the entire domain. The procedure for the calculation of the time history kernel function is detailed in [2]. Since the nodes in the mesh have two degrees of freedom, at each instant in time, $\boldsymbol{\theta}(t)$ is a 2×2 matrix.

It is interesting to observe that this matrix is not symmetric, i.e. $\theta_{12} \neq \theta_{21}$. It has been shown [2] that, since the effects of m decays quickly with m itself, it is sufficient to retain contributions from $3 \div 5$ values of m. For reference, Fig. 8.19a, b respectively show the behavior of θ_{11} and θ_{22} over the fine-scale simulation time domain for some values of m.

Figure 8.20a represents a coarse-scale description of the wave propagation over the entire rectangular domain, while Fig. 8.20b is the fine-scale description of the

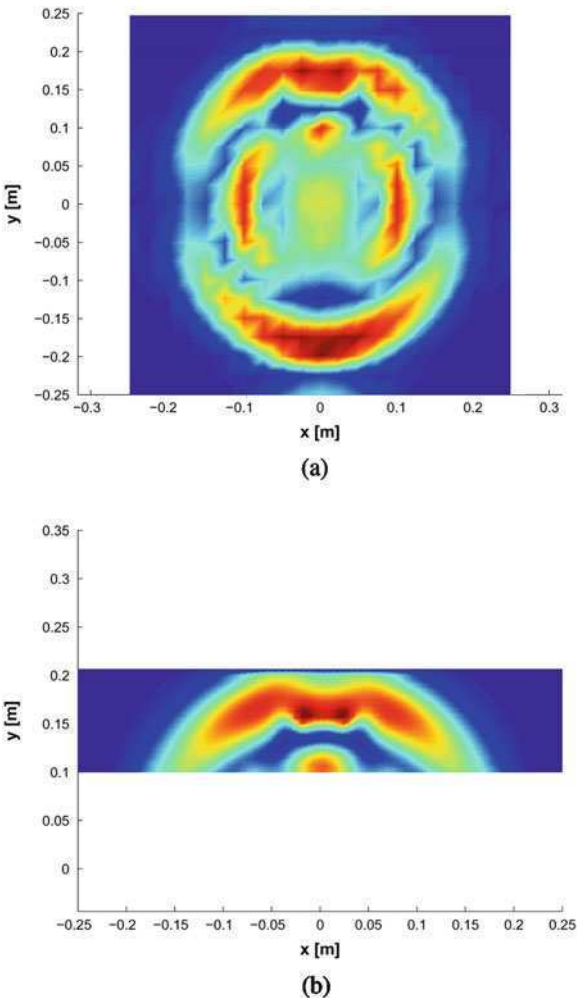

Fig. 8.21 Snapshot of incident travelling wave-Damaged Plate. **a** Coarse-scale simulation. **b** Fine-scale simulation

wavefield within the small rectangular window where the fine mesh is available. Two considerations can be made: first, the fine-scale analysis provides a more detailed representation of the phenomenon, therefore a detailed inspection of a region of the plate is available without solving the full fine-scale problem. Second, the BSM takes care of the interface between the meshes and no spurious reflections are observed.

A discontinuity is introduced as a region of material characterized by higher density and stiffness to simulate a stiff inclusion. The stiff region is modeled as a 10×1 fine-scale element strip located symmetrically with respect to the vertical axis at $\bar{y} = 0.15$ m. The results of the simulation are shown in Fig. 8.21a, b. As in the previous examples, the two scales provide two complementary yet compatible pieces of information about the wave motion. Figure 8.21a provides a low-resolution

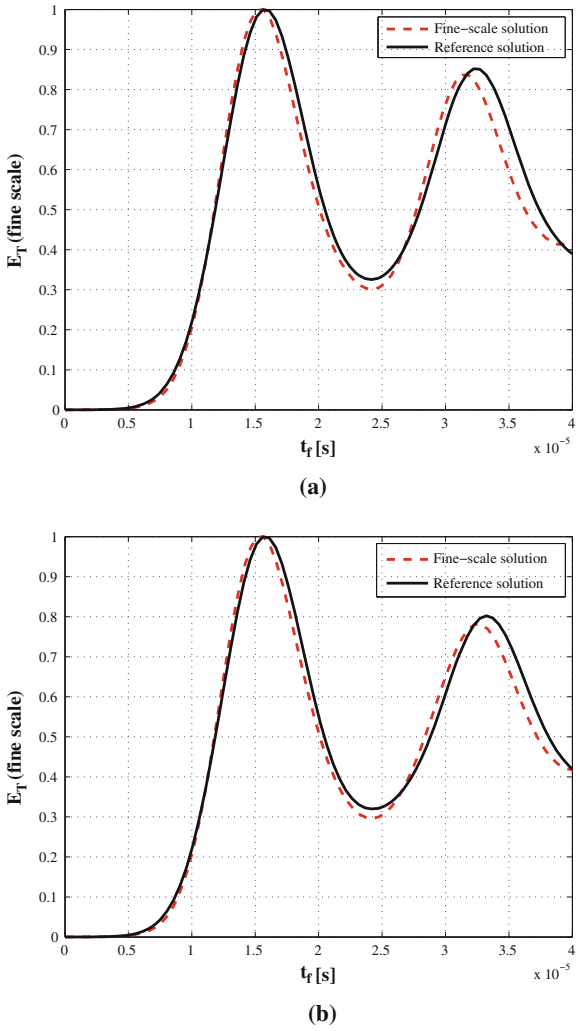

Fig. 8.22 Energy-based accuracy test or bridging scales simulation. **a** Undamaged plate. **b** Damaged plate

picture of the complete wavefield including both the pressure and shear mode and allows visualization of the wave interaction with the plate boundaries.

Figure 8.21b clearly shows that the presence of the stiff inclusion is properly detected and provides a crisp picture of the reflection generation mechanism. The absence of spurious waves due to the scale interface, documented in Fig. 8.20a, b and the compatibility between the result in Fig. 8.21a with the one in Fig. 8.21b suggest that the analysis is accurate. The fine-scale simulation provides a precise representation of the wavefield and shows the extent of the defect. The accuracy of the BSM is again quantified by monitoring the total mechanical energy over the fine-scale region. The energy is normalized by its value at $t = 0$ and is plotted versus time in Fig. 8.22a, b for the damaged and undamaged cases, respectively.

The plots show considerable agreement with the reference solution over a simulation interval corresponding to the time required by the pressure wave to reach the upper edge of the plate, be reflected and travel through the fine-scale region. Comparison of Fig. 8.22b with Fig. 8.22a also shows the presence of a defect: the returning wave is in fact associated with a slightly lower level of mechanical energy as a consequence of the localized reflection caused by the stiff inclusion.

8.4 Results for Frequency-Domain Bridging

8.4.1 Time Domain Spectral Element Discretization

Although independent of the approximation technique, the considered multiscale approach is applied in conjunction with a time domain spectral element (SE) discretization of the wavefield due to the significant advantages offered in modeling elastic waves in complex structures.

Within a SE framework, high-order Lagrange's polynomials are used as interpolation/shape functions of the field variables. The $n+1$ Lagrange polynomials of degree n are defined in terms of the control points $\xi_i \in [-1,1], i = 1,\ldots,n+1$:

$$\psi(\xi)_i^n = \frac{(\xi-\xi_1)\cdots(\xi-\xi_{i-1})(\xi-\xi_{i+1})\cdots(\xi-\xi_{p+1})}{(\xi_i-\xi_1)\cdots(\xi_i-\xi_{i-1})(\xi_i-\xi_{i+1})\cdots(\xi_i-\xi_{p+1})} \tag{8.35}$$

The $n+1$ control points ξ_i used in Eq. 8.35 are chosen to be the Gauss–Lobatto–Legendre (GLL) points, which are the roots of the following equation:

$$(1-\xi^2)\mathscr{L}'_n(\xi) = 0 \tag{8.36}$$

where $\mathscr{L}'_n(\xi)$ denotes the first derivative of the Legendre polynomial of degree n. Note that the GLL points always include $+1$ and -1 therefore in a SE mesh some nodes always lie exactly on the boundaries of the elements. The shape functions for 2D elements are conveniently generated by the cartesian product of 1D shape functions in the x and y direction.

This method is characterized by the high accuracy of spectral method while maintaining the flexibility of FE methods when dealing with complex geometries. Similarly to classical finite elements, the governing partial differential equations of a waveguide are discretized and transformed to a set ordinary differential equation in time. Let $\boldsymbol{u}$ denote the global vector of unknown degrees of freedom, the discretized system of governing differential equation results:

$$\boldsymbol{M}\ddot{\boldsymbol{u}}(t) + \boldsymbol{K}\boldsymbol{u}(t) = \boldsymbol{f}(t) \tag{8.37}$$

where $\boldsymbol{M}$ and $\boldsymbol{K}$ are the mass and stiffness matrices of the system and $\boldsymbol{f}$ the vector of externally applied nodal loads.

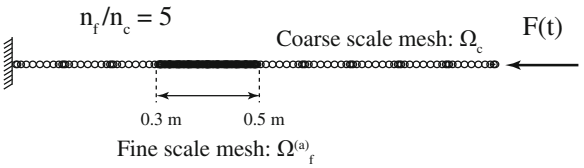

Fig. 8.23 One dimensional uniform rod and corresponding multi scale mesh

8.4.2 Rod

The propagation of axial waves in a one dimensional (1D) homogeneous rod is first studied as a test problem.

The system under consideration (Fig. 8.23) consists of a uniform aluminum rod $(E = 71.0\,\text{GPa}, \rho = 2700\,\text{kg/m}^3)$ clamped at the left end and excited by a concentrated force at the opposite boundary. To avoid the onset of numerical noise during simulations, dissipation is added to the system by a complex Young's modulus: $\tilde{E} = E(1 + 0.01i)$. The same figure also shows that the waveguide is simultaneously discretized using two meshes: a coarse-scale mesh is defined over the entire domain, and a fine-scale mesh is limited over a selected portion of the structure: $\Omega_f^{(a)} = [0.3L\ 0.5L]$ with $L = 1.0\,\text{m}$ denoting the length of the rod. The underlying assumption of the BSM is that the coarse-scale region must be accurate enough to capture the global wave motion. The SE approach adopted in this chapter, allows to discretize the coarse-scale mesh with only 6 nodes per shortest wavelength, while a refinement ratio $n_f/n_c = 5$ is chosen for the fine-scale region.

Wave propagation results are obtained for a four cycles sine burst at 200 kHz. Figure 8.24a shows the computed wavefield in the coarse-scale region for a simulation time that allows the wave to travel the length of the rod twice. As expected, when the main wave intersects the boundaries between the two meshes, the wavefield remains free from spurious reflections from the interface. Figure 8.24b illustrates that also the displacement field solved in the fine-scale region is free from reflections at the boundaries: both the incoming and outgoing waves are free to propagate undisturbed through the two regions.

Figure 8.25 show a snapshot of the wave traveling across the two regions and illustrate the perfect matching between the coarse and fine scale solutions. This can be better observed in Fig. 8.25b that shows how the fine-scale displacement overlaps the coarse-scale solution, with a better spatial resolution and no spurious reflections.

8.4.3 Damaged Timoshenko Beam

The present multiscale approach is also applied to model the wave propagation characteristics of an aluminum Timoshenko beam with imperfections. Figure 8.26

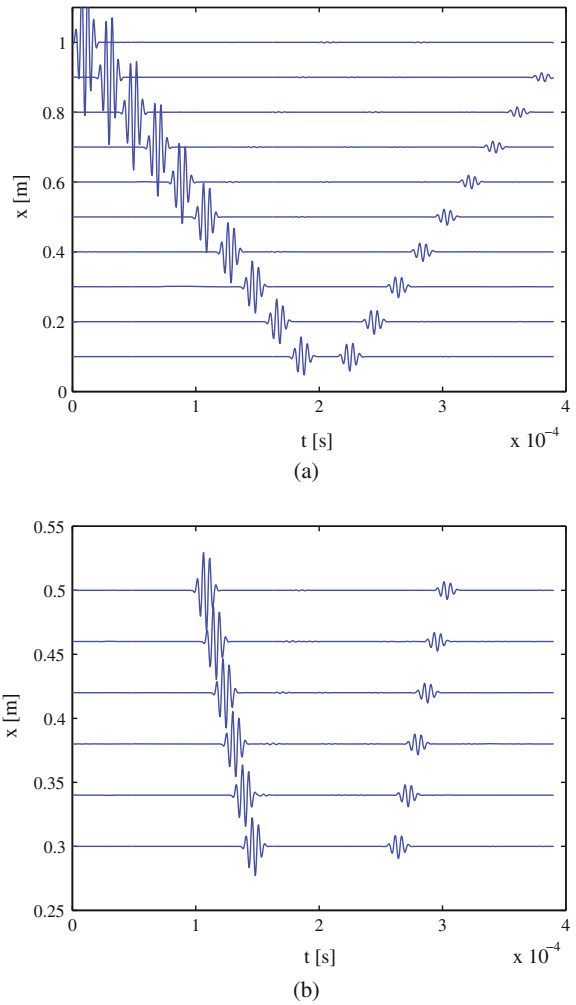

Fig. 8.24 Computed wavefield **a** coarse-scale simulation, **b** fine-scale simulation

illustrates the considered structure in which damage is modeled as a reduction of the effective stiffness of a section located at $x_d = 0.35$ m from the clamped end.

The fine-scale mesh is chosen to provide a fine discretization in the damaged region $\Omega_f^{(a)} = [0.3L\ 0.5L]$. The coarse-scale mesh, that discretizes the entire beam, includes 40 elements, while the fine-scale mesh correspond to a refinement ratio $n_f/n_c = 5$. With the present approach, the presence of a discontinuity is modeled only at the fine-scale level, since in many cases the size of the damaged area in the fine scale region is smaller than that of the size of a single finite element of the coarse-scale. On the contrary, the coarse-scale model simply considers homogeneous properties applied throughout the entire domain.

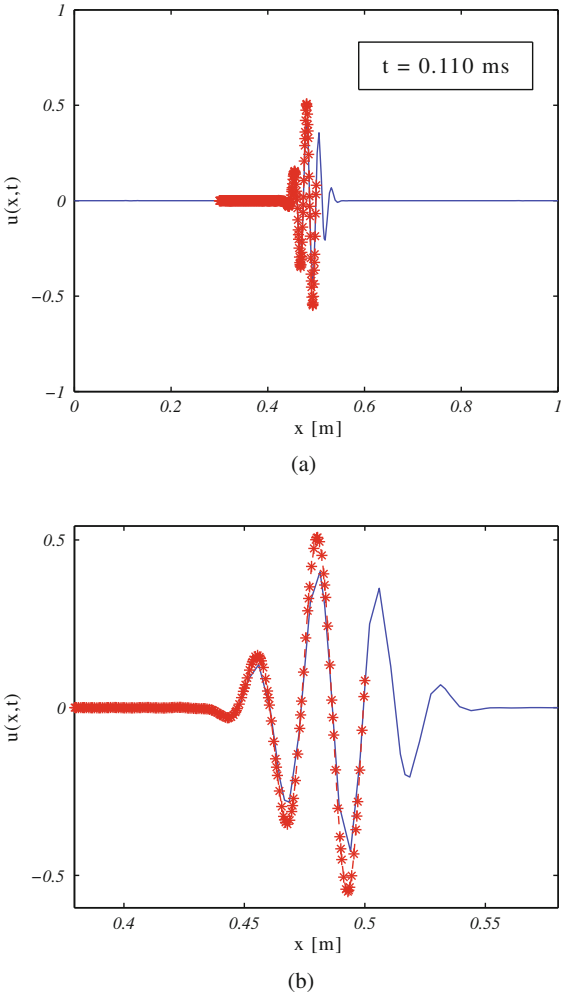

Fig. 8.25 **a** Snapshot of the response when the incident wave is traveling through the refined zone, and **b** a detail of the fine-scale solution. Coarse scale solution: *solid line* (—), fine-scale solution: *star markers* (-- ∗ --)

Numerical results are presented for the beam being excited by a four-cycle sine burst at 100 kHz. Figures 8.27 and 8.28 show how incident and reflected waves are able to propagate throughout the entire structure without spurious reflections at

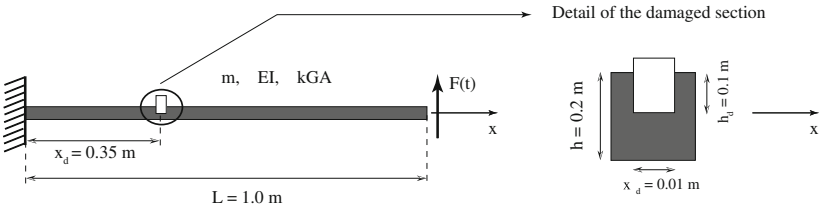

Fig. 8.26 Sketch of the considered Timoshenko beam with damage

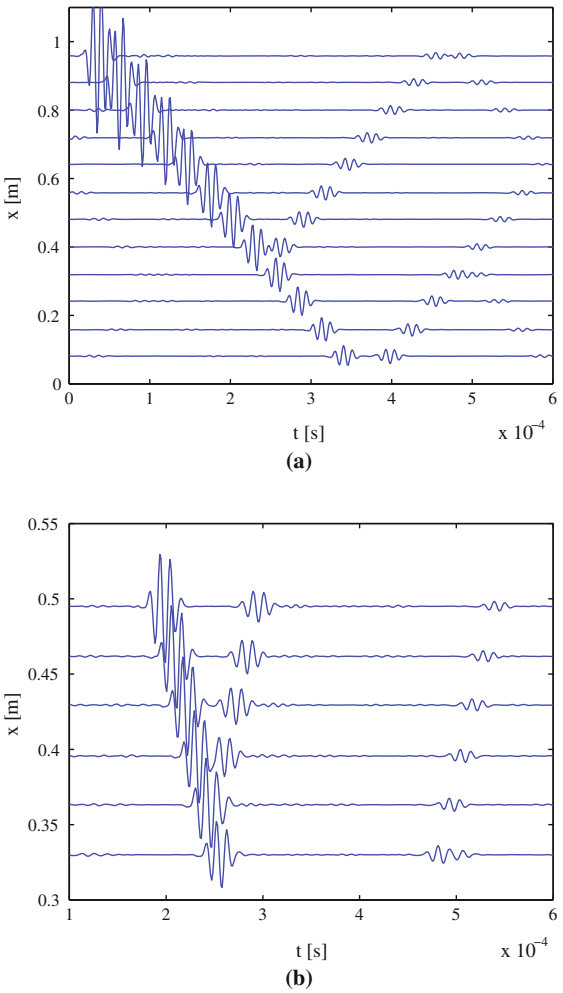

Fig. 8.27 **a** Computed coarse-scale wavefield of the vertical displacement degrees of freedom, and **b** corresponding fine-scale solution

the interface between the two meshes. Specifically, Figs. 8.27a and 8.28a illustrate the coarse-scale wavefield corresponding to the beam vertical displacement and sectional rotation respectively. These results show how the coarse-scale mesh is able to describe the global behavior of the structure, including the interaction with damage, but fails in giving a detailed representation of the reflections induced by the discontinuity. Figures 8.27b and 8.28b show how the displacement field resolved at the fine-scale level is free from spurious reflections, and give a more detailed description of the interaction between the incident wave and the damaged section. Snapshots of the displacement field at the fine and coarse scales are illustrated in Fig. 8.29. These results illustrate the perfect overlapping between the

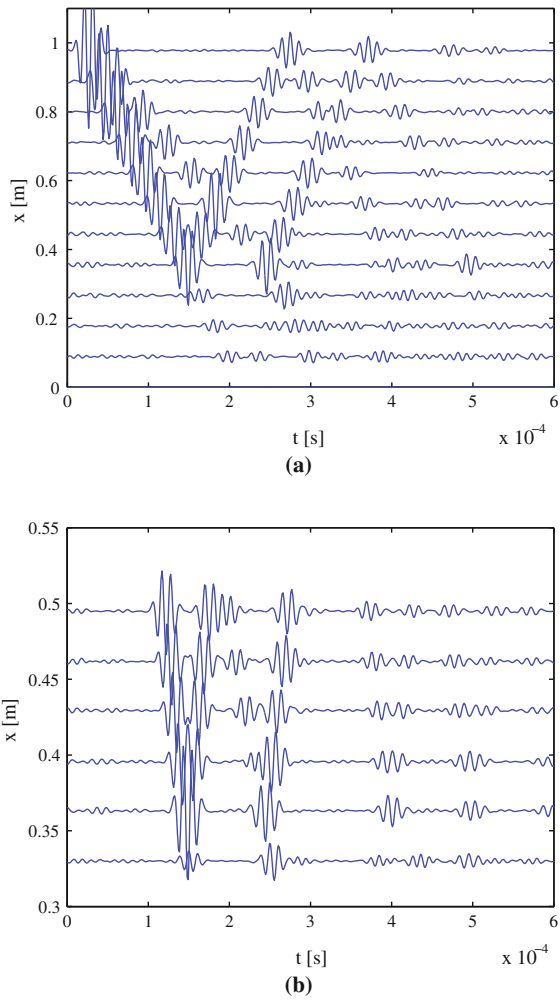

Fig. 8.28 **a** Computed coarse-scale wavefield of the sectional rotation degrees of freedom, and **b** corresponding fine-scale solution

two scales for both the transverse displacement and sectional rotation degrees of freedom.

8.4.4 Two Dimensional Waveguides

As a final example, let us consider the problem of in-plane wave propagation in a thin rectangular membrane. The structure consist of an aluminum ($E = 71.0\,\text{GPa}$, $\rho = 2700\,\text{kg/m}^3$, $v = 0.33$) two dimensional (2D) waveguide of out-of-plane thickness $t = 1.0\,\text{mm}$. The structure is clamped at the left edge and excited by a

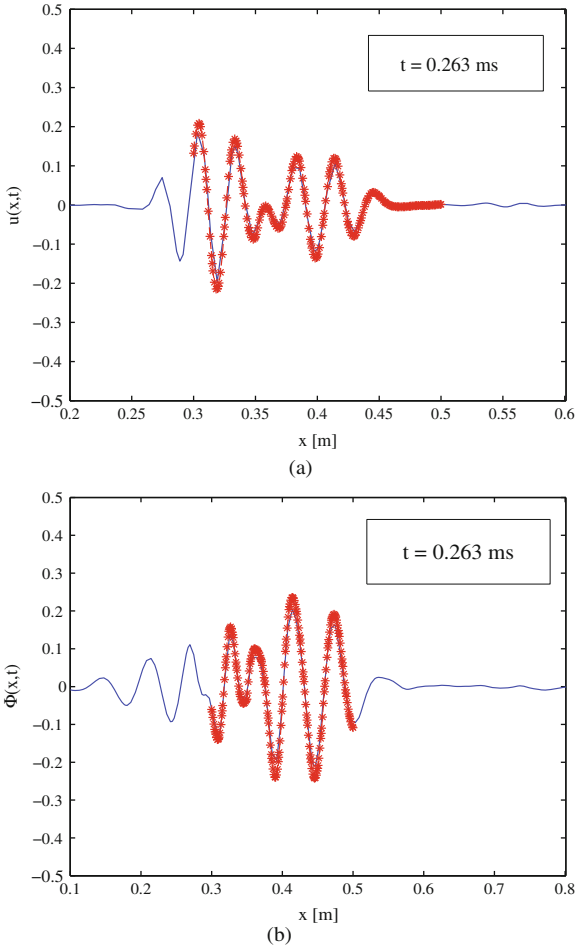

Fig. 8.29 Snapshots of the transmitted and reflected waves across the two meshes: **a** vertical beam displacement, and **b** sectional rotation

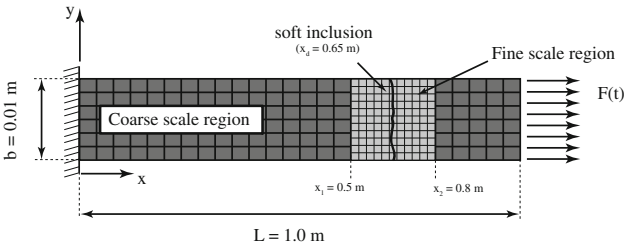

Fig. 8.30 Schematic of the structure discretized with a coarse and fine multi scale mesh

uniform line load on its right boundary as illustrated in Fig. 8.30. A uniform coarse mesh of 40×2 spectral elements characterized by polynomial shape functions of order 4 in both directions is considered. The fine-scale region, discretized with

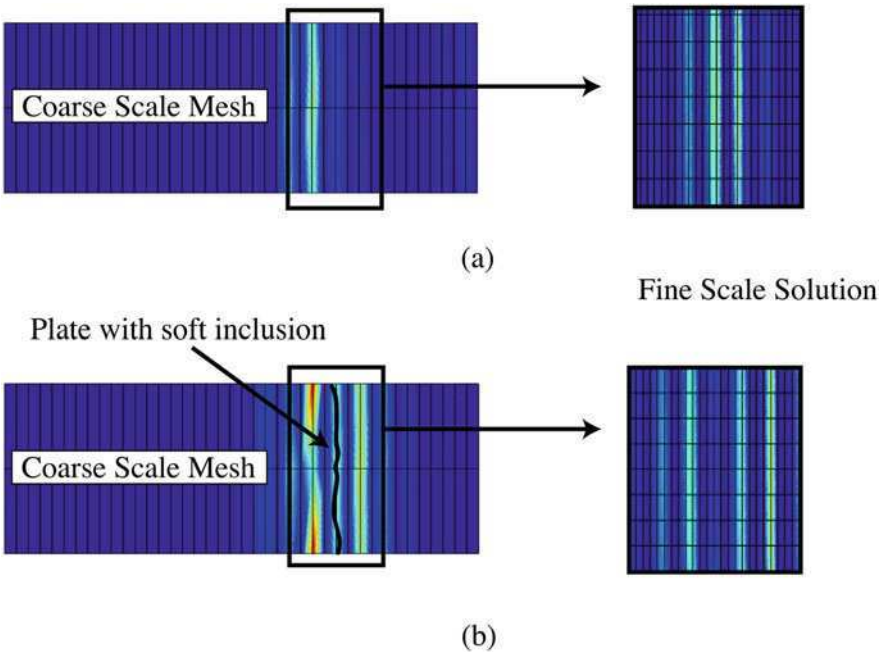

Fig. 8.31 Snapshot of the 2D wavefield for the undamaged plate (**a**) and the damaged plate (**b**)

24×8 elements, is located between $x_1 = 0.5\,\text{m}$ and $x_2 = 0.8\,\text{m}$ and covers for the entire width of the membrane: $\Omega_f = [0.5\ 0.8] \times [0.0\ 0.01]\,\text{m}$. Numerical simulation are conducted to demonstrate the flexibility of the proposed approach in dealing with 2D structures in which a discontinuity is modeled only at the fine-scale level. Results for the undamaged structure are also presented as a reference case. Within the fine-scale region, a soft inclusion is modeled by reducing the Young's modulus of a vertical strip of 8×1 elements at $x_d = 0.65\,\text{m}$ such that $E_d = 0.025\,E$. Figure 8.31 illustrate a snapshot of the undamaged and damaged structures when the input wave is traveling through the refined region. Figure 8.31a, representing the undamaged case, shows that the coarse-scale solution is capable to capture the global wave propagation phenomenon without spurious reflections arising at the interface between the two meshes. At the same time the fine-scale solution provides a more detailed representation of the wave motion within the refined region. On the other hand, Fig. 8.31b shows that the coarse-scale model detects the presence of a discontinuity in the structure, which only occurs at the fine-scale level. Figure 8.32 show snapshots of the horizontal displacement of the plate vertical midline $(y = 5.0\,\text{mm})$. In the undamaged case, presented in Fig. 8.32a, b, the coarse and fine scale results are almost coincident, with the fine-scale solution improving the accuracy of the coarse-scale discretization. In the damaged case, Fig. 8.32c, d show that the coarse-scale is updated with the informations provided

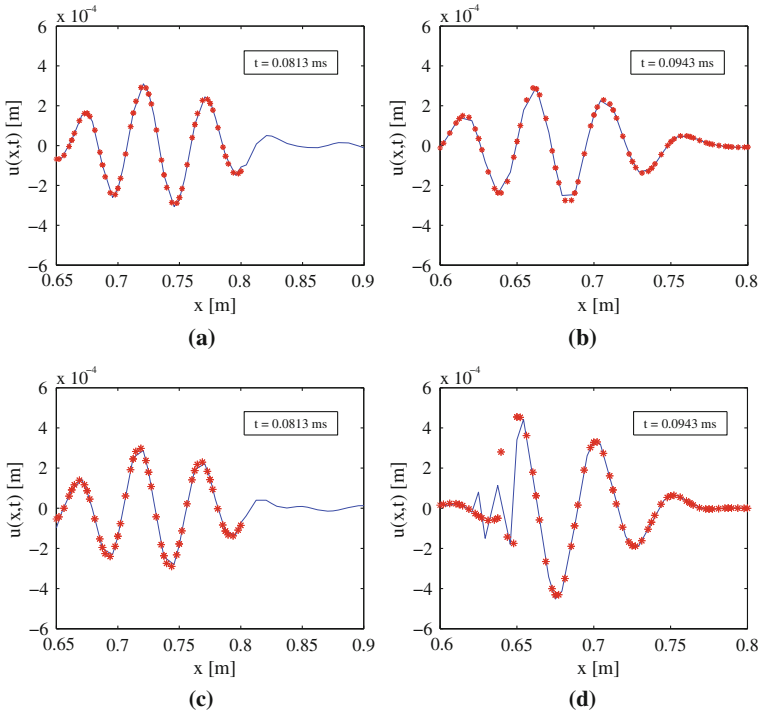

Fig. 8.32 Snapshots of the horizontal displacement at $y = 5.0$ mm of the undamaged structure (**a**), (**b**) and the damaged structure (**c**), (**d**). Coarse scale solution: *solid line* (—), fine-scale solution: *star markers* (-- ∗ --)

by the refined region in which the damage is actually modeled. Specifically, in Fig. 8.32d, only the refined solution is effectively able to capture the local behavior of the structure, especially in the presence of a damage smaller than a single coarse-scale element.

8.5 Conclusions

This chapter describes a multiscale method which allows proper coupling of two meshes of two levels of refinement. The coarse scale mesh covers the entire computational domain to capture its overall behavior, while a fine mesh is defined at a local level where details such as damage need to be resolved with fine spatial resolution. The approach, develops proper coupling relations through which the two discretizations share information without the generation of spurious terms associated with the numerical process. The formulation of the coupled two-scale problem is carried out in the time and frequency domain. The time domain

formulation conveniently exploits time integration schemes, which need to adopt time step sizes which are compatible with the spatial discretization of the domains, in addition to their geometrical features. A convolution operator also needs to be evaluated at each time step for proper coupling of the two scales. The frequency domain approach leads to a considerably simpler implementation of the coupling relations, and does not need to satisfy mesh requirements outside of those imposed by the geometry of the domain, but is affected by the need to evaluate the system matrices at every time step. Results for both formulations are presented to illustrate the capabilities of the general approach and its time and frequency domain implementations.

References

1. Gonella S, Ruzzene M (2008) Bridging scales analysis of wave propagation in heterogeneous structures with imperfections. Wave Motion 45:481–497
2. Kadowaki H, Liu WK (2004) Bridging multi-scale method for localization problems. Comput Methods Appl Mech Eng 193(30–32):3267–3302
3. Liu WK, Chen Y, Chang C, Belytschko T (1996) Advances in multiple scale kernel particle methods. Comput Mech 18(2):73–111
4. Liu WK, Karpov E, Park H (2006) Nano mechanics and materials. Theory, multiscale methods and applications. Wiley, New York
5. Liu WK, Park HS, Qian D, Karpov EG, Kadowaki H, Wagner GJ (2006) Bridging scale methods for nanomechanics and materials. Comput Methods Appl Mech Eng 195(13–16):1407–1421
6. McVeigh C, Vernerey F, Liu WK, Brinson LC (2006) Multiresolution analysis for material design. Comput Methods Appl Mech Eng 195(37–40):4291–4310
7. Park HS, Liu WK (2004) An introduction and tutorial on multiple-scale analysis in solids. Comput Methods Appl Mech Eng 193(17–20):1733–1772
8. Wagner G, Liu W (2003) Coupling of atomistic and continuum simulations using a bridging scale decomposition. J Comput Phys 190(1):249–274
9. Weeks W (1966) Numerical inversion of laplace transforms using laguerre functions. J Assoc Comput Mach 13(3):419
10. Weideman J (1999) Algorithms for parameter selection in the weeks method for inverting the laplace transform. SIAM J Sci Comput 21(1):111–128

Chapter 9
Modeling of Actuators and Sensors for SHM

9.1 Introduction

The chapter is divided in three main parts. The first deals with the description of modeling techniques for the efficient simulation of guided wave generation in plate structures, while the second part discusses the application of such techniques for the analysis of two-dimensional periodic arrays and the prediction of their directional characteristics. A final part presents the models for sensing through patches of different shapes.

The generation of guided waves is a common approach for the interrogation of the state of health of structural components [12, 22]. The development of proper interpretation procedures to analyze the response of the monitored structures, and the optimization of the excitation strategies benefit much from the availability of efficient simulation tools, which are capable of accurate prediction of the propagation of waves generated through various sources, and their interaction with damage or structural defects. Generally, the application of finite elements for the analysis of wave propagation problems leads to large models which tend to be too computationally costly to be used for parametric or optimization studies. For this reason, the development of semi-analytical approaches for wave propagation analysis is an area of research of growing activity. Examples of such techniques include the spectral finite element method described [8] in Chap. 5 of this book, the Semi Analytical Finite Element (SAFE) approach presented in [1] among others, or boundary element-based techniques of the kind illustrated in [4]. Of particular importance is the estimation of guided waves generated by surface mounted or embedded piezoelectric patches or wafer transducers [11, 12, 13], for which accurate models are essential for the selection of geometry, dimensions, and excitation bandwidth suitable for the excitation of specific modes and the detection of various damage types. A common methodology is based on the solution of the wave equation in the spatial Fourier domain [23]. This technique has been applied to the analysis of waves generated by several actuator configurations in isotropic

S. Gopalakrishnan et al., *Computational Techniques for Structural Health Monitoring*, Springer Series in Reliability Engineering, DOI: 10.1007/978-0-85729-284-1_9,

structures in [12, 13], where it is shown how the size of the actuator is a very important parameter for tuning the excitation to a specific frequency and wave mode. These results, which are limited to one-dimensional (1D) wave propagation, are extended to the 2D analysis of crested waves propagation in plates in [20], where an analytical model allows the investigation of the effects of the in-plane shape of the piezo-patch. The formulation of [20] relies on the solution of the 3D equations of elasticity with the stress field generated by the surface bonded piezo as a boundary condition.

Efficient modeling of wave generation is particularly important for the design of novel actuation strategies, and for the optimization of existing ones. The effective interrogation of the health of a structural component often requires sensors and actuators with the ability to perform directional scanning. This enhances the sensitivity of the inspection and simplifies the determination of the location of damage [16, 17, 25]. Wave steering through phased arrays is a well-established technique, used extensively in ultrasonic imaging for medical as well as NDE applications [3, 10, 15, 24–26]. Recent research has investigated the application of piezoelectric phased arrays for guided waves-based structural health monitoring [25]. Promising results demonstrate the potential benefits of beam steering. However, an underlying limitation is associated with the need to excite the array elements individually, which implies hardware and software complexity. Recently, periodic actuator arrays have been proposed for the generation of strong, frequency-dependent directional beaming, which allows beam steering to occur through a simple sweep of the excitation frequency. The concept enables in-situ monitoring of critical components through strongly focused actuation (and/or sensing) and directional scanning capability, which may be achieved with very limited hardware requirements. This different approach to beam steering exploits interference phenomena generated by the spatial periodicity of the array and the simultaneous activation of its components. Such interference phenomena produce waves with frequency dependent directional characteristics, which allow directional scanning to be performed simply through a frequency sweep. The need for beam-forming algorithms and associated hardware is thus avoided. In addition, spatially periodic piezoelectric actuators can be exploited for tuning the excitation to a specific wave mode [3, 26], thus combining mode tuning and beam steering capabilities in a single device.

The chapter first presents modeling techniques for the simulation of guided wave generation. Such techniques are then applied to the estimation of the performance of two-dimensional periodic arrays. The concept of beam steering, and frequency-based directionality is described in detail as a background. The application of the concept for directional sensing is also illustrated in the final section of the chapter.

9.2 Modeling of Lamb Wave Generation

This section describes basic analytical tools for the evaluation of the guided wave field generated in a thin plate by surface-bonded actuators of arbitrary shape.

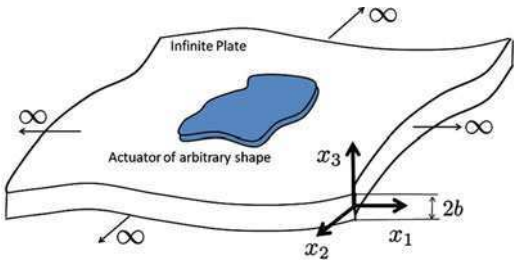

Fig. 9.1 Infinite isotropic plate with arbitrary shape piezoelectric transducer bonded on the top surface

The formulation follows the approach presented in [20], which is based on the solution of the three-dimensional (3D) equations of elasticity in the spatial Fourier domain. Actuation is modeled as an assigned surface stress distribution which is defined by the shape of the actuator.

9.2.1 Governing Equations

Consider an infinite isotropic plate of thickness $2b$ and bonded to its top surface ($x_3 = b$) Fig. 9.1. For convenience, the origin of the reference frame is located on the mid-plane of the plate, which is contained in the x_1, x_2 plane, while the x_3 axis is normal to the plate surface. The dynamic equilibrium of the 3D domain corresponding to the plate, in the absence of external body forces, has the well known form:

$$(\lambda + \mu)\nabla\nabla \cdot \boldsymbol{u} + \mu\nabla^2\boldsymbol{u} = \rho\ddot{\boldsymbol{u}} \tag{9.1}$$

where $\boldsymbol{u} = \{ u_1 \quad u_2 \quad u_3 \}^T$ denotes the displacement vector, μ, λ are the Lamé coefficients, and ρ is the density of the plate material.

Equation 9.1 can be decomposed into Helmholtz components by introducing the scalar potential Φ and the vector potential $\boldsymbol{H}$, for which the following holds:

$$\begin{aligned} \boldsymbol{u} &= \nabla\Phi + \nabla \times \boldsymbol{H}, \\ \nabla \cdot \boldsymbol{H} &= 0 \end{aligned} \tag{9.2}$$

By using Eq. 9.2, Eq. 9.1 reduces to the following two decoupled expressions:

$$\nabla^2\Phi = \frac{\ddot{\Phi}}{c_p^2} \tag{9.3}$$

$$\nabla^2\boldsymbol{H} = \frac{\ddot{\boldsymbol{H}}}{c_s^2} \tag{9.4}$$

where $c_p^2 = (\lambda + 2\mu)/\rho$, and $c_s^2 = \mu/\rho$ are the speeds of the P-wave and S-wave, respectively.

The three-dimensional Fourier Transform (3D FT) of the generic function $f(x_1, x_2, x_3, t)$ is defined as:

$$\bar{f}(\xi_1, \xi_2, x_3, \omega) = \int_{-\infty}^{\infty} \int_{-\infty}^{\infty} \int_{-\infty}^{\infty} f(x_1, x_2, x_3, t) e^{-j(\omega t + \xi_1 x_1 + \xi_2 x_2)} dt dx_1 dx_2 \tag{9.5}$$

Transforming both sides of Eq. 9.4 gives:

$$\frac{\partial^2 \bar{\Phi}}{\partial x_3} - (\xi_1^2 + \xi_2^2)\bar{\Phi} = \frac{\omega}{c_p^2}\bar{\Phi} \tag{9.6}$$

$$\frac{\partial^2 \bar{\boldsymbol{H}}}{\partial x_3} - (\xi_1^2 + \xi_2^2)\bar{\boldsymbol{H}} = \frac{\omega}{c_s^2}\bar{\boldsymbol{H}} \tag{9.7}$$

whose solutions are of the form

$$\begin{aligned} \bar{\phi} &= c_1 \sin(\alpha x_3) + c_2 \cos(\alpha x_3) \\ \bar{\boldsymbol{H}} &= \boldsymbol{c}_3 \sin(\beta x_3) + \boldsymbol{c}_4 \cos(\beta x_3) \end{aligned} \tag{9.8}$$

where ξ_1 and ξ_2 are the wave numbers in x_1 and x_2 directions and

$$\alpha^2 = \frac{\omega^2}{c_p^2} - (\xi_1^2 + \xi_2^2), \tag{9.9}$$

$$\beta^2 = \frac{\omega^2}{c_s^2} - (\xi_1^2 + \xi_2^2) \tag{9.10}$$

The integration constants $c_1, \boldsymbol{c}_3$, are associated with wave modes which are symmetric through the thickness, whereas $c_2, \boldsymbol{c}_4$, correspond to antisymmetric modes. The derivations are here presented for symmetric modes only, with the understanding that the antisymmetric contributions are obtained in a similar manner.

The actuator applies a surface stress distribution on the portion of the upper face of the plate it covers. Accordingly, the stress field at the plate surface ($x_3 = b$) can be expressed as follows:

$$\begin{aligned} \sigma_{33}(x_1, x_2, b, t) &= 0 \\ \sigma_{32}(x_1, x_2, b, t) &= F_2(x_1, x_2) V_0(t) \\ \sigma_{31}(x_1, x_2, b, t) &= F_1(x_1, x_2) V_0(t) \end{aligned} \tag{9.11}$$

where $V_0(t)$ denotes the applied voltage, and F_i and $(i = 1, 2)$ are the stress distribution functions, whose numerically-based computation is the object of the next section. Typically, the applied surface stress state relies on common

assumptions made for thin layer modeling, whereby the normal stress in the active layer is neglected ($\sigma_{33}(x_1, x_2, b) = 0$), along with the dynamic behavior of the actuator [6]. This approximation is acceptable when the product of the thickness times the Young's modulus of the piezoelectric material is significantly smaller than that of the supporting structure, and when the bonding layer is thin and can be considered as rigid.

Application of the stresses as boundary conditions allows the evaluation of the integration constants in Eq. 9.8. Assuming an harmonic applied voltage $V_0(t) = V_0(\omega)e^{j\omega t}$ leads to the estimation of the 3D FT of the three components of the plate displacement. The corresponding spatial displacement distribution is subsequently obtained through an inverse 3D FT. These derivations, whose detailed description can be found in [20], lead to expressions for the three components of the plate displacement. For example, the out-of-plane component u_3 for symmetric modes is given by:

$$\begin{aligned} u_3(x_1, x_2, \omega) = \frac{1}{4\pi^2\mu} V_0(\omega) \int_{-\infty}^{\infty} \int_{-\infty}^{\infty} \frac{ie^{j(\xi_1 x_1 + \xi_2 x_2)}}{D_s(\xi, \omega)} \\ \left[2\alpha\beta \sin(\alpha b)\cos(\beta b) + (\xi^2 - \beta^2)\cos(\alpha b)\sin(\beta b)\right] \\ (\xi_1 \bar{F}_1(\xi_1, \xi_2) + \xi_2 \bar{F}_2(\xi_1, \xi_2)) d\xi_1 d\xi_2 \end{aligned} \tag{9.12}$$

where

$$\xi^2 = \xi_1^2 + \xi_2^2$$

and

$$D_s(\xi) = (\xi^2 - \beta^2)^2 \cos(\alpha b)\sin(\beta b) + 4\xi^2 \alpha\beta \sin(\alpha b)\cos(\beta b).$$

Expressions for the other components u_1, u_2 can be found in [20]. The displacement expressions all contain integrals which are singular for values of the wavenumber ξ which are real roots of functions $D_s(\xi)$ or $\sin(\beta b)$ and correspond to Rayleigh-Lamb symmetric and horizontally polarized shear modes (SH waves), as obtained from the solution of the dispersion relation of the plate for the assigned value of frequency ω.

9.2.2 Harmonic Far Field Response

For given $F_i(x_1, x_2)$, the plate displacements can be computed from Eq. 9.12. The evaluation of the integrals for generic piezoelectric shapes requires the numerical integration over the 2D wavenumber domain, which needs to be performed in a computationally efficient way. This is achieved through the procedure illustrated in what follows. Letting:

$$F_s(\xi,\omega) = j\,\frac{\left[2\alpha\beta\sin(\alpha b)\cos(\beta b) + (\xi^2-\beta^2)\cos(\alpha b)\sin(\beta b)\right]}{D_s(\xi,\omega)} \tag{9.13}$$

Equation 9.12 can be rewritten as:

$$u_3(x_1,x_2,\omega) = \frac{V_o(\omega)}{4\pi^2\mu}\int_{-\infty}^{\infty}\int_{-\infty}^{\infty} e^{j(\xi_1 x_1+\xi_2 x_2)}F_s(\xi,\omega)(\xi_1\bar{F}_1(\xi_1,\xi_2) + \xi_2\bar{F}_2(\xi_1,\xi_2))d\xi_1 d\xi_2 \tag{9.14}$$

The function $F_s(\xi,\omega)$ tends to infinity when $D_s(\xi,\omega)=0$, i.e. when (ξ,ω) correspond to a point on the Rayleigh Lamb dispersion curve and in this case, for a symmetric wave mode. This singularity can be handled through the application of the residue theorem as in [20]. This requires knowledge of the Laurent development of $e^{j(\xi_1 x_1+\xi_2 x_2)}F_s(\xi,\omega)(\xi_1\bar{F}_1(\xi_1,\xi_2)V_o(\omega) + \xi_2\bar{F}_2(\xi_1,\xi_2)V_o(\omega))$, which is not generally available for a generic functions F_i [5, 9].

The evaluation of the integral relies on the expression of Eq. 9.14 in cylindrical coordinates, which is given by:

$$u_3 = \frac{V_0(\omega)}{4\pi^2\mu}\int_0^{\infty}\xi^2 F_s(\xi,\omega)\int_0^{2\pi}\bar{F}_r(\xi,\varphi)e^{j\xi r\cos(\varphi-\theta)}d\varphi d\xi \tag{9.15}$$

The integration over the angular coordinate φ is approximated through the stationary phase theorem, which stipulates that, for large r:

$$\int_{\psi_1}^{\psi_2} f(\psi)e^{jrh(\psi)}d\psi \approx \sqrt{\frac{\pi}{2rh''(\psi_0)}}f(\psi_o)e^{j(rh(\psi_o)+\sin(h''(\psi_o))\frac{\pi}{4})} + O\left(\frac{1}{r}\right) \tag{9.16}$$

where $h'(\psi_0)=0$, $f()$ is a generic function, and ψ_1,ψ_2 are arbitrary end-points of the interval of integration, which contains ψ_0.

Assuming $r\to+\infty$ the following asymptotic expression is obtained:

$$u_3(r,\theta) = -\frac{jV_0(\omega)}{4\pi^2\mu}\sqrt{\frac{\pi}{2r}}\int_0^{\infty}\frac{\xi^2}{\sqrt{\xi}}e^{-j\sin(\xi)\frac{\pi}{4}}F_s(\xi,\omega)\bar{F}_r(\xi,\theta)e^{j\xi r}d\xi \tag{9.17}$$

The evaluation of the integral in Eq. 9.17 can be efficiently performed through the application of the 1D Fast Fourier Transform (FFT) algorithm for assigned values of θ. In order to avoid numerical noise induced by the discretization of the F_s function, material damping is introduced by considering a complex Young's Modulus, which effectively regularizes the singularities in the $D_s(\xi,\omega)$ term.

9.2.3 Actuator Directivity

The proposed methodology allows the convenient estimation of the directivity. Specifically, as the $F_s(\xi, \omega)$ function is singular (or closely singular when damped systems are considered) when (ξ, ω) lie on one of the dispersion branches, most of the generated input is represented in wavenumber space by the function $F_s(\xi, \omega)\bar{F}_r(\xi, \theta)$. At a given frequency ω, the angular variation of the function defines the directivity of the actuator. Such directivity d is evaluated as the locus of the maximum amplitude of the peaks over all ξ:

$$d_s(\omega, \theta) = max_{\xi}(|F_s(\xi, \omega)\bar{F}_r(\xi, \theta)|) \tag{9.18}$$

This definition provides the directivity of a given wave mode s. The directivity of symmetric and anti-symmetric modes is compared by normalizing the function $d(\omega, \theta)$ by the maximum for the A_0 mode at a given frequency. The normalized directivity for the S_0 mode is for example given by:

$$\mathcal{D}_{S_0}(\omega, \theta) = \frac{d_{S_0}(\omega, \theta)}{max_{\theta}[d_{A_0}(\omega, \theta)]} \tag{9.19}$$

9.2.4 Example: Circular Actuator

The procedure is illustrated for the case of a circular actuator. The simple geometry allows the application of the analytical procedure based on an assumed distribution of the interface stresses. Such assumptions will be validated later in the chapter, where a procedure for the numerical estimation of the stress distribution based on a local FE analysis is presented, and where the limitations of the current assumptions will be specifically illustrated in light of the prediction of the tuning conditions for the actuator.

A circular bonded piezo is modeled as an externally applied surface tangential traction distribution, which yields the following surface stress components:

$$\begin{aligned} \sigma_{31}(r, \theta, t) &= \tau(t)\delta(r - a)\cos\theta \\ \sigma_{32}(r, \theta, t) &= \tau(t)\delta(r - a)\cos\theta \\ \sigma_{33}(r, \theta, t) &= 0 \end{aligned} \tag{9.20}$$

where r, θ are polar coordinates with origin at the center of the piezo Fig. 9.2, and $\tau(t)$ defines the time history of the surface shear stress. It is convenient to consider a harmonic input $\tau(t) = \tau_0(\omega)e^{j\omega t}$, and formulate the solution in the wavenumber domain, so that the applied surface stress at frequency ω can be expressed as:

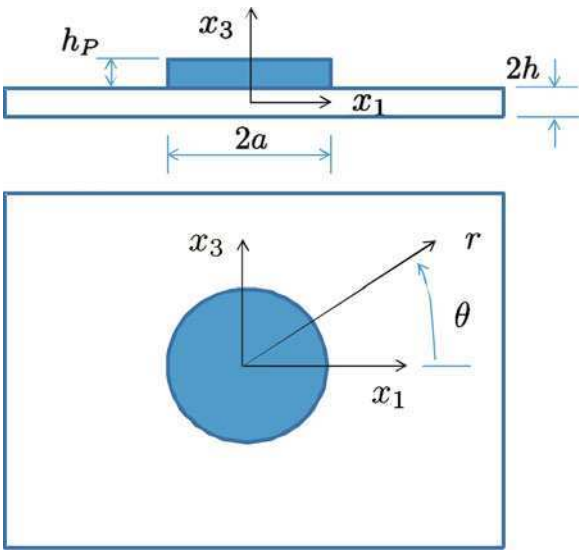

Fig. 9.2 Dimensions and reference system used for the circular actuator analysis

$$\begin{aligned}\hat{\sigma}_{31}(\xi_1,\xi_2,\omega) &= -ia\tau_0(\omega)J_1(a\xi)\frac{\xi_1}{\xi},\\ \hat{\sigma}_{32}(\xi_1,\xi_2,\omega) &= -ia\tau_0(\omega)J_1(a\xi)\frac{\xi_2}{\xi}\\ \hat{\sigma}_{33}(\xi_1,\xi_2,\omega) &= 0\end{aligned} \tag{9.21}$$

In Eq. 9.21, $\xi^2 = \xi_1^2 + \xi_2^2$, while $J_1(\cdot)$ is the Bessel Function of the first kind and order 1. Following the approach presented in [20], a change in coordinates is convenient due to the particular symmetry of the problem. Polar coordinates ξ, γ in the wavenumber domain ($\xi_1 = \xi\cos\gamma, \xi_2 = \xi\sin\gamma$) are used to express the radial and out-of-plane displacement components, with the tangential displacement being equal to zero due to the axi-symmetric configuration of the actuator. Application of the residue theorem from complex analysis, and imposing wave propagation conditions, leads to the following expression for the radial displacement $u_r = [u_1^2 + u_2^2]^{1/2}$:

$$\begin{aligned}u_r(r,\theta,\omega,h) = -\pi j\frac{\tau_0 a}{\mu}\Bigg[&\sum_{\xi_S} J_1(a\xi_S)\frac{N_S(\xi_S)}{D_S'(\xi_S)}H_1^{(2)}(\xi_S r)\\ &+\sum_{\xi_A} J_1(a\xi_A)\frac{N_A(\xi_A)}{D_A'(\xi_A)}H_1^{(2)}(\xi_A r)\Bigg]\end{aligned} \tag{9.22}$$

where

$$\begin{aligned}N_S &= \xi\beta(\xi^2+\beta^2)\cos\alpha h\cos\beta h\\ D_S &= (\xi^2-\beta^2)^2\cos\alpha h\sin\beta h + 4\xi^2\alpha\beta\sin\alpha h\cos\beta h\end{aligned}$$

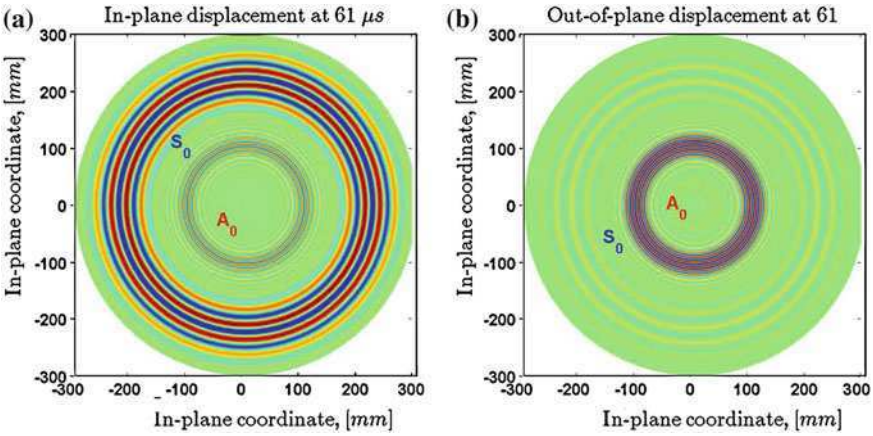

Fig. 9.3 Displacements as function in-plane spatial coordinates showing both S_0 and A_0 Lamb modes: **a** Radial (*in-plane*) displacement; **b** transverse displacement

and

$$N_A = \xi\beta(\xi^2 + \beta^2)\sin\alpha h \sin\beta h$$
$$D_A = (\xi^2 - \beta^2)^2 \sin\alpha h \cos\beta h + 4\xi^2\alpha\beta\cos\alpha h \sin\beta h$$

Also in Eq. 9.22, $H_1^{(2)}$ is the complex Hankel function of the second type and order 1.

The out-of-plane component is obtained through a similar procedure and can be expressed as:

$$u_3(r,\theta,\omega,h) = -\pi j\frac{\tau_0 a}{\mu}\left[\sum_{\xi_S} J_1(a\xi_S)\xi_S^2\frac{N_S^*(\xi_S)}{D_S'(\xi_S)}H_0^{(2)}(\xi_S r) + \sum_{\xi_A} J_1(a\xi_A)\xi_A^2\frac{N_A^*(\xi_A)}{D_A'(\xi_A)}H_0^{(2)}(\xi_A r)\right] \tag{9.23}$$

where

$$N_S^* = 2\alpha\beta\sin\alpha h\cos\beta h + (\xi^2 - \beta^2)\sin\alpha h\cos\beta h$$
$$N_A^* = 2\alpha\beta\cos\alpha h\sin\beta h + (\xi^2 - \beta^2)\cos\alpha h\sin\beta h$$

and $H_0^{(2)}$ is the complex Hankel function of the second type and order 0.

Figure 9.3 shows the in-plane and out-of-plane displacement components of the plate response generated by an actuator of thickness $h_P = 2.1$ mm and diameter $2a = 20$ mm, mounted on an aluminum plate of thickness $2h = 1.5$ mm. The input describing applied to the actuator is a Hanning-modulated sine burst at 200 kHz. The plots clearly show the omni-directional nature of the waves generated by the actuator.

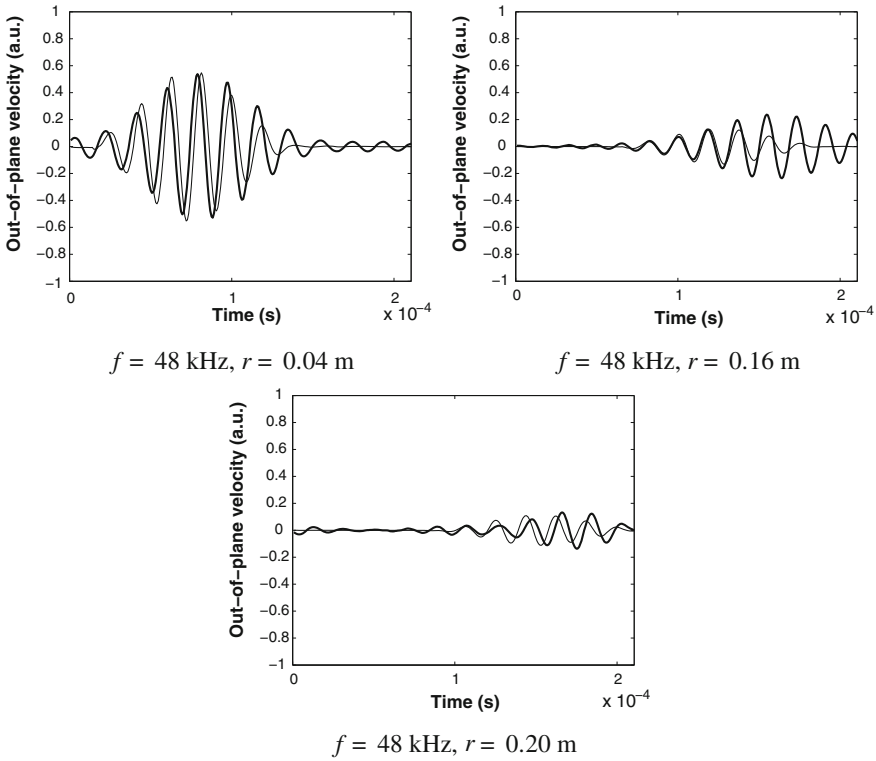

Fig. 9.4 Comparison of analytical predictions (*thin line*) and measured response (*solid line*) at 48 kHz and various distances r from center of actuator

9.2.5 Experimental Validation

The formulation presented above is validated through a wave propagation experiment performed on a square aluminium plate (Young's modulus $E = 71$ GPa, Poisson's ration $v = 0.33$, density $\rho = 2700$ kg/m^3). The plate has a thickness of $2h = 161$ mm thickness, and measures $L = 45.7$ cm per side. The excitation is provided by a circular piezoelectric disc (StemInc, Model SMD20T21F1000) of diameter $2a = 20$ mm and thickness $h_p = 2.1$ mm. The actuator is bonded to the center of the plate and is actuated by a voltage signal controlled by a signal generator through a voltage amplifier. The considered excitation signal is a sine burst of selected frequency, modulated by a Hanning window. The excitation frequency considered for the tests is in the considered range where only the first symmetric and antisymmetric mode (S_0 and A_0) are excited.

The plate response is measured by a scanning Laser Vibrometer (Polytec PSV 400M) over a fine grid to record full wavefield data on the considered plate. The recorded response measured at a selected number of points is compared to the one

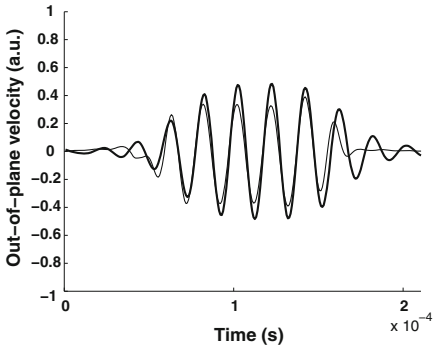

$f = 55$ kHz, $r = 0.09$ m

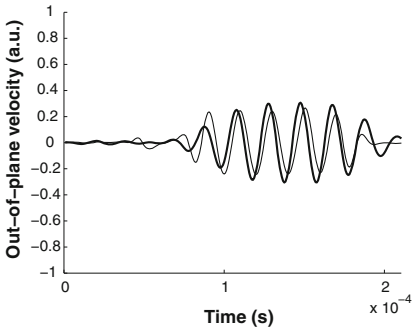

$f = 55$ kHz, $r = 0.14$ m

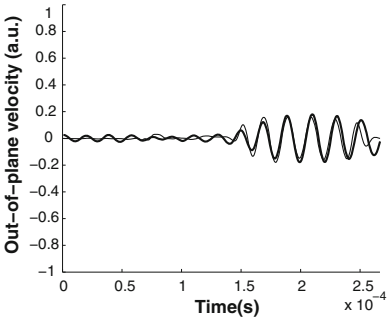

$f = 55$ kHz, $r = 0.22$ m

Fig. 9.5 Comparison of analytical predictions (*thin line*) and measured response (*solid line*) at 50 kHz and various distances r from center of actuator

predicted analytically in Figs. 9.4 and 9.5, where results are reported for excitation frequencies of 48 kHz and 55 kHz. Similar levels of agreement can be found at other frequencies, whose corresponding plots are here omitted for the sake of brevity. The figures show a good match between experimental data and analytical predictions, and suggest the accuracy of the formulation. The analytical predictions can therefore be employed to investigate the response of the plate due to an array of sources, as illustrated later in this chapter.

9.2.6 Finite Element Evaluation of the Interface Stresses

Previously, equation were derived using the assumptions introduced in [6] to obtain an analytical description of the stress induced by a thin layer of piezoelectric material. The corresponding analytical expression lends itself to the analytical solution of the problem as described in the previous section, but is affected by some limitations. These commonly used assumptions consider the piezoelectric composite

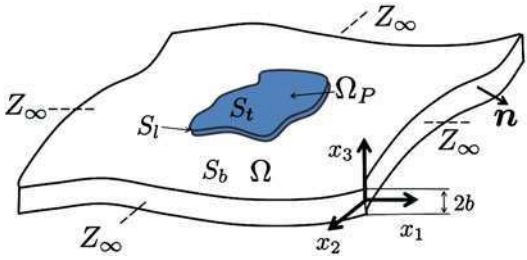

Fig. 9.6 Multilayered piezocomposite system

as a Love-Kirkchoff layered system characterized by linear variations of displacements through the layers' thickness. Furthermore, the induced interface shear stress computation assumes that no reacting forces are applied to the piezo-composite element. In addition, electro-mechanical coupling effects are largely simplified by considering a constant electrostatic field within the piezoelectric layer. This standard assumption allows removing the electrical degrees of freedom from the fully coupled electro-mechanical formulation. A review of such simplifying assumptions and their implications is found in [2], where it is shown how important inaccuracies are introduced especially when electromechanical coupling becomes relevant [7].

The limiting assumptions discussed above can be avoided by performing the analysis of the fully coupled electro-mechanical behavior of the layered structure. The resulting equations and associated boundary conditions can in fact be discretized through a three-dimensional (3D) FE formulation, whose generality can be exploited to investigate complex geometries and bonding conditions between the layers. The fully coupled model is used specifically to estimate the interface stresses through the numerical estimation of the functions $F_i(x_1, x_2, t)$.

The considered computational domain, depicted schematically in Fig. 9.6 consists of a mechanical structure on an open domain Ω and of a piezoelectric domain Ω_p. The constitutive equations for the piezoelectric domain are expressed as: piezoelectric material:

$$\begin{aligned} \sigma &= [\boldsymbol{c}]^E \varepsilon - [\boldsymbol{e}]^\sigma \boldsymbol{E} \\ \boldsymbol{D} &= [\boldsymbol{e}]\varepsilon + [\varepsilon]^\varepsilon \boldsymbol{E} \end{aligned} \tag{9.24}$$

where $\sigma = \{\, \sigma_x \quad \sigma_y \quad \sigma_z \quad \tau_{xz} \quad \tau_{yz} \quad \tau_{xy} \,\}^T$ and $\varepsilon = \{\, \varepsilon_x \quad \varepsilon_y \quad \varepsilon_z \quad \gamma_{xz} \quad \gamma_{yz} \quad \gamma_{xy} \,\}^T$ respectively are the mechanical stress and strain vectors, $\boldsymbol{D} = \{\, D_1 \quad D_2 \quad D_3 \,\}^T$ is the electric charge vector, and $\boldsymbol{E} = \{\, E_1 \quad E_2 \quad E_3 \,\}^T$ is the electric field vector. Also, $[\boldsymbol{c}]^E$, $[\boldsymbol{e}]^\sigma$, and $[\varepsilon]^\varepsilon$ denote the mechanical stiffness matrix at constant electric field, the piezoelectric stress coupling matrix evaluated at constant stress, and the permittivity matrix at constant strain. The behavior of the system is governed by the 3D electro-mechanical equations which are expressed in the form:

$$\begin{aligned} \rho \ddot{\boldsymbol{u}} - \nabla\sigma &= \boldsymbol{f}, \quad \forall \boldsymbol{x}\Omega \cup \Omega_p \\ \nabla \boldsymbol{D} &= \boldsymbol{0} \quad \forall \boldsymbol{x} \in \Omega_p \end{aligned} \tag{9.25}$$

The considered mechanical and electrical boundary conditions are:

$$\begin{aligned} \sigma \cdot \boldsymbol{n} &= Z_\infty(\boldsymbol{u}, t), \quad \forall \boldsymbol{x} \in S_\infty \\ \sigma \cdot \boldsymbol{n} &= 0, \quad \forall \boldsymbol{x} \in S/(S_\infty \cup S_b) \\ [\boldsymbol{u}] = [\sigma \cdot \boldsymbol{n}] &= 0, \quad \forall \boldsymbol{x} \in S_b \end{aligned} \tag{9.26}$$

and

$$\begin{aligned} V &= 0, \quad \forall \boldsymbol{x} \in S_b \\ V &= V_0(t), \quad \forall \boldsymbol{x} \in S_t \\ \boldsymbol{D} \cdot \boldsymbol{n} &= 0, \quad \forall \boldsymbol{x} \in S_l \end{aligned} \tag{9.27}$$

In Eq. 9.27, $Z_\infty()$ denotes an infinite impedance operator. Also in Eq. 9.26[] represents the interface jump operator (i.e $[u] = u^{(+)} - u^{(-)}$ where $u^{(+)}$ and $u^{(-)}$ denotes the generic function u on each side of the considered interface). This set of equilibrium equations is complemented by the dual counterpart of the imposed non-homogenous electrical Dirichlet boundary condition on S_t:

$$q_o = -\int_{S_t} D_n dS \tag{9.28}$$

The FE discretization of Eq. 9.25 is based on the formulation of its weak form, augmented by the Lagrange multipliersT_{s_b} and q_0 respectively associated with the non-homogeneous Dirichlet boundary conditions in Eqs. 9.27 and 9.28.

Application of a suitable discretization scheme with associated shape functions, leads to the discretized equations of motion in matrix form for the elastic domain

$$\begin{bmatrix} M^s_{ii} & M^s_{ic} & 0 \\ M^{sT}_{ic} & M^s_{cc} & 0 \\ 0 & 0 & 0 \end{bmatrix} \begin{bmatrix} \ddot{\boldsymbol{u}}_{si} \\ \ddot{\boldsymbol{u}}_{sc} \\ \ddot{\boldsymbol{T}}_{S_b} \end{bmatrix} + \begin{bmatrix} K^s_{ii} & K^s_{ic} & 0 \\ K^{sT}_{ic} & K^s_{cc} & I \\ 0 & I & 0 \end{bmatrix} \begin{bmatrix} \boldsymbol{u}_{si} \\ \boldsymbol{u}_{sc} \\ \boldsymbol{T}_{S_b} \end{bmatrix} = \begin{bmatrix} Z_\infty(\boldsymbol{u}_{si}, t) \\ 0 \\ \boldsymbol{u}_{pc} \end{bmatrix} \tag{9.29}$$

and for the piezoelectric layer

$$\begin{bmatrix} M_{ii} & M_{ic} & 0 & 0 & 0 \\ M^T_{ic} & M_{cc} & 0 & 0 & 0 \\ 0 & 0 & 0 & 0 & 0 \\ 0 & 0 & 0 & 0 & 0 \\ 0 & 0 & 0 & 0 & 0 \end{bmatrix} \begin{bmatrix} \ddot{\boldsymbol{u}}_{pi} \\ \ddot{\boldsymbol{u}}_{pc} \\ \ddot{\boldsymbol{T}}_{S_b} \\ \ddot{V} \\ \ddot{V}_0 \end{bmatrix} + \begin{bmatrix} K_{ii} & K_{ic} & 0 & E_i & E_{ip} \\ K^T_{ic} & K_{cc} & -I & E_c & E_{cp} \\ 0 & I & 0 & 0 & 0 \\ -E^T_i & -E^T_c & 0 & C & C_p \\ -E^T_{ip} & -E^T_{cp} & 0 & C^T_{cp} & C_{pp} \end{bmatrix} \begin{bmatrix} \boldsymbol{u}_{pi} \\ \boldsymbol{u}_{pc} \\ \boldsymbol{T}_{S_b} \\ V \\ V_0 \end{bmatrix}$$
$$= \begin{bmatrix} 0 \\ 0 \\ \boldsymbol{u}_{sc} \\ 0 \\ Q_0 \end{bmatrix} \tag{9.30}$$

where, for simplicity, the same notation is used for the continuous functions and their discretized representation. In Eq. 9.29, $\boldsymbol{u}_{si}$ denotes the internal structural degrees of freedom, while $\boldsymbol{u}_{sc}$ defines the interface degrees of freedom. Similarly, the degrees of freedom of the piezo patch are split as $\boldsymbol{u}_{pi}$ for the inner part and $\boldsymbol{u}_{pc}$ for the boundary ones. Partition of the voltage term is introduced by using V for unknown voltage degrees of freedom and V_0 for the applied potential.

An interesting aspect of the approach consists in the fact that the homogeneous Dirichlet boundary conditions have not been directly removed from the model in order to improve numerical convergence of the interface stresses $\boldsymbol{T}_{S_b}$, which correspond to the Lagrange multipliers. This vector effectively defines the applied stress functions F_i in Eq. 9.12. Also, the formulation does not rely on assumptions on the stress and displacement variations through the thickness of the piezo, and allows the estimation of electro-mechanical coupling effects, as well as the introduction of additional layers for example corresponding to a bonding agent. Finally, according to [2], this fully coupled model permits the consideration of the "induced electrical potential" and does not introduce constraints on each surface's charge fields q_0 dual to the applied voltages V_0, even if it does not explicitly appear in Eq. 9.30, but only through its integral form $Q_0 = \sum q_0$.

The piezocomposite system in Fig. 9.6 is modeled by considering a representative element which is sufficiently large to compute the local piezoelectric coupling effect in conditions where the obtained solution is insensitive to the applied boundary impedance Z_∞. The solution leads to expressions for the functions $F_i(x_1, x_2)(i = 1, 2)$ in Eq. 9.12. The corresponding 2D FT is evaluated in a cylindrical coordinate system, which is convenient for the subsequent estimation of the corresponding far-field plate response. The computed expressions of $\bar{F}_i(\xi, \varphi)$ are given by:

$$\bar{F}_i(\xi, \varphi) = \int_{-\infty}^{+\infty} \int_{0}^{\pi} F_i(r\cos(\theta), r\sin(\theta)) e^{-j\xi . r . \cos(\theta - \varphi)} r dr d\theta \tag{9.31}$$

The integral in Eq. 9.31 is evaluated numerically on a mesh surface in the plane (ξ, φ). Its computation is efficient because the F_i functions are defined on a small bounded domain and are null outside, which significantly limits the range of integration along the radial coordinate r.

9.2.7 Example: Circular Patch

The numerical procedure described above is applied to compute the plate response generated by a circular actuator. This allows a comparison of the results obtained with the numerical technique, with those based on the analytical description of the interface stresses.

Table 9.1 PZT 5H piezoelectric material characteristics

$c_{11}^E = 1.2710^{11}$ Pa	$c_{22}^E = 1.2710^{11}$ Pa	$c_{33}^E = 1.1710^{11}$ Pa
$c_{12}^E = 8.0210^{10}$ Pa	$c_{13}^E = 8.4610^{10}$ Pa	$c_{23}^E = 8.4610^{10}$ Pa
$c_{44}^E = 2.3010^{10}$ Pa	$c_{55}^E = 2.3010^{10}$ Pa	$c_{66}^E = 2.3410^{10}$ Pa
$e_{31} = 6.62$ C/m^{-2}	$e_{33} = -23.24$ C/m^{-2}	$e_{32} = 6.62$ C/m^{-2}
$e_{24} = -17.03$ C/m^{-2}	$e_{15} = -17.03$ C/m^{-2}	$\rho = 7500$ kg m $^{-3}$
$\varepsilon_{11}^S = 1704\varepsilon_0$ C V^{-1} m^{-1}	$\varepsilon_{22}^S = 1704\varepsilon_0$ C V^{-1} m^{-1}	$\varepsilon_{33}^S = 143.361\varepsilon_o$ C V^{-1} m^{-1}

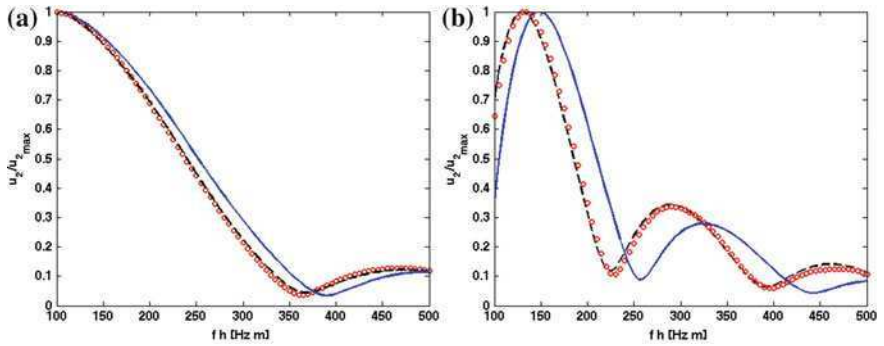

Fig. 9.7 Variation of amplitude of the plate in-plane displacement versus excitation frequency at 5 cm from the source. Comparison of analytical (*circle*), semi-analytical with Dirac applied stress (*dashed line*) and semi-analytical results with FE-evaluated interface stresses (*solid line*) for the S_0 (**a**) and A_0 mode (**b**)

The response computed through the developed process are directly compared with the ones of the analytical approach of [20]. For the purpose of this comparison, we consider an infinite isotropic aluminum plate of 2 mm of thickness, excited by a 0.9 cm radius actuator made of PZT-2 material (see Table 9.1). A first set of results is obtained through the implementation of the analytical approach of [20], where the applied stresses are assumed concentrated at the edge of the actuator as described by a Dirac function. A second computation is performed through the present approach with the applied stress field still modeled as a Dirac function. Finally, a last case employs the interface stresses evaluated through the FE procedure described above, with no assumptions made regarding their distribution. Figure 9.7 compares the amplitude of the plate radial displacement $((u_1^2 + u_2^2)^{1/2})$ at a distance $r = 5$ cm from the center of the disc resulting from the three computations. The results confirm the validity of the developed solution scheme when the delta function is considered to describe the interface stress distribution. For both modes, there is however an observable shift of the response curves associated with the detailed modeling of the interface stress. This shift can have important practical consequences for the evaluation of the accurate frequencies for optimal tuning of Lamb wave excitation and for proper actuator sizing.

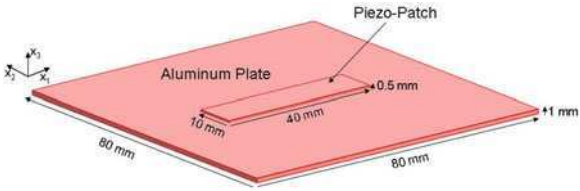

Fig. 9.8 Geometry of rectangular piezo patch and of the portion of the plate considered for detailed FE modeling

9.2.8 Rectangular Isotropic Piezo Patch

A second example considers a rectangular PZT-2 patch of 0.5 mm of thickness Fig. 9.8. FE model of a square portion of the plate measuring 56 mm per side is developed to compute the stress distribution functions F_i. The applied electrical and mechanical boundary conditions are equivalent to those used for the circular piezo presented in the previous section. The wavenumber domain distribution of the shear stresses presented in Fig. 9.9a clearly shows the non-isotropic behavior of the patch, which is characterized by a set of peaks in the the ξ_2 direction, and by a secondary set of peaks along ξ_1. This suggests that the patch radiates preferentially along the direction perpendicular to its length. Figure 9.9b shows the plate out-of-plane response at the frequency corresponding to the circles in Fig. 9.9a, which is equal to 480 kHz for a 1 mm thick aluminum plate. The out-of-plane response clearly shows the strong directivity of the actuator, and illustrates how the response is dominated by the A_0 mode. This is due to the fact that the strain distribution peaks intercepted by the dispersion circles at the corresponding frequency are higher for the A_0 mode, and also that the polarization for A_0 is predominantly out-of-plane, while S_0 is mostly in-plane. The directivity of the two modes at the considered frequency is depicted in Fig. 9.9c.

9.3 Beamforming Through One-Dimensional Phased Arrays: A Quick Overview

The analytical and numerical procedures for the evaluation of wave generation are applied for the design and optimization of actuation configurations for SHM. Specifically, directional actuation is of great interest for the effective detection and localization of structural defects. This section provides a quick overview of array configurations which provide directional control of the generated waves. The basic concepts introduced here are then applied in the next section, which illustrates the performance of two-dimensional arrays capable of frequency-based beam steering.

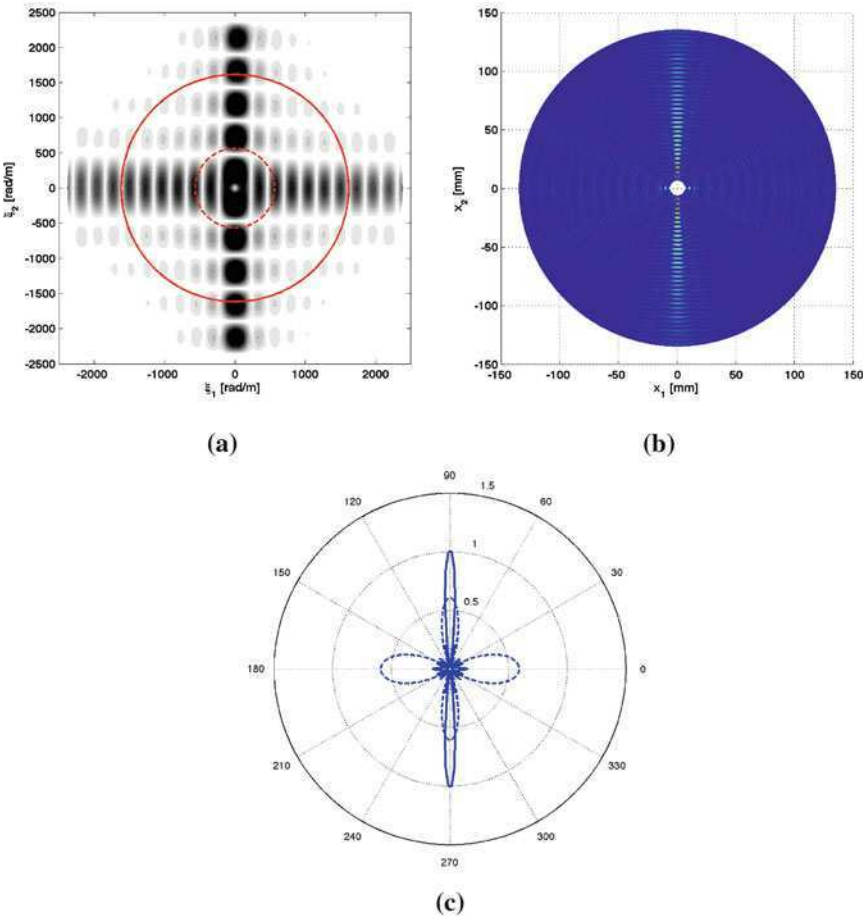

Fig. 9.9 Rectangular isotropic patch: wavenumber representation of the stress distribution function and symmetric S_0 (*dashed*)/antisymmetric A_0 (*plain*) wave number (**a**), plate harmonic vertical response u_3 at 480 kHz (**b**), and (**c**) corresponding directivity diagrams for the S_0 (*dashed line*) and the A_0 mode (*solid*)

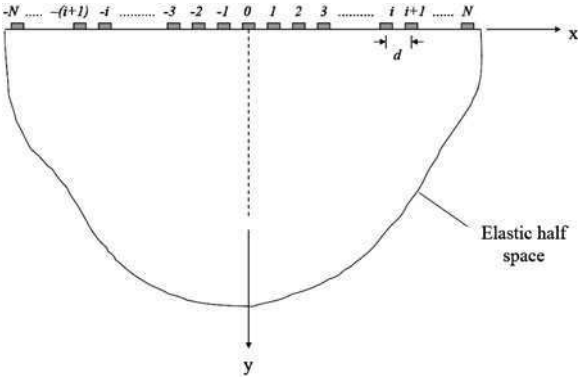

Fig. 9.10 Considered configuration of phased arrays

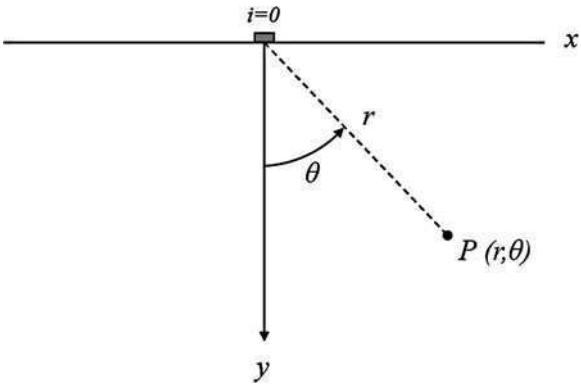

Fig. 9.11 Coordinate system and generic response point

Consider a linear array mounted on the free surface of an elastic half-space. The array contains $2N + 1$ elements, which all act as point sources. The considered configuration is depicted schematically in Fig. 9.10. The analysis is based on the following assumptions: (1) each component acts as a point source, (2) the elastic half-space is homogeneous, isotropic, and in plane strain conditions the medium sustains the propagation of two modes: a longitudinal (P) wave of phase speed c_P and a shear (S) wave mode of speed c_S, and each i-th component generates a signal in the time domain denoted as $g_i(t)$.

9.3.1 Response Due to a Single Component

The response at point P due to the excitation of the array component $i = 0$ (see Fig. 9.11) can be expressed as:

$$w_0(r, \theta, t) = \frac{1}{r} g_0(t - \tau_0), \tag{9.32}$$

where the term $\frac{1}{r}$ introduces a spherical spreading loss factor related to the distance of the response point from the source. Also, τ_0 denotes the propagation time from the source at $O(0, 0)$ to $P(r, \theta)$. Under the assumption that a single mode, say the P-mode, is propagating non-dispersively at speed c_P, the propagation time can be expressed as:

$$\tau_0 = \frac{r}{c_P}, \tag{9.33}$$

The response at P due to the generic source i generic can be written as:

$$w_i(r, \theta, t) \approx \frac{1}{r} g_i(t - \tau_i), \tag{9.34}$$

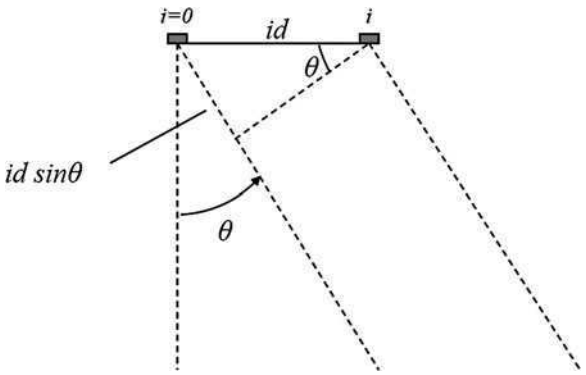

Fig. 9.12 Far-field approximation of difference in paths of propagation of waves emanating from sources $i = 0$ and generic i

where τ_i is the corresponding propagation time. Within the far-field assumption, τ_i can be expressed in terms of τ_0 through a set of simple geometric considerations, which are based on the schematic configuration shown in Fig. 9.12. The far-field assumptions assumes that the waves generated by the actuators $i = 0$ and generic i have essentially parallel wavefronts, and that the propagation distance only differs by a quantity which is related to the spacing between the two actuators, which is equal to id, with d denoting the spatial period of the array. Hence the relation between τ_i and τ_0 can be approximated as:

$$\tau_i = \frac{r + id\sin\theta}{c_P} = \tau_0 + \frac{id\sin\theta}{c_P}. \tag{9.35}$$

9.3.2 Array Response

Based on the derivations and simplifying assumptions described in the previous section, the response of the entire array can be easily expressed as the superposition of the contributions from the various sources. This gives:

$$\begin{aligned} w(r,\theta,t) &= \sum_{i=-N}^{+N} w_i(r,\theta,t) \\ &= \sum_{i=-N}^{+N} \frac{1}{r} g_i\left(t - \tau_0 - \frac{id\sin\theta}{c_P}\right) \\ &= \frac{1}{r}\sum_{i=-N}^{+N} g_i\left(t - \frac{r}{c_P} - \frac{id\sin\theta}{c_P}\right) \end{aligned} \tag{9.36}$$

An additional parameter can be introduced to allow the possibility for each array component to be actuated with a specified, controllable delay. Such delay, denoted as τ_{c_i}, must therefore be added to the physical delay associated with the difference in propagation distance. Accordingly, the array response becomes:

$$w(r,\theta,t) = \frac{1}{r}\sum_{i=-N}^{+N} g_i\left(t - \frac{r}{c_P} - \frac{id\sin\theta}{c_P} + \tau_{c_i}\right), \tag{9.37}$$

9.3.3 Beam Steering Strategies

The array response expressed in Eq. 9.37 can be used as a basis to describe typical strategies for directing the array response at desired, controllable angles. Specifically, two strategies will be here explored, one based on the specific selection of the controlled delay τ_{c_i}, and the next by exploiting the physical, inherent delay due to the difference in propagation paths. The first strategy is well known and applied in a number of fields such as Sonar, Radar, antenna technology, medical imaging, as well as in NDE and SHM. The second is less known, and less flexible in terms of angle controllability and resolution, but has the great advantage of avoiding the need for complex electronics and related components on each array element.

For beam steering, it is typically assumed that all the components generate the same signal $g(t)$, so that the array response becomes:

$$w(r,\theta,t) = \frac{1}{r}\sum_{i=-N}^{+N} g\left(t - \frac{r}{c_P} - \frac{id\sin\theta}{c_P} + \tau_{c_i}\right), \tag{9.38}$$

In addition, it is convenient to carry out the analysis in the frequency domain:

$$\begin{aligned} w(r,\theta,\omega) &= \int_{-\infty}^{\infty} w(r,\theta,t)e^{-j\omega t}dt \\ &= \frac{1}{r}\sum_{i=-N}^{+N}\int_{-\infty}^{\infty} g(t-\Delta t_i)e^{-j\omega t}dt \end{aligned} \tag{9.39}$$

where:

$$\Delta t_i = \frac{r}{c_P} + \frac{id\sin\theta}{c_P} - \tau_{c_i},$$

Application of the Fourier Transfom gives:

$$w(r,\theta,\omega) = \frac{G(\omega)}{r}\sum_{i=-N}^{+N} e^{-j\omega\Delta t_i}, \tag{9.40}$$

where

$$G(\omega) = \int_{-\infty}^{\infty} g(t)e^{-i\omega t}dt$$

is the Fourier transform of the input signal. Explicit expression of the time delay Δt_i leads to the following simplifications:

$$\begin{aligned} w(r,\theta,\omega) &= \frac{G(\omega)}{r}\sum_{i=-N}^{+N} e^{-j\omega\frac{r}{c_P}}e^{-j\omega\frac{id\sin\theta}{c_P}}e^{j\omega\tau_{c_i}}, \\ &= \frac{e^{-j\omega\frac{r}{c_P}}}{r}G(\omega)\sum_{i=-N}^{+N} e^{-j\omega\left[\frac{id\sin\theta}{c}-\tau_{c_i}\right]}. \end{aligned} \tag{9.41}$$

The analysis of Eq. 9.41 allows the convenient description of the beam steering strategies to be investigated. It is worth noting that the formulation so far holds for any type of input $g(t)$, for which no specific assumption has been made.

9.3.3.1 Strategy 1: Linear Phase Delay

The first strategy assumes the ability to impose a controlled delay to each array component. Specifically, the controlled delay on the i-th actuator can be set to be:

$$\tau_{c_i} = \frac{i}{c_P}d\sin\theta_f, \tag{9.42}$$

where θ_f is the angle defining the orientation of the steered beam. Substituting Eq. 9.42 in Eq. 9.41 gives:

$$w(r,\theta,\omega) = G(\omega)\frac{e^{-j\frac{\omega}{c_P}r}}{r}\sum_{i=-N}^{+N} e^{-j\frac{\omega}{c_P}i\left(\sin\theta-\sin\theta_f\right)d}. \tag{9.43}$$

Equation 9.43 can be simplified by recalling the identity:

$$\sum_{n=1}^{N} e^{-jn\alpha} = \frac{\sin N\alpha}{\sin\alpha}$$

whose application leads to:

$$w(r,\theta,\omega) = \frac{e^{-j\frac{\omega}{c_P}r}}{r}G(\omega)\frac{\sin\left[(2N+1)\frac{\omega}{c_P}d(\sin\theta-\sin\theta_f)\right]}{\sin\left[\frac{\omega}{c_P}d(\sin\theta-\sin\theta_f)\right]} \tag{9.44}$$

The response reaches a maximum when

$$\sin\theta = \sin\theta_f$$
$$\theta_f = \theta$$

which defines a first lobe of maximum response. Additional lobes are found for:

$$\sin\theta - \sin\theta_f = \frac{p\pi c_P}{\omega d}. \tag{9.45}$$

with p integer.

The directionality of the array can be conveniently represented through polar plots of the directionality factor, which is here given by:

$$d(\theta,\omega) = \frac{\sin\left[(2N+1)\frac{\omega}{c_P}d(\sin\theta - \sin\theta_f)\right]}{\sin\left[\frac{\omega}{c_P}d(\sin\theta - \sin\theta_f)\right]} \tag{9.46}$$

Examples of directionality plots are presented in Fig. 9.13.

9.3.3.2 Strategy 2: Frequency Based Steering

An alternative strategy consists in actuating all elements of the array simultaneously, and letting the spacing between each element introduce the proper phase delay to achieve preferential radiation in a given direction. The phase delay in this case is clearly associated with the wavelength of the excitation, and its relation with the array periodicity. Directionality is therefore based on the frequency of excitation.

The relation between excitation frequency and direction of radiation can be found by letting the controlled phase delay in Eq. 9.44 equal to zero, which corresponds to imposing that $\theta_f = 0$. This gives

$$w(r,\theta,\omega) = \frac{e^{-j\frac{\omega}{c_P}r}}{r}G(\omega)\frac{\sin\left[(2N+1)\frac{\omega}{c_P}d\sin\theta\right]}{\sin\left[\frac{\omega}{c_P}d\sin\theta\right]} \tag{9.47}$$

whose maximum response value is obtained for:

$$\sin\theta = \frac{p\pi c_P}{\omega d}. \tag{9.48}$$

with $p = 0, 1, ..$ is an integer. The case for $p = 0$ is somewhat trivial as it corresponds to the obvious situation when the preferential direction of radiation occurs for $\theta = 0$. More interesting to the study at hand are the cases for which $p \neq 0$ where a direction of maximum radiation can be associated to the proper combination of p and ω. The problem with this configuration consists in the fact that conditions need

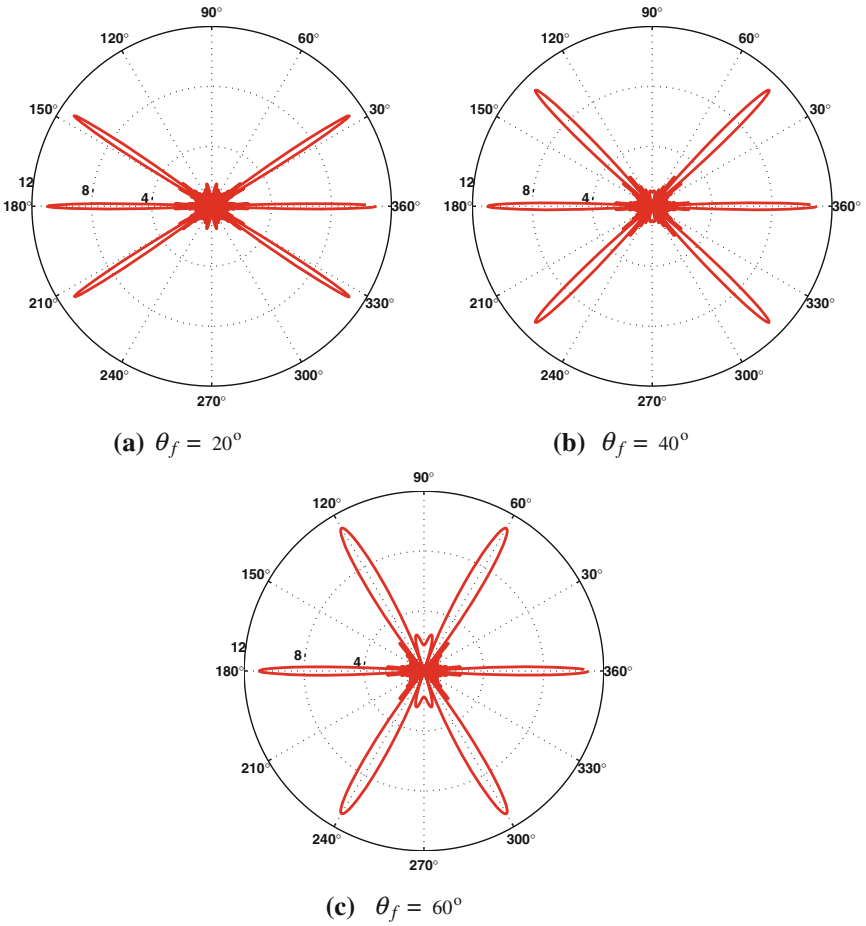

(a) $\theta_f = 20^o$ **(b)** $\theta_f = 40^o$

(c) $\theta_f = 60^o$

Fig. 9.13 Actuator directionality for selected steering angles

to be imposed in order to avoid the occurrence of many directionality lobes, corresponding to multiple directions of preferential radiation. A mathematical limitation for the existence of lobes at $p \neq 0$ is related to the fact that:

$$|\sin\theta| \leq 1 \tag{9.49}$$

which leads to the following condition:

$$\frac{p\pi c_p}{\omega d} = \frac{p\pi\lambda}{d} \leq 1 \tag{9.50}$$

where $\lambda = \frac{2\pi c_p}{\omega}$ is the wavelength corresponding to excitation frequency ω. Another condition consists in imposing the existence of a single beaming angle for $p \neq 0$.

This is enforced by imposing the requirement that:

$$\frac{p\pi c_p}{\omega d} = \frac{p\pi\lambda}{d} \geq \frac{1}{2} \tag{9.51}$$

If this condition is not satisfied, a peak would occur at p as well as at integer multiples of p up to the order for which condition in Eq. 9.50 is no longer satisfied. Equations 9.50 and 9.53 can be translated as the following conditions for the wavelength:

$$\frac{d}{p} < \lambda \leq \frac{2d}{p} \tag{9.52}$$

which lead to the following restrictions on the beaming angle:

$$30^o < \theta \leq 90^o \tag{9.53}$$

Within these two limit angles, every value can be obtained through proper selection of frequency ω and the corresponding value of wavelength. The excitation frequency corresponding to a desired beaming direction θ_b (under the limitations expressed in Eq. 9.53 is given by:

$$\omega_b = \frac{c_P d}{p\pi} \sin\theta_b \tag{9.54}$$

Examples of directivity plots corresponding to excitation at selected frequencies corresponding to selected beaming angles are shown in Fig. 9.14. The plots demonstrate the ability of the considered strategy to allow directional scanning through a sweep in the excitation frequency. The results in figures also highlight the main drawbacks of this strategy:

1. A beam at $\theta = 0$ always occurs regardless of the excitation frequency.
2. The aperture of the array is limited to the angular range $[-30^o, 30^o]$.
3. Within the angular aperture, the array produces two beams at $\pm\theta_b$.

The resolution of these problems requires proper signal processing tools, and/or the development of more complex array topologies which eliminate the $\theta = 0$ radiation, the limited angular aperture of the array, and possibly resolve the issue of double beaming at $\pm\theta_b$. Some of these issues can for example be addressed through the extension of this concept to two-dimensional array topologies described in the next section.

9.4 Two Dimensional Arrays for Frequency Based Beam Steering

The effective interrogation of the health of a structural component often requires sensors and actuators with the ability to perform directional scanning. This

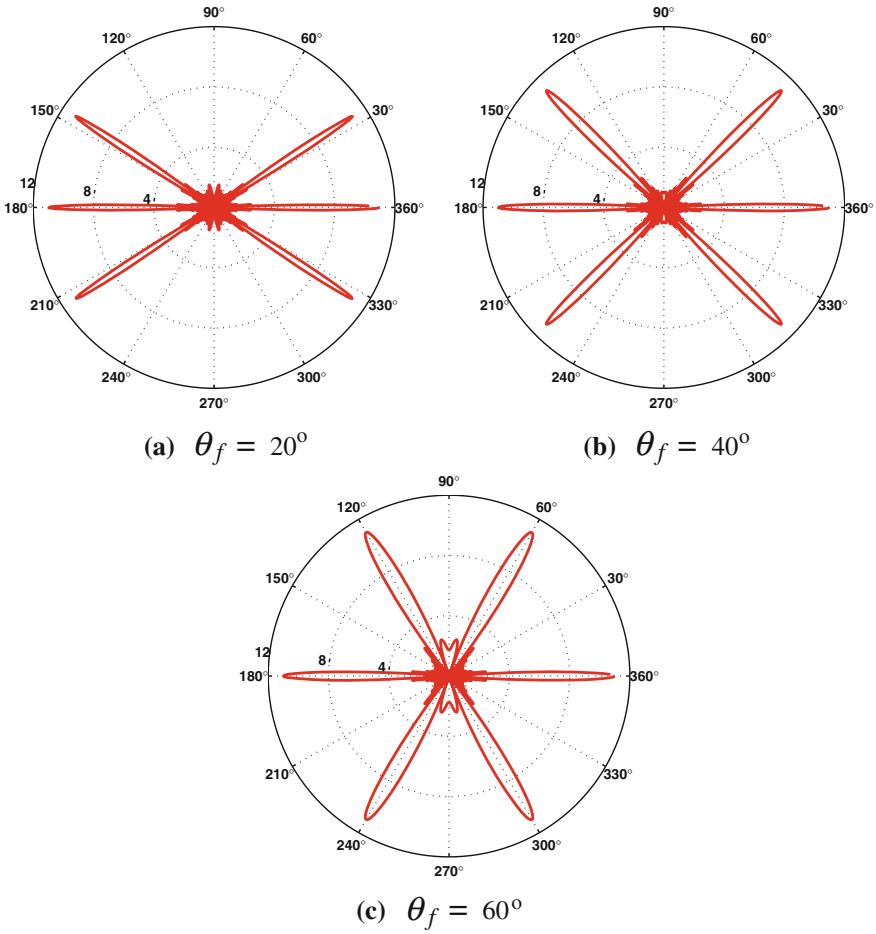

(a) $\theta_f = 20^o$ (b) $\theta_f = 40^o$

(c) $\theta_f = 60^o$

Fig. 9.14 Actuator directionality for selected steering angles

enhances the sensitivity of the inspection and simplifies the determination of the location of damage [16, 17, 25]. Wave steering through phased arrays is a well-established technique, used extensively in ultrasonic imaging for medical as well as NDE applications [3, 10, 15, 24–26]. Recent research has investigated the application of piezoelectric phased arrays for guided waves-based structural health monitoring [25]. Promising results demonstrate the potential benefits of beam steering. However, an underlying limitation is associated with the need to excite the array components individually, which implies hardware and software complexity.

The second beam steering strategy discussed in the previous section exploits interference phenomena generated by the spatial periodicity of the array and the simultaneous activation of its components. Such interference phenomena produce

waves with frequency dependent directional characteristics, which allow directional scanning to be performed simply through a frequency sweep. The need for beam-forming algorithms and associated hardware is thus avoided. Effective focusing and steering can be controlled and significantly enhance through the use of two-dimensional arrays of sources, which are arranged according to specific spatial topologies. Spatially periodic piezoelectric actuators can be also exploited for tuning the excitation to a specific wave mode [3, 26], and therefore are able to combine mode tuning with beam steering capabilities in a single device. The concept is first illustrated for the case of SV waves in a membrane-like medium, which can be treated through a simple mathematical formulation and does not introduce the complexity associated with multi-modal generation and propagation. The preliminary analysis is subsequently extended to the case of guided waves in homogeneous, isotropic plates, excited by a periodic array of piezoelectric discs. The analysis is supported by the analytical prediction of the plate response due to excitation of a single, circular piezoelectric disc and of multiple sources periodically bonded to the plate surface. The directionality of the array and its mode tuning capabilities are investigated through the analysis of the plate dispersion characteristics and of the excitation distribution in wavenumber space. Subsequently, the response of the plate resulting from the harmonic excitation of the array is predicted to demonstrate its ability to focus the plate response in directions which depend on the excitation frequency. The directivity of the array is maintained in the presence of multiple wave modes, which suggests that the proposed beam steering strategy may be a cost effective solution to achieve scanning capabilities for guided wave inspection of plate-like structures.

9.4.1 Application to SV Waves in a Membrane

The concept to be explored can be illustrated for the case of SV waves (Shear Vertical polarized waves) propagating in an isotropic, two-dimensional elastic medium, which is excited by a generic loading distribution. The governing equation is:

$$\mu(\nabla^2 u_3 + f_3) = \rho \ddot{u}_3 \tag{9.55}$$

where μ, ρ respectively denote the shear modulus and the density of the domain, $u_3 = u_3(x_1, x_2, t)$ is the out-of-plane displacement, while $f_3 = f_z(x_1, x_2, t)$ defines the loading distribution. In here and in the following developments, the plate geometry and its state of motion are described in terms of a reference frame x_1, x_2, x_3, with x_1, x_2 defining the plane of the structure. Under the assumption of harmonic load at frequency ω, $f_3(x_1, x_2, t) = f_3(x_1, x_2, \omega)e^{-j\omega t}$, Eq. 9.55 becomes:

$$\nabla^2 u_3 - k^2 u_3 = -f_3 \tag{9.56}$$

where $k^2 = \omega^2/c_s^2$ is the wavenumber, $c_s^2 = \mu/\rho$ is the phase velocity of the SV waves, and $u_3(x_1, x_2, t) = u_3(x_1, x_2, \omega)e^{-j\omega t}$.

The solution of Eq. 9.56 can be formally obtained through the application of the two-dimensional Fourier transform (FT) to displacements and force distribution. Application of the FT to Eq. 9.56 leads to:

$$(\xi_1^2 + \xi_2^2 - k^2)\hat{u}_3 = \hat{f}_3 \tag{9.57}$$

which can be solved in terms of the unknown displacement transform, to obtain:

$$\hat{u}_3(\xi_1, \xi_2, \omega) = \frac{\hat{f}_3(\xi_1, \xi_2, \omega)}{\xi_1^2 + \xi_2^2 - k^2} \tag{9.58}$$

This relation illustrates how the displacement amplitudes appear dependent upon two main factors: (1) the structure's behavior, and (2) the actuator's behavior as a function of the excitation frequency. Following the approach described in [15], the transformed displacement can be expressed in the following general form:

$$\hat{u}_3(\xi_1, \xi_2, \omega) = \mathcal{D}^{-1}(\xi_1, \xi_2, \omega)\hat{f}_3(\xi_1, \xi_2, \omega) \tag{9.59}$$

where $\mathcal{D}(\xi_1, \xi_2, \omega)$ explicitly denotes the contribution of the structure under consideration. The response of more complex structures due to a generic surface force distribution can be represented in the same form, whereby the expression of $\mathcal{D}(\xi_1, \xi_2, \omega)$ is defined by the differential operator corresponding to the governing equation of the medium under consideration. Equation 9.59 also indicates that maximum displacement amplitudes are obtained for excitation frequencies ω whose corresponding wavenumber k maximizes both $\mathcal{D}^{-1}(\xi_1, \xi_2, \omega)$ and $\hat{f}_3(\xi_1, \xi_2, \omega)$. The first term is clearly maximized when:

$$\mathcal{D}(\xi_1, \xi_2, \omega) = 0 \tag{9.60}$$

which corresponds to the dispersion relation of the domain under consideration, in this case $\mathcal{D}(\xi_1, \xi_2, \omega) = \xi_1^2 + \xi_2^2 - k^2$. In conclusion, the maximum output is obtained at the wavenumber, and associated frequency, corresponding to the intersection between the medium's dispersion relation, and the locus in the ξ_1, ξ_2 plane defining the maximum of $\hat{f}_3(\xi_1, \xi_2, \omega)$. This simple consideration is at the basis of the design procedure to be undertaken, and it is based on criteria introduced for the design of comb-type actuators for mode tuning as presented for example in [15, 21].

9.4.1.1 Rectangular Two Dimensional Periodic Array of Point Sources

The concept described above can be illustrated through the application of the analysis to the simple case of a two-dimensional (2D) periodic array of point sources. The force distribution in this case is expressed as:

$$f(x_1, x_2, \omega) = f_0(\omega) \sum_{n=-N}^{N} \sum_{m=-M}^{M} \delta(x_1 - nd_1)\delta(x_2 - md_2) \tag{9.61}$$

where, $f_0(\omega)$ denotes the amplitude of the excitation at frequency $\omega, 2N + 1,\ 2M + 1$ respectively define the number of sources along the x_1, x_2 directions, while d_1, d_2 denote the spacings, or the periods, of the array in the two directions. Application of the 2D FT in space yields:

$$\hat{f}(\xi_1, \xi_2, \omega) = f_0 \sum_{n=-N}^{N} \sum_{m=-M}^{M} e^{jn\xi_1 d_1} e^{jm\xi_2 d_2} \tag{9.62}$$

whose expression can be simplified to obtain:

$$\hat{f}(\xi_1, \xi_2, \omega) = f_0 \frac{\sin\left(\frac{(2N+1)\xi_1 d_1}{2}\right) \sin\left(\frac{(2M+1)\xi_2 d_2}{2}\right)}{\sin\left(\frac{\xi_1 d_1}{2}\right) \quad \sin\left(\frac{\xi_2 d_2}{2}\right)} \tag{9.63}$$

This expression is maximized when:

$$\xi_{1_p} = p\frac{2\pi}{d_1}, \xi_{2_q} = q\frac{2\pi}{d_2} \tag{9.64}$$

where p, q are integers. Equation 9.64 identifies a pair of values in wavenumber space, whose substitution in the dispersion relation for the medium identifies a corresponding value of frequency:

$$\omega_{p,q} = 2\pi c_s \sqrt{\left(\frac{p}{d_1}\right)^2 + \left(\frac{q}{d_2}\right)^2} \tag{9.65}$$

which in turns defines preferential directions of radiation for the source array. In fact, letting $\xi_1 = \xi \cos\theta$ and $\xi_2 = \xi \sin\theta$, with θ defining the direction of the wave vector ξ, and taking the ratio of the two equations in Eq. 9.64, provides a value for the direction of maximum direction corresponding to excitation at frequency $\omega_{p,q}^M$. This expression is:

$$\tan(\theta_{p,q}) = \frac{qd_1}{pd_2} \tag{9.66}$$

Equations 9.64 and 9.66 show that the proper selection of the frequency of excitation of the array components can be exploited to achieved preferential radiation of the array in directions, which are defined by the periodicity d_1, d_2 and by the selected integers' pair p, q. This concept and its implication to the design of actuators with frequency-dependent directionality can be illustrated by considering the 7×7 array shown in Fig. 9.15. The array comprises of point sources with non-dimensional periods $d_1/c_s = 0.5$ and $d_2/c_s = 0.4$. The directionality of the array can be expressed as:

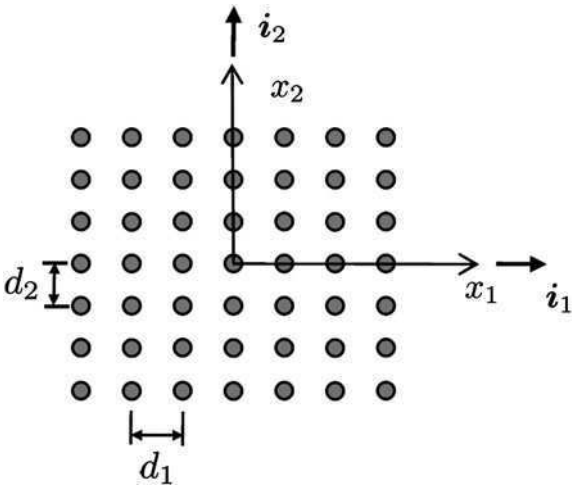

Fig. 9.15 Rectangular point source array

$$d(\theta, p, q) = \frac{\sin\left(\pi\Omega_{p,q}\cos\theta(2N+1)\right)}{\sin\left(\pi\Omega_{p,q}\cos\theta\right)}\frac{\sin\left(\pi\Omega_{p,q}\sin\theta(2M+1)\right)}{\sin\left(\pi\Omega_{p,q}\sin\theta\right)} \tag{9.67}$$

where Ω defines a non-dimensional values of frequency

$$\Omega = \omega d_1/2\pi c_s. \tag{9.68}$$

As explicitly indicated, the directionality of the array depends on the excitation frequency, which in turn is defined by the integer pair p, q according to Eq. 9.77. Examples of directionality plots for various values of integer pairs and corresponding frequencies are presented in Fig. 9.16. The results show how the proper selection of the excitation frequency can be used to obtain different directional characteristics of the array. In particular, simultaneous excitation of all the array components at $\Omega_{p,q} = 2\pi, 2.5\pi$ produces strong radiations respectively along the horizontal and vertical directions, while excitation at $\Omega_{p,q} = 3.2\pi$ corresponds to main lobes at $\theta_{p,q} = \pm 51^o$ and $\theta_{p,q} = \pm 128^o$. This last result shows how proper design of the array must include considerations which reduce the number of lobes appearing for a given value of the excitation frequency, so that proper scanning capabilities can be achieved, and motivates the need for the formulation of design strategies leading to a minimum number of principal lobes for a given excitation frequency. A first attempt is presented in the following section, while a dedicated effort in this direction is currently underway. The predictions obtained through the analysis of the dispersion relations and their intersection with the loci of maximum actuator output can be validated with the response of the considered domain computed for the considered excitation frequencies. The expression for the wave field generated by the source array can be obtained analytically through a straightforward extension of the formulation for the single point source presented

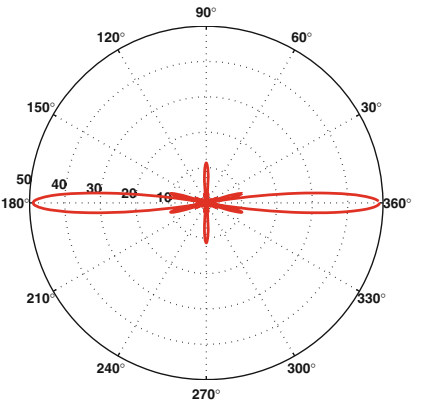

(a) $\Omega_{p,q} = 2\pi, \theta_{p,q} = 0^o, 180^o$

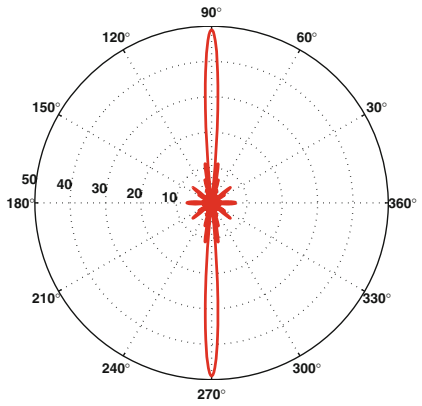

(b) $\Omega_{p,q} = 2.5\pi, \theta_{p,q} = \pm 90^o$

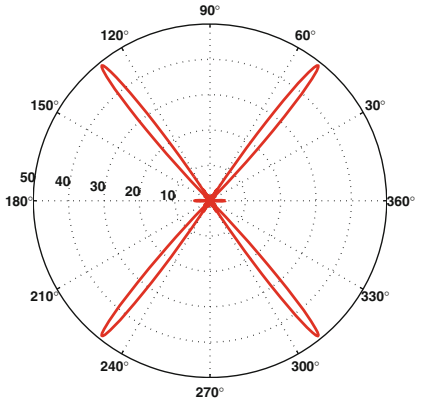

(c) $\Omega_{p,q} = 3.2\pi, \theta_{p,q} = \pm 51^o, 128^o$

Fig. 9.16 Rectangular array directivity at different excitation frequencies

in [14]. The displacement at location x_1, x_2 due to a point force at location x_{1_n}, x_{2_m} of amplitude f_0 and frequency ω can be expressed as:

$$u_3(\boldsymbol{r}, \omega) = f_0 \, \mathcal{G}(\boldsymbol{r}, \boldsymbol{r}_{n,m}, \omega) \tag{9.69}$$

where $\boldsymbol{r} = x_1 \boldsymbol{i}_1 + x_2 \boldsymbol{i}_2$ is a vector defining the response location, $\boldsymbol{r}_{n,m} = x_{1_n} \boldsymbol{i}_1 + x_{2_m} \boldsymbol{i}_2$ is the source location, and $\mathcal{G}$ is the Green's function defining the response to a unit source, which is given by:

$$\mathcal{G}(\boldsymbol{r}, \boldsymbol{r}_{n,m}, \omega) = \int_{-\infty}^{+\infty} \int_{-\infty}^{+\infty} \frac{e^{-j[\xi_1(x_1 - x_{1_n}) + \xi_2(x_2 - x_{1_m})]}}{\xi_1^2 + \xi_2^2 - k^2} dx_1 dx_2 \tag{9.70}$$

which upon integration gives:

$$\mathcal{G}(\boldsymbol{r}, \boldsymbol{r}_{n,m}, \omega) = j\pi^2 H_0^{(1)}(kR) \tag{9.71}$$

where $H_0^{(1)}$ is the Hankel function of the first kind and order 0, while $R = |\boldsymbol{r} - \boldsymbol{r}_{n,m}|$ denotes the distance between source and point under consideration. Equation 9.69 can be readily extended to superimpose the effects of the various sources of the array. This gives:

$$u_3(\boldsymbol{r}, \omega) = f_0(\omega) \sum_{n=1}^{N} \sum_{m=1}^{M} \mathcal{G}(\boldsymbol{r}, \boldsymbol{r}_{n,m}, \omega) \tag{9.72}$$

Equation 9.72 is applied to evaluate the response of the D domain when the array is excited at the frequency values considered in the previous section. The estimated response amplitudes are shown in Fig. 9.17, which confirms the prediction regarding directionality of the actuator array and its frequency dependency.

9.4.1.2 Quadrilateral Array of Point Sources

The basic configuration presented above can be modified through a simple change in coordinates, through which the frequency dependent directionality of the actuator can be improved. The objective is to increase the number of combinations of in-plane wavenumbers and corresponding frequencies, which uniquely define a preferential direction of radiation for the actuator. The discussion presented in the previous section can be generalized by considering an array of sources located according to a quadrilateral topology defined by the unit vectors $\boldsymbol{e}_1, \boldsymbol{e}_2$, the associated angles α, β, and the periods d_1, d_2. A schematic of the quadrilateral array is presented in Fig. 9.18. The corresponding force distribution can be expressed as:

$$f(x_1, x_2, \omega) = f_0(\omega) \sum_{n=-N}^{N} \sum_{m=-M}^{M} \delta(x_1 - x_{1_{n,m}}) \delta(x_2 - x_{2_{n,m}}) \tag{9.73}$$

where $x_{1_{n,m}}, x_{2_{n,m}}$ denote the coordinates of the n, m-th actuator of the array. The spatial FT of the force distribution defined in Eq. 9.73 is given by:

$$\hat{f}(\xi_1, \xi_2, \omega) = f_0(\omega) \sum_{n=-N}^{N} \sum_{m=-M}^{M} e^{jnd_1(\xi_1 \cos\alpha + \xi_2 \sin\alpha)} e^{jmd_2(\xi_1 \cos\beta + \xi_2 \sin\beta)} \tag{9.74}$$

which can be simplified as follows:

$$\hat{f}(\xi_1, \xi_2, \omega) = f_0(\omega) \frac{\sin((2N+1)d_1(\xi_1 \cos\alpha + \xi_2 \sin\alpha))}{\sin(d_1(\xi_1 \cos\alpha + \xi_2 \sin\alpha))} \frac{\sin((2M+1)d_2(\xi_1 \cos\beta + \xi_2 \sin\beta))}{\sin(d_2(\xi_1 \cos\beta + \xi_2 \sin\beta))} \tag{9.75}$$

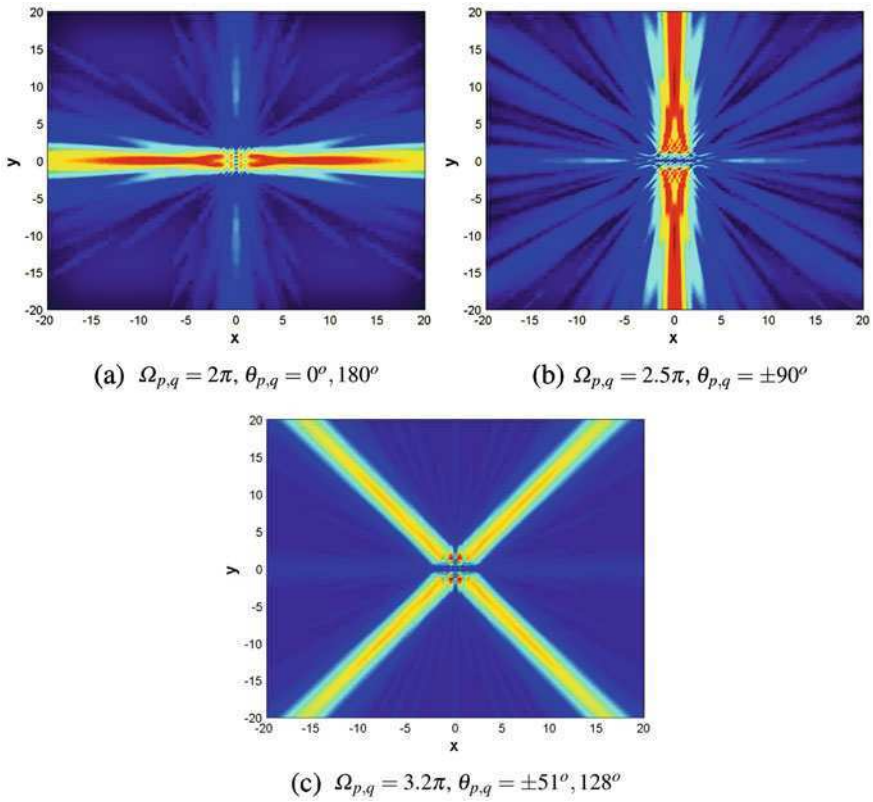

Fig. 9.17 Displacement amplitudes resulting from excitation at selected frequencies

The wavenumber values which maximize the actuators output are obtained as solutions for the following system of algebraic equations defined by a selected integer pair p, q:

$$\begin{aligned} \xi_1 \cos\alpha + \xi_2 \sin\alpha &= \frac{2p\pi}{d_1}, \\ \xi_1 \cos\beta + \xi_2 \sin\beta &= \frac{2q\pi}{d_2} \end{aligned} \tag{9.76}$$

As before, the corresponding frequency $\omega_{p,q}$ is obtained upon substitution of the wavenumber values in the dispersion relation for the medium, which in this case gives:

$$\omega_{p,q} = 2\pi c_s \sqrt{\left(\xi_{1_{p,q}}\right)^2 + \left(\xi_{2_{p,q}}\right)^2} \tag{9.77}$$

The directionality of the array corresponding to excitation at one the frequencies $\omega_{p,q}$ of maximum actuator output can be expressed as:

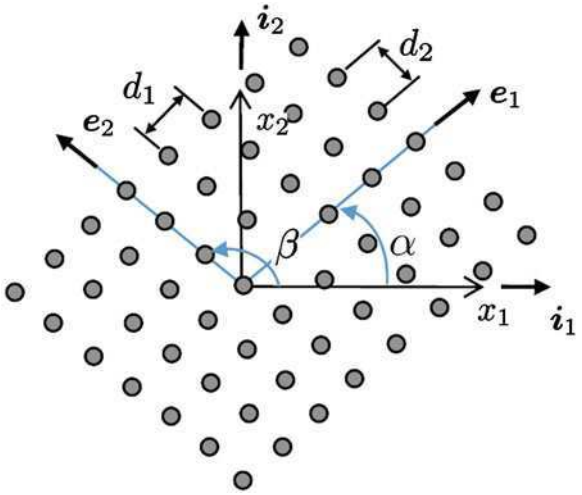

Fig. 9.18 Quadrilateral point source array

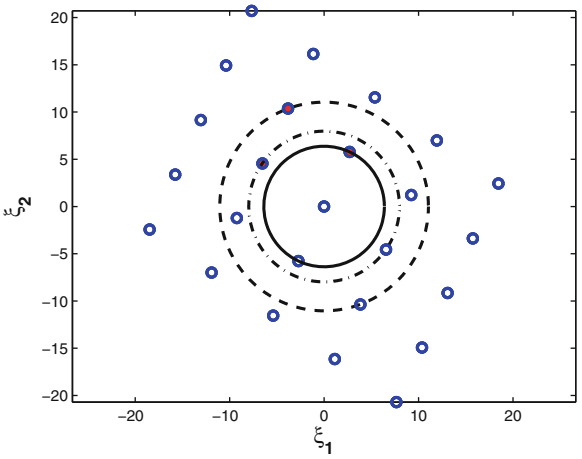

Fig. 9.19 Location of force maxima in the wavenumber space, and intersection with dispersion relation at selected values of frequency ($\Omega_{p,q} = 1.01\pi$ *solid line*, $\Omega_{p,q} = 1.26\pi$ *dashed line*, $\Omega_{p,q} = 1.75\pi$ *dash-dotted line*)

$$d(\theta,p,q) = \frac{\sin\left(2\pi\Omega_{p,q}(2N+1)(\cos\theta\cos\alpha+\sin\theta\sin\alpha)\right)}{\sin\left(2\pi\Omega_{p,q}(\cos\theta\cos\alpha+\sin\theta\sin\alpha)\right)} \frac{\sin(2\pi\Omega_{p,q}(2M+1)\frac{d_2}{d_1}(\cos\theta\cos\beta+\sin\theta\sin\beta))}{\sin(2\pi\Omega_{p,q}\frac{d_2}{d_1}(\cos\theta\cos\beta+\sin\theta\sin\beta))} \tag{9.78}$$

where frequency is non-dimensionalized according to $\Omega = d_1\omega/c_s$. Results for a 7×7 array defined by the angles $\alpha = 55^o$ and $\beta = 165^o$ are shown in Figs. 9.19, 9.20 and 9.21. In Fig. 9.19, the locations of the wavenumber maxima defined by Eq. 9.76 are presented together with circles representing the cross-section of the dispersion relation at the frequencies $\omega_{p,q}$. This representation graphically illustrates the concept under investigation, whereby the intersection between the

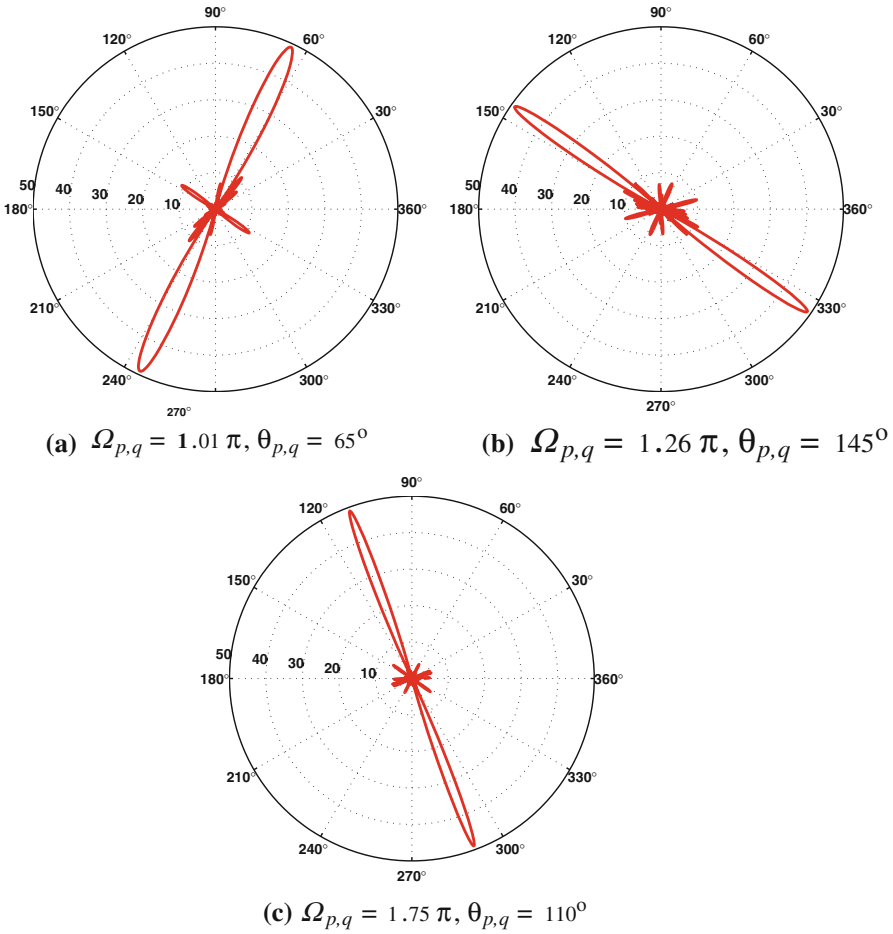

(a) $\Omega_{p,q} = 1.01\,\pi$, $\theta_{p,q} = 65^{\circ}$ **(b)** $\Omega_{p,q} = 1.26\,\pi$, $\theta_{p,q} = 145^{\circ}$

(c) $\Omega_{p,q} = 1.75\,\pi$, $\theta_{p,q} = 110^{\circ}$

Fig. 9.20 Actuator directionality at selected frequencies

dispersion relation at a given frequency with one of the maxima of the force distribution in wavenumber space leads to the maximum actuator output. Such intersection also defines a direction of preferential direction, which is given by $\tan(\theta_{p,q}) = \xi_{2_{p,q}}/\xi_{1_{p,q}}$, where $\xi_{1_{p,q}}, \xi_{2_{p,q}}$ denote the wavevector components of maximum radiation, as defined by the solution of Eq. 9.76. Directionality plots corresponding to the frequency values highlighted in Fig. 9.19 are presented in Fig. 9.20 to illustrate the frequency-dependent directionality obtained through the periodic array topology. Of note is the fact that the considered configuration, in contrast to the rectangular array design, leads to a broader set of combinations for which a single beaming angle is achieved. The directional behavior of the actuator array is verified through the estimation of the harmonic response of the medium subjected to the simultaneous excitation of all the array components. Examples of

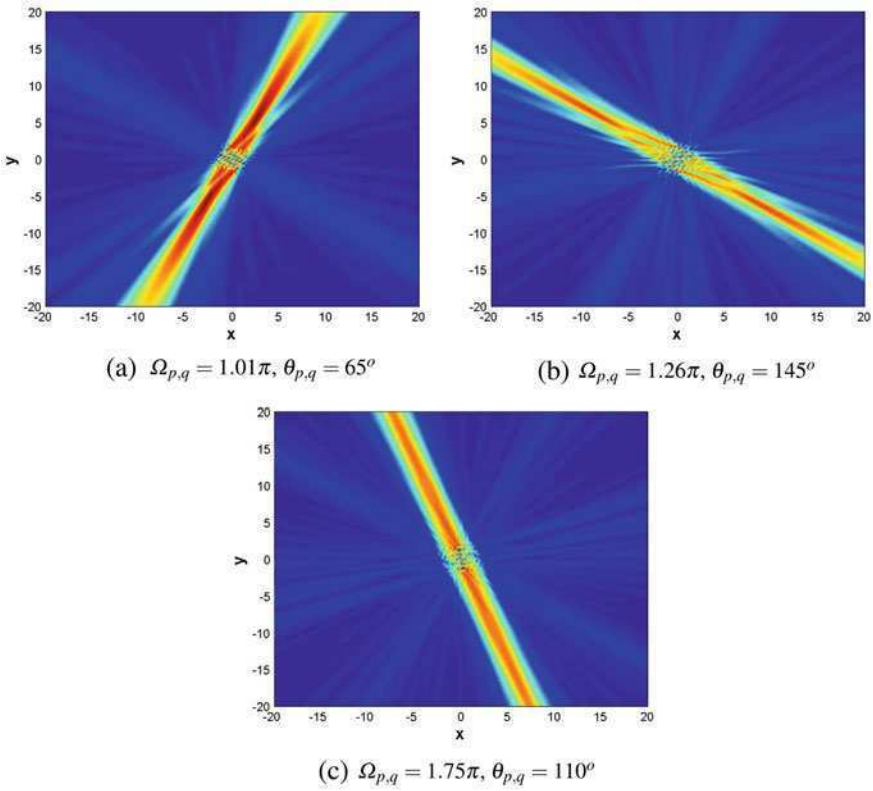

Fig. 9.21 Displacement amplitudes resulting from excitation at selected frequencies

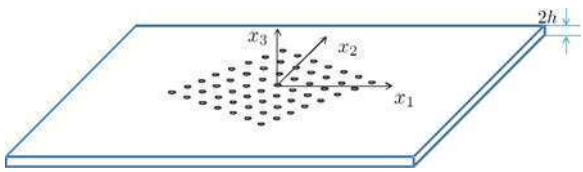

Fig. 9.22 Configuration of plate with piezo array

harmonic response computed through the procedure described in the previous section for selected frequencies are presented in Fig. 9.21.

9.4.2 Application to Guided Waves in Thin Plates

The concept investigated above is applied to the directional excitation of guided waves in plate structures. The considered configuration features an array of surface mounted piezoelectric discs as depicted in Fig. 9.22. The discs are operated in

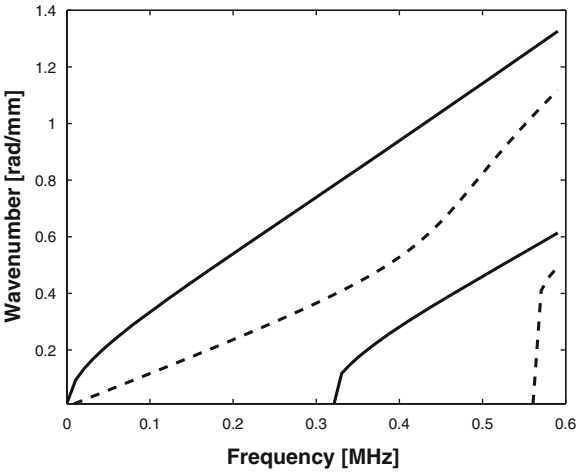

Fig. 9.23 Dispersion relation of the plate: detail of frequency range of excitation (Asymmetric modes *solid line*, symmetric modes *dashed line*)

shear and excite Lamb waves by applying a surface traction distribution corresponding to the in-plane shape of each actuator disc and to the topology of the array. The extension of the concept previously illustrated for the case of SV waves in an elastic medium requires the analysis of the dispersion properties of the plate and their matching with the array topology. A complicating factor in this regard is the multi-modal nature of wave propagation in the plate, which causes several modes to be excited at a given frequency. A detailed discussion devoted to this aspect illustrates the validity of the concept of directional excitation for a multi-modal waveguide and highlights the opportunity for it to be combined with mode tuning capabilities. The prediction of the dispersion analysis are subsequently verified through the computation of the plate response resulting from the piezoelectric discs array, which is based on the analytical formulation also presented in what follows.

9.4.2.1 Plate and Array Configuration

The analysis considers an aluminum plate (Young's modulus $E = 71$ GPa, Poisson's ration $v = 0.33$ density $\rho = 2700$ kg/m^3) of thickness $2h = 5$ mm. The dispersion relations for the plate are shown in Fig. 9.23. For simplicity, the excitation frequency range is limited by an upper bound coinciding with the cut-off frequency for the A_1 mode, in this case approximately at 0.33 MHz, so that only two modes are simultaneously excited in the plate. A 7×7 array of piezoelectric disc arranged according to a quadrilateral topology is considered. The array angles are $\alpha = 55^o$ and $\beta = 165^o$, and the periods are $d_1 = 0.043$ m $d_2 = 0.035$ m. The choice of the array configuration is based the preliminary results presented in the previous section, and on trial and error studies performed to identify the array

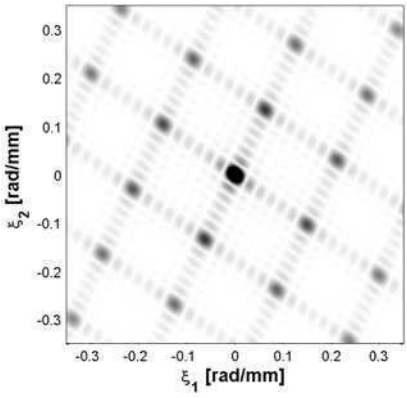

Fig. 9.24 Amplitude of $\hat{F}_1(\xi_1, \xi_2)$ for the considered array

configuration providing a large combination of frequency-radiation direction pairs within the limitations of the considered frequency range.

9.4.2.2 Dispersion Analysis for Directional Excitation of Lamb Waves

Each array component applies a distribution of shear stresses on the plate surface, which can be described as follows:

$$\begin{aligned}\sigma_{31}(x_1, x_2, t) &= \tau(t) F_1(x_1, x_2) = \sum_{n,m} F_1^{n,m}(x_1, x_2) \\ \sigma_{32}(x_1, x_2, t) &= \tau(t) F_2(x_1, x_2) = \tau(t) \sum_{n,m} F_2^{n,m}(x_1, x_2) \\ \sigma_{33}(x_1, x_2, t) &= 0\end{aligned} \tag{9.79}$$

where $\tau(t)$ defines the time history of the applied excitation, while $F_1^{n,m}(x_1, x_2), F_2^{n,m}(x_1, x_2)$ define the contribution to the surface stresses of the array component n, m. In this study, each actuator is considered to be a circular piezoelectric disc of radius a, so that the functions F_1, F_2 can be reasonably expressed as [19]:

$$\begin{aligned}F_{1_{n,m}}(r^{(n,m)}, \theta^{(n,m)}) &= \delta(r^{(n,m)} - a) \cos\theta^{(n,m)} \\ F_{2_{n,m}}(r^{(n,m)}, \theta^{(n,m)}) &= \delta(r^{(n,m)} - a) \sin\theta^{(n,m)}\end{aligned} \tag{9.80}$$

where $r^{(n,m)}, \theta^{(n,m)}$ define a set of polar coordinates with origin at the center of the component n, m. Simple coordinate transformations can be applied to transform the local polar coordinates with the global reference system x_1, x_2 on the plane of the plate. The functions F_1, F_2 in the wavenumber space (denoted $\hat{F}_1, \hat{F}_2$) are evaluated through a combination of numerical and analytical procedures. The resulting amplitude plot for the function $\hat{F}_1$ is presented in Fig. 9.24, in the form of contour plots with scale of intensity varying from white to black. The plot,

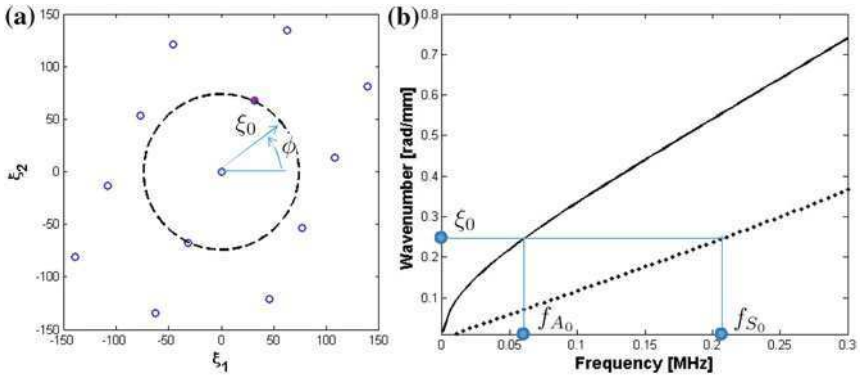

Fig. 9.25 Dispersion analysis for selective directionality and mode tuning

corresponding to the array configuration described above (see Fig. 9.18), shows that maxima in the wavenumber domain occur at locations, which are conveniently approximated by the formulas presented in the previous section for an array of point sources (see Eq. 9.76). The amplitude plot for $\hat{F}_2$ show a similar behavior and is therefore omitted for the sake of brevity. The analysis of the dispersion relations has the objective of determining the excitation frequency leading to strong radiation directionality for the array. This is achieved by identifying a wavenumber ξ_0 defining the radius of a circle intersecting a set of peaks of the excitation distribution in wavenumber space. The circle, in the case of an isotropic plate, corresponds to the cross section of the dispersion relation for the given wavenumber ξ_0. The associated frequency values are obtained by evaluating the dispersion relations for the corresponding wavenumber. Within the considered frequency range, this procedure leads to two frequencies f_{A_0}, f_{S_0}, respectively associated with symmetric (S_0) and anti-symmetric (A_0) modes. The process is schematically represented in Fig. 9.25, which shows how the selection of f_{A_0} or f_{S_0} determines both the directionality of the array radiation, which occurs at the angle ϕ defined by the wavevector components in Fig. 9.25a, and the mode (symmetric versus anti-symmetric) excited in the plate. Results for the considered plate/array configuration are shown in Figs. 9.26 and 9.27. Excitation at 16, 28, and 36 kHz for example (see Fig. 9.26) produces A_0 modes of wavenumbers equal to $\xi_0 = 0.23, 0.34, 0.40$ rad/mm, which also correspond to preferential radiations at three different angles, namely $\phi = 65°, 8°, 70°$. Same radiation angles and same wavenumbers can be induced in the plate through excitation at $f = 128, 185, 220$ kHz, when S_0 modes are mostly produced (see Fig. 9.27). The generation of two wave modes for excitation at any one frequency is particularly clear in the case of S_0 mode tuning as presented in Fig. 9.27, where circles corresponding to the S_0 and A_0 wavenumbers are depicted respectively as dashed and solid lines. The A_0 mode excitation in this case occurs at much higher wavenumber values, which are typically associated with significantly weaker radiation efficiency of the actuator, as indicated by the decrease in the peaks' amplitude for increasing wavenumbers.

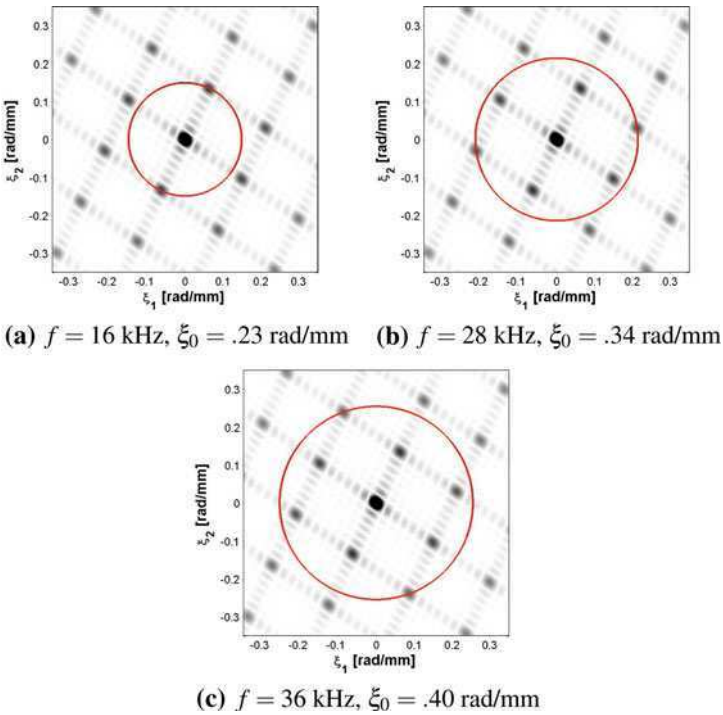

(a) $f = 16$ kHz, $\xi_0 = .23$ rad/mm **(b)** $f = 28$ kHz, $\xi_0 = .34$ rad/mm

(c) $f = 36$ kHz, $\xi_0 = .40$ rad/mm

Fig. 9.26 Directional characteristics with A_0 tuning

In addition, the A_0 mode circle does not intersect specific peaks of the forcing function distribution, and therefore is not associated with a preferential direction of radiation. In other words, mode tuning at S_0 generates low amplitude A_0 modes, which do not interfere with the directional characteristics of the array. Similar considerations can be made in the case of A_0 tuning Fig. 9.26, where the circles corresponding to the S_0 modes are too small to be drawn effectively. In addition, the large difference in the propagation speeds for the two modes naturally decouples their contributions and therefore limits their potential interaction. Table 9.2 lists a number of radiation angles and corresponding excitation frequencies for A_0 and S_0 mode tuning. The response due to an array of circular piezo-electric discs can be computed simply through linear superposition. The response for a single disc is first computed in a local reference system with origin at the center of the disc as in the previous formulation. A change in coordinate then transforms the response into a global coordinate frame, where the contributions of the array components are superimposed. The array configuration considered is the one presented above with a total of 49 elements arranged according to a quadrilateral topology Fig. 9.18. The results from the dispersion analysis in Sect. 5.3.5 guide the selection of excitation frequencies to be applied to simultaneously achieve mode tuning as well as directional radiation. Results for asymmetric mode tuning and a selected combinations of

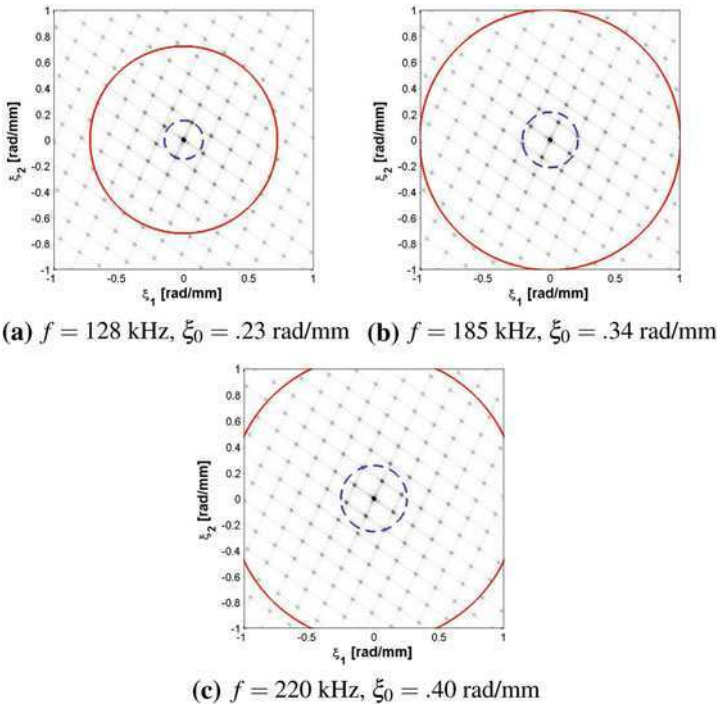

(a) $f = 128$ kHz, $\xi_0 = .23$ rad/mm **(b)** $f = 185$ kHz, $\xi_0 = .34$ rad/mm

(c) $f = 220$ kHz, $\xi_0 = .40$ rad/mm

Fig. 9.27 Directional characteristics with S_0 tuning

frequency and radiation directions are illustrated in Fig. 9.28, which present the amplitude of the out-of-plane response of a 2×2 m plate featuring the considered array mounted at its center. The results clearly show the directional characteristics of radiation at the considered frequencies, and confirm the direction of radiation predicted through the dispersion analysis previously presented. The results for S_0 mode tuning presented in Fig. 9.29 show identical behavior, which is induced however at higher frequencies as a result to the tuning of the excitation to the specific wave propagation mode. Also, it is a fact that the tuning capabilities of the actuator array minimize the interference of other modes, which are not necessarily directional, and which therefore do not prevent the directionality of the actuator to occur along the desired direction.

9.4.2.3 Plate Response Due to the Actuator Array: Narrow Band Burst Excitation

The directionality of the plate is also investigated in the presence of narrow-band burst inputs, which allows analyzing excitation configurations which are commonly used for structural inspection. The use of a sine burst simultaneously allow the spectrum of the input signal to be centered at a desired frequency, while

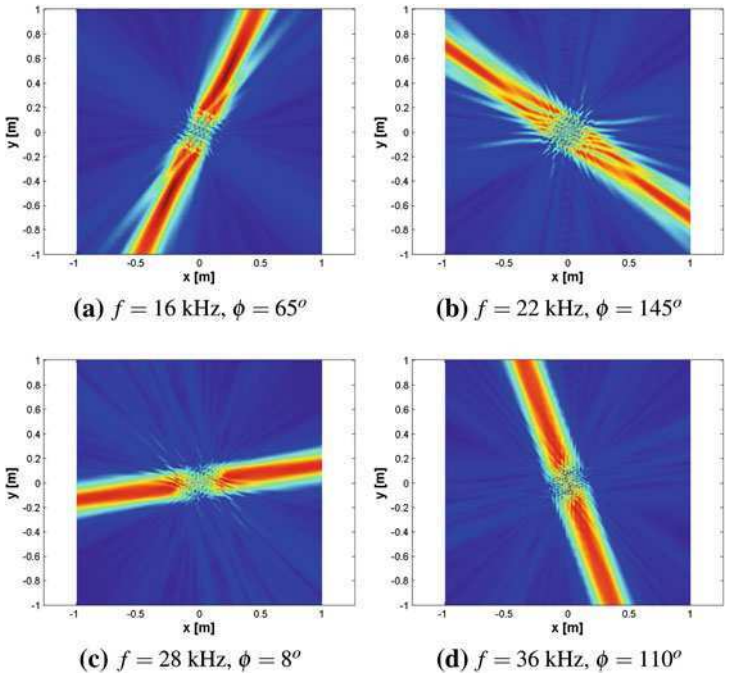

(a) $f = 16$ kHz, $\phi = 65^o$ **(b)** $f = 22$ kHz, $\phi = 145^o$

(c) $f = 28$ kHz, $\phi = 8^o$ **(d)** $f = 36$ kHz, $\phi = 110^o$

Fig. 9.28 Directional response for A_0 tuning

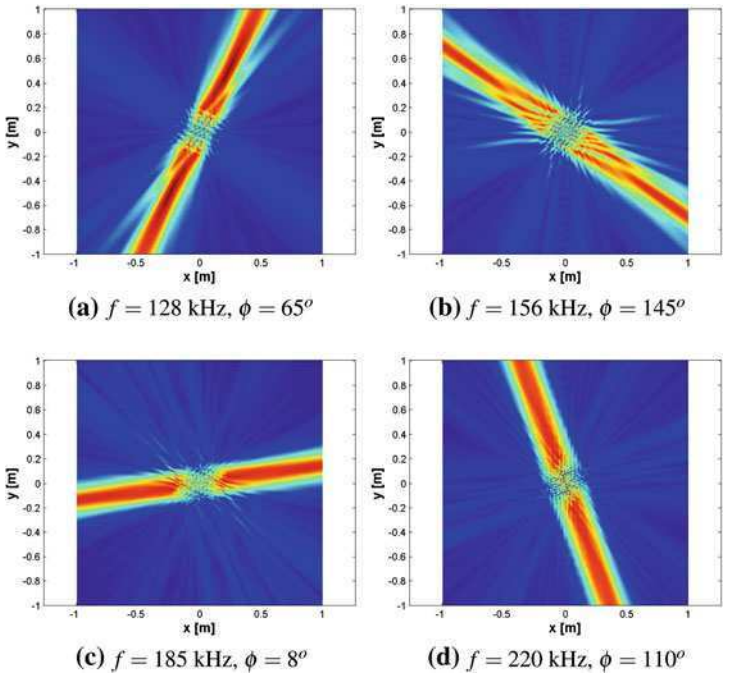

(a) $f = 128$ kHz, $\phi = 65^o$ **(b)** $f = 156$ kHz, $\phi = 145^o$

(c) $f = 185$ kHz, $\phi = 8^o$ **(d)** $f = 220$ kHz, $\phi = 110^o$

Fig. 9.29 Directional response for S_0 tuning

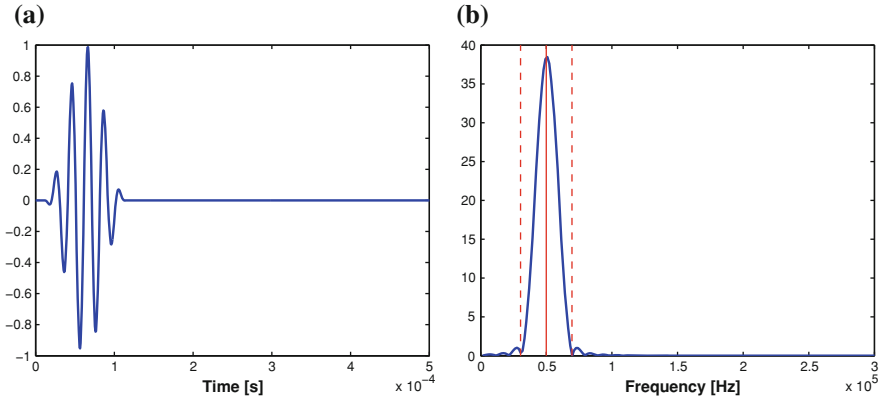

Fig. 9.30 Sine burst excitation and associated bandwidth

producing a transient wave which can be reflected by a structural discontinuity along its path. This assumes that the considered design is employed in a pulse-echo scheme, where a scan is performed by sweeping through a number of input frequencies thus producing wave propagation in the corresponding directions. Future studies of the proposed concept will assess the ability of the periodic array to image a defect through the considered beam forming configuration. The study presented in what follows consider a 5-cycle sine burst at selected frequencies. A typical signal and its frequency domain representation are shown in Fig. 9.30. Specifically, Fig. 9.30b highlights the bandwidth of excitation, which is considered equal to:

$$f \in \left[f_0 - \frac{2}{T_0},\ f_0 + \frac{2}{T_0} \right] \tag{9.81}$$

where f_0 is the center frequency, while T_0 is the duration of the signal. The representation of the bandwidth in the wavenumber domain is presented in Fig. 9.31, which shows the results obtained for center frequency $f_0 = 48$ kHz and duration T_0 corresponding to a 5 cycles, hanning modulated harmonic function. Figure 9.31 shows how the bandwidth of excitation must be selected so that it intersects a single pair of peaks corresponding to the excitation distribution in the wavenumber domain. This ensures that the directionality properties, previously illustrated for the case of a pure harmonic input, are preserved in the presence of a time-limited input. Figures 9.32 and 9.33 show snapshots of the plate response when the array is actuated by 5-cycle sine burst respectively at $f_0 = 16$ and $f_0 = 22$ kHz. The plate response clearly shows the presence of a wave packet which travels along the plate in the direction predicted by the dispersion analysis, identified according to the procedure illustrated in the previous section. For simplicity, the results show the response in the top portio of the plate, so that a single beam is observed. Results similar to those presented in Figs. 9.32 and 9.33 can be produced for all excitation frequencies and angles listed in Table 9.2.

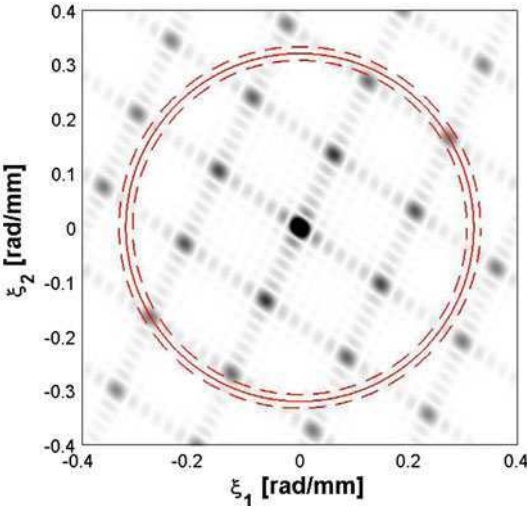

Fig. 9.31 Wavenumber content of a sine burst excitation (*solid line* center frequency, *dashed line* bandwidth limits)

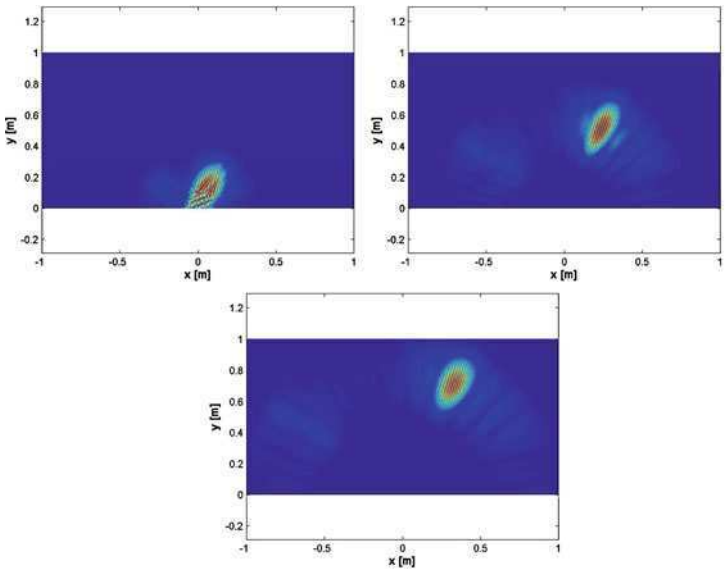

Fig. 9.32 Snapshots of directional response resulting from sine burst excitation at 16 kHz

9.5 Modeling of Lamb Wave Sensors

In this section, we present the equations that govern sensing of elastic waves (Lamb waves) through surface mounted patches. As in generation, the case of a patch of arbitrary shape is illustrated as a general framework for the subsequent illustration of the principles of directional sensing through properly shaped patches.

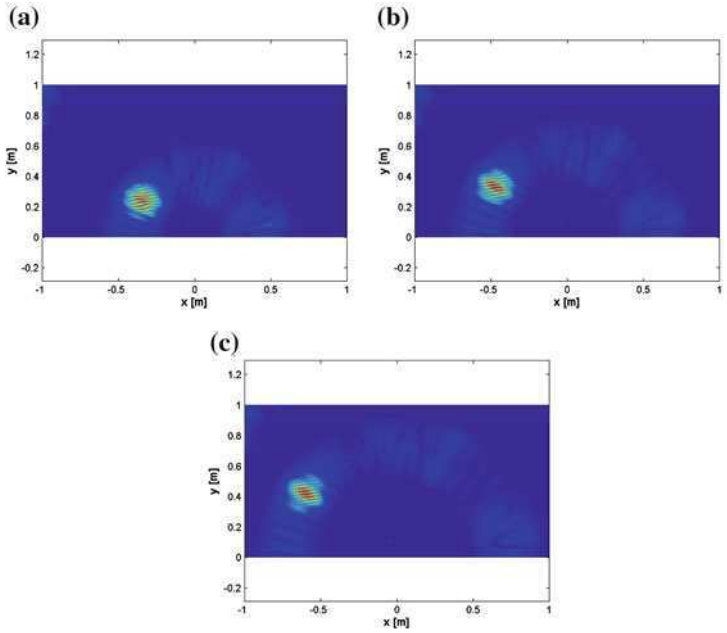

Fig. 9.33 Snapshots of directional response resulting from sine burst excitation at 22 kHz

Table 9.2 Radiation directions, excitation frequencies and mode tuning

ϕ [^{o}]	f_{A_0} [kHz]	f_{S_0} [kHz]	ξ_0 [rad/mm]
65	16	128	0.23
145	22	156	0.29
8	28	185	0.34
110	36	220	0.40
48	51	276	0.48

9.5.1 Plate Configuration and Piezoelectric Constitutive Relations

The system under consideration is illustrated in Fig. 9.34. The domain of interest consists of a mechanical structure (thin plate) on an open domain Ω and of a piezoelectric domain Ω_p of thickness t_P. The reference system used for the analysis is located at the mid-surface of the structure, with coordinates x_1, x_2 defining the plane of the structure.

The constitutive equations for the piezoelectric domain are expressed in Eq. 9.24, which hold over the domain of the structure covered by the piezoelectric patch, defined by $\boldsymbol{x} \in \Omega_P$, where $\boldsymbol{x} = x_1\boldsymbol{i}_1 + x_2\boldsymbol{i}_2$ denotes a position vector on the plane of the structure. It is here convenient to extend the validity of the piezoelectric constitutive relation to the entire domain of analysis Ω by introducing a functional $f(\boldsymbol{x})$ defined as:

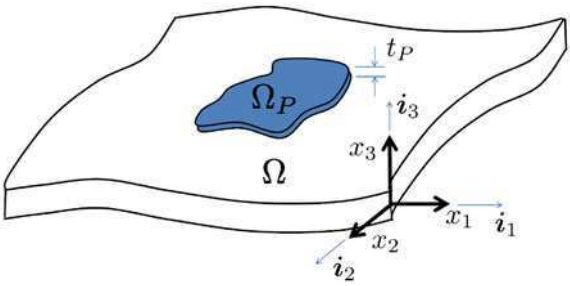

Fig. 9.34 Plate with arbitrarily shaped piezoelectric sensor bonded on the top surface, and considered coordinate system

$$\varphi(\boldsymbol{x}) = \begin{cases} 1, & \boldsymbol{x} \in \Omega_P \\ 0, & \boldsymbol{x} \in \Omega - \Omega_P \end{cases} \tag{9.82}$$

which describes the shape of the patch. A second function $\psi(\boldsymbol{x})$ is introduced to allow for different polarizations to be present within the piezoelectric domain. For simplicity, and in light of practicality, the case of alternating polarizations over specified sub-regions of Ω_P is considered, so that the function $\psi(\boldsymbol{x}) = \pm 1, \boldsymbol{x} \in \Omega_P$ depending on the polarization distribution.

Accordingly, Eq. 9.24 can be rewritten as:

$$\begin{Bmatrix} \sigma \\ \boldsymbol{D} \end{Bmatrix} = \varphi(\boldsymbol{x}) \begin{bmatrix} \boldsymbol{C}^E & -\psi(\boldsymbol{x})\boldsymbol{e}^T \\ \psi(\boldsymbol{x})\boldsymbol{e} & \varepsilon^\varepsilon \end{bmatrix} \begin{Bmatrix} \varepsilon \\ \boldsymbol{E} \end{Bmatrix}, \boldsymbol{x} \in \Omega \tag{9.83}$$

For operation of the patch in a sensing mode, the second of Eq. 9.83 is of particular importance and will be analyzed in detail. The analysis is simplified by introducing a number of assumptions which reduce the size of the problem. First, it is assumed that the piezoelectric material is polarized along its thickness direction x_3, so that two of the components of the electric displacement vector are zero ($D_1 = D_2 = 0$). The sensor is also considered in a state of plane strain, i.e. $\varepsilon_{33} \approx \gamma_{13} \approx \gamma_{23} \approx 0$, and $\varepsilon = \{ \varepsilon_{11} \quad \varepsilon_{22} \quad \gamma_{12} \}^T$. The second of Eqs. 9.83 reduces to:

$$D_3 = f(\boldsymbol{x})\boldsymbol{b}^T\boldsymbol{D} = \varphi(\boldsymbol{x})\boldsymbol{b}^T(\psi(\boldsymbol{x})\boldsymbol{e}\varepsilon + \varepsilon^\varepsilon \boldsymbol{E}), \boldsymbol{x} \in \Omega \tag{9.84}$$

where $\boldsymbol{b} = [0, 0, 1]^T$. Considering the strain-charge form of the piezoelectric constitutive equations, Eq. 9.84 can be rewritten as follows:

$$D_3 = \varphi(\boldsymbol{x})\boldsymbol{b}^T[\psi(\boldsymbol{x})\boldsymbol{d}^\sigma \boldsymbol{C}^E \varepsilon + (\varepsilon^\sigma - \boldsymbol{d}^\sigma \boldsymbol{C}^E \boldsymbol{d}^{\sigma^T})\boldsymbol{E}], \boldsymbol{x} \in \Omega \tag{9.85}$$

where $\boldsymbol{d}^\sigma, \varepsilon^\sigma$ respectively denote the matrix of the piezoelectric strain constants and of the permittivity constants evaluated at constant stress.

9.5.2 Voltage Generated by Piezo Sensors of Arbitrary Shape

In sensing mode, the total charge developed over the piezoelectric area is $\int_{\Omega_P} D_3 d\boldsymbol{x} = \int_{\Omega} \varphi(\boldsymbol{x}) D_3 d\boldsymbol{x} \approx 0$. Integration of both sides of Eq. 9.85 therefore gives:

$$\boldsymbol{b}^T \boldsymbol{d}^\sigma \boldsymbol{C}^E \int_{\Omega} \varepsilon \varphi(\boldsymbol{x}) \psi(\boldsymbol{x}) d\boldsymbol{x} = \boldsymbol{b}^T (\boldsymbol{d}^\sigma \boldsymbol{C}^E \boldsymbol{d}^{\sigma^T} - \varepsilon^\sigma) \int_{\Omega} \varphi(\boldsymbol{x}) \boldsymbol{E} d\boldsymbol{x} \tag{9.86}$$

where it was assumed that all properties of the piezoelectric patch are constant over the area Ω_P. Equation 9.86 can be simplified by imposing that $E_1 = E_2 = 0$, and that the voltage varies linearly across the thickness of the piezo t_P which gives:

$$E_3 = \frac{V}{t_P} \tag{9.87}$$

where V is the total voltage measured at the electrodes of the piezos. Accordingly, in Eq. 9.86, the electric field vector can be expressed as:

$$\boldsymbol{E} = \frac{V}{t_P} \boldsymbol{b} \tag{9.88}$$

Substituting in Eq. 9.86, and solving for the measured voltage V gives:

$$V = \frac{t_P}{A_P [\boldsymbol{b}^T (\boldsymbol{d}^\sigma \boldsymbol{C}^E \boldsymbol{d}^{\sigma^T} - \varepsilon^\sigma) \boldsymbol{b}]} \boldsymbol{b}^T \boldsymbol{d}^\sigma \boldsymbol{C}^E \int_{\Omega} \varepsilon f(\boldsymbol{x}) d\boldsymbol{x} \tag{9.89}$$

where $A_P = \int_{\Omega} \varphi(\boldsymbol{x}) d\boldsymbol{x}$ is the area occupied by the piezoelectric patch, and where $f(\boldsymbol{x}) = \varphi(\boldsymbol{x}) \psi(\boldsymbol{x})$ is introduced to simplify the notation. The sensing voltage expressed in Eq. 9.89 can be evaluated in the presence of a plane wave propagating in the plane of the structure at frequency ω. The surface displacement can in general be expressed as:

$$\boldsymbol{u}(\boldsymbol{x}, \omega) = \boldsymbol{U}_0(\omega) e^{-j \boldsymbol{k}_0(\omega) \cdot \boldsymbol{x}} \tag{9.90}$$

where $\boldsymbol{U}_0$ defines the amplitude and the polarization of the wave at the considered frequency, and $\boldsymbol{k}_0(\omega) = k_0(\omega) \boldsymbol{i'}_1 = k_0(\omega)(\cos\theta \boldsymbol{i}_1 + \cos\theta \boldsymbol{i}_2)$ is the considered wave vector defining plane wave propagation at an angle θ Fig. 9.35. Assuming that the considered wave is characterized by a displacement field such that:

$$\boldsymbol{u}(\boldsymbol{x}, \omega) \cdot \boldsymbol{i'}_2 = 0 \tag{9.91}$$

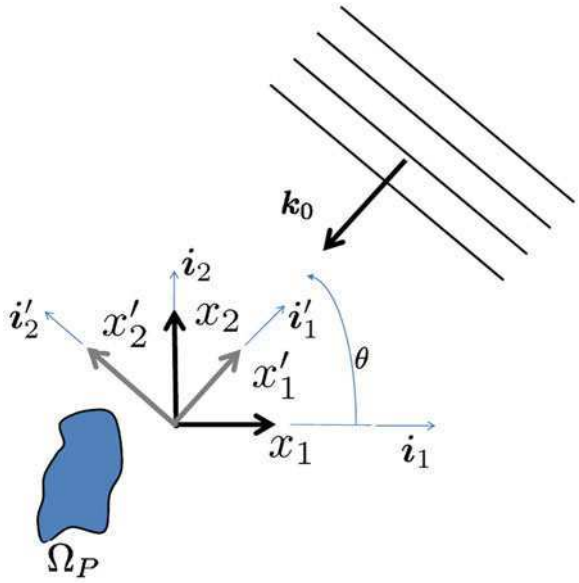

Fig. 9.35 Schematic of plane wave propagating at angle θ on the plane of the structure $\boldsymbol{x}$

the only strain component relevant to the surface mounted sensor is given by:

$$\varepsilon_{1'1'} = \frac{\partial u_1'}{\partial x_1'} = jU_{1_0'}(\omega)k_0(\omega)e^{-jk_0(\omega)x_1'} \tag{9.92}$$

while $\varepsilon_{1'1'} = \gamma_{1'2'} = 0$. In this case, the plane strain field in Eq. 9.89 can be written as:

$$\varepsilon = \varepsilon_{1'1'}[\cos^2\theta, \sin^2\theta, 0]^T \tag{9.93}$$

$$\varepsilon = \varepsilon_{1'1'}\boldsymbol{r}(\theta) \tag{9.94}$$

Substituting Eq. 9.93 into Eq. 9.89 gives:

$$V(\omega) = jU_{1_0'}(\omega)k_0(\omega)\mathcal{H}(\theta)\mathcal{D}(\omega,\theta) \tag{9.95}$$

where:

$$\mathcal{H}(\theta) = \frac{t_P}{A_P}\frac{\boldsymbol{b}^T\boldsymbol{d}^\sigma\boldsymbol{C}^E\boldsymbol{r}(\theta)}{[\boldsymbol{b}^T(\boldsymbol{d}^\sigma\boldsymbol{C}^E\boldsymbol{d}^{\sigma^T} - \varepsilon^\sigma)\boldsymbol{b}]} \tag{9.96}$$

and

$$\mathcal{D}(\omega,\theta) = \int_\Omega e^{jk_0(\omega)(x_1\cos\theta + x_2\sin\theta)}f(\boldsymbol{x})d\boldsymbol{x} \tag{9.97}$$

Table 9.3 PZT 5H piezoelectric material characteristics

$c_{11}^E = 1.27\ 10^{11}$ Pa	$c_{22}^E = 1.27\ 10^{11}$ Pa	$c_{33}^E = 1.17\ 10^{11}$ Pa
$c_{12}^E = 8.02\ 10^{10}$ Pa	$c_{13}^E = 8.46\ 10^{10}$ Pa	$c_{23}^E = 8.46\ 10^{10}$ Pa
$c_{44}^E = 2.30\ 10^{10}$ Pa	$c_{55}^E = 2.30\ 10^{10}$ Pa	$c_{66}^E = 2.34\ 10^{10}$ Pa
$\varepsilon_0 = 8854 \times 10^{-12}$ F/m	$d_{15} = 741 \times 10^{-12}$ C/N	$d_{24} = 741 \times 10^{-12}$ C/N
$d_{31} = -274 \times 10^{-12}$ C/N	$d_{32} = -274 \times 10^{-12}$ C/N	$d_{33} = 593 \times 10^{-12}$
$\varepsilon_{11}^\sigma = 3130\ \varepsilon_0$	$\varepsilon_{22}^\sigma = 3130\ \varepsilon_0$	$\varepsilon_{33}^\sigma = 3400\ \varepsilon_0$

define two separate contributions to the measured voltage. The first quantity $\mathcal{H}$ contains the material properties of the piezo-structure system, and can have a directional component in case of non-isotropic properties. For the case of a PZT 5H material, whose properties are listed in Table 9.3, the quantity $\mathcal{H}$ is constant with respect to the angle of wave propagation θ, and therefore no directionality is introduced. Other common piezo patches, such as the Macro Fiber Composite sensors discussed in [18], have non-isotropic piezoelectric properties which lead to significant directional behaviors.

In contrast, parameter $\mathcal{D}$ describes the effect of the distribution of material as defined by the function $f(\boldsymbol{x})$. Specifically, the definition of $\mathcal{D}$ provides the opportunity of selecting specific material and polarization distributions to tune the sensor to specific wavelengths and associated wave modes, and to achieve desired directionality properties. Examples of specific design configurations are provided in the following sections. Of interest, is the further development of Eq. 9.97, which can be rewritten as follows:

$$\mathcal{D}(\omega, \theta) = \int_{-\infty}^{+\infty} e^{-j\boldsymbol{k}_0(\omega)\cdot\boldsymbol{x}} f(\boldsymbol{x}) d\boldsymbol{x} \tag{9.98}$$

exploits the limited support of the function $f(\boldsymbol{x})$ so that the integration limits can be extended to infinity without affecting the value of the integral. Equation 9.98 can be easily recognized as the spatial Fourier Transform (FT) of the function $f(\boldsymbol{x})$, with the understanding that its dependence upon frequency is based on its direct relation with the wave vector $\boldsymbol{k}_0$ as defined by the dispersion relations for the considered medium. This simple observation leads to the convenient estimation of the directivity for various sensor shapes and polarizations through the identification of the proper FT pairs:

$$\mathcal{D}(\boldsymbol{k}_0(\omega), \theta) = \mathcal{F}[f(\boldsymbol{x})] \tag{9.99}$$

where $\mathcal{F}[\cdot]$ denotes the FT. Equation 9.99 suggests the possibility of evaluating the sensor directivity through FFT algorithms in the case of complex material distributions.

9.5.3 Examples of Directivities for Simple Geometries

9.5.3.1 Circular Sensor

The case of a circular piezo sensor can be modeled through the following expression for the function $f(\boldsymbol{x})$:

$$f(\boldsymbol{x}) = \text{rect}\left(\frac{|\boldsymbol{x}|}{a}\right) \tag{9.100}$$

where the function rect is defined as follows:

$$\text{rect}(x) = \begin{cases} 1, & |x| <= 1 \\ 0, & |x| > 1 \end{cases} \tag{9.101}$$

and where a defines the radius of the disc. Figure 9.36 shows a configuration of the disc, where the black domain identifies the location of the piezoelectric material.

The corresponding directivity is given by:

$$\mathcal{D}(\boldsymbol{k}_0(\omega), \theta) = a\,\text{sinc}(k_0 a) \tag{9.102}$$

The directivity function clearly shows the absence of any sensing directivity, and indicates that preferential tuning occurs for wave modes corresponding to local maxima of the sinc function. Such maxima can be found at $k_0 a = (2n-1)\frac{\pi}{2}$, where $n = 1, 2, \ldots$ is an integer. The directivity function in the wavenumber domain, as well as the directivity curve for $k_0 = \frac{\pi}{2a}$ is presented in Fig. 9.37 to confirm the absence of any preferential direction of sensitivity.

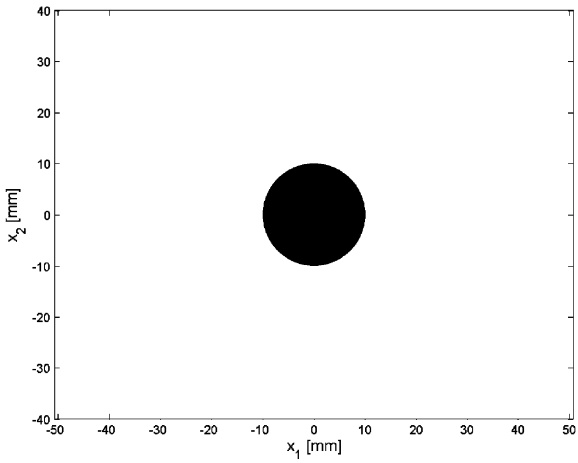

Fig. 9.36 Circular piezo disc of radius $a = 10$ mm

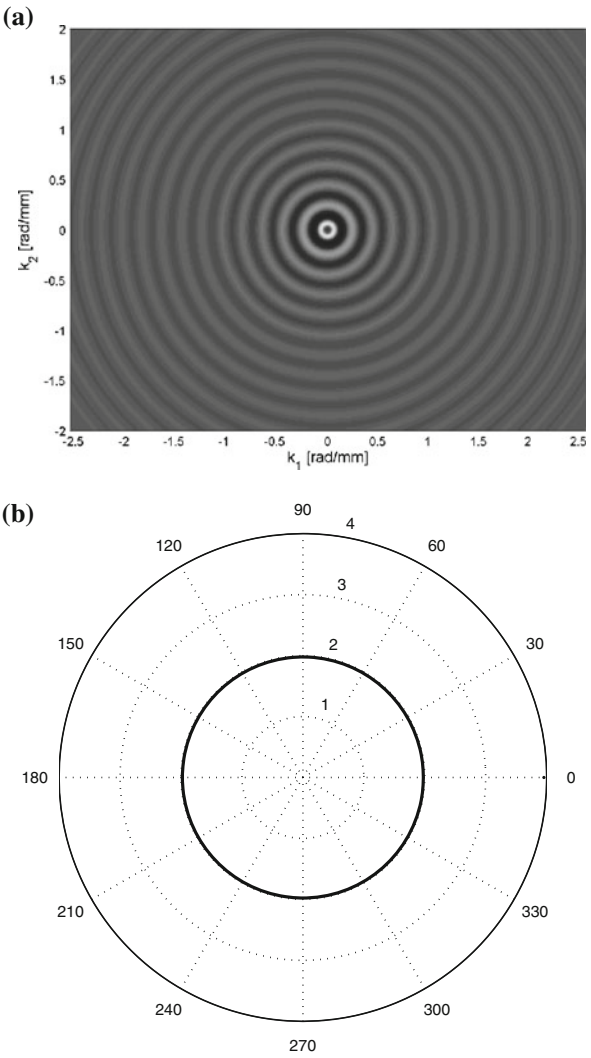

Fig. 9.37 Wavenumber representation of the directivity function of the piezo disc of radius $a = 10$ mm (**a**), and directivity curve at $k_0 = \frac{\pi}{2a}$ (**b**)

9.5.3.2 Rectangular Sensor

A second example considers the case of the rectangular piezo, which can be described by the following function:

$$f(\boldsymbol{x}) = \text{rect}\left(\frac{x_1}{a_1}\right)\text{rect}\left(\frac{x_2}{a_2}\right) \tag{9.103}$$

where $2a_1, 2a_2$ define the dimensions of the rectangular patch along the x_1 and x_2 direction, here assumed aligned with the principle directions of the rectangle. A sensor of dimensions $a_1 = 5$ mm, $a_2 = 7$mm is displayed in Fig. 9.38.

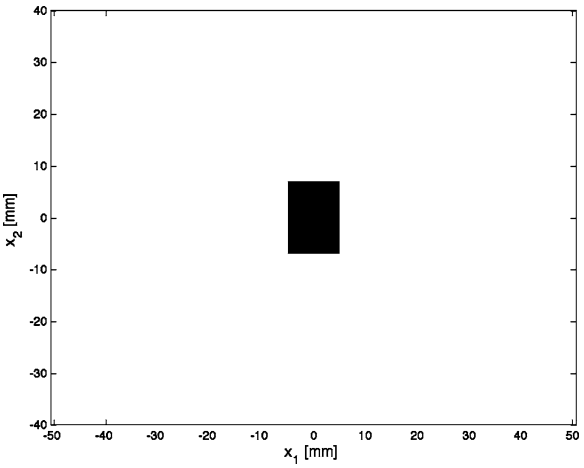

Fig. 9.38 Rectangular piezo disc of dimensions $a_1 = 5$ mm, $a_2 = 7$ mm

The sensor's directivity, given by:

$$\mathcal{D}(\boldsymbol{k}_0(\omega), \theta) = a_1 a_2 \,\mathrm{sinc}(a_1 k_0 \cos\theta)\,\mathrm{sinc}(a_2 k_0 \sin\theta) \tag{9.104}$$

indicates that preferential directions of sensitivity are aligned with the main dimensions of the rectangle, along which tuning occurs for wavenumber values which maximize the two sinc functions in Eq. 9.104. Specifically, for an incoming wave at $\theta = 0$, maximum sensitivity occurs for wavenumbers $k_0 a_1 = (2n_1 - 1)\frac{\pi}{2}$, where $n_1 = 1, 2, ...$, while for waves propagating along the direction $\theta = \pi/2$, the sensor is tuned for $k_0 a_2 = (2n_2 - 1)\frac{\pi}{2}$, where $n_2 = 1, 2, ...$ Given the dependence of wavenumber upon frequency, one could consider situations where the sensor can discriminate between the two directions of maximum sensitivity ($\theta = 0$ and $\theta = \pi/2$), based on the frequency value (and corresponding wavenumber) it senses. In other words, the rectangular sensor can act as a spatial filter which is tuned to the $\theta = 0$ or $\theta = \pi/2$ direction depending on the frequency it receives. The polar directivity curves of Fig. 9.39 illustrate the different directional patterns with strong lobes at $\theta = 0$ (Fig. 9.39b) and at $\theta = \pm\pi/2$ (Fig. 9.39c) for different wavenumber values.

9.5.4 Frequency Steerable Acoustic Transducer Periodic Array

The method outlined above can be applied to the analysis of the sensing directionality of a periodic array of piezo discs. The concept relies on similar considerations made above for the rectangular piezo, whereby directionality is observed as the result of matching with maximum values of directivity which occur for specific directions of the wave vector.

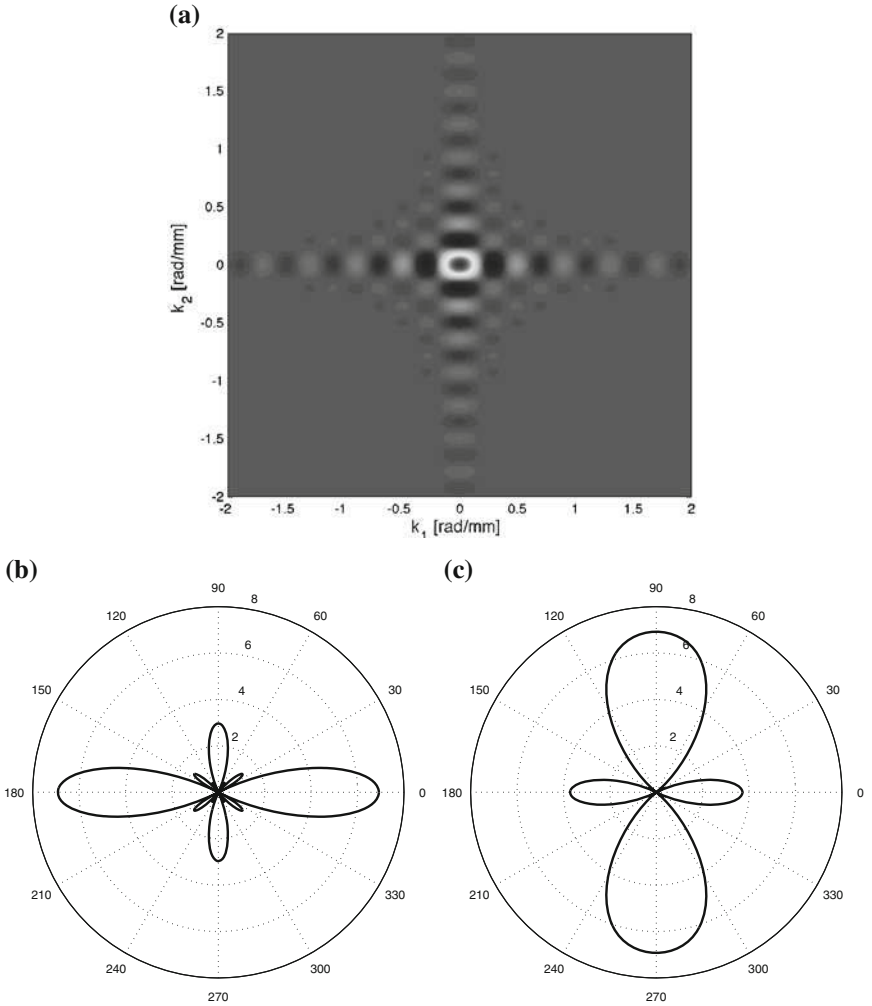

Fig. 9.39 Wavenumber representation of the directivity function of the rectangular piezo (**a**), and directivity curve at $k_0 = \frac{\pi}{2a_1}$ (**b**) and at $k_0 = \frac{\pi}{2a_2}$ (**c**)

The material distribution function $f(\boldsymbol{x})$ for the array is expressed as:

$$f(\boldsymbol{x}, \omega) = \sum_{n_1} \sum_{n_2} \text{rect}(a|\boldsymbol{x} - \boldsymbol{x}_{n_1,n_2}|) \tag{9.105}$$

where a is the radius of each disc, while $\boldsymbol{x}_{n_1,n_2}$ defines the location of the center of the disc n_1, n_2, where the integers $n_i \in [-\frac{1}{2}(N_i - 1), \frac{1}{2}(N_i - 1)]$, with N_i defining the number of elements of the array in the i-th direction. Such location can be expressed as:

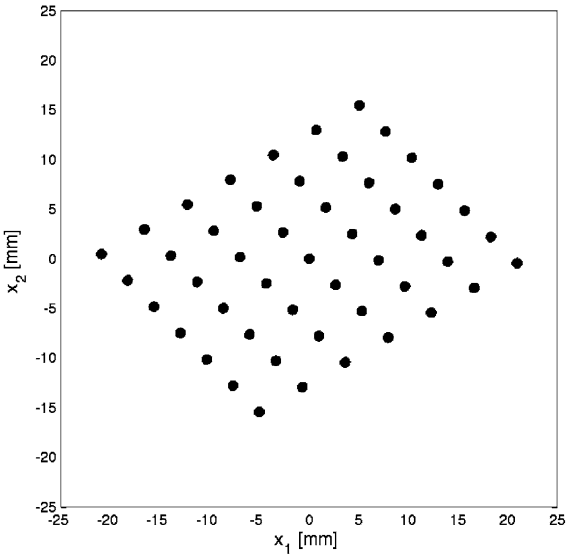

Fig. 9.40 Periodic piezo array

$$\boldsymbol{x}_{n_1,n_2} = n_1\boldsymbol{e}_1 + n_2\boldsymbol{e}_2 \tag{9.106}$$

In Eq. 9.106, $\boldsymbol{e}_1, \boldsymbol{e}_2$ are two vectors defining the periodicity of the array, which according to the configuration proposed in Sect. 9.4, can be generally written as:

$$\begin{aligned} \boldsymbol{e}_1 &= d_1 \cos\alpha \boldsymbol{i}_1 + d_1 \sin\alpha \boldsymbol{i}_2 \\ \boldsymbol{e}_2 &= d_2 \cos\beta \boldsymbol{i}_1 + d_2 \sin\beta \boldsymbol{i}_2 \end{aligned} \tag{9.107}$$

where d_1, d_2 define the spacing of the array elements along the array directions, while α, β are two generic angles. Figure 9.40 shows an example of the periodic array obtained for $a = 0.5$ mm, $N_1 = 7, N_2 = 7, d_1 = 5, d_2 = 3.75$ mm, $\alpha = 30\pi/180, \beta = 135\pi/180$.

The corresponding directivity can be evaluated through the spatial FT of the material distribution function in Eq. 9.105, which is given by

$$\begin{aligned} \mathcal{D}(\boldsymbol{k}_0(\omega), \theta) &= a\,\mathrm{sinc}(a\,k_0) \sum_{n_1}\sum_{n_2} e^{-i\boldsymbol{k}_0\cdot\boldsymbol{x}_{n_1,n_2}} \\ \mathcal{D}(\boldsymbol{k}_0(\omega), \theta) &= a\,\mathrm{sinc}(a\,k_0) \sum_{n_1}\sum_{n_2} e^{-i(n_1\boldsymbol{e}_1\cdot\boldsymbol{k}_0 + n_2\boldsymbol{e}_2\cdot\boldsymbol{k}_0)} \end{aligned} \tag{9.108}$$

Upon manipulation, Eq. 9.108 can be conveniently rewritten as:

$$\mathcal{D}(\boldsymbol{k}_0(\omega), \theta) = a\,\mathrm{sinc}(a\,k_0) \frac{\sin(\frac{N_1}{2}\boldsymbol{e}_1\cdot\boldsymbol{k}_0)\sin(\frac{N_2}{2}\boldsymbol{e}_2\cdot\boldsymbol{k}_0)}{\sin(\frac{1}{2}\boldsymbol{e}_1\cdot\boldsymbol{k}_0)\ \sin(\frac{1}{2}\boldsymbol{e}_2\cdot\boldsymbol{k}_0)} \tag{9.109}$$

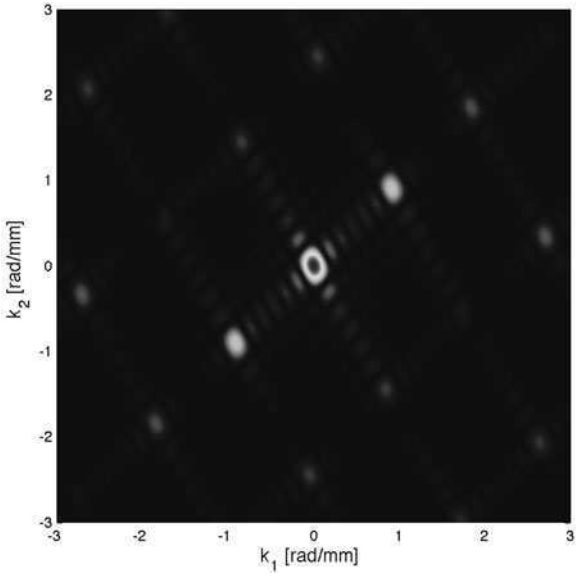

Fig. 9.41 Array directivity function

The variation of the directivity in terms of the wave vector components shown in Fig. 9.41. The wavenumber values which maximize Eq. 9.108 are obtained as solutions of the following system for a given pair of integers p, q:

$$\begin{aligned} \boldsymbol{e}_1 \cdot \xi &= 2p\pi \\ \boldsymbol{e}_2 \cdot \xi &= 2q\pi \end{aligned} \tag{9.110}$$

The solution of Eq. 9.110 is associated with a wave vector $\boldsymbol{k}_{0_{p,q}}$ whose direction is given by:

$$\theta_{p,q} = \arctan\left(\frac{k_{02_{p,q}}}{k_{01_{p,q}}}\right) \tag{9.111}$$

The selection of a particular peak in the directivity distribution can be performed by determining the wavenumber corresponding to the radius of a circle intersecting the peak of interest. This wavenumber value corresponds to a specific frequency of the measured wave as defined by the dispersion relations of the structure, which is then associated with the direction corresponding to the wavenumber components identifying the peak under consideration. Directivity curves for various combinations of the integer pairs p, q are shown in Fig. 9.42. Directional sensing at the considered 3 directions corresponding to the main lobes in Fig. 9.42 occurs at the values of frequencies which satisfy the following relation:

$$(\xi_{p,q}, \omega) = 0 \tag{9.112}$$

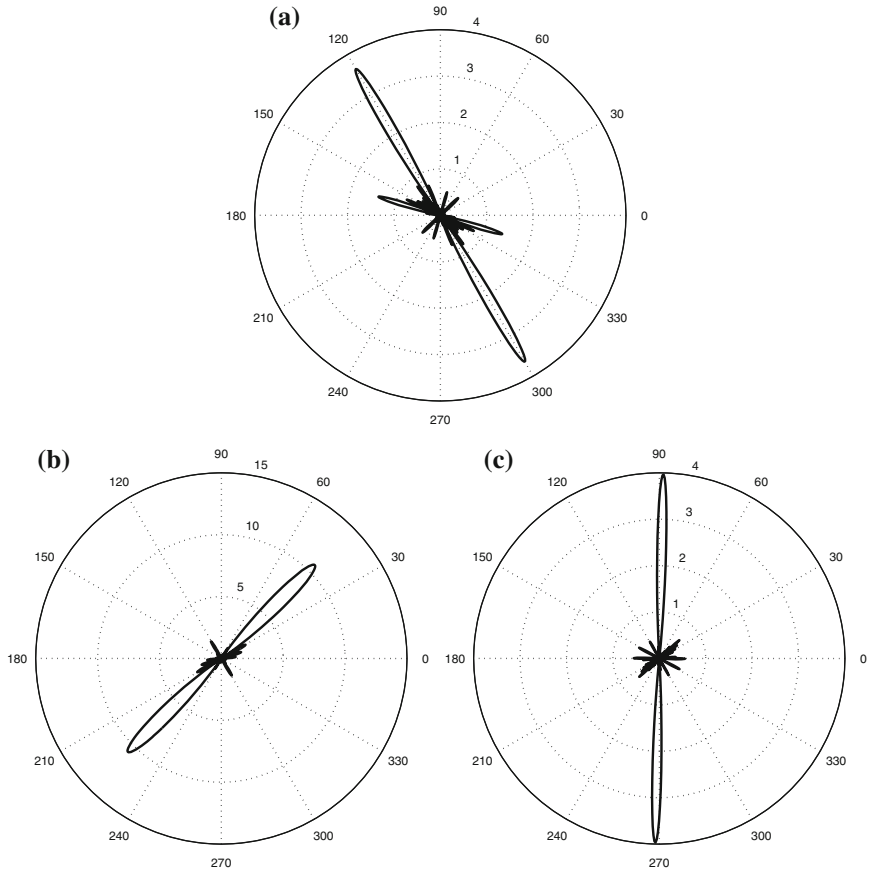

Fig. 9.42 Array directivity curves for various values of the p, q pair: $p = 1, q = 0$ **a**, $p = 0, q = 1$ **b**, $p = 1, q = 1$ **c**

which defines the dispersion relation of the considered medium, whose solution provides the value of frequency $\omega_{p,q}$ at which the array radiates at the angle $\theta_{p,q}$.

References

1. Bartoli I, Marzani A, Lanza di Scalea F, Viola E (2006) Modeling wave propagation in damped waveguides of arbitrary cross-section. J Sound Vib 295(3–5):685–707
2. Benjeddou A (2000) Advances in piezoelectric finite element modeling of adaptive structural elements: a survey. Comput Struct 76(1–3):347–363
3. Bruce WD, Paul DW (2006) Ultrasonic arrays for non-destructive evaluation: a review. IEEE Trans Ultrason Ferroelectr Freq Control 39:525–541

4. Cho YH, Rose JL (1996) A boundary element solution for a mode conversion study oil the edge reflection of Lamb waves. J Acoust Soc Am 99(4, Part 1):2097–2109
5. Cooray TMJA (2006) Complex analysis with vector calculus. Alpha Science
6. Crawley EF (1987) Use of piezoelectric actuators as elements of intelligent structures. AIAA J 25:1373–1385
7. Cunefare KA, Collet M (2008) Modal synthesis and dynamical condensation methods for accurate piezoelectric systems impedance computation. J Int Mat Syst and Struct 19(11):1251–1271
8. Doyle JF (1997) Wave propagation in structure. Springer, New York
9. Freitag E, Busam R (2005) Complex analysis. Springer, Heidelberg
10. Fromme P, Wilcox PD, Michael Lowe JS, Peter Cawley P (2006) On the development and testing of a guided ultrasonic wave array for structural integrity monitoring. IEEE Trans Ultrason Ferroelectr Freq Control 53(4):777–784
11. Giurgiutiu V, Bao J, Zhao W (2003) Piezoelectric wafer active sensor embedded ultrasonics in beams and plates. Exp Mech 42(4):428–449
12. Giurgiutiu V (2007) Structural health monitoring: with piezoelectric wafer active sensors. Academic Press, New York
13. Giurgiutiu V (2005) Tuned lamb wave excitation and detection with piezoelectric wafer active sensors for structural health monitoring. J Intell Mater Syst Struct 16(4):291–305
14. Graff KF (1991) Wave motion in elastic solids. Dover, New York
15. Li J, Rose JL (2001) Implementing guided wave mode control by use of a phased transducer array. IEEE Trans Ultrason Ferroelectr Freq Control 48(3):761–768
16. Lin B, Giurgiutiu V (2005) Review of in-situ fabrication methods of piezoelectric wafer active sensor for sensing and actuation applications. Proc SPIE Int Soc Opt Eng 5765:1033–1044
17. Lin B, Giurgiutiu V (2005) PVDF and PZT piezoelectric wafer active sensors for structural health monitoring. Am Soc Mech Eng Nondestruct Eval Eng Div (Publ) NDE 26 NDE:69–76
18. Matt HM, di Scalea FL (2007) Macro-fiber composite piezoelectric rosettes for acoustic source location in complex structures. Smart Mater Struct 16:1489–1499
19. Raghavan A, Cesnik CES (2005) Finite-dimensional piezoelectric transducer modeling for guided wave based structural health monitoring. Smart Mater Struct 14:1448–1461
20. Raghavan A, Cesnik CES (2005) Finite-dimensional piezoelectric transducers modeling for guided wave based structural health monitoring. Smart Mater Struct 14:1448–1461
21. Rose JL, Pelts SP, Quarry MJ (1998) A comb transducer model for guided wave nde. Ultrasonics 36:163–169
22. Staszewski WJ, Boller C, Tomlinson G (2004) Health monitoring of aerospace structures. Smart sensors and signal processing. Wiley, Chichester
23. Viktorov IA (1967) Rayleigh and Lamb waves. Plenum, New York
24. Wilcox PD (2003) Omni-directional guided wave transducer arrays for the rapid inspection of large areas of plate structure. IEEE Trans Ultrason Ferroelectr Freq Control 50(6):699–709
25. Yu L, Giurgiutiu V (2005) Using phased array technology and embedded ultrasonic structuralnradar for active structural health monitoring and nondestructive evaluation. Am Soc Mech Eng Nondestruct Eval Eng Div (Publ) NDE 26:53–60
26. Zhu W, Rose JL (1999) Lamb wave generation and reception with time-delay periodic linear arrays: a BEM simulation and experimental study. IEEE Trans Ultrason Ferroelectr Freq Control 46(3):654–64

Part III
Computational Methodologies for Damage Detection and Quantification

Chapter 10
Computational Techniques for Damage Detection, Classification and Quantification

10.1 Overview

The objective of a SHM system is to identify anomalies or damages such as cracks, delaminations and disbonds in structures. The term identification includes the determination of the existence of damages, their location and their size as accurately as possible. In the literature, the amount of information that can be obtained regarding a damaged structure is typically classified into five levels: (1) identification of the presence of damage, (2) determination of the location of the damage, (3) classification of the type of damage, (4) quantification of its extent, and (5) estimation of the remaining life of the component under investigation. These levels were discussed in Chap. 1. The definition of an effective measure of damage responds to the requirements of the first four stages of the information, and ideally provides inputs to step number (5). Damage measures proposed in the literature from an SHM perspective are meant to identify and locate the damage, and, in some cases, provide an indication regarding the extent of the damage and its progression.

Many SHM techniques developed over the years are based on the detection of changes in the dynamic behavior of the monitored components. Valuable reviews of the state-of-the-art in dynamics-based SHM can be found in [13, 42, 43]. The existing techniques vary on the basis of the type of dynamic response signals used for the analysis, and on the features or parameters considered as damage indicators. Such features or parameters must obviously be sensitive to damage, and vary monotonically with the extent of the damage. Dynamics-based inspection techniques are typically classified as vibration-based methods, and wave propagation methods. Vibration-based damage detection techniques typically monitor changes in modal frequencies, in measured mode shapes (and their derivatives), and changes in measured flexibility coefficients, while wave propagation inspections look for reflections and mode conversion phenomena caused by the presence of damage.

S. Gopalakrishnan et al., *Computational Techniques for Structural Health Monitoring*, Springer Series in Reliability Engineering, DOI: 10.1007/978-0-85729-284-1_10,

Early studies in vibration-based techniques evaluated the influence on the natural frequencies of localized stiffness reductions caused by damage. These investigations have shown that natural frequencies are damage indicators, which generally show low sensitivity, and do not allow the determination of the location of damage. More recent studies have investigated the effects of localized and distributed damage on mode shapes, operational deflection shapes (ODS) and corresponding curvatures. The detection of small changes in the deformed configuration of the structure can be used to localize damage and potentially estimate its severity. In particular, small variations from an undamaged state can be highlighted by successive spatial differentiations of the deflections, as typically required for estimating curvature modes and the associated strain energy. These modal-based methods are very attractive as they provide information regarding the general state of health of the structure. However they tend to have limited sensitivity and generally they are not accurate enough to provide detailed information regarding damage type and its extent.

10.2 A General Introduction to Vibration-Based Techniques

The analysis of the modal properties of the structure and their variation due to damage have received great attention by researchers over the last 30 years. An excellent and thorough review of the research in the area can be found in [13]. Most of the damage measures proposed assume the possibility of comparing current measurements with baseline information regarding the undamaged state of the structure. This may be a significant drawback as it assumes the availability of data on the component under test in its pristine state, and the basic assumption that any measured change is due to damage only, and not to changing environmental or boundary conditions applied to the component. The techniques presented below are examples of solutions proposed over the years, whose practicality can be significantly improved if coupled with procedures aimed at generating data approximating the undamaged response of the structure. Details of such a procedure, proposed in [40], is presented in Sect. 10.3.1

10.2.1 Early Techniques Based on Natural Frequency Shifts

Modal parameters are global properties of a vibrating structure, and their change can indicate the presence of damage, without performing direct measurements at or near the damage site. Analytical quantification of the change in modal frequencies related to loss of stiffness in simple beam and plate structures can be found for example in [26, 30, 41], where perturbation methods are applied to estimate modal properties in the presence of notch-type defects. It is nowadays quite accepted that simple monitoring of frequency changes is not a reliable and sensitive enough

method for early damage detection, and cannot easily provide location information [13]. Noteworthy attempts include the work of Cawley and Adams [7], who investigated frequency shifts due to damage in composite materials. The ratio between shifts at various modes $\Delta\omega_i/\Delta\omega_j$ is used to construct an error term which allows estimating the damage location. This technique, which does not account for multiple damage sites, was revisited in [44, 45] using the sensitivity of modal frequency changes in terms of local stiffness and mass changes. The following error function for the ith mode and pth structural member was introduced:

$$e_{ip} = \frac{z_i}{\sum_j z_j} - \frac{F_{ip}}{\sum_j F_{jp}} \tag{10.1}$$

where z_i is ith term in the array of squared modal frequency changes, which is defined as:

$$\{z\} = [F]\{\alpha\} - [G]\{\beta\} \tag{10.2}$$

with $[F]$ and $[G]$ respectively denoting changes in elemental stiffness and mass magnitudes. The member that minimizes the error in Eq. 10.1 is determined to be the damaged one, again under the assumption of single defect. The estimation of the frequency change sensitivity is based on the FE model of the structure under consideration, which may be problematic in the case of complex structures. In [19], authors employed the FE formulation to introduce a damage severity parameter for structural member n representing the element's stiffness loss, i.e.:

$$[\Delta k_n] = \alpha_n [k_n] \tag{10.3}$$

which, under the assumption of single damage location, can be directly related to a frequency shift according to the following expression:

$$\Delta\omega_i^2 = \alpha_n \frac{\{\epsilon_n(\phi_i)\}^T [k_n] \{\epsilon_n(\phi_i)\}}{\{\phi_i\}^T [M] \{\phi_i\}} \tag{10.4}$$

where $\{\epsilon_n(\phi_i)\}$ are the nth member's deformations computed on the basis of the undamaged mode shapes ϕ_i, while $[M]$ and $[k_n]$ describe the mass of the structure and the stiffness of the nth member. This equation directly relates the effect of damage on a specific component n to the corresponding shift in frequency, under the assumption that the evaluation of this direct relation can be performed on the basis of pre-damage modal information. The hypothesis that damage only produces a change in stiffness $[\delta K]$ is exploited in [35], where the orthogonality properties of the damaged and undamaged structure is used to obtain the following sensitivity equation:

$$\{\phi_i\}^T [\delta K] \{\phi_i\} = (\omega_i^{(d)})^2 - (\omega_i^{(u)})^2 \tag{10.5}$$

where it is again assumed that the damage causes a negligible change in the mode shapes.

10.2.2 Mode Shape Analysis

Mode shape changes are found to be quite sensitive to damage, especially when higher modes are considered, and are able to directly provide damage location information. The problem associated with mode shape monitoring is clearly related to the need of sufficient spatial measurement resolution, which complicates the experimental procedures. The required measurement resolution can be easily achieved through the use of a Scanning Laser Doppler Vibrometer, which has become an important tool for dynamic testing. Alternatively, the number of measurement locations can be reduced if the FE model of the structure under investigation is available for its use in increasing the information on the structure's behavior and for interpolation purposes. Most of the early work on mode shape analysis consider the Modal Assurance Criterion (MAC) to compare measured, or damaged, modes, with undamaged or numerical ones. For example, West [47] used the MAC to correlate the modes of an undamaged Space Shuttle Orbiter body flap with those after the flap has been exposed to acoustic loading. Another technique presented in [50], considered a damage measure based on changes in the mode shape and mode shape slope. Changes were simulated for stiffness reductions in each structural member and compared to measured changes to determine the damage location. Other techniques of various nature exploit comparisons through modal correlation criteria. For example, Fox [16] proposed the concept of a MAC based on measurement points close to a node point for a particular mode ("Node line MAC"). In [22], authors investigated the use of the Partial MAC (PMAC) to compare the MAC values of coordinate subsets of the modal vectors, and Ko et al. [24] presented a method that uses a combination of MAC, COMAC and sensitivity analysis to detect damage in steel framed structures. Finally, a damage signature based on the mode shape normalized by the change in the modal frequency of another mode is proposed in [25], as a way to combine frequency shift and changes in mode shapes as damage indicators.

More recent investigations apply the Wavelet transform as a signal processing tool to highlight the presence of discontinuities in the modal deflections. The spatial information resulting from multi-point measurements are fed to wavelet algorithms to obtain information regarding anomalies related to damage in the deformed shapes. Plots obtained upon the wavelet analysis localize the damage and may be used, after proper calibration, to quantify the damage extent [8, 37, 52]. Specifically, Zhong and Oyadiji [52] employed the WT of the spatial modal signal to locate the damage along the beam length and potentially monitor its progression through the thickness. Results for plates using a similar approach are presented in [37].

10.2.3 Mode Shape Curvature Changes

An alternative to using mode shapes to obtain spatial information about structural changes consists in using mode shape derivatives, such as curvatures or strain

energy distributions obtained from spatial integration of modes. For example, in 1991 [33], authors demonstrated the use of absolute changes in curvature as good indicators of damage for a beam-type structure. They used a central difference-based numerical differentiation technique to compute the curvature from numerically obtained mode shapes. Their results showed that the absolute changes in curvature were localized around the damaged region, and that damage could be quantified by establishing a relationship between changes in curvature and damage extent. The evaluation of changes in the curvature of dynamic deflection shapes as a tool for damage detection and localization were also investigated in [30] and subsequently in [26]. In these studies, the dynamic behavior of beams with notch defects and delaminations was studied analytically and experimentally. Analytical models described the dynamic behavior and the curvature modes of cracked beams through perturbation of the modal parameters of the undamaged beams, so that approximated analytical expressions for the damaged modes were obtained. The analytical studies were supported by experimental investigations performed on simple beam structures. Their results show the potentials of the technique when applied to the first mode of the beam. The limitation to a single mode was mainly dictated by the limited spatial resolution available in the accelerometers-based experiments. Ho and Ewins [21] formulated a damage index defined as the quotient squared of the corresponding modal curvatures of the undamaged and damaged structure. The damage index was found to be highly susceptible to noise as measurement errors were amplified due to second derivatives based on numerical techniques. They also demonstrated that spatially sparse measurements adversely affect the performance of the damage index. As an alternative Ho and Ewins [21] investigated the changes in the square of the slope of mode shapes of beams. Oscillations in the slopes were reduced through polynomial fit of the measured mode shape as compared to the use of finite difference approximation. They also reported that higher derivatives can be more sensitive to damage, but are more subject to numerical errors.

10.3 Damage Measure Based on Energy Functional Distributions

The approach of [21] has been pursued for example by [23] to formulate a damage index based on the comparison of strain energy distributions for damaged and undamaged structures. In [23] and in subsequent papers by the same authors, the technique is applied to beam structures using mode shapes, or time-domain data to obtain information on both damage location and extent. The same technique has then been extended to plate structures in [12], where accelerometers are used to measure the deflections to be interpolated for successive differentiation. The results presented in [23, 12], show the effectiveness of the technique, and are used as a basis for the developments presented in what follows. Specifically, practical application of energy based techniques for damage detection relies on the

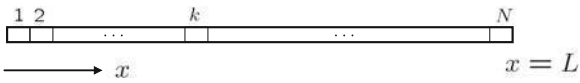

Fig. 10.1 Schematic of beam divisions

availability of high spatial measurement resolution, which can conveniently obtained through a SLDV. The laser beam placement is controlled by a user-defined set of grid points on the structure, which offers the possibility of accurately estimating deflection derivatives of various orders and in turn allows the estimation of curvatures and strain energy distributions. Such measurement refinement is unattainable in a timely manner using accelerometers and/or strain gauges. Furthermore, the damage index formulation presented in [12, 23] requires the use of data from an undamaged structure to be used as a reference. This can also represent a problem towards the practical implementation of the technique, as historical data may not always be available, and variations may be induced by a number of reasons other than structural damage. The developments presented in this chapter introduce a technique which allows the generation of baseline information directly from the measured data set. Reference data are synthesized by under-sampling measurements recorded directly on the damaged specimen. The term "under-sampling" implies that we use the same set of measurements, but analyze them over a coarser grid which is less sensitive to the damage size of concern.

10.3.1 Formulation for Beams and Plates

The strain energy for a Euler Bernoulli beam is given by:

$$U = \frac{1}{2}\int_0^L EI(x)w(x)_{,xx}^2 dx \tag{10.6}$$

where L is the beam length, EI the flexural rigidity of the beam, and w the beam deflection, with the notation $()_{,x} = \frac{\partial}{\partial x}$ adopted to indicate partial derivatives with respect to the spatial coordinate. We denote with $\phi_i(x)$ the amplitude of the beam deflection when excited at its ith natural frequency. In the literature, $\phi_i(x)$ is denoted as ODS at the ith natural frequency. The strain energy associated to $\phi_i(x)$ can be expressed as:

$$U_i = \frac{1}{2}\int_0^L EI(x)\phi_i^2(x)_{,xx} dx \tag{10.7}$$

The beam is subdivided into N regions so that the total strain energy of the beam can be expressed as [12] (Fig. 10.1):

$$U_i = \frac{1}{2}\sum_{k=1}^{N} EI_k \int_{x_k}^{x_{k+1}} \phi_i^2(x)_{,xx} dx$$
$$U_i = \sum_{k=1}^{N} U_{i_k} \tag{10.8}$$

where it is assumed that the flexural rigidity of the beam over each region is constant. In addition, it is assumed that damage is localized in a single region $k = p$, and that at the damage location:

$$\frac{U_{i_p}}{U_i} \approx \frac{U_{i_p}^*}{U_i^*} \tag{10.9}$$

so that an estimation of the reduction in stiffness rigidity can be obtained as:

$$\frac{EI_p^*}{EI_p} \approx \frac{U_i^* \int_{x_p}^{x_{p+1}} \phi_i^2(x)_{,xx} dx}{U_i \int_{x_p}^{x_{p+1}} \phi_i^{*2}(x)_{,xx} dx} = f_{i_p} \tag{10.10}$$

where $\phi_i^*(x)_{,xx}$ is the curvature corresponding to the ODS of the undamaged beam, and where the ratio f_{i_p} is denoted as strain energy ratio (SER). The SER potentially provides indications of both damage location, as well as its extent. Specifically, it is expected to be equal to 1 over the undamaged regions, and different than one over a damaged region. It is well known how damage affects the strain energy distribution when it is located near, or in regions of maximum strain energy. Hence, the visibility of damage is affected by the frequency of excitation. For this reason, it is convenient to combine information obtained from the analysis of several modes (I) and therefore to consider a cumulative strain energy ratio, defined as

$$f_k = \frac{1}{I}\sum_{i=1}^{I} f_{i_k} \tag{10.11}$$

This cumulative index provides a single piece of information which combines the results from several ODSs and associated strain energy distributions. ODSs not affected by damage because its particular location will not contribute, i.e. they will give unit contributions, whereas the index for modes altered by the defect will be combined to provide a robust indication of defect. The definition of SER given above can be easily extended to plate structures. The procedure follows the presentation made in Chap. 7 (Sect. 7.2) on plates with notch and line damage. The strain energy for a plate can be expressed as

$$U_i = \frac{1}{2}\int_A D\left[\phi_{i_{,xx}}^2 + \phi_{i_{,yy}}^2 + 2v\phi_{i_{,yy}}\phi_{i_{,xx}} + 2(1-v)\phi_{i_{,xy}}^2\right] dA \tag{10.12}$$

where $\phi_i = \phi_i(x, y)$ defines the plate ODS when excited harmonically at its ith natural frequency. Also, A denotes the plate surface, $D = D(x, y) = Eh^3/12(1 - v^2)$

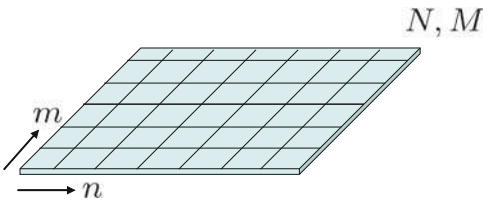

Fig. 10.2 Schematic of plate divisions

is the plate rigidity, with $h = h(x, y)$ denoting the plate thickness, while E and v are the Young's modulus and the Poisson's ratio of the plate material. The plate is subdivided into an $N \times M$ grid (Fig. 10.2), so that the strain energy associated to the n, m area can be expressed as:

$$U_{i_{nm}} = \frac{1}{2} D_{nm} \int_{A_{nm}} \left[\phi^2_{i,xx} + \phi^2_{i,yy} + 2v\phi_{i,yy}\phi_{i,xx} + 2(1-v)\phi^2_{i,xy} \right] dA \tag{10.13}$$

where it is assumed that the plate rigidity is constant over each region. Following the procedure outlined for beams, we define

$$\frac{D^*_{nm}}{D_{nm}} \approx \frac{U^*_{nm} \int_{A_{nm}} [\phi^2_{i,xx} + \phi^2_{i,yy} + 2v\phi_{i,yy}\phi_{i,xx} + 2(1-v)\phi^2_{i,xy}] dA}{U_{nm} \int_{A_{nm}} [\phi^{*2}_{i,xx} + \phi^{*2}_{i,yy} + 2v\phi^*_{i,yy}\phi^*_{i,xx} + 2(1-v)\phi^{*2}_{i,xy}] dA} = f_{i_{nm}} \tag{10.14}$$

where D^*_{nm} and ϕ^*_i are respectively the rigidity and the ODS of the damaged plate. A cumulative SER can be again defined by combining the contributions from the SER obtained at several excitation frequencies (I) to obtain, for region n, m

$$f_{nm} = \frac{1}{I} \sum_{i=1}^{I} f_{i_{nm}} \tag{10.15}$$

10.3.2 Spline Interpolation of Operational Deflection Shapes

The SER provides a comparison between damaged and undamaged strain energy over the considered region of the structure. In practice however, it may be difficult to obtain baseline information from structures to be analyzed. This in fact assumes that either an undamaged specimen, or that historical data of the same kind as those currently being collected are available. For this reason, we propose a technique which allows synthesizing undamaged information directly from the measured response. In the proposed approach, the ODS are measured at several locations over the structure, so that spatial derivatives required for the evaluation of SER can be accurately estimated. This is done by performing the spline interpolation of the measured data. Based on the procedure outlined in [5], the ODS$\phi(x, y)$ for a plate structure can be approximated as:

$$\phi(x,y) \cong \sum_{p,q} h_p(x) h_q(y) \Phi_{p,q} \tag{10.16}$$

where $\Phi_{p,q}$ defines the value of the ODS at location p, q over the plate, while $h_p(x), h_q(y)$ are spline basis function [14]. The value of $\Phi_{p,q}$ is the quantity measured experimentally at the sensor location, or at a point of a SLDV grid. Alternatively, in numerical simulations using finite elements, it may represent the value of the nodal displacement at the considered location. The spline interpolation of the plate deflection at discrete locations can be used for accurate prediction of the derivative of the deflection. The curvature estimations can be obtained by taking derivatives of the spline functions, while keeping the nodal or measured values as weighting parameters. The presence of noise on these parameters hence does not significantly affect the estimation of curvatures. This concept can be described in a concise manner by expressing the plate curvatures as:

$$\begin{aligned}
\phi_{,xx}(x,y) &\cong \sum_{p,q} h_{p,xx}(x) h_q(y) \Phi_{p,q} \\
\phi_{,yy}(x,y) &\cong \sum_{p,q} h_p(x) h_{q,yy}(y) \Phi_{p,q} \\
\phi_{,xy}(x,y) &\cong \sum_{p,q} h_{p,x}(x) h_{q,y}(y) \Phi_{p,q}
\end{aligned} \tag{10.17}$$

This process reduces the numerical errors associated with the presence of noise in the measurements, which is unavoidable, and makes the experimental evaluation of SER feasible. In addition, the interpolation procedure briefly described above offers the opportunity of calculating SER, without the need for baseline data. The availability of measurements on a supposedly undamaged structure to be directly compared with those on a damaged structure is an assumption upon which many damage detection techniques rely heavily [23, 42]. In a real test scenario, however, it is very unlikely that historical data are available, and/or that such data can be considered reliable for damage detection purposes. Changes may in fact result from a number of uncontrollable sources, such as temperature variations, operating conditions, boundary conditions, etc. In here, we propose a technique whereby damage or anomalies can be obtained from a single measurement. Baseline information is generated by using a subset of the measurement points. The baseline interpolated deflection can be expressed as:

$$\phi^*(x,y) \cong \sum_{r,s} h_r(x) h_s(y) \Phi_{r,s} \tag{10.18}$$

where r, s are a subset of the measurement grid points p, q, such that $r < p,\ s < q$. The resulting under-sampling of the data has the purpose of intentionally "missing" any discontinuity or anomaly corresponding to damage, which can generally be detected only through a refined measurement grid. The baseline information can be then differentiated and used for the estimation of the strain energy generically denoted as U^*.

10.3.3 Numerical Results on Beams

The procedure presented above has been first tested on numerically simulated results, the case of a beam structure being initially considered for simplicity. The beam is made of steel ($E = 2.1 \times 10^{11}$ MPa, $\rho = 7{,}800\,\mathrm{kg/m^3}$), it has a rectangular cross section of thickness $h_0 = 5$ mm and out-of-plane width $b = 1$ cm, and it is 1 m long. The beam is considered simply supported at both ends and loaded by a harmonic unit load of varying frequency. The behavior of the beam is predicted through a FE model, formulated using classical Euler–Bernoulli beam elements. The length of the beam is discretized using 80 elements. This large number of elements is selected to replicate experimental measurement density available with SLDV. The nodal displacements corresponding to a harmonic load at a specified frequency are computed and used for the calculation of beam curvature, and SER. A subset of the nodal displacements is used to generate reference data. The subset is defined by under-sampling the available nodal displacements, according to a so-called "decimation factor", which is here defined as:

$$d = 100 \times \left(1 - \frac{N_i}{N_t}\right) \tag{10.19}$$

where N_i is the number of nodal displacements used for the interpolation, while N_t is the total number of nodal displacements available from the analysis. For example, in this case, the analysis provides $N_t = 80$, and a decimation factor $d = 75\%$ indicates that the under-sampling is performed by considering one out of four nodal displacements.

Damage in the beam is simulated as a thickness reduction occurring over a single element of the FE mesh. The thickness of the damaged element is denoted as h, while h_0 denotes the thickness of the undamaged beam. Example of the ODS amplitude and related curvature for excitation at the first and second natural frequency of the beam are shown in Fig. 10.3. The plots, obtained for damage at mid-length of the beam with $h/h_0 = 0.9$, confirm the sensitivity of curvature as opposed to displacement amplitudes. Also, the example demonstrates how the influence of both displacements and curvatures depends upon the location of damage with respect to nodal points of ODS and curvature. The curvature of the second mode in this case does not reveal the presence of damage, while the first curvature mode clearly highlights it. The selection of the decimation parameter is critical to the formulation of the SER. A low d in fact does not provide adequate baseline information, as the interpolated ODS captures all the features associated to damage, while a high d may not be sufficient to provide an appropriate description of the ODS. While further studies regarding to optimal choice of d are being performed, we here report on the effects of decimation on the accuracy of the damage detection methodology.

Figure 10.4 illustrates the influence of the decimation parameter on the synthesized data and on the resulting estimated SER. The plots are obtained for a damage at mid-length equal to $h/h_0 = 0.9$. For low decimations ($d = 50\%$), the

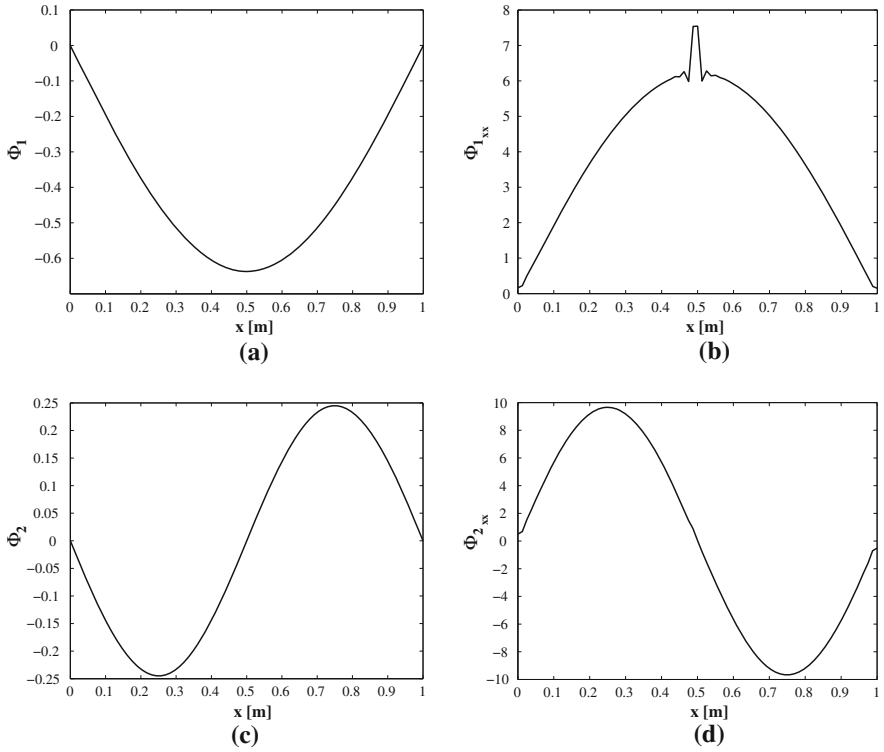

Fig. 10.3 Effect of damage at 50% length on displacement and curvature amplitudes. **a** Displacement first mode. **b** Culvature first mode. **c** Displacement second mode. **d** Culvature second mode $(h/h_0 = 0.9)$

synthesized baseline data, indicated as $'o'$ in the plots, replicate very closely the interpolation obtained from the full data set. The resulting SER estimation highlights some deviation from the unit value at mid-length, but does not give clear indication of the location of damage. The predictions can be significantly improved by increasing the decimation number, which allows synthesing baseline information, which resembles very closely the undamaged configuration. The proper selection of the decimation parameters provides a good estimation for the SER, which, in principle, can be used to assess both damage location and extent. Figure 10.5 shows how the amplitude of the deviation from unity is in fact proportional to the damage extent. The plots correspond to the SER for excitation at the first and third natural frequency, and for two damage locations. The cumulative SER value is an effective way to combine the results from the excitation of several modes and to avoid lack of sensitivity associated to damage located close to nodal points. The cumulative SER is also proportional to the damage extent, as shown in Fig. 10.6, which presents the results of the combination of the first 10 modal SER for both single and multiple damage locations.

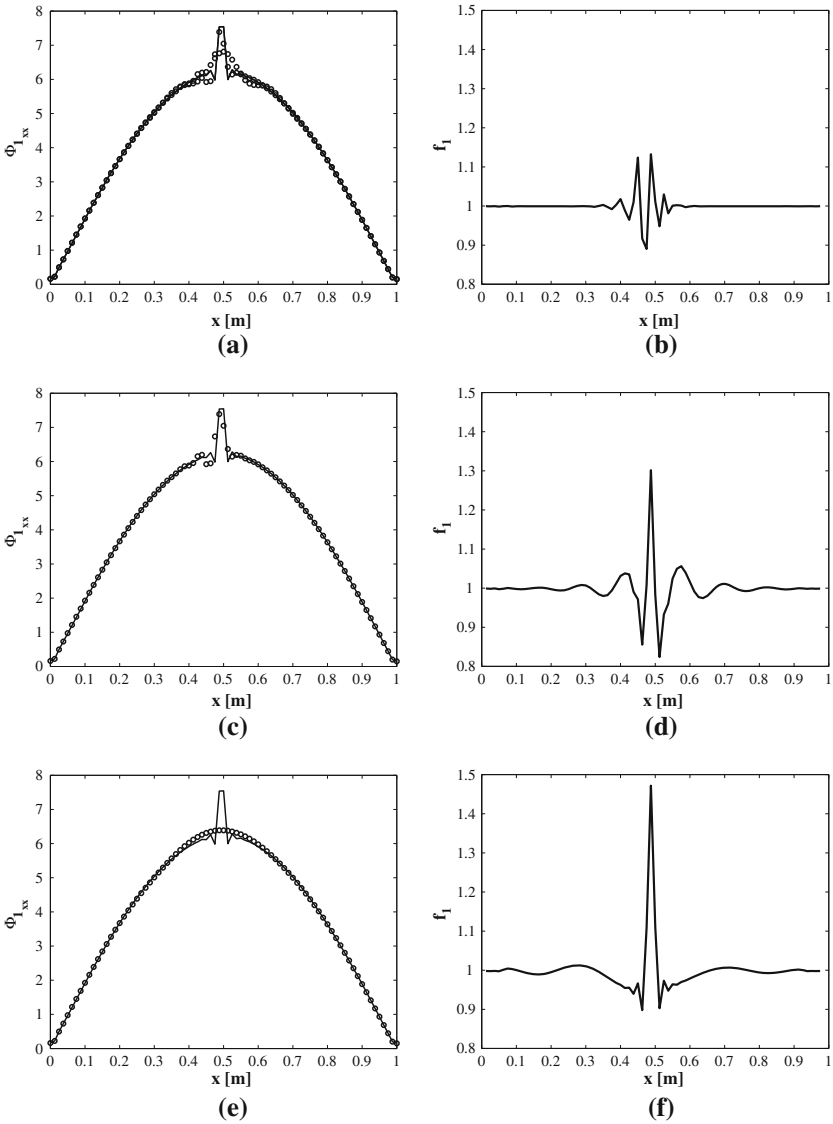

Fig. 10.4 Influence of order of decimation on modal curvature and SER estimation (first mode). **a** Curvature, 50% decimation, **b** Model SER, **c** Curvature, 75% decimation, **d** Model SER, **e** Curvature, 90% decimation, **f** Model SER

10.3.4 Numerical Results on Plates

Additional numerical tests are performed on a plate structure. A FE model is formulated according to Kirchhoff Plate Theory to predict the dynamic behavior of

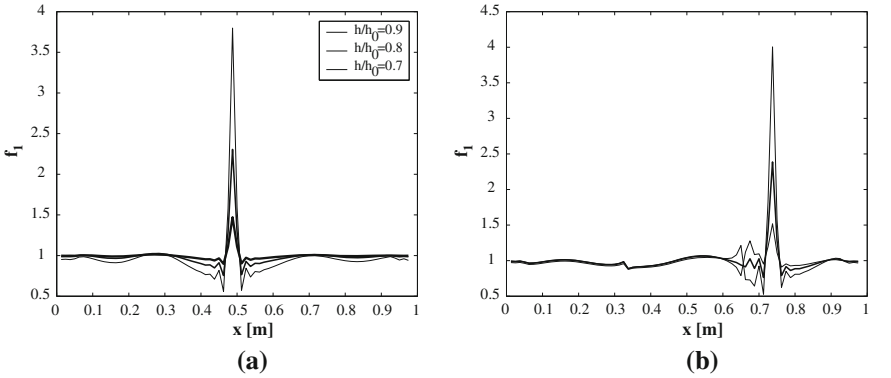

Fig. 10.5 Influence of damage extent on modal SER. **a** Damage at 50% length, first mode. **b** Damage at 75% length, first mode

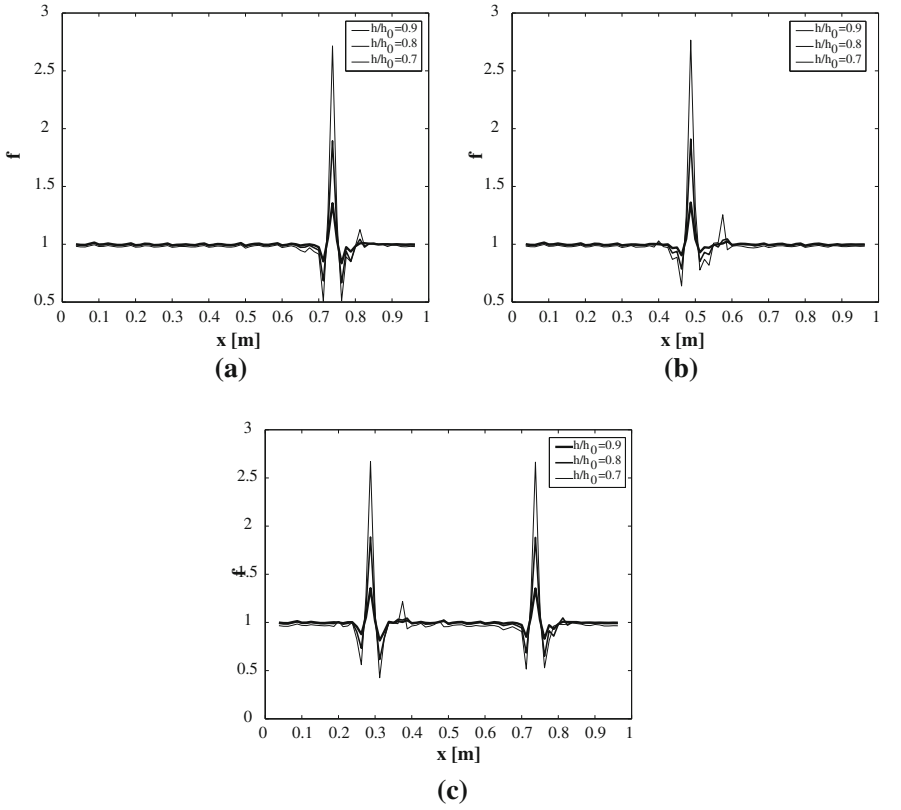

Fig. 10.6 Cumulative SER for different damaged configurations. **a** Damage at 75% length, **b** damage at 50% length, **c** damage at 75 and 30% length

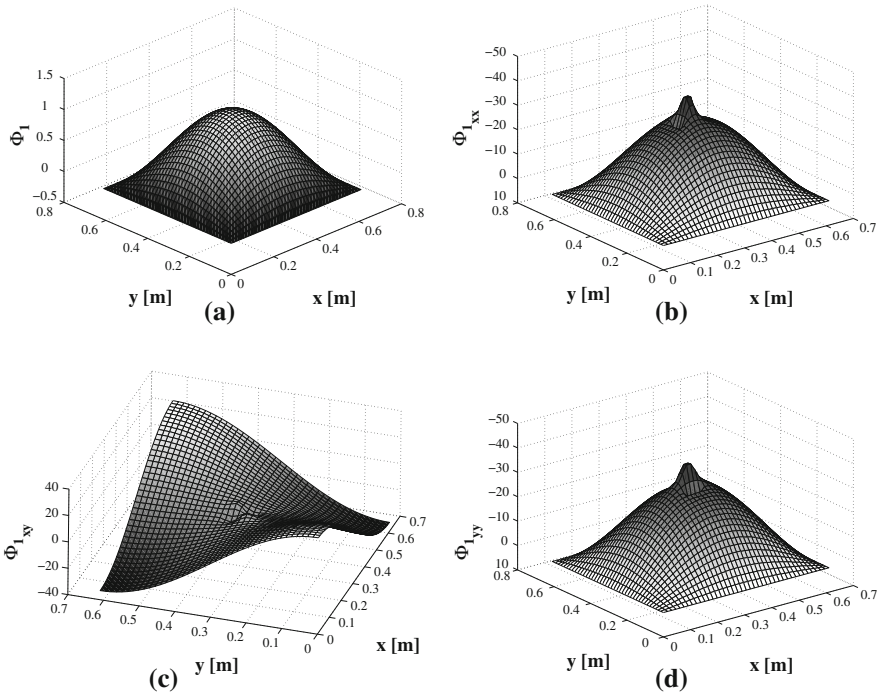

Fig. 10.7 First mode operational deflection shape and curvatures for plate with damage near center $(h/h_0 = 0.9)$

a thin steel plate $(E = 2.1 \times 10^{11}\,\text{MPa},\ \rho = 7,800\,\text{kg/m}^3,\ \nu = 0.3)$. The plate, which is square and measures 60 cm per side, is discretized using a 40×40 element grid, and it is supported on all sides. Damage is simulated again as a thickness reduction over a single element of the considered mesh. The curvatures corresponding to the harmonic excitation of the plate at its natural frequencies are obtained for a concentrated vertical load applied at coordinates $x_l = y_l = 0.16$ m from the lower left corner of the plate. Examples of curvatures for excitation at modes 1, 2 are shown in Figs. 10.7 and 10.8.

The considered damage corresponds to $h/h_0 = 0.9$ and it is located at coordinates $0.27 \le x_D \le 0.32$ m, $0.27 \le y_D \le 0.32$ m, which is the location of the element near the plate center. Figures 10.7 and 10.8 demonstrate the sensitivity of the curvature mode with respect to damage as opposed to the ODS, and again indicate how modes with maximum curvature near the damage location are mostly affected. The generation of baseline data through decimation of the available nodal information is also tested on simulated plate data. The results of this investigations are shown in Fig. 10.9, which show the influence of the decimation parameter on the first modal SER evaluation. The same damaged configuration considered for the results shown in Fig. 10.7 and 10.8 is again selected, and the decimation parameter now indicates the reduction of the nodal information along each side of

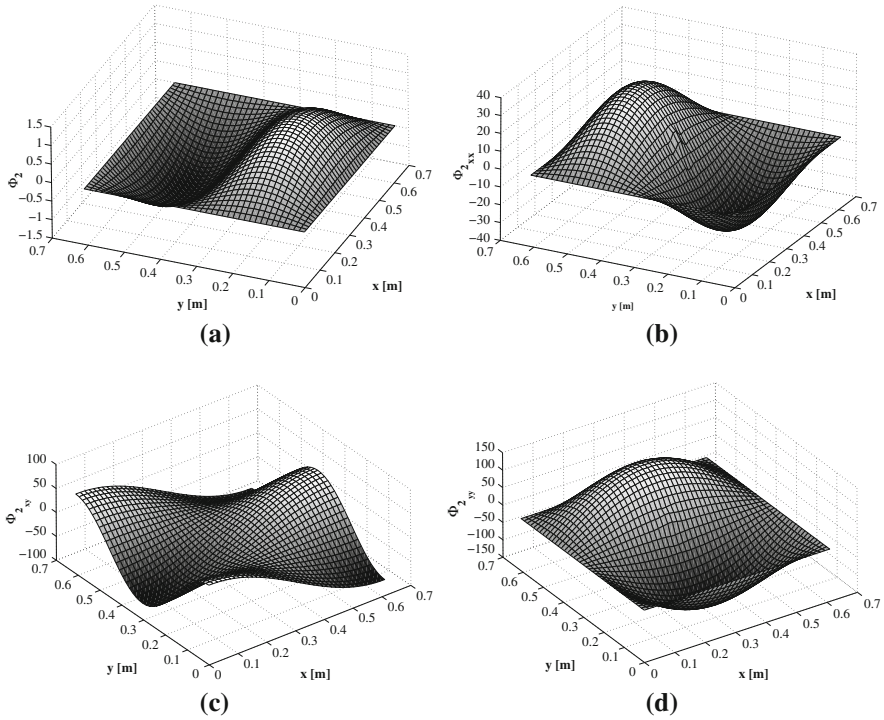

Fig. 10.8 Second mode operational deflection shape and curvatures for plate with damage near center $(h/h_0 = 0.9)$

the plate. The curvature plots shown in Fig. 10.9a, c and e are obtained by taking a cross section of the curvature surfaces at $y = 0.3$ m. The SER distributions are represented as contour maps, where the white background corresponds to unitary values, and the iso-level colors vary from black, corresponding to values of $f \cong 1.01$, to white again for $f \geq 2$. The SER contours confirm the results obtained from the beam analysis, which indicate how the decimation parameter can be selected to improve the damage sensitivity of the technique. Finally, Fig. 10.10 shows examples of cumulative SER distribution for various damage locations. The plots, obtained from the superposition of the first 10 modal contributions, indicate the effectiveness of the cumulative SER in identifying the correct location of single or multiple damaged elements.

10.3.5 Experimental Results on Beams

The beams used in the tests are 1.5″ wide and are cut from a plate fabricated with 12 layers of woven cloth with 0 and 90° fiber orientation. The matrix is a polyester resin type. The fiberglass beam used in the tests is shown in Fig. 10.11a. A

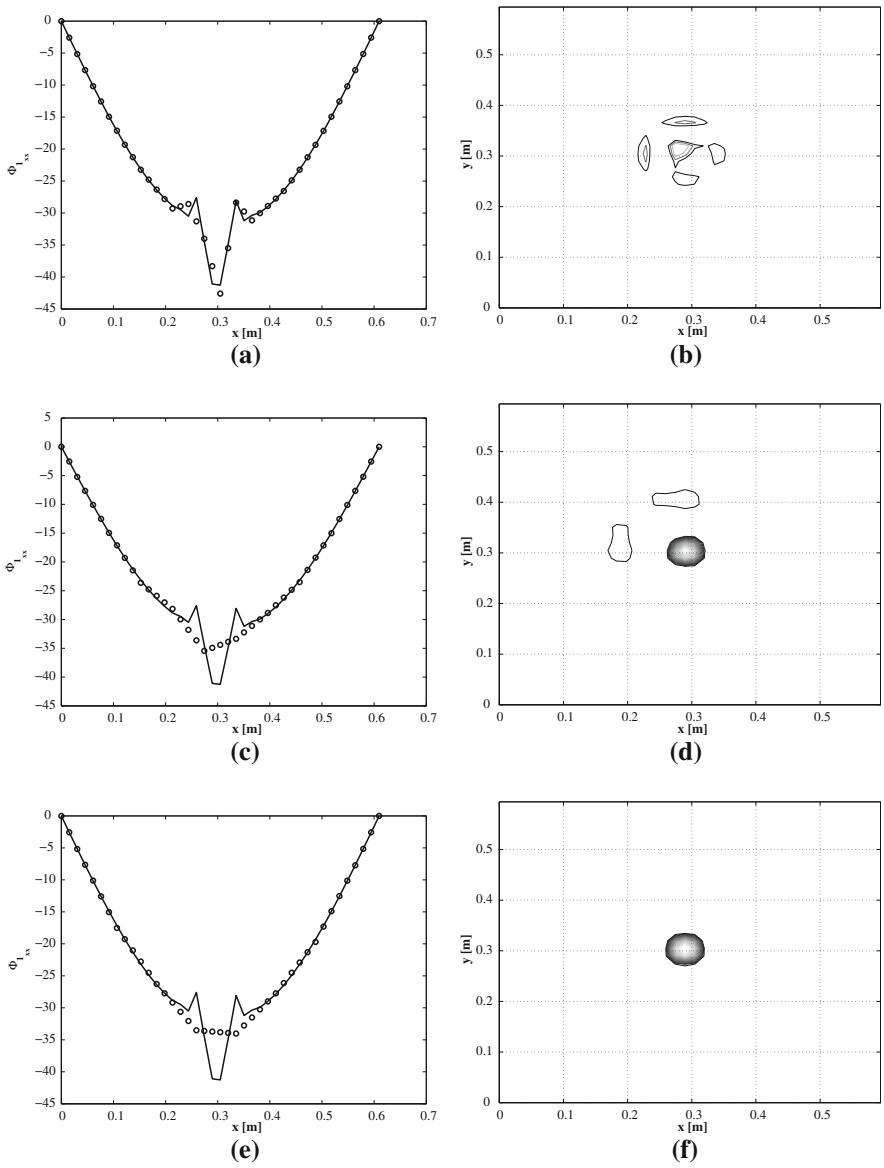

Fig. 10.9 Influence of order of decimation on first modal curvature and SER for plate. **a** $d = 50\%$, Curvature. **b** $d = 50\%$, Model SER. **C** $d = 75\%$, Curvature. **d** $d = 75\%$, Model SER. **e** $d = 80\%$, Curvature. **f** $d = 80\%$, Model SER $(h/h_0 = 0.9)$

cantilevered configuration is chosen for convenience. The beam is excited by an electrodynamic shaker (Ling Dynamics, Model 102A), and its response velocity is measured using a SLDV. The shaker stinger is purposely positioned off the centerline to allow excitation of both torsion and bending modes. The measurement

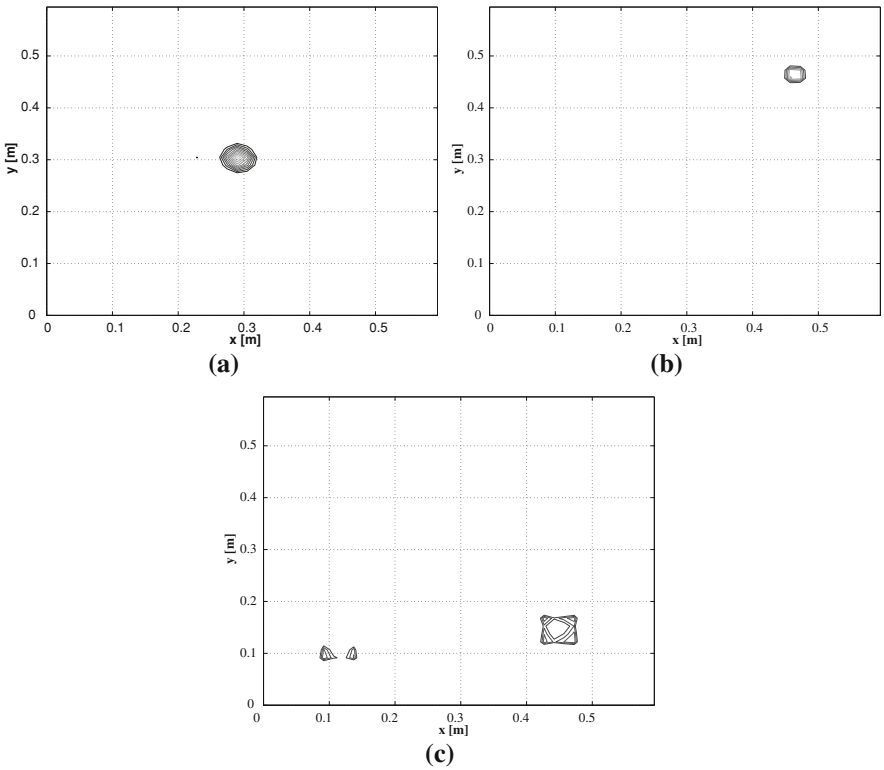

Fig. 10.10 Plate Cumulative SER for damage $h/h_0 = 0.9$ at various locations **a** $0.27 \leq x_D \leq 0.32\,\text{m},\ 0.27 \leq y_D \leq 0.32\,\text{m}$, **b** $0.43 \leq x_D \leq 0.46\,\text{m},\ 0.43 \leq y_D \leq 0.46\,\text{m}$, **c** $0.09 \leq x_D \leq 0.15\,\text{m},\ 0.09 \leq y_D \leq 0.14\,\text{m},\ 0.43 \leq x_D \leq 0.49\,\text{m},\ 0.12 \leq y_D \leq 0.18\,\text{m}$

grid and the damaged configuration with both cuts are shown in Fig. 10.11b and c. Damage is inflicted by cutting rectangular grooves using a hand saw. The first considered cut $(\sharp 1)$ is applied normally to the length of the beam. A second cut $(\sharp 2)$ is inclined with respect to the beam axis to ensure that the effectiveness of the technique is not affected by a particular orientation of the damage. The depth of each cut is kept at approximately $0.050''$, with tolerance requirements, which are not strict, as the objective at this time is to simply detect the presence of the damage in the test specimen. The vibration tests were conducted using pseudo-random excitation over the 0–1,000 Hz frequency range. The shaker is driven by the internal function generator available on SLDV. The recorded data are exported and post-processed in MATLAB® Examples of recorded ODSs are shown in Fig. 10.12.

The deflection measured along the beam center line is first analyzed, in order to perform an initial one-dimensional analysis. The measured ODS at various resonant frequencies are extracted and then interpolated using splines. The analytical differentiation of the splines functions is used to estimate the beam curvatures at

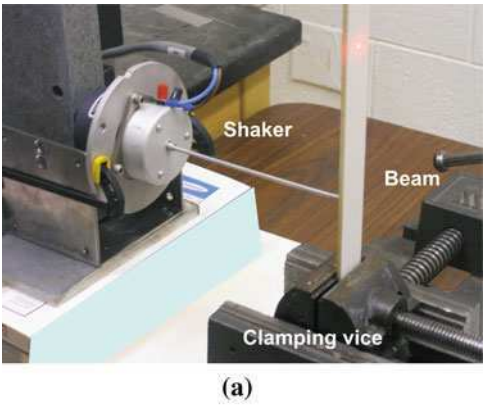

Fig. 10.11 Experimental set-up and configuration of damaged composite beam. **a** Experimental set-up, **b** measurement grid, **c** damaged beam

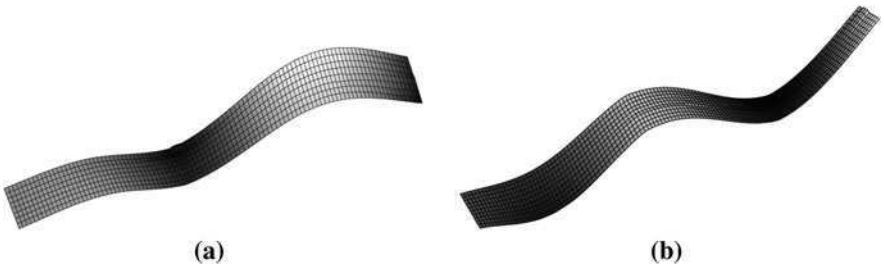

Fig. 10.12 Examples of ODS measured during beam experiments **a** ODS at 639 Hz, **b** ODS at 770 Hz

various frequencies. The results of the analysis of the beam with a single damage (cut (♯1)) are shown in Fig. 10.13. The displayed curvature and SER correspond to an excitation at 639 Hz, which is the fourth mode of the damaged beam. In the curvature plots, the solid line indicates the curvature computed from the full data set, while the circles correspond to the curvature obtained from decimated data. The SER estimations in Fig. 10.13b and d are obtained for two values of decimation to show how proper choice of the parameter d can substantially improve the accuracy of damage identification.

The results for the beam with two damages are shown in Fig. 10.14. The considered excitation frequency is 657 Hz, which corresponds to the fifth mode

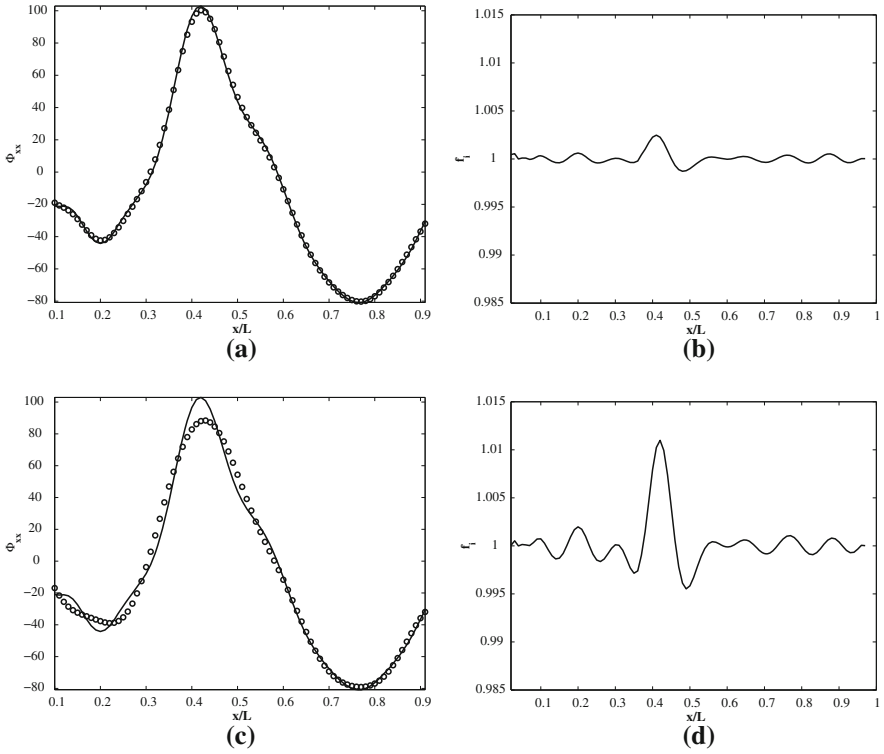

Fig. 10.13 Influence of order of decimation on the 639 Hz ODS curvature and SER for composite beam specimen with a single damage. **a** $d = 50\%$, Curvature, **b** $d = 50\%$, Model SER, **C** $d = 75\%$, Curvature, **d** $d = 75\%$, Model SER

of the beam. It is noted that higher decimation is now required in order to obtain an unambiguous damage indication. A low decimation parameter does not provide any identification of the damage using curvature data and provides a marginal indication using the SER information. This is similar to what was observed using the numerical simulation data due to the fact that a low decimation parameter does not provide an adequate baseline information. A decimation parameter of 90% provides identification of the location correctly for both damages in the beam.

The results of two-dimensional SER evaluation for the composite beam are presented in Fig. 10.15. The SER contours are evaluated by using data from the complete measurement grid shown in Fig. 10.11b, and by superimposing the contributions of the five modes of the beam, which contribute to the response in the 0–1,000 Hz frequency range. Both damages are correctly identified in terms of their location as well as orientation. The advantage of this latter approach is that no expert intervention is required for the selection of the mode to be analyzed, which may facilitate the process of automating the technique.

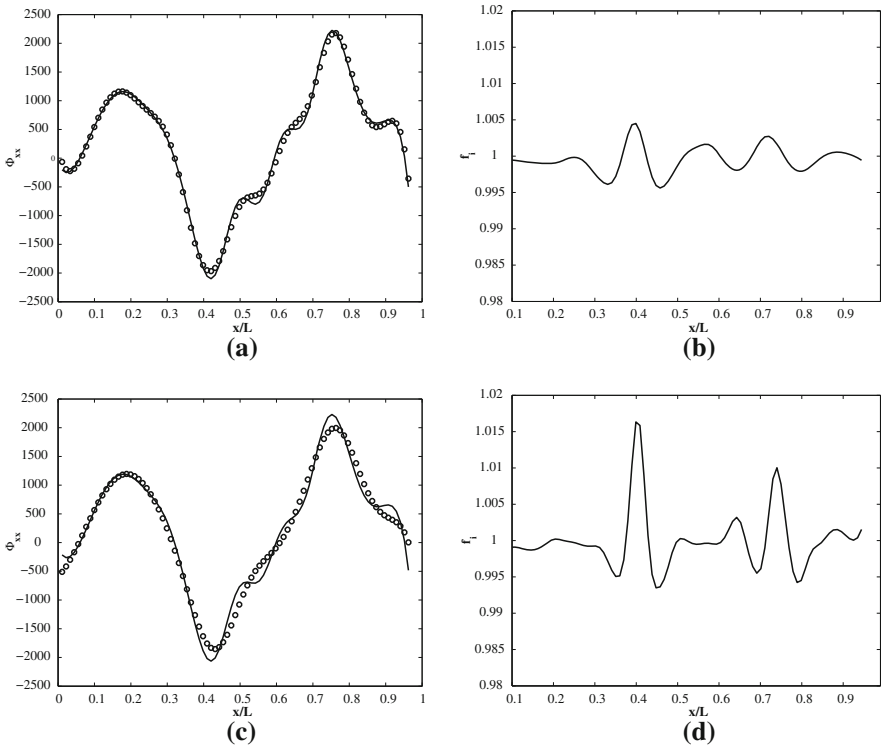

Fig. 10.14 Influence of order of decimation on the 657 Hz ODS curvature and SER for composite beam specimen with two damages. **a** d = 75%, Curvature, **b** d = 75%, Model SER, **c** d = 95%, Curvature, **d** d = 90%, Model SER

10.3.6 Experimental Results on Plates

The next step of validation of the damage detection methodology using SER includes tests on a thin aluminum plate with artificially induced damage.The plate measures $14'' \times 14'' \times 0.040''$, and it is cantilevered at the base. A piezoceramic disc of $1.1''$ diameter and $0.030''$ thickness is used as an exciter. The placement of the actuator is selected in order to excite the highest number of modes of the structure. Plate, with actuator and damage location is shown in Fig. 10.16a. The actuator is simply bonded to the plate using a Loctite Quick Set epoxy. The disc is also fully encased in a layer of epoxy to provide it with an adequate backing to impart sufficient force to its base. A set of simple tests are conducted to ensure that the effectiveness of the actuator in exciting the vibration modes and to check for durability of the bonding epoxy, which demonstrates to be excellent. The damage is a $1.41''$ long, $0.05''$ wide and 0.015 deep groove, which is cut in the plate at the location shown in Fig. 10.16a. Figure 10.16b shows the measurement grid utilized for the plate tests.

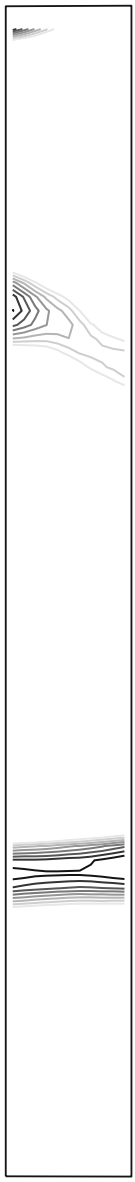

Fig. 10.15 Cumulative SER estimated using first five modes of beam with two damages

The plate is excited in the 0–500 Hz range using pseudo-random excitation. The forced response at the plate natural frequencies in the excitation range, and the corresponding curvatures are evaluated. Figure 10.17 shows for example the measured ODS at 270 and 293 Hz, while Fig. 10.18 shows the plate curvature at 293 Hz, and the corresponding modal SER. The plate curvature in this case does

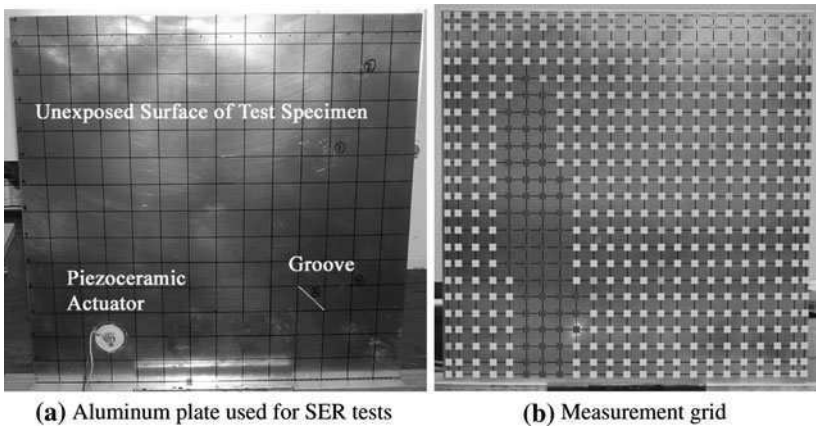

Fig. 10.16 Cantilevered aluminum plate with detail of actuator and damage locations (**a**), and measurement grid (**b**)

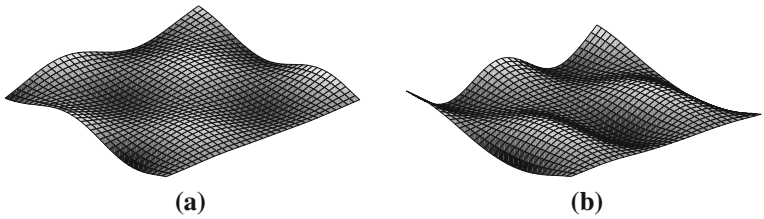

Fig. 10.17 Examples of experimentally measured ODS. **a** ODS at 270 Hz, **b** ODS at 293 Hz

not reveal any noticeable distortions due to the presence of damage. This is probably due to the particular orientation considered for the artificial cut versus the curvature shape. A direct comparison with the curvature associated with the corresponding mode of the undamaged plate, showed differences around the damage location. The results for the undamaged plate are not reported here as they do not add any relevant information. The modal SER shown in Fig. 10.18b on the contrary clearly highlights the location of damage in the plate. Some deviation from unity can be observed at other locations, one of them being located close to the exciter, and the other most likely due to measurement and/or numerical noise. This spurious information can be effectively filtered out by considering a cumulative SER obtained from the superposition of several modal information. The cumulative SER obtained from the superposition of the first five modes of the plate is shown in Fig. 10.19, which provides an unambiguous indication about damage presence and location.

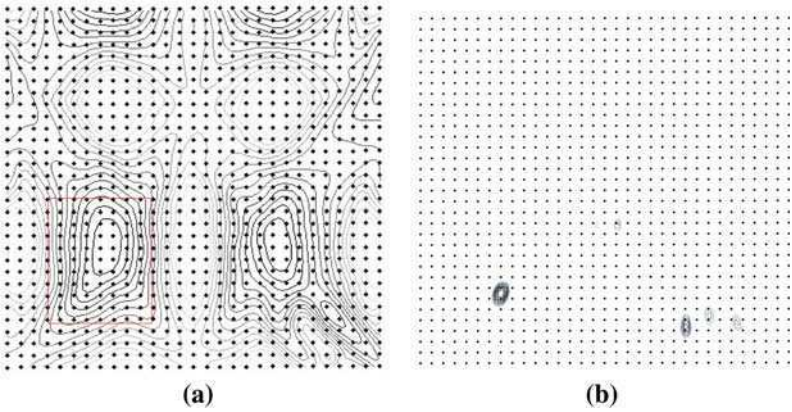

Fig. 10.18 Curvature and modal SER at 293 Hz. **a** Curvature, **b** Model SER

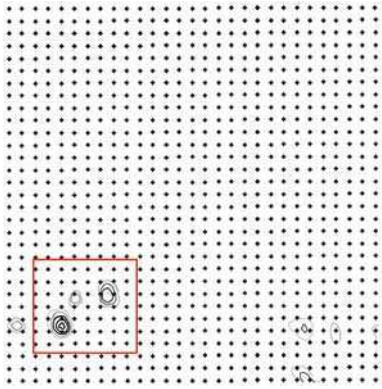

Fig. 10.19 Experimentally evaluated SER through the superposition of first five modes

10.4 Wave Propagation Techniques: Time Domain Damage Measure

The lack in sensitivity and capability of discriminating damage from changes in the operating conditions of modal-based methods can be overcome by applying inspection techniques based on Guides Ultrasonic Waves (GUWs) propagation [34, 36, 43]. Guided waves, show sensitivity to a variety of damage types and, as opposed to bulk waves used in traditional ultrasonics techniques, they have the ability to travel relatively long distances within the structure under investigation. For this reason, GUWs are particularly suitable for SHM applications, which may employ a built-in sensor/actuator network to interrogate and assess the state of health of the structure. These aspects were discussed in Chap 1. In most applications, GUWs are generated and received by piezoelectric transducers, which can both excite the structure, and record its response. As an alternative, an array of

transducers and actuators can be distributed over the structure's surface according to convenient patterns [17, 31, 36, 43]. The fundamentals of this type of operation consist in evaluating the characteristics of the propagation along the wave path between each transducer/receiver pair, and detecting reflections associated with damage. The interpretation of the signals characteristics and the detection of reflections is however complicated by the multi-modal and dispersive nature of GUW signals. For this reason, significant efforts are being devoted to improvements in the defect characterization procedures. Advanced signal processing techniques are being employed to highlight signal features, which are sensitive to the presence of damage, and which can be used for its classification and for the estimation of its extent [34].

10.4.1 Theoretical Background

The approach presented below is similar to the vibration based method discussed in Sect. 10.3.2. As in the vibration based method, the approach to be presented in this section relies heavily on the SLDV measurements. The major difference between these two methods is that in the former ODS is used, while in the latter, GUWs generated through piezo actuators is used in the estimation of the damage index (DI).

The damage index is formulated on the basis of the distribution of an energy functional over the monitored surface. The ratio of the measured energy distribution to a reference, baseline value is considered as the damage indicator. This formulation follows the developments presented for example in [12, 23], and heavily relies on the notation used in finite element analysis. In particular, we consider the expression of the displacement field at some location x, y as:

$$w(x, y) = \sum_k h_k(r, s) w_k \tag{10.20}$$

where $w(x, y)$ is the out-of-plane displacement at location x, y, while w_k is the out-of-plane displacement at the kth grid point. This displacement value is the one obtained directly from SLDV measurements, or represents the displacement at a nodal location in a numerical simulation. Depending on the type of dynamic tests that are being conducted, $w_k = w_k(t)$ defines the amplitude of the response at a specific time instant t, else $w_k = w_k(\omega)$ may quantify the amplitude of the steady-state response when the structure is excited at a frequency ω. Finally in Eq. 10.20, h_k is the kth interpolation function defined in terms of a set of non-dimensional coordinates r, s. The interpolation considers grid points around the location of interest x, y, in order to basically reproduce the process used in FEA with plane elements. The order of the function h_k is defined by the number of grid point displacements used for the interpolation. The quadrilateral element analogy is generally considered as in the great majority of the tests we expect to utilize rectangular grids. The expression of the interpolation functions in terms of

non-dimensional coordinates however allows mapping general grid patterns into non-dimensional squares, as traditionally done with isoparametric elements [10]. Equation 10.20 can be expressed in the following matrix form:

$$w_g(x,y) = \boldsymbol{H}_g(r,s)\boldsymbol{w}_g \tag{10.21}$$

where $w_g(x,y)$ is the out-of-plane displacement within the gth region of the scanned surface, $\boldsymbol{H}_g(r,s)$ is the matrix of the interpolation functions, while $\boldsymbol{w}_g$ is the array of the measured out-of-plane displacements used for interpolation.

Equations 10.20 and 10.21 can be used to formulate an energy functional which is closely related to the strain energy of the structure under investigation. We rely on the assumption that the portion of the structures under investigation is relatively thin compared to their in-plane dimensions. This assumption certainly holds true for the examples presented in this chapter. The following strain–displacement relations are here considered:

$$\boldsymbol{\varepsilon} = -z\left[w_{,xx} w_{,yy} w_{,xy}\right]^T \tag{10.22}$$

where z is the thickness coordinate, while the following notation $(.)_{,x}$ indicates a partial derivative with respect to the coordinate x. Imposing the matrix form of the displacement interpolation relations, we obtain the following expression for the interpolated strain distribution:

$$\boldsymbol{\varepsilon}_g = -z\boldsymbol{B}(r,s)\boldsymbol{w}_g \tag{10.23}$$

where $\boldsymbol{B}$ is a matrix containing the derivatives corresponding to the strain–displacement relations in Eq. 10.20. This expression is utilized to evaluate the energy functional over the gth region of the measurement grid, which is defined as follows:

$$\mathscr{E}_g(t) = \frac{b_g^3}{24}\boldsymbol{w}_g^T(t)\int_{A_g} \boldsymbol{B}^T\,\boldsymbol{B}dA\;\boldsymbol{w}_g(t) \tag{10.24}$$

where b_g is the thickness of the region g of area A_g. It is here assumed that the thickness over each grid region is constant. One should note how the expression in Eq. 10.24 resembles very closely the expression for the elemental strain energy in FEA. In here, we do not include the constitutive matrix of the material, as direct measurement on the structure under investigation are generally not available. The total energy functional $\mathcal{E}$ for the monitored area can be estimated as:

$$\mathscr{E}(t) = \sum_g \mathcal{E}_g(t) \tag{10.25}$$

Time dependence is here explicitly indicated to underline that, in case of transient, time domain measurements, the procedure can provide a value for the total energy as well as for the energy distribution over the monitored region at any time step.

Alternatively, $\mathscr{E}(\omega)$, $\mathscr{E}_g(\omega)$ can be computed from the measured steady-state response when the structure is excited at frequency ω.

We denote with the superscript $()^*$ quantities associated with an undamaged test structure, while the absence of the superscript indicates properties of the damaged structure. Following the developments presented in [12, 23], it is assumed that damage is located at a particular location $g = p$, and that at this location:

$$\frac{\mathscr{E}_p}{\mathscr{E}} \approx \frac{\mathscr{E}_p^*}{\mathscr{E}^*} \tag{10.26}$$

Equation 10.26 can be used to formulate a damage index measuring the reduction in stiffness over the region p, according to the following expression:

$$f_p = \left(\frac{b_p^*}{b_p}\right)^3 = \frac{\mathcal{E}^*}{\mathcal{E}} \frac{\boldsymbol{w}_p^T \int_{A_p} \boldsymbol{B}^T \boldsymbol{B} dA \, \boldsymbol{w}_p}{\boldsymbol{w}_p^{*T} \int_{A_p} \boldsymbol{B}^T \boldsymbol{B} dA \, \boldsymbol{w}_p^*} \tag{10.27}$$

where f_p is the considered DI for the pth region. The DI potentially provides indications of both damage location, as well as its extent. Specifically, f_p is expected to be equal to 1 over undamaged regions, and different than 1 over a damaged region. It is well known how damage affects the strain energy distribution when it is located near, or in regions of maximum strain energy. Hence, the visibility of damage is affected by the frequency range of excitation and associated response wavelength, and on the considered measurement grid refinement.

The considered DI formulation requires knowledge of deflections and its partial derivatives along two reference directions, say $w_{,x}$ and $w_{,y}$. These derivatives are obtained through spline interpolation of the measured deflections and the successive differentiation of the interpolating spline. This minimizes errors related to the numerical differentiation of measured values, as the differentiation of the splines can be performed analytically, with the measured deflections acting as weighing parameters. Baseline information is generated by using a subset of the measurement points. The data decimation along one of the reference direction, say x, is quantified by a "decimation factor" (see Sect. 10.3.3).

As previously discussed, two versions of the DI can be defined depending on the data used for its evaluation. The frequency domain formulation utilizes the ODS for excitation at the structure's natural frequencies. The DI expression defined in Eq. 10.27 can be also formulated in the time domain, and can be applied to the analysis of propagating waves. Results from this formulation are DI maps that evolve over time as waves propagate within the structure. The advantages of a time domain DI include the possibility of limiting the investigation to a particular time window. A recognized problem in wave propagation-based inspections arises when the incoming wave hides the presence of damage and resulting wave reflections. The analysis of the trailing part of the wave, after the main pulse has decayed, is often rich in information regarding damage location and extent, as damage generally behaves like a secondary wave source. The considered time

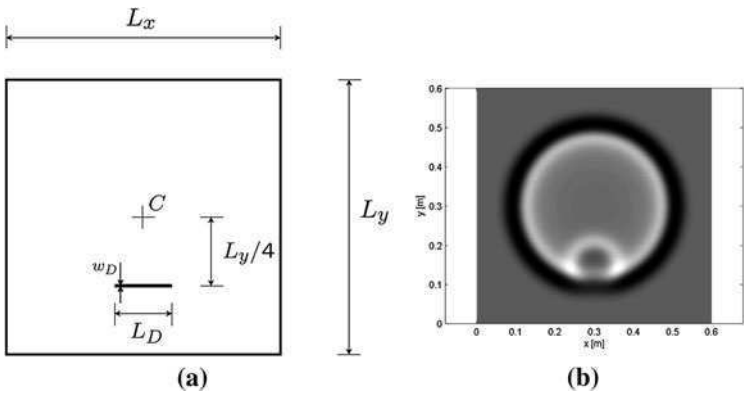

Fig. 10.20 **a** Computational domain and **b** snapshot of response showing propagating wave and reflection caused by damage

domain DI allows selecting the time interval where structural response and associated energy distribution are most affected by damage.

10.4.2 Numerical Examples: Wave Propagation in a Homogeneous Medium

The mass Spring Lattice Model (MSLM) presented in [49] is used to simulate the propagation of elastic waves in the considered homogeneous medium. MSLM utilizes the formalism of finite difference methods to discretize the medium into a lattice, for which elastodynamic equations are formulated. Discontinuities and in general changes to the material properties of the medium are treated by simply modifying the properties of the lattice at the corresponding locations. The approach is very simple, easy to implement, and therefore very convenient for simulating wave propagation in a damaged specimen. Here, the approach is used for simulating ultrasonic waves in a thin two-dimensional elastic domain, with the assumption that all displacement components are constant through the thickness, i.e. $u = u(x, y), v = v(x, y), w = w(x, y)$. This allows the out-of-plane displacement component to be decoupled from the in-plane behavior of the domain, which yields a significant reduction in the cost. The goal of the simulations is to test the DI concept as applied to transient wave propagation. The considered domain is discretized using a 200×200 lattice, with damage being modeled as a localized loss of stiffness. A schematic of the considered computational domain and of the location of damage is shown in Fig. 10.20a. The domain is square with $L_x = L_y = 0.6$ m, and features a local reduction in thickness over a region with $w_D = 3$ mm, and length L_D. A snapshot of the propagating wave in the considered domain is presented in Fig. 10.20b, which shows the response obtained for a 30% reduction in thickness, and for $L_D = 1.8$ cm, given an initial gaussian

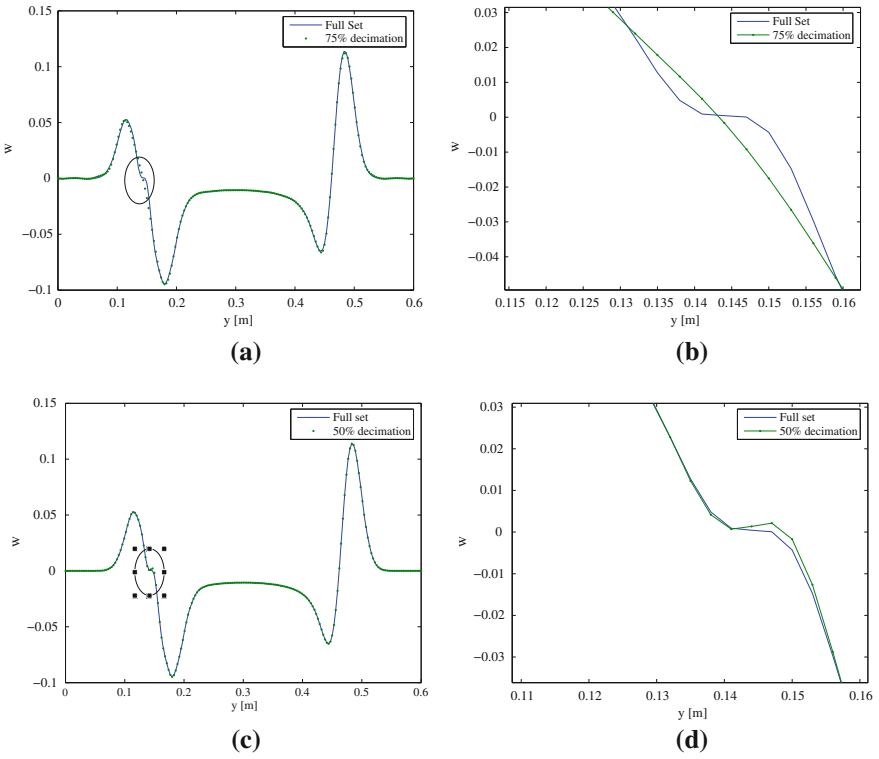

Fig. 10.21 Comparison of deformed configuration obtained from full and decimated data set (cross section at $x = L_x/2$) **a** d = 75%, **b** d = 75%, detail, **c** d = 50%, **d** d = 50%, detail

displacement distribution centered at the plate center C. The presence of a reflected wave anticipating all edge reflections clearly highlights the presence of damage and its interaction with the propagating wave. The DI is evaluated at every time instant considered in the simulations. The decimation procedure is applied to obtain baseline information. The effect of the decimation factors on the evaluation of the domain deformed configuration is shown in Fig. 10.21, which compares the out-of-plane deflections estimated at a specific instant of time using full and decimated nodal information. The figures show a cross section of the deformed configuration of the plate at $x = L_x/2$. The specific snapshot corresponds to the instant immediately following the interaction with the main wave with the defect. The full response shows the effect of damage as a localized discontinuity at the damage location. This discontinuity is not captured by a 75% decimated data set (see details shown in Fig. 10.21b, d), while it is partially described by interpolated values obtained through a 50% decimation. Damage index maps obtained using 75% decimation show with vivid detail the location and the extension of damage over the computational domain (Fig. 10.22). The maps are obtained at a specific time instant which corresponds to the initial interaction of the propagating pulse

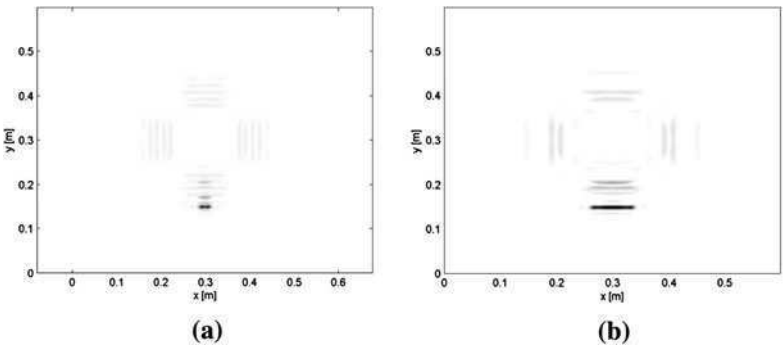

Fig. 10.22 Snapshots of DI maps corresponding to linear cracks of different lengths. **a** L_D=1.8 cm, **b** L_D=9.6 cm

with the longitudinal crack, and correspond to two damage lengths, specifically $L_D = 1.8$ cm (Fig. 10.22a), and $L_D = 9.6$ cm (Fig. 10.22b).

10.4.3 Experimental Results: Aluminum Plate

The approach presented in the previous section is validated experimentally on simple plate structures. Both frequency domain tests, as well as wave propagation investigations are performed to implement the integrated approach described in Sect. 10.4.1. The two types of dynamic investigations are performed using the same actuator and sensor pair. Piezo-ceramic discs are employed as actuators, and they are placed at locations which are selected so that adequate modal excitation is achieved, and elastic waves suitable for damage detection are generated [17, 43]. The SLDV is used to detect the resulting plate vibrations and the wavefield. More details on SLDV operation is given in Chap. 1.

For the wave propagation tests, The excitation signal is a 5-cycle sinusoidal burst at 50 kHz. This frequency is selected through a manual sweep over the 20–100 kHz range performed to evaluate the frequency corresponding to the maximum plate response. This procedure can be improved by carefully matching the size of the actuator with the desired excitation frequency through methodologies of the kind described in [17].

A snapshot of the plate time domain response and of the corresponding DI are shown in Fig. 10.23. A qualitative analysis of the time domain signal suggests that the considered time instant corresponds to the interaction between the symmetric Lamb mode and the defect. The symmetric mode travels faster than the anti-symmetric mode, which is the one mostly excited by the considered actuator set-up. The DI shown in Fig. 10.23b is obtained with a 67% decimation in both directions, and clearly shows orientation and length of the damage.

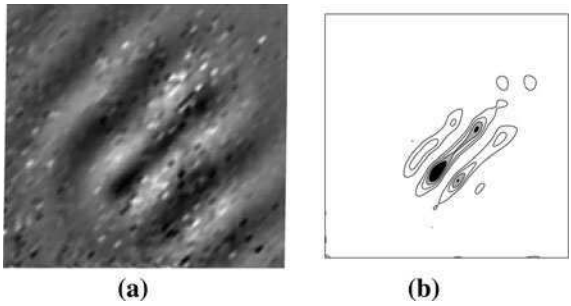

Fig. 10.23 Snapshot of plate displacement and corresponding DM. **a** Displacement, **b** Time domain DI

10.5 Phase Gradient and Conversion Coefficients Evaluation for Damage Localization and Quantification

In terms of damage detection, much of the literature considers excitation configurations where the first symmetric (S_0) mode is typically used for interrogation, and utilizes a frequency range which is below the cut-off frequency for the second antisymmetric (A_1) mode. Mode conversion is a key aspect to damage quantification with Lamb waves, and is defined as the phenomen whereby partial energy transfer may result in the particle to move out-of-plane given an in-plane incident mode [17]. For example, a launched S_0 mode partially converts to an A_0 mode upon arrival at the defect location, or vice-versa. It is quite intuitive to expect that mode conversion does not occur in the presence of defects which are symmetric through the thickness [4]. Partial reflection of the incident S_0 wave in the presence of defects has for example been predicted using the boundary element method [51] or modal decomposition [15].

The variation of reflection, transmission or/and conversion coefficients with respect to defect size has been utilized to quantify the degree of damage [9, 15, 28]. The reflection, transmission and conversion coefficients are defined as the ratios between the amplitudes of reflected, transmitted and converted modes and the amplitude of the incident wave. These ratios can be defined in the time [1] or frequency domain [29], at one location [29, 53] or as a spatially averaged quantity [6]. Finite elements [29], global-local or hybrid techniques [2], boundary elements [51], as well as analytical methods [15], higher order plate theory [46] and experimental results [27] have all been used to estimate the wave coefficients and to relate them with the damage size for different configurations. Most of the literature shows that these coefficients are strongly dependent on the frequency-thickness product, on the mode type (symmetric or antisymmetric), and on the ratio between the wavelength and a characteristic length of the defect [2, 46].

In what follows, spatially dense measurements are used to estimate the location of damage along one-dimensional waveguides, and subsequently evaluate mode conversion/reflection coefficients in the presence of simple notch-like defects. The available spatial resolution is exploited to define an integral definition of the mode coefficients, in an attempt to reduce the influence of noise, along with problems

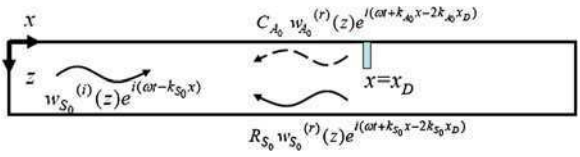

Fig. 10.24 1D waveguide with damage

with the selection of the point to be considered for the estimation of the modal amplitudes.

10.5.1 Simplified Description of a Multi-Modal Wave

The concepts is here illustrated for simplicity by considering the one-dimensional (1D) propagation of a multi-modal wave. The formulation is restricted to the frequency range of the first two Lamb waves, but it may be extended to higher order modes. It is assumed that the first symmetric Lamb mode (S_0) is generated to interrogate the structure, and that the interaction with a defect causes reflection and partial mode conversion into the A_0 mode of the injected wave (Fig. 10.24).

Accordingly, the wave in the region $x < x_D$ can be expressed as:

$$w(x,t) = e^{j\omega_0 t}\left[w_{S_0}^{(i)} e^{-jk_{S_0}x} + w_{S_0}^{(r)} e^{j(k_{S_0}x - 2k_{S_0}x_D)} + w_{A_0}^{(r)} e^{j(k_{A_0}x - 2k_{A_0}x_D)}\right] \tag{10.33}$$

or

$$w(x,t) = w_{S_0}^{(i)} e^{j\omega_0 t}\left[e^{-jk_{S_0}x} + R_{S_0}^{j(k_{S_0}x - 2k_{S_0}x_D)} + C_{A_0} e^{j(k_{A_0}x - 2k_{A_0}x_D)}\right] \tag{10.34}$$

where $w(x,t)$ defines the displacement distribution along the longitudinal coordinate x, measured on the top surface of the waveguide. Also in Eq. 10.33, w_{S_0}, w_{A_0} define the amplitudes the two modes propagating simultaneously in the waveguide, while the subscripts (i), (r) respectively denote 'incident' and 'reflected' wave components. Finally, R_{S_0}, C_{A_0} are the reflection and mode conversion coefficients, under the assumption that the injected wave contains only one mode (S_0), and that damage causes its partial reflection and conversion into the mode A_0. The adopted notation suggests that we are considering the propagation of Lamb waves in a thin plate, even though the description in Eq. 10.33 should be considered as general, and not completely accurate for the case of Lamb waves. It is however sufficient and simple enough to illustrate the concepts under investigation.

10.5.2 Phase Gradient for Damage Localization

The contributions from incident and reflected wave modes can be conveniently separated through filtering in the frequency wavenumber domain as illustrated in

Chap. 3. Assuming that the converted/reflected A_0 mode is of interest, a filtered w_f response can be obtained upon filtering such that:

$$w_f(x,t) \approx w_{S_0}^{(i)} C_{A_0} e^{j(k_{A_0}(x-2k_{A_0}x_D)} e^{j\omega_0 t}, \quad x \leq x_D \tag{10.35}$$

The phase of the Fourier transform of the converted A_0 wave can be used to estimate the location of damage. After obtaining the filtered A_0 wave, its spatial distribution can be evaluated through the application of FT. This gives the spatial distribution of the converted mode, at the excitation frequency ω_0. The converted A_0 wave originates at the damage location, so its mathematical expression should read:

$$w_{A_0}^{(r)}(x,\omega_0) \cong w_{S_0}^{(i)} C_{A_0} e^{jk_{A_0}(x-2k_{A_0}x_D)}, \quad x \leq x_D \tag{10.36}$$

The magnitude of the of the converted wave is given by:

$$|w_{A_0}^{(r)}(x,\omega_0)| = w_{S_0}^{(i)} C_{A_0}, \quad x \leq x_D \tag{10.37}$$

while its phase can be expressed as:

$$\angle w_{A_0}^{(r)}(x,\omega_0) \cong k_{A_0}(x-2x_D)U(x_D-x), \quad x \leq x_D \tag{10.38}$$

The linear variation of the phase can be used to obtain the precise location of the damage. This can be achieved by estimating the phase of the recorded response at a number of measuring points, and by subsequently identifying the location at which the phase becomes constant, through linear regression of the data. A more robust technique consists in taking the second derivative of the phase in terms of the spatial coordinate, which gives:

$$\frac{\partial^2}{\partial x^2}\left[\angle w_{A_0}^{(r)}(x,\omega_0)\right] \cong \delta(x-x_D) \tag{10.39}$$

where δ is the Dirac Delta function centered at the damage location.

This simple technique, which can generally be applied to any propagating wave, defines the location of the damage as origin of the reflected signal. The approach has great potentials for two important reasons:

1. The presence of a linearly varying phase originating at the source of a reflection occurs independently from the amplitude of the signal, which provides the means to highlight the presence of small reflected waves, resulting from very small damages.
2. The linear variation of the phase may be used to reduce the number of measurement points while still enabling the precise localization of damage through linear regression of the phase values.

The application of this concept for damage localization is illustrated in the following sections as applied to simulated and experimental data.

10.5.3 Reflection, Transmission and Conversion Coefficients for Damage Quantification

Upon filtering and evaluation of the individual modes and their FT at the frequency of interest ω_0, and following the simplified notation introduced above, one may express the filtered incident and reflected/converted modes as:

$$w_{A_0}^{(r)}(x,\omega_0) \cong w_{S_0}^{(i)} C_{A_0} e^{jk_{A_0}(x-2k_{A_0}x_D)}, \quad x \le x_D \tag{10.40}$$

and,

$$w_{S_0}^{(i)}(x,\omega_0) \cong w_{S_0}^{(i)} e^{-jk_{S_0}x}, \quad x \le x_D \tag{10.41}$$

Similarly, the reflected S_0 mode may be expressed as:

$$w_{S_0}^{(i)}(x,\omega_0) \cong w_{S_0}^{(i)} R_{S_0} e^{jk_{S_0}(x-2x_D)}, \quad x \le x_D \tag{10.42}$$

Taking the ratio of the magnitudes of the various separated mode components can lead to an estimation of the reflection and conversion coefficients. Specifically, the conversion coefficient A_0 can be estimated as:

$$C_{A_0} \approx \frac{|w_{A_0}^{(r)}(x,\omega_0)|}{|w_{S_0}^{(i)}(x,\omega_0)|} \tag{10.43}$$

while the reflection coefficient can be found from:

$$R_{S_0} \approx \frac{|w_{S_0}^{(r)}(x,\omega_0)|}{|w_{S_0}^{(i)}(x,\omega_0)|} \tag{10.44}$$

Previous work has investigated the evaluation of the mode coefficients and has provided recommendations in regards to the distance where they can be evaluated to avoid influence of near field phenomena developing near the damage [27, 28, 46]. The recommended distance is typically defined as a multiple of the wavelength of the incident wave λ, with a typical recommended value of 4λ. Such recommendation clearly drives the positioning of the transducer to be used for the measurement. Wavefield data however, provide the opportunity to select various points over the measured distance, so that the value of the mode coefficients can be estimated at various locations. This allows the estimation of its spatial-independence, and more importantly of a spatially averaged value, which is less affected by amplitude fluctuations due to noise, or by general trends associated with geometrical spreading. The spatial averaging procedure can be mathematically described as an integral operation over a portion of the measurement domain defined by two coordinates x_1, x_2.

Considering the relation between incident, converted and reflected amplitudes corresponding to Eqs. 10.43 and 10.44:

$$\left|w_{A_0}^{(r)}(x,\omega_0)\right| \approx C_{A_0}\left|w_{S_0}^{(i)}(x,\omega_0)\right| \tag{10.45}$$

and

$$\left|w_{S_0}^{(r)}(x,\omega_0)\right| \approx R_{S_0}\left|w_{S_0}^{(i)}(x,\omega_0)\right| \tag{10.46}$$

and integrating both sides of the equations between x_1, x_2 gives:

$$C_{A_0} \approx \frac{\int_{x_1}^{x_2}|w_{A_0}^{(r)}(x,\omega_0)|dx}{\int_{x_1}^{x_2}|w_{S_0}^{(i)}(x,\omega_0)|dx} \tag{10.47}$$

$$R_{S_0} \approx \frac{\int_{x_1}^{x_2}|w_{S_0}^{(r)}(x,\omega_0)|dx}{\int_{x_1}^{x_2}|w_{S_0}^{(i)}(x,\omega_0)|dx} \tag{10.48}$$

10.5.4 Application to Simulated Data

10.5.4.1 Model Configuration

The model of an isotropic, homogeneous plate with a rectangular notch defect is developed using the commercial software ABAQUS. The model considers a cross section of the plate, which is assumed infinite along the out-of-plate direction. Such conditions are enforced by imposing a state of plane strain on the model. The plate dimensions are: thickness $h = 2 \times 10^{-3}$ m, out-of-plane width 5×10^{-1} width, and length 1 m. The material properties are: density 2,800 kg/m^3, elastic modulus 72 GPa and Poisson's ratio 0.33. The rectangular notch has a length of 1×10^{-3} m and a non-dimensional depth $\varepsilon = h_d/h \in [0,1]$, where h_d is the notch depth.

The governing equations of motion are solved through an explicit central-difference time integration scheme. To ensure stability, the integration time step Δt, is chosen such that $\Delta t = 1/f_0/20$, where f_0 is the highest frequency of interest, measured in hertz [48]. The element size ($\Delta l = \Delta t c_L$, where c_L is the longitudinal wave speed) is selected on the basis of the minimum wavelength of elastic waves propagating in the plate [32].

A longitudinal uniform tip load is applied at one end of the plate whereas the opposite end is fixed. The symmetry of the applied in-plane load ensures that the S_0 mode is primarily excited [3]. The broad-band impulse load in Fig. 10.25a is the considered excitation time history. The frequency/wavenumber representation of the corresponding plate response displayed in Fig. 10.25b shows the bandwith of the signal as well as the agreement with the analytical dispersion curves for Lamb waves, which highlights the accuracy of the FE discretization.

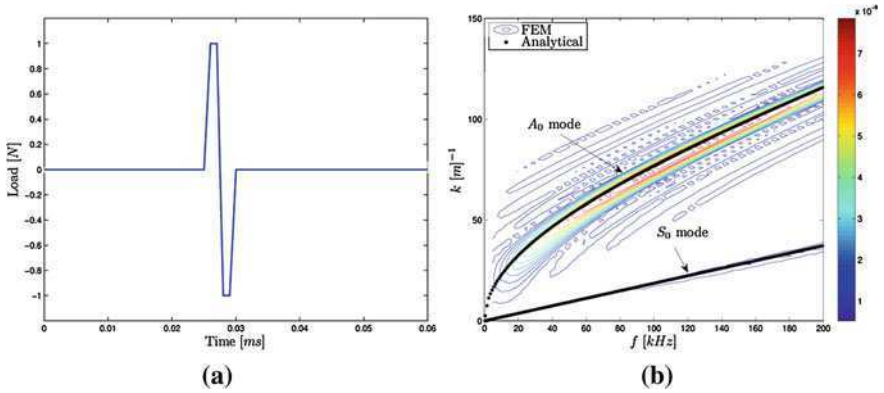

Fig. 10.25 **a** Broad-band square impulse tip load, **b** analytical and FE dispersion relations for the transverse response

10.5.4.2 Damage Localization Through Phase Gradient Estimation

The response corresponding to a 5-cycle in-plane tone burst modulated by a Hanning window is recorded and post-processed to separate different modes and to calculate phase gradients of the reflected A_0 mode at the frequency of maximum amplitude. For the given simulations, the excitation frequency, damage depth, and damage width are parametrically varied, whereas the plate height and width remain constant. For the given parametric studies, ε, the non-dimensional ratio of the damage depth (h_d) to plate thickness (h) ranges from 0 to 1 at increments of 0.1. For the given plate dimensions and material properties, the frequency range is 0 to 0.8 MHz. Upon selecting an applicable frequency, the resulting wavelength is directly extracted from the dispersion relations. A non-dimensional ratio (Λ) of excitation wavelength (λ) to damage width (Δl) is used to quantify the damage size versus the excitation wavelength: $\Lambda = \lambda/\Delta l$.

The results at $\Lambda = 40.8$ for three depths $(\varepsilon = 0.1, 0.5, 0.9)$ are presented in Fig. 10.26, whereas the results at a constant notch depth of $\varepsilon = 0.5$ for varying normalized excitation wavelengths, Λ, are shown in Fig. 10.27. For the given parametric studies, the non-dimensionalized Lamb wavelengths, Λ, ranges from 10 to 40, which is consistent with previous low frequency Lamb wave reflection studies per notch width [28]. Figures 10.26 and 10.27a show the variation of the phase of the converted A_0 mode with the longitudinal coordinate whereas Figs. 10.26 and 10.27b show the variation of the second derivative of the phase of the same converted A_0 mode with respect to the longitudinal coordinate. From Fig. 10.26a, the amplitude of the phase are identical for three notch depths at a constant wavelength, and upon taking the second derivative, the damage location is successfully identified at $x_D = 0.5$ by virtue of the derivative peaks at the discontinuity. Conversely, for varying wavelengths at a constant notch depth, the results in Fig. 10.27a depict the phase amplitude discrepancy for each wavelength with a similar discontinuity at $x_D = 0.5$, from which the converted mode

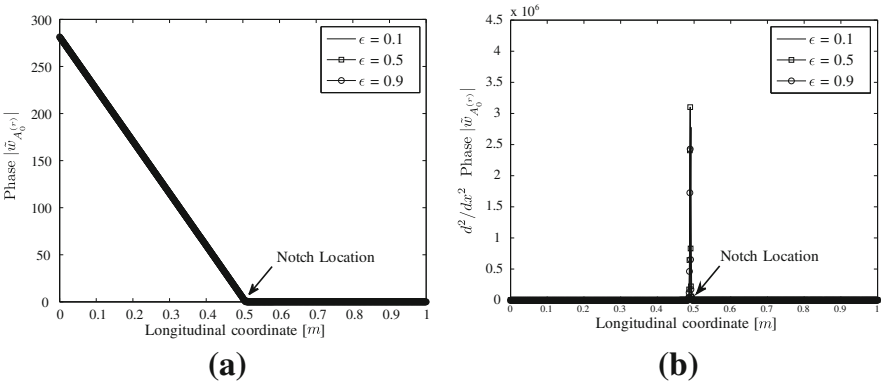

Fig. 10.26 Variation of **a** phase of $\tilde{w}_{A_0^{(r)}}$ and **b** phase gradient versus notch depth

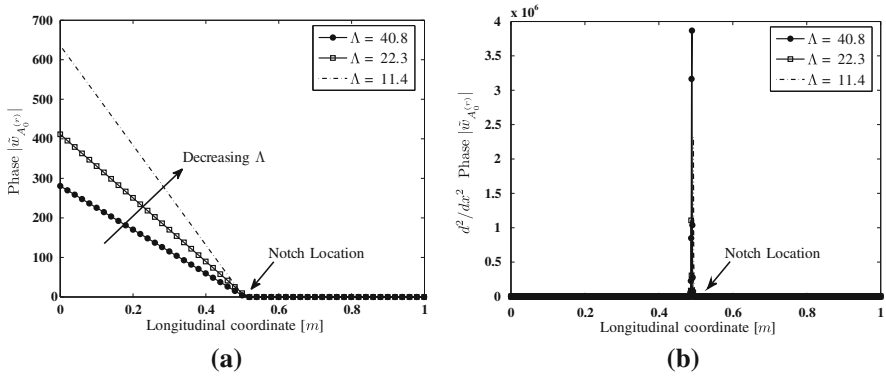

Fig. 10.27 Variation of **a** phase of $\tilde{w}_{A_0^{(r)}}$ and **b** phase gradient versus excitation frequency/wavelength

originates. Thus, the damage localization method is independent of both damage size and excitation wavelength, making this technique attractive for blind damage localization tests. One question that arises from a damage localization method, which implements the second derivative of the converted A_0 phase to accurately identify the notch location, is the method's sensitivity to noise. As a case study, noise is simulated by taking the root mean square (RMS) of the original FEM displacement results at each scanned node along the FEM model. Upon taking a percentage of the RMS, ranging from 0 to 50%, and then multiplying by a randomized set of data whose mean is 0 with a standard deviation of 1, the resulting noise vector is summed with the original displacement data at time history in each node. Figure 10.28 shows the phase and second derivative for a notch size of $\epsilon = 0.5$ and excitation wavelength of $\Lambda = 40.8$ for varying noise levels. From Fig. 10.28, it is evident that the damage location does not vary with the increasing noise levels.

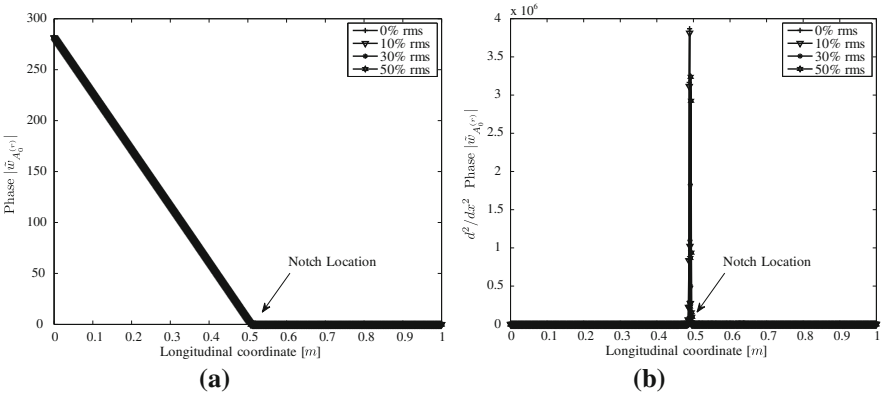

Fig. 10.28 Variation of **a** phase of $\tilde{w}_{A_0^{(r)}}$ and **b** phase gradient at varying noise percentage RMS levels for constant $\Lambda = 40.8$ and $\varepsilon = 0.5$

10.5.4.3 Numerical Estimation of Mode Conversion

Figure 10.29a displays the amplitude of the filtered incident and transmitted S_0 mode for different damage depths along the span of the plate at 200 kHz excitation frequency. For stability purposes damping is introduced into the FEM by way of the linear bulk viscosity parameter, which is intended to damp out high frequency ringing. The inclusion of damping helps explain the decay in mode amplitude from the source in Fig. 10.29. However, it is observed in Fig. 10.29a that the incident S_0 mode has the same amplitude for all frequencies prior to the notch location $(x < x_D = 0.5\,\text{m})$. The modes distinctly separate in amplitude after the S_0 mode propagates past the notch $(x > x_D = 0.5\,\text{m})$, such that the amplitude of the transmitted S_0 mode is proportional to the damage depth. From Fig. 10.29a, it is concluded that this transmitted coefficient will decrease when the depth of the notch increases. In contrast, the reflected S_0 mode in Fig. 10.29b conveys the expected trend of an increase in damage depth leading to an increase in the amplitude of the reflected S_0 mode. In the case of the converted A_0 mode, Fig. 10.29c, the peak amplitude occurs when $\varepsilon \approx 0.7$ which is consistent with published results [15, 28]. This result indicates that for blind tests based solely on the converted A_0, aliasing of the damage depth can occur, and further information is required.

Figures 10.30 and 10.31 provide the integrated mode coefficients (Eqs. 10.47, 10.48) as a function of damage depth to plate thickness for different wavelengths to notch widths, Λ. Qualitatively, the reflected S_0 mode coefficients, shown in Fig. 10.30a, increase almost linearly with increasing notch depth, which is consistent with previous single point studies by [28]. In addition, Fig. 10.30b demonstrates a relative linear variation in the R_{S_0} mode coefficient over the given wavelength range per damage depth, where the maximum relative difference of 143% occurs at the notch depth of $\varepsilon = 0.1$, where the maximum and minimum amplitudes are 0.053 and 0.022, respectively. The maximum absolute R_{S_0}

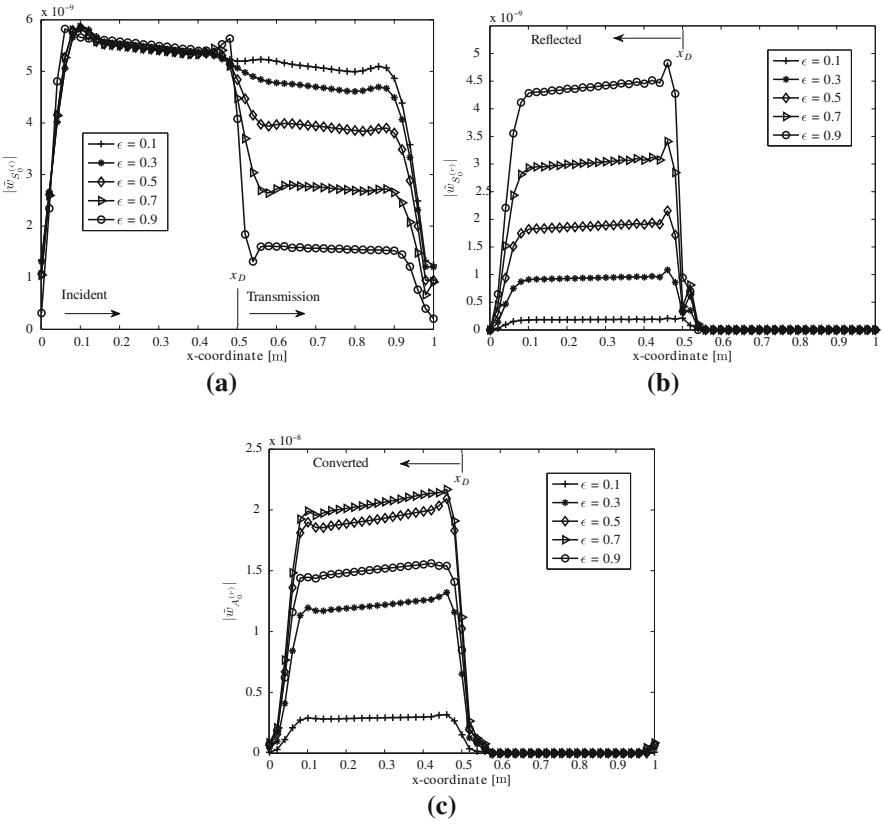

Fig. 10.29 Filtered modes along the length of the plate at 200 kHz excitation frequency, for a plate whose notch width of 1 mm is centered at $x = 0.5$, and where ε is a ratio of notch depth to beam thickness: **a** incident and transmitted S_0 mode, **b** reflected S_0 mode, and **c** converted A_0 mode

difference exists at the $\varepsilon = 0.5$ notch depth of 0.12. The importance of these findings is that R_{S_0} is relatively sensitive to the applied excitation wavelength, where the notch depth is held constant, and the practitioner in the field cannot accurately assume that the measured R_{S_0} mode coefficient is universally applicable to other wavelengths. In contrast to the R_{S_0} mode coefficient, the converted C_{A_0} mode coefficients shown in Fig. 10.31a, whose peak amplitude at $\varepsilon \approx 0.7$, result in mode coefficient amplitudes greater than unity. This may be explained by Eq. 10.48, where the converted A_0 mode has a larger out-of-plane amplitude than the out-of-plane amplitude of the incident S_0 mode. Also, the slope of the parabolic profile in Fig. 10.31a increases with Λ, and Fig. 10.31b further accentuates this wavelength dependency, such that at $\varepsilon = 0.7$ and $\varepsilon = 0.9$, the maximum relative difference is approximately 507 and 741%, respectively. Thus, by way of ranking, the maximum relative sensitivity to wavelength variation for constant notch depths is greatest for the C_{A_0} mode coefficient, followed by the T_{S_0} mode coefficient, and the R_{S_0} mode coefficient.

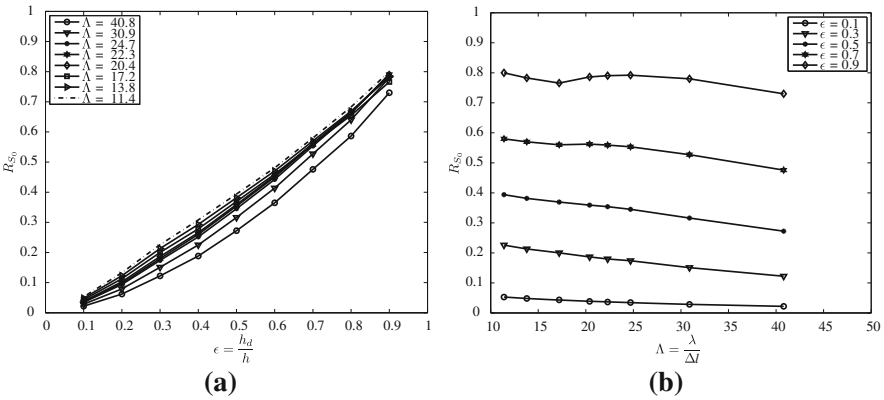

Fig. 10.30 Integrated reflected S_0 mode coefficients as function of: **a** ϵ, damage depth to total plate height, and **b** Λ, the ratio of excitation wavelength to notch width

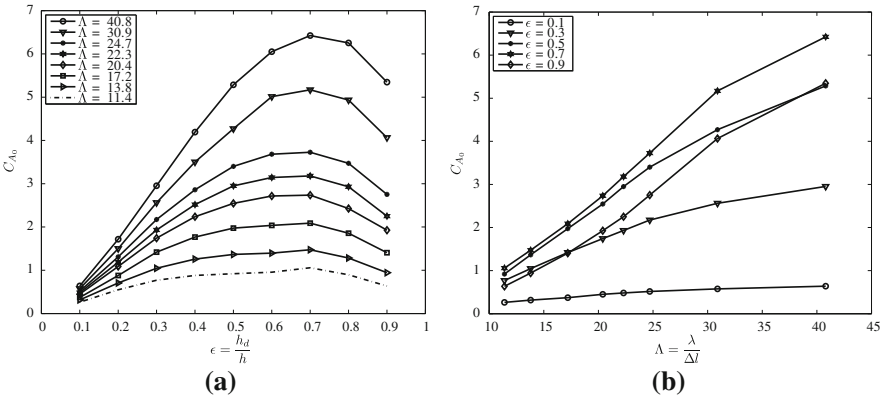

Fig. 10.31 Integrated converted A_0 mode coefficients as function of: **a** ϵ, damage depth to total plate height, and **b** Λ, the ratio of excitation wavelength to notch width

In order to investigate the damage depth for which the C_{A_0} mode coefficient peaks, the resolution of ε is refined, varying from 0.55 to 0.75 at increments of 0.01 for a selected wavelength, $\Lambda = 24.7$. The results are shown in Fig. 10.32 for both the integrated formulation and at a single point four wavelengths away from the damage. It is evident that the peak amplitude occurs at $\epsilon \approx 2/3$, for both the integrated and single point mode coefficients at this excitation wavelength. A comparison of single point and the spatially integrated formulations for R_{S_0} and C_{A_0} mode coefficients is provided in Figs. 10.33 and 10.34. In order to highlight the benefits and limitations of the spatially-integrated formulation, numerical noise is introduced to the response, as described in Sect. 10.5.4.2. Ranging from 0 to 50% levels of the RMS of the response, the resulting noise vector is summed with the original displacement data at each node for every time sample. Qualitatively for each excitation wavelength as a function of damage depth, Fig. 10.33a

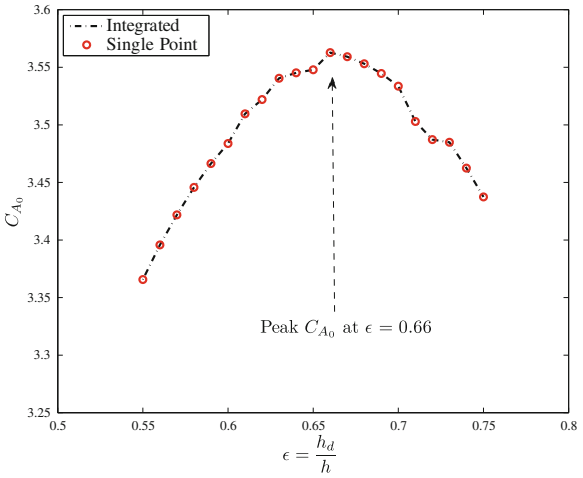

Fig. 10.32 Magnified view of FEM C_{A_0} mode coefficient as a function of ε for both integrated and single point formulation at excitation wavelength of $\Lambda = 24.7$

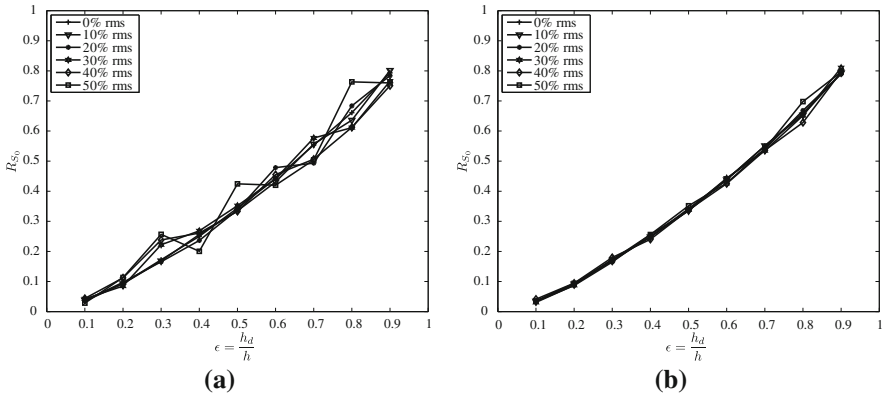

Fig. 10.33 R_{S_0} mode coefficient comparison with numerical noise at varying RMS levels for: **a** single point, and **b** spatially integrated formulations

demonstrates the discrepancy produced by the single point formulation for the increasing percentage RMS levels throughout the damage depth range, whereas the integrated mode coefficients in Fig. 10.33b display a slight variation at the latter notch levels for ε greater than 0.7.

10.5.5 Application to Experimental Data

10.5.5.1 Set up

An aluminum (Al 6061-T6) plate of 1.19 mm thickness with a notch of 12.65 mm length and 0.8 mm width is considered for the experiments. In order to excite an

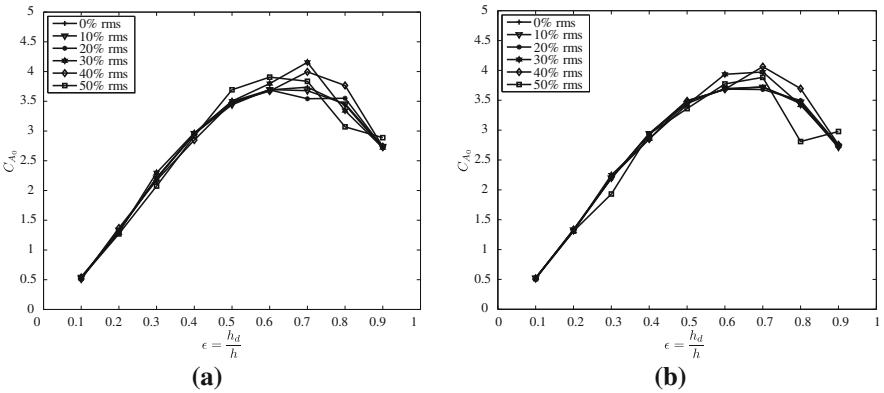

Fig. 10.34 C_{A_0} mode coefficient comparison with numerical noise at varying RMS levels for: **a** single point, and **b** Spatially integrated formulations

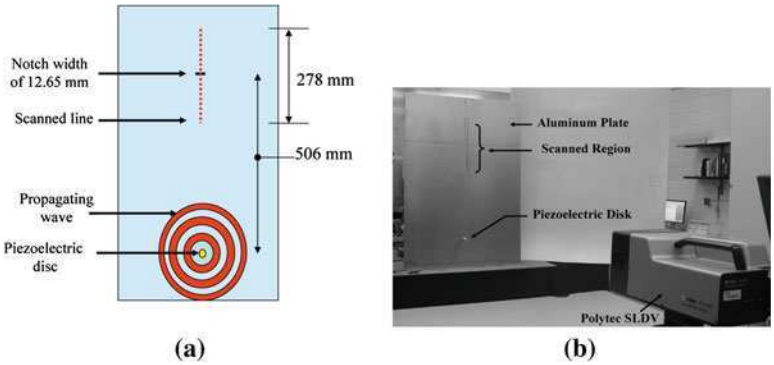

Fig. 10.35 **a** Schematic of the test plate; **b** experimental setup to measure interaction of S_0 waves with notch type defect

enhanced S_0 mode, two actuators are placed on the opposite faces of the plate, and synchronized to impart a dominant symmetrical loading into the plate. The plate is excited by a four cycle tone burst modulated by a Hanning window over a range of frequencies from 100 kHz up to 300 kHz. A Polytec PSV-400 SLDVis used to control the experiment and acquire the response data. The dynamic response of the plate is recorded along a line covering a distance of 140 mm on either side of the notch, with a total of 227 points measured at a spatial resolution of 1.2 mm. The plate schematic and experimental setup are shown in Fig. 10.35. The spatial resolution is empirically optimized after several iterations of post-processing of the data, where spatial resolution is reduced until the mode conversion from the notch is apparent per the minimum excitation wavelength at 300 kHz. The recorded wave are separated using the wavenumber/frequency domain procedure presented in [38].

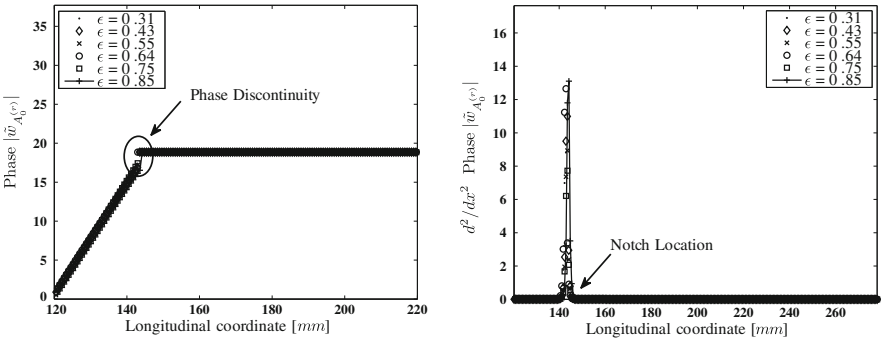

Fig. 10.36 **a** Spatial detail of the phases of $\tilde{w}_{A_0^{(r)}}(x, \omega_{\max})$ (for six notch depths) in terms of the spatial coordinate; **b** spatial detail of the second derivative of the phase of $\tilde{w}_{A_0^{(r)}}(x, \omega_{\max})$ in terms of the spatial coordinate; the location of the notch is $x_D \approx 140$ mm

10.5.5.2 Damage Localization

The phase of the reflected A_0 modes of the experimental data are calculated and plotted in Fig. 10.36. From the notch depth point of view, six cases cases are considered: $\epsilon \approx 0.3 - 0.9$. Fig. 10.36a presents the phase variation of the reflected A_0 for all the cases along the scan line and shows that the phase mode varies linearly with the spatial coordinate and is constant in the $x > x_D$ region ($x_D = 140\,\text{mm}$). Also, the phase of the converted A_0 mode is not a function of the notch's depth. Figure 10.36b presents the second derivative of the phase in terms of the spatial coordinate (Eq. 10.39) which highlights the location of the notch.

10.5.5.3 Mode Conversion Estimation

Figure 10.37 displays the amplitudes of the filtered converted A_0 mode for given damage depths along the scanned line of the plate. The considered excitation signal is a 160 kHz sinusoidal modulatedwith a Hanning window. It is observed that the response approximately attenuates from the notch, located at $x_D = 140$ mm at a decay rate proportional to $\frac{1}{\sqrt{r}}$, where r is the distance from the notch due to geometric spreading of the circular crested waves generated by the piezoelectric transducer [18]. These generated crested waves differ from the plane strain FEM simulation plane wave S_0 loading, where no attenuation from the source exists. Therefore, the separated mode responses are modified to account for this attenuation by evaluating the proportionality constant at each frequency case prior to calculating the damage mode coefficients. The minimum converted A_0 response is the $\varepsilon = 0.31$ damage case, which follows intuitively that the lowest damage level produces the least magnitude converted A_0. However, the maximum

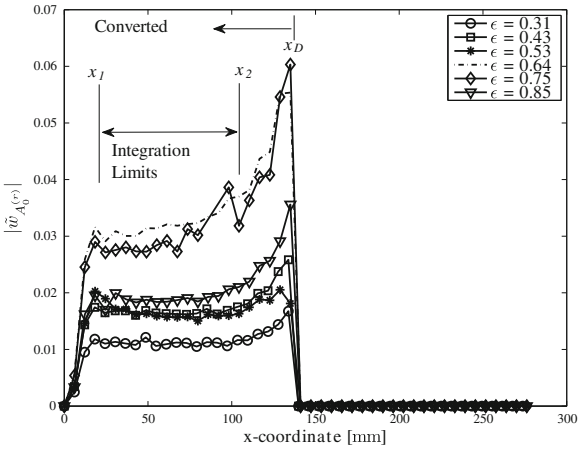

Fig. 10.37 Filtered converted $\tilde{w}_{A_0^{(r)}}$ mode along the scanned length of an aluminum plate whose notch width of 0.8 mm is centered at $x_D \approx 140$ mm, and is excited at 160 kHz. The integration limits are identified as x_1 and x_2, which are located at the x-coordinates 10 and 110 mm, respectively

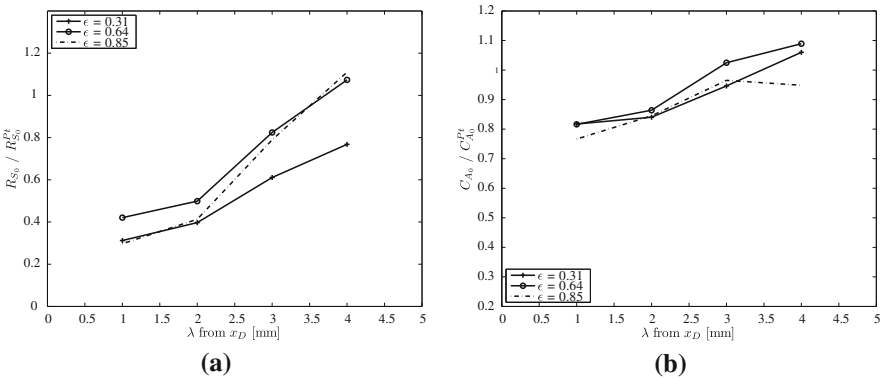

Fig. 10.38 Comparison of single point mode coefficients as a function of wavelength, λ, and notch depth, ε, from the notch location, x_D at an excitation of 160 kHz: **a** R_{S_0} mode coefficient, and **b** C_{A_0} mode coefficient

converted A_0 response does not correlate to the maximum degree of damage, but rather at the $\varepsilon = 0.64$ damage case. For the given length of 140 mm prior to the notch location, the integration limits of the C_{A_0} mode coefficients are selected at a sufficient distance away from the local effects of the notch. For single point mode coefficient formulations of straight crested wave excitation, this distance was previously selected as 60 plate thicknesses [28]. In practice, a 60 plate thickness region may be unattainable for structures of complex geometry where the suggested scan distance is unreachable, and thus it is of interest to investigate the ability of the spatially integrated mode coefficient to accurately estimate the mode conversion. For circular crested waves, it has been shown analytically that three to four wavelengths of the circular crested excitation is to within 0.1% of the straight crested behavior [18]. Figure 10.38a and b demonstrates this gradual convergence to unity with increasing wavelengths away from the notch, where the ratio is the

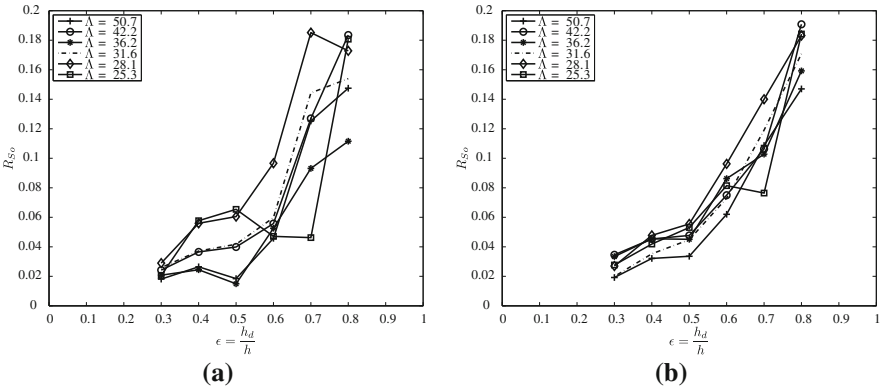

Fig. 10.39 Reflected S_0 mode coefficients, where Λ is a ratio of wavelength to notch width: **a** results at a $x = 4\lambda x_D$, **b** results for the spatially-integrated results value

integrated coefficient C_{A_0} to the amplitude of the single point converted mode, $C_{A_0}^{Pt}$. Thus, it may be interpreted that the integrated formulation provides greater accuracy within the scanning region where x is less than four wavelengths, as a result of the single point being more susceptible to the amplitude variation from the local notch effects. Furthermore, Figs. 10.39 and 10.40 provide the reflected and converted integrated mode coefficients as a function of damage depth to plate thickness for different wavelengths to notch widths, Λ. Figures 10.39 and 10.40a are the single point results of the reflection S_0 and converted A_0 mode coefficients, respectively, taken at 4 wavelengths, or 4 λ, from the identified notch location at 140 mm. In terms of the R_{S_0} mode coefficient, the discrepancy between the formulated single point and spatially-integrated mode coefficients is evident per each wavelength excitation, and highlights the advantage of integrating over a spatial domain versus relying upon a single measurement point. However, the C_{A_0} mode coefficient for both the single point and integrated formulations are almost identical in both amplitude and trend for each wavelength, and this is attributed to the the 4λ distance away from the point source.

Although the trends from Fig. 10.39b compare favorably with the FEM trend shown in Figs. 10.30, the apparent maximum amplitude discrepancy from 0.8 to 0.2 may be attributed to factors, such as the inclusion of a single displacement component, and the variation from straight to circular crested waves albeit the described $\frac{1}{\sqrt{r}}$ adjustment.

10.6 Damage Force Indicator Technique

The damage force indicator (DFI) is yet another damage detection technique that is based on the measured wave propagation responses. The concept does not require baseline responses and the nature and form of load history is not very important in

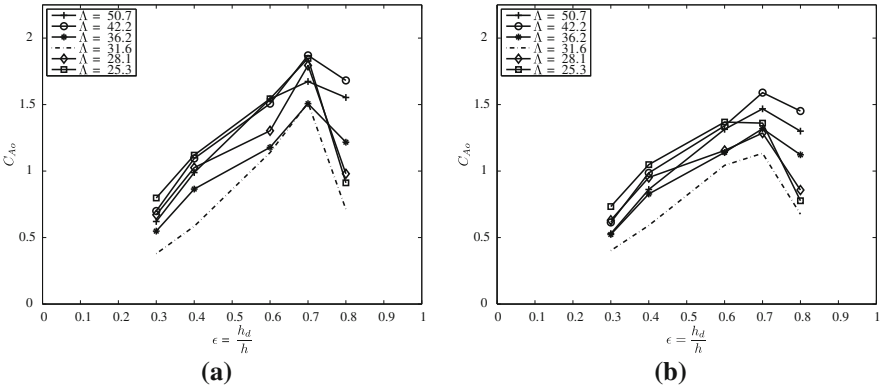

Fig. 10.40 Converted A_0 mode coefficients, where Λ is a ratio of wavelength to notch width: **a** results at a $x = 4\lambda x_D$, **b** results for the spatially-integrated results value

this technique. The concept uses the healthy dynamic stiffness matrix derived from SFE model explained in detail in Chap. 5 and the measured transient response to determine the location of the damage.

The concept of damage force was first used in [39] to derive a damage indicator for detecting the elements having flaws. The dynamic stiffness matrix of the reference healthy structure along with the nodal displacements of the damaged structure are required to find which elements contain damage. This technique bounds the damage location within the region of the sensing points. Keeping the objective of on-line health monitoring in mind, a similar strategy is implemented here. But the basic difference is that the finite element system is constructed entirely in the frequency domain under the framework of SFEM. One advantage is that a much lower number of sensors are sufficient, since the number of measurements complying with SFEM degrees of freedom (dof) is smaller than that required when using conventional FEM. The only limiting factor when using fewer sensors is that the measured signal must be reliable enough to differentiate the effect of wave scattering in the presence of slight damage along with the effect of damping. For polymer composite, this is an important issue because a sensor placed too far from the damage location may not be able to capture the measurable fluctuations when damage is present.

The global dynamic stiffness matrixof the healthy structure $\hat{\mathbf{K}}_h(\omega_n)$ at each FFT sampling frequency ω_n is obtained using a standard finite element assembly for all spectral elements. The spectral amplitude of global displacement vector $\hat{\mathbf{u}}$ consists of axial displacement $\hat{u}^o$, transverse displacement $\hat{w}$ and rotation $\hat{\phi}$ at each node. Now, the damage force vector is defined as

$$\Delta\hat{\mathbf{f}} = \hat{\mathbf{K}}_h\hat{\mathbf{u}}_d - \hat{\mathbf{f}}_d \tag{10.49}$$

where the subscript h denotes healthy structure and d denotes for delaminated (or cracked) structure. If delamination occurs, the vector $\Delta\hat{\mathbf{f}}$ will have non-zero entries only at the dofs connected to the elements with damage. The above expression

requires the excitation force ($\hat{\mathbf{f}}_d$) or the internal forces at the nodes to be known. Direct measurement of this requires force sensors and may not always be feasible [39]. The damage indicator proposed by Schulz [39] overcomes this limitation by computing the damage force directly as $\hat{\mathbf{K}}_h\hat{\mathbf{u}}_d$. In this section, the same expression is used assuming the vector $\hat{\mathbf{f}}_d$ is unknown in the simulation. However, in SFEM, the inverse problem can be solved to obtain $\hat{\mathbf{f}}_d$ from other types of measurement such as displacements, strains or their rates. For delamination identification, we already have the spectral element for a waveguide with embedded delamination (see Chap. 6, Sect. 6.3) that can be inserted in the healthy structure by comparing damage force indicator from experimentally obtained and post-processed signals. For this purpose, a combined force vector $\hat{\mathbf{r}}(\omega_n)$ is considered

$$\hat{\mathbf{r}}(\omega_n) = \Delta\hat{\mathbf{f}} + \hat{\mathbf{f}}_d = \hat{\mathbf{K}}_h\hat{\mathbf{u}}_d. \tag{10.50}$$

Multiplying $\hat{\mathbf{r}}$ by transpose of its complex conjugate $\hat{\mathbf{r}}^*$, we get one $(m \times m)$ square matrix $\hat{\mathbf{R}}(\omega_n)$:

$$\hat{\mathbf{R}}(\omega_n) = \hat{\mathbf{r}}\hat{\mathbf{r}}^* \tag{10.51}$$

where m is the total number of dofs in the model. Now, if the delamination is expected in the ith element, the existing element can be replaced by the spectral element for delamination. There will be non-zero diagonal entries in $\hat{\mathbf{R}}(\omega_n)$ corresponding to the dofs associated with the ith element. The rest of the diagonal entries will be zero. The magnitude of these non-zero diagonal entries will depend on the applied load, and the configuration of delamination. Summing up the absolute values of the diagonal entries in $\hat{\mathbf{R}}(\omega_n)$ over all frequency steps $n = 1, \ldots, N$ (N = Nyquist frequency in FFT), a damage force indicatorvector $\mathbf{d}$ of length m is obtained as

$$d_i = \sum_{\omega_n} |\hat{R}_{ii}|\,, \quad i \in [1,\ m]\,, \quad n = 1,\ \ldots,\ N. \tag{10.52}$$

10.6.1 Identification of Single Delamination Through Damage Force Indicator

One infinite graphite–epoxy beam of 10 mm × 10 mm cross-section is considered as shown in Fig. 10.41 Eight SFEs of equal length (100 mm) are assumed between two throw-off elements at the ends. $\hat{\mathbf{K}}_h$ is stored for each FFT sampling frequency. A broadband load (Fig. 3.7) is applied in transverse direction (dof-26) on the right node of the 8th element. Each time, one mid-plane delamination of length 20 mm is introduced (Fig. 10.42a) in one of these elements and $\hat{\mathbf{u}}_d$ is computed. The damage force indicator$\mathbf{d}$ is computed for each of these delamination configurations

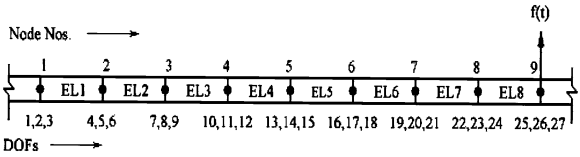

Fig. 10.41 An infinite beam considered to study the identification of delaminations using a damage force indicator

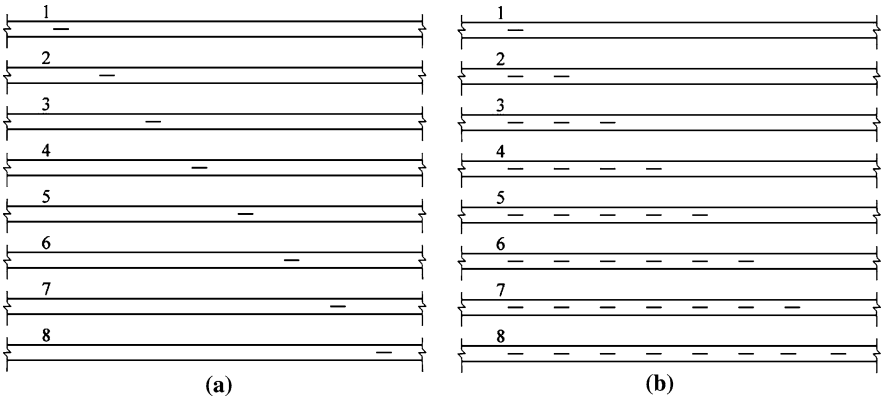

Fig. 10.42 Different configurations considered for the infinite beam with delamination; **a** with single delamination and **b** with multiple delaminations

using Eqs. 10.49–10.52 and plotted in Fig. 10.43. Peaks at the dofs associated with the delaminated elements can be seen in the bar-plots. All the entries in $\mathbf{d}$ are normalized with respect to $\text{Max}(\mathbf{d})$, separately for transverse and rotational dofs. It is also found that $\mathbf{d}$ is in decreasing order from the point of application of load. This is because of attenuation and gradual dissipation of energy in a slightly damped system. Some small non-zero amplitudes of $\mathbf{d}$ can be noticed at the dof of the applied load $(i = 26)$ for all cases. This appears because the applied load was not eliminated from the dof while computing $\mathbf{d}$, presuming it to be an unknown in a practical problem (see Eq. 10.50).

10.6.2 Identification of Multiple Delamination Through Damage Force Indicator

For the same infinite beam and applied load considered in the last example (Fig. 10.41), multiple delaminations are introduced progressively, i.e., first in element 1, then simultaneously in elements 1 and 2 and so on (see Fig. 10.42b). For these varying configuration, normalized $\mathbf{d}$ is plotted in Fig. 10.44. Normalization is done with respect to the maximum of $\mathbf{d}$ among all the delaminated configurations. But, due to this normalization, no peaks for the first configuration are visible. The peaks are also not in any ordered magnitude as in the previous study. This can be attributed to the interference between the reflected waves

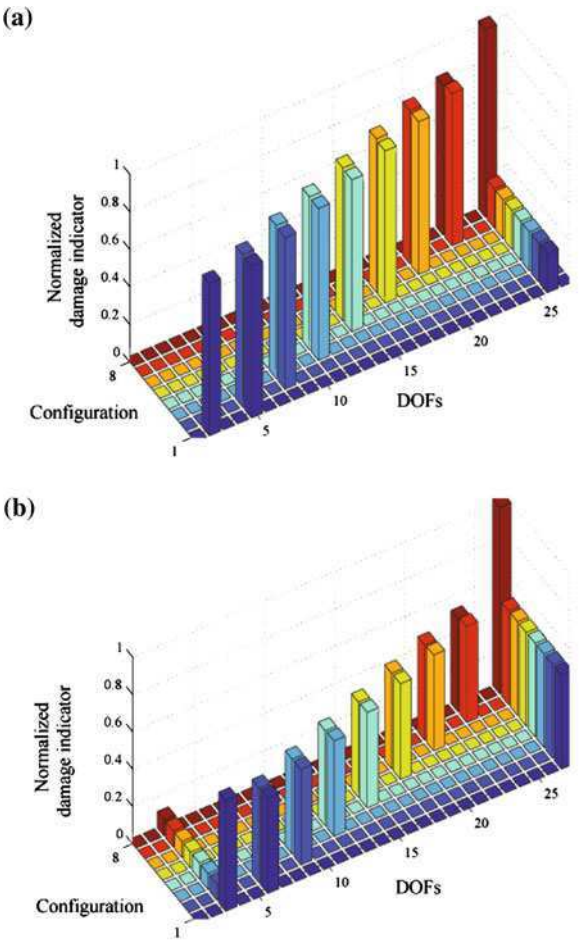

Fig. 10.43 Normalized damage force indicator **d** for **a** transverse and **b** rotational dofs for different configurations (varying location of a single delamination shown in Fig. 10.42a) modeled using single spectral element for delamination

generated by different delamination tips. Computation time to obtain **d** is plotted in Fig. 10.45. This shows cubic polynomial time complexity [11] for increasing numbers of delaminations. Therefore with this same identification strategy and further development of spectral elements for plates and shells, a real-scale structural health monitoring task appears tractable.

10.6.3 Sensitivity of Damage Force Indicator Due to Variation in Delamination Size

The aim of the following studies is to determine whether the damage force indicator can also quantify the intensity of the delamination. For this purpose, a 2 m

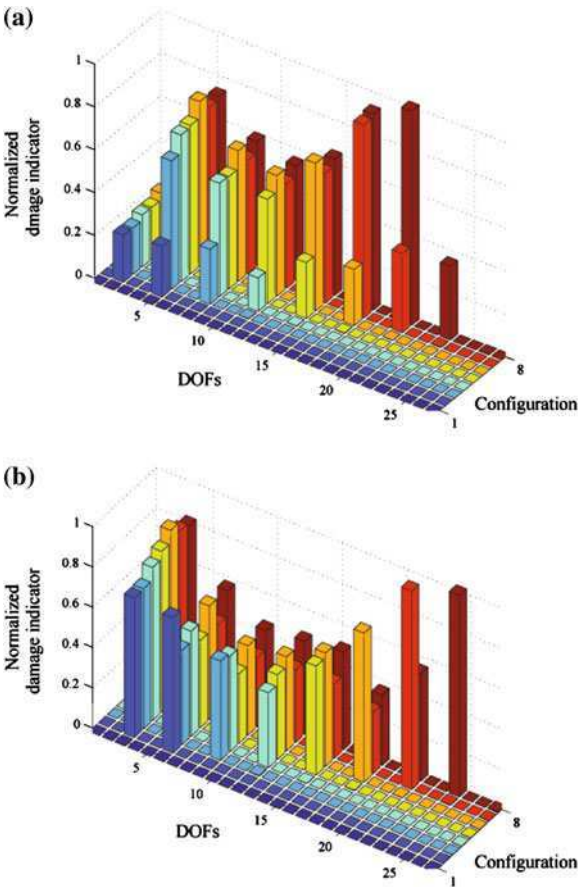

Fig. 10.44 Normalized damage force indicator **d** for **a** transverse and **b** rotational dofs for different configurations (varying number of delaminations shown in Fig. 10.42b) modeled using one spectral element for each delamination

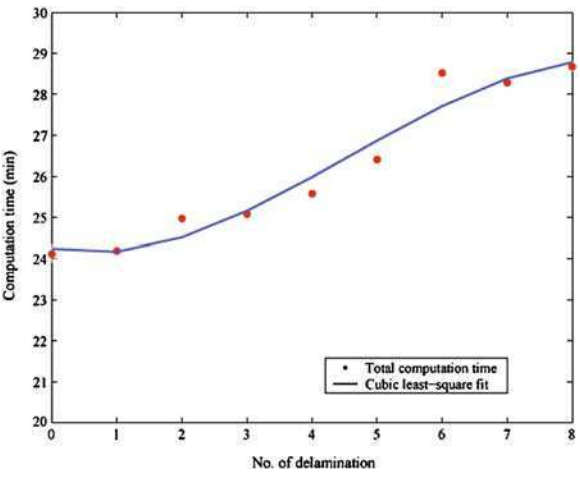

Fig. 10.45 Computation time for damage force indicator in the case of an increasing number of delaminations (shown in Fig. 10.42b)

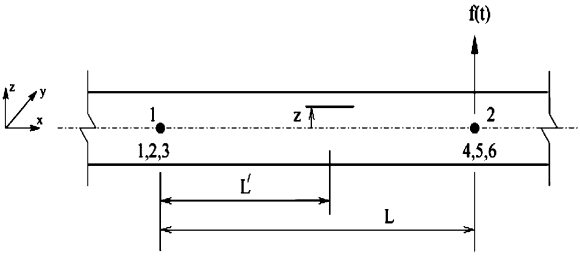

Fig. 10.46 Infinite beam with single delamination for sensitivity analysis of delamination parameters on damage force indicator. The node numbers (in *bold letters*) and the dofs are shown

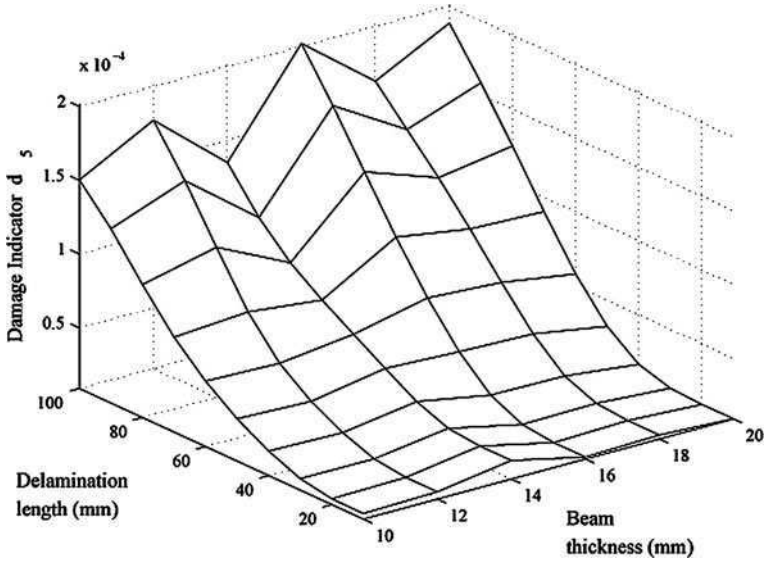

Fig. 10.47 Damage force indicator for transverse dofs at node 2 (Fig. 10.46) for different lengths of single delamination ($z = 0$) and various beam thicknesses. Delamination length is varied from its center, left and right simultaneously by equal amounts

long spectral element for delamination with throw-off elements connected to both ends is considered (Fig. 10.46). The width of the beam is kept fixed at 10 mm, while the beam thickness is varied from 10 to 20 mm in uniform steps of 2 mm. For each different beam thickness, the length of mid-plane delamination is varied from 10 to 100 mm in uniform steps of 5 mm in both directions equally about the center.

Component of **d** for the transverse and rotational dofs at node 2 (i.e., d_5 and d_6) are computed for all of these configurations and are plotted in Figs 10.47 and 10.48. Exponential increments in **d** with the delamination length are observed for the transverse case. This shows that with increasing delamination length, change in the dynamic response increases exponentially. However, the variation with beam thickness for a fixed size of delamination is not monotonous. For the rotational dofs, these fluctuations are more pronounced. The transverse damage force

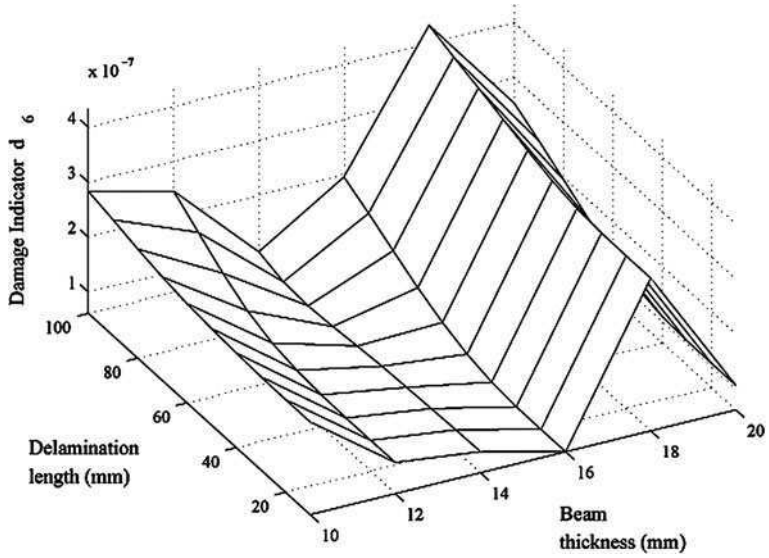

Fig. 10.48 Damage force indicator for rotational dofs at node 2 (Fig. 10.46) for different lengths of single delamination ($z = 0$) and various beam thicknesses. Delamination length is varied from its center, left and right simultaneously by equal amounts

indicator is a minimum for a delamination length of 10 mm when the beam thickness is 20 mm and maximum when they are 100 and 16 mm, respectively.

10.6.4 Sensitivity of Damage Force Indicator Due to Variation in Delamination Depth

For the same element length and different beam thicknesses considered in the previous study, the location of the delamination along thickness was varied from $z = -3$ mm to $z = +3$ mm. Delamination length was kept fixed at 20 mm. Damage force indicators in transverse and rotational dofs are plotted respectively in Figs. 10.49 and 10.50. Due to significant scale variation in the damage force indicator with change in beam thickness, the magnitudes are plotted relative to Min($\mathbf{d}$) (separately for transverse and rotational dofs) for corresponding beam thicknesses. With variation in the delamination depth, a non-linear relationship symmetric about the mid-plane ($z = 0$) is observed in Figs. 10.49 and 10.50. In the case of the transverse dof (Fig. 10.49), the depth for which the minima occurs (zero value in the plot for some beam thicknesses), is different for different beam thickness. However, they are always maximum for a mid-plane delamination. In the case of the rotational dof (Fig. 10.50), the maxima does not always occur for a mid-plane delamination. From these plots, it can be concluded that for thin beams, the effect of mid-plane delamination can be captured with maximum reliability.

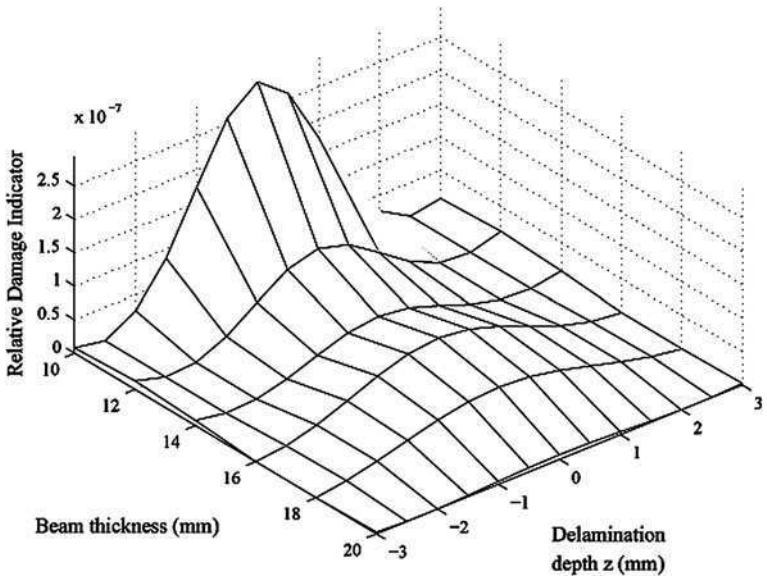

Fig. 10.49 Relative damage force indicator for transverse dofs at node 2 (Fig. 10.46) for different depth (z) of single delamination of length 20 mm for various beam thicknesses

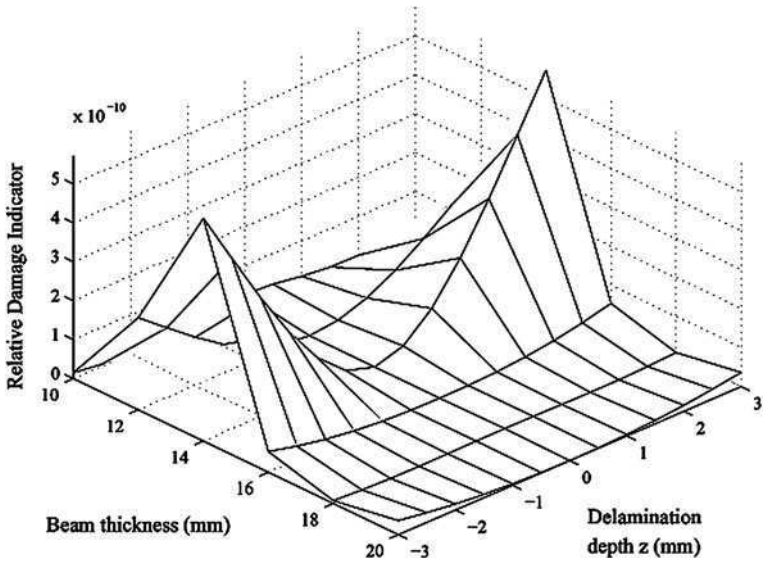

Fig. 10.50 Relative damage force indicator for rotational dofs at node 2 (Fig 10.46) for different depth (z) of single delamination of length 20 mm for various beam thicknesses

Whereas, for asymmetrically delaminated beams, predictions are much easier for moderate thicknesses.

10.7 Summary

The chapter presents an overview of various techniques for the detection and the quantification of damage. Vibration-based techniques are presented through an initial historical perspective, and by introducing some novel concepts such as the residual(damage) force method, and the strain energy-based damage index formulation. Numerical and experimental results are illustrated in support of these techniques to demonstrate the concepts they rely on, and to show their output in the presence of various forms of damage. The strain energy damage index is also extended to the analysis of time-domain data, as obtained for example from guided-wave inspections. Wavefield data are also used to formulate a procedure for the detection of the damage location through the analysis of a phase operator, obtained through Fourier analysis in the spatial domain. Finally, mode conversion and reflection coefficients are presented as a way to quantify damage. A formulation based on spatial average is proposed to reduce the influence of noise, and to reduce the sensitivity of the estimates upon the selection of the measurement point. The last part of this chapter introduces a novel concept of damage force to detect the flaw location. This approach requires only the stiffness matrix of the healthy structure, which is readily available and the approach does not require any baseline measurements. The approach is well suited to work with spectral element models and hence has great potential to provide rapid answers regarding the state of the structures. This requires further research in this area.

References

1. Alleyne D, Cawley P (1992) The interaction of Lamb waves with defects. IEEE Trans Ultrason Ferroelectr Freq Contr 39(3):381–397
2. Al-Nassar Y, Datta S, Shah A (1991) Scattering of Lamb waves by a normal rectangular strip weldment. Ultrasonics 292:125–132
3. Basri R, Chiu W (2004) Numerical analysis on the interaction of guided Lamb waves with a local elastic stiffness reduction in quasi-isotropic composite plate structures. Comp Struct 66(1–4):87–99
4. Benmeddour F, Grondel S, Assaad J, Moulin E (2008) Study of the fundamental Lamb modes interaction with asymmetrical discontinuities. NDT E Int 415:330–340
5. Blotter JD, West RL, Sommerfeldt SD. Spatially continuous power flow using a scanning laser Doppler vibrometer. J Vib Acoust Trans ASME 124(4):476–482
6. Castaings M, Clezio EL, Hosten B (2002) Modal decomposition method for modeling the interaction of Lamb waves with cracks. J Acoust Soc Am 1126:2567–2582
7. Cawley P, Adams RD (1979) The locations of defects in structures from measurements of natural frequencies. J Strain Anal 14(2):49–57

8. Chang CC, Chen L-W (2005) Detection of the location and size of cracks in the multiple cracked beam by spatial wavelet based approach. Mech Syst Signal Process 19:139–155
9. Cho Y, Hongerholt D, Rose J (1997) Lamb wave scattering analysis for reflector characterization. IEEE Trans Ultrason Ferroelectr Freq Contr 44(1):44–52
10. Cook RD, Malkus DS, Plesha ME, Witt RJ (2001) Concepts and applications of finite element analysis, 4th edn. Wiley, New York
11. Cormen TH, Leiserson CE, Rivest RL (1998) Introduction to algorithms. Prentice-Hall, Engle-wood Cliffs
12. Cornwell P, Doebling SW, Farrar CR (1999) Application of the strain energy damage detection method to plate-like structures. J Sound Vib 224(2):359–374
13. Doebling SW, Farrar C, Prime MB, Daniel WS (1996) Damage identification and health monitoring of structural and mechanical systems from changes in their vibration characteristics: a literature review, May 1996, LA-13070-MS
14. Farin G (2002) Curves and surfaces for CAGD: a practical guide, 5th edn. Academic Press, New York
15. Flores-Lopez M, Gregory R (2006) Scattering of Rayleigh–Lamb waves by a surface breaking crack in an elastic plate. J Acoust Soc Am 1194:2041–2049
16. Fox CHJ (1992) The location of defects in structures: a comparison of the use of natural frequency and mode shape data. In: Proceedings of the 10th international modal analysis conference, pp 522–528
17. Giurgiutiu V, Bao J, Zhao W (2003) Piezoelectric wafer active sensor embedded ultrasonics in beams and plates. Exp Mech 43(4):428–449
18. Giurgiutiu V (2007) Structural health monitoring with piezoelectric wafer active sensors. Academic Press, New York
19. Hearn G, Testa RB (1991) Modal analysis for damage detection in structures. J Struct Eng 117(10):3042–3063
20. Ho YK, Ewins DJ (2000) Numerical evaluation of the damage index, 2000, International workshop on structural health monitoring. Stanford University, Palo Alto, CA, pp 995–1011
21. Ho YK, Ewins DJ (2000) On the structural damage identification with mode shapes. European COST F3 conference on system identification and structural health monitoring. Madrid, Spain, pp 677–686
22. Kim J-H, Jeon H-S, Lee C-W (1992) Application of the modal assurance criteria for detecting and locating structural faults. In: Proceedings of the 10th international modal analysis conference, pp 1992536–1992540
23. Kim JT, Stubbs N (2003) Crack detection in beam type structures using frequency data. J Sound Vib 259(1):146–160
24. Ko JM, Wong CW, Lam HF (1994) Damage detection in steel framed structures by vibration measurement approach. In: Proceedings of the 12th international modal analysis conference, pp 280– 286
25. Lam HF, Ko JM, Wong CW (1995) Detection of damage location based on sensitivity analysis. In: Proceedings of the 13th international modal analysis conference, pp 1499–1505
26. Lestari W (2001) Damage of Composite structures: detection technique, dynamic response and residual strength. Ph.D thesis, Georgia Institute of Technology
27. Lowe M, Cawley P, Kao J, Diligent O (2000) Prediction and measurement of the reflection of the fundamental anti-symmetric Lamb wave from cracks and notches. In: Thompson DO, Chimenti DE (eds) Review of progress in quantitative nondestructive evaluation, AIP, pp 193–200
28. Lowe M, Diligent O (2002) Low-frequency reflection characteristics of the S(0) Lamb wave from a rectangular notch in a plate. J Acoust Soc Am 111(1):64–74
29. Lu Y, Ye L, Su Z, Yang C (2008) Quantitative assessment of through-thickness crack size based on Lamb wave scattering in aluminium plates. NDT E Int 411:59–68
30. Luo H, Hanagud S (1997) An integral equation for changes in the structural dynamics characteristics of undamaged structures. Int J Solids Struct 34(35–36):4557–4579

31. Michaels TE, Michaels JE (2004) Ultrasonic signal processing for structural health monitoring. In: Thompson DO, Chimenti DE (eds) Review of progress in QNDE, 23. American Institute of Physics
32. Moser F, Jacobs L, Qu J (1999) Modeling elastic wave propagation in waveguides with the finite element method. NDT E Int 324:225–234
33. Pandey AK, Biswas M, Samman MM (1991) Damage detection from changes in curvature mode shapes. J Sound Vib 145(2):321–332
34. Raghavan A, Cesnik CES (2007) Review of guided-wave structural health monitoring. Shock Vib Digest 39(2):91–114
35. Richardson MH, Mannan MA (1992) Remote detection and location of structural faults using modal parameters. In: Proceedings of the 10th international modal analysis conference, pp 502–507
36. Rose JL (2003) A baseline and vision of ultrasonic guided wave inspection potential. J Pressure Vessel Technol 124:273–282
37. Rucka M, Wilde K (2006) Application of continuous wavelet transform in vibration based damage detection method for beams and plates. J Sound Vib 297:536–550
38. Ruzzene M (2007) Frequency/wavenumber filtering for improved damage visualization. Smart Mater Struct 16(6):2116–2129
39. Schulz MJ, Naser AS, Pai PF, Chung J (1998) Locating structural damage using frequency response reference functions. J Intell Mater Syst Struct 9:899–905
40. Sharma V, Ruzzene M, Hanagud S (2006) Damage index estimation in beams and plates using laser vibrometry. AIAA J 44:919–923
41. Sharma V, Ruzzene M, Hanagud S (2006) Perturbation analysis of damaged plates. Int J Solids Struct 43(16):4648–4672
42. Sohn H, Farrar CR, Francois MH, Devin DS, Daniel WS, Nadler BR (2003) A review of structural health monitoring literature: 1996–2001. Los Alamos National Laboratory Report, LA-13976-MS
43. Staszewski WJ, Boller C, Tomlinson G (2004) Health monitoring of aerospace structures. Smart Sensors Signal Process. Wiley, New York
44. Stubbs N, Osegueda R (1990) Global damage detection in solids-experimental verification. Modal analysis. Int J Anal Exp Modal Anal 5(2):81–97
45. Stubbs N, Osegueda R (1990) Global non-destructive damage evaluation in solids. Modal analysis. Int J Anal Exp Modal Anals 5(2):67–79
46. Wang C, Rose L (2003) Wave reflection and transmission in beams containing delamination and inhomogeneity. J Sound Vib 2644:851–872
47. West WM (1984) Illustration of the use of modal assurance criterion to detect structural changes in an orbiter test specimen. In: Proceedings of the air force conference on aircraft structural integrity, pp 1–6
48. Yang C, Ye L, Su Z, Bannister M (2006) Some aspects of numerical simulation for Lamb wave propagation in composite laminates. Comp Struct 75(1–4):267–275
49. Yim H, Sohn Y (2000) Numerical simulation and visualization of elastic waves using mass-spring lattice model. IEEE Trans Ultrason Ferroelectr Freq Contr 47(3):549–558
50. Yuen MMF (1985) A numerical study of the eigenparameters of a damaged cantilever. J Sound Vib 103:301–310
51. Zhao X, Rose J (2003) Boundary element modeling for defect characterization potential in a wave guide. Int J Solids Struct 40(11):2645–2658
52. Zhong S, Oyadiji SO (2007) Crack detection in simply supported beams without baseline modal parameters by stationary wavelet transform. Mech Syst Signal Process 21:1853–1884
53. Zhou W, Ichchou M, Mencik J (2008) Analysis of wave propagation in cylindrical pipes with local inhomogeneities. J Sound Vib 319(1):335–354

Chapter 11
Use of Soft Computing Tools for Damage Detection

11.1 Genetic Algorithms

It was explained earlier that damage detection is essentially an inverse problem, wherein the input (force history) and the output (displacement, velocity, acceleration or strain histories) are known and using these, it is necessary to determine the location and extent of the damage present in a given structure. In essence, damage detection is a system identification problem, wherein for a given set of input–output parameters the location and extent of the damage is identified by using a set of functions called the *objective functions*, minimum through certain process. This process is called the genetic algorithms (GA) and hence GA can be thought of as an optimization problem. This section briefly explains the utility of GAs for detecting damages in structures.

11.1.1 A Brief Introduction to Genetic Algorithms

Genetic algorithms (GA) are powerful and broadly applicable stochastic search and optimization algorithms based on the principle of natural selection and natural genetics [3, 4]. They are finding increasing attention in engineering optimization problems. The conventional search and optimization techniques are usually calculus based. They use gradient of the function to find the local minima or maxima. These search techniques are problem dependent and can work well for simple and smooth functions. Practical problems (like what we are trying to solve here) are complex in nature, and these methods cannot give any satisfactory solution. The difference between the conventional search algorithms and GA is shown in Fig. 11.1. The main efficiency of genetic algorithms lies on their robustness. They can find the global optimum and does not lock on to local points. GAs do not

S. Gopalakrishnan et al., *Computational Techniques for Structural Health Monitoring*, Springer Series in Reliability Engineering, DOI: 10.1007/978-0-85729-284-1_11,

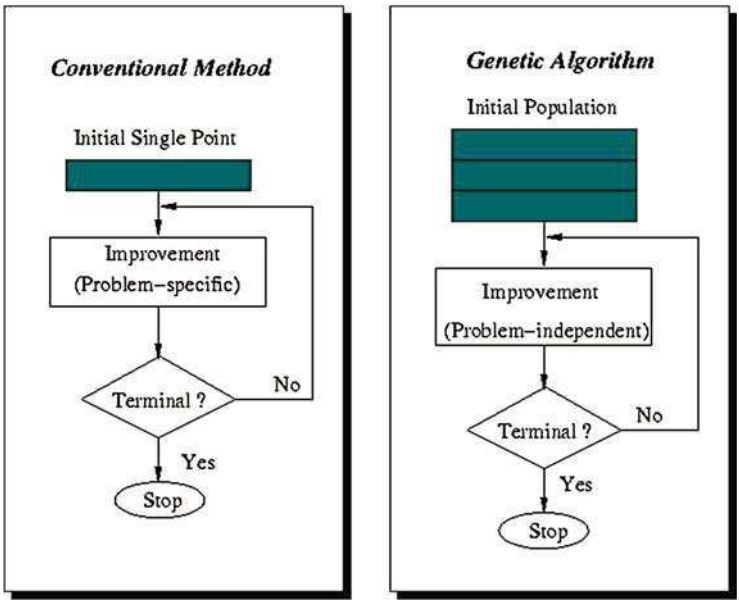

Fig. 11.1 Comparison between conventional search methods and genetic algorithms

require much mathematical operation to perform, and are not problem dependent. They can handle all types of objective functions and constraints, linear or non-linear. The differences between the GAs from the conventional method as summarized by Goldberg [4] are as follows.

- GAs start from a collection of solution points called *population*, and not from a single point solution.
- GAs work with the symbolic coded form of the solutions and not the solutions themselves. A solution in the coded form is called *chromosome*. A number of chromosomes creates a population.
- GAs use payoff information (fitness function) and not the derivatives or other auxiliary information.
- GAs use probabilistic transition rules, not deterministic rules.

A genetic search starts with randomly created *chromosomes* which makes the initial *population*. The chromosomes are coded from of the solutions. Coding is usually done using binary bit-strings. Each variable is mapped into coded strings and they are appended one after another to form a single chromosome. In living organism, a chromosome is some cell entity that encodes the prescription specifying all biological mechanism. Population is the solution space of each generation holding a fixed number of chromosomes. For instance a population of five members may appear like this:

1000100110
0011100001
1010001011
1100010000
1111001000

Parent chromosomes undergo two types of genetic operations, *crossover* and *mutation* to create offsprings. Crossover is the main genetic operation the parent chromosomes undergo. The performance of a GA depends largely on the performance of the crossover operator used [3]. It operates on one pair of chromosomes at a time and generates one or two offsprings retaining some features of both the parent chromosomes. There may be numerous ways of performing crossover; a simple crossover operation is illustrated here. A pair of parent chromosomes are selected randomly or based on their fitness. A crossover point is selected randomly after the fourth digit. The strings are exchanged across this point and the offsprings are created.

$$\left.\begin{array}{l}\text{Parent 1:1010} \bullet \text{001011} \\ \text{Parent 2:1111} \bullet \text{001000}\end{array}\right\} \longrightarrow \left\{\begin{array}{l}\text{Child 1:1010} \bullet \text{001000} \\ \text{Child 2:1111} \bullet \text{001011}\end{array}\right.$$

This is a single point crossover operation. It can also be two points or multi points operation. A *crossover probability* or *crossover rate* (p_c) is defined as the probability that a member of a population will be selected for crossover. Typical value of p_c is 0.5–0.8. A $p_c = 1.0$ implies that all the member of a population will go for crossover. Higher p_c makes better exploration of the solution space and reduces chances of local trapping; but it increases the computation time by increasing the number of function evaluation [3].

The other genetic operator mutation, creates offsprings by randomly changing one or more genes in the parent chromosome. For example, if the 5th gene of the 2nd member of the population is selected for mutation, the chromosome of the child after the mutation will be as shown.

$$\text{Parent: } 0011\underset{\uparrow}{1}00001 \longrightarrow \text{Child: } 0011000001$$

The *probability of mutation* $(p_m)$is defined by the probability that a single gene in the entire population will be altered. A typical value of p_m is 0.01. If it is 10 bit chromosome, then the probability that a member will undergo the mutation operation is 0.1.

The most crucial part of a GA is the *selection* procedure. A new generation created from an old one by this genetic operation. Selection is the driving force for any genetic search. Selections are always based on the fitness of the member. The better members are having higher chances of being selected in the next generation. Fitness of a member is usually done using the optimizing function itself. The selection pressure i.e., the weight on the healthy members for selection, plays a critical role in the selection procedure. High selection pressure may lead to premature convergence; on the other hand low selection

pressure makes the convergence slow [3]. The selection can be from the *regular sampling space* or from *enlarged sampling space*. The regular sampling space is usually created by replacing the parents by their offsprings after their birth. Hence the size of this space is always equal to the size of the population size. The replacements may also take place randomly or based on their fitness values. The enlarged sampling space contains both parent and offspring subspaces. The parents and offsprings get the same chance to compete in the selection. The size of this space will change as the number of offsprings changes.

A wide variety of selection mechanisms are experimented till date. The three basic mechanism as outlined in [3] are the following

- Stochastic selection
- Deterministic selection, and
- Mixed Selection

In *stochastic selection* the members are assigned some selection probability based on their fitness. This probabilities may be directly proportional to their fitness values or may be obtained by scaling up their fitness values or the rank in the sample space. A well known scaling procedure is exponential scaling. In *deterministic selection*, first best members of the population size is selected. This can be done only with enlarged sampling space discussed earlier. Here the prohibition of duplicate chromosome in the population is automatically maintained. This prevents the stronger chromosomes from maintaining more than one copy in the population, which otherwise may lead to premature convergence. *Mixed selection* is a combination of both stochastic and deterministic selection. An example of mixed sampling is the tournament selection. Here a set of chromosomes are randomly picked and the best one from that set is selected.

11.1.2 Genetic Algorithm Process for Damage Detection and Definitions

In the search problem, one may possibly locate the delaminations (or cracks) and their sizes by maximizing certain norms constructed from experimentally obtained and computationally simulated data for known location and size of the damage. However, a clear rational needs to be developed to determine the level of information that is required from damage matrix construction that needs to be fed into GA to start the spatially local search procedure. This process is implemented to work with the simplified damaged elements that were formulated in Chap. 6. An overview of the GA search adopted here is schematically presented in Fig. 11.2. Two major features followed here are; (1) selection from a enlarged sampling space, consisting of parent and offspring pools, and (2) prohibition of duplicate chromosomes in the early generations. At this stage, it is necessary to define some of the standard terminologies used in GA:

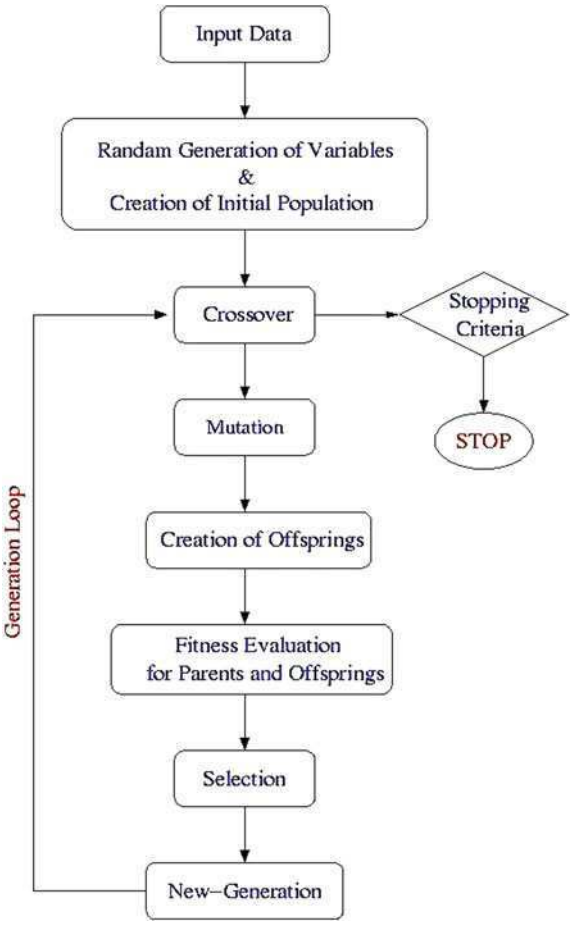

Fig. 11.2 Flowchart of genetic search

- *Chromosome*—The damage configuration in coded form
- *Genes*—The individual parameters or variables to represent the damage configuration.
- *Locus*—The position of the gene or in other words the order of significance of the variables and the relative extent to which they affect the behavior of the damaged structure in measurable form.
- *Alleles*—Values of the gene, or in other words the number of delamination, their location and size.
- *Phenotype*—Decoded solution or the possible damaged configuration of the structure.
- *Genotype*—Encoded solution or the set of values of the variables in binary string in our problem, that represent the damaged structure when decoded.

11.1.3 Objective Functions in GA for Delamination Identification

The performance of a GA largely depends upon the objective function. With a smooth function or a function with few local extrema, GAs converge rapidly than a function with large number of peaks and troughs, that are normally found in spectral functions. In this section, we will examine the behavior of different possible objective functions towards the determination of delamination parameters in a composite beam, i.e. the delamination location, depth and its size. Two physical parameters, namely displacement and power are proposed and these will be examined on a cantilever beam and a fixed beam, respectively. The configurations of the beam is shown in Fig. 11.3

11.1.3.1 Displacement Based Functions

Four possible displacement-based objective functions are examined. These functions compares the baseline or experimental response of the structure with the simulated response. Functions J_1, J_2, J_3 and J_4, which are given in Eqs. 11.1–11.4, require displacement coefficients $(\hat{u}^o,\ \hat{w},\ \hat{\phi})$, measured at a spectral element node at sampling frequency (ω_n) under the SFEM environment.

$$\mathbf{J}_1 = \frac{1}{1+\frac{1}{N}\sum_{\omega_n}\frac{\left|\hat{u}^o_{\text{comp}}-\hat{u}^o_{\text{expt}}\right|}{\left|\hat{u}^o_{\text{expt}}\right|}}, \quad n=1,\ldots,N. \tag{11.1}$$

$$\mathbf{J}_2 = \frac{1}{1+\frac{1}{N}\sum_{\omega_n}\frac{\left|\hat{w}_{\text{comp}}-\hat{w}_{\text{expt}}\right|}{\left|\hat{w}_{\text{expt}}\right|}}, \quad n=1,\ldots,N. \tag{11.2}$$

$$\mathbf{J}_3 = \frac{1}{1+\frac{1}{N}\sum_{\omega_n}\frac{\left|\hat{\phi}_{\text{comp}}-\hat{\phi}_{\text{expt}}\right|}{\left|\hat{\phi}_{\text{expt}}\right|}}, \quad n=1,\ldots,N. \tag{11.3}$$

$$\mathbf{J}_4 = \frac{1}{1+\frac{1}{3N}\sum_{\omega_n}\left\{\frac{\left|\hat{u}^o_{\text{comp}}-\hat{u}^o_{\text{expt}}\right|}{\left|\hat{u}^o_{\text{expt}}\right|}+\frac{\left|\hat{w}_{\text{comp}}-\hat{w}_{\text{expt}}\right|}{\left|\hat{w}_{\text{expt}}\right|}+\frac{\left|\hat{\phi}_{\text{comp}}-\hat{\phi}_{\text{expt}}\right|}{\left|\hat{\phi}_{\text{expt}}\right|}\right\}}, \quad n=1,\ldots,N. \tag{11.4}$$

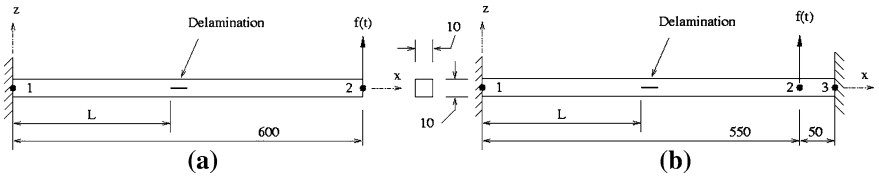

Fig. 11.3 The configurations of the **a** cantilever and **b** fixed beams considered to examine the sensitivity of the GA objective functions

Here, $\hat{u}^o$, $\hat{w}$, $\hat{\phi}$ correspond to the axial, transverse and the rotational motions respectively. N is the Nyquist point in FFT. The subscripts$_{\text{comp}}$ in the above equations indicate the computationally simulated response data, obtained using *damaged spectral element* model explained in Sect. 6.3. The subscript$_{\text{expt}}$ stands for measured baseline response data. However no experimentation is performed here as a part of this study, and these response data are also generated using the *damaged spectral element* for known configurations. All of these objective functions are maximizing functions and they achieve the maximum value (equal to 1) when the simulated results match exactly with the experimental data. The delamination parameters corresponding to that of simulated response are the identified parameters.

The cantilever beam considered is shown in Fig. 11.3a and the fixed beam in Fig. 11.3b. Sensitivity for each of the three delamination parameters on these functions are studied separately, keeping other two parameters fixed. In the study with delamination location, the reference data is generated by keeping a 20 mm mid-plane delamination at location $L = 250$ mm. Load is applied at node-2, transversely, upward. The delamination location is varied from $L = 0$ to 500 mm and the corresponding function values are computed. For the cantilever beam, the function values are plotted in Fig. 11.4a and for the fixed fixed beam in Fig. 11.4b. None of these functions is found to be smooth; all of them are having many local maxima. The most important feature one should examine for an objective function with multiple peaks, is the band-width of the primary variable around the optimum point, where function values are higher than the neighboring area. This band-width is found to be almost equal for all the functions. In case of depth z, the function values are plotted in Fig. 11.5a for the cantilever beam and in Fig. 11.5b for the fixed beam for varying depth of delamination. The reference response data is generated with a 20 mm long delamination at a depth $z = -3$ mm. It is interesting to note here that the functions based on the transverse and rotational components of response (i.e. J_2 and J_3 respectively), the maximum fitness value, 1 occurs at the actual depth of delamination and also for the depth which is the mirror image of the actual depth about the mid-plane. However the other two functions (i.e. $J_1$and J_4) do not behave this way. This phenomenon can be explained by the fact that the net bending stress for these two configurations of delamination (one at a depth which is mirror image of other about the mid-plane) are identical at any instant of time. The net axial stress however are different. The overall nature of the functions is found to be quite smooth. All of the functions are found to be most well behaved when it comes to delamination length or size identification. The reference data is generated for a delamination of length 20 mm located at distance $L = 250$ mm from the left node and at the mid-plane of the beams. In the plots (Fig. 11.6a, b) it can be noticed that functions J_2 and J_3 are overlapping.

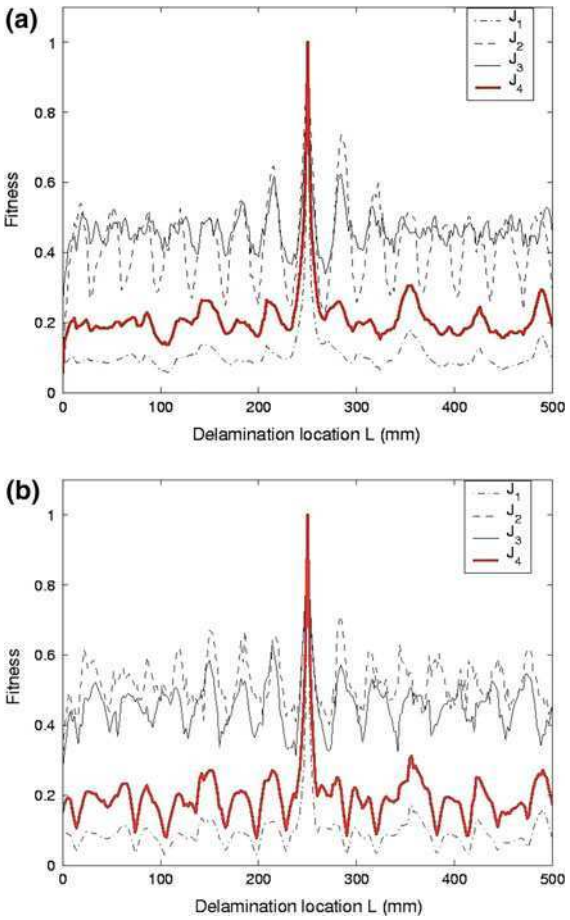

Fig. 11.4 The GA objective functions $J_1 - J_4$ (Eqs. 11.1–11.4) plotted with varying location of delamination for **a** cantilever and **b** fixed beams

11.1.3.2 Power Based Objective Functions

The displacement-based objective functions studied in the previous section are quite well behaved except for the delamination location (L). Search for a better function is extended with the spectral power flow [6] expressed as

$$\hat{P}(x, \omega_n) = \hat{\mathbf{f}}(x, \omega_n)^T (i\omega_n \hat{\mathbf{u}}(x, \omega_n))^* \tag{11.5}$$

where the superscript * represents the complex conjugate. The reason for choosing power as a measure is that for a non-dissipative medium, the real part of it is space invariant [7]. The objective function based on spectral power is derived as

$$J_5 = \left[1 + \frac{1}{N} \sum_n \frac{\left| \hat{\mathbf{f}}^T_{\text{comp}} \left(i\omega_n \hat{\mathbf{u}}_{\text{comp}} \right)^* - \hat{\mathbf{f}}^T_{\text{expt}} \left(i\omega_n \hat{\mathbf{u}}_{\text{expt}} \right)^* \right|}{\left| \hat{\mathbf{f}}^T_{\text{expt}} \left(i\omega_n \hat{\mathbf{u}}_{\text{expt}} \right)^* \right|} \right]^{-1} \tag{11.6}$$

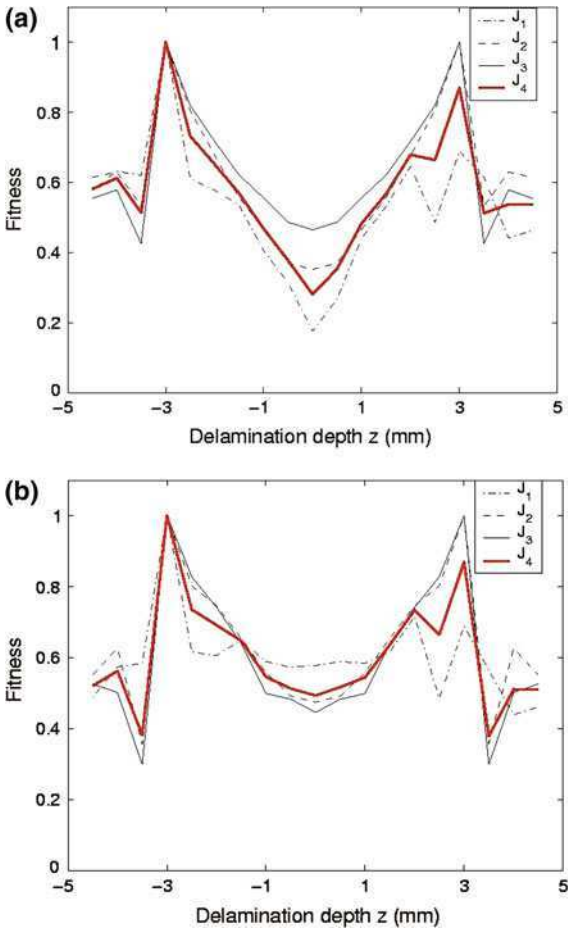

Fig. 11.5 The GA objective functions $J_1 - J_4$ Eqs. 11.1–11.4 plotted with varying depth of delamination for **a** cantilever and **b** fixed beams

The fitness plot of the function J_5 for identification of location L is shown in Fig. 11.7 in comparison with the displacement-based function J_4. However, J_5 can in no way be said to be better behaved than J_4. Also, it shows many more fluctuations compared to the other displacement-based functions. Hence, it stresses the fact that any quadratic measure as objective function (representative of the energy components in different frequency bands) will have similar drawbacks and one needs to explore further for better functional space. This can provide improved performance of GA-based identification strategies for non-smooth problems as in the present case. Other directions to improve the performance such as rank-based non-domination [9] and immune diversity [2] are less likely to ensure global optima unless better objective functions (e.g., J_4 in the present case, which includes the effect of axial–flexural coupling) are used. Similar observation in the context of a benchmark problem called the Traveling Salesman Problem (TSP) can

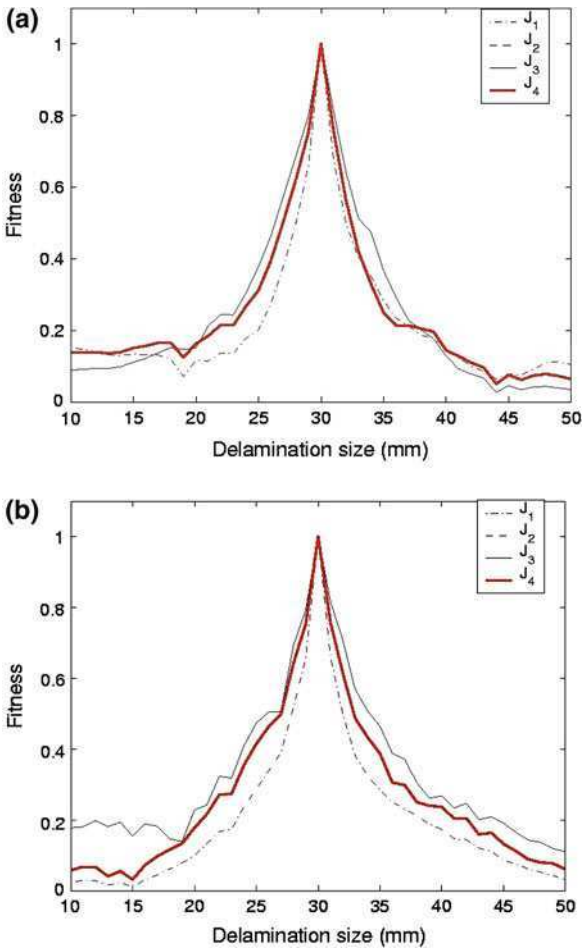

Fig. 11.6 The GA objective functions $J_1 - J_4$ Eqs. 11.1–11.4 plotted with varying size of delamination for **a** cantilever and **b** fixed beams

be found in [1]. In the present study, we restrict simulations to using only the objective functions discussed so far and show the performance of the proposed GA-based identification strategy in terms of the accuracy of the converged result and computational cost in the following section.

11.1.4 Case Studies with a Cantilever Beam

The cantilever beam shown in Fig. 11.3a is now considered for identification. Short duration Gaussian excitation having frequency content up to 40 kHz (Fig. 3.7) is applied at the cantilever tip in the transverse direction. First, single parameter

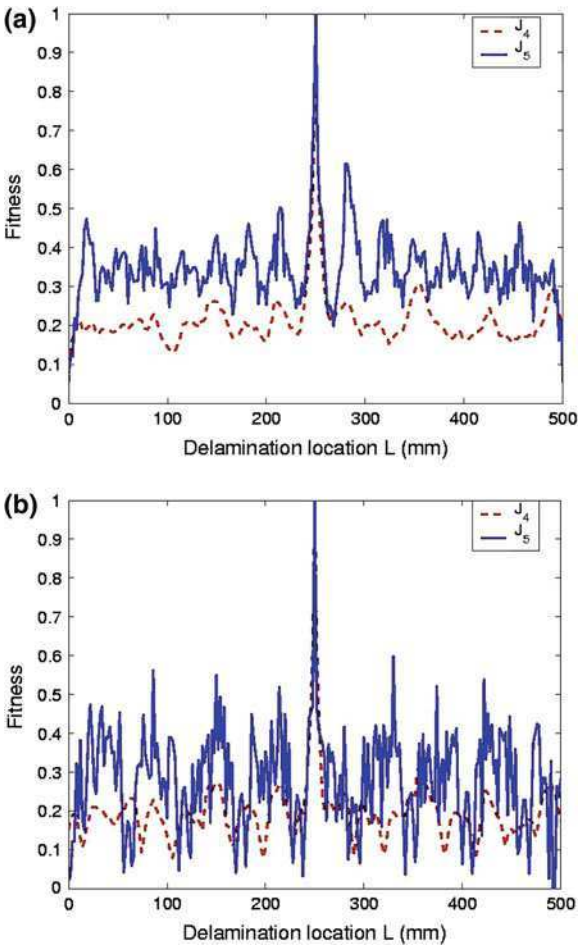

Fig. 11.7 The GA objective functions J_4 and J_5 Eqs. 11.4 and 11.6 plotted with varying location of delamination for **a** cantilever and **b** fixed beams

identification is performed. Later, it is extended to two parameters and finally three-parameter identification is performed. Unless otherwise mentioned, function J_2 is considered as the objective function. Although J_4 is ideal as discussed earlier, the reason for choosing J_2 is to demonstrate the efficiency of the proposed SFEM-GA strategy in terms of computational cost as well as accuracy, while using an inferior objective function.

11.1.4.1 Identification of Delamination Location

In this case study, the size and depth of delamination is assumed to be known. The reference data is generated by considering a 20 mm delamination at a depth $z = -2$ mm. The location of delamination X from the root is identified with the following input data.

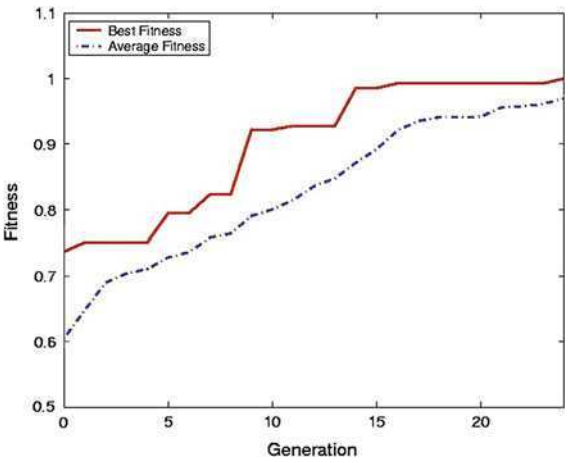

Fig. 11.8 Fitness curve of the GA run for identification of delamination location

Variable limits : $0 \leq X \leq 500\,\text{mm}$
Population size : 15
Crossover type : two point
Selection type : deterministic
Crossover rate p_c : 0.6
Mutation rate p_m : 0.04

The fitness curve is given in Fig. 11.8. Location of the delamination ($X = 200\,\text{mm}$) is identified exactly. The number of generations passed is 24. In total, 251 function evaluations are performed and the time required to complete this computation is only 25 min. Note that the structural analysis here must involve the dynamics up to the frequency content of the excitation signal (here 40 kHz). Such high frequency excitation is particularly useful when smaller damage zones (typically a few centimeters in most composite beams and panels) need to be detected. The plot in Fig. 11.8 shows that the run reached a very good fitness value at generation 14. The total number of function evaluations up to generation 14 is 161 and the corresponding computation time is found to be 17 min. The computational cost shows huge improvement over the available GA-based strategies for similar problem complexity and accuracy. Similar improvement can be observed in all the other case studies presented below.

11.1.4.2 Identification of Delamination Size

In this case study, the delamination size (X) is considered as the only unknown parameter. The delamination location ($L = 200\,\text{mm}$) and depth ($z = -2\,\text{mm}$) are presumed to be known parameters. The input data for the GA run is given below.

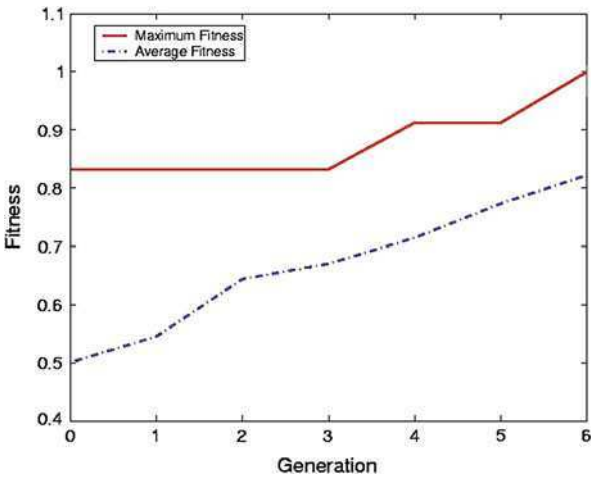

Fig. 11.9 Fitness curve of the GA run for identification of delamination size

Variable limits : $0 \leq X \leq 50\,\text{mm}$
Population size : 7
Crossover type : two point
Selection type : deterministic
Crossover rate p_c : 0.6
Mutation rate p_m : 0.04

A lower population size is considered because of the reduced complexity of the problem The exact size of the delamination ($X = 20\,\text{mm}$) is identified from the search. The fitness curve is given in Fig. 11.9. The number of generations passed is six. A total of 25 function evaluations is performed and total the computation time is only 3 min. Much better performance is found with this problem compared to location identification. This was expected as the fitness function behaves much better with variations in delamination size. The narrow bound in the variable limits is also another reason for this better convergence.

11.1.4.3 Identification of Delamination Location and Size

In this case study, two variables, delamination location (X_1) and its size (X_2) are identified in a single run. The delamination depth ($z = -2\,\text{mm}$) is assumed to be the only known parameter. The input data for the GA run is shown below.

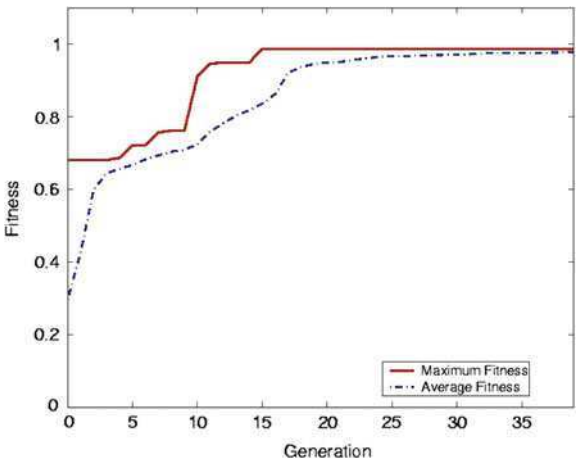

Fig. 11.10 Fitness curve of the GA run for identification of delamination location and size

Variable limits : $0 \leq X_1 \leq 500\,\text{mm}; 0 \leq X_2 \leq 50\,\text{mm}$
Population size : 20
Crossover type : two point
Selection type : deterministic
Crossover rate p_c : 0.6
Mutation rate p_m : 0.04

The fitness curve is given in Fig. 11.10. The search results are tabulated in Table 11.1. The number of generations passed is 39. In total, 438 function evaluations are performed and the total computation time is 41 min.

11.1.5 Identification of Delamination Location, Size and Depth

In this case study, all three parameters of a delamination; i.e., delamination location (X_1), its size (X_2) and depth (X_3) are identified in a single GA run. Since the function J_2 is not sensitive to the delamination depth, function J_4 is used instead. The input data for the GA run is shown below.

Table 11.1 Results of genetic search for delamination location and size

Parameter	Actual value (mm)	Identified value (mm)
Location (X_1)	250	250
Size (X_2)	20	19.9

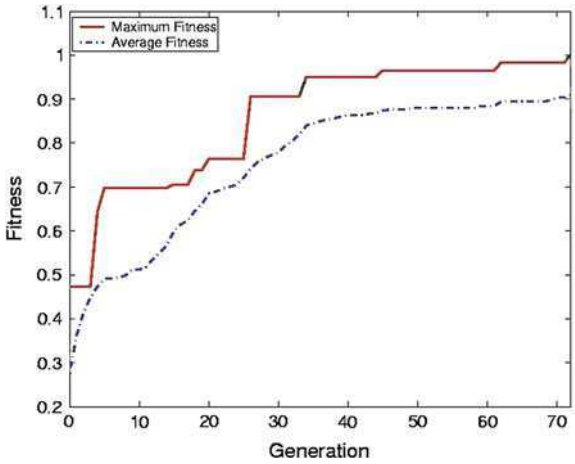

Fig. 11.11 Fitness curve of the GA run for identification of delamination location, depth and size

$$\begin{aligned}
\text{Variable limits} &: 0 \leq X_1 \leq 500\,\text{mm}; 0 \leq X_2 \leq 50\,\text{mm}; \\
&\quad -\ 4\,\text{mm} \leq X_3 \leq\ +\ 4\,\text{mm} \\
\text{Population size} &: 20 \\
\text{Crossover type} &: \text{two point} \\
\text{Selection type} &: \text{deterministic} \\
\text{Crossover rate } p_c &: 0.8 \\
\text{Mutation rate } p_m &: 0.1
\end{aligned}$$

The crossover and mutation rates are increased to enable better exploration of the solution space. The fitness curve over the generations is shown in Fig. 11.11. The results of the search are tabulated in Table 11.2. The number of generations required for convergence is 72. A total of 660 function evaluations are performed and total computation time is 2 h and 52 min. Total computation time is comparatively higher than the previous studies. This is because the function J_4 needs all three displacement components, which increases the computation time inside the fitness evaluation module. The net time is indeed very much attractive considering the complexity involved in the problem.

Table 11.2 Results of genetic search for delamination location, depth and size

Parameter	Actual value	Identified value
Location (X_1)	200 mm	200 mm
Size (X_2)	20 mm	20 mm
Depth (X_3)	−1 mm from mid-plane	−1 mm from mid-plane

11.2 Artificial Neural Networks

An artificial neural network is a framework consisting of many numbers of interconnected neuron like processing units. Each neuron unit is stimulated by the sum of the incoming weighted signals and transmits the activated response to the other connected neuron units [5]. A neural network is a massively parallel distributed processor made up of simple processing units, which has a natural propensity for storing experiential knowledge and making it available for use. It resembles the brain in two respects:

1. Knowledge is acquired by the network from its environment through a learning process.
2. Inter neuron connection strengths, known as synaptic weights are used to store the acquired knowledge.

11.2.1 Simple Model of Neuron

A neuron is an information-processing unit that is fundamental to the operation of a neural network. The block diagram shown in Fig. 11.12 shows the model of a neuron, which forms the basis for designing neural networks. The three basic elements of the neural network are:

1. *Synapses*: It represents the connecting links, each of which has strength of its own. Specifically, a signal $\mathbf{x}_j$ at the input of synapse **j** connected to neuron **k** is

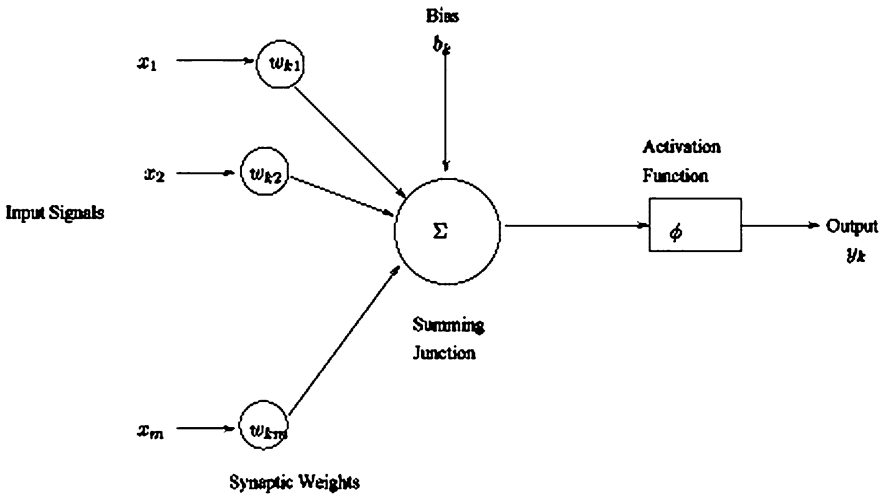

Fig. 11.12 Simple neuron showing the input, output and activation function with 1 hidden layer

multiplied by the synaptic weight $\mathbf{w_{ij}}$. Here i denotes the present neuron and j represent the next neuron.

2. *Adder*: An *adder* is used for summing the input signals, weighted by a respective synapses of the neuron. The operations described here constitute a linear neuron.
3. *Activation Function*: An *activation function* is used for limiting the amplitude of the output of a neuron. This activation function also includes the bias, which is externally applied and this bias $\mathbf{b}_k$ has the effect of increasing or decreasing the net input of the activation function.

In mathematical terms, the neuron may be described as

$$u_k = \sum_{j=0}^{m} w_{kj} x_j \tag{11.7}$$

and

$$y_k = \phi(u_k + b_k) \tag{11.8}$$

where

$$x_1, \ldots, x_m$$

are the input signals.

$$w_{k_1}, w_{k_2}, \ldots, w_{k_m}$$

are the synaptic weights of the neuron $\mathbf{k}, \mathbf{u}_k$ is the *linear combiner output* due to the input signals, and $\mathbf{b}_k$ is the bias, while $\phi(.)$ is the activation function.

There are three types of network architectures

1. *Single Layer Feedforward Networks*: In a layered neural network, the neurons are organized in the form of layers. In the simplest form of a layered network, we have *input layer* of source nodes that projects onto an output layer of neurons. This type of network is called as single layer network.
2. *Multilayer Feedforward Networks*: This class has one or more *hidden layers* whose computation nodes are called *hidden neurons*. By adding one or more hidden layers, the network is enabled to extract higher-order statistics. The neural network is said to be fully connected in the sense that every node in each layer is connected to every other node in the adjacent forward layer. If some of the communication links are missing from the network, we say that the network is partially connected.
3. *Recurrent-Networks*: A *recurrent neural network* distinguishes itself from a feedforward neural network in that it has at least one feedback loop. For example, a recurrent network may consist of a single layer of neurons with each neuron feeding its output signal back of the inputs of all the other neurons.

11.2.2 Types of Activation Function

The activation function ϕ defines the output of a neuron in terms of the induced local field **v**. The three types of activation function are

1. *Threshold Function*: In this type of activation function, we have

$$\phi(y_k) = \begin{cases} 1 & \text{if } v_k \geq 0 \\ 0 & \text{if } v_k < 0 \end{cases}$$

   This type of function is known as Heaviside function. The above neuron shows *all or none property*, which is shown in Fig. 11.13a
2. *Piecewise-Linear Function*: For the piece-wise linear function described as in the Fig. 11.13b, we have

$$\phi(.) = \begin{cases} 1 & \text{if } v \geq 0 \\ v & +\frac{1}{2} > v > -\frac{1}{2} \\ 0 & \text{if } v < 0 \end{cases}$$

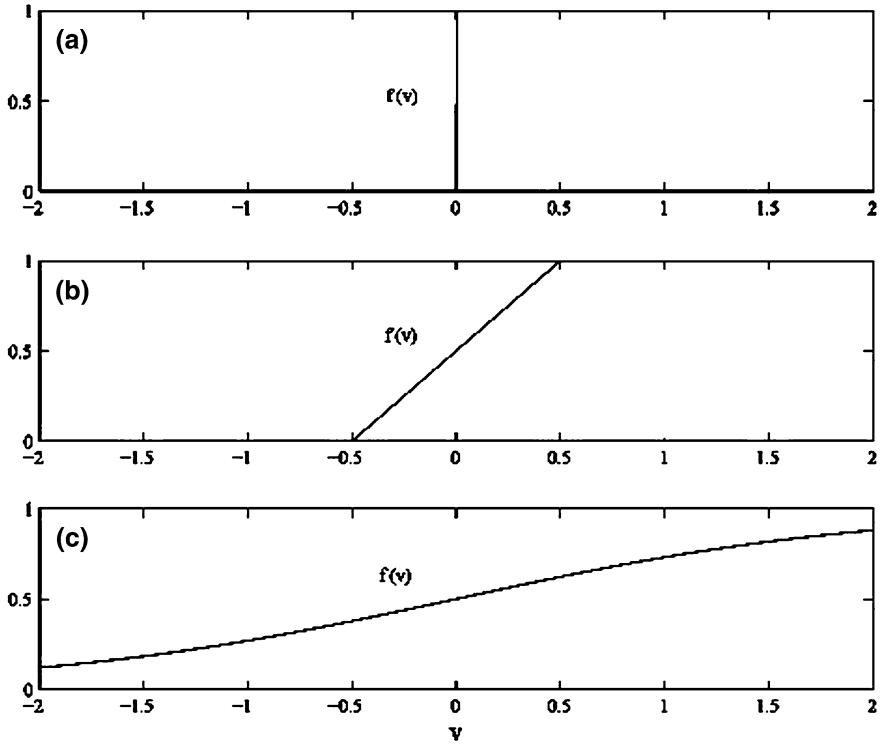

Fig. 11.13 Plot showing various activation functions. **a** Threshold function, **b** piecewise-linear function, **c** sigmoid function

This form of an activation function may be viewed as an *approximation* to a non linear amplifier.

3. *Sigmoid Function*: The sigmoid function, whose graph is shaped as shown in Fig. 11.13c, is the common activation function used in neural networks. An example of the sigmoid function is the logistic function, defined by

$$\phi(v) = \left(\frac{1}{1 + \exp(-av)}\right)$$

where a is the slope parameter of the sigmoid function. As the slope parameter approaches infinity, the function becomes simply a threshold function. Sigmoid function is continuous and differentiable. The other sigmoidal function is

$$\phi(v) = \tanh(v)$$

These functions are pictorially shown in Fig. 11.13

11.2.3 Multilayer Feedforward Networks

The number of nonlinear layers of a multilayer network is defined to be the number of the weight layers, instead of neuron layers. An excessive number of layers causes slower convergence in the backpropagation learning. Generally two layer is found to be adequate.

The steps (algorithm) in backpropagation learning are the following:

1. *Initialization*: Assuming that no prior information is available, the synaptic weights and threshold are picked from the uniform distribution whose mean is zero and whose variance is chosen to make the standard deviation of the induced local fields of the neurons lie at the transition between the linear and saturated parts of the sigmoid activation function.
2. *Presentation of Training Samples*: Next, the network is presented with an epoch of training samples. For each example in the set, which is ordered in some fashion, the sequence of forward and backward computations described in the next steps are performed.
3. *Forward Computation*: Let a training example in the epoch be denoted by $(\mathbf{x}(\mathrm{n}), \mathbf{d}(\mathrm{n}))$, where the input vector $\mathbf{x}(\mathrm{n})$ is applied to the input layer of sensory nodes and the desired response vector $\mathbf{d}(\mathrm{n})$ is presented to the output layer of computation nodes. Next, the local fields and function signals of the network, layer by layer are computed. The local field $v_j^{(l)}(n)$ for neuron j in layer l is given by

$$v_j^{(l)}(n) = \sum_{i=0}^{m_o} w_{ji}^{(l)}(n) y_i^{(l-1)}(n) \tag{11.9}$$

where $y_i^{(l-1)}(n)$ is the output(function) signal of neuron i in the previous layer $l-1$ at the iteration n and $w_{ji}^{(l)}(n)$ is the synaptic weight of neuron j in layer l that is fed from neuron i in layer $l-1$. For $i=0$, we have $y_0^{(l-1)}(n)=+1$ and $w_{j0}^{(l)}(n)=b_j^{(l)}(n)$ is the bias applied to the neuron j in layer l. Assuming the use of a sigmoid function, the output signal of neuron j in layer l is

$$y_j^{(l)} = \phi_j(v_j(n))$$

If the neuron j is in the output layer (i.e., $l=L$, where L is referred to as the depth of the network), then, we set

$$y_j^{(L)} = o_j(n)$$

The error signal is then computed as

$$e_j(n) = d_j(n) - o_j(n)$$

where $d_j(n)$ is the jth element of the desired response vector $\mathbf{d}(n)$

4. *Backward Computation*: Next, the δs (i.e. local gradients) of the network is computed, which is defined by

$$\delta_j^{(l)}(n) = \begin{cases} e_j^{(L)}(n)\phi_j'(v_J^{(L)}(n)) & \text{for neuron } j \text{ in output layer } L \\ \phi_j'(v_j^{(n)}) \sum_k \delta_k^{(l+1)}(n) w_k j^{(l+1)}(n) & \text{for neuron } j \text{ in hidden layer } l \end{cases} \tag{11.10}$$

where the prime in $\phi_j'(.)$ denotes differentiation with respect to the argument. After this operation, the synaptic weights of the network in layer l are adjusted according to the generalized delta rule.

$$w_{ji}^{(l)}(n+1) = w_{ji}^{(l)}(n) + \alpha[w_{ji}^{l}(n-1)] + \eta\delta_j^{(l)}(n) y_j^{l-1}(n) \tag{11.11}$$

where η is the learning rate parameter and α is the momentum constant.

5. *Iteration*: Lastly, the forward and backward computations are iterated in the 3th and 4th step by presenting new epochs of training samples to the network until the stopping criteria is met.

In the next section, we will use the multi layer feedforward network for identification of flaws, especially the degraded zones, under the FSFEM environment

11.2.4 Neural Network Integrated with SFEM

An Multi-Layer Perceptron (MLP) feedforward neural network using an error back propagation (BP) algorithm is trained and tested to estimate (1) the span-wise location of the damage (L_1), (2) the approximate length of the degraded zone (L_2) and (3) the

stiffness degradation factors α_{ij} for damage in the composite beam. Here, the spectral element damage model, developed in Chap. 6 is used here to demonstrate the effectiveness of feedforward network in damage detection. Among the two degraded spectral element model presented in Chap. 6, the Average Degraded Model reported in Sect. 6.7.2 is used in the simulation. Detailed discussion on such network models can be found in [5]. A schematic flow-chart on the use of frequency domain spectral analysis tools and model-generated data to train and test neural networks was reported in [10]. The main difference in the strategy developed here compared to that reported in [10] is that the measurement is assumed to be carried out at a single sensor location, especially for univariate data (i.e., data containing the information of a single damage configuration), whereas in [10], the data from several sensor locations (as many as the number of input nodes) at a particular frequency need to be fed as inputs while using that network. In the present model, we assume that broadband spectral data is available from a single sensor measurement. In SFEM, the spectral band ranges from ω_1 to ω_N, where N is the Nyquist frequency. Hence, the number of input nodes in the input layer needs to be fixed by considering the frequency resolution in the model during training. Therefore, if one needs to use the complete spectrum of the vector $\hat{\mathbf{u}}(\omega_n)_i$ (for beam it consists of $\hat{u}^o$, $\hat{w}$ and $\hat{\phi}$) at the nth sampling frequency and from the ith sensor location, then N complete sets (each containing three displacement components) of neurons in the input layer can be included. The network model is shown in Fig. 11.14. Since the broadband spectral data consist of real and imaginary components at every sampling frequency, the number of neurons in the input layers is assigned as follows. First the amplitude and phase of the spectral data for each displacement component are

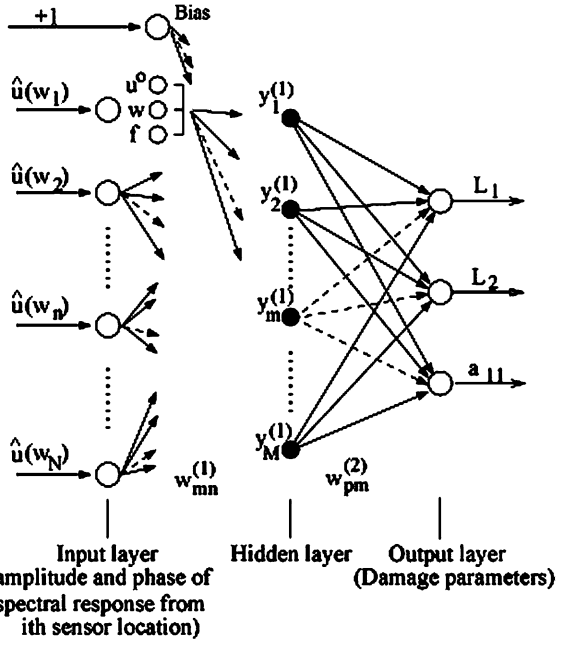

Fig. 11.14 Multi-layer perceptrons feed forward neural network for estimation of damage parameters from broadband spectral data

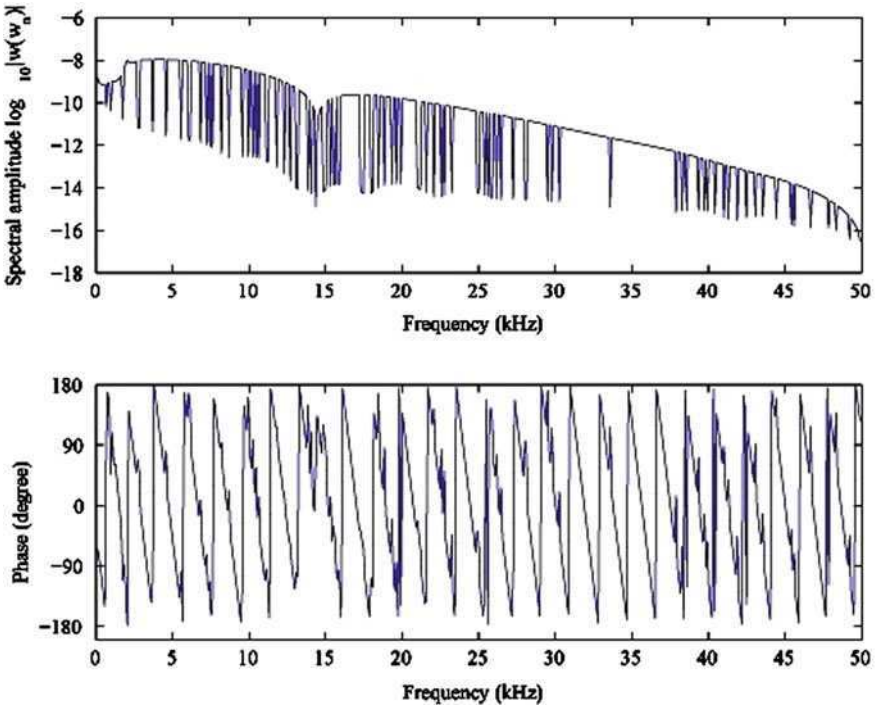

Fig. 11.15 Typical amplitude and phase spectra of transverse displacement used as the neural network input

computed at each sampling frequency. This doubles the length of the data array. Fig. 11.15 shows typical spectra of amplitude and phase of transverse displacement used as the network input. The data set corresponding to the first sample (at $\omega_n = 0$) is removed as it does not contribute to the dynamic characteristics. The input data to the input layer are formed by adding one additional element of unity as input bias with the previous array. The output from the neurons in the output layer are the damage location (L_1), the length of degraded zone (L_2) and the stiffness degradation factor α_{11} (in general a set of α_{ij} as seen in Eq. 6.84 depending on the importance and reliability of the diagnostic measurement). It should be noted that for higher resolution spectral data obtained through the simulation or measurements for neural network training, the number of neurons in the input layer will increase in proportion. As a result, the number of hidden layers and the number of neurons in each of these hidden layers also must increase to provide optimal evolution of the information pattern to be embedded in the network. However, there is an inherent drawback to such a large network in that an excessive number of hidden layers causes slower convergence in the learning when using error back propagation. Hence, for better network performance when dealing with spectral data having low, medium or high resolution, it is essential to restrict the number of neurons in the input layers. Depending on the resolution (frequency sampling) and the extent of useful diagnostic information, any FFT spectral data set

can be transformed to a data set with pre-assigned and smaller dimension but having the same bandwidth. Although we restrict our study to estimation of a single damage configuration, the model shown in Fig. 11.14 can be extended to a two-dimensional network to deal with broadband spectral data from multiple sensor locations. Obviously, in such a case, it would be more practical to use a number of measurement sensors in proportion to the number of damage incidents to be monitored. However, dealing with problems of such enormous complexity remains a future area of development. The following network details are chosen for the training and performance testing. A graphite–epoxy cantilever beam with one damage configuration (defined by the damage parameters L_1, L_2 and α_{11}) as discussed Sect. 6.7.2, is considered. One single spectral element with embedded degraded zone is used to generate the data sets. Only the transverse displacement spectrum $\hat{w}(\omega_n)$ obtained at the tip of the cantilever is used. Training is carried out in sequential mode using S data sets. For each of these cases, the FSFEM computation is performed through automated scripts by varying the damage parameters randomly. The number of neurons in the input layer is fixed at 1023 (511 neurons for amplitude, 511 neurons for phase and one neuron for bias). The amplitudes are normalized as

$$y_n^{(0)} = 1.6\left(\frac{\bar{w}_n - \mathrm{Min}[\mathrm{w_n}, \theta_\mathrm{n}]_\mathrm{S}}{\mathrm{Max}[w_n, \theta_n]_S - \mathrm{Min}[w_n, \theta_n]_S}\right) - 0.8 \quad \in [-0.8, 0.8], \tag{11.12}$$

$$\bar{w}_n = \log_{10}|\hat{w}(\omega_n)|\,, \qquad \theta_n = \tan^{-1}\left(\frac{\mathrm{Im}[\hat{w}(\omega_n)]}{\mathrm{Re}[\hat{w}(\omega_n)]}\right) \quad \in [0, 2\pi] \tag{11.13}$$

and the phases are normalized as

$$y_n^{(0)} = 1.6\left(\frac{\theta_n - \mathrm{Min}[w_n, \theta_n]_S}{\mathrm{Max}[w_n, \theta_n]_S - \mathrm{Min}[w_n, \theta_n]_S}\right) - 0.8 \quad \in [-0.8, 0.8], \tag{11.14}$$

where $\mathrm{Max}[\,]_S$ and $\mathrm{Min}[\,]_S$ are respectively the maximum and minimum values in the S input data set. The S output data sets are also normalized in a similar way within the range $[-0.8, 0.8]$. In the present numerical study, we have only one hidden layer having 512 neurons. The synaptic weights between the neurons of the input layer and the neurons of the hidden layer are initialized as a matrix $\mathbf{w}(0)^{(1)}_{(512\times1023)}$. The synaptic weights between the neurons of the hidden layer and the neurons of the output layer are initialized as a matrix $\mathbf{w}(0)^{(2)}_{(3\times512)}$. Both $\mathbf{w}(0)^{(1)}_{(512\times1023)}$ and $\mathbf{w}(0)^{(2)}_{(3\times512)}$ consist of normally distributed random numbers (with mean zero, variance one and standard deviation one).

11.2.4.1 Feedforward Computation

Following the standard algorithm for the feedforward MLP network [5], the input to the mth neuron in the lth layer during the rth learning step can be expressed as

$$v(r)_m^{(l)} = \sum_{n=1}^{N} w(r)_{mn}^{(l)} y(r)_n^{(l-1)} \tag{11.15}$$

where $y(r)_n^{(l-1)}$ is the output of the nth neuron in the previous layer $l-1$ at the rth learning step. $w(r)_{mn}^{(l)}$ is the synaptic weight of the mth neuron in the lth layer that is fed from neuron n in layer $l-1$. In the present case $y(r)_n^{(0)} = y_n^{(0)}$ is the input spectral data in normalized form as given in Eqs. 11.13 and 11.14, $y_1^{(0)} = +1$ is the bias to one neuron in the input layer. $y(r)_m^{(2)}, m = 1, 2, 3$, is the output of the three neurons in the output layer at the rth learning step, where $\mathbf{o}^{(2)} = \{L_1\ L_2\ \alpha_{11}\}^T$ is the expected output vector from the three neurons in the output layer. The output of the mth neuron in the lth layer through the activation function of the input to the mth neuron can be expressed as

$$y(r)_m^{(l)} = \Phi_m^{(l)}\left(v(r)_m^{(l)}\right). \tag{11.16}$$

In the present case, a *bipolar sigmoidal* function is given by

$$\Phi_m^{(l)} = \frac{1 - e^{v(r)_m^{(l)}}}{1 + e^{v(r)_m^{(l)}}} \tag{11.17}$$

is used as the activation function in all neurons in the hidden layer as well as in the output layer. The error signal at the output of the mth neuron in the output layer $l = 2$ is defined as

$$e(r)_m^{(l)} = o_m^{(l)} - y(r)_m^{(l)}. \tag{11.18}$$

For a total number of M neurons in the output layer, the Mean Squared Error (MSE) in the network output when training in sequential mode over S training data sets is then defined as

$$\text{MSE} = \frac{1}{2S}\sum_{m=1}^{M}\left[e(r)_m^{(L)}\right]^2. \tag{11.19}$$

During supervised learning, the MSE, which is also called the training error (TE), is used as the stopping criteria over the number of epochs (number of learning steps) when training is performed. Additional quantifications of network performance are given by the MSE during testing, which is also called the generalization error (GE), and the total error is given by

$$\text{total error} = \frac{S \times \text{TE} + \text{S}' \times \text{GE}}{(S + S')}, \tag{11.20}$$

where S' is the number of test data sets.

11.2.4.2 Error Back Propagation

The error in the output signal from the neuron in the output layer (given in Eq. 11.18) is back propagated using a gradient descent algorithm, where the local gradient is computed as

$$\delta(r)_m^{(l)} = \begin{cases} (e(r)_m)^{(L)} \phi_m{}^{(L)'} & \text{for neuron } m \text{ in output layer } L \\ \phi_m^{(l)'} \sum_n \delta(r)_n^{(l+1)} w(r)_{nm}^{(l+1)} & \text{for neuron } m \text{ in hidden layer } l, \end{cases} \tag{11.21}$$

where $\phi(r)_m^{(l)'}$ denotes differentiation with respect to the function argument defined in Eqs. 11.16 and 11.17. In the next epoch $r+1$, the synaptic weightsconnecting layer l to layer $l+1$ are updated according to the generalized delta rule [8] as

$$w(r+1)_{mn}^{(l)} = w(r)_{mn}^{(l)} + \Delta w(r)_{mn}^{(l)}, \tag{11.22}$$

$$\Delta w(r)_{mn}^{(l)} = \beta^{(l)} \Delta w(r-1)_{mn}^{l} + \eta^{(l)} \delta(r)_m^{(l)} y(r)_m^{(l-1)}, \tag{11.23}$$

where $\eta^{(l)}$ is the learning rate parameter and $\beta^{(l)}$ is the momentum constant for the neurons in layer l.

For optimal performance of the network, especially in the present problem where the amount of input spectral data is voluminous and highly non-smooth, it is important to choose the learning rate parameters for each of the layers carefully. After observation of the numerical performance of the network over a small number of training data sets as a trial, the learning rate parameters for the neurons in the hidden layer and output layer were fixed at $\eta^{(1)} = 0.03$ and $\eta^{(2)} = 0.03$. Without using any momentum constant ($\beta^{(l)} = 0$) for additional stability, good convergence of the MSE has been achieved along with closely matching damage parameters. The numerical results are presented in the following section.

11.2.5 Numerical Results and Discussion

The case study performed here is with the spectrum of the transverse displacement $\hat{\mathbf{w}}(\omega_n)$ at the tip of the 0.8 m long graphite–epoxy cantilever beam with single damage configuration subjected to the broadband pulse (Fig. 3.7) applied in transverse direction at the tip. From SFE computation, spectral data having 512 sampling points up to the Nyquist frequency are taken directly into the neural network training and testing. Sampling is done at $\Delta\omega = 97.66$ Hz. No frequency scaling or dimensionality reduction is made when the data are taken for normalization. Sets of damage parameters used during generation of input data sets for training and testing are taken as combination of two different sets S_1 and S_2, where

Table 11.3 Error-level in the network output after 600 epochs

	L_1	L_2	α_{11}
$(\text{TE})^{1/2}$	0.0095	0.0304	0.0115
$(\text{GE})^{1/2}$	0.0224	0.0265	0.0632
$(\text{Total error})^{1/2}$	0.0141	0.0100	0.0332
Maximum error	0.0412	0.0632	0.1749

$$
\begin{aligned}
S_1: \quad & L_1 \in [0.1\,\text{m}, 0.6\,\text{m}] \text{ in steps of } 0.1\,\text{m} \\
& L_2 \in [0.01\,\text{m}, 0.21\,\text{m}] \text{ in steps of } 0.05\,\text{m} \\
& \alpha_{11} \in [0.1, 0.9] \text{ in steps of } 0.2 \\
S_2: \quad & L_1 \in [0.2\,\text{m}, 0.45\,\text{m}] \text{ in steps of } 0.05\,\text{m} \\
& L_2 \in [0.01\,\text{m}, 0.26\,\text{m}] \text{ in steps of } 0.05\,\text{m} \\
& \alpha_{11} \in [0.1, 0.85] \text{ in steps of } 0.15
\end{aligned}
$$

The total number of training data sets is 316 and the total number of test data sets is 20 (randomly selected from S_1). Table 11.3 shows the error-level in the network output after 600 epochs. It can be seen that the error in α_{11} is highest. Although one can proceed with training the network further to obtain optimal network parameters, the network performance at the end of 600 epochs shows acceptable accuracy in estimating the damage parameters. The accuracy of these results is discussed next. Figure 11.16a, b show the nature of neural estimation compared to the actual values of L_1 during training and testing respectively. Similar comparisons for L_2 and α are shown in Figs. 11.17a, b and 11.18a, b respectively. It can be seen from these figures that L_1 is estimated most accurately, except for test sample number 18. Corresponding actual damage parameters are $L_1 = 0.3\,\text{m}, L_2 = 0.15\,\text{m}$ and $\alpha_{11} = 0.3$. Interestingly, $L_2 = 0.15$ m represents, comparatively, a large-size damage. However, the $L_1 = 0.3$ m i.e., the first interface where the waves are scattered, is sufficiently far away, hence is expected to transmit less energy through the first interface into the damaged zone. The corresponding $\alpha_{11} = 0.3$ indicates very high degradation in stiffness, so that it is obvious that only a very small amount of energy is left to scatter back from the second interface (with L_2 information) and arrive at the measurement location (cantilever tip). This is why L_2 is predicted with maximum deviation from the actual for test sample number 18. Subsequently, α_{11} is also predicted for this sample with maximum error (see Table 11.3). Table 11.3 also indicates small training and testing errors, which shows the generalization capability of the network. However, the overall estimate of the damage parameters is made with acceptable accuracy.

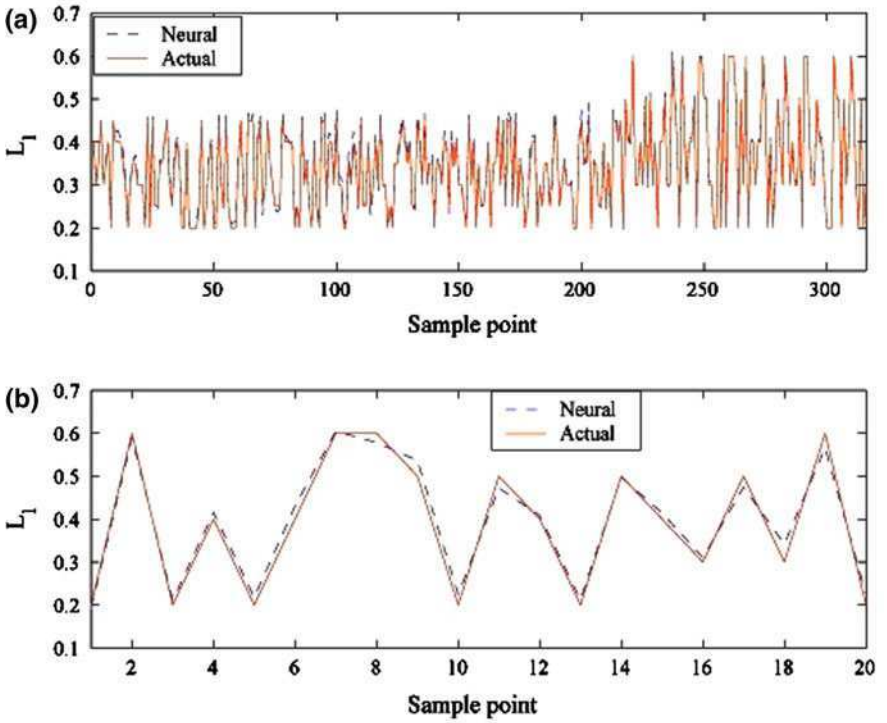

Fig. 11.16 Actual and estimated values of damage location L_1 during **a** training and **b** testing at the end of 600 epochs

11.2.5.1 Effect of Noise

Noise is inherent to any spectral estimation from on-line sensor signals, especially in SHM based on acoustic wave excitation. This is because of (1) features due to manufacturing defects in the structure, (2) ambient environment and interference in the sensor hardware, (3) limitations on the transducer bandwidth, and (4) other unknown sources of scattered waves which are unaccounted for in the case of finite element model-based training of the neural network. Therefore, it is important to study the effect of different levels of noise on the network, which has already been trained. To numerically simulate such a situation, random noise is added to some of the test data sets. This is done by adding noise to the amplitude and phase of the spectra separately. Only those data sets are selected for which the addition of noise does not exceed the normalization range $[-0.8, 0.8]$ for which that network has already been trained.

Figures 11.19, 11.20 and 11.21 show the percentage deviation of the estimated L_1, L_2 and α_{11} with respect to the actual values in the presence of a noise-to-signal ratio up to 10%. In these figures, the results are shown for three different sets A, B and C of damage parameters. These three sets correspond to test sample numbers

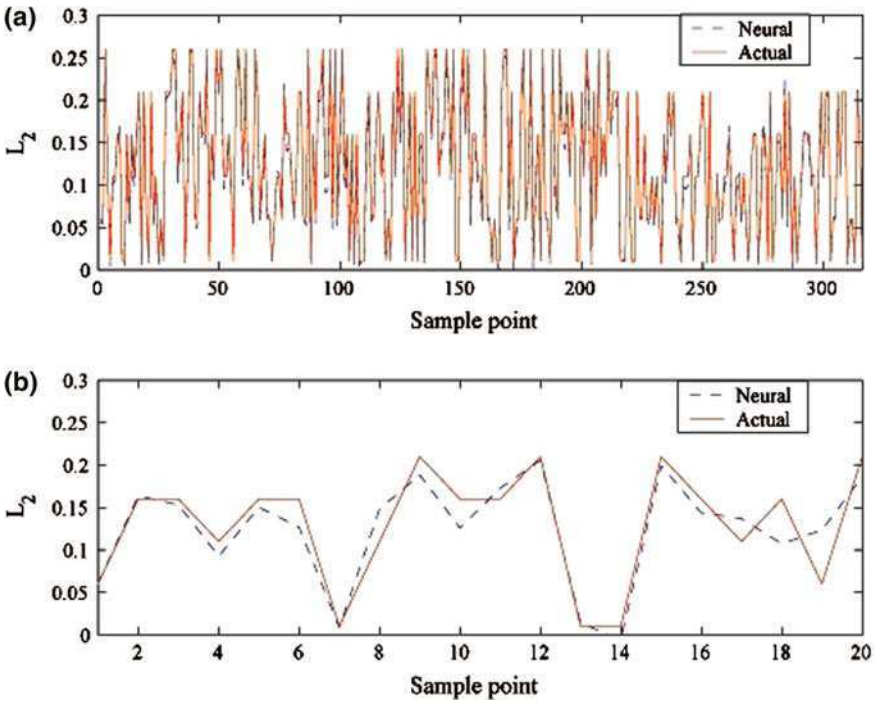

Fig. 11.17 Actual and estimated values of damage size L_2 during **a** training and **b** testing at the end of 600 epochs

4, 6 and 8 (see Figs. 11.16, 11.17, 11.18). It can be seen from Fig. 11.20 that L_2 is highly sensitive to noise, whereas Fig. 11.21 shows that α_{11} is less sensitive to noise until high noise-to-signal levels are present. It can also be noted from Figs. 11.18 and 11.21 that α_{11} of Set B (test sample number 6) is estimated accurately and so also is L_1 of Set B (as seen from Figs. 11.16, 11.19). On the other hand, since the estimation of L_2 of Set B is less accurate in the absence of noise (see Fig. 11.17), it is further affected leading to a higher sensitivity to noise.

11.3 Summary

In this chapter, the use of soft computing tool such as GA and ANN for damage detection under spectral FE environment is demonstrated. Both these approaches needs a number of measured experimental responses, which in this chapter were generated using the simplified spectral element damaged models described in Chap. 6. The chapter first gave a overall GA procedure and its implementation under spectral FE environment for damage detection. Various objective functions and their merits and demerits for damage detection is discussed in detail.

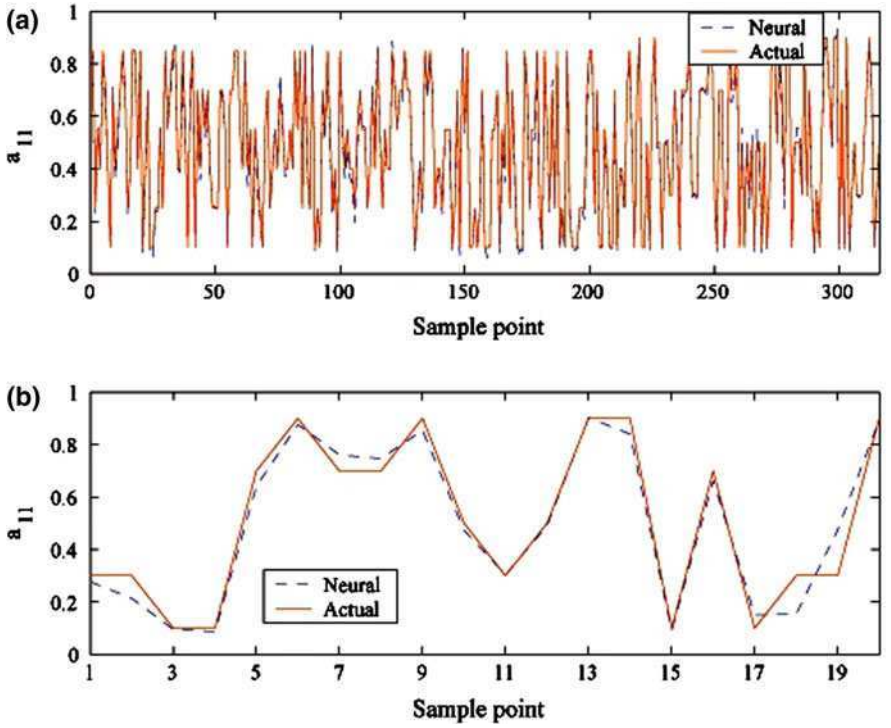

Fig. 11.18 Actual and estimated values of stiffness degradation factor α_{11} during **a** training and **b** testing at the end of 600 epochs

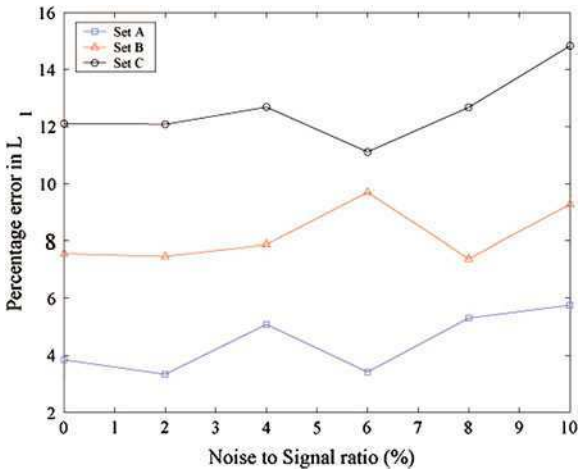

Fig. 11.19 Percentage deviation of estimated L_1 compared to the actuals when using a noisy input to the neural network during testing

A number of examples involving detection of location, size and depth is given to demonstrate the efficiency of GA under SFEM. In the next part of the chapter, the procedure to detect damage using ANN is discussed. This part began with the

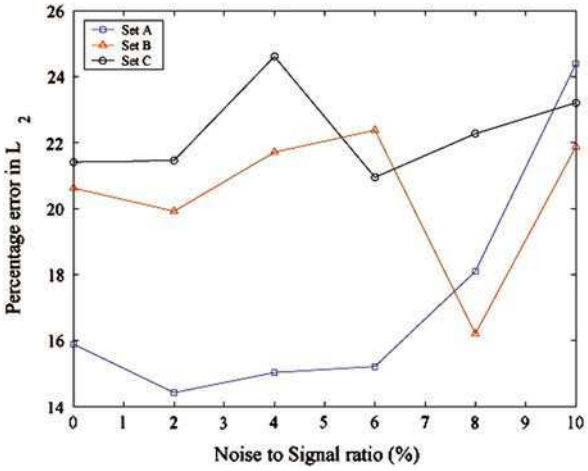

Fig. 11.20 Percentage deviation of estimated L_2 compared to the actuals when using a noisy input to the neural network during testing

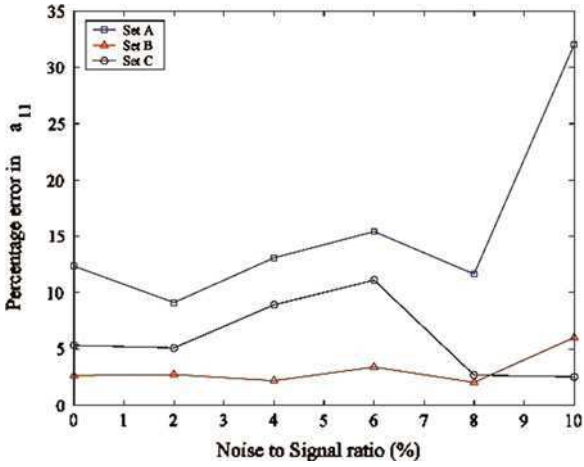

Fig. 11.21 Percentage deviation of estimated α_{11} compared to the actuals while using noisy input to the neural network during testing

definition and components of a neural network. In particular, the choice of weight functions, their merits and demerits in the context of damage detection is discussed. Next, the implementation of this technique under SFEM is given, which includes the complete network design. The efficiency of the designed network to detect the degraded zones in a composite beam is demonstrated. This study includes the detection studies using noise polluted responses. These studies shows that the time taken for identifying many damage parameters by both GA and ANN approaches is quite small compared to other optimization based techniques.

References

1. Alander JT (1999) Population size, building blocks, fitness landscape and genetic algorithm search efficiency in combinatorial optimization: an empirical study. In: Chambers LD (eds) Practical handbook of genetic algorithms: complex coding systems, Chapter 13. CRC Press, New york
2. Gao F, Shen Y, Li L (2000) The optimal design of piezoelectric actuator for plate vibroacoustic control using genetic algorithms with immune diversity. Smart Mater Struct 9:485–491
3. Gen M, Cheng R (1997) Genetic algorithms and engineering design. Wiley, New York
4. Goldberg DE (1989) Genetic algorithm in search, optimization, and machine learning. Addison-Wesley Publishing Company, Inc., Reading
5. Haykins S (2001) Neural networks: a comprehensive review. Pearson Educational Asia, Singapore (reprint)
6. Langley RS (1990) Analysis of power flow in beams and frameworks using the direct dynamic stiffness method. J Sound Vib 136(3):439–452
7. Roy Mahapatra D (2003) Development of spectral finite element models for wave propagation studies, health monitoring and active control of waves in laminated composite structures. PhD Thesis, Indian Institute of Science, Bangalore, India
8. Rumelhart DE, Hinton GE, Williams RJ (1986) Learning representations of back-propagation errors. Nature 323:533–536
9. Srinivas N, Deb K (1993) Multiobjective optimization using non-dominated sorting in genetic algorithm. Technical Report, Department of Mechanical Engineering, Indian Institute of Technology-Kanpur, India
10. Xu YG, Liu GR, Wum ZP, Huang XM (2001) Adaptive multilayer perceptron network for detection of cracks in anisotropic laminated plates. Int J Solids Struct 38:5625–5645

Index

S. Gopalakrishnan et al., *Computational Techniques for Structural Health Monitoring*, Springer Series in Reliability Engineering, DOI: 10.1007/978-0-85729-284-1,